JAERI-Conf
98-003

INDC(JPN)-180/U

PROCEEDINGS OF THE 1997 SYMPOSIUM ON NUCLEAR DATA
NOVEMBER 27-28, 1997, JAERI, TOKAI, JAPAN

March 1998

(Eds.) Tadashi YOSHIDA* and Tokio FUKAHORI

日本原子力研究所
Japan Atomic Energy Research Institute

本レポートは，日本原子力研究所が不定期に公刊している研究報告書です。
入手の問合わせは，日本原子力研究所研究情報部研究情報課（〒319-1195　茨城県那珂郡東海村）あて，お申し越しください。なお，このほかに財団法人原子力弘済会資料センター（〒319-1195　茨城県那珂郡東海村日本原子力研究所内）で複写による実費頒布をおこなっております。

This report is issued irregularly.
Inquiries about availability of the reports should be addressed to Research Information Division, Department of Intellectual Resources, Japan Atomic Energy Research Institute, Tokai-mura, Naka-gun, Ibaraki-ken, 319-1195, Japan.

© Japan Atomic Energy Research Institute, 1998

編集兼発行　日本原子力研究所
印　　刷　いばらき印刷㈱

JAERI-Conf 98-003 INDC(JPN)-180/U

Proceedings of the 1997 Symposium on Nuclear Data
November 27-28, 1997, JAERI, Tokai, Japan

(Eds.) Tadashi YOSHIDA* and Tokio FUKAHORI

Japanese Nuclear Data Committee
Tokai Research Establishment
Japan Atomic Energy Research Institute
Tokai-mura, Naka-gun, Ibaraki-ken

(Received February 3, 1998)

The 1997 Symposium on Nuclear Data was held at Tokai Research Establishment, Japan Atomic Energy Research Institute (JAERI), on 27th and 28th of November 1997. Japanese Nuclear Data Committee and Nuclear Data Center, JAERI organized this symposium. In the oral sessions, presented were 18 papers on nuclear fuel cycle and nuclear data, status of JENDL, international collaboration, applying JENDL-3.2 to fission reactors, delayed neutron, new experimental facilities and nuclear data needs, and some topics. In the poster session, presented were 40 papers concerning experiments, evaluations, benchmark tests and on-line database on nuclear data. Those presented papers are compiled in this proceedings.

Keywords: Nuclear Data, Symposium, Proceedings, Nuclear Reaction, JENDL, Experiment, Evaluation, Benchmark Test, Cross Section.

*Musashi Institute of Technology

1997年核データ研究会報文集
1997年11月27日～28日，東海研究所，東海村

日本原子力研究所東海研究所
シグマ研究委員会
（編）吉田　正*・深堀　智生

(1998年2月3日受理)

1997年核データ研究会が，1997年11月27日と28日の両日，日本原子力研究所東海研究所において開催された。この研究会は，日本原子力研究所のシグマ研究委員会と核データセンターが主催して開いたものである。口頭発表では、核燃料サイクルと核データ、JENDLの進捗、核データの国際動向、核分裂炉への応用、新しい実験施設と核データへのニーズ、トピックスについての18件の報告があった。ポスター発表では、40件の発表があり、それらは、核データの測定、評価や評価済核データのベンチマークテスト、オンラインデータベース等に関するものであった。本報文集は、それらの論文をまとめたものである。

東海研究所：〒319-1195 茨城県那珂郡東海村白方白根2-4
* 武蔵工業大学

Program Committee

Tadashi YOSHIDA(Chairman)	Musashi Institute of Technology
Tokio FUKAHORI	Japan Atomic Energy Research Institute
Kazuki HIDA	Toshiba, Co.
Hideo HIRAYAMA	High Energy Accelerator Research Organization
Makoto ISHIKAWA	Power Reactor and Nuclear Fuel Development, Co.
Osamu IWAMOTO	Japan Atomic Energy Research Institute
Jun-ichi KATAKURA	Japan Atomic Energy Research Institute
Ken NAKAJIMA	Japan Atomic Energy Research Institute
Yutaka NAKAJIMA	Research Organization for Information Science and Technology
Etsuro SAJI	Toden Software Inc.
Hiroshi TAKADA	Japan Atomic Energy Research Institute
Teiko TAKADA	Japan Atomic Energy Research Institute
Yoshitomo UWAMINO	The Institute of Physical and Chemical Research
Takashi WATANABE	Kawasaki Heavy Industries, Co. Ltd.

プログラム委員会

吉田　正（委員長）	武蔵工業大学
深堀　智生	日本原子力研究所
肥田　和毅	（株）東芝
平山　英夫	高エネルギー加速器研究機構
石川　真	動力炉・核燃料開発事業団
岩本　修	日本原子力研究所
片倉　純一	日本原子力研究所
中島　健	日本原子力研究所
中島　豊	（財）高度情報科学技術研究機構
佐治　悦郎	東電ソフトウェア（株）
高田　弘	日本原子力研究所
高田　禎子	日本原子力研究所
上蓑　義明	理化学研究所
渡部　隆	川崎重工業（株）

This is a blank page.

Contents

1. Introduction 1

2. Paper Presented at Oral Session 7
2.1 Fuel Cycle and Nuclear Data 9
2.1.1 Development of Libraries for ORIGEN2 Code Based on JENDL-3.2. 9
K. Suyama, J. Katakura, M. Ishikawa and Y. Ohkawachi
2.1.2 Status of Criticality Safety Research at NUCEF 15
K. Nakajima
2.1.3 Neutron Intensity of Fast Reactor Spent Fuel 21
M. Takamatsu and T. Aoyama
2.2 Status of JENDL 27
2.2.1 Current Status of JENDL-3.3. 27
A. Hasegawa
2.3 International Trends of Nuclear Data 37
2.3.1 Nuclear Data and Reactor Physics Activities in Indonesia. 37
Liem Peng Hong
2.3.2 Status of Nuclear Data Activities in Korea. 49
Young-Ouk Lee and Jonghwa Chang
2.3.3 Progress of International Evaluation Cooperation. 55
K. Shibata
2.3.4 Results from ISTC Frame Work 60
T. Fukahori
2.4 Fission Reactor Application 67
2.4.1 Nuclear Characteristics of Pu Fueled LWR and Cross Section Sensitivities 67
T. Takeda
2.4.2 Analysis of Reactivity Characteristics of the MONJU Initial Core Using JENDL-3.2 73
K. Sasaki, T. Suzuki, N. Suzuki and Y. Itagaki
2.4.3 Uncertainty of Doppler Reactivity Worth due to Uncertainties of JENDL-3.2 Resonance Parameters 79
A. Zukeran, H. Hanaki, T. Nakagawa, K. Shibata and M. Ishikawa
2.5 Topics 93
2.5.1 Present Status of Research on Optical Potential for Neutron 93
M. Matoba
2.5.2 Evaluation Method of Nuclear Data: Half-Lives, Gamma-Ray Intensities etc 95
Y. Yoshizawa, O. Miyatake and M. Toyama
2.5.3 Energy Distribution of Projectile Fragment Particles in Heavy Ion Therapeutic Beam 101
N. Matsufuji, H. Tomura, Y. Futami, H. Yamashita, A. Fukumura, T. Kanai, A. Higashi, T. Akagi, H. Komami and T. Kohno
2.6 New Facilities and Nuclear Data Needs 107
2.6.1 Present Status and Future Plan of Neutron Experiments by using TIARA 107
M. Baba
2.6.2 Neutron Science Project at JAERI 113
Y. Oyama
2.6.3 Japan Hadron Facility 119
T. Shibata
2.6.4 Nuclear Data for Designing the IFMIF Accelerator 124
M. Sugimoto

3. Papers Presented at Poster Session 131
3.1 Critical Experiments Analyses by Using 70 Energy Group Library Based on ENDF-B/VI 133
Y. Tahara, H. Matsumoto, H.C. Huria and M. Ouisloumen
3.2 Measurement of Neutron Inelastic Scattering Cross Section of ^{238}U 139
T. Miura, M. Baba, M. Ibaraki, T. Sanami, Than Win, Y. Hirasawa, S. Matsuyama and N. Hirakawa

3.3 Accuracy of Helium Accumulation Fluence Monitor for Fast Reactor Dosimetry 144
C. Ito and T. Aoyama
3.4 Recommended Evaluation Procedure for Photonuclear Cross Section 150
Young-Ouk Lee, Jonghwa Chang and T. Fukahori
3.5 Systematics in Delayed Neutron Yields 156
T. Ohsawa
3.6 Decay Heat Measurement on Fusion Reactor Materials and Validation of Calculation Code System 162
F. Maekawa, Y. Ikeda and M. Wada
3.7 Benchmark Experiment on Vanadium Assembly with D-T Neutrons -In-situ Measurement- 168
F. Maekawa, Y. Kasugai, C. Konno, M. Wada, Y. Oyama, Y. Ikeda I. Murata, Kokooo and A. Takahashi
3.8 Benchmark Validation by means of Pulsed Sphere Experiment at OKTAVIAN 174
C. Ichihara, Shu A. Hayashi, I. Kimura, J. Yamamoto and A. Takahashi
3.9 Helium Production Cross Section Measurement of Pb and Sn for 14.9 MeV Neutrons 180
Y. Takao, T. Fujimoto, S. Ozaki, M. Muramasu, H. Nakashima, Y. Kanda and Y. Ikeda
3.10 Apparatus to Measure Low Level Helium for Neutron Dosimetry 186
S. Ozaki, Y. Takao, M. Muramasu, T. Hida, H. Sou, H. Nakashima and Y. Kanda
3.11 (n,α) Cross Section Measurement of Light Nuclei using Gridded Ionization Chamber and Gaseous Sample 192
T. Sanami, M. Baba, K. Saito, Y. Ibara, T. Yamazaki, J. Sato and N. Hirakawa
3.12 Some Remarks on Multigroup Library 198
C. Konno, F. Maekawa and M. Wada
3.13 Benchmark Experiment on Vanadium Assembly with D-T Neutrons -Leakage Neutron Spectrum Measurement- 204
Kokooo, I. Murata, D. Nakano, A. Takahashi, F. Maekawa and Y. Ikeda
3.14 Measurement of Reaction Cross Sections of Fission Products Induced by DT Neutrons 210
D. Nakano, I. Murata and A. Takahashi
3.15 Resonance Analysis of the ^{12}C, $^{13}C(\alpha,n)$ Reactions and Evaluation of Neutron Yield Data of the Reaction 215
T. Murata
3.16 Measurements of Neutron Cross Section of the $^{243}Am(n,\gamma)^{244}Am$ Reaction 221
Y. Hatsukawa, N. Shinohara and K. Hata
3.17 Fission Cross Section Measurement of Am-242m using Lead Slowing-down Spectrometer 225
T. Kai, K. Kobayashi, S. Yamamoto, Y. Fujita, I. Kimura, Y. Ohkawachi and T. Wakabayashi
3.18 Measurements of Fast Neutron-Induced Fission Data of Np-237 231
Than Win, K. Saito, M. Baba, T. Iwasaki, M. Ibaraki, T. Miura, T. Sanami, Y. Nauchi and N. Hirakawa
3.19 Measurement of the Effective Thermal Cross Section of ^{134}Cs by Triple Neutron Capture Reaction 237
S. Nakamura, H. Harada, T. Katoh, Y. Hatsukawa, N. Shinohara, K. Hata, K. Kobayashi, S. Motoishi and M. Tanase
3.20 Measurement of MA Fission Cross Sections at YAYOI 242
Y. Ohkawachi, S. Ohki and T. Wakabayashi
3.21 Multiplicity and Energy of Neutrons from $^{233}U(n_{th},f)$ Fission Fragments 247
K. Nishio, I. Kimura and Y. Nakagome
3.22 Measurements of Gamma Rays from keV-Neutron Resonance Capture by Odd-Z Nuclei in the 2s-1d Shell Region 253
M. Igashira, Sam Yol Lee, S. Mizuno, J. Hori and H. Kitazawa
3.23 Direct Capture of Low-Energy Neutrons by ^{16}O 259
H. Kitazawa and M. Igashira
3.24 Measurements of Effective Total Macroscopic Cross Sections and Effective Energy of Continuum Beam 264
H. Kobayashi

3.25 Measurements of (n,xp), (n,xd) Double Differential Cross Sections of Al and C for Neutrons at 75 and 65 MeV 270
Y. Nauchi, M. Baba, T. Iwasaki, T. Sanami, T. Tabei, T. Suzuki, M. Ibaraki, S. Tanaka, H. Nakashima, S. Meigo, H. Takada, N. Nakao, T. Nakamura, Y. Watanabe, M. Harada, T. Nunomiya and N. Hirakawa

3.26 Study of the p+^{12}C Reaction at Energies up to 30MeV 276
M. Harada, A. Yamamoto, S. Yoshioka, K. Sato, T. Nakashima, H. Ijiri, Y. Watanabe, H. Yoshida, Y. Uozumi, S. Chiba, T. Fukahori, S. Meigo and O. Iwamoto

3.27 Improvements on Semi-Classical Distorted-Wave Model 282
Sun Weili, Y. Watanabe, R. Kuwata, M. Kohno, K. Ogata and M. Kawai

3.28 Neutron and Gamma-ray Emission Double Differential Cross Sections for the Nuclear Reaction by 1.5 GeV π^+ Incidence 288
K. Iga, K. Ishibashi, N. Shigyo, N. Matsufuji, T. Nakamoto, K. Maehata, M. Numajiri, S. Meigo, H. Takada, S. Chiba, T. Nakamura and Y. Watanabe

3.29 Calculations for Nuclear Data Evaluation for Nb, Zr and W in the High Energy Region 294
H. Kitsuki, S. Maruyama and K. Ishibashi

3.30 Measurement of Continuum Spectrum from ^{12}C (p,p'x) at Energy of 392 MeV 299
H. Yoshida, D. Konishi, Y. Uozumi, G. Wakabayashi, T. Sakae, M. Matoba, A. Nohtomi, T. Maki and N. Koori

3.31 Proton Induced Nuclide Production Cross Section by HETC-3STEP/FRG-R 303
N. Shigyo, K. Ishibashi, N. Yoshizawa and H. Takada

3.32 Development of Twin Ge Detector for High Energy Photon Measurement and Its Performance 307
Y. Shigetome and H. Harada

3.33 Development of the Multistep Compound Process Calculation Code 312
T. Kawano

3.34 Measurement of Cross Sections Producing Short-lived Nuclei by 14 MeV Neutron -Cd, Sn, Te, Nd, Gd, Re- 318
H. Sakane, T, Iida, A. Takahashi, H. Yamamoto and K. Kawade

3.35 Intercomparison of Delayed Neutron Summation Calculations among JEF2.2, ENDF/B-VI and JNDC-V2 322
M. Sagisaka, K. Oyamatsu and Y. Kukita

3.36 Easy-to-use Application Programs for Decay Heat and Delayed Neutron Calculations on Personal Computers 328
K. Oyamatsu

3.37 Consistency among Integral Measurements of Aggregate Decay Heat Power 334
H. Takeuchi, M. Sagisaka, K. Oyamatsu and Y. Kukita

3.38 Quantum Recurrence and Integer Ratios in Neutron Resonances 340
M. Ohkubo

3.39 A Database for Transmutation of Nuclear Materials on Internet 346
M. Fujita, M. Utsumi and T. Noda

3.40 Systematics of Nuclear Mass and Level Density Formulas 352
H. Nakamura

APPENDIX : Participants List 358

目　次

1. はじめに 1

2. 口頭発表論文 7
2.1 核燃料サイクルと核データ 9
2.1.1 JENDL-3.2 に基づく ORIGEN2 用ライブラリの作成 9
須山賢也、片倉純一、石川　眞、大川内靖
2.1.2 NUCEF における臨界安全性研究の現状 15
中島　健
2.1.3 使用済高速炉燃料の中性子放出率 21
高松　操、青山卓史
2.2 JENDL の進捗 27
2.2.1 JENDL-3.3 の進捗 27
長谷川明
2.3 核データの国際動向 37
2.3.1 インドネシアにおける核データ及び炉物理に関する研究活動 37
Liem Peng Hong
2.3.2 韓国における核データ活動 49
Young-Ouk Lee、Jonghwa Chang
2.3.3 評価国際協力活動(WPEC/WPMA)の進展 55
柴田恵一
2.3.4 ISTC からのこれまでの成果 60
深堀智生
2.4 核分裂炉への応用 67
2.4.1 プルトニウム燃料軽水炉特性と断面積感度 67
竹田敏一
2.4.2 JENDL-3.2 によるもんじゅ炉物理試験解析 73
佐々木研治、鈴木隆之、鈴木教倫、板垣善彦
2.4.3 JENDL-3.2 共鳴パラメータの不確かさによるドップラー反応度価値の不確かさ 79
瑞慶覧篤、花木　洋、中川庸雄、柴田恵一、石川　眞
2.5 ピックス 93
2.5.1 中性子光学ポテンシャル研究の現状 93
的場　優
2.5.2 半減期、ガンマ線強度等の核データの評価方法 95
吉沢康和、宮武　修、遠山正男
2.5.3 治療領域の重粒子線から生じる入射核フラグメントのエネルギー分布 101
松藤成弘、外村浩美、二見康之、山下晴男、福村明史、金井達明、
東　明男、赤城　卓、駒見英明、河野俊之
2.6 新しい実験施設と核データへのニーズ 107
2.6.1 TIARA を用いた中性子実験の現状と今後の計画 107
馬場　護
2.6.2 原研における中性子科学研究計画 113
大山幸夫
2.6.3 大型ハドロン計画 119
柴田徳思
2.6.4 IFMIF 設計のための核データ 124
杉本昌義

3. ポスター発表論文 131
3.1 ENDF/B-VI に基く 70 群断面積を用いた臨界実験解析 133

田原義壽、松本英樹、H.C. Huria、M. Ouisloumen
3.2 U-238 の中性子非弾性散乱断面積の測定 139
三浦孝子、馬場 護、茨木正信、佐波俊哉、Than Win、平沢善孝、松山成男、平川直弘
3.3 高速炉ドシメトリー用 He 蓄積型中性子フルエンスモニタの精度評価 144
伊藤主税、青山卓史
3.4 光核反応断面積評価手法の推奨 150
Young-Ouk Lee、Jonghwa Chang、深堀智生
3.5 遅発中性子収率の系統性 156
大澤孝明
3.6 核融合炉材料の崩壊熱測定と計算コードシステムの検証 162
前川藤夫、池田裕二郎、和田政行
3.7 D-T 中性子によるバナジウム体系ベンチマーク実験 －体系内測定－ 168
前川藤夫、春日井好巳、今野 力、和田政行、大山幸夫、池田裕二郎、村田 勲、Kokooo、高橋亮人
3.8 OKTAVIAN パルス球実験による核データベンチマーク 174
市原千博、林 脩平、木村逸郎、山本淳治、高橋亮人
3.9 鉛、錫の 14.9 MeV 中性子照射による He 生成断面積測定 180
鷹尾良行、藤本智弘、小崎修司、村益将友、中島秀紀、神田幸則、池田裕二郎
3.10 中性子線量測定のための低レベル He 測定装置の開発 186
小崎修司、鷹尾良行、村益将友、樋田知也、宗 裕文、中島秀紀、神田幸則
3.11 グリッド電離箱とガス状試料を用いた軽核の(n,α)断面積測定 192
佐波俊哉、馬場 護、斉藤佳一郎、井原康貴、山崎哲朗、佐藤 潤、平川直弘
3.12 多群ライブラリーに関する注意点 198
今野 力、前川藤夫、和田政行
3.13 D-T 中性子によるバナジウム体系ベンチマーク実験 －漏洩中性子スペクトル測定－ 204
Kokooo、村田 勲、中野大介、高橋亮人、前川藤夫、池田裕二郎
3.14 D-T 中性子による FP の反応断面積測定 210
中野大介、村田 勲、高橋亮人
3.15 ^{12}C, ^{13}C(α,n)反応の共鳴解析と中性子収率の評価 215
村田 徹
3.16 ^{243}Am(n,γ)^{244}Am 反応の中性子断面積の測定 221
初川雄一、篠原伸夫、畑健太郎
3.17 鉛スペクトロメータを用いた Am-242m の核分裂断面積測定 225
甲斐哲也、小林捷平、山本修二、藤田薫顕、木村逸郎、大川内靖、若林利男
3.18 ^{237}Np の高速中性子核分裂データの測定 231
Than Win、斉藤佳一郎、馬場 護、岩崎智彦、茨木正信、三浦孝子、佐波俊哉、名内泰志、平川直弘
3.19 三重中性子捕獲反応による ^{134}Cs の熱中性子実効断面積の測定 237
中村詔司、原田秀郎、加藤敏郎、初川雄一、篠原伸夫、畑健太郎、小林勝利、本石章司、棚瀬正和
3.20 弥生炉を用いた MA 核分裂断面積の測定 242
大川内靖、大木繁夫、若林利男
3.21 ^{233}U 熱中性子核分裂片から放出される中性子の多重度及びエネルギー 247
西尾勝久、木村逸郎、中込良廣
3.22 2s-1d 殻領域の奇 Z 核の keV 中性子共鳴捕獲ガンマ線の測定 253

井頭政之、李　三烈、水野　哲、堀　順一、北沢日出男
3.23 ^{16}O の低エネルギー中性子直接捕獲.....259
北沢日出男, 井頭政之
3.24 連続中性子ビームにおける実効的巨視的断面積と実効エネルギー測定.....264
小林久夫
3.25 75, 76 MeV 中性子に対する Al と C の(n,xp)、(n,xd)二重微分断面積の測定.....270
名内泰志、馬場　護、岩崎智彦、佐波俊哉、田部井高志、鈴木敬典、
茨木正信、田中　進、中島　宏、明午伸一郎、高田　弘、中尾徳晶、
中村尚司、渡辺幸信、原田正英、布宮智也、平川直弘
3.26 30MeV 以下の領域における p+^{12}C 反応の研究.....276
原田正英、山本晃央、吉岡　聡、佐藤一道、中嶋俊幸、井尻秀信、
渡辺幸信、吉田博喜、魚住祐介、千葉　敏、深堀智生、明午伸一郎、
岩本　修
3.27 半古典的歪曲波モデルの改良.....282
SUN Weili、渡辺幸信、桑田良作、河野通郎、緒方一介、河合光路
3.28 1.5GeV π^+入射による中性子及びγ線生成二重微分断面積.....288
伊賀公紀、石橋健二、執行信寛、松藤成弘、中本建志、前畑京介、
沼尻正晴、明午伸一郎、高田　弘、千葉　敏、中村尚司、渡辺幸信
3.29 高エネルギー領域における Nb, Zr, W についての核データ評価.....294
木附洋彦、丸山晋一、石橋健二
3.30 392 MeV における ^{12}C (p,p'x)反応からの連続スペクトルの測定.....299
吉田博喜、小西大輔、魚住裕介、若林源一郎、榮　武二、的場　優、
納冨昭弘、牧　孝、桑折範彦
3.31 HETC-3STEP/FRG-R による陽子入射核種生成断面積.....303
執行信寛、石橋健二、義澤宣明、高田　弘
3.32 高エネルギー光子測定用双子型 Ge 検出器の開発とその性能.....307
重留義明、原田秀郎
3.33 多段階複合核過程計算コードの開発.....312
河野俊彦
3.34 14MeV 中性子による短寿命核生成断面積の測定 -Cd, Sn, Te, Nd, Gd, Re-.....318
坂根　仁、飯田敏行、高橋亮人、山本　洋、河出　清
3.35 日米欧核データライブラリーを用いた遅発中性子総和計算の比較.....322
匂坂充行、親松和浩、久木田豊
3.35 パソコン上での崩壊熱及び遅発中性子に関する簡易アプリケーションソフト.....328
親松和浩
3.37 崩壊熱の積分測定間の整合性.....334
竹内弘樹、匂坂充行、親松和浩、久木田豊
3.38 中性子共鳴における量子回帰と整数比.....340
大久保牧夫
3.39 インターネット上の材料用核変換情報データベース.....346
藤田充苗、内海美砂子、野田哲二
3.40 原子核質量系統式と準位密度公式.....352
中村　久

付　録：　参加者リスト.....358

1. Introduction

The 1997 symposium on nuclear data was held at Tokai Research Establishment, Japan Atomic Energy Research Institute (JAERI), on 27th and 28th of November 1997. Japanese Nuclear Data Committee and Nuclear Data Center, JAERI organized the symposium.

The program of the symposium is listed below. In the topics session, three invited talks were addressed on present status of research on optical potential for neutron, evaluation method of nuclear data such as half life and gamma-ray strength function, and energy distribution of projectile fragmentation. As an international session, nuclear data research activities in Indonesia and Korea, present status of OECD/NEA/NSC Working Party on Evaluation Cooperation, and review of results from ISTC projects were presented. In the other sessions, total 12 papers were presented on delayed neutron, new experiments, JENDL special purpose file and high energy nuclear data. In the poster session, presented were 40 papers concerning nuclear data experiments, evaluations, benchmark tests and on-line database on nuclear data. Those papers are compiled in this proceedings.

Program

Oral Presentation [Talk + Discussion (min.)]

Nov. 27 (Thu.)

10:00 – 10:10

1. Opening Address — M. Nakagawa (JAERI)

10:10 – 12:00

2. Fuel Cycle and Nuclear Data — Chairman: M. Ishikawa (PNC)

2.1 Development of Libraries for ORIGEN2 Code Based on JENDL-3.2 [25+5] — K. Suyama (JAERI)

2.2 Status of Criticality Safety Research at NUCEF [30+10] — K. Nakajima (JAERI)

2.3 Neutron Intensity from Spent Fuel Subassembly of Fast Reactor [25+5] — M. Takamatsu (PNC)

12:00 – 13:00 LUNCH

13:00 – 13:30

3. Status of JENDL — Chairman: Y. Nakajima (RIST)
3.1 Status of Revision Work for JENDL-3.3 [20+5] — A. Hasegawa (JAERI)

13:30 – 15:30

4. International Trends of Nuclear Data — Chairman: A. Hasegawa (JAERI)
4.1 Nuclear Data and Reactor Physics Activities in Indonesia [30+5] — Liem Peng Hong(BATAN)
4.2 Status of Nuclear Data Activities at Korea [20+5] — Lee Young-Ouk (KAERI)
4.3 Present Status of NEAR/NSC/WPEC and WPMA [20+5] — K. Shibata (JAERI)
4.4 Results from ISTC Frame Work [20+5] — T. Fukahori (JAERI)

15:30 – 15:50 COFFEE BREAK

15:50 – 17:50

5. Fission Reactor Application — Chairman: E. Saji (TSI)
5.1 Cross Section Sensitivity Analysis of Burn-up Characteristics of Pu-Thermal Reactors [25+5] — T. Takeda (Osaka Univ.)
5.2 Analysis of Reactivity Characteristics of the MONJU Initial Core using the JENDL-3.2 [30+10] — K. Sasaki (PNC)
5.3 Uncertainty of Dopplar Reactivity Worth due to Uncertainties of JENDL-3.2 [30+10] — A. Zukeran (Hitachi, Ltd.)

18:10 – 20:00 RECEPTION at Akogi-ga-ura Club

Nov. 28 (Fri.)

9:00 – 10:50

6. Topics — Chairman: T. Fukahori (JAERI)
6.1 Present Status of Research on Optical Potential for Neutron [30+10] — M. Matoba (Kyushu Univ.)
6.2 Evaluation Method of Nuclear Data such as Half Life and Gamma-ray Strength Function [25+5] — Y. Yoshizawa (Hiroshima Univ.)
6.3 Energy Distribution of Projectile Fragmentations in Heavy Ion Therapeutic Beam [25+5] — N. Matsufuji (NIRS)

10:50 – 12:00

7. Poster Session 1

12:00 – 13:00 LUNCH

13:00 – 14:00

8. Poster Session 2

14:00 – 16:10

9. New Facilities and Nuclear Data Needs Chairman: Y. Uwamino (RIKEN)

9.1 Present Status and Future Plan of Neutron Experiment by Using TIARA Facility [25+5] M. Baba (Tohoku Univ.)

9.2 JAERI Neutron Science Project [25+5] Y. Oyama (JAERI)

9.3 Japan Hadron Facility [25+5] T. Shibata (KEK)

9.4 Nuclear Data for Designing the IFMIF Accelerator [25+5] M. Sugimoto (JAERI)

16:10 – 16:25

10. Summary Talk M. Igashira (TIT)

Poster Session

Nov. 28 (Fri.) 10:50 – 12:00 and 13:00 – 14:00

P.1 Critical Experiment Analyses with 70 Energy Groups Cross Section Library Based on ENDF-B/VI H. Matsumoto and Y. Tahara (MHI)

P.2 Measurement of Inelastic Scattering Cross Section of U-238 T. Miura (Tohoku Univ.)

P.3 Accuracy of HAFM for Fast Reactor Dosimetry C. Ito (PNC)

P.4 Activities of WPEC SG10 and SG17 in WPEC on FP Nuclear Data M. Kawai (Toshiba)

P.5 Systematics in Delayed Neutron Yields T. Ohsawa (Kinki Univ.)

P.6 Decay Heat Measurement on Fusion Reactor Materials and Validation of Calculation Code System F. Maekawa (JAERI)

P.7 Benchmark Experiment on Vanadium Assembly with D-T Neutrons -In-situ Measurement- F. Mekawa (JAERI)

P.8 The Benchmark Study for Fusion Related Nuclear Data with Pulsed Sphere Experiment at OKTAVIAN C. Ichihara (Kyoto Univ.)

P.9 Helium Production Cross Section Measurement of Pb and Sn for 14 MeV Neutrons Y. Takao(Kyushu Univ.)

P.10 An Apparatus to Measure Very Low Level Helium for Neutron Dosimetry S. Ozaki (Kyushu Univ.)

P.11 (n, α) Cross Section Measurement of Light Nuclei using Gridded Ionization Chamber and Gaseous Sample T. Sanami (Tohoku Univ.)
P.12 Some Remarks on Multigroup Library C. Konno (JAERI)
P.13 Benchmark Experiment on Vanadium Assembly with D-T Neutrons -Leakage Neutron Spectrum Measurement- Kokooo (Osaka Univ.)
P.14 Measurement of Reaction Cross Sections of Fission Products Induced by D-T Neutrons D. Nakano(Osaka Univ.)
P.15 Resonance Analysis of the Li-7+ α Reaction and the Evaluation of the Neutron Yield by the Li-7(α ,n)B-10 Reaction T. Murata (AITEL)
P.16 Cross section of the Reaction Am-243(n,g)Am-244 Y. Hatsukawa (JAERI)
P.17 Fission Cross Section Measurement of Am-242m using Lead Slowing-down Spectrometer T. Kai(Kyoto Univ.)
P.18 Measurement of Fast Neutron Induced Fission Data of Np-237 Than Win(Tohoku Univ.)
P.19 Measurement of the Effective Cross Section of ^{134}Cs by the Triple Neutron Capture Reaction S. Nakamura (PNC)
P.20 Measurement of MA Fission Cross Sections at YAYOI Y. Ohkawachi (PNC)
P.21 Multiplicity and Energy of Neutrons from Fission Fragments for U-233(n_{th},f) K. Nishio (Kyoto Univ.)
P.22 Measurements of Gamma Rays from keV-Neutron Resonance Capture by Odd-Z Nuclei in the 2s-1d Shell Region M. Igashira (TIT)
P.23 Low-energy Neutron Direct Capture by O-16 H. Kitazawa (TIT)
P.24 Measurements of Effective Total Macroscopic Cross Section and Effective Energy of Continuum Neutron Beam H. Kobayashi (Rikkyou Univ.)
P.25 Measurements of (n,xp), (n,xd) Double Differential Cross Sections of Al and C for up to 75 MeV Neutrons Y. Nauchi (Tohoku Univ.)
P.26 Study of the p+^{12}C Reaction at Energies up to 30MeV M. Harada (Kyushu Univ.)
P.27 Improvements on Semi-Classical Distorted Wave Model Sun Weili (Kyushu Univ.)
P.28 Neutron and Gamma-ray Emission Double Differential Cross Sections for the Nuclear Reaction by 1.5 GeV π^+ Incidence K. Iga (Kyushu Univ.)
P.29 Nuclear Data Evaluation for Zr,Nb and W up to 1.5 GeV H. Kitsuki (Kyushu Univ.)
P.30 Measurement of Continuum Spectrum from C-12(p,p') Reaction at 392 MeV H. Yoshida (Kyushu Univ.)
P.31 Analysis on the Quasi-elastic Scattering Cross Sections of ^{4}He, ^{12}C at 1GeV M. Nishimura(Kyushu Univ.)
P.32 Development of Twin Ge Detector for High Energy Photon Measurement and Its Performance Y. Shigetome (PNC)
P.33 Development of the Multistep Compound Process Calculation Code T. Kawano (Kyushu Univ.)

P.34 Measurement of Cross Sections Producing Short-lived Nuclei by 14 MeV Neutron -Ge,Cd,Sn,Te,Nd,Re- H. Sakane (Nagoya Univ.)

P.35 Intercomparison of Delayed Neutron Summation Calculations among JEF-2.2, ENDF/B-VI and JNDC-V2 M. Sagisaka (Nagoya Univ.)

P.36 An Easy-to-use Application for Decay Heat Power and Delayed Neutron Calculation on Personal Computers K. Oyamatsu (Nagoya Univ.)

P.37 Consistency among Integral Measurements of Aggregate Decay Heat Power H. Takeuchi (Nagoya Univ.)

P.38 Quantum Recurrence and Integer Ratios in Neutron Resonances M. Ohkubo

P.39 Database of Transmutation for Materials on Internet M. Fujita (NRIM)

P.40 Nuclear Mass and Level Density Formula H. Nakamura (Fuji Electric)

This is a blank page.

2. Papers Presented at Oral Session

This is a blank page.

2.1 Fuel Cycle and Nuclear Data

2.1.1

Development of Libraries for ORIGEN2 Code Based on JENDL-3.2*

Kenya SUYAMA
Dept. of Fuel Cycle Safety Research, JAERI, Tokai-mura, Ibaraki-ken, 319-11, JAPAN
e-mail: kenya@cyclone.tokai.jaeri.go.jp

Jun-ichi KATAKURA
Nuclear Data Center, JAERI, Tokai-mura, Ibaraki-ken, 319-11, JAPAN
e-mail: katakura@cracker.tokai.jaeri.go.jp

Makoto ISHIKAWA
O-arai Engineering Center, PNC, O-arai-machi, Ibaraki-ken, JAPAN
e-mail:ishikawa@oec.pnc.go.jp

Yasushi OHKAWACHI
O-arai Engineering Center, PNC, O-arai-machi, Ibaraki-ken, JAPAN
e-mail: okawachi@oec.pnc.go.jp

The working Group of JNDC "Nuclide Generation Evaluation" has launched a project to make libraries for ORIGEN2 code based on the latest nuclear data library "JENDL-3.2" for current design of LWR and FBR fuels. Many of these libraries are under validation.

1. INTRODUCTION

ORIGEN2 code[1] is one of the most widely used burnup codes for many purposes, such as analysis of transmutation of radioactive waste, evaluation of the source of radiation, etc. The advantage of using ORIGEN2 is that it has a variety of data libraries for various reactor systems.

However, the libraries in ORIGEN2 have at least two problems. One is that the libraries are based on obsolete design of reactors and the other is to have used old nuclear data libraries such as ENDF/B-IV, ENDF/B-V, and LENDL for development, since ORIGEN2 code had been mainly developed from the end of 1960's to early 1980's. This means that ORIGEN2 code has no adequate library based on the latest nuclear data libraries for the current reactors.

To overcome these problems, JNDC launched the project to make libraries of ORIGEN2 code based on the current reactor design using JENDL-3.2[2]. The aim of making these libraries is to evaluate assembly averaged isotopic composition as correctly as possible.

This paper describes the background and method developing the new libraries of ORIGEN2 code based on JENDL-3.2.

2. OBJECTIVE

Four kinds of libraries are prepared in ORIGEN2 as shown in **Table 1**. "One-grouped cross

*This study uses the part of the work carried out by the Japan Atomic Energy Research Institute (JAERI) under the entrustment by the Science and Technology Agency (STA) of JAPAN.

section libraries" are data storage of one-grouped cross sections for various reactor systems. For FP and activation products, the one-grouped cross sections of (n, γ), (n,2n), (n,p) and (n, α) are contained in these libraries. Also, for actinides, those of (n, γ), (n,2n), (n,3n), (n,f) are preserved in them. "Subroutines of variable actinide cross section" are source programs written in FORTRAN for each reactor system. It contains the one-grouped cross sections depending on burnup. A user can take into account the effect of change of a neutron spectrum during burnup using one of these subroutines. "Libraries of decay and fission yield" are database of decay constants, branching ratios of radioactive decay, recoverable energy of decay, and direct fission yields, etc. "A photon spectrum library" has 18 grouped photon spectrum data for various radio active isotopes.

In this project, all of the data libraries are compiled for the current reactor systems based on JENDL-3.2 library except for the photon spectrum data library. The library of decay and fission yield, it is compiled from JNDC fission products library 2nd version (JNDCFPV2)[3].

Table 1 Libraries in ORIGEN2

Libraries	Make New Library
One-grouped Cross Section Libraries	YES
Subroutines of Variable Actinide Cross Section	YES
Decay and Fission Yield	YES
Photon Spectrum (18 groups)	NO

Target reactor specifications for LWR are shown in **Table 2**. The parameters are selected from the current design of each reactor system. **Table 3** indicates the parameters for FBR libraries. These are chosen by requests from analyst of fast reactor, since no fixed specification of FBR exists especially for a commercial reactor.

3. METHOD

To make libraries for LWR, we use single pin cell models that are equivalent to the target assembly. We should evaluate applicability of our single pin cell model comparing the results with these of explicit assembly model. This comparison shows that the differences between the models are small. Especially for BWR, though assembly of BWR has complicated enrichment and void ratio distribution, the maximum difference between the two models for 70 % void ratio of STEP-II assembly, which is considered to show the largest difference, is about 10% at 50 GWd/t. This result supports the validity of this single pin cell model.

For making LWR libraries, integrated burnup code system SWAT[4] is used. SWAT has an additional package "SWAT2ORI2" to make a subroutine for the variable actinide cross section.

To compile FBR libraries, new system is developed. This system is based on diffusion

calculation of whole core using JFS3-J3.2[5]. Libraries of blancket region are prepared as well as those of core regions.

Table 2 Parameters for LWR Libraries

	PWR	BWR		
Fuel Assembly	17×17 Assembly	STEP-I Assembly	STEP-II Assembly	STEP-III Assembly
U-235 Initial Enrichment	3.4, 4.1, 4.7	2.7	3.7	4.7
Maximum Burnup(GWd/t)	55	40	40	40
Void Ratio(%)	NODATA	40	0,40, 70	40
Identifiers of Libraries	PWR34J32[1] PWR41J32 PWR47J32	BS140J32[2]	BS200J32 BS240J32 BS270J32	BS340J32

1 - Library for PWR initial U-235 enrichment is 3.4 % based on JENDL-3.2

2 - Library for BWR STEP-I assembly, void ratio is 40 % based on JENDL-3.2

Table 3 Parameters for FBR Libraries

Type of Reactors	Fuel	Initial Pu Content
Small Experimental Reactor(JOYO)	MOX	LWR
Prototype Reactor (MONJU)	MOX	LWR
600 MW Demonstration Reactor	MOX	LWR
600 MW Demonstration Reactor	MOX	FBR
600 MW Demonstration Reactor	METAL	LWR
600 MW Demonstration Reactor	NITRIDE	LWR
1300 MW Commercaial Reactor	MOX	LWR
Pu Burner		

Figure 1 inditates a flowchart of compilation of the libraries. As this figure shows, 73 groups infinite diluted cross section library is compiled with CRECTJ5[6] using a standard neutron spectrum (70 groups) which was used for making JFS3-J3.2 and prompt fission neutron spectrum of Pu-239. Data in this 73 groups library is collapsed to infinite diluted one grouped data with 73 group neutron spectrum prepared from diffusion calculation with JFS3-J3.2 and the prompt fission neutron spectrum of Pu-239. Finally, the infinite diluted cross sections are substituted with

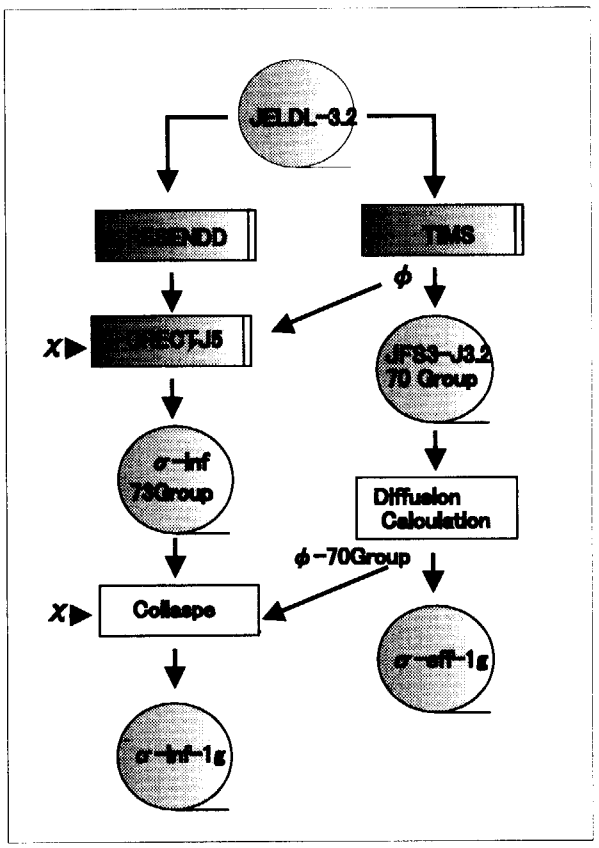

Figure 1 Flow of Compilation of Libraries for FBR

Table 4 Averaged Ratios of Calculation to Experiment(C/E) using several libraries for analysis of PIE of PWR.

	PWR-US	PWR-UE	PWR41J32
U-235	0.88	0.95	1.00
U-236	1.01	1.00	0.95
U-238	1.00	1.00	1.00
Pu-238	0.83	1.02	0.87
Pu-239	0.85	0.98	1.00
Pu-240	0.95	0.99	1.02
Pu-241	0.78	0.96	1.00
Pu-242	0.83	0.92	0.98
Am-241	0.85	1.07	1.12
Cm-244	0.66	0.92	0.82

the effective cross section data from diffusion calculation. This system will be distributed for users to make a new library for satisfying each user's purpose.

The fission yield and decay libraries are also compiled based on JNDCFPV2 for each LWR and FBR systems. The decay heat values calculated using these libraries have been recommended by the Atomic Energy Society of Japan for analysis of reactor decay heat. The direct fission yield for LWR is calculated based on the data in JNDCFPV2 considering the energy range of fission reaction evaluated by SWAT.

4. RESULTS

LWR Libraries

The examples of results using new library are shown in **Figure 2, 3, 4** and **5**, respectively for U-235, Pu-239, Pu-240 and Pu-241. In these figures, the results are compared with five PIE data for PWR 17×17 type assembly (Marks in the figures are PWR). The initial enrichment of U-235 of these samples is 4.1%. Averaged C/E values (ratio of calculated result to experimental result) of these five samples are indicated in **Table 4**. This table reveals improved results for U and Pu isotopes using our new library PWR41J32 except for Pu-238. The results of Am and Cm is also rather good. These figures and tables conclude that our libraries based on JENDL-3.2 are adequate for analysis of the current fuel.

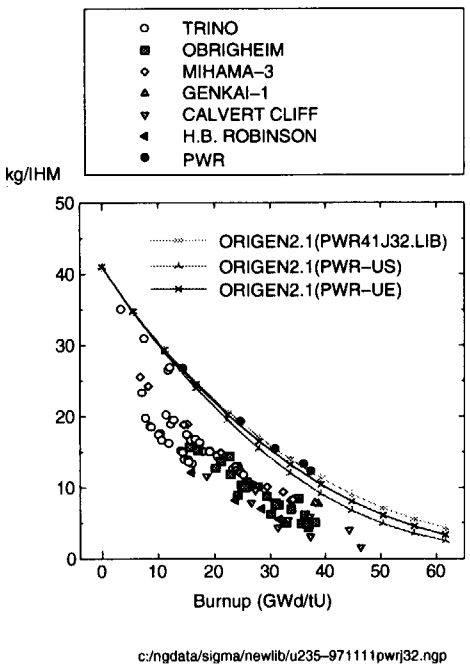

Figure 2 Comparison of Results of PIE and Calculations by ORIGEN2(U-235)

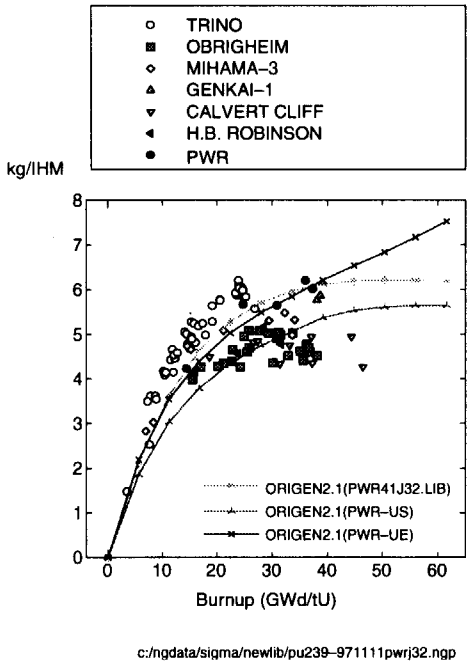

Figure 3 Comparison of Results of PIE and Calculations by ORIGEN2(Pu-239)

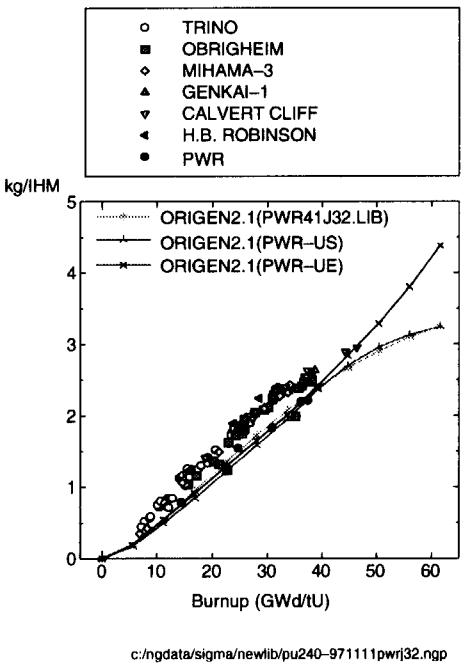

Figure 4 Comparison of Results of PIE and Calculations by ORIGEN2(Pu-240).

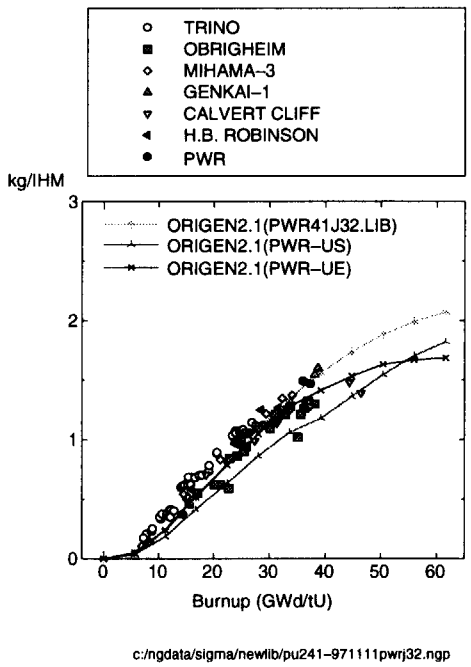

Figure 5 Comparison of Results of PIE and Calculations by ORIGEN2(Pu-241).

FBR Libraries

Since there is no disclosed PIE data, calculated amounts of generation or depletion of isotopes are compared between the old and new libraries. **Table 5** presents the comparison between them. Old Library is "LMFBR: Advanced oxide, LWR-Pu/U/U/U" in ORIGEN2. As this table shows, some isotopes have large difference of results.

Table 5 Comparison of Change of Weight(g) using Old and New Libraries for FBR.

	Old Lib.	New Lib.	N/O
U-235	1.15e+03	1.20e+03	1.05
U-238	6.99e+04	7.24e+04	1.04
Pu-238	2.09e+03	2.06e+03	0.99
Pu-239	2.60e+03	1.88e+03	0.72
Pu-240	-9.30e+02	-1.93e+03	2.08
Pu-241	9.80e+03	9.34e+03	0.95
Pu-242	4.20e+02	3.20e+02	0.76
Np-237	-3.25e+02	-2.09e+02	0.64
Am-241	-2.07e+03	-2.05e+03	0.99
Am-243	-1.23e+03	-1.45e+03	1.18
Cm-244	-1.53e+02	-3.12e+02	2.04

5. CONCLUSION

New libraries for ORIGEN2 were developed based on JENDL-3.2 using the latest core parameters. The objective reactors for LWR are PWR (17×17 fuel assembly) and BWR (step I, II or III assembly). The single pin cell model is employed as to be equivalent to the target assemblies. For PWR fuel, initial enrichment of U-235 (3.4, 4.1 and 4.7%) is taken as a parameter for the libraries. For BWR fuel, initial enrichment of U-235 (2.7, 3.7 and 4.7%) and axial void ratio (0, 40 and 70%) are taken as parameters. To make libraries for LWR, an integrated burnup code system SWAT is used.

For FBR libraries, several types of cores(JOYO, MONJU, 600 MW prototype and 1300 MW commercial) and fuels (MOX, metal or nitride) are parameters. Libraries for not only core but also blanket region are developed. For this case, the results of core calculations using JFS-3-J3.2 are compiled for making FBR libraries.

Current status of these libraries are under evaluation. After extensive tests, these libraries will be distributed to use in many fields of nuclear engineering.

6. Acknowledgments

Authors are deeply indebted to the members of Analytical Chemistry Laboratory of JAERI. They carried out PIE for PWR assembly.

7. REFERENCES

1. Croff, A.G.: *ORNL-5621*(1980).
2. Nakagawa,T. et al: *J. Nucl. Sci. Technol.*,**32**[12],1259(1995).
3.Tasaka,K. et al: *JAERI-1320(1990)*
4. Suyama,K. et al: *JAERI-Data/Code 97-047*, (1997)(in Japanese).
5. Takano,H. et al: *Private Communication*(1994)
6. Nakagawa, T.: *Private Communication*(1984).

2.1.2 Status of Criticality Safety Research at NUCEF

Ken NAKAJIMA
Criticality Safety Laboratory, Department of Fuel Cycle Safety Research
Japan Atomic Energy Research Institute
Tokai-mura, Naka-gun, Ibaraki 319-1195
e-mail: nakajima@melody.tokai.jaeri.go.jp

Two critical facilities, named STACY and TRACY, at the Nuclear Fuel Cycle Safety Engineering Research Facility (NUCEF) started their hot operations in 1995. Since then, basic experimental data for criticality safety research have been accumulated using STACY, and supercritical experiments for the study of criticality accident have been performed using TRACY.

In this paper, the outline of those critical facilities and the main results of TRACY experiments are presented.

1. Introduction

The Japan Atomic Energy Research Institute has built two critical facilities, STACY and TRACY in the Nuclear Fuel Cycle Safety Engineering Research Facility (NUCEF)[1,2] for the experimental research on criticality safety. STACY(Static Experiment Critical Facility) is operated to obtain basic criticality data on the solution fuel of low enriched uranium, plutonium and their mixture. In TRACY(Transient Experiment Critical Facility), a supercritical experiment is performed using the solution fuel of low enriched uranium to simulate the criticality accident in a reprocessing plant.

In this paper, the outline of STACY and TRACY and the main results of TRACY experiments are presented.

2. Critical facilities, STACY and TRACY

2.1 STACY[3-5]

STACY consists of the core tank containing fuel solution, solution transfer system, fuel storage system, solution adjusting system, and water reflector system. For the core tank, several sizes of cylindrical and slab tanks are used. The nitrate solution of low-enriched uranium, plutonium or their mixture is used as fuel solution. The fuel solution is fed from the storage tank to the core tank through a critical approach. The flow diagram of STACY is shown in Fig. 1. Reactivity is

controlled by adjusting the solution height in the core tank. The solution height in the core tank is measured using contact type height gauge with the accuracy of ±0.2 mm. Safety rods containing B_4C pellets are positioned at the upper part of the core tank, and are dropped by gravity for an emergency shutdown.

STACY achieved its first criticality on 23 February, 1995. After the first criticality, a series of experiment using 10wt% enriched uranyl nitrate aqueous solution with a cylindrical tank(60cm-diam.) and a slab tank(28cm-thick) has been performed. For the detailed description of STACY experiment, see references[3-5].

2.2 TRACY[6,7]

TRACY is a critical facility to conduct a supercritical experiment using low-enriched uranium solution. Major components of TRACY are an experimental assembly, a solution transfer system, a solution storage system, and an off-gas ventilation system as illustrated in Fig. 2. The experimental assembly consists of a core tank, a transient rod, three safety rods, and instruments. In Fig. 3, the configuration of experimental core is shown. The core tank has an annular shape with an outer and inner diameter of 50 and about 8 cm, respectively. The central hole in the core tank is used for positioning the transient rod, which controls the reactivity for supercritical experiments. The instruments for TRACY experiment are shown in Fig. 3.

The reactivity of TRACY is controlled by two methods. One method changes the solution level in the core tank by feeding or draining fuel solution. The other method moves the transient rod, which contains B_4C pellets, along the guide tube positioned at the center of the core tank. In the supercritical experiments, an excess reactivity of up to three dollars can be inserted into the core. For these experiments, TRACY is operated with one of the following operation modes.

a) Step withdrawal, b) Ramp withdrawal, and c) Ramp feed.

At the step withdrawal, the transient rod is withdrawn pneumatically in about 0.2 sec. At the ramp withdrawal, the reactivity is inserted by withdrawal of the transient rod using motor drive. At the ramp feed, the reactivity insertion is conducted by feeding fuel solution into the core tank. The major specifications of TRACY are listed in Table I.

The first criticality of TRACY was achieved on 20 December, 1995, and a series of supercritical experiment has been performed since June, 1996.

3. Main results of TRACY Experiment

3.1 Criticality measurements

The first critical approach experiment was performed using 9.97 wt% ^{235}U enriched uranyl nitrate aqueous solution fuel. The uranium concentration of the solution was 433.4 gU/*l* and the acid molarity was 0.89 N. The experiment started by feeding the solution to the core tank with the transient rod withdrawn. The measured critical height was 45.0 cm. The critical height, for the core

with the transient rod inserted, was also measured afterwards. The obtained height was 49.8 cm for the fuel of 432.3 gU/*l* with 0.87 N acid molarity. The effective neutron multiplication factors for the critical cores were calculated using the continuous energy Monte Carlo code MCNP-4A[8] with the JENDL-3.2 nuclear data library[9]. The results of calculations are shown in Table II. The multiplication factors of two critical cores show that the calculations overestimate the criticality by more than 1 %. This tendency of overestimation was observed for the STACY experiment, too. This was probably caused by the uncertainty of nuclear data used in the calculations.

3.2 Supercritical experiments

Up to the present, the following supercritical experiments were performed.

a) Step withdrawal

- Inserted reactivity : 0.25 to 2.8$, rod withdrawal time : about 0.1s for core height.

b) Ramp withdrawal

- Inserted reactivity : 1.8, 2.8$, rod withdrawal speed : 300, 600, 900cm/min.

c) Ramp feed

- Inserted reactivity : 1.6, 2.7$, solution feed rate : 20, 40, 60 *l*/s.

As the results of supercritical experiments, power profiles for three different operation modes are shown in Fig. 4 to 6. As seen in those figures, small power peaks appear after the first large peak. Especially for the ramp feed mode, in which the reactivity insertion rate is very small, the power peaks appear regularly and it oscillates. Such power behaviors are caused by the production and disappearance of radiolytic gas void. In the supercritical experiment, the power increases due to the inserted reactivity, then the temperature rises and the radiolytic gas void is produced. Since the radiolytic gas void has a large negative reactivity effect, the power decreases rapidly. After a while, the void disappears from the surface of solution due to the buoyancy, and the power increases again. These increase and decrease of power repeat until the temperature rises enough to shutdown the system by its negative reactivity effect. Therefore, it is clear that the radiolytic gas void effect is very important for the analysis of power behavior.

4. FUTURE SCHEDULE

The experiment schedules of STACY and TRACY are shown in Fig. 7 and 8, respectively. In STACY, the experiment for a cylindrical core tank with 80cm-diameter and two slab tanks with 35cm-thickness using 10wt% uranyl nitrate solution will be performed. After that, a series of experiments using 6wt% uranyl nitrate solution will start. In 2002, The experiment using plutonium nitrate solution is planned. In TRACY, the transient power behavior for the various conditions of reactivity insertion will be investigated with the present core. Then, the experiments using the water-reflected core will be performed. During these experiments, the radiation dose surrounding the core tank and the transportation behavior of fission products in the off-gas line will be studied, too.

REFERENCES

1. Tonoike, K. et al.: *Proc. Fifth Int. Conf. on Nucl. Criticality Safety*, September, 1995, Albuquerque, NM, p 10·25 (1995).
2. Takeshita, I. et al.: *Genshiryokukogyo*, **43**, 2 (1997) [in Japanese].
3. Miyoshi, Y. et al.: *Proc. 1995 Symposium on Nuclear Data*(JAERI-Conf 96-008), November, 1996, Tokai, Japan, p 23 (1996).
4. Miyoshi, Y. et al.: *Nucl. Technol.*, **118**, 69 (1997).
5. Miyoshi, Y. et al.: *Genshiryokukogyo*, **43**, 5 (1997) [in Japanese].
6. Nakajima, K. et al.: *Proc. Int. Conf. on Physics of Reactors*, September, 1996, Mito, Japan, p L-83 (1996).
7. Nakajima, K. et al.: *Genshiryokukogyo*, **43**, 14 (1997) [in Japanese].
8. Briesmeister, J. F. Ed.: LA-12625 (1993).
9. Kikuchi, Y.: *Proc Int. Conf on Nuclear Data and Science Technology*, May, 1994, Gatlinburg, p 685 (1994).

Table I Major specifications of TRACY

Core	500mmϕ cylindrical tank with a channel for the transient rod movement. Bare or water reflected.
Fuel	Uranyl nitrate solution (10 wt% ^{235}U enriched) Maximum concentration : 500 gU/*l*
Reactivity insertion	Transient rod withdrawal or fuel solution feed.
Maximum excess reactivity	Static operation mode : 0.8 $ Transient operation mode : 3 $
Maximum power	Static operation mode : 10 kW Transient operation mode : 5 GW
Maximum energy	32 MJ(= 10^{18} fissions)/experiment
Maximum pressure	880 kPa (= 9 kg/cm^2)

Table II Calculated effective multiplication factors

Transient rod position	Multiplication factor	Core condition
Out of core	1.0106 ± 0.0003	Height:45.0 cm 433.3 gU/*l* 0.89 N(H^+)
In core	1.0114 ± 0.0003	Height:49.8 cm 432.3 gU/*l* 0.87 N(H^+)

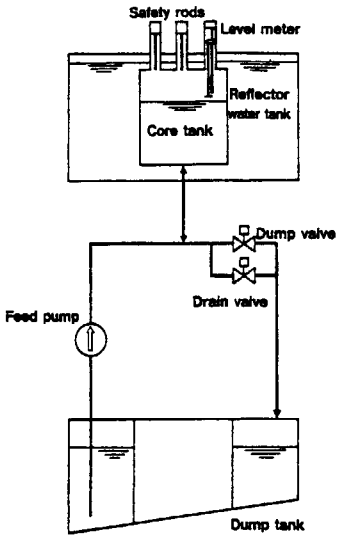

Fig. 1 Flow diagram of STACY

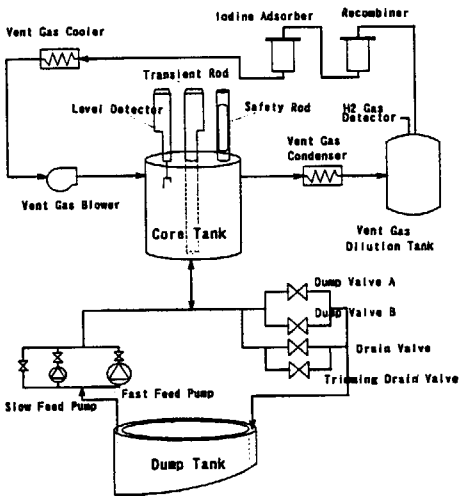

Fig. 2 Flow diagram of TRACY

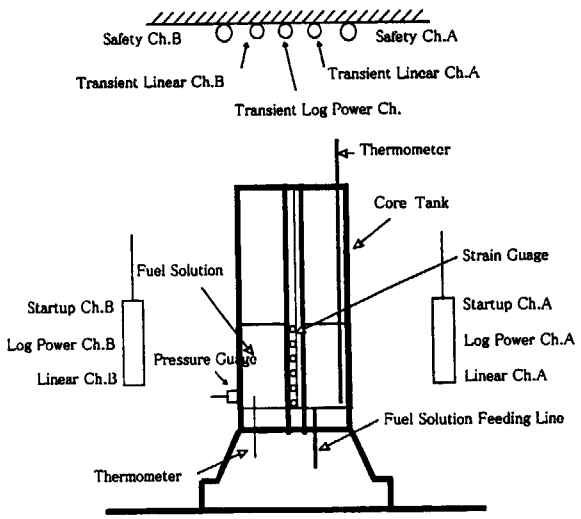

Fig. 3 Configuration of TRACY core

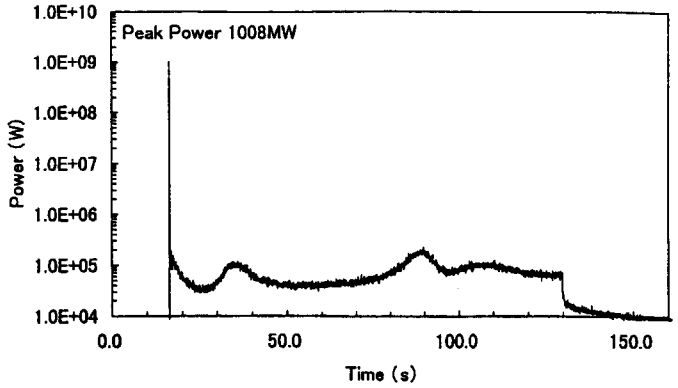

Fig. 4 TRACY power profile for step withdrawal mode (Inserted reactivity : 2.8 $)

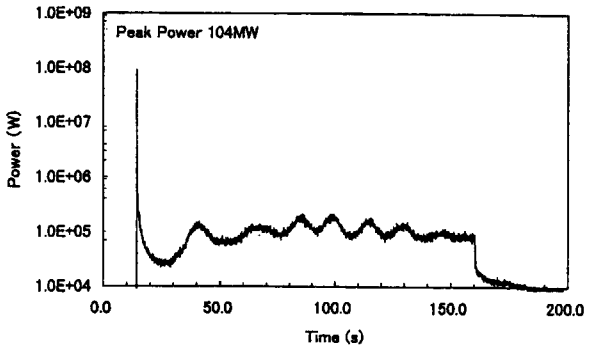

Fig. 5 TRACY power profile for ramp withdrawal mode (Inserted reactivity : 2.8 $)

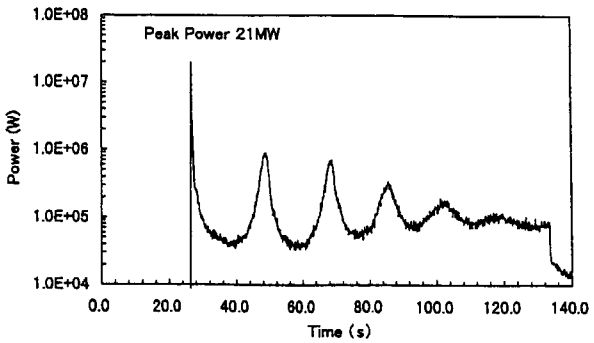

Fig. 6 TRACY power profile for ramp feed mode (Inserted reactivity : 2.6 $)

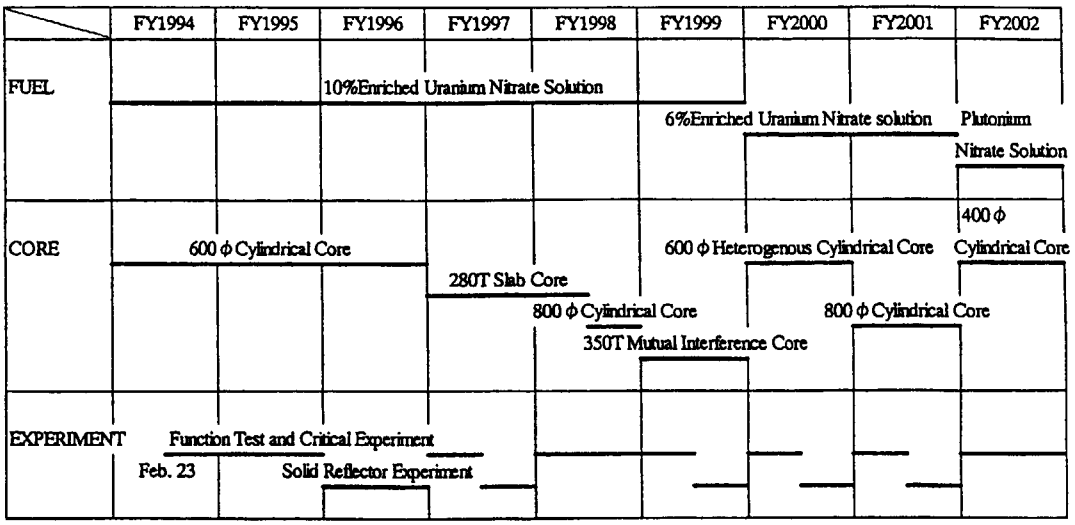

Fig. 7 STACY experiment schedule

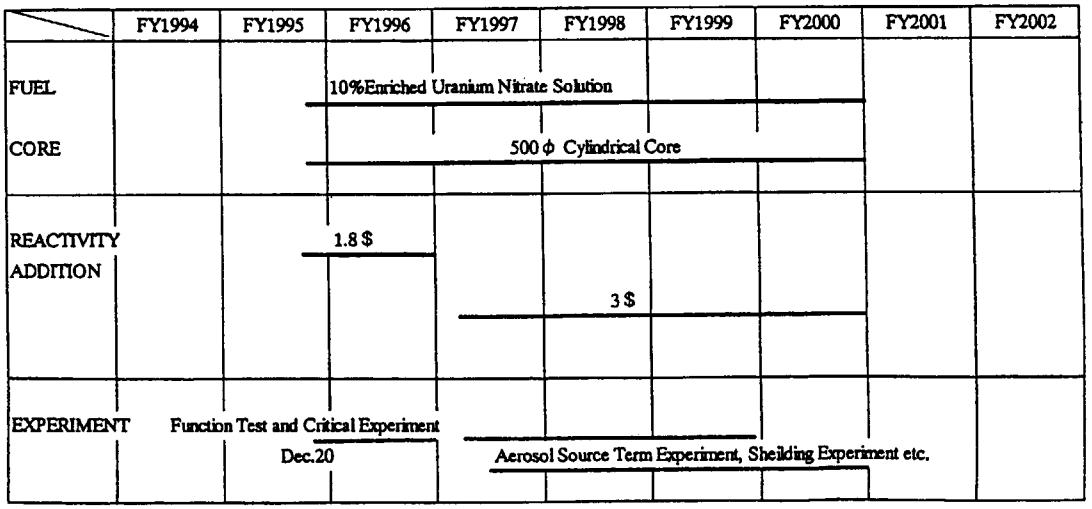

Fig. 8 TRACY experiment schedule

2.1.3 Neutron Intensity of Fast Reactor Spent Fuel

Misao TAKAMATSU and Takafumi AOYAMA

Reactor Technology Section, Experimental Reactor Division, Oarai Engineering Center
Power Reactor and Nuclear Fuel Development Corporation
4002 Narita-cho, Oarai-machi, Ibaraki-ken 311-1393 JAPAN
E-mail : misao@oec.pnc.go.jp

Neutron intensity of spent fuel of the JOYO Mk-II core with a burnup of 62,500MWd/t and cooling time of 5.2 years was measured at the spent fuel storage pond. The measured data were compared with the calculated values based on the JOYO core management code system "MAGI", and the average C/E approximately 1.2 was obtained. It was found that the axial neutron intensity didn't simply follow the burnup distribution, and the neutron intensity was locally increased at the bottom end of the fuel region due to an accumulation of ^{244}Cm.

1. Introduction

Neutron intensity of spent fuel is important not only for the shielding design and dose evaluation of the reprocessing plant and the transportation of the mixed oxide (MOX) fuel, but also for the core management, because it contains more minor actinides than that of LWR fuel. The accuracy of neutron intensity depends on each neutron intensity from spontaneous fission and (α, n) reactions of individual nuclide, and burnup calculation for its production and transmutation. Due to the lack of accumulated data, obtaining an evaluation of neutron intensity accuracy has not been achieved yet.

In order to obtain the experimental data and to improve the accuracy of burnup calculation, the neutron intensity from a spent fuel subassembly of the experimental fast reactor JOYO Mk-II core was measured. The measured data were compared with the calculated values based on the JOYO core management code system.

2. Measurement

The neutron intensity measurement was taken in the spent fuel storage pond at JOYO as illustrated in Fig. 1. The measurement system consists of a neutron detector, a gamma-ray detector and the fuel scanning device which contains the spent fuel inside. Axial and circumferential distribution of neutron and gamma-ray emitted from a spent fuel was measured by moving the fuel scanning system vertically and by rotating itself around the fixed detectors. B-10 proportional counters with sensitivity of 0.78cps/nv$_{th}$ or 5.83cps/nv$_{th}$ were used for the neutron detector depending on the neutron intensity of spent fuel. Cadmium shield was covered around the neutron detector to improve the S/N ratio by reducing the thermal neutron which was moderated in the water and became the background in the measurement. Gamma-ray spectrum of the spent fuel was measured with a high purity germanium (Ge) detector to obtain burnup distribution by counting 2.186MeV peak of ^{144}Pr which is one of the representative fission products. The stainless steel collimator with lead slits was used to increase the position resolution for the gamma-ray measurement. Spent fuel

of the JOYO Mk-II core with a burnup of 62,500MWd/t and cooling time of 5.2 years was measured in this study. The outline of measured spent fuel subassembly is shown in Table 1.

3. Calculation

3.1 Detector Response Calculation

Because the neutron distribution was measured without collimation, neutrons emitted from the whole fuel region contributed to the counts by a B-10 proportional counter. Therefore, the detector response per neutron released from the spent fuel was required to convert the neutron counting rate into the neutron intensity. The detector response matrix as shown in Fig. 2 was calculated using the Monte Carlo code "MCNP-4A" [1] in the water moderated condition. Some calculation conditions by "MCNP-4A" were shown in Table 2. The neutron cross section set used in this calculation was the FSXLIB[2] processed from the JENDL-3.2 library.[3]

As the detector counts the primary neutron from the spent fuel produced by spontaneous fission and (α, n) reactions, but also the secondary neutron which was generated by the induced fission reaction in the spent fuel with a moderated neutron. Therefore, the effect of the neutron multiplication was also considered in the calculation.

3.2 Neutron Intensity Calculation

The neutron intensity was then calculated by multiplying the atomic number of actinide nuclides by spontaneous fission and (α, n) reaction rates. The burnup calculation to obtain the change of fissile composition of U, Pu and the transmutation of minor actinides was conducted using the JOYO core management code system "MAGI".[4] The details of the calculation method of "MAGI" is shown in Table 3. The neutron flux distribution was calculated on the basis of a 3-D diffusion theory with seven energy groups. The neutron cross section was collapsed from the 70 group JFS-3-J2 cross section set [5] processed from the JENDL-2 library. The reactor power history and the core configuration in each operational cycle of the JOYO Mk-II core was simulated exactly in the "MAGI" calculation.

The accuracy of the neutron flux calculation was evaluated to be less than 5% in the fuel region according to the comparison between "MAGI" and reactor dosimetry test results based on the foil activation method. The axial neutron flux by "MAGI" was corrected so that the relative distribution (see Fig. 3) of calculated and measured (^{144}Pr) burnup could match.

4. Result and Discussion

Comparison of measured and calculated neutron intensity is shown in Fig. 4 and Table 4. The measured neutron intensity in the whole fuel was about 2.4×10^{6} n/s, and it was about 2.5 times as much as that of fresh (unirradiated) fuel which is calculated to be about 9.7×10^{5} n/s. The ratio of calculated to measured value (C/E) ranged from 0.89 to 1.47 in each fuel region with the average C/E of 1.22. The error of C/Es ranged from 14% to 32% and was mainly due to an uncertainty in solving the inverse matrix of detector response to obtain neutron intensity.

The measured ^{144}Pr distribution (Fig. 3) showed that the axial peak of burnup was slightly shifted downward due to the control rod insertion during irradiation. Different from the roughly symmetrical shape of axial burnup distribution, it was observed in Fig. 4 that the neutron intensity at the bottom of fuel region was apparently higher than that at the top. The

"MAGI" calculation shown in Table 5 indicates that neutron intensity from ^{244}Cm amounts to about 50% of the total number. Therefore, the neutron intensity depends on the ^{244}Cm distribution in the fuel which had been mainly produced by ^{243}Am (n, γ) reaction.

In order to investigate the ^{244}Cm distribution, the neutron spectra and ^{243}Am (n, γ) reaction rates at the top, center and bottom of the fuel region are compared in Fig. 5 and Fig. 6, respectively. As the JOYO Mk-II driver fuel has axial reflectors of stainless steel with an insulator pellet of depleted uranium between MOX fuel and the axial reflector, the neutron spectrum at the bottom of the fuel region is softer than that of the center. This effect is less at the top because of the neutron absorption by the control rod. As a result, ^{243}Am (n, γ) reaction rate at the bottom is higher than that of the top, and the increase of the neutron intensity from ^{244}Cm as shown in Fig.7 was also due to the same reason. Similar phenomena was observed concerning the ^{243}Am distribution from Am isotope ratio analysis conducted in post irradiation examination.[6] However, the increase of the measured neutron intensity at the bottom end was significant, and is even larger than that of the center. It appears due to the error in solving the inverse matrix of detector response, so further investigation is required.

5. Conclusion

Neutron intensity of spent JOYO Mk- II fuel with a burnup of 62,500MWd/t and cooling time of 5.2 years was measured and compared with the calculation based on the JOYO core management code system. The measured neutron intensity in the whole fuel was about 2.4×10^6n/s, and the average C/E approximately 1.2 was obtained. It was found that the axial neutron intensity didn't simply follow the burnup distribution, and the neutron intensity was locally increased at the bottom end of the fuel region due to an accumulation of ^{244}Cm.

Acknowledgements

The authors would like to note the contribution of Mr. T. MASUI and Mr. T. SAIKAWA of Inspection Development Company for the neutron and gamma-ray measurement, and Mr. M. NAGATANI of Information Technologies Japan Inc. for the neutron flux and burnup calculation by "MAGI". We also appreciated the cooperation of Mr. O. SATO and Ms. S. FURIHATA of Mitsubishi Research Institute Inc. for the detector response calculation.

References

1) J. F. Brismeister Ed.: "MCNP-A General Monte Carlo N-Particle Transport Code Version 4A," *LA*- 12625-*M* (1993)
2) K. KOSAKO et al.: "FSXLIB-J3: MCNP Continuous Energy Cross Section Library Base on JENDL-3," *JAERI-M* 91-187 (1991)
3) T. NAKAGAWA et al.: "Japanese Evaluated Nuclear Data Library Version 3 Revision-2: JENDL-3.2," *J. Nucl. Sci. Technol.*, **32**, 1259 (1995)
4) T. AOYAMA et al.: "Core Management Experience of the Experimental Fast Reactor JOYO," *Proc. Int. Conf. Fast Reactor Core and Fuel Structural Behavior, British Nuclear Energy Society, UK*, p.299 (1990)
5) H. TAKANO and K. KANEKO: "Revision of Fast Reactor Group Constant Set JFS-3-J2," *JAERI-M* 89-141 (1989)
6) S. KOYAMA et al.: "Results of Am Isotopic Ratio Analysis in Irradiated MOX Fuels," *PNC TN* 9410 97-054 (1997)

Table 1 Outline of Measured Spent Fuel Subassembly

Fuel Composition	^{235}U Enrichment : 12.8 % Pu Content : 26.8 %
Irradiation Condition	Core Resident Period : 1989.5.8～1992.6.17 1) ϕ_{total} : 3.4×10^{15} n/cm^2/s Irradiation Days : 181 days (at the Second Row) 2) ϕ_{total} : 2.6×10^{15} n/cm^2/s Irradiation Days : 240 days (at the Fourth Row)
Φ_{total}	1.07×10^{23} n/cm^2 (Subassembly Averaged)
Burnup	62,500MWd/t (Subassembly Averaged)
Cooling Time	1,900 days (Measured Date : 1997.8.30)

Table 2 Condition of Detector Response Calculation

Calculation Code	MCNP-4A
Cross Section	FSXLIB(JENDL-3.2)
Neutron Source Spectrum	Spontaneous Fission Watt Type (^{244}Cm) (α 、 n) Reaction α -ray Energy : 5.5MeV
History	5,000,000
FSD	Less than 1% for Detector Responses

Table 3 Condition of Neutron Flux and Burnup Calculation

Item	MAGI
Cross Section	JFS-3-J2(JENDL-2)
Geometry	3D Hex-Z
Energy Group	7
Flux Calculation	Diffusion
Burnup Calculation	Matrix Exponential

Table 4 Comparison of Neutron Intensity

Neutron Intensity (n/s/Subassembly)		C/E
Measurement	MAGI + ORIGEN2	
2.39×10^6	2.91×10^6	1.22

Table 5 Neutron Intensity of Individual Nuclide (by MAGI Calculation)

Nuclide	Neutron Intensity (n/s/Subassembly)			Ratio (%)
	(α , n) Reaction	Spontaneous Fission	Total	
^{238}Pu	2.8×10^{5}	4.5×10^{4}	3.2×10^{5}	11.0
^{239}Pu	8.3×10^{4}	—	8.3×10^{4}	2.85
^{240}Pu	1.2×10^{5}	6.1×10^{5}	7.3×10^{5}	25.1
^{242}Pu	—	1.3×10^{5}	1.3×10^{5}	4.62
^{241}Am	2.0×10^{5}	—	2.0×10^{5}	6.81
^{242}Cm	4.8×10^{3}	2.3×10^{4}	2.8×10^{4}	0.96
^{244}Cm	1.2×10^{4}	1.4×10^{6}	1.4×10^{6}	48.6
Total	6.9×10^{5}	2.2×10^{6}	2.9×10^{6}	100

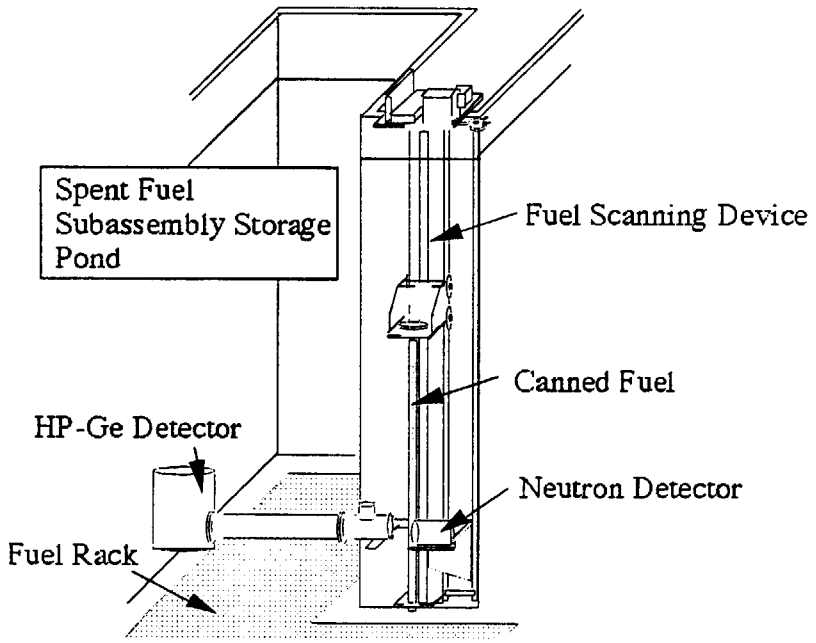

Fig. 1 Schematic Diagram of Measurement System

$$(Ri)=(Mij)(Sj) \rightarrow (Sj)=(Mij)^{-1}(Ri)$$

Ri : Neutron Counting Rate (cps)
Rj : Neutron Intensity (n/s)
Mij : Response Matrix

Fig. 2 Neutron Detector Response Matrix

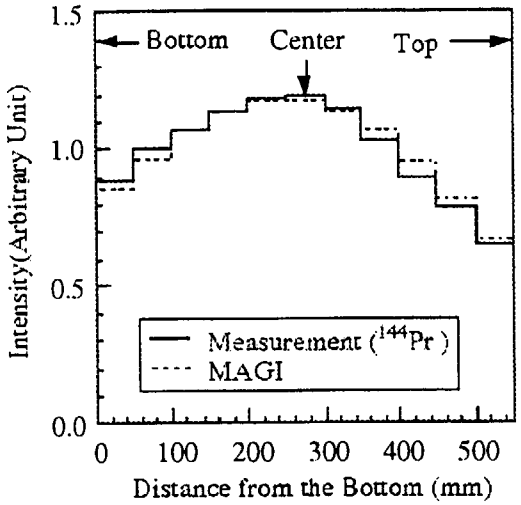

Fig. 3 Axial Burnup Distribution

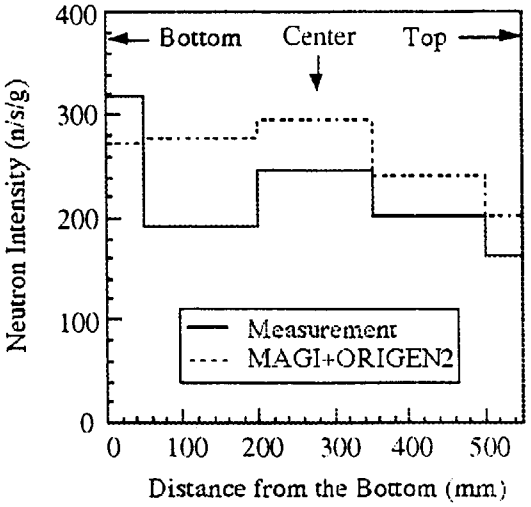

Fig. 4 Axial Neutron Intensity Distribution

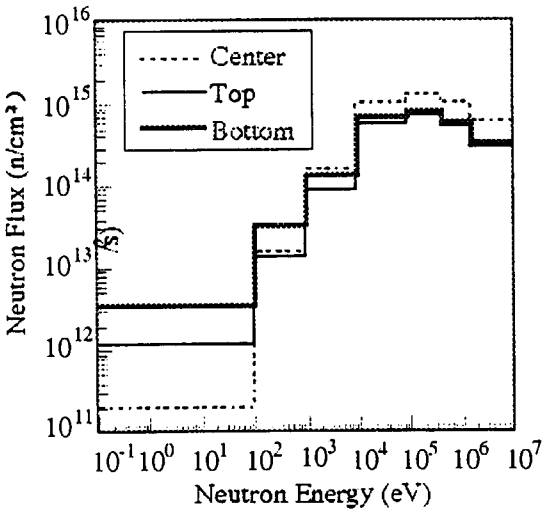

Fig. 5 Comparison of Neutron Spectrum

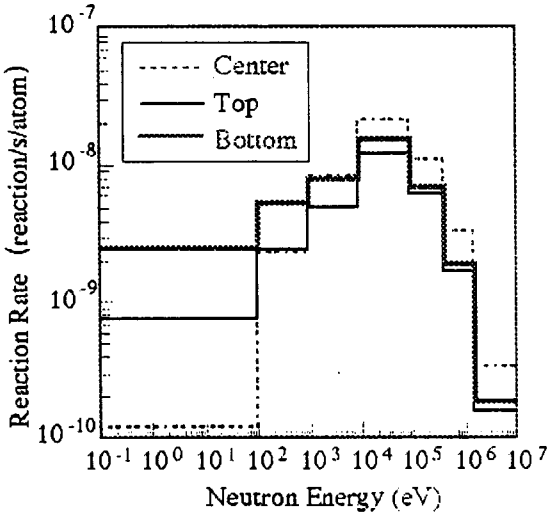

Fig. 6 Comparison of ^{243}Am(n , γ) Reaction Rate

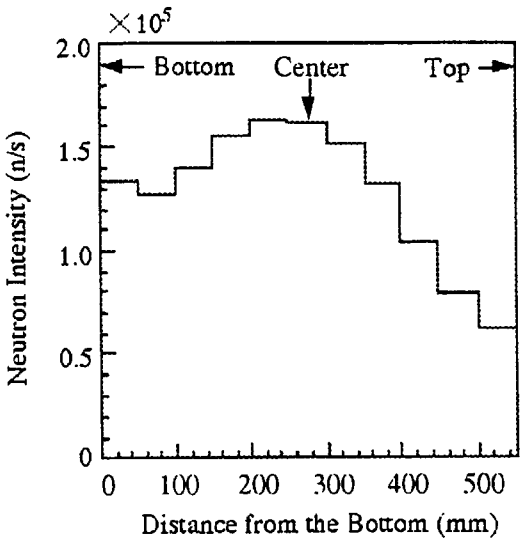

Fig. 7 Axial Neutron Intensity Distribution from ^{244}Cm

2.2 Status of JENDL

2.2.1 Current Status of JENDL-3.3

Akira HASEGAWA

Nuclear Data Center, Japan Atomic Energy Research Institute
Tokai-mura, Naka-gun, Ibaraki-ken, 319-1195 Japan

Abstract

Current status of JENDL-3.3 is presented. Reevaluation work toward JENDL-3.3 has started last April for three years project to supply a consolidated new versions of JENDL by JAERI NDC (Nuclear Data center) with the cooperation of JNDC (Japanese Nuclear Data Committee). The working schedule has been fixed by the careful review of the summary report, "The problems of JENDL-3.2", submitted to JNDC last March after one year discussions by a small advisory group: "Identifying the problems of JENDL-3.2". To cope with the problems, two new subgroups are set up in the Subcommittee of Nuclear Data of JNDC. One is Heavy Mass Elements Evaluation Working Group for the re-evaluation of major actinides (Th-232, U-233,235,236,238 Pu-236,239,241,242). The other is Intermediate Mass Elements Evaluation Working Group for solving the inconsistencies between calculations and integral experiments relating to the fields of fusion neutronics and shielding applications as well as new evaluations such as Er elements. Supplying covariance data for important nuclides are one of the main feature of JENDL-3.3. Re-evaluated data will be released as JENDL-3.3 in the individual bases after the reviewing process by the experts.

1. Introduction

Reevaluation work toward JENDL-3.3 has started last April for three years project to supply a consolidated new versions of JENDL by JAERI NDC (Nuclear Data center) with the cooperation of JNDC (Japanese Nuclear Data Committee). The work has started based on the summary report submitted to JNDC last March after one year discussions made by a small advisory group "Identifying the problems of JENDL-3.2".[1] The outline was presented in this Symposium held in the last year.[2] In the report, many problems are listed up from several view points such as evaluators of JENDL-3.2, users in the applications for the individual fields like reactor applications, fusion neutronics, shielding or basic sciences, or big potential users like ITER.

This article treats the current status of JENDL-3.3. In the section 2, the scope of

JENDL-3.3 is outlined. In the section 3, development schedule and organization scheme for newly formed working group(WG) are presented. Following sections are devoted to the work assigned to each WG.

2. Scope of JENDL3.3

JENDL-3.3 is a revision work of current version of JENDL-3.2[3]. JENDL3.3 will be supplied as a consolidated new versions of JENDL by JAERI NDC (Nuclear Data center) with the cooperation of JNDC (Japanese Nuclear Data Committee). It's main features are followings:

1) Covariance data supplemented for major elements such as major actinides, structural materials and main coolants for the applications of FBR, LWR and Fusion reactors, to enable the estimation of quantitative contribution of nuclear data uncertainty to design accuracy or safety margin. No covariance data were supplied up to the JENDL-3.2.

2) New material evaluations such as Er for burnable poisons in LWR high burn-up applications.

3) Adoption of isotope evaluation policy rather than natural element evaluation policy. Up to now for natural elements JENDL supports natural element evaluation policy, i.e., for the transport calculations in nuclear reactors, natural elements data are recommended to use and for the dosimetry or activation application data of isotope evaluation are recommended. From time to time, this policy has caused several problems for unfamiliar users of JENDL to use constructed data from isotope evaluations as natural element data in the transport calculations. In some cases, consistency between these two data is not always guaranteed in the JENDL-3.2 evaluations.

Other individual items are presented in the section 4.

3. Development schedule and organization scheme for the JENDL-3.3

3.1 Schedule

A rough schedule and mile stones for JENDL-3.3 development since JENDL3.2 release is given in Fig.1. JENDL-3.2 was released at June 1994. Two years later a small advisory group for discussing the problems of JENDL-3.2 was organized to identify the problems of the current version of JENDL. Summary report was submitted to JNDC at March 1997. Based on this report, a working schedule for 3 years project of JENDL-3.3 and a new organization scheme has been set up. We are expecting the final release of JENDL-3.3 at Mar. 2000. Re-evaluated data will be released in the individual bases

after the reviewing process is finished

3.2 Organization scheme

To cope with the problems listed up in the summary report by the advisory group, we set up two new working groups (WG) in the Subcommittee of Nuclear Data in JNDC. One is Heavy Mass Elements Evaluation Working Group, this group has 9 members and is headed by Dr.T. Kawano of Kyusyu University. Re-evaluation of major actinides (Th-232, U-233,235,236,238 Pu-236,239,241,242) are the main mission of this group. The other is Intermediate Mass Elements Evaluation Working Group, this group has 6 members and is headed by Dr. K. Shibata of JAERI. Main topics of this group are the inconsistencies between calculations and integral experiments relating to fusion neutronics and shielding applications. Inconsistencies in the neutron and gamma-ray spectrum leaked from massive substances appeared by the benchmark experiments for 14 MeV neutrons are also the problems .

As supplying covariance data for important nuclides are one of the main feature of JENDL-3.3, much efforts are foreseen by the Covariance Working Group of JNDC. This group is expected to supply the guideline of the covariance evaluations. For the delayed neutron spectrum evaluation, Delayed Neutron Data Evaluation Working Group is concerned. A Compilation Group of JENDL-3.2 are also set up in NDC organizing the coordination of the works such as evaluations, file productions and reviewing of the re-evaluated data submitted by evaluators.

In Fig. 2, related organizations for JENDL-3.3 developments are presented.

4. Assigned works for newly established WG.

4.1 Heavy Mass Element Evaluation Working Group

In Fig.3 working group members and their responsible nuclides are shown.

Main items for this WG are followings:

(1) Secondary energy distribution for neutron emission reactions in some nuclides[4)]

As shown in Fig.4, incorrect(unphysical) neutron spectra are given for some heavy elements like U-233, U-235 in the JENDL-3.2 for the energy distribution of neutron emission reactions (continuum of inelastic cross sections). For these nuclides, consistent evaluations are requested among competing channels. Re-evaluations will be made using GNASH and GAMFIL codes.

(2)Capture cross-section in MeV range

As in Fig.5, direct capture process is not included in JENDL-3.2. Therefore always very low capture data is given in JENDL-3.2 Re-evaluation is requested for these

energy regions to supply correct data for the name of general purpose file.

(3)U-238 inelastic scattering cross sections

To fix the cross-section shape and energy distributions is the main task for U-238 evaluation. These problems are long standing ones in the evaluators. The data have not been converged yet even in the major files like ENDF/B-VI[5] and JENDL-3.2 as seen in Fig.6.

(4) U-235 capture cross-sections in resolved resonance region

Decision for the adoption of the latest evaluation of U-235 resolved resonance parameters by Leal/Derrien[6] is one of the main jobs for this nuclide. As seen in Fig.7, if we adopt this data, as much as 80 % difference will be introduced compared with current data in JENDL-3.2. We must check very carefully the consistency among other data in the benchmark performance for this data.

(5) Over estimation of Keff by 0.3 to 1.1% for thermal system compared with JENDL-3.1[7]

As seen in Fig. 8, consistent over estimation on Keff is observed for thermal system such as research reactors in JAERI. This tendency is common for all thermal systems calculated by JENDL-3.2. The root cause should be identified and removed.

4.2 Intermediate Mass Elements

In Fig.9 working group members and their missions are shown.

One of the main problems for this group is to up-date the resonance region data based on the recent high resolution measurements for the main structural materials such as Cr, Fe, Ni. As seen in Fig.10 JENDL-3.2 data gives fairly poor data among other evaluations.

5. Conclusions

Brief descriptions of the current status of JENDL-3.3 development were given. This revision work started in April 1997 by JAERI NDC with the close cooperation by JNDC. A new version of JENDL-3.3 will be scheduled at the end of FY 1999 i.e., within 3 years. This does not mean that new data will be available after 3 years from now. Any new revised data (nuclide wise) will be open to the publics at the time when the evaluation work is completed and their critical review is finished.

5. References

1) Advisory group for the problems of JENDL-3.2 (Ed.), "Summary reports for the problems in JENDL-3.2" , unpublished work in Japanese (1997).

2) Hasegawa,A. : JAERI-Conf 97-005, pp27-43 (1997).

3) Nakagawa,T., et al.:J. Nucl.Sci. Technol.,32[12], 1259 (1995)

4) Porodzinskij,Y.V., Sukhovitskij,E.S.,: Private communication,(1995).

5) Rose, P.F., (ed.) : "ENDF/B-VI Summary Documentation", BNL-NCS-17541 (ENDF-201), (1991), Data Library ENDF/B-VI. Update, 1995, by the U.S. National Nuclear Data Center.

6) Leal,L C., Derien,H., et al. : "Final report on evaluation of U-235 cross sections", distributed NEA NSC WPEC 8th meeting,(1996).

7) Shibata, K., et al.: JAERI-1319, (1990)

Fig. 1 Schedule & Milestone for JENDL-3.3

- Release of JENDL-3.2: **June 1994** (I)
- A small Advisory Group for Discussing
  the Problems of JENDL-3.2 Evaluations Apr. 1996 ➔ Mar. 1997 (II)
- **JENDL-3.3 Three Year Project:** Apr. 1997 ➔ Mar. 2000 (III)
  Based on the summary report submitted by above group (JNDC)

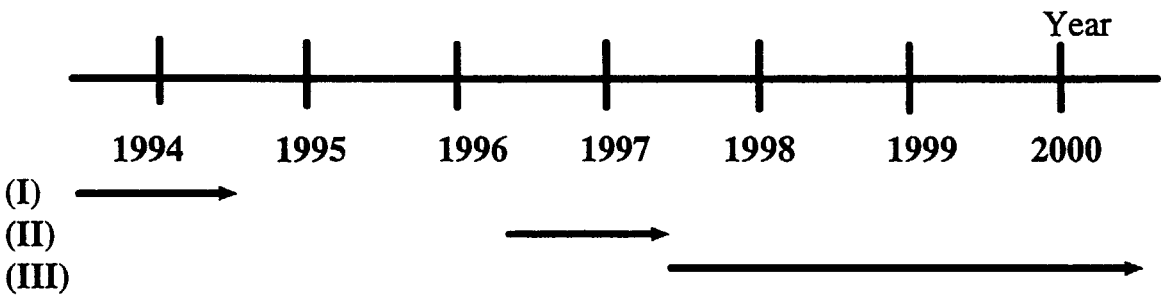

Release of JENDL-3.3: in the individual bases after review

Fig. 2 Organization Scheme for Re-evaluation

Subcommittee on Nuclear Data

2 New adhoc Subgroups + existing WG

- **Heavy Mass Elements Evaluation** WG
  Head: **T. Kawano** (Kyusyu Univ) **10** members
- **Intermediate Mass Elements Evaluation** WG
  Head: **K. Shibata** (JAERI) **6** members
- **Covariance Data Evaluation** WG
  supply **guide line** of evaluation for covariance data
- Delayed Neutron Data Evaluation WG
  Head: **T.Yoshida** (MUSASHI-Tec)
  supply delayed neutron spectrum
- **Compilation Group of JENDL-3.3** (Standing Group)
  file creation and coordination of evaluation
  administration of **reviewing** of submitted evaluations

Fig. 3 Heavy Mass Elements Evaluation Working Group

Responsible Persons

U-233 U-235: H.Matsunobu (Data Eng.)
U-236 : T.Yoshida (Musashi-Tec)
U-238 : T.Kawano (Kyushu Univ.)
Pu-236 : O.Iwamoto (JAERI)
Pu-239 : M.Kawai (Toshiba)
Pu-240 : T.Murata (AITEL) & A.Zukeran (Hitachi)
Pu-241 : Y.Nakajima (RIST)
Pu-242 : T.Murata & M.Kawai
Th-232 : T.Osawa (Kinki Univ.)

Delayed Neutron Spectrum : SWG T.Yoshida
Fission Spectrum: Covariance data deduction

Fig. 4 Secondary Energy Distribution for (n,n')

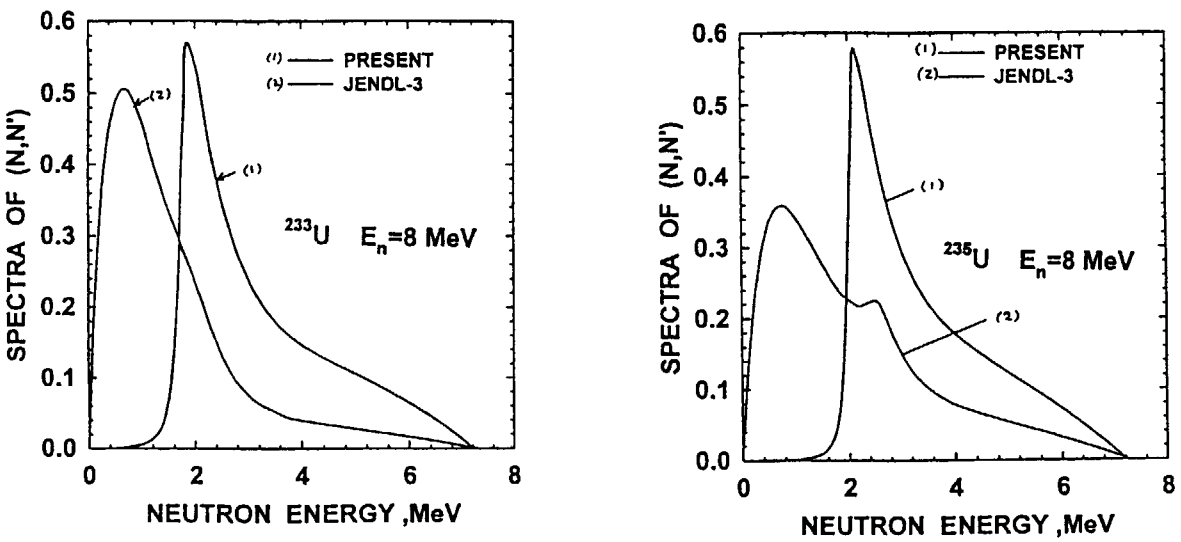

Consistent evaluation among competing reaction channels

GNASH + GAMFIL

Fig. 5 Capture cross-section in MeV range

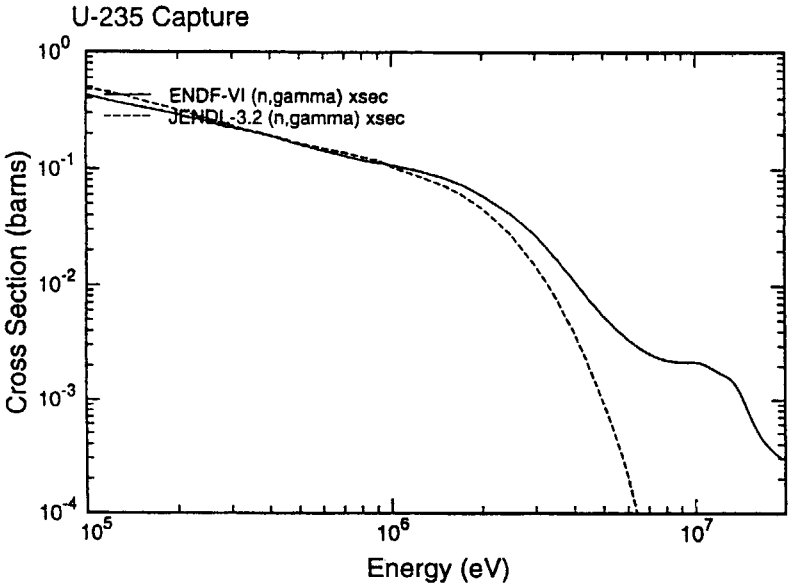

Taking into direct capture process.

Fig.6 U-238 Inelastic Scattering Cross-section

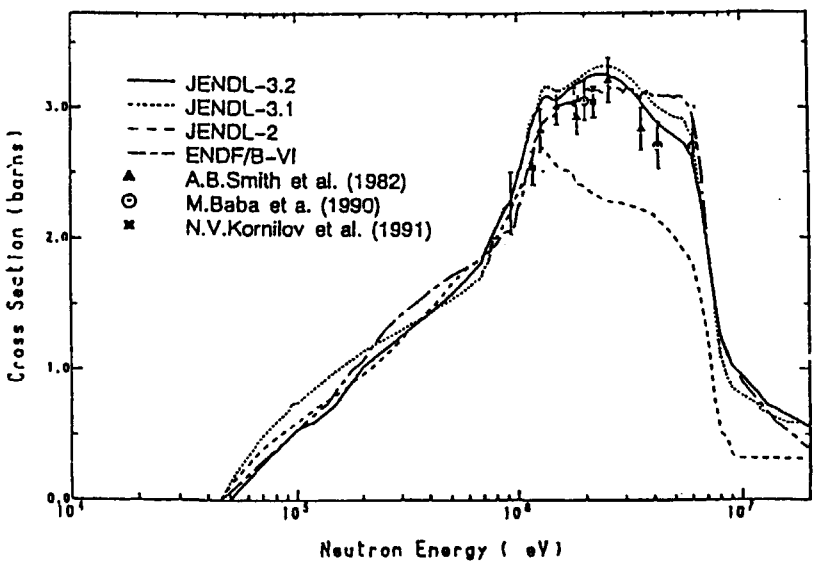

Settling the long standing problems !

Fig. 7 U-235 Resolved Resonance Parameters

Leal/Derrien Evaluation (Latest evaluation WPEC SG-18)

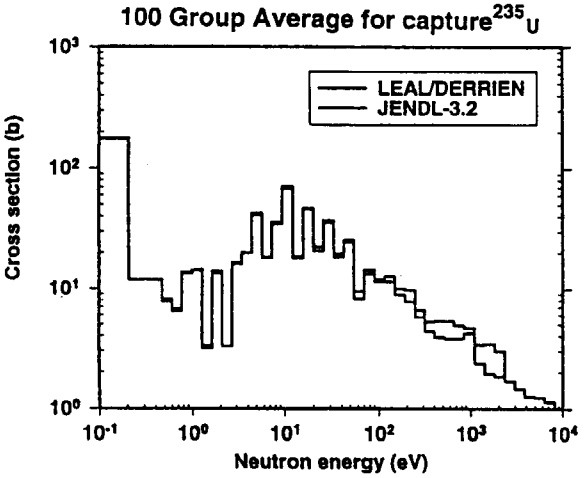

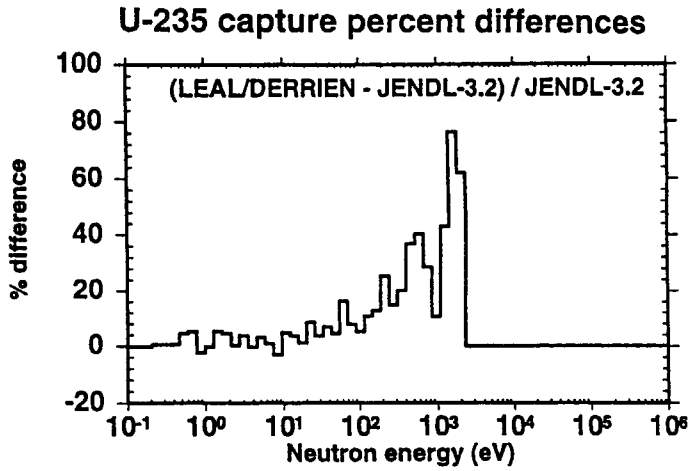

Unresolved Part
Consistency against the Benchmark Test

Fig. 8 U-235 data revision from JENDL-3.1 to JENDL-3.2

keff: 0.3 – 1.1 % more reactive for thermal System than JENDL-3.1

C/E of Keff	JENDL-3.1	JENDL-3.2	J3.2-J3.1
A-12 (JRR-4)	0.9976	1.0063	0.877 %
A-4+B-12 (JRR-4)	0.9933	1.0030	0.974
First Critical (JRR-3)	0.9988	1.0076	0.876
First Core (JRR-3)	1.0019	1.0104	0.841
VHTRC-1(HTTR)	0.9968	1.0054	0.865
VHTRC-4(HTTR)	1.0004	1.0083	0.803
VHTRC-6(HTTR)	0.9971	1.0062	0.916
STACY (Water Ref.)	1.0014	1.0080	0.66
STACY (No Reflect)	0.9994	1.0063	0.69

Fig. 9 Current Status of Cr data

New evaluation is requested by new experimental Data

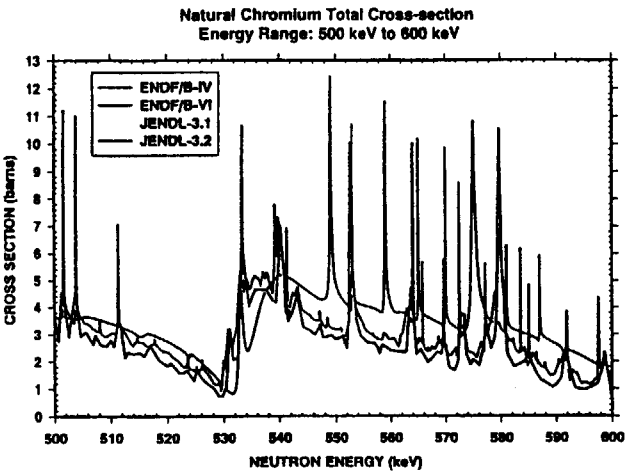

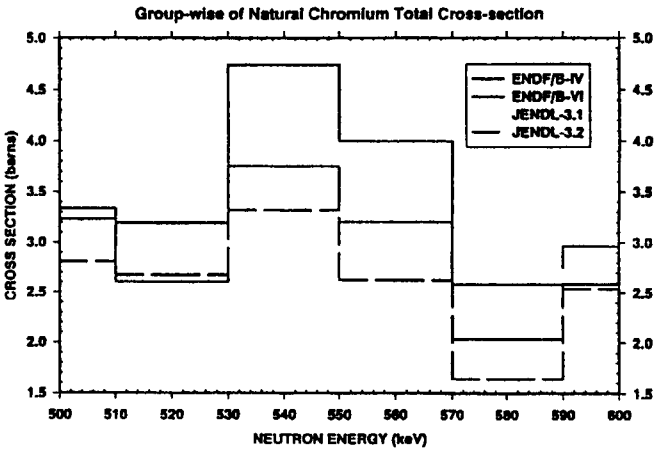

High Resolution Measurements for Cr , Fe, Ni

Fig. 10 Individual Evaluations for Intermediate Mass Elements

Na-23:	elastic, inelastic scattering	(Shibata)
Fe :	total, elastic, inelastic	(Shibata)
Ni ,Ta-181 :	(n,alpha)	(Shibata)
Cu :	resonance parameters	(Shibata)
Si :	neutron spectra	(Kitazawa)
Ti :	neutron & secondary gamma-ray spectra	(Asami)
Cr :	secondary gamma-ray spectra	(Asami)
W :	gamma-ray energy balance & spectra	(Asami)
Co :	neutron spectra	(Watanabe: Kawasaki Industry)
V-51:	resonance parameter	(Watanabe: Kawasaki Industry)
Nb-95:	secondary gamma-ray spectra	(Watanabe: Kyusyu Univ.)
Er :	new evaluation	(Igashira)

2.3 International Trends of Nuclear Data

2.3.1 Nuclear Data and Reactor Physics Activities in Indonesia

LIEM Peng Hong
Center for Multipurpose Reactor (PRSG),
National Atomic Energy Agency (Batan),
Puspiptek Complex, Serpong, Tangerang, Indonesia 15310
e-mail: liemph@uninet.net.id

The nuclear data and reactor physics activities in Indonesia, especially, in the National Atomic Energy Agency are presented. In the nuclear data field, the Agency is now taking the position of a user of the main nuclear data libraries such as JENDL and ENDF/B. These nuclear data libraries become the main sources for producing problem dependent cross section sets that are needed by cell calculation codes or transport codes for design, analysis and safety evaluation of research reactors. In the reactor physics field, besides utilising the existing core analysis codes obtained from bilateral and international co-operation, the Agency is putting much effort to self-develop Batan's codes for reactor physics calculations, in particular, for research reactor and high temperature reactor design, analysis and fuel management. Under the collaboration with JAERI, Monte Carlo criticality calculations on the first criticality of RSG GAS (MPR-30) first core were done using JAERI continuous energy, vectorized Monte Carlo code, MVP, with JENDL-3.1 and JENDL-3.2 nuclear data libraries. The results were then compared with the experiment data collected during the commissioning phase. Monte Carlo calculations with both JENDL-3.1 and -3.2 libraries produced k_{eff} values with excellent agreement with experiment data, however, systematically, JENDL-3.2 library showed slightly higher k_{eff} values than JENDL-3.1 library.

1. Introduction

Through bilateral and international co-operation, as well as self development by the Agency, the availability of nuclear data, nuclear data processing codes, and reactor physics calculation codes in the Agency is growing increasingly. This is partly attributed to the growing needs of the Agency to operate and utilise efficiently and safely three research reactors, i.e., two, relatively low power, Triga-type research reactors located in Bandung and Yogyakarta, and one 30 MWth multipurpose reactor (RSG GAS, formerly called MPR-30) located in Serpong, Tangerang. Of course, as a long term objective, the activity is expected to support the power reactor technology transfer and development.

Nuclear Data and Libraries

Concerning the nuclear data and their relevant processing codes, within the Agency's organisation, up to the present date, there is no special center for nuclear data, however, an ad-hoc team consisting of several persons for maintaining the existing nuclear data and the relevant processing codes has long been established. The team's members were elected from the Informatics Development Center, Center for Multipurpose Reactor, and the Center for Assessment of Nuclear Technology.

As shown in Table 1, the main nuclear data libraries maintained by the team are the Japan Evaluated Nuclear Data Library (JENDL) and the Evaluated Nuclear Data File (ENDF/B). A general nuclear data processing code for these nuclear data libraries available in the Agency is the NJOY91.38 code [1]. The processing code is used for generating additional cross sections in the WIMS/D4 cell calculation code [2]. This work has to be done since many new radioisotope targets are being inserted in the RSG GAS, or new irradiation facilities were installed. However, the original WIMS/D4 library is still in use. Besides the original WIMS/D4 library, through bilateral co-operation, the new WIMS/D4 libraries that was adjusted for Triga reactors have been installed and used.

The MGCL-137 library with its processing code systems [3] is being used for control rod studies in the Center for Multipurpose Reactor. However, the library is relatively old and its scattering cross sections are limited to P_0 and P_1 scattering cross sections at room temperature.

The author has also compiled problem dependent cross section sets for high temperature reactor, especially for the pebble bed HTR-200 module using JAERI's DELIGHT-7 [4] and V.S.O.P [5] cell calculation codes. These libraries, together with self-developed Batan-MPASS code [6], a code for pebble bed HTR fuel management, have been used for design evaluation of the HTR-200 module which is being conducted by the Agency's HTR team under the Center for Nuclear Technology Assessment.

Core Analysis Codes

The reactor physics codes available in Batan are summarised in Table 2. A workstation version of SRAC-95 [7] has been successfully installed and used in Batan for research reactor analyses. The code is found very useful for detailed analyses of research reactors which require full 3-D many group neutron diffusion calculations, or 2-D few group neutron transport calculations. However, for routine fuel management activity of our research reactors it seem still too heavy. Therefore, instead of SRAC-95, we use TRIGAP [8], IAFUEL [9] and self-developed Batan-FUEL [10] codes for routine fuel management purposes. The recently available MCNP-4B Monte Carlo code [11] will be used for more advance applications where accuracy is of the most importance.

Batan-FUEL code, an in-core fuel management code for research reactors has been developed by the Agency to support the RSG core conversion program from oxide to silicide fuel [12]. The code is designed to simulate and record the fuel burnup in a reactor core within the framework of multigroup neutron diffusion theory in 2-D XY or RZ reactor geometry. Although not for routine fuel management, Batan-FUEL code has a 3-D diffusion module to treat the axial dependent problems such as when the axial position of the control rods must be evaluated accurately. Several important options for reactor design and analysis are available:

(1) External source problem solver,
(2) Adjoint eigenvalue problem solver,
(3) Kinetic parameter calculation,
(4) Calculation of reactivity changes based on the first order perturbation theory,

(5) Special treatment for xenon and samarium poisoning effects,
(6) Special treatment for strong absorbers using the effective diffusion parameters (blackness theory) and logarithmic derivative constants (internal boundary conditions), and
(7) Equilibrium core searching option; using this option the reactor designer can directly obtain the core equilibrium condition without simulating the transition cores [13,14].

Batan-MPASS was developed as a general fuel management code for calculating the core equilibrium condition of pebble-bed high temperature reactors with multipass and Once-Through-Then-Out (OTTO) refuelling schemes. The code adopts an iterative method to obtain directly both the equilibrium core and critical conditions of the reactors without simulating the transition cores. 2-D, RZ reactor geometry as well as 1-D reactor geometry options are available. The code is also equipped with 1-D and 2-D thermal-hydraulic routines to assess the coolant flow pattern and fuel temperature distribution in the core. With these options the designers can obtain comprehensive results from neutronics, fuel management, and thermal aspects of the reactor.

For peu a peu refuelling scheme, a similar code, Batan-PEU [15] was developed. This code is almost identical with Batan-MPASS code except for the fuel burnup calculation. The fuelling operation which increases the core height is simulated in the code by moving the boundary between the core and upper core void regions.

Batan-MPASS and Batan-PEU have been successfully used in the assessment and prefeasibility study on the utilisation of high temperature gas reactors for future industrialisation programs, particularly in the fields of (1) process heat applications, (2) process steam and electricity co-generation, and (3) electric generation for isolated/remote islands [16].

2. Evaluation (JAERI MVP Code with JENDL-3.1 and JENDL-3.2 Libraries)

In the next subsection, as one output of the reactor physics activity in the Agency, Monte Carlo calculation results for the first core of RSG GAS will be presented and compared with the experiment data. The first core was chosen because of, first, the completeness of the experiment data, and secondly, the fuel elements, absorber and beryllium reflectors were still fresh so that uncertainties raised from the fuel burnup and absorber depletion calculations, and from the calculation of lithium poisoning in the beryllium reflectors can be eliminated. The vectorized, continuous energy Monte Carlo code, MVP [17], developed by JAERI, was used for the entire calculations. In the present evaluation work, as the nuclear data libraries for the code, the third version Japanese Evaluated Nuclear Data Library, JENDL-3.1 [18] and JENDL-3.2 [19] were used and compared with the experiment data.

Criticality Experiments on the First Core of RSG GAS

Firstly, the RSG GAS is briefly reviewed here. RSG GAS is a 30 MWth open pool type, light water moderated and cooled, beryllium reflected reactor (Table 3). Fuel elements (FEs) used for RSG GAS are of the material testing reactor, i.e. plate-type FEs, and one FE consists of 21 fuel plates assembled by two side plates. One fuel plate consists of 19.75 % enriched uranium oxide meat (with uranium density of

2.96 gU/cc) embedded in aluminium matrix, and aluminium clad. The active length of the fuel element (or the meat height) is 60 cm. The nominal ^{235}U loading per FE is 250 g. Control fuel elements (CEs) with identical outer dimension consist of 15 fuel plates, that is, three fuel plates at both outer sides of the FE are removed to provide space for absorber blades, and therefore the nominal ^{235}U loading for a CE reduces to 178.57 g. At both sides of the CE, two absorber guide plates (aluminium) are installed. A fork type control rod (0.38 cm thick Ag-In-Cd absorber meat with SS-321 cladding) can be inserted into or withdrawn out of the CE.

The full configuration of the first core of RSG GAS consists of 12 fresh FEs and 6 CEs while the configuration for the first criticality needs only fresh 9 FEs and 6 CEs. First, estimation of the number of FEs and CEs required for the first criticality was conducted. Six control fuel elements were first loaded in the core with the absorber plates were all fully inserted. ^{252}Cf neutron source was then inserted at the E-7 grid position to initiate fission chain reactions, and then loading of standard FEs was done step by step. At each loading step, the inverse multiplication rates were plotted for four control rod configurations to estimate the critical loading. The first core configuration when the first criticality was achieved is shown in Fig. 1. Thirdly, after first criticality, loading of FEs and reflector elements were conducted to achieve a full core configuration with sufficient excess reactivity for one core cycle. Following the excess reactivity loading, control rod calibrations were conducted for the six control rods with various methods. During the calibrations one can find many combinations of control rods' position which gave a critical core condition suitable for our Monte Carlo calculations. In the present work, the combinations of control rods' position occurred during control rod calibration with bank compensation method will be checked with Monte Carlo calculations.

Monte Carlo Calculations

The active part (7.71 x 8.1 x 60 cm^3) of both FE and CE were modelled as their exact geometry and dimensions while the top- and end-fitting of the elements were modelled in an approximate manner since their geometry are very complicated, that is, the structure materials were homogenised with water by volume weighting. Exact modelling approach was also taken for the active parts of the beryllium reflector elements, beryllium block elements and irradiation positions. Considering their complicated geometry, the core grid and bottom support were also treated approximately as for the top or end-fitting of fuel elements. This approximation did not deteriorate the accuracy of the Monte Carlo calculation results since it was applied in the non active parts of the core. The movable control rods (absorber blades) were modelled as their exact geometry and dimensions. Consequently, 60 cm water layer above the core had to be included in the calculation to provide enough space for the absorber blades when a control rod was fully withdrawn. Approximately 30 cm water layers were included below the core bottom support, and around the beryllium block and element reflectors. Vacuum boundary conditions were imposed on the outer boundary of the reactor system.

All Monte Carlo calculations in the present work were conducted with libraries from JENDL-3.1 and JENDL-3.2 for temperature of 300 K. The measured critical effective multiplication factors were corrected when the core isothermal temperature was not identical with 300 K. The total number of particles simulated was 600.000 for all cases considered.

Results and Discussion

Table 4 shows the comparison between experiment data and Monte Carlo calculation results for first criticality and excess reactivity of RSG GAS first core. The first criticality predictions by Monte Carlo method were very close to the experiment data, especially the one with JENDL-3.1 library. JENDL-3.2 library produced a slightly higher effective multiplication factor although the relative difference with the experiment data was still below 1 %.

For the full configuration of the RSG GAS first core, the (corrected) excess reactivity data and Monte Carlo calculation results also showed a good agreement. However, again JENDL-3.2 library gave a slightly higher effective multiplication factor. It should be noted here that the measured excess reactivity must be converted from $ to absolute value to get the (absolute unit) effective multiplication factor, and therefore, the accuracy depended on the accuracy of the calculated β_{eff} (=0.00765). No measured data were available for β_{eff} so that further assessment on the accuracy of the calculated β_{eff} was not possible. This factor contributed also in the difference between the experiment data and Monte Carlo results.

The total control rod worth shown in Table 4 was obtained by a simple arithmetic summation of single control rod worth, while the single control rod worth was measured by a reactivity meter with shim rod bank compensation method. It is well known that the interference between control rods to some extent may deteriorate the accuracy of the total control rod worth obtained by the summation of single control rod worth. Combined with the uncertainty of the calculated β_{eff} value, the Monte Carlo results can be judged to be well agreed with the experiment data.

Table 5 shows the comparison between Monte Carlo results with several critical conditions of the RSG GAS first core occurred during control rod calibrations. These critical conditions were achieved when the calibrated rod was fully inserted and the other rods were in a certain bank position. The measured critical conditions shown in the table were already corrected for the Joule effect (which turned out to be negligible) of the primary cooling pumps. It can be observed from the table that Monte Carlo results using JENDL-3.1 library gave excellent agreement with experiment data. JENDL-3.2 library results systematically produced slightly higher effective multiplication factors but still below 1 % differences.

The slightly higher effective multiplication factors calculated with JENDL-3.2 library are consistent with the evaluation reported by Nakagawa [19]. Firstly, it is attributed to the smaller ^{235}U capture cross sections in the unresolved region (below 30 keV) in JENDL-3.2 than the one in JENDL-3.1, and secondly, it was pointed out recently by Takano [20] that the thermal fission cross section of JENDL-3.2 was slightly higher than the one of JENDL-3.1. The latter is expected to influence the results predominantly.

3. Conclusion

The nuclear data and reactor physics activities in Indonesia, especially, in the National Atomic Energy Agency has been presented. In the nuclear data field, the

Agency is now taking the position of a user of the main nuclear data libraries such as JENDL and ENDF/B. These nuclear data libraries become the main sources for producing problem dependent cross section sets that are needed by cell calculation codes or transport codes for design, analysis and safety evaluation of research reactors. In the reactor physics field, besides utilising the existing core analysis codes obtained from bilateral and international co-operation, the Agency is putting much effort to self-develop Batan's codes for reactor physics calculations, in particular, for research reactor and high temperature reactor design, analysis and fuel management.

As an example of the reactor physics activity of the Agency, Monte Carlo benchmark calculations have been conducted on the first core of the Indonesian 30 MWth Multipurpose Reactor, RSG GAS. Vectorized, continuous energy Monte Carlo code, MVP, developed by JAERI combined with nuclear data derived from JENDL-3.1 and -3.2 libraries was used for the whole calculations and the results were compared with experiment data. Monte Carlo calculations with both JENDL-3.1 and -3.2 libraries produced k_{eff} values with excellent agreement to experiment data. Systematically, JENDL-3.2 library showed a slightly higher k_{eff} values than JENDL-3.1 library.

Acknowledgements

The author expresses his gratitude to the commissioning group of RSG GAS for providing the criticality experiment data, and to Mr. Nakano Yoshihiro, Department of Research Reactor, JAERI, for his collaborative work in the evaluation using the MVP code during the author stay in JAERI.

References

[1] LANL, "NJOY91.38, A Code System for Producing Pointwise and Multigroup Neutron and Photon Cross Sections from ENDF/B Evaluated Nuclear Data", PSR-171, RSICC (1992).
[2] Askew, J.R., Fayers, F.J. and Kemshell, P.B., "A General Description of the Code WIMS", Jour. of Brit. Nuc. Energy Soc., **5**, 4 (1966).
[3] Naito, Y. *et al.*, "MGCL-PROCESSOR: A Computer Code System for Processing Multigroup Constants Library MGCL", JAERI-M 9396 (1981).
[4] Shindo R., Yamashita K. and Murata I., "DELIGHT-7; One Dimensional Fuel Cell Burnup Analysis Code for High Temperature Gas-Cooled Reactors (HTGR)", JAERI-M 90-048 (1990).
[5] Teuchert, E., Hansen, U. and Haas, K.A., "V.S.O.P.; Computer Code System for Reactor Physics and Fuel Simulation", Jul-1649 (1980).
[6] Liem, P.H., "Batan-MPASS: A General Fuel Management Code for Pebble-Bed High-Temperature Reactors", Ann. of Nucl. Energy, **21**, 5 (1994).
[7] Tsuchihashi K., Ishiguro Y., Kaneko K., and Ido M., "Revised SRAC Code System", JAERI 1302 (1986).
[8] Mele, I. and Ravnik, M., "TRIGAP, A Computer Programme for Research Reactor Calculations", IJS-DP-4228 (1985).
[9] Wickert M., "Concept and Methods of the Program MAIN: Controlling the IAFUEL Program Cycle for Neutronic Calculations Regarding Research Reactor", Interatom Bericht/Report Ident-No: 54.07100.4 (1986).
[10] Liem, P.H., "Batan-FUEL: A General In-Core Fuel Management Code", Atom Indonesia, **22**, 2 (1996).

[11] Transport Methods Group, LANL, "MCNP4B, Monte Carlo N-Particle Transport Code System", CCC-660, RSICC (1997)
[12] Liem, P.H. *et al.*, "Fuel Management Strategy for the New Equilibrium Silicide Core Design of RSG GAS (MPR-30)", accepted to be published in Nuclear Engineering and Design.
[13] Bakrie, A., Liem, P.H. and Prayoto, "A Procedure for Searching the Equilibrium Core of A Research Reactor", 19-th Reduced Enrichment for Research and Test Reactor, Seoul, South Korea (1996).
[14] Liem, P.H., "Development of An In-Core Fuel Management Code for Searching Core Equilibrium Condition in 2-D Reactor Geometry (Batan-EQUIL-2D)", Atom Indonesia, **23**, 1 (1997).
[15] Liem, P.H., "Batan-PEU: Fuel Management Code for Pebble Bed HTGR with Peu A Peu Fuelling Scheme", Batan Seminar on HTR Technology and Application II, Jakarta (1995).
[16] Liem, P.H., "Design Procedures for Small Pebble-Bed High Temperature Reactors", Ann. Nucl. Energy, **23**, 3 (1996).
[17] Mori, T. and Nakagawa, M., "MVP/GMVP: General Purpose Monte Carlo Codes for Neutron and Photon Transport Calculations based on Continuous Energy and Multigroup Methods", JAERI-Data-Code 94-007 (1994).
[18] Shibata, K. *et al.*, "Japanese Evaluated Nuclear Data Library, Version-3, JENDL-3", JAERI 1319 (1990).
[19] Nakagawa, T. *et al.*, "Japanese Evaluated Nuclear Data Library, Version 3 Revision-2: JENDL-3.2", J. Nucl. Sci. Technol., **32**, 1259 (1995).
[20] Takano, H., Personal Communications (1997).
[21] LANL, "MCNPXS, Standard Neutron, Photon, and Electron Data Libraries for MCNP4B", DLC-189, RSICC (1997)
[22] Villarino, E.A., "MTR_PC V2.6", INVAP/CNEA, Argentina.
[23] Fowler, T.B. and Vondy, D.R., "Nuclear Reactor Core Analysis Code: CITATION", ORNL-TM-2496, Rev. 2 (1971).
[24] Little, Jr., W.W. and Hardie, R.W., "2DB User's Manual – Revision I", BNWL-831 Rev. 1. See also 2DBUM (2DB University of Michigan) documentation on tape.
[25] Little, Jr., W.W. and Hardie, R.W., "3DB User's Manual", documentation on tape.

Table 3. Reactor Main Design Data of RSG GAS.

General

Reactor Type	Pool Type
Fuel Element Type	LEU Oxide MTR
Cooling System	Forced Convection Down Flow
Moderator/Coolant	H_2O
Reflector	Be & H_2O
Maximum Power (MWt)	30

Fuel/Control Elements

Fuel/Control Element Dimension (mm)	77.1x81x60
Fuel Plate Thickness (mm)	1.3
Coolant Channel Width (mm)	2.55
No. of Plate per Fuel Element	21
No. of Plate per Control Element	15

Fuel Plate Clad Material	$AlMg_2$
Fuel Plate Clad Thickness (mm)	0.38
Fuel Meat Dimension (mm)	0.54x62.75x600
Fuel Meat Material	U_3O_8Al
U-235 Enrichment (w/o)	19.75
Uranium Density in Meat (g/cc)	2.96
U-235 Loading per Fuel Element (g)	250
U-235 Loading per Control Element (g)	178.6
Absorber Meat Material	Ag-In-Cd
Absorber Thickness (mm)	3.38
Absorber Clad Material	SS-321
Absorber Clad Thickness	0.85

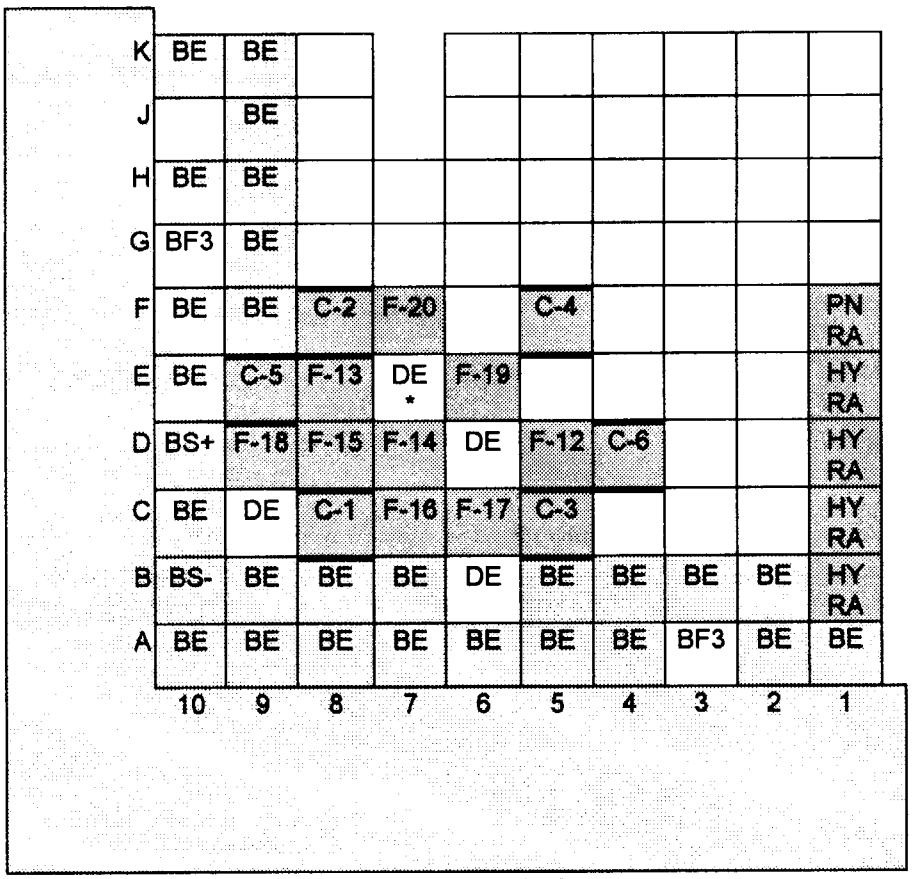

Beryllium Block Reflector

F	: Fuel Element	BS-	: Be Refl. El. without Stopper
C	: Control Element	BS+	: Be Refl. El. with Stopper
BE	: Be Reflector Element	DE	: Dummy Element
PNRA	: Pneu. Rabbit System	HYRA	: Hydraulic Rabbit System
BF3	: BF_3 Neutron Detector	*	: Neutron Source (Cf-252)

Figure 1. First criticality core configuration of the RSG GAS first core.

Table 1. Original and processed nuclear data installed in Batan (1997)

NUCLEAR DATA		PROCESSING CODE	SPECIFIC LIBRARY OUTPUT
ORIGINAL	PROCESSED		
	MGCL-137 (JAERI)	MAIL, REMAIL etc. [3] (JAERI)	• P_0, P_1 cross section library for transport code (ANISN-Jr)
ENDF/B-IV ENDF/B-VI JENDL-3.2		NJOY93.38 [1] (IAEA)	• Irradiation target, RI cross sections for WIMS/D4 library or for direct core calculation (Batan-FUEL code)
ENDF/B-VI			• MCNPXS (DLC-189) [21]
ENDF/B-IV ENDF/B-III		DELIGHT-7 [4] *) (JAERI)	• Operational parameters dependent cross section libraries for Batan-MPASS code (limited to HTR-200 Module)
ENDF/B-IV		V.S.O.P [5] *) (KFA-JULICH)	

*) Not available in Batan

Table 2. Reactor physics analysis codes used in Batan (1997)

ORIGIN	CODE NAME	CELL CALC.	CORE CALC.	FUEL MNGT.	APPLICATION In BATAN
JAERI (Japan)	SRAC-95 [7]	Yes	Yes	yes	• Research reactor analyses
CNEA/INVAP (Argentina)	MTR-PC [22]	Yes	Yes	yes	• Research reactor analyses
ANL (USA)	CITATION [23] 2-DB, 3-DB [24,25]	Yes	Yes		• Code verification
RSICC (USA)	MCNP-4B [11]	Yes	Yes		• Criticality calculation
J. Stefan Inst. (Ljubljana)	TRIGAP [8]		Yes	Yes	• Two Triga research reactors fuel management
Interatom/ Siemens	IAFUEL [9]			Yes	• RSG GAS (MPR-30) oxide core fuel management (present)
Batan (Indonesia)	Batan-FUEL [10]		Yes	Yes	• RSG GAS silicide core conversion program • RSG GAS silicide core fuel management • RPI-10 reactor design and fuel management
	Batan-MPASS [6]		Yes	Yes	• Pebble bed HTGR design and fuel management

Table 4. Comparison of Monte Carlo calculation results with experiment data for first criticality and excess reactivity of RSG GAS first core (300 K).

Core configuration		Experiment Data	Monte Carlo calculations	
			JENDL-3.1 MVP code	JENDL-3.2 MVP code
First criticality (9 FEs, 6 CEs, RR=475 mm)	K_{eff}	1.0	0.999780±0.001136	1.00919±0.00123
	C/E		1.000	1.009
Full core (9 FEs, 6 CEs, CRs all up)	K_{eff}	1.09242 a)	1.09531±0.00097	1.10177±0.00085
	C/E		1.003	1.009
Full core (9 FEs, 6 CEs, CRs all down)	K_{eff}	n.c. b)	0.917270±0.001198	0.924893±0.001168
	C/E		-	-
Control rods worth	$\Delta\rho$(%)	17.80 c)	17.72	17.36
	C/E		0.996	0.975

Note :

a) β_{eff} = 0.00765, excess reactivity was already corrected (see text)

b) n.c. = not conducted

c) Shim rod bank compensation method, measured by reactivity meter, summation of single control rod worth

Table 5. Comparison of Monte Carlo calculation results with several critical conditions of RSG GAS first core occurred during control rod calibrations (300 K).

Calibrated rod / grid position (calibrated rod position / other rod bank position)		Experiment data	Monte Carlo calculations	
			JENDL-3.1 MVP code	JENDL-3.2 MVP code
JDA06 / C-8	K_{eff}	1.00008 a)	0.998454±0.001370	1.00794±0.001171
(600 mm / 290 mm)	C/E		0.998	1.008
JDA01 / E-9	K_{eff}	1.00008	0.997867±0.001064	1.00811±0.001218
(600 mm / 284 mm)	C/E		0.998	1.008
JDA03 / F-8	K_{eff}	1.00008	1.00015±0.001174	1.00736±0.001144
(600 mm / 293 mm)	C/E		1.000	1.007
JDA05 / C-5	K_{eff}	1.00008	0.999951±0.001081	1.00775±0.001154
(600 mm / 288 mm)	C/E		1.000	1.008
JDA04 / F-5	K_{eff}	1.00008	0.998557±0.001175	1.00812±0.001217
(600 mm / 290 mm)	C/E		0.998	1.008
JDA07 / D-4	K_{eff}	1.00008	0.997683±0.001205	1.00493±0.001196
(600 mm / 282 mm)	C/E		0.998	1.005

Note: a) β_{eff} = 0.00765, excess reactivity was already corrected (see text)

2.3.2 Status of Nuclear Data Activities in Korea

LEE, Young-Ouk and CHANG, Jonghwa
Nuclear Data Evaluation Lab.
Korea Atomic Energy Research Institute
P.O. Box 105, Yusung, Taejon, 305-600, Korea
Phone: +82-42-868-2964 e-mail: yolee@lui.kaeri.re.kr

ABSTRACT

Although nuclear data activities in Korea are still in the early stage, considerable demands for more accurate and wide-range nuclear data from nuclear R&D fields activated a new nuclear data project titled as "Development of Nuclear Data System". It was launched this year as one of nation-wide long-term nuclear R&D programs in Korea for the next decade. Its main goals are 1) to establish nuclear data system, 2) to build up the infra-structure for utilization of nuclear data and 3) to develop highly reliable nuclear data system. To achieve these goals, international cooperation and cultivation of human resource as well as construction of measurement facilities will be indispensable. This report briefly describes the demands of nuclear data from the nuclear R&D programs, current nuclear data activities and future plan with its strategy.

I. Introduction

Nuclear power shares more than 40 % of the electric supply in Korea. There are now 10 PWRs and 2 CANDU plants in operation and 4 PWRs and 2 CANDUs under construction. Consequently Nuclear design technologies have been one of the most active research and development programs throughout the country. Nuclear design tool consists of the numerical method and the nuclear data. But the nuclear data, which is the basis of all the nuclear technologies, has not been paid as much attention as the numerical method in Korea. It was only several years ago that a consensus had risen in the fields of nuclear research and industries realizing the importance of the nuclear data[1]. It is now widely accepted in Korea that without the nuclear data technologies, research activities in the nuclear fields will not be able to catch up the contemporary level of the developed countries. The cultivation of human resources as well as the construction of the experimental facilities is also considered essential to participate the international cooperation for acquiring wide range of nuclear data. In the previous year's symposium, we outlined some of our nuclear data activities and future plan proposed as one of the nation-wide nuclear

R&D program. The plan has gone through many feedbacks and modifications in various aspects for the last 1 year, and finally launched this year for the next decade[2].

Following chapter describes shortly the demand of nuclear data from the related nuclear R&D programs in Korea. Current nuclear data activities, which are considered as the initiative step for the future plan, are briefly explained in chapter III. Our future plan and its strategy are explained in Chapter VI.

2. Demand for Nuclear Data

New long-term nuclear R&D program which was started this year in Korea consists of 33 projects, grouped as:

Nuclear reactor	: 2 projects
Reactor safety	: 6 projects
Nuclear fuel	: 4 projects
Waste treatment	: 4 project
Radioisotope	: 8 projects
Radiation protection	: 2 projects
Basic nuclear technologies	: 6 projects

The project "Development of Nuclear data system" belongs to "Basic nuclear technologies" group and all projects in the other 6 groups are more or less demanding the nuclear data.

As for the R&D on the nuclear reactor, reactor safety and nuclear fuel, high quality of nuclear data ensures accuracy of the nuclear design which is the key factor for the safety and efficiency of nuclear system. For example, insufficient/inaccurate nuclear data for decay heat, moderator temperature coefficient, radiation in the pressure tube, minor actinide cross sections for high burnup or MOX fuel and fission product yields lead to conservative design and accordingly undermine the economical efficiency of PWR when in operation. Introducing new poison material and high actnides require more accurate nuclear data than the currently used ones. Design of New type of reactor will demand wider range of nuclear data while the neutron scattering, absorption and fission cross sections under 5 MeV had been mainly studied for the existing reactor.

The accelerator-driven transmutation project, which is a major project in the waste treatment group, requires cross sections for the long-lived fission fragments with higher precision than those of the conventional power reactors. it also demands more measurements and much accurate nuclear reaction models for the the nuclear data of the spallation target and higher energy neutron/proton source.

Projects in the radioisotope and radiation protection groups also require highly precise nuclear data of neutron, proton and photon for the improvement of analysis.

Besides the direct demand for the nuclear data from the R&D programs mentioned

so far, Better knowledge and understanding on the nuclear structure and its reaction mechanism will improve public acceptance for the nuclear facilities and people working in those places.

III. Nuclear Data Activities

In this chapter, current nuclear data activities in Korea are introduced in three categories: data measurement, evaluation and processing. In fact, nuclear data activities in Korea are in the early stage. It was only at 1993 that the importance of the nuclear data was raised via the project "Strategy to establish nuclear data system for the nuclear design". Since then, Korea Atomic Energy Research Institute (KAERI)[3-5] has been taking the main role in the nuclear data activities as well as in other nuclear R&Ds.

As for the data measurement, there are only a few experiences. Nuclear structure data studied at universities and proton reaction data measured by cyclotron were the main measurement activities before 1990's. However, two major facilities had started their operation in 1995, HANARO reactor[5] and a light source from accelerated electrons at Pohang Accelerator Laboratory[6] (PAL). HANARO is a multi-purpose research reactor at KAERI. It is a pool type 30 MW reactor of which neutron flux level is 5E+14. On the other hand, PAL has a 150m-long LINAC to provide electrons to the storage ring. Three electron beam exits, from 100 MeV to 2 GeV, were prepared. In 1996, the conceptual study on the usage of Pohang Accelerator facility was initiated and its feasibility study was performed by KAERI and Pohang Accelerator Laboratory (PAL). It is expected that these facilities will promote the measurement activity in the future. Recently it is decided that the construction of a high energy proton accelerator will be initiated in 3 years. This facilities will widen the range of measurement activities in Korea.

As for the evaluation, a database construction has been the major work scope. Evaluated nuclear data have been collected since 1979 and processed for the domestic applications. Since 1994, Network system in World Wide Web (WWW) form has been developed to redistribute the collected nuclear cross sections and structure data[4]. Since then, the projects "Development of nuclear database", "Establishment of nuclear data system" and some other projects related to nuclear database system had been performed by KAERI. In 1996, necessary evaluation for the nuclear data the transmutation, accelerator and radiation therapy have been surveyed through the feasibility study of the construction of high energy proton accelerator.

For the evaluation work itself, many well known models and methodologies are under review in parallel with manpower buildup. Recently some of photonuclear reaction data have been evaluated for the target system of pulse neutron source using electron accelerator.

As for the processing of the evaluated data libraries, Korea has some experiences

through the conventional PWR projects and HANARO R&D. NJOY system has been used to process ENDF/B, JENDL and JEFF. WIMS/D library for HANARO and CANDU reactor is one of the major libraries produced. MCNP4A library was produced for HANARO simulation, CASMO library for Mixed Oxide (MOX) fuel research, and SPINX, TRANSX/MATX libraries for the fast reactor nuclear design. Also a benchmark test of evaluated Fe data for OECD/NEA is one of the examples in the processing activities.

IV. Long-term plan and its strategy

As one of 33 projects under New long-term nuclear R&D program, "Development of Nuclear Data System" has started this year for the next decade. The major goals for 3 stages are:

1) to establish nuclear data system,
2) to build up the infra-structure for the utilization of nuclear data,
3) to develop highly reliable nuclear data system, respectively.

In the Table, main activities were listed in three categories, for each 3 stage. This project will provide a firm foundation for the future nuclear R&D fields in Korea.

For the actual performance, some strategies are set up as follows:

Measurement

- request domestic or foreign laboratories for the required measurements
- perform feasibility and validity study for the construction of pulse neutron source using proton and electron accelerators.
- consign development of detector system in HANARO to domestic universities

For 100 MeV electron accelerator

- utilize the infra-facilities and specialties of PAL
- design target assembly in cooperation with RPI, KURRI, JINR
- develop data aquisition system in PAL
- design detectors in cooperation with domestic universities and laboratories
- consign safety analysis to PAL and domestic Institutes

Evaluation

- periodically introduce nuclear DB in cooperation with OECD/NE and IAEA/NDS to derive necessary nuclear data for the R&D project in Korea
- cooperate with JAERI, KURRI, BNL, LANL, RPI, ECJRC IPPE, and CIAE to acquire latest measurements and evaluated data
- develop nuclear models and codes to produce nuclear data for Nuclear R&D in Korea

Processing

- improve processing and validation methodologies, develop multi-group libraries to

Table. Main activities in the long-term project "Development of Nuclear Data System"

	stage I (1997-2000)	stage II (2001-2004)	stage III (2005-2006)
Goal	**Establish nuclear data system**	**Building up infra-structure**	**Develop reliable nuclear data system**
Evaluation	-Database setup -Data supply -Model develop (intermediate energy)	-Stable isotope -Improve model (intermediate energy)	-Fission data -Fission fragment -Spallation data
Measurement (activities)	-Poison/structural mat. (HANARO) -Proton reaction (Cyclotron)	-Fission/Neutron Capture -Intermediate energy data	-Polarized neutron -Fission fragment
(facilities)	-Feasibility Study	-Lead slowing down asm. -100 MeV Accelerator	-Develop spallation facility
Processing	Neutron data	Proton data	Breeder/ Transmutation

support long-term nuclear R&D projects.
- consider cooperation with JAERI and OECD/NEA to validate processed libraries
- develop validation technique by sensitivity analysis experiments

V. Summary

In response to considerable demands for the more accurate and wide range nuclear data from the nuclear R&D fields, a new nuclear data project are launched this year as one of the long-term nuclear R&D projects in Korea for the next 10 years. Its main goals are: 1) to establish nuclear data system, 2) to build up the infra-structure for the utilization of nuclear data, 3) to develop highly reliable nuclear data system. To achieve these goals, the international cooperation and the cultivation of human resource as well as the construction of the measurement facilities will be indispensable.

References

[1] Cho N.Z., "Nuclear Energy Policy and R&D Prospects: The Korean Case", Proc. Int. Conf. on the Physics of Reactors (PHYSOR 96), Vol. 1, O-21. Sept. 16-20, 1996. Mito, Japan

[2] Mistry of Science and Technology Korea (1997), "1997 Request for Project on Long-Term Nuclear R&D Program"

[3] http://www.kaeri.re.kr

[4] http://hpngp01.kaeri.re.kr

[5] http://hanaro.kaeri.re.kr

[6] http://pal.postec.ac.kr

2.3.3 Progress of International Evaluation Cooperation

Keiichi SHIBATA
Nuclear Data Center, Japan Atomic Energy Research Institute
Tokai-mura, Naka-gun, Ibaraki-ken 319-11
e-mail: shibata@cracker.tokai.jaeri.go.jp

The international evaluation cooperation started to remove the differences among major nuclear data libraries such as JENDL, ENDF, and JEF. The results obtained from the cooperation have been used to improve the quality of the libraries. This paper describes the status of the ongoing projects and several remarkable results so far obtained from the projects already finished.

1. Introduction

It is eight years since the international evaluation cooperation started under the NEA Nuclear Science Committee. The objective of the cooperation was to remove the differences among major nuclear data libraries such as JENDL, ENDF, and JEF. Moreover, the problems common to the libraries have been also examined.

There are two working parties (WPs) under the NEANSC auspices, i.e., a working party on evaluation cooperation (WPEC) and a working party on measurements activities (WPMA). There exist four subgroups within the framework of WPMA: standards, activation cross section, inelastic scattering cross section of ^{238}U, and intermediate energy data. In WPEC, more than ten subgroups and two standing groups have been formed.

This paper summarizes the outcome obtained from the subgroup activities in WPEC as well as the status of the ongoing projects.

2. Outcome of WPEC

2.1 Comparison of evaluated data for ^{52}Cr, ^{56}Fe and ^{58}Ni [1]

Comparison of the cross section data for the three nuclei was made among the libraries JENDL-3, ENDF/B-IV, JEF-2 and EFF-2. It was found that the data on the ^{58}Ni(n,α) reaction were most discrepant, as shown in Fig. 1. As for ^{58}Ni, the (n,p) reaction cross section is almost comparable to the (n,n') cross section except for the threshold energies. An investigation showed that the discrepancy came from the use of different level density parameters. Therefore, a new subgroup was proposed to deal with the level density parameters for structural material nuclei.

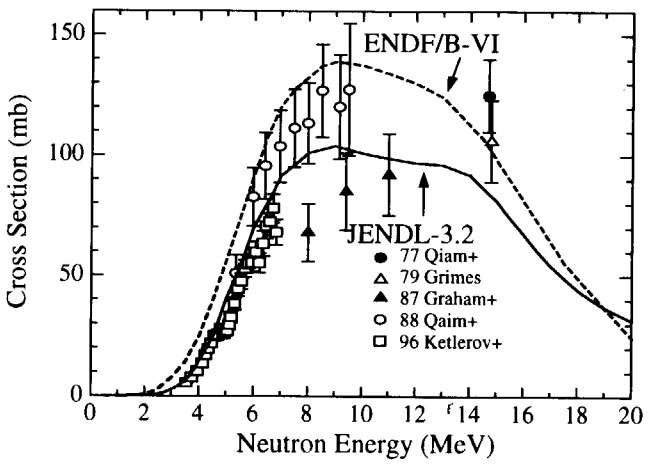

Fig. 1 ^{58}Ni(n,α) reaction cross section.

2.2 Generation of covariance files for ^{56}Fe and natural iron [2]

Covariances were generated by Japan, USA and EU with different methods. A large difference was shown among the results obtained. The subgroup did not draw any conclusion, but raised several problems concerning the data format and the covariances of nuclear model calculations.

2.3 Actinide data in the thermal range [3]

Thermal data on ^{232}Th, ^{233,235,238}U, and ^{239,240}Pu were reviewed. The energy dependence of η for ^{235}U was carefully examined. There had been a discrepancy of the η measurements between the Geel-ILL data [4,5] and Harwell-ORNL data [6,7] below 100 meV. The discrepancy was resolved by using a new measurement [8] of α at Geel and by R-matrix analyses using the resonance parameters given by Leal et al. [9] It was found that the η value should be energy-dependent below 100 meV. This energy dependence was also taken into account in JENDL-3.2, as shown in Fig. 2.

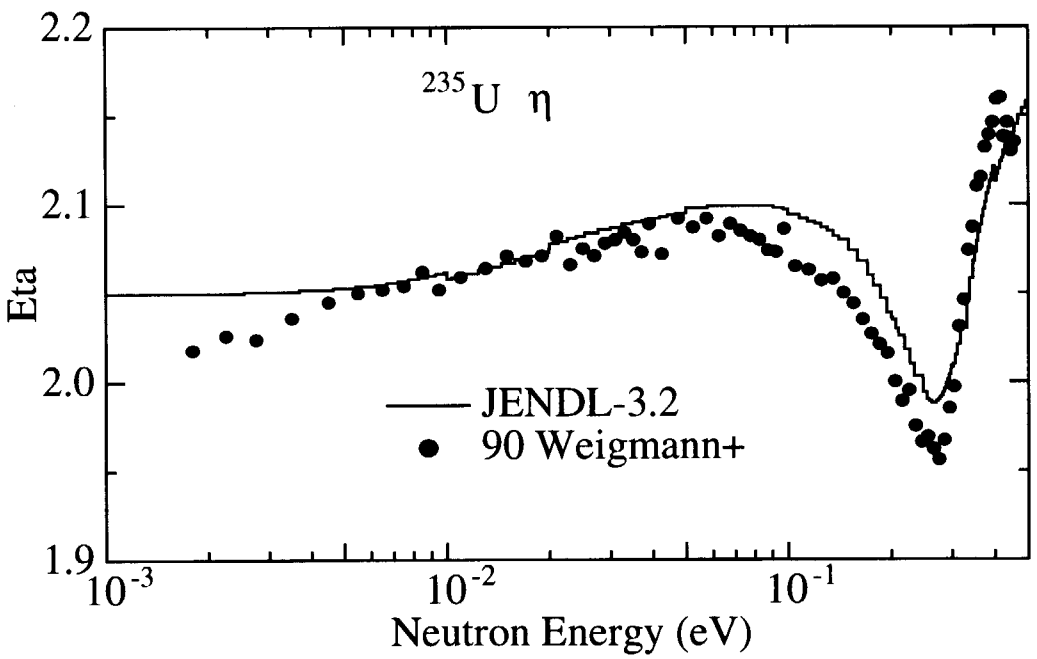

Fig. 2 η values of ^{235}U

2.4 Fission cross section of ^{239}Pu between 1 and 100 keV [10]

The fission cross section measured by Weston and Todd [11] was 5% lower than recent measurements and major evaluations in the energy region from 1 to 100 keV. This discrepancy led to two new experiments [12,13] at ORNL and Geel. The two measurements were consistent with each other giving the fission integral between 100 and 1000 eV, I_f = 9275 b•eV, but higher than the Weston-Todd data with I_f = 8996 b•eV. It was concluded that there was a normalization problem in the Weston-Todd experiment.

2.5 Cross section fluctuations and self-shielding effects in the unresolved resonance region [14]

The objectives of the subgroup were to understand the effects of self-shielding above the resonance region of structural materials, to determine the importance of a correct treatment of the effects, and to recommend procedures representing the physics in this region.

High resolution total cross section data on structural materials were measured at ORNL and Geel. It was found that the measured fluctuations of the iron total cross section is predicted by the Hauser-Feshbach theory, although the calculated relative spread is less than 10% above 4 MeV. The fluctuations of the measured cross sections above 4 MeV mainly come from counting statistics. Benchmark calculations [15,16] with and without fluctuations in the iron cross sections were performed at Petten and Frascati. The main result was that self-shielding effects are important up to 2 or 3 MeV, but negligible above 4 to 5 MeV. Therefore, the subgroup recommended that the high resolution data should be stored unsmoothed in data files up to 4 MeV. Above 4 MeV where self-shielding effects are not quite important, it is better to store smoothed cross sections.

3. Status of Ongoing Activities

3.1 ^{238}U capture and inelastic cross sections

The capture cross section was already fixed, but there is still an open problem for the inelastic scattering cross section. Prof. Kanda, the coordinator of the subgroup, proposed that the evaluation by V. Maslov [17] should be adopted. However, the WPEC has not reached the consensus of opinion yet. At present, it seems that there is nothing to do until new measurements appear. The WPEC concluded that a final report should be written and circulated to members of the subgroup.

3.2 FP inelastic cross sections

This subgroup started to investigate the inconsistency with the STEK integral experiments [18] for weak absorbers. In JENDL-3.1, no direct-interaction process was not taken into account. Considering the direct-interaction process with DWBA, the inelastic scattering cross sections of FP in JENDL-3.2 were much improved [19]. However, there is an opinion that the coupled-channel method should be extensively used. Figure 3 shows the ^{92}Mo(n,n$_1$) cross section. Between 2 and 3 MeV, the JENDL-3.2 data are larger than the latest measurements at Geel. The overshoot near the threshold might be due to the inappropriateness of DWBA. The applicability of DWBA is examined by the working group on evaluation and calculation system, Japanese Nuclear Data Committee, and recommendation would be given before the next WPEC meeting.

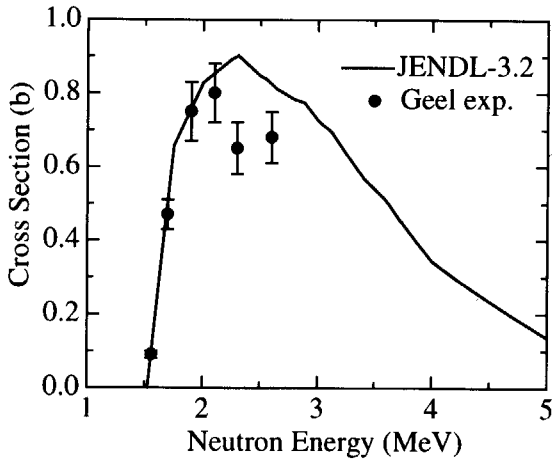

Fig. 3 ^{92}Mo(n,n$_1$) cross section.

3.3 Epithermal cross sections of ^{235}U

The subgroup aims at improving the accuracy of the ^{235}U capture cross section in the epihthermal region. Two preliminary evaluations, one by L. Leal et al. and the other by M.

Moxon, had been provided to the subgroup for testing. The most prominent difference was found in the g-factor for capture (0.99 for Leal et al. vs. 0.95 for Moxon). Final data will be provided for benchmark testing at ORNL and Cadarache. Table 1 summarizes the present status of ^{235}U data.

Table 1 Present status of ^{235}U data

	I_γ (b)	I_f (b)	α	$<\Gamma_\gamma>$ (meV)
Mughabghab[20]	144±6	275±5	0.523±0.24	
JENDL-3.2	134	279	0.478	35
ENDF/B-VI.2	133.5	279.1	0.478	35
Leal-Derrien	140	275	0.509	41.9

3.4 Delayed neutron data

The subgroup activity will be terminated after having identified the most important delayed neutron precursors for actinides, proposed a new representation of the time dependence more accurate than six groups, and written a report giving recommendations of the best delayed neutron yield data for major actinides. A new subgroup will start on the isotopes for transmutation and Th fuel cycle applications.

3.5 Intermediate energy nuclear data evaluation

The objectives of the subgroup were to investigate data needs, to recommend new measurements, to compile experimental data, to perform benchmark calculations, and to propose data format. Some of them were already achieved. However, the activity has become too vast for one group to deal with. Therefore, the group will be divided into several groups with small specific tasks.

3.6 Nuclear model validation

It was decided to limit the scope of the subgroup and to concentrate on the status of nuclear model codes used for evaluation work for incident nucleon energies below 150 MeV. After completing the work, the subgroup will be closed and a new one could be opened on a specific subject.

3.7 FP cross sections

The lumped one-group cross sections were compared, and systematic differences were found among data libraries. However, it was concluded that the status of the lumped cross sections is satisfactory for fast systems.

3.8 Minor actinide data

There had been no progress in the work. It was proposed to write a final report on the results available and to close the subgroup.

3.9 Resonance parameters of ^{52}Cr, ^{56}Fe, ^{58}Ni, and ^{60}Ni

There had been no progress in the work. The coordinator would be asked to write a final report.

3.10 Level density parameters of ^{52}Cr, ^{56}Fe and ^{58}Ni

There had been no progress in the work. The coordinator had written a draft report, and it would be reviewed for the final report.

3.11 Data for the Th fuel cycle

This subgroup has just started, but manpower is lacking.

4. Concluding Remarks

A brief review was given of the subgroup activities in the international evaluation cooperation. Useful results have been obtained, and some of them were already taken into account in the JENDL-3.2 evaluation. Some results will be considered in the new version JENDL-3.3. There are still open problems in nuclear data. New proposals for the international evaluation cooperation are anticipated.

References

[1] Fu C.Y. and Larson D.C.: "Comparison of Evaluated Data for Chromium-52, Iron-56 and Nickel-57", NEA/WPEC-1, OECD/NEA (1996).
[2] Vonach H. and Gruppelaar H.: "Generation of Covariance Files for Iron-56 and Natural Iron", NEA/WPEC-2, OECD/NEA (1996).
[3] Tellier et al.: "Actinide Data in the Thermal Energy Range", NEA/WPEC-3, OECD/NEA (1996).
[4] Wartena J.A. et al.: Report IAEA Tecdoc 491, 123 (1987).
[5] Wartena J.A. et al.: Report NEANDC(E) 312, III (1989).
[6] Moxon M. et al.: Proc. Int. Conf. Nuclear Data for Science and Technology, Mito 1988, p. 75 (1988).
[7] Moxon M. et al.: Private communication (1990).
[8] Weigmann H. et al.: Proc. Int. Conf. Nuclear Data for Science and Technology, Juelich 1991, p.38 (1992).
[9] Leal L.C. et al.: Nucl. Sci. Eng., **109**, 1 (1991).
[10] Fort E. and Salvatores M.: "Plutonium-239 Fission Cross Section between 1 and 100 keV", NEA/WPEC-5, OECD/NEA (1996).
[11] Weston L.W. and Todd J.: Nucl. Sci. Eng., **88**, 567 (1984).
[12] Weston L.W. et al.: Nucl. Sci. Eng., **115**, 164 (1993).
[13] Wagemans C. et al.: Nucl. Sci. Eng., **115**, 173 (1993).
[14] Froehner F.H. and Larson D.C.: "Cross-Section Fluctuations and Self-Shielding Effects in the Unresolved Resonance Region", NEA/WPEC-15, OECD/NEA (1996).
[15] Hogenbirk A.: ECN-C-95-045 (1995).
[16] Petrizzi L.: Private communication (1994).
[17] Maslov V. et al.: "U-238 Inelastic Scattering Cross Section", presented at Int. Conf. Nuclear Data for Science and Technology, Trieste 1997, to be published.
[18] Veenema J.J. and Janssen A.J.: ECN-10 (1976).
[19] Nakagawa T. et al.: J. Nucl. Sci. Technol., **32**, 1259 (1995).
[20] Mughagbghab S.F.: "Neutron Cross Sections", Vol. 1, Part B, Academic Press (1984).

2.3.4 Results from ISTC Frame Work

Tokio FUKAHORI
Nuclear Data Center, Japan Atomic Energy Research Institute,
Tokai-mura, Naka-gun, Ibaraki-ken, 319-11 Japan
e-mail: *fukahori@cracker.tokai.jaeri.go.jp*

Under International Science Research Center (ISTC) projects, JAERI Nuclear Data Center has been taking a role of collaborator and monitor for following items; 1) Measurement of the Fission Neutron Spectra of the Minor Actinides and Spontaneous Fission of Curium Isotopes (ISTC#183: V.I. Khlopin Radium Institute, KRI, St. Petersburg, Russia), 2) Measurement and Analysis of the Basic Nuclear Data for Minor Actinides (ISTC#304: Institute of Physics and Power Engineering, IPPE, Obninsk, Russia), and Evaluation of Actinide Nuclear Data (ISTC#CIS-3: Radiation Physics and Chemistry Problems Institute, RPCPI, Minsk, Belarus). These are related to the Japanese OMEGA Project and expected to supply minor actinide (MA) nuclear data, since Russia has good quality MA samples, experimental technique and nuclear data evaluation experiences. In this report, out-line and some results of above three projects are reviewed.

1. Introduction

International Science Research Center (ISTC) was organized in 1994 in order to support Russian nuclear scientists financially by governments of Japan, European countries and US after the former Soviet Union fell down. Under ISTC projects, JAERI Nuclear Data Center has been taking a role of collaborator and monitor for following items.

- ISTC#183: Measurement of the Fission Neutron Spectra of the Minor Actinides and Spontaneous Fission of Curium Isotopes (V.I. Khlopin Radium Institute, KRI, St. Petersburg, Russia, 1995-1997)
- ISTC#304: Measurement and Analysis of the Basic Nuclear Data for Minor Actinides (Institute of Physics and Power Engineering, IPPE, Obninsk, Russia, 1995-1997)
- ISTC#CIS-3: Evaluation of Actinide Nuclear Data (Radiation Physics and Chemistry Problems Institute, RPCPI, Minsk, Belarus, 1995-1997)

These are related to the Japanese OMEGA Project and expected to supply minor actinide (MA) nuclear data, since Russia has good quality MA samples, experimental technique and nuclear data evaluation experiences.

In this report, out-line and some results of above three projects are reviewed.

2. Measurement of the Fission Neutron Spectra of MA and Spontaneous Fission of Curium Isotopes

Experimental data of fission neutron spectra for curium isotopes were measured at V.I. Khlopin Radium Institute (KRI, St. Petersburg, Russia) as the ISTC project number of ISTC#183. For an example of obtained results, prompt neutron spectrum ratios of ^{244}Cm to ^{252}Cf obtained at the various experimental conditions are shown in **Fig.1**. This figure shows

the prompt neutron spectrum of ^{244}Cm is softer than that of ^{252}Cf.

3. Measurement and Analysis of the Basic Nuclear Data for MA

Various measurements and evaluations have been performed at Institute of Physics and Power Engineering (IPPE, Obninsk, Russia) under the ISTC project of ISTC#304. The project are divided into following five categories.

- Fission Cross Section Measurements for MA
- Measurements of Primary Fragment Yields for ^{237}Np
- Measurements of Inelastic Neutron Scattering and Prompt Fission Neutron Spectra for ^{237}Np
- Analysis of Discrepancies between the Evaluated Data for MA and Development of Improved Evaluations
- Measurements of Total Yields and Group Constants of Delayed Neutrons from Fast Neutron Induced Fission of ^{237}Np

Fission cross sections for ^{238}Pu, ^{242m}Am, $^{243, 244, 245, 246, 247, 248}$Cm were measured in the energy range of E_n=0.1～7 MeV. In **Fig.2,** the experimental results for ^{238}Pu fission cross section are compared with JENDL-3 and the other experimental data. The IPPE results has a tendency of slightly lower than the other experimental data. The JENDL-3 data are larger than the IPPE results in all energy region, especially above 4 MeV.

Primary fragment yields for ^{237}Np were measured in the energy range of E_n=0.8～5 MeV. Mass yields of fission products for ^{237}Np (n,f) at the incident neutron energy of 1, 5 and 18 MeV are shown in **Fig.3**. This result indicates mass distribution depends on the incident energy. The distribution goes to be symmetry according to incident energy increase. The result is very useful to obtain higher energy fission yield needed to estimate radioactivity after transmutation of MA waste by accelerator-driven system.

Inelastic neutron scattering and prompt fission neutron spectra for ^{237}Np were measured in the energy range of E_n=0.5～2.5 MeV. **Figure 4** shows the one of results of neutron spectrum for of ^{237}Np as well as evaluated nuclear data files. Both experimental and evaluated data are almost in good agreement.

Analysis of discrepancies between the evaluated data for MA was done and nuclear data evaluation was improved. The neutron total cross section for ^{237}Np is compared with experimental data and different evaluations in **Fig.5.** It can be obtained JENDL-3 evaluation cannot reproduce the recent IPPE experimental data while ENDF/B-VI and IPPE evaluated data agree with the experimental data. **Figure 6** shows comparison of the evaluated fission cross sections for ^{243}Cm with experimental data. Only new IPPE evaluation can reasonably reproduce the recent experimental results.

Total yields and group constants of delayed Neutrons from fast neutron induced fission of ^{237}Np were measured and dependence of the total delayed neutron yield for ^{237}Np fission on incident neutron energy is shown in **Fig.7**. It seems that tendency of energy dependent delayed neutron yield of JENDL-3 does not agree with the IPPE evaluation.

4. Evaluation of Actinide Nuclear Data

Actinide nuclear data were evaluated by Radiation Physics and Chemistry Problems Institute (RPCPI, Minsk, Belarus) under the ISTC project of ISTC#CIS-3. Following three items were obtained as the results.

- Missing excited levels were estimated by using Soft Rotator Model
- Multi-chance fission cross sections were evaluated simultaneously with other reaction channels like (n, γ), (n,n') and (n,2n) reactions.
- A problem of continuum inelastic scattering spectra in JENDL-3 was pointed out.

An example of missing excited levels estimated by using Soft Rotator Model are shown in **Fig.8** as a level scheme for ^{246}Cm compared with experimental data (ENSDF). Levels shown by solid line are stored in ENSDF database and those of dashed line are newly estimated. The result seems to be reasonable and is useful to calculate discrete inelastic scattering data.

Multi-chance fission cross sections were evaluated simultaneously with other reaction channels like (n, γ), (n,n') and (n,2n) reactions. For an example, the evaluated results of ^{242}Pu fission cross section are shown in **Fig.9** with experimental data. The evaluated result can reproduce the various experimental data. This approach makes evaluation consistent with the calculation of the other reaction channels.

During the evaluation process, a problem of continuum inelastic scattering spectra in JENDL-3 was pointed out. **Figure 10** shows the neutron spectra of continuum inelastic scattering for ^{235}U at incident neutron energy of 8 MeV as an example. The JENDL-3 spectrum distributes below about 2 MeV where emitted neutrons from (n,2n) reaction channel, since decay should go the father neutron emission process after low energy neutron emission. The evaluated data of JENDL-3 partly includes the emitted neutron of (n,xn) reactions (x=2,3,...). This caused by compilation error. This problem is not serious for ordinary calculations such as reactor design and shielding and will be solved in the JENDL-3.3 evaluation stage.

5. Summary

Various MA nuclear data are obtained under ISTC project. Here results from only three projects, which were reviewed and reported to JAERI Nuclear Data Center, were introduced. They are useful for producing JENDL Actinide File needed to OMEGA project. Final reports from all the institutes are available at Nuclear Data Center, JAERI. Many of other projects related to nuclear data are reported to other laboratories, institutes, organizations, etc. They are also useful and available.

"ISTC#609: Neutron Induced Fission Cross Sections of Some Actinides and Other Heavy Nuclei in Energy Region 1-200 MeV (Khlopin Radium Institute & Petersburg Nuclear Physics Institute, St. Petersburg, Russia)" is now on going. Other projects under ISTC framework will be done not only for nuclear data but also for other nuclear engineering field.

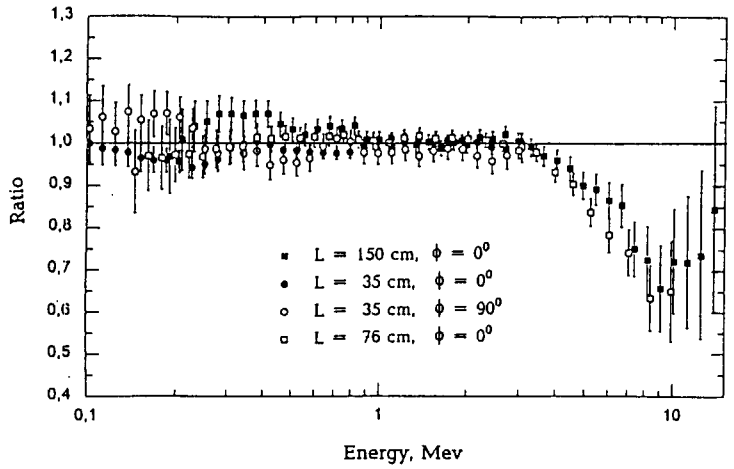

Fig.1 Prompt neutron spectrum ratios of ^{244}Cm to ^{252}Cf obtained at the various experimental conditions. L is flight path and ϕ is angle relative to fission chamber axis.

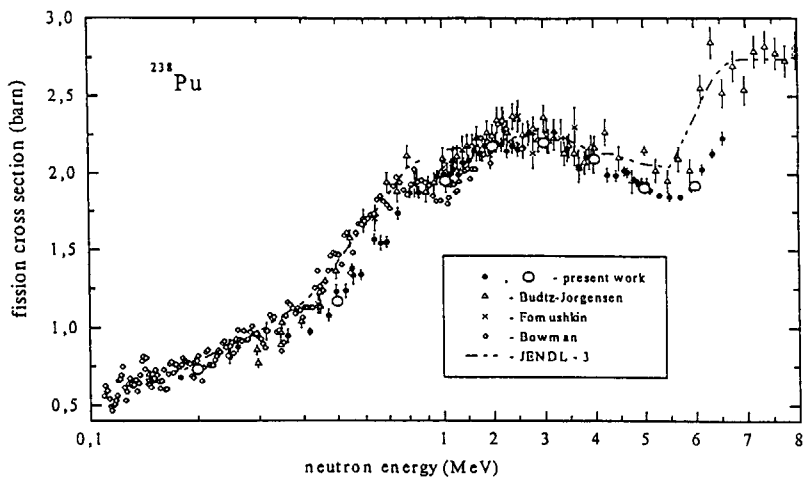

Fig.2 ^{238}Pu fission cross section.

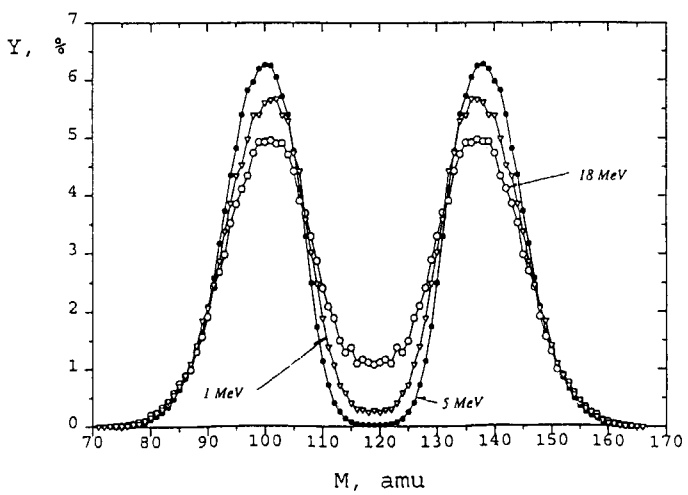

Fig.3 Mass yields of fission products for ^{237}Np (n,f) .

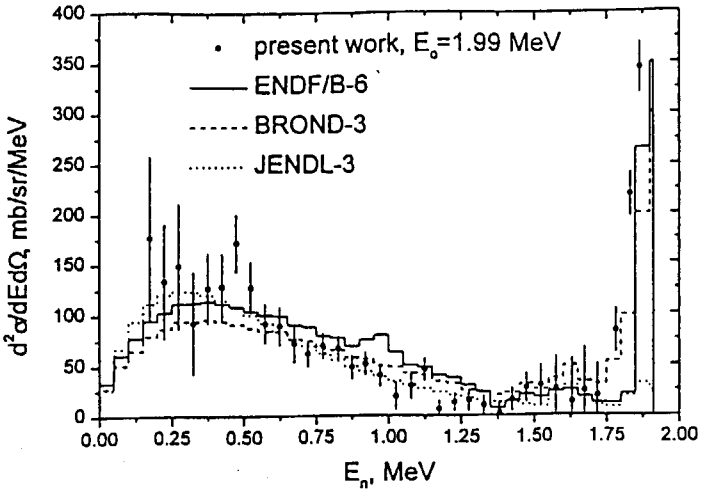

Fig.4 Neutron spectrum for neutron induced reaction of ^{237}Np.

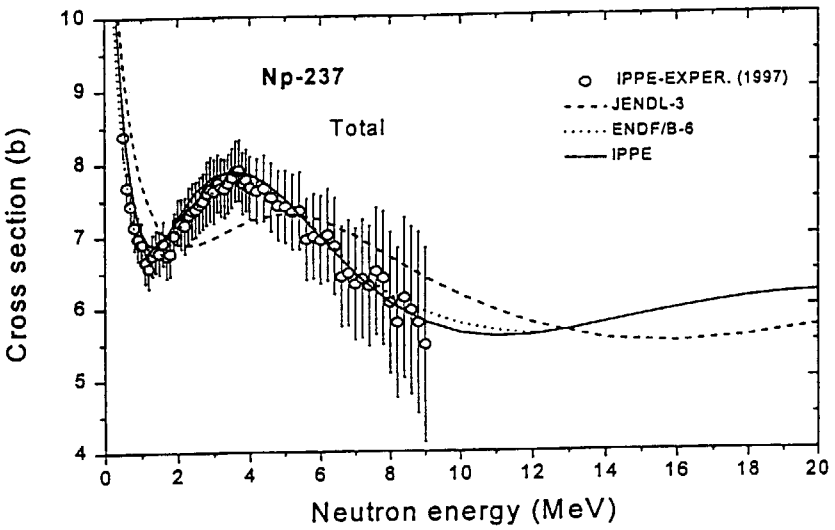

Fig.5 Comparison of the neutron total cross section for ^{237}Np with experimental data and different evaluations.

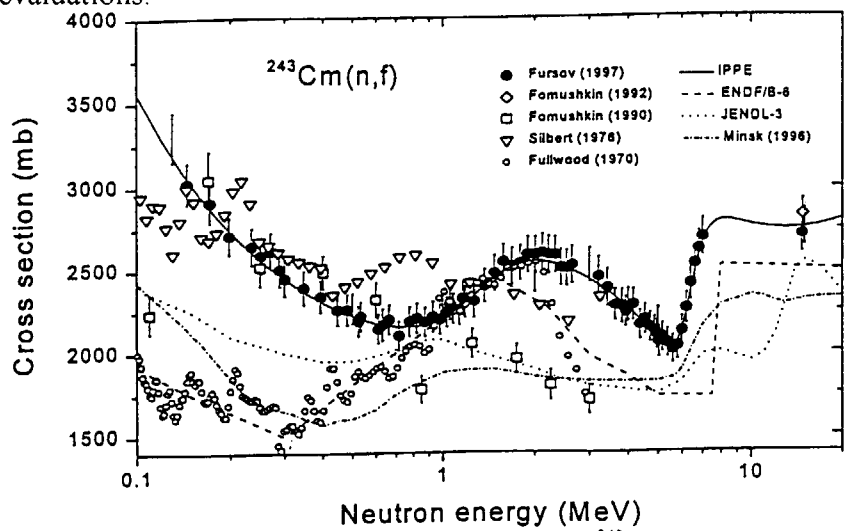

Fig.6 Comparison of the evaluated fission cross sections for ^{243}Cm with experimental data.

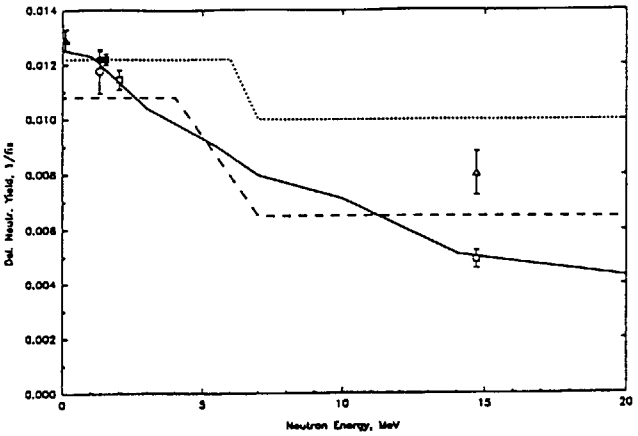

Fig.7 Dependent of the total delayed neutron yield for ^{237}Np fission on incident neutron energy. Solid line shows present evaluation, dashed line ENDF/B-VI, and dotted line JENDL-3, open squares Koldobskij evaluation, closed triangles Saleh's experimental data, closed circles Benedetti's experimental data, open circle and triangles Gudkov's experimental data, and closed square Cesana's experimental data.

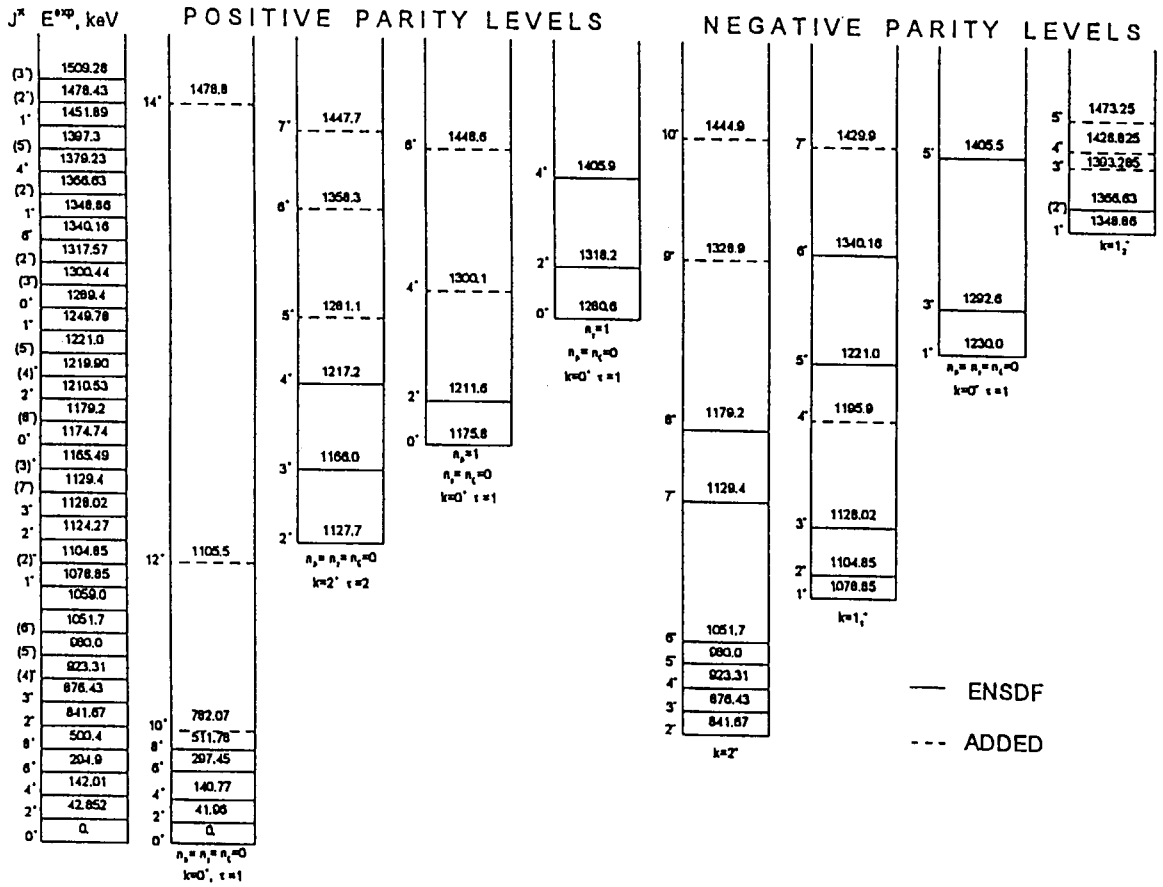

Fig.8 Level scheme for ^{246}Cm estimated by the soft rotator model with experimental data (ENSDF).

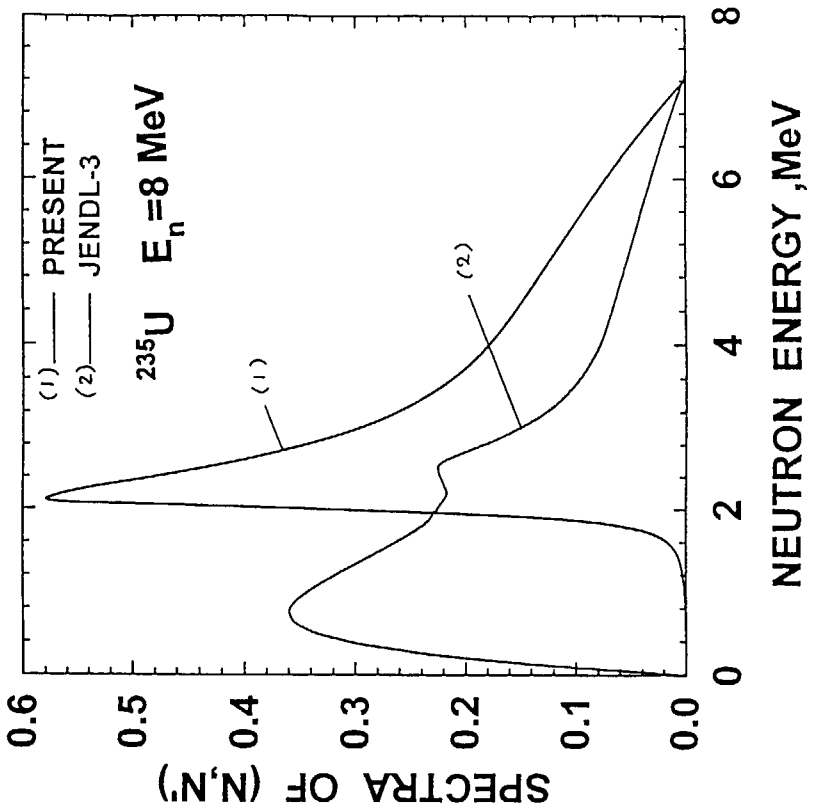

Fig.10 Neutron spectra of continuum inelastic for ^{235}U.

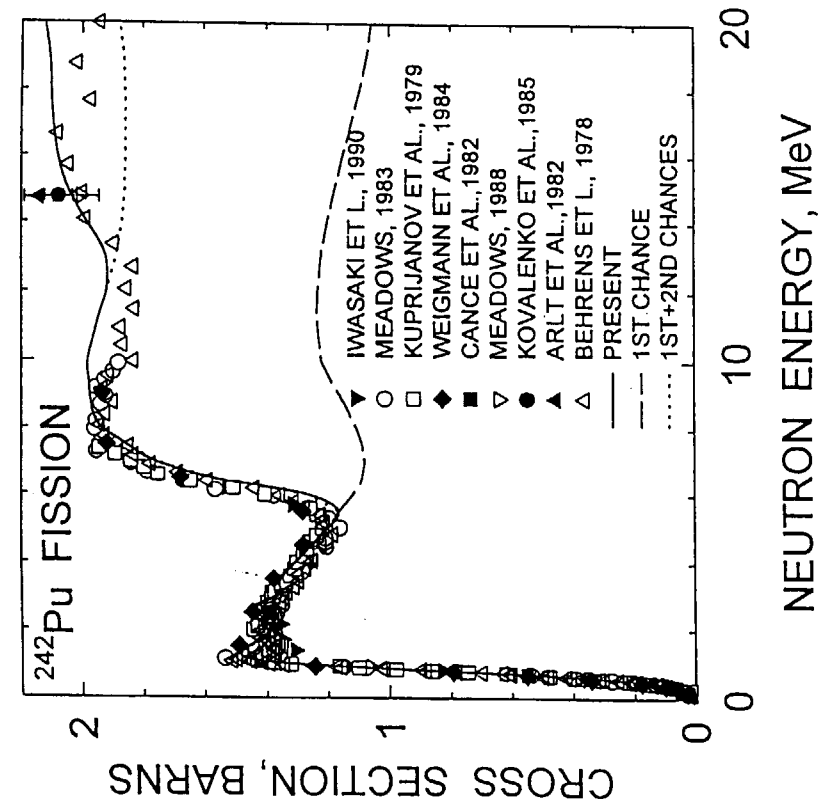

Fig.9 ^{242}Pu fission cross section.

2.4 Fission Reactor Application

2.4.1 Nuclear Characteristics of Pu Fueled LWR and Cross Section Sensitivities

Toshikazu TAKEDA
Dep. of Nuclear Engineering, Osaka Univ., Suita 565, Japan

The present status of Pu utilization to thermal reactors in Japan, nuclear characteristics and topics and cross section sensitivities for analysis of Pu fueled thermal reactors are described. As topics we will discuss the spatial self-shielding effect on the Doppler reactivity effect and the cross section sensitivities with the JENDL-3.1 and 3.2 libraries.

1. Introduction

As the critical experiments for obtaining data of nuclear characteristics of Pu fueled LWRs the VENUS program (VIP) and the MISTRAL program were conducted. For the VIP, there are BWR and PWR cores both of which have a central PuO_2 test zone surrounded by a driver zone of UO_2. To obtain data for large Pu-thermal reactors the MISTRAL program was launched in 1996, which has 7.0% MOX fuel. In addition to the critical experiments a few MOX assemblies were loaded into MIHAMA-1, and TSURUGA-1, and the integrity of the irradiated fuel assemblies were investigated. The nuclear characteristics of Pu fueled thermal reactors are presented from the points of Pu cross sections at thermal and resonance regions.

As topics we will discuss the spatial self-shielding effect on the Doppler reactivity effect and the cross section sensitivities. When the spatial distribution of the self-shielding effects within fuel rods and the spatial temperature distribution are taken into account, the Doppler reactivity effect was decreased by about 20%. The k-inf values of Pu-fueled cells are calculated using the nuclear libraries JENDL 3.1 and 3.2, and the results are compared for cells with various moderation ratios. In general the agreement is good, but there are some points where the k-inf behavior vs. void fraction is different for the JENDL 3.1 and 3.2.

2.Critical experiments for Pu-thermal reactors

2.1 VIP-PWR-MOX program[1]

The VENUS International Program (VIP) PWR MOX fuel critical experiment was performed as a joint research program among the utilities and vendors in nuclear industry in Japan and European countries. The aim is to obtain nuclear physics data for validating the nuclear design codes against high-plutonium content PWR/MOX fuels. The feature of the experiment was that wide variety of Pu content was investigated(Pu^{tot}: 14.4/9.7/5.4wt%) so that the range of Japanese PWR MOX utilization plan, and typical light water reactor plutonium composition(Pu^f/Pu^{tot}~70wt%) were both covered. The critical experiment was performed using the VENUS critical facility located at SCK/CEN in Mol, Belgium. The geometry of the critical experiment simulated a configuration of 17 × 17-type MOX and UO_2 PWR assemblies(Fig.1). This experiment was composed of two mockups: MOX mockup, in which a standard MOX assembly was loaded at the center of the core, and MOX-gadolinium mockup, in which a MOX-gadolinium assembly including 20 UO_2 fuel rods bearing Gd_2O_3 was loaded at the center of the core.

Table1 shows the comparison of the criticality between the measurement and 2-D calculations using SIMULATE-3. There is a considerable difference among the calculational models applied in the code. However, the use of the improved SIMULATE model leads to good results. Fig. 2 describe the comparison of power distributions in the MOX-gadolinium mockup obtained from CASMO-4 code. A good agreement is seen inside the MOX-gadolinium assembly; the rms. error is less than 2%. Figures 3 and 4 describe the comparison of power distributions obtained from SIMULATE-3 for the two mockups. Especially in the MOX-gadolinium assemblies in Fig. 4, a considerable difference is observed among the calculational models.

2.2 VIP-BWR-MOX program[2]

The critical core configuration is shown in Fig. 5. The test bundles and the reference bundles were arranged to simulate 8×8BWR lattices with 2×2 large central water holes. The moderator water density was reduced by 27%, to simulate the hot operating conditions, by inserting aluminum rods or tubes among fuel pins. The MOX fuels, for which fissile plutonium concentrations were 3.4-9.9 wt%, were loaded in the test bundles along with 14 pins of 7.2wt% Gd_2O_3-UO_2. For comparison, the experiments were also done using 3.3wt% UO_2 fuels with eight gadolinium pins in the test bundles. Table 2 shows the comparison of calculated k-eff to the measurement using CASMO-4 (C-4) and/or SIMULATE-3 (S-3). The C-4/S-3 results were somewhat less accurate compared with the full-core C-4 results because of difficulty in evaluating the amount of neutron leakage for such a small core by the nodal diffusion calculation. Fig. 6 describes the error distributions within the MOX and UO_2 test bundles, respectively. In the MOX core, the errors by C-4/S-3 were somewhat larger than the C-4 results along the MOX/UO2 bundle interface. This tendency can be attribute to the steep thermal flux gradient across at the interface. Table 3 gives the summary for the bundle-averaged fission rate. Although the results in the MOX core were slightly less accurate than those in the UO_2 core, the calculations and the measurements agreed very well.

2.3 MISTRAL program[3]

The MISTRAL program is an extended experimental program which was undertaken in the EOLE critical facility in a framework of cooperation between CEA, NUPEC and their industrial partners. The aim was to measure the main core physics parameters of 100% MOX loaded cores of light water reactors. Table 4 summarizes the four core configurations and the parameters to be measured. The main profile of the cores are:

Core1: a uranium core of homogeneous square lattice with H/HM (hydrogen to heavy metal atomic number ratio) ~5, which is a reference for MOX cores.

Core2: a 100%MOX core of homogeneous square lattice with H/HM~3, which us dedicated to obtain basic characteristics of the 100%MOX core with high moderator to fuel ratio.

Core 3: same as Core2, except that H/HM is ~6, which is dedicated to obtain the effect of increasing moderator to fuel ratio.

Core 4: a mock up core of an APWR loaded with 100% MOX.

The configuration of the Core 1 is shown in Fig. 7. The Core 1 has about 740 fuel rods located in a rod pitch of 1.32 cm, 16 guided tubes for safety rods and one guide tube for a pilot rod. The boron concentration was about 300 ppm and the core temperature was regulated to be 20℃.

The radial and axial fission rate distribution were measured with miniature fission chambers of ^{237}Np and ^{235}U, and integral gamma scanning technique of the fuel rods. An example of radial distribution measured by using the gamma scanning is shown in Fig. 8.

2.4 Demonstration experiments in commercial reactors

Several demonstration experiments have been conducted using commercial PWR and BWR reactors. In Tsuruga-1, two MOX fuel subassemblies were loaded and irradiated from 1986 to 1990[4]. In Mihama-1, four MOX fuel subassemblies were loaded and irradiated from 1988 to 1991[4]. The average burnup was 23.2-23.5GWd/t. For the both experiments, the post irradiation experiments were performed and the fuel performance under irradiation was investigated.

3. Core characteristics of Pu-thermal reactors

The nuclear characteristics of the MOX fueled LWR are strongly influenced by the difference of characteristics of plutonium compared with uranium: 1) larger absorption cross section at thermal and resonance energy , 2) smaller delayed neutron fraction, 3) the presence of ^{240}Pu, which absorption cross section is large, and so on. These tendencies lead to the following core characteristics which are common to the MOX fueled LWR:1) decreased worth of rod worth and boron, 2) increase of the magnitude of negative moderator temperature coefficient and Doppler coefficient, 3) local power peaking at the peripheral pins of the MOX assemblies, and 4) increase of internal conversion ratio owning to the production of ^{241}Pu from ^{240}Pu. Figure 9 shows the comparison of neutron spectrum in MOX and U fuels. It is seen that the fraction of thermal neutron is smaller in MOX fuel. This leads to the decreased worth of rod worth and boron, and increase of the

magnitude of negative moderator temperature coefficient and Doppler coefficient. In order to take into account the above mentioned tendency, several measures are taken in the reactor design: 1) increase of control rod by modifying the MOX loading pattern, and increase of boron concentration, 2) use of fuel pins with multiple Pu enrichments in a MOX subassembly to avoid the local power peaking problem, and so on. Figure 10 describes an example of pin arrangement in a MOX subassembly.

4. Topics and sensitivity analysis

4.1. Doppler reactivity[5]

The Doppler reactivity worth is usually calculated using self-shielded cross sections averaged over a fuel rod. This approximation of constant cross sections is satisfactory for fast reactor cells. However, for thermal reactor fuel cells, the self-shielding effect has space dependence within a fuel rod. Here there are three methods by considering the space dependence of temperature and cross sections within a fuel rod.

Method 1: The average self-shielded cross section is calculated by using the average temperature within a fuel rod. (This method is the commonly used method.)

Method 2: Space dependent cross section is calculated by dividing the fuel rod into 10 regions, however, the average temperature is used for calculating the cross section.

Method 3: Space dependent cross section is used with space-dependent temperature instead of the average temperature.

The space-dependence of the ^{238}U microscopic capture cross section shown in Fig.11 may have an effect on the capture rate, and so on the difference between capture rates of different temperatures, which is the main contribution to the Doppler reactivity worth. The difference between capture rates of different temperatures is shown in Fig.12.

The Doppler reactivity worth calculated by the three methods for the UO_2 cell and the MOX cell are shown in Table 5. The methods 1 and 2 produce almost the same results. The method 3 which uses the space-dependent self-shielded cross section and temperature leads to smaller Doppler reactivity. The Doppler reactivity worth is smaller by 15-18% than that for methods 1 and 2.

From the above results, we can conclude that it is important to take into account the space-dependence of the self-shielding and temperature within a fuel rod for calculating the Doppler reactivity worth in thermal reactor cells.

4.2 Comparison of k-inf calculated by JENDL-3.2 and 3.1 for Pu LWR cells

We calculated the k-inf factor for Pu LWR cells by using the continuous energy Monte Carlo code MVP[6] developed at JAERI, and the difference between JENDL-3.2 and 3.1 were investigated by changing the three parameters: ratio of moderator to fuel volume by changing the cell pitch, Pu enrichment and void fraction.

The results are shown in Fig.13. From this figure we can find that the difference of infinite multiplication factor between JENDL-3.2 and 3.1 becomes larger especially for 100% of void fraction. It is found that this difference comes from the following facts.

The difference of microscopic cross section of ^{238}U capture and ^{239}Pu fission between JENDL-3.2 and 3.1 are shown in Figs. 14 and 15 for Vm/Vf = 0.5 and void fraction = 80% case. As shown in Figs. 14 and 15, the difference of ^{238}U capture cross section is up to +5% at the resonance energy region, and for the ^{239}Pu fission cross section the difference is up to -14% at about 3keV. These facts cause the decrement of infinite multiplication factor of JENDL-3.2 compared to that of JENDL-3.1.

4.3 Sensitivity analysis

Burnup sensitivity analysis for LWR MOX cell based on transport theory were performed to obtain the sensitivity coefficient and the uncertainty. Table 6 shows the sensitivity coefficient for ^{241}Am number density at EOC(10GWd/t). It is obvious that the ^{241}Am number density at EOC becomes large if the ^{240}Pu capture cross section becomes large, thus the sensitivity coefficient becomes positive and large compared to the other cross sections. However by multiplying the difference of cross sections between JENDL-3.2 and 3.1, the uncertainty of ^{241}Pu fission cross section

has a large effect on the ^{241}Am number density at EOC. Fig.16 shows the energy dependence of the difference of ^{241}Pu fission cross section for ^{241}Am number density at EOC. It is found from this figure that the uncertainty of the cross section at about resolved resonance energy region(10eV-100eV) is dominant for the uncertainty of ^{241}Am number density at EOC.

References

(1) Saji, E., et al.: Nucl. Sci. Eng. 121, 52-56 (1995).
(2) Mori, M., et al: ibid., 41-51 (1995).
(3) Yamamoto, T., et al.: Proc. Int. Conf. on Future Nuclear Systems, Global 97', Oct. 5-10, Yokohama, Vol.1, p.395 (1997).
(4) Takeda, T., et al.: J. At. Energy Soc. Japan, 37[7], 561 (1995) (in Japanese).
(5) Takeda, T., et al.: J. Nucl. Sci. Technol., 33[7], 604 (1996).
(6) Mori., T., et al: MVP/GMVP: General purpose Monte Carlo codes for neutron and photon transport calculations based on continuous energy and multigroup methods, JAERI-Data/Code 94-007, (1994).

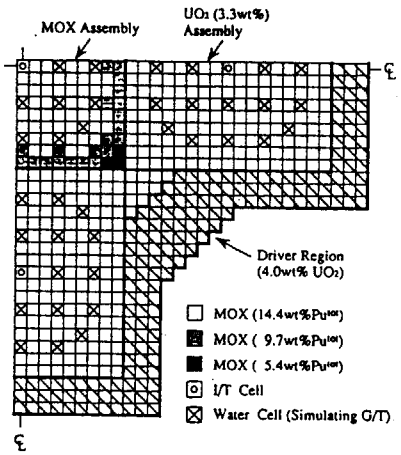

Note: A MOX-Gd fuel assembly including 20 UO_2 fuel rods bearing Gd_2O_3 was loaded at the center of the MOX-Gd Mock-up core.

Fig. 1 Configuration of the VIP-PWR MOX mockup

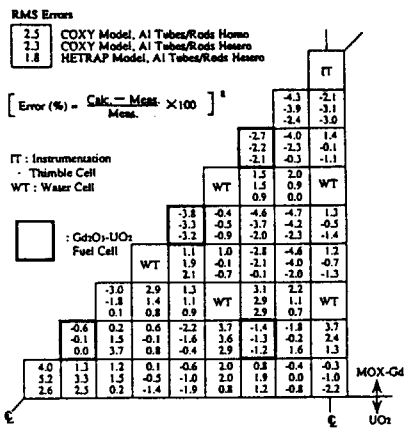

[a] Both the measured and the calculated fuel rod power distributions are normalized to unity inside each fuel assembly

Fig. 2 Errors of calculated fuel rod power distribution by CASMO-4 inside the MOX-gadolinium assembly

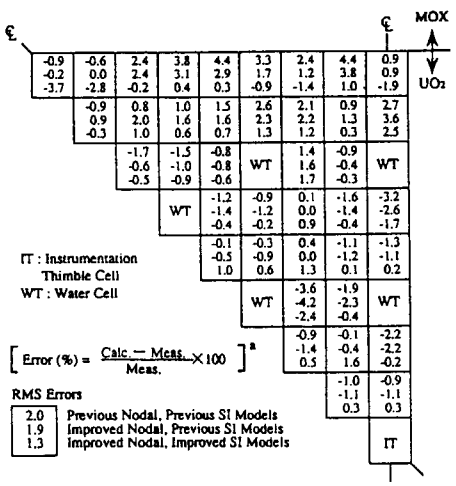

[a] Both the measured and the calculated fuel rod power distributions are normalized to unity inside each fuel assembly

Fig. 3 Errors od calculated fuel rod power distribution by SIMULATE-3 inside the UO_2 assembly

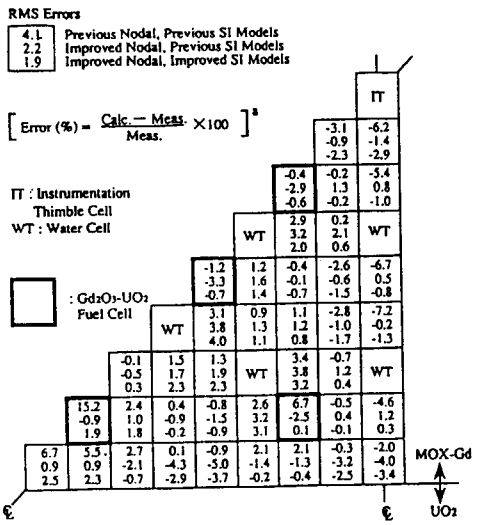

[a] Both the measured and the calculated fuel rod power distributions are normalized to unity inside each fuel assembly

Fig. 4 Errors od calculated fuel rod power distribution by SIMULATE-3 inside the MOX-gadolinium assembly

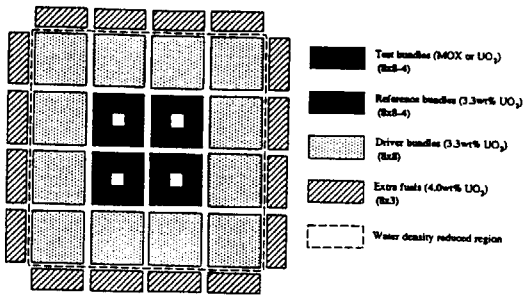

Fig. 5 Critical core configuration

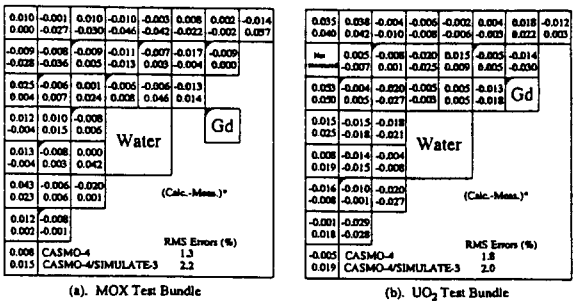

Fig. 6 Differences in fission rate distributions in the test bundles between calculations and measurements

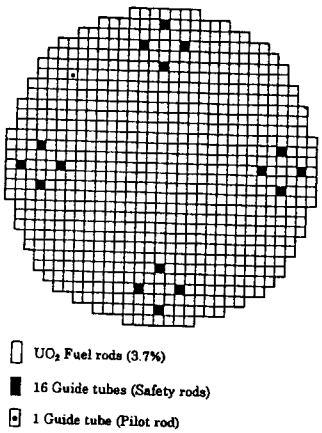

Fig. 7 Core configuration of Core 1

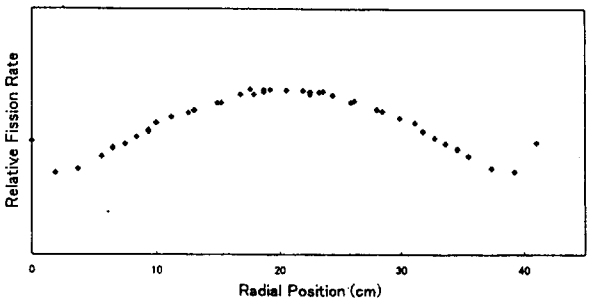

Fig. 8 Measured radial fission rate distribution

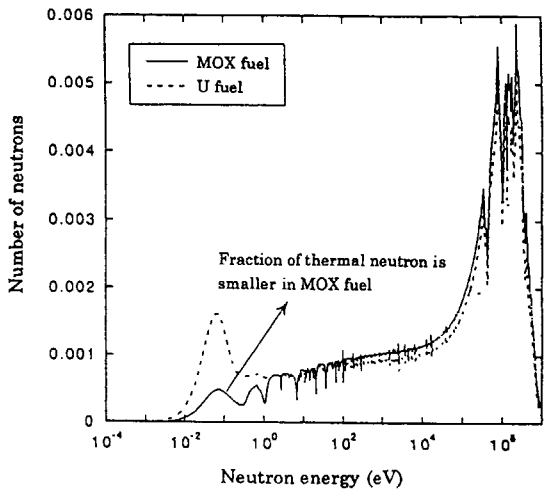

Fig. 9 Neutron spectrum for UO_2 and MOX fuel

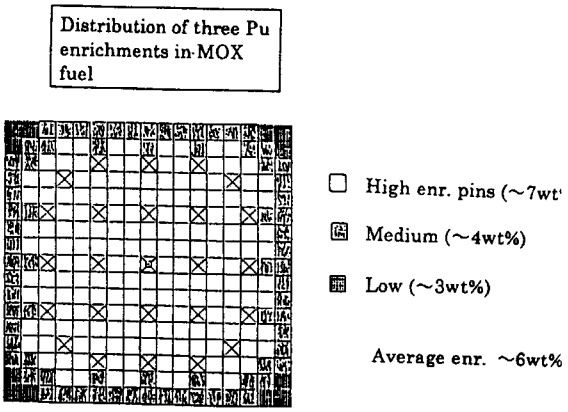

Fig. 10 Distribution of Pu enrichment for MOX assembly

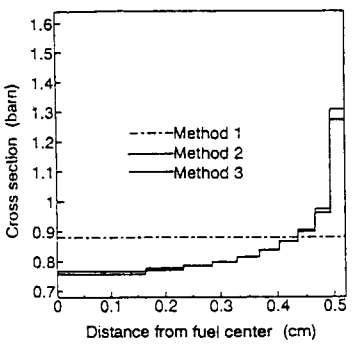

Fig. 11 Space dependence of ^{238}U capture cross sections for UO_2 fuel

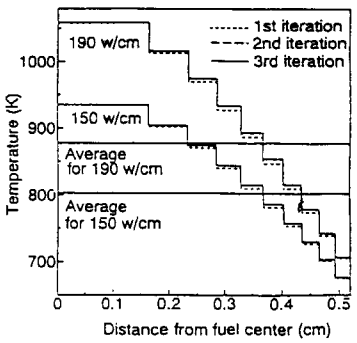

Fig. 12 Temperature distribution within a UO_2 fuel

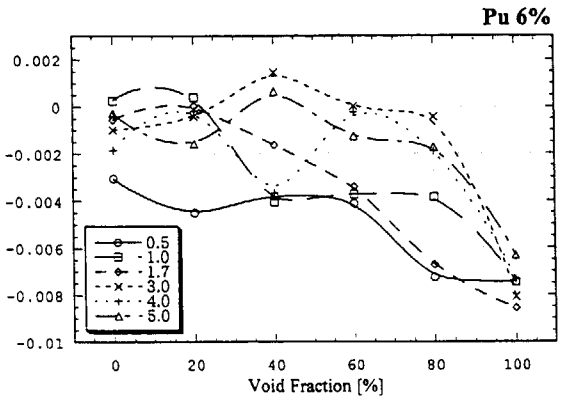

Fig. 13 Difference of k_{inf} in % between JENDL-3.2 and 3.1

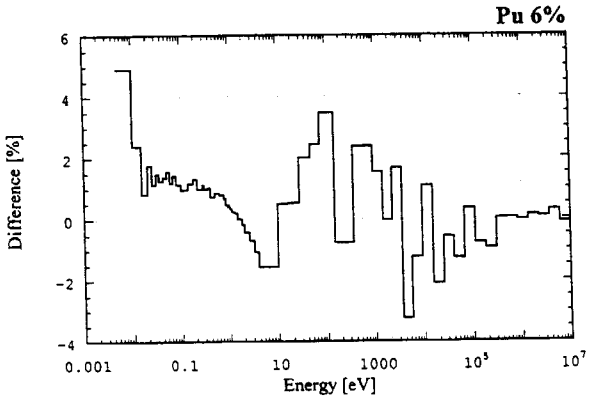

Fig. 14 Difference of ^{238}U capture cross section between JENDL-3.2 and 3.1

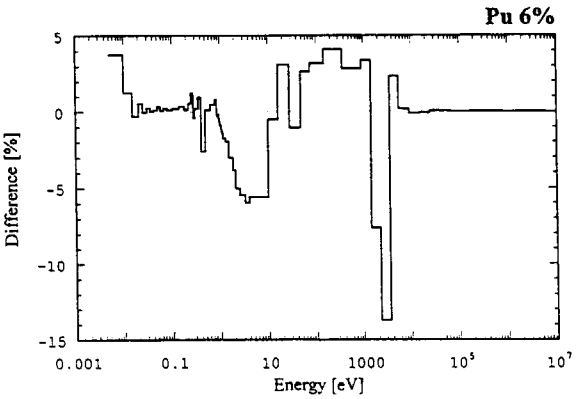

Fig. 15 Difference of ^{239}Pu fission cross section between JENDL-3.2 and 3.1

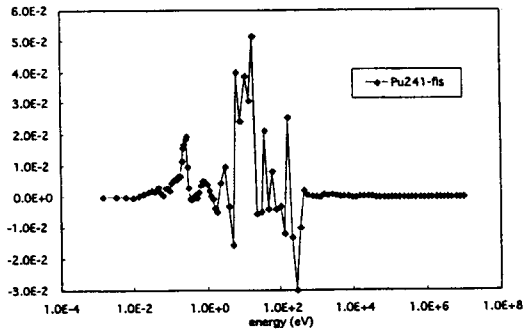

Fig. 16 Energy dependence of the difference of ^{241}Pu fission cross section for ^{241}Am number density at EOC

Table 1 Calculated k_{eff} by SIMULATE-3

SIMULATE-3 Models		Calculated k_{eff} (Error % $\Delta K/K$)	
Nodal Models	SI Models	MOX Mockup Core	MOX-Gadolinium Mockup Core
Previous	Previous	1.009(+0.9)	1.007(+0.7)
Improved	Previous	1.008(+0.8)	1.006(+0.6)
Improved	Improved	1.003(+0.3)	1.000(0.0)

Table 2 Comparison of the calculated eigenvalues

Cases	C-4[a]	C-4/S-3[b]
MOX core	1.0014	0.9937
UO_2 core	1.0014	0.9921

[a]Full-core transport calculation.
[b]Nodal diffusion calculation with single-bundle C-4 constants.

Table 3 Bundle-averaged fission rate

Cases	Measured	Calculated by C-4/S-3
MOX core		
UO_2 reference bundle / MOX test bundle	1.160 / 0.840	1.153 / 0.847
UO_2 core		
UO_2 reference bundle / UO_2 test bundle	1.147 / 0.853	1.147 / 0.853

Table 4 Core confugurations and measured parameters in the MISTRAL program

	Core-1	Core-2	Core-3	Core-4
Volumetric Moderation Ratio	~1.8	~1.8	~2.1	*to be defined*
Atomic Moderation Ratio	5.11	5.15	6.21	*to be defined*
Fuel	UO_2-3.7%	MOX-7.0%	MOX-7.0%	MOX-7.0%
Critical Mass	O	O	O	O
Boron Concentration	O	O	O	O
Spectrum Indices	O	O	O	
Radial Power Distribution	O	O	O	O
Axial Power Distribution	O	O	O	O
Iso. Temp. Coef.	O	O	O	
Boron Worth	O	O	O	O
Absorber Worth	O	O	O	
Fuel Substitution	O	O	O	
Cluster Worth				O
2D Void			O	
$\beta_{effective}$	O	O		

Table 6 Sensitivity coefficient for ^{241}Am number density at EOC

	Each Term of Sensitivity Coefficient			Total Sensitivity Coefficient	Direct Calculation	Difference* (J3.1&J3.2) (%)
	Flux Term	Power Term	Number Density Term			
U238-capture	2.46e-6	0.0	1.89e-3	1.89e-3	5.18e-4	6.2e-4
Pu239-fission	6.37e-6	1.31e-1	-2.43e-3	1.28e-1	7.94e-2	6.3e-2
Pu240-capture	2.14e-6	0.0	2.81e-1	2.81e-1	1.79e-1	6.6e-2
Pu241-fission	1.67e-6	4.38e-2	-2.04e-1	-1.60e-1	-1.30e-1	3.1e-1

* (J32-J31)/J31 x (Sens. Coeff.) x100 (%)

Table 5 Doppler reactivity worths for each calculation method

	Method (1)	Method (2)	Method (3)
UO_2 cell	−2.704[†]	−2.718	−2.296
MOX cell	−3.139	−3.151	−2.730

[†] $10^{-5}\ \Delta k/k/°C$

2.4.2 Analysis of Reactivity Characteristics of the MONJU Initial Core Using JENDL-3.2

Kenji Sasaki*, Takayuki Suzuki*, Norimichi Suzuki* and Yoshihiko Itagaki**

* Reactor and Systems Engineering Sections, Monju Construction Office
Power Reactor and Nuclear Fuel Development Corporation
2-1, Shiraki, Turuga-shi, Fukui-ken, 919-12 Japan
E-mail: esasaki@monju.pnc.go.jp

** Tsuruga Office, Nuclear Energy System Inc.
2-1, Shiraki, Turuga-shi, Fukui-ken, 919-12 Japan

Abstract

This paper describes the evaluated results of criticality, absorber rod worth and coolant worth in the MONJU initial cores based on the JENDL-3.2[1] library compared with those of the JENDL-2[2] library. We confirm that the ratios of calculated and experimental (C/E) values using the JENDL-3.2 library are slightly better than those based on the JENDL-2 library.

1. Introduction

The Japanese prototype fast breeder reactor MONJU achieved initial criticality on April 5, 1994. Afterwards, the configuration of the initial full core loaded with 198 fuel sub-assemblies was completed on May 20, 1994. A series of core loading, criticality and physics tests[3] on the MONJU initial cores were carried out by November 1994. The principal design and performance data of MONJU and the schedule of these measurements show table 1 and table 2. In these tests, we measured criticality, absorber rod worth and coolant worth. We also measured fixed absorber worth and fuel worth. In addition, we carried out foil irradiations[4] and reactivity coefficient measurements. This paper describes the comparison of the C/E values for criticality, absorber rod worth and coolant worth of the MONJU initial cores based on the JENDL-3.2 library and those of the JENDL-2 library. The analyses were carried out by using the JUPITER (Japanese-United States Program of Integral Tests and Experimental Research under US DOE and PNC of Japan) analysis system[5] and the sensitivity analysis system.

2. Calculation Method

2.1 Analysis of Criticality and Reactivity Worth

The calculations of criticality, absorber rod worth and coolant worth were performed using the JUPITER analysis system. The flow scheme is shown in Fig.1. For the cell calculations, the SLAROM[6] code was used to produce 70 energy group effective cross-sections by inputting atomic number densities, geometries and the 70 energy group constant set JFS-3-J3.2[7] (referred to as J3.2 hereafter) based on the JENDL-3.2 library or JFS-3-RJ2(1989)[8] (referred to as J2 hereafter) based on the JENDL-2 library. For the reactor calculations, the CITATION[9] diffusion code (or TWOTRAN transport code) was used to evaluate the basic results of criticality and reactivity worth. The effective multiplication factor (k_{eff}) values were calculated by using the calculation methods shown in table 3. The final results were evaluated from the basic results by considering correction factors as shown in table 4.

2.2 Sensitivity Analysis

Reactivity changes when using J3.2 or J2 were investigated by the sensitivity analysis system. Its flow scheme is shown in Fig.2. The cross-sections were calculated by using infinite dilution cross-sections collapsed from 70 energy groups to 18 energy groups. The sensitivity coefficients were calculated by using the CITATION code and the SAGEP code.

3. Measurements and Calculation Results

3.1 Criticality

3.1-1 Measurements

The fuel loading of MONJU was started in October 1993. The first sub-assemblies to be loaded into the core were two auxiliary neutron source assemblies containing californium 252 in temporary positions for the approach to criticality. The entire inner core was then loaded row by row, and counting rates were monitored with the neutron instrumentation system. Loading of the first batch was completed by the loading of 80 inner core fuel sub-assemblies. This marked the first "rods up" point in the approach to criticality. The approach to criticality was carried out in 9 steps. The counting rate evolution during the approach to criticality was simulated by 2-dimensional transport calculations. Criticality was first achieved with 168 fuel sub-assemblies; all the control rods were withdrawn except for one half-inserted in the core. The "rods up" experimental k_{eff} value was estimated by calibrating the control rod. The measurements of absorber rod worth were carried out on the initial critical core and on the core in which one more fuel sub-assembly was loaded. The 29 fuel sub-assemblies required to complete the loading of the outer core were then added. After the final fuel loading on May 20 1994, the initial full core was taken critical. The excess reactivity of this core was determined from the results of control rod calibration.

3.1-2 Calculation Results

In order to evaluate the criticality of the initial critical core and the initial full core, the basic results were calculated by using the CITATION code with its 3-dimensional Hex-Z calculational model, 70 energy group cross-sections and 1 mesh per assembly in the horizontal plane. The final results were evaluated from the basic results by considering the correction effects shown in table 4. The comparison of calculated and measured values for criticality is shown in Fig.3. As the difference of correction factors between J3.2 and J2 was small, the difference of the final results of each library was due to the difference of the basic results. The C/E values using J3.2 were 0.993 for the initial critical core and 0.992 for the initial full core. They are only 0.1 % greater than those based on J2.

The contributions of specific nuclear reactions to the worth differences between J3.2 and J2 were analyzed. For example, the components of the k_{eff} difference for the initial full core are shown in Fig.4. Although the contributions of each individual reaction, especially the fission cross-section of plutonium 239, in J3.2 are different from those in J2, the overall effect is small.

3.2 Absorber Rod Worth

3.2-1 Measurements

The arrangement of the absorber rods in MONJU is shown in Fig.5. The absorber rods are composed of 10 coarse control rods (CCR), 3 fine control rods (FCR) and 6 back-up rods (BCR). CCR1 is the center of the core. The 1st ring contains 3 CCRs and 3 BCRs and the 2nd ring contains 6 CCRs, 3 FCRs and 3 BCRs. The measurements were performed for CCR1 by using the periodic method. It consisted of running a series of positive reactivity steps by raising CCR1 and lowering the other control rods. The operations were monitored on the reactivity meter which immediately gave the reactivity. For the measurement of the other absorber rod worth, the balancing method was used. That is, obtaining the reactivity difference between the "just critical" control rod positions before and after moving the considered sub-assembly. This required the S-curve of the reactivity standard rod (CCR1) which was based on the control rod calibration results.

3.2-2 Calculation Results

In order to evaluate the absorber rod worth, the basic results were produced using the CITATION code with its 3-dimensional Tri-Z calculational model, 6 energy group cross-sections and 6 meshes per assembly in the horizontal plane. The final results were evaluated from the basic results by considering correction effects shown in table 4. The comparison of the absorber rod worth using J3.2 and J2 and the measurements is shown in Fig.6. The C/E values are shown in Fig.7. The C/E values using J3.2 are from 0.98 to 0.99 and about 3 % greater than those based on J2. The difference of the final results of each library was due to the difference of the basic results.

The contributions of specific nuclear reactions to the worth differences between J3.2 and J2 were analyzed. For example, the components for CCR1 are shown in Fig.8. Although the contributions of each individual reaction, especially the fission cross-section of plutonium 239, in J3.2 are different from those in J2, the overall effect is small.

3.3 Coolant Worth

3.3-1 Measurements

The coolant worth was another "replacement reactivity". Non-fissile dummy sub-assemblies with helium gas (void) region of 60 cm length around core mid-plane were replaced by dummy sub-assemblies which had the same region filled with sodium. The key parameters of these dummy sub-assemblies are shown in table 5. The coolant worth was measured with 6 dummy sub-assemblies loaded around CCR1. The arrangement of the dummy sub-assemblies is shown in Fig.9. Since the dummy sub-assemblies do not contain fuel material, the coolant worth is not same as the sodium void worth. To evaluate the influence of CCR1 position on the coolant worth, 2 measurements were carried out, one with CCR1 fully withdrawn and the other with the rod fully inserted. The balancing method was used for measuring the coolant worth.

3.3-2 Calculation Results

We performed diffusion and transport theory calculations for the coolant worth. The C/E values are shown in table 6. The comparison between the calculation results using diffusion and transport theory and the measurements is shown in Fig.10. Transport theory and J3.2 are used as reference calculations. Their C/E values are 1.6 for CCR1 fully withdrawn and 1.7 for CCR1 fully inserted. They are about 10 and 40 %, respectively, smaller than those based on J2. When transport theory is replaced by diffusion theory, the C/E values are about 0.9 for CCR1 fully withdrawn and fully inserted.

The contributions of specific nuclear reactions to the worth differences between J3.2 and J2 were analyzed. The components of the coolant worth difference in diffusion theory are shown in Fig.11. The capture cross-section of manganese has a similar contribution as the capture cross-section of plutonium 239, the elastic cross-section of oxygen and the inelastic scattering cross-section of sodium.

4. Conclusions

The C/E values using J3.2 for the criticality of the initial critical core and the initial full core of 0.993 and 0.992, respectively, are only 0.1 % greater than those based on J2. The C/E values using J3.2 for the absorber rod worth are from 0.98 to 0.99 and about 3 % greater than those based on J2. The C/E values of the coolant worth using J3.2 and transport theory are 1.6 for CCR1 fully withdrawn and 1.7 for CCR1 fully inserted. They are about 10 and 40 %, respectively, smaller than those based on J2. For this difference, the capture cross-section of manganese has a similar contribution as the capture cross-section of plutonium 239, the elastic cross-section of oxygen and the inelastic scattering cross-section of sodium.

In future, we will evaluate the fixed absorber and fuel worth using J3.2.

5. References

1. T.NAKAGAWA, et al., "Japanese Evaluated Nuclear Data Library Version 3 Revision-2: JENDL-3.2," Journal of Nuclear Science and Technology, 32[12], P1259-1271 (1995).
2. T.NAKAGAWA, "Summary of JENDL-2 General Purpose File," JAERI-M 84-103, Japan Atomic Energy Research Institute (1984).
3. S.SAWADA, et al., "REACTIVITY CHARACTERISTICS EVALUATIONS OF THE INITIAL CORE OF MONJU" in Proc. International Conference on the Physics of Reactors, Sept. 16-20, 1996, Mito, Japan Vol.2, pE-76.
4. S.USAMI, et al., "Evaluation of the FBR MONJU Core Breeding Ratio and the Power Distribution from the Reaction Rate Distribution Measurement" in Proc. International Conference on the Physics of Reactors, Sept. 16-20, 1996, Mito, Japan Vol.2, pE-86.
5. K.SHIRAKATA, et al.,"Development of Concept and Neutronic Calculation Method for Large LMFBR Core," in Proc. International Conference on Fast Reactors and Related Fuel Cycles, Oct. 28 - Nov. 1, 1991, Kyoto, Japan, Vol.I, P3.5-5.

6. M.NAKAGAWA and K.TSUCHIHASHI, "SLAROM: A Code for Cell Homogenization Calculation of Fast Reactor," JAERI 1294, Japan Atomic Energy Research Institute (1984).
7. H.TAKANO, "Benchmark Tests of JENDL-3.2 for Thermal and Fast Reactors," in Proc. International Conference on Nuclear Data for Science and Technology, May 9-13, 1994, Gatlinburg, Tennessee USA, P809.
8. H.TAKANO, "Revised Edition of Fast Reactor Group Constant Set JFS-3-J2," JAERI-M 89-141, in Japanese, Japan Atomic Energy Research Institute (1989).
9. T.B.FOWLER, et al., "Nuclear Reactor Analysis Code: CITATION," ORNL-TM-2498, Oakridge National Laboratory (1971).

Table 1 Principal Design and Performance Data of MONJU

Reactor type	Sodium-cooled loop-type
Thermal output	714 MW
Electrical output	280 MW
Fuel material	PuO_2-UO_2
Core dimensions	
Equivalent diameter	179 cm
Height	93 cm
Plutonium enrichment (Pu fissile %)	(inner core / outer core)
Initial core	15 / 20
Equilibrium core	16 / 21
Fuel inventory	
Core(U+Pu metal)	5.9 t
Blanket(U metal)	17.5 t
Average burnup	80,000 MWD/T
Cladding material	SUS316
Cladding outer diameter/thickness	0.65 / 0.047 cm
Blanket thickness Upper / lower / radial	30 / 35 / 30 cm

Table 2 Schedule of Measurements

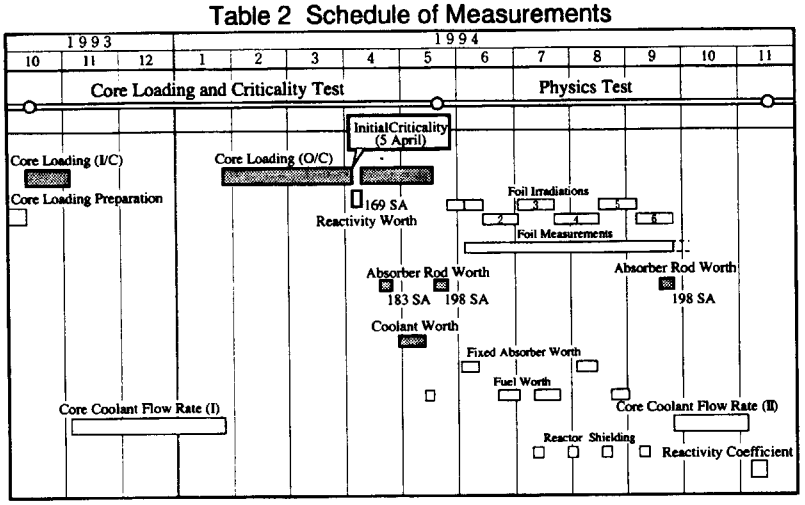

Table 3 Calculation Method

Items		Measurements		
		Criticality	Absorber Rod Worth	Coolant Worth
70 Multigroup Constant Set		JENDL-3.2 [JFS-3-J3.2] JENDL-2 [JFS-3-RJ2(1989)]		
Cell Calculation	Used Code	SLAROM		
	Fuel Sub Assembly	Homogeneous		
	Absorber Rod	Heterogeneous		
Reactor Calculation	Used Code	CITATION(diffusion)		TWOTRAN (transport) CITATION
	No. of Energy Groups	70	6	70
	Geometry	Hex-Z	Tri-Z	RZ

Table 4 Correction Items

Items	Measurements		
	Criticality	Absorber Rod Worth	Coolant Worth
Finite Mesh Size	○	○	○
Transport	○	○	○
Group Collapsing	–	○	○
Heterogeneity	○	○	△
Temperature	○	○	×
Real Composition of Steel	○	×	×
Pu-241 Decay	○	×	×
CR interaction	–	○	–
Dimension	–	–	△

○…used △…check of the effect, but not used
×…not used –…not needed

Table 5 Key Parameters of Dummy Sub-Assemblies of the Coolant Worth Measurement

Items		Dummy Sub-Assembly	
		Void region	Sodium region
Length of Void or Sodium Region		~60cm	
Volume Fraction	Steel	18%	18%
	Sodium	19%	82%
	Void	63%	-

Table 6 C/E values of the Coolant Worth

Items		C/E			
		CCR1 Fully Withdrawn		CCR1 Fully Inserted	
		JENDL-2	JENDL-3.2	JENDL-2	JENDL-3.2
Diffusion (RZ.Homo. 70gr.)		1.7	0.9	1.2	0.9
Transport (RZ.Homo. 70gr.)		2.5	1.6	1.9	1.7
Finite Mesh Size (RZ.Homo.70gr.Dif)		-	1.0	-	1.0
Group Collapsing (RZ.Homo.transp.)	70gr.	-	1.6	-	1.7
	18gr.	-	2.2	-	1.8
Heterogeneity (RZ.70gr.)	diff.(Hetero)	2.5	-	1.9	-
	transp.(Hetero)	2.6	-	1.6	-
Dimensional (Homo.18gr.transp.)	RZ	-	2.2	-	-
	3D.XYZ	-	2.1	-	-

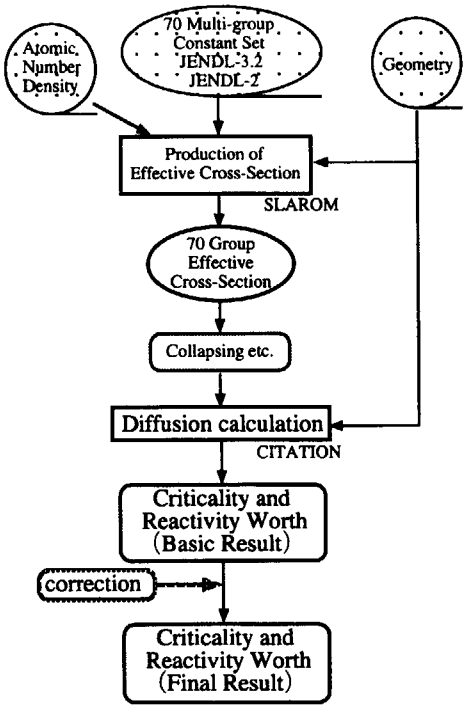

Fig.1 Flow Scheme of JUPITER Analysis System

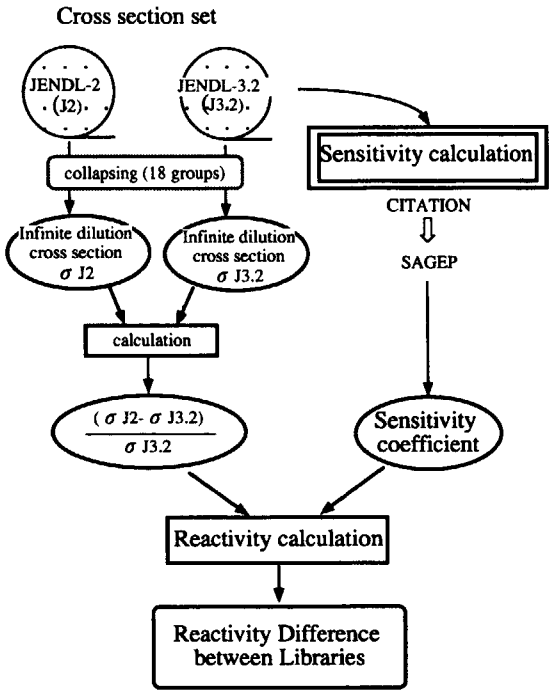

Fig.2 Flow Scheme of Sensitivity Analysis System

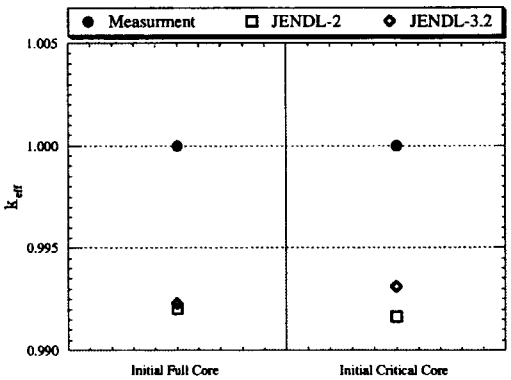

Fig.3 Comparison of Criticality

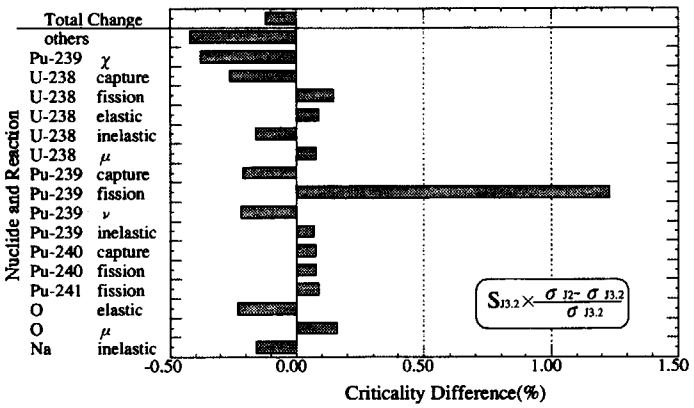

Fig.4 Components of the Criticality Difference between JENDL-3.2 and JENDL-2 (Initial Full Core)

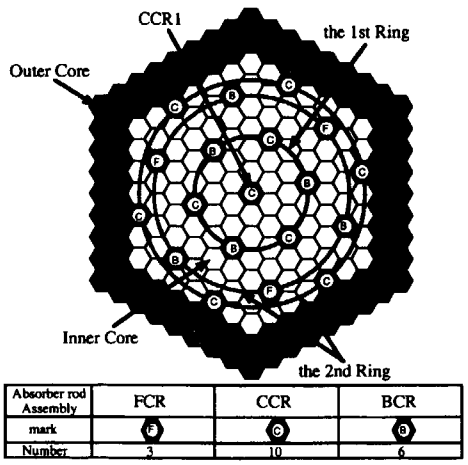

Fig.5 Arrangement of Absorber Rods in MONJU

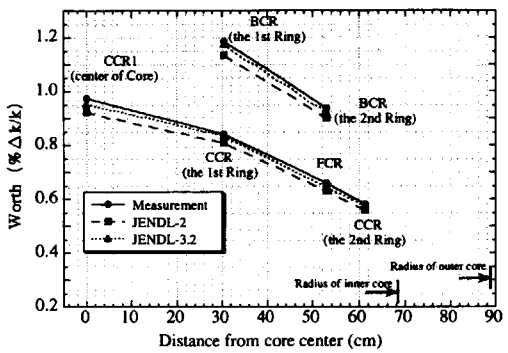

Fig.6 Comparison of the Absorber Rod Worth

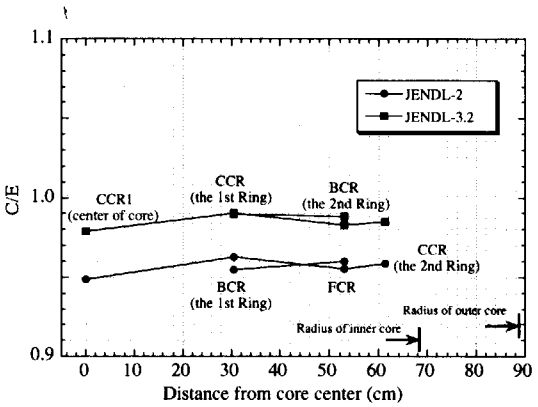

Fig.7 C/E Values of the Absorber Rod Worth

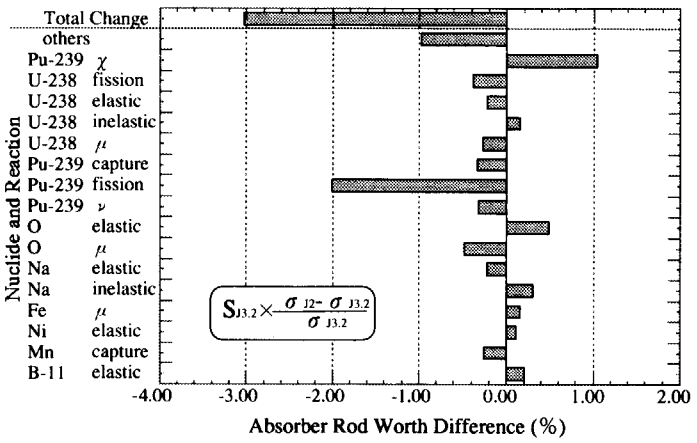

Fig.8 Components of the Absorber Rod Worth Difference between JENDL-3.2 and JENDL-2(CCR1)

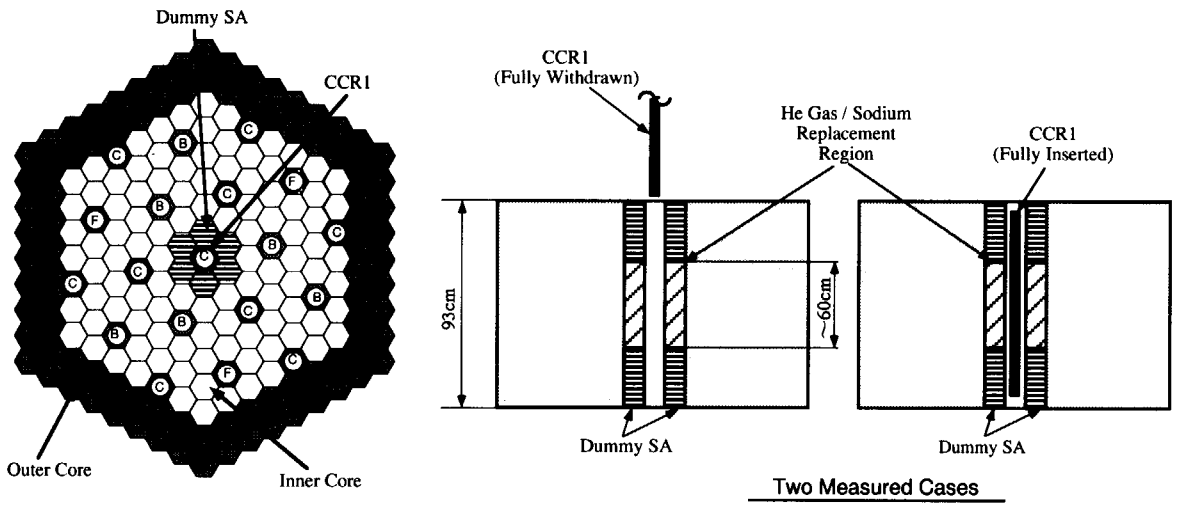

Fig.9 Arrangement of Dummy Assemblies for the Coolant Worth Measurements

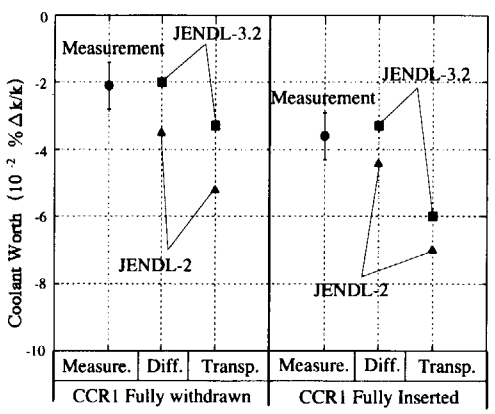

Fig.10 Comparison of the Coolant Worth

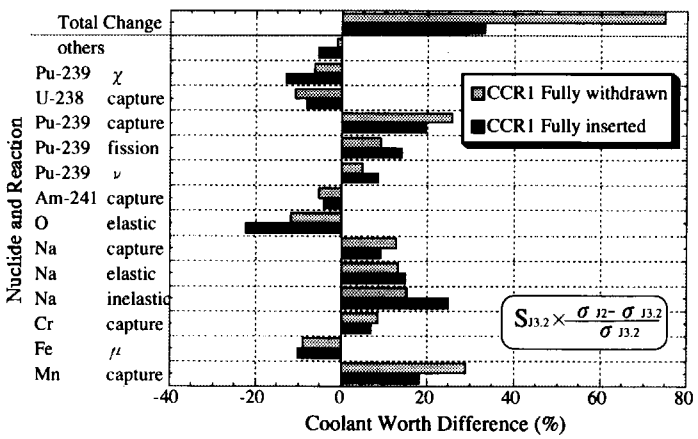

Fig.11 Components of the Coolant Worth Difference between JENDL-3.2 and JENDL-2 in Diffusion

2.4.3

Uncertainty of Doppler Reactivity Worth due to Uncertainties of JENDL-3.2 Resonance Rapameters

Atsushi ZUKERAN
Power & Industrial System R & D Division, Hitachi, Ltd.
7-2-1 Omika-cho, Hitachi-shi, Ibaraki-ken, 319-12 Japan

Hiroshi HANAKI
Fast Breeder Engineering Department, Hitachi Works, Hitachi, Ltd.
3-1-1 Saiwai-cho, Hitachi-shi, Ibaraki-ken, 317 Japan

Tuneo NAKAGAWA* and Keiichi SHIBATA
Nuclear Data Center
Japan Atomic Energy Research Institute
Tokai-mura, Naka-gun, Ibaraki-ken, 319-11 Japan

Makoto ISHIKAWA
Advanced Technology Division
O-arai Engineering Center
Power Reactor & Nuclear Fuel Development Corporation
Narita-cho,O-arai-machi,Higashi-Ibaraki-gun,Ibaraki-ken, 311-13,JAPAN

November 27, 1997

Abstract

Analytical formula of Resonance Self-shielding Factor (f-factor) is derived from the resonance integral (J-function) based on NR approximation and the analytical expression for Doppler reactivity worth (ρ) is also obtained by using the result. Uncertainties of the f-factor and Doppler reactivity worth are evaluated on the basis of sensitivity coefficients to the resonance parameters. The uncertainty of the Doppler reactivity worth at $487\,^0K$ is about 4 % for the PNC Large Fast Breeder Reactor.

1 Introduction

Doppler reactivity worth is an important nuclear characteristics for safe operations of fast breeder reactors as well as thermal ones. It has been requested to evaluate the prediction accuracy for the Doppler reactivity worth from viewpoints of the nuclear data and calculational method. The current accuracy, however, is hardly evaluated from nuclear data point of view since the resonance self-shielding factor (f-factor), key property of Doppler effect, is tremendous mixing effects arising from about several thousands of resonances.

Present work aims at estimating the Doppler reactivity uncertainty though those of resonance self-shielding factors due to resonance parameters. The following items are in the scope of present work,

*Present address, Nuclear Power Engineering Corporation

1) Uncertainties of JENDL-3.2 resonance Parameters[1],
2) Analytical formulations of f-factor and Doppler reactivity worth,
3) Uncertainty evaluation of the f-factor and Doppler reactivity worth.

The uncertainty of f-factor has been estimated by two different methods, namely, (a) previously, numerical method using the fast reactor cross section processing code MC^2-2[2] and (b) at present an analytical method based on narrow-resonance approximation for effective cross sections. Only the latter is limited in this work. In the analytical method, the integrand of the resonance integral function (so-called J-function), which is a functional function of Doppler broadening functions ψ, χ, was expanded as the power series of these broadening functions.

2 Uncertainty of Resonance Parameter

Reich-Moore resonance parameters for ^{239}Pu of JENDL-3.2 are converted to Breit-Wigner Multilevel expression in order to link the conventional resonance integral formula expressed in terms of Doppler broadening functions. The two kind of fission widths are collapsed into a single value by $\Gamma_f = \sqrt{\Gamma_{f1}^2 + \Gamma_{f2}^2}$. Uncertainty of resolved resonance parameters are shown in **Fig. 1** for ^{238}U as the most important nuclide for Doppler reactivity worth. Constant error of about 4.3 % for capture width Γ_γ is assigned for almost all levels but some levels has larger errors than 11% as shown in **Table 1**. Errors of p-wave neutron widths are assumed to be 15% for errors of all p-wave resonances. Errors for subthreshold fissions are neglected.

3 Derivation of Analytical Formula for Resonance Self-Shielding Factor and Doppler Reactivity Worth

Effective cross section $\sigma_{eff\,x}$ of reaction x in a neutron flux ϕ is defined by a flux-weighted average cross section as

$$\sigma_{eff\,x}(T) = \frac{\int \sigma_x(E,T,)\,\phi(E,T,)\,dE}{\int \phi(E,T,)\,dE} \tag{1}$$

where、E: neutron energy, $\phi_i^K(E,T)$: neutron flux, $\sigma_x(E,T)$: micro-scopic cross section. For instant, capture cross section $\sigma_{\gamma ik}$ for k-th level at temperature T can be shown as a function of Doppler broadening symmetric function ψ_i^k as

$$\sigma_{\gamma i}^k(E,T) = \sigma_{0i}^k(E)\frac{\Gamma_{\gamma i}^k}{\Gamma_i^k}\cdot\psi_i^k(T,E) \tag{2}$$

$$\sigma_{0i}^k(E) = \frac{cnst}{E_{ri}^k}\cdot\frac{g\Gamma_{ni}^k}{\Gamma_i^k}, \qquad (cnst = 2.603995\times 10^6) \tag{3}$$

$$\psi_i^k\left\{\theta_i^k(T),x\right\} = \frac{\theta_i^k}{\sqrt{4\pi}}\int_{-\infty}^{+\infty}\frac{\exp\left[-\frac{(\theta_i^k)^2}{4}\cdot(x-y)^2\right]}{1+y^2}dy \tag{4}$$

$$= \frac{\theta_{ik}\sqrt{\pi}}{2}\cdot\Re\,W\left(\frac{\theta_i^k x_{ik}}{2},\frac{\theta_i^k}{2}\right) \tag{5}$$

$x_{ik} = \frac{2(E-E_{ri}^k)}{\Gamma_i^k}$, σ_{oi}^k: peak cross section, $\theta_i^k = \frac{\Gamma_i^k}{\Delta_i^k}$: total width relative to Doppler width、

Δ_i^k: Doppler width、x:dimensionless energy, complex W-function $W(z)$ $(W-table)$

$$W(z) = W(x,y) = \exp(-z^2)\cdot erfc(-iz) \tag{6}$$
$$z = x+iy \tag{7}$$

The broadening of ^{240}Pu capture cross section superimposed by 1/v-term is shown in **Fig. 2** as function of neutron energy and temperature up to solor inner temperature.

Resonance self-shielding factor $f(T,\sigma_0)$, when the mutual interference terms are neglected, can be defined by the following expression

$$f(T,\sigma_0) = \frac{1}{\pi}\int_{-\infty}^{\infty}\frac{\beta\psi(\theta,x)}{\beta+\psi(\theta,x)+a_p\chi(\theta,x)}dx \qquad = \frac{1}{\pi}\int_{-\infty}^{\infty}Q(\beta,\theta,x)dx \tag{8}$$

where $\beta = \sigma_p/\sigma_0$ and σ_p: potential scattering function per resonant absorber atom. The surfixes and/or superscripts are omitted unless they are especially needed hereafter.

The integrand $Q(\beta,\theta,x)$ of Eq.(8) can be expressed in terms of $E(\beta,\theta,x)$-function as shown below

$$Q(\beta,\theta,x) = \frac{\beta\psi(\theta,x)}{\beta+\psi(\theta,x)+a_p\chi(\theta,x)} \tag{9}$$
$$= \frac{\beta}{\beta+1}\psi(\theta,x)\sum_{n=0}^{\infty}\{E(\beta,\theta,x)\}^n \tag{10}$$
$$= \frac{\beta}{\beta+1}\sum_{n=0}^{\infty}\sum_{r=0}^{n}\sum_{s=0}^{n-r}(-1)^{n-r}\omega^n\binom{n}{r}\binom{n-r}{s} \times a_p{}^{n-r-s}\psi^{s+1}\chi^{n-r-s} \tag{11}$$
$$\omega(\beta) = 1/(\beta+1) \tag{12}$$
$$E(\beta,\theta,x) = \frac{1-[\psi(\theta,x)+a_p\chi(\theta,x)]}{\beta+1} \tag{13}$$

The power series converses as long as the $E(\beta,\theta,x)$ is smaller than 1 as shown in Fgi. 3. Analytical integration of the product $\psi^k\times\chi^l$ can be made as long as $k+l\leq 3$ but the higher order terms in Eq.(11) are replaced by the approximated ψ function for high temperature.

Finally an analytical form of resonance self-shielding factor $f(\beta,\,\theta)$ for a single resonance is shown by

$$\begin{aligned} f(\beta,\,\zeta) &= (1-\omega(\beta))\left[1+\omega(\beta)+\left\{1-\frac{\sqrt{\pi}}{4}(\frac{1-\theta}{p\theta})fz2(\theta)\right\}\omega(\beta)^2\right. \\ &- 0.5\left\{\omega(\beta)+2\omega(\beta)^2-\frac{\sqrt{\pi}}{2}(\frac{1-\theta}{p\theta})fz1(\theta)\omega(\beta)^2\right\}\psi_0(\theta) \\ &+ \left.\sum_{n=3}^{nmax}\omega(\beta)^n\sum_{m=0}^{n}\frac{(-1)^{n-m}}{\sqrt{n-m+1}}\binom{n}{m}\left\{\sqrt{\frac{\pi}{\sqrt{2}}}\frac{(1-\theta)}{p\theta}\right\}^{n-m}\right] \end{aligned} \tag{14}$$

where, $fz1(\theta)$ and $fz2(\theta)$ are polynomial functions of $\theta(T)$, and $\psi_0(\theta)$ is the ψ-function at the resonance energy $(x=0)$ whose trace is the peak line of Doppler broadened cross section shown in Fig. 2.

Resonance Self-Shielding Factor $f_{xi}^g(\beta,\theta)$ for a multigroup containing k-th resonance is the weighted average of the single level resonance self-shielding factor $f_{xi}^k(\beta,\theta)$ as

$$f_{xi}^{g} = \sum_{g \exists k}^{g} \Lambda_{xi}^{k} \cdot f_{xi}^{k} \tag{15}$$

$$\Lambda_{xi}^{k} = \frac{\sigma_{\infty,xi}^{k} \cdot \psi^{k} \Delta U^{k}}{\sum_{g \exists l}^{g} \sigma_{\infty,xi}^{l} \cdot \psi^{l} \Delta U^{l}} \tag{16}$$

where、$\sigma_{\infty,xi}^{l}$: infinitely diluted cross section, ψ^{l}: neutron flux, ΔU^{l}: lethargy width。

The sensitivity coefficient $S_{\Gamma_p}^{f_{xi}^{k}}$ of resonance self-shielding factor $f_{xi}^{k}(\beta, \zeta)$ to the change of "generalized" resonance parameter Γ_p ($p = xjl, x = n, \gamma, f, j : isotope, l : resonanceNo.$) including the resonance energy is defined by

$$S_{\Gamma_p}^{f_{xi}^{k}} = \frac{\Gamma_p}{f_{xi}^{k}(\beta, \zeta)} \cdot \frac{\partial f_{xi}^{k}(\beta, \zeta)}{\partial \Gamma_p} \tag{17}$$

where suffix p and x mean the resonance parameter to be changed and reaction type whose f-factor sensitivity coefficient is of interest.

3.1 Doppler Reactivity Worth

The Doppler reactivity worth ρ_i^k for a single resonance (k) of a nuclide (i) can be expressed in terms of resonance parameters and resonance self-shielding factor as shown below,

$$\rho_{xi}^{k}(T, T_0) = w_{xi}^{k} \cdot \frac{(\overline{\nu} - k_{eff})\Gamma_{fi}^{k} - k_{eff}\Gamma_{\gamma i}^{k}}{\Gamma_{fi}^{k} + \Gamma_{\gamma i}^{k}} \cdot \frac{f_{xi}^{k}(T) - f_{xi}^{k}(T_0)}{f_{xi}^{k}(T_0)} \tag{18}$$

where w_{xi}^{k} means the weighting function for Doppler reactivity worth of k-th resonance, and T and T_0 are temperature and its standard one, respectively.

Sensitivity coefficient $S_{\Gamma_p}^{\rho,xik}$ can be obtained from Eqs.(18) and (14) as

$$\mathbf{S}_{\Gamma_p}^{\rho,xik} = \begin{pmatrix} S_{Ern,p} & S_{Er\gamma,p} & S_{Erf,p} & S_{ErEr,p} \\ S_{nn,p} & S_{n\gamma,p} & S_{nf,p} & S_{nEr,p} \\ S_{\gamma n,p} & S_{\gamma\gamma,p} & S_{\gamma f,p} & S_{\gamma Er,p} \\ S_{fn,p} & S_{f\gamma,p} & S_{ff,p} & S_{fEr,p} \end{pmatrix} \tag{19}$$

$$S_{nn,p} = \left(1 - \frac{\Gamma_{ni}^{k}}{\Gamma_{i}^{k}}\right) \cdot F_{\beta xi}^{k} \cdot S_{\Gamma_p}^{\Gamma_{nik}^{k}} \tag{20}$$

$$S_{\gamma\gamma,p} = -\frac{\Gamma_{\gamma i}^{k}}{\Gamma_{i}^{k}} \left[\frac{k_{eff}\Gamma_{i}^{k}}{(\overline{\nu} - k_{eff})\Gamma_{fi}^{k} - k_{eff}\Gamma_{\gamma i}^{k}} + F_{\beta xi}^{k}\right] \cdot S_{\Gamma_p}^{\Gamma_{\gamma i}^{k}} \tag{21}$$

$$S_{ff,p} = -\frac{\Gamma_{\gamma i}^{k}}{\Gamma_{i}^{k}} \left[\frac{k_{eff}\Gamma_{i}^{k}}{(\overline{\nu} - k_{eff})\Gamma_{fi}^{k} - k_{eff}\Gamma_{\gamma i}^{k}} + F_{\beta xi}^{k}\right] \cdot S_{\Gamma_p}^{\Gamma_{\gamma i}^{k}} \tag{22}$$

$$S_{ErEr,p} = -\left(F_{\beta xi}^{k} + F_{\theta xi}^{k}\right) \cdot S_{\Gamma_p}^{E_{ri}^{k}} \tag{23}$$

$$S_{a \neq b} = 0.0 \quad \text{(off-diagonal terms)} \tag{24}$$

with

$$F^k_{\beta xi} = 1 - \frac{f^k_{xi}(T)\cdot S^{\beta ik}_{\Gamma_p}(T) - f^k_{xi}(T_0)\cdot S^{\beta ik}_{\Gamma_p}(T_0)}{f^k_{xi}(T) - f^k_{xi}(T_0)} \tag{25}$$

$$F^k_{\theta i} = 1 - \frac{f^k_{xi}(T)\cdot S^{\theta ik}_{\Gamma_p}(T) - f^k_{xi}(T_0)\cdot S^{\theta ik}_{\Gamma_p}(T_0)}{f^k_{xi}(T) - f^k_{xi}(T_0)} \tag{26}$$

where the second terms of right-hand sides come from the resonance self-shielding factors giving the Doppler reactivity worth as expected from Eq.(18) and the second terms $f^k_{xi}(T_0)\cdot S^{\beta_{ik},\theta_{ik}}_{\Gamma_p}(T_0)$ means the deviation of the standard point.

The error of Doppler reactivity worth $\frac{\delta\rho^k_i}{\rho^k_i}$ of the k-th resonance of i-th isotope can be expressed by the weighted sum

$$\frac{\delta\rho^k_i}{\rho^k_i} = \sum_x\sum_k W^k_{\rho xi}\times \mathbf{S}^{\rho,ik}_{\Gamma_p}\times \begin{pmatrix} \delta Er^{ik}/Er^{ik} \\ \delta\Gamma^{ik}_{ni}/\Gamma^{ik}_{ni} \\ \delta\Gamma^{ik}_{\gamma i}/\Gamma^{ik}_{\gamma i} \\ \delta\Gamma^{ik}_{fi}/\Gamma^{ik}_{fi} \end{pmatrix} \tag{27}$$

As expected from the numerators of Eqs.(25) and (26), strong cancellations are taken placed between the temperature T and T_0 states since the equations were derived under the assumption that the same errors of resonance parameters arise in the two different temperature systems. However, the errors belongs to some statistical (normal) distribution and thus the same error statistically appears at the other system. Therefore, in practice, the expectation value of the second term due to the randomness of error in T- and T_0-systems can be expressed by a probabilistic correlation coefficients as shown below,

$$\begin{aligned} < f^k_i(T)S^{\beta ik}_{\Gamma_p}(T) - f^k_i(T_0)S^{\beta ik}_{\Gamma_p}(T_0) >= & [\{f^k_i(T)S^{\beta ik}_{\Gamma_p}(T)\}^2 + \{f^k_i(T_0)S^{\beta ik}_{\Gamma_p}(T_0)\}^2 \\ & -2.0\cdot Prb(T)\cdot Prb(T_0)\cdot f^k_i(T)S^{\beta ik}_{\Gamma_p}(T)\cdot f^k_i(T_0)S^{\beta ik}_{\Gamma_p}(T_0)]^{1/2} \end{aligned} \tag{28}$$

where the probability, $Prb(T)$, finding a error set $\{\Gamma'_p s\}$ is

$$Prb(T) = \frac{1}{\sqrt{2\pi}\cdot\sigma_p}\int_{-\epsilon}^{+\epsilon}\exp[-\frac{1}{2}(\frac{\epsilon_p}{\sigma_p})]d\epsilon_p \tag{29}$$

$$\simeq \frac{1}{\sqrt{2\pi}}\int_{-1}^{+1}\exp[-\frac{1}{2}t^2]dt = 0.682694 \tag{30}$$

where $\epsilon_p = \delta\Gamma_p$ means a generarized error of resonance parameter and σ_p variance of $\delta\Gamma_p$. The errors of resonance parameters are ordinary given as a 1 standard(1σ) deviation and then the magnitude of probability becomes 0.68269 as shown above. Two temperature systems ($T, \{\Gamma'_p s\}$ and $T, \{\Gamma'_p s\}$) are closed and independent, whose probabilities are the same each other. Therefore,

$$Prb(T)\cdot Prb(T_0) \simeq 0.46606 \tag{31}$$

3.2 Temperature Gradienet of Resonance self-shielding Factor

In order to adjust the resonance self-shielding factor $f-factor$, it is expressed in terms of the temperature gradient $\alpha^g_{f\,xi}$ and the log-tenperature difference as shown below,

$$f^g_{xi}(T) = f^g_{xi}(T_0)\cdot\left[1+\alpha^g_{f\,xi}\{\log(T)-\log(T_0)\}\right] \tag{32}$$

$$\alpha^g_{f\,xi} = \frac{f^g_{xi}(T) - f^g_{xi}(T_0)}{f^g_{xi}(T_0)\cdot\{\log(T)-\log(T_0)\}} \tag{33}$$

By using the analytical expression Eq.(14), the relative error due to errors of resonance parameters $\frac{\delta\alpha^g_{fxi}}{\alpha^g_{fxi}}$ can be shown by

$$\frac{\delta\alpha^g_{fxi}}{\alpha^g_{fxi}} = \frac{f^g_{xi}(T)}{f^g_{xi}(T) - f^g_{xi}(T_0)} \quad [\sum_{k\in g} \langle \{G^{\alpha\,ik}_{Er}(\frac{\delta Er^{ik}}{Er^{ik}})\}^2 + \{G^{\alpha\,ik}_{\Gamma_n}(\frac{\delta\Gamma^{ik}_n}{\Gamma^{ik}_n})\}^2 + \{G^{\alpha\,ik}_{\Gamma_\gamma}(\beta,\theta,\theta_0)(\frac{\delta\Gamma^{ik}_\gamma}{\Gamma^{ik}_\gamma})\}^2 + \{G^{\alpha\,ik}_{\Gamma_f}(\frac{\delta\Gamma^{ik}_f}{\Gamma^{ik}_f})\}^2 \rangle]^{1/2} \quad (34)$$

where $G^{\alpha\,ik}_{\Gamma_p}$, means the sensitivity coefficient of α^g_{fxi} as function of β, $\theta(T)$ and $\theta_0(T_0)$, and k and g indicate the resonance number and broad group number, respectively.

4 Uncertainty Evaluation of Resonance Self-Shielding Factor and Doppler Reactivity Worth

4.1 Uncertainty of Resonance Self-Shielding Factor

Uncertainty of f-factor is estimated by using the sensitivity coefficient defined by Eq.(17) and the errors of resonance parameters in the section 2. The level-wise uncertainties of f-factor are collapsed into multigroup structure of JFS-3-J2 70 group library. The resultant uncertainties of f-factor for the potential scattering cross section per absorber atom $\sigma_p = 37$ (b) used for ZPPR-9 critical assembly and room temperature $T = 300^0$k is shown in **Table 2** and some groups having larger uncertainties were shown in **Table 1** together with the resonance energy and σ_0 defined by Eq.(3).

Famous s-wave resonance at 6.67 eV and the next p-wave one at 7.7 eV are included in the broad group 57. The former one mainly contributes to the group uncertainty since the σ_0-value is extremely larger than the later. In this case, the resonance parameters themselves have high accuracies and the resultant uncertainty is small. The 50 group has three p-wave resonances whose errors of Γ_n-values are about 15 % together with those Γ_γ about 4.4 %, and the group uncertainty is about 4.4% where equal contributions from three levels are expected. The largest uncertainty at group 45 is due to the significantly larger error of Γ_γ as shown in the **Table 1**.

The f-factor uncertainty tends to be gradually reduced with the σ_p and T-values since the f-factor tends to be flattened for larger σ_p- and T-values. The f-factor uncertainties for ^{239}Pu and ^{240}Pu are shown in **Tables 4,6,8** and **10**.

4.2 Temperature Gradient α_f for Resonance Self-Shielding Factor

The calculated α^g_{fxi}-values for ^{238}U capture reaction in a typical fast breeder reactor with the potential scattering cross section 37 b are shown in **Table 3**. The larger error of Γ_γ of 145.7 eV resonance begonging to the 45 broad group significantly affects the α_f-value. The α-value uncertainties for ^{239}Pu and ^{240}Pu are shown **Tables 5, 7, 9** and **11**.

4.3 Uncertainty of Doppler Reactivity Worth

The uncertainty of Doppler reactivity worth is estimated as shown in **Table 12** as the group contributions, and in **Table 13(a)** as total uncertainty as functions of σ_p anf T. As indicated by the 45 group value with 1.08×10^{-2}, the significantly larger error $\frac{\delta\Gamma_\gamma}{\Gamma_\gamma} = 44.783$ % as shown in **Table 1** results larger Doppler uncertainty.

The total Doppler reactivity worth uncertainties of the other fuel elements such as ^{239}Pu and ^{240}Pu were negligibly small as the result of their smaller contributions to the Doppler reactivity worths as shown in **Tables 13(b)** and **13(c)**.

5 Conclusion

1. Resonance self-shielding factor Uncertainty due to Resonance Parameter
   (a) Maximum 16 % due to the errors of neutron capture width at 145.7 and 165.3 eV resonances of ^{238}U,
   (b) In general, the assumed error 15% of p-wave neutron width tends to give remarkable uncertainty.
2. Doppler Reactivity Worth Uncertainty due to Resonance Parameter.
   (a) For large fast breeder reactor, about 4% mainly due to ^{238}U.
   (a) This uncertainty is enhanced about a few % by taking into account the unresolved resonance contribution.
3. Request for Nuclear Data
   (a) Further evaluation of covariance matrix.
   (b) Reevaluation p-wave neutron widths and some capture widths.

References

[1] T. Nakagawa and K. Shibata, "Estimation of Uncertainties of Resonance Parameters of ^{56}Fe, ^{239}Pu, ^{240}Pu, and ^{238}U", JAERI-Research 97-035, Japan Atomic Energy Research Institute, (1997)

[2] H. Henryson II, B.J. Toppel and C.G. Stenberg, "MC^2-2: A Code to Calculate Fast Neutron Spectra and Multigroup Cross Section", ANL-8144(ENDF 239), Argonne National Laboratory, (1979)

Table 1 Errors of Resonance Parameters giving Larger Resonance Self-Shielding Factor Uncertainties for ^{238}U.

Res. No.(i)	Group No.	Er (eV)	*l-wave*	$\sigma_{0i}^{*)}$ (barn)	Error of resonance Parameter (%)				
					$\frac{\delta Er}{Er}$	$\frac{\delta\Gamma_n}{\Gamma_n}$	$\frac{\delta\Gamma_\gamma}{\Gamma_\gamma}$	$\frac{\delta\Gamma_f}{\Gamma_f}$	$\frac{\delta\Gamma}{\Gamma}$
2	57	6.674E+00	S	2.398E+04	0.003	0.154	0.183	0.0	0.172
3	57	7.709E+00	P	1.333E -01	0.100	14.963	4.348	0.0	4.348
11	50	4.331E+01	P	7.469E -01	0.100	15.059	4.348	0.0	4.348
12	50	4.520E+01	P	1.768E+00	0.004	14.286	4.348	0.0	4.348
13	50	4.676E+01	P	2.930E -01	0.100	15.000	4.348	0.0	4.348
31	45	1.332E+02	P	2.284E+00	0.038	25.000	4.348	0.0	4.346
32	45	1.359E+02	P	8.397E -01	0.100	15.000	4.348	0.0	4.348
33	45	1.457E+02	S	6.403E+02	0.007	4.959	44.783	0.0	43.192
						$\Gamma_\gamma =$	0.023		
						$\Delta\Gamma_\gamma =$	0.0103		
							(44.78%)		
34	45	1.524E+02	P	1.320E+01	0.013	5.453	4.348	0.0	4.338
35	45	1.589E+02	P	4.548E+00	0.019	16.632	4.348	0.0	4.346
36	45	1.645E+02	P	4.627E -01	0.100	15.000	4.348	0.0	4.348
37	45	1.653E+02	S	2.029E+03	0.006	0.223	11.391	0.0	9.937
						$\Gamma_\gamma =$	0.023		
						$\Delta\Gamma_\gamma =$	0.0026		
							(11.30%)		

*):**Peak cross section:** $\sigma_{0i} \simeq \frac{2.6\cdot 10^6}{Er} \cdot \frac{g\Gamma_n}{\Gamma}$

Table 2 Uncertainty of $^{238}U(n,\gamma)$ Resonance Self-Shielding Factor for Large Fast Breeder Reactor at $\sigma_0 = 37$ barn and $T = 487.5^0$k

IBG	EH (eV)	Uncertainty Components (absolute)				
		$\frac{\delta f}{f}(\frac{\delta Er}{Er})$	$\frac{\delta f}{f}(\frac{\delta \Gamma_n}{\Gamma_n})$	$\frac{\delta f}{f}(\frac{\delta \Gamma_\gamma}{\Gamma_\gamma})$	$\frac{\delta f}{f}(\frac{\delta \Gamma_f}{\Gamma_f})$	$\frac{\delta f}{f}(\frac{\delta \Gamma}{\Gamma})$
28	1.1709E+4	5.49E-06	5.65E-03	9.78E-03	0.0	1.13E-02
29	9.1188E+3	3.94E-05	4.75E-03	6.04E-03	0.0	7.68E-03
30	7.1017E+3	4.51E-05	5.02E-03	6.20E-03	0.0	7.98E-03
31	5.5308E+3	9.49E-06	3.19E-03	6.43E-03	0.0	7.18E-03
32	4.3074E+3	1.64E-06	1.83E-03	7.38E-03	0.0	7.60E-03
33	3.3546E+3	1.80E-06	2.22E-03	7.66E-03	0.0	7.98E-03
34	2.6126E+3	1.05E-06	1.30E-03	8.55E-03	0.0	8.65E-03
35	2.0347E+3	3.24E-06	4.51E-03	9.03E-03	0.0	1.00E-02
36	1.5846E+3	2.19E-06	1.46E-03	9.57E-03	0.0	9.68E-03
37	1.2341E+3	1.84E-06	1.39E-03	8.90E-03	0.0	9.01E-03
38	9.6122E+2	4.05E-06	4.70E-03	7.87E-03	0.0	9.17E-03
39	7.4852E+2	6.02E-06	7.83E-03	5.11E-03	0.0	9.36E-03
40	5.8295E+2	4.06E-06	6.44E-03	1.85E-03	0.0	6.70E-03
41	4.5400E+2	6.75E-06	1.09E-02	1.20E-02	0.0	1.62E-02
42	3.5358E+2	2.67E-05	4.52E-03	9.87E-03	0.0	1.08E-02
43	2.7536E+2	4.84E-06	6.50E-04	9.64E-03	0.0	9.67E-03
44	2.1445E+2	3.01E-05	7.69E-04	5.54E-04	0.0	9.48E-04
45	1.6702E+2	3.08E-05	1.63E-02	1.59E-01	0.0	1.60E-01
46	1.3007E+2	4.79E-05	1.84E-03	3.38E-03	0.0	3.85E-03
47	1.0130E+2	3.93E-05	1.11E-02	2.55E-02	0.0	2.78E-02
48	7.8893E+1	1.78E-05	1.12E-03	3.44E-03	0.0	3.62E-03
49	6.1442E+1	1.31E-04	3.27E-02	4.66E-07	0.0	3.27E-02
50	4.7851E+1	2.24E-04	4.94E-02	3.11E-06	0.0	4.94E-02
51	3.7267E+1	3.34E-05	4.53E-04	1.22E-03	0.0	1.30E-03
52	2.9023E+1	5.04E-04	7.57E-02	7.05E-07	0.0	7.57E-02
53	2.2603E+1	5.77E-05	7.41E-04	1.70E-03	0.0	1.85E-03
54	1.7603E+1	0.0	0.0	0.0	0.0	0.0
55	1.3710E+1	1.30E-08	3.12E-06	3.77E-06	0.0	4.90E-06
56	1.0677E+1	4.07E-07	1.04E-04	2.09E-04	0.0	2.33E-04
57	8.3153E+0	3.66E-05	1.48E-03	2.48E-03	0.0	2.89E-03
58	6.4760E+0	0.0	0.0	0.0	0.0	0.0
59	5.0435E+0	1.07E-08	2.09E-06	2.46E-06	0.0	3.23E-06

Table 3 Uncertainty of The Temperature Gradient α of $^{238}U(n,\gamma)$ f-factor for Large Fast Breeder Reactor at $\sigma_0 = 37$ barn and $T = 487.5^0$k

IBG	Uncertainty Components (absolute)				
	$\frac{\delta \alpha}{\alpha}(\frac{\delta Er}{Er})$	$\frac{\delta \alpha}{\alpha}(\frac{\delta \Gamma_n}{\Gamma_n})$	$\frac{\delta \alpha}{\alpha}(\frac{\delta \Gamma_\gamma}{\Gamma_\gamma})$	$\frac{\delta \alpha}{\alpha}(\frac{\delta \Gamma_f}{\Gamma_f})$	$\frac{\delta \alpha}{\alpha}(\frac{\delta \Gamma}{\Gamma})$
28	2.81E-06	2.71E-03	9.82E-05	0.0	2.71E-03
29	2.96E-05	1.92E-03	5.26E-05	0.0	1.92E-03
30	5.05E-05	3.04E-03	7.36E-05	0.0	3.04E-03
31	5.80E-06	1.47E-03	1.77E-04	0.0	1.48E-03
32	2.27E-06	1.06E-03	1.40E-04	0.0	1.07E-03
33	2.38E-06	1.33E-03	2.63E-04	0.0	1.35E-03
34	2.13E-06	9.70E-04	3.09E-04	0.0	1.01E-03
35	9.24E-06	6.70E-03	3.28E-04	0.0	6.71E-03
36	6.31E-06	1.38E-03	8.18E-04	0.0	1.60E-03
37	5.82E-06	1.25E-03	8.57E-04	0.0	1.51E-03
38	9.96E-06	4.16E-03	1.08E-03	0.0	4.30E-03
39	1.49E-05	8.11E-03	2.73E-03	0.0	8.55E-03
40	1.54E-05	9.27E-03	3.36E-03	0.0	9.86E-03
41	2.15E-05	1.96E-02	1.14E-02	0.0	2.27E-02
42	4.39E-05	7.50E-03	4.09E-03	0.0	8.54E-03
43	4.42E-05	4.08E-03	7.21E-03	0.0	8.29E-03
44	6.80E-05	1.39E-03	4.21E-04	0.0	1.45E-03
45	6.35E-05	2.11E-02	1.58E-01	0.0	1.59E-01
46	1.21E-04	3.55E-03	3.41E-03	0.0	4.92E-03
47	3.73E-05	1.49E-02	2.17E-02	0.0	2.64E-02
48	2.63E-05	1.66E-03	1.08E-03	0.0	1.99E-03
49	1.32E-08	4.48E-06	4.38E-07	0.0	4.50E-06
50	5.47E-09	1.38E-05	2.53E-06	0.0	1.41E-05
51	4.90E-05	6.68E-04	2.65E-04	0.0	7.21E-04
52	3.08E-08	3.77E-06	5.98E-07	0.0	3.81E-06
53	8.51E-05	1.09E-03	6.93E-04	0.0	1.29E-03
54	0.0	0.0	0.0	0.0	0.0
55	2.41E-08	5.75E-06	2.66E-06	0.0	6.34E-06
56	6.63E-07	1.69E-04	1.56E-04	0.0	2.30E-04
57	5.38E-05	2.17E-03	1.25E-03	0.0	2.51E-03
58	0.0	0.0	0.0	0.0	0.0
59	2.05E-08	3.97E-06	1.46E-06	0.0	4.23E-06

Table 4 Uncertainty of $^{239}Pu(n,\gamma)$ Resonance Self-Shielding Factor for Large Fast Breeder Reactor at $\sigma_0 = 37$ barn and $T = 487.5^0$k

IBG	EH (eV)	Uncertainty Components (absolute)				
		$\frac{\delta f}{f}(\frac{\delta Er}{Er})$	$\frac{\delta f}{f}(\frac{\delta \Gamma_n}{\Gamma_n})$	$\frac{\delta f}{f}(\frac{\delta \Gamma_\gamma}{\Gamma_\gamma})$	$\frac{\delta f}{f}(\frac{\delta \Gamma_f}{\Gamma_f})$	$\frac{\delta f}{f}(\frac{\delta \Gamma}{\Gamma})$
34	2.6126E+3	3.07E-06	8.29E-03	7.03E-03	6.06E-03	1.24E-02
35	2.0347E+3	3.28E-06	8.97E-03	8.76E-03	6.62E-03	1.41E-02
36	1.5846E+3	3.40E-06	8.09E-03	7.42E-03	9.12E-03	1.42E-02
37	1.2341E+3	6.36E-06	1.25E-02	1.20E-02	8.64E-03	1.94E-02
38	9.6122E+2	9.20E-06	1.98E-02	7.17E-03	1.35E-02	2.50E-02
39	7.4852E+2	1.04E-05	2.08E-02	7.23E-03	1.78E-02	2.83E-02
40	5.8295E+2	1.15E-05	2.32E-02	1.70E-02	1.39E-02	3.20E-02
41	4.5400E+2	1.28E-05	2.59E-02	1.72E-02	1.52E-02	3.46E-02
42	3.5358E+2	1.16E-05	2.35E-02	8.16E-03	1.85E-02	3.10E-02
43	2.7536E+2	1.10E-05	2.31E-02	1.38E-02	1.99E-02	3.35E-02
44	2.1445E+2	1.63E-05	2.96E-02	3.44E-02	1.77E-02	4.87E-02
45	1.6702E+2	1.64E-05	3.28E-02	3.57E-02	2.51E-02	5.47E-02
46	1.3007E+2	9.55E-06	1.84E-02	1.60E-02	1.76E-02	3.01E-02
47	1.0130E+2	7.18E-06	1.67E-02	2.72E-02	1.78E-02	3.66E-02
48	7.8893E+1	1.75E-05	3.37E-02	2.40E-02	3.16E-02	5.21E-02
49	6.1442E+1	2.97E-05	5.07E-02	7.06E-02	1.70E-02	8.86E-02
50	4.7851E+1	3.57E-05	6.22E-02	9.65E-02	1.42E-02	1.15E-01
51	3.7267E+1	2.08E-05	4.15E-02	4.86E-02	3.34E-02	7.21E-02
52	2.9023E+1	1.28E-05	2.51E-02	1.66E-02	2.54E-02	3.94E-02
53	2.2603E+1	4.56E-05	8.89E-02	6.90E-02	6.51E-02	1.30E-01
54	1.7603E+1	1.78E-05	3.46E-02	4.17E-02	2.32E-02	5.90E-02
55	1.3710E+1	7.35E-06	1.43E-02	1.46E-02	3.96E-02	4.46E-02
56	1.0677E+1	0.0	0.0	0.0	0.0	0.0
57	8.3153E+0	4.96E-05	9.82E-02	6.08E-02	8.88E-02	1.45E-01

Table 5 Uncertainty of The Temperature Gradient α of $^{239}Pu(n,\gamma)$ f-factor for Large Fast Breeder Reactor at $\sigma_0 = 37$ barn and $T = 487.5^0$k

IBG	Uncertainty Components (absolute)				
	$\frac{\delta \alpha}{\alpha}(\frac{\delta Er}{Er})$	$\frac{\delta \alpha}{\alpha}(\frac{\delta \Gamma_n}{\Gamma_n})$	$\frac{\delta \alpha}{\alpha}(\frac{\delta \Gamma_\gamma}{\Gamma_\gamma})$	$\frac{\delta \alpha}{\alpha}(\frac{\delta \Gamma_f}{\Gamma_f})$	$\frac{\delta \alpha}{\alpha}(\frac{\delta \Gamma}{\Gamma})$
34	4.82E-09	8.43E-06	7.65E-06	1.35E-06	1.14E-05
35	5.31E-09	9.19E-06	6.96E-06	1.87E-06	1.16E-05
36	5.93E-09	1.24E-05	1.44E-05	2.44E-06	1.92E-05
37	1.79E-08	2.14E-05	1.16E-05	6.87E-06	2.54E-05
38	2.71E-08	2.67E-05	1.42E-05	3.12E-06	3.04E-05
39	3.68E-08	5.16E-05	3.94E-05	4.54E-06	6.51E-05
40	1.32E-07	1.64E-04	8.03E-05	4.06E-05	1.87E-04
41	1.07E-07	1.88E-04	5.42E-05	2.42E-05	1.97E-04
42	8.12E-08	1.24E-04	6.81E-05	1.42E-05	1.42E-04
43	2.76E-07	3.81E-04	2.52E-04	4.36E-05	4.60E-04
44	1.17E-07	1.73E-04	1.12E-04	1.40E-05	2.07E-04
45	9.63E-07	1.72E-03	1.39E-03	7.04E-05	2.21E-03
46	2.12E-07	3.56E-04	1.41E-04	4.20E-05	3.86E-04
47	8.32E-06	1.37E-02	6.70E-03	1.64E-03	1.53E-02
48	3.48E-07	6.60E-04	1.17E-04	3.28E-05	6.72E-04
49	5.11E-05	8.73E-02	7.54E-02	3.33E-03	1.15E-01
50	6.09E-05	1.07E-01	1.14E-01	1.90E-03	1.56E-01
51	1.24E-09	2.47E-06	2.57E-06	8.42E-09	3.57E-06
52	4.97E-05	9.73E-02	2.66E-02	1.92E-03	1.00E-01
53	7.22E-08	1.40E-04	5.40E-05	2.42E-06	1.50E-04
54	4.87E-05	9.50E-02	4.49E-02	1.56E-03	1.05E-01
55	5.27E-05	1.04E-01	1.43E-02	1.12E-03	1.05E-01
56	0.0	0.0	0.0	0.0	0.0
57	3.52E-07	6.97E-04	1.69E-04	5.04E-07	7.17E-04

Table 6 Uncertainty of $^{239}Pu(n,f)$ Resonance Self-Shielding Factor for Large Fast Breeder Reactor at $\sigma_0 = 37$ barn and $T = 487.5^0$k

IBG	EH (eV)	Uncertainty Components (absolute)				
		$\frac{\delta f}{f}(\frac{\delta Er}{Er})$	$\frac{\delta f}{f}(\frac{\delta \Gamma_n}{\Gamma_n})$	$\frac{\delta f}{f}(\frac{\delta \Gamma_\gamma}{\Gamma_\gamma})$	$\frac{\delta f}{f}(\frac{\delta \Gamma_f}{\Gamma_f})$	$\frac{\delta f}{f}(\frac{\delta \Gamma}{\Gamma})$
34	6.6126E+3	4.64E-06	8.00E-03	3.80E-03	5.99E-03	1.07E-02
35	2.0347E+3	4.09E-06	9.79E-03	4.29E-03	8.34E-03	1.35E-02
36	1.5846E+3	4.09E-06	9.55E-03	4.65E-03	1.01E-02	1.47E-02
37	1.2341E+3	5.31E-06	1.11E-02	5.69E-03	1.21E-02	1.74E-02
38	9.6122E+2	9.69E-06	1.90E-02	6.06E-03	1.53E-02	2.51E-02
39	7.4852E+2	1.07E-05	2.10E-02	7.54E-03	1.86E-02	2.91E-02
40	5.8295E+2	1.05E-05	2.08E-02	1.09E-02	1.69E-02	2.89E-02
41	4.5400E+2	1.27E-05	2.53E-02	9.31E-03	2.11E-02	3.42E-02
42	3.5358E+2	1.21E-05	2.41E-02	9.22E-03	2.12E-02	3.34E-02
43	2.7536E+2	1.18E-05	2.36E-02	1.05E-02	2.14E-02	3.36E-02
44	2.1445E+2	1.35E-05	2.72E-02	1.59E-02	2.51E-02	4.03E-02
45	1.6702E+2	1.51E-05	3.03E-02	2.32E-02	2.71E-02	4.68E-02
46	1.3007E+2	1.75E-05	3.52E-02	1.73E-02	3.14E-02	5.03E-02
47	1.0130E+2	1.92E-05	3.86E-02	2.58E-02	3.77E-02	5.98E-02
48	7.8893E+1	1.51E-05	2.97E-02	1.96E-02	2.39E-02	4.29E-02
49	6.1442E+1	2.16E-05	4.13E-02	4.04E-02	3.14E-02	6.58E-02
50	4.7851E+1	2.20E-05	4.01E-02	6.35E-02	3.03E-02	8.10E-02
51	3.7267E+1	2.10E-05	4.20E-02	6.04E-02	3.32E-02	8.07E-02
52	2.9023E+1	1.04E-05	2.08E-02	1.23E-02	1.78E-02	3.01E-02
53	2.2603E+1	4.21E-05	8.22E-02	6.48E-02	5.95E-02	1.20E-01
54	1.7603E+1	1.31E-05	2.62E-02	3.13E-02	1.92E-02	4.52E-02
55	1.3710E+1	7.26E-06	1.46E-02	2.79E-02	1.55E-02	3.51E-02
56	1.0677E+1	0.0	0.0	0.0	0.0	0.0
57	8.3153E+0	4.96E-05	9.82E-02	6.08E-02	8.88E-02	1.45E-01

Table 7 Uncertainty of The Temperature Gradient α of $^{239}Pu(n,f)$ f-factor for Large Fast Breeder Reactor at $\sigma_0 = 37$ barn and $T = 487.5^0$k

IBG	Uncertainty Components (absolute)				
	$\frac{\delta \alpha}{\alpha}(\frac{\delta Er}{Er})$	$\frac{\delta \alpha}{\alpha}(\frac{\delta \Gamma_n}{\Gamma_n})$	$\frac{\delta \alpha}{\alpha}(\frac{\delta \Gamma_\gamma}{\Gamma_\gamma})$	$\frac{\delta \alpha}{\alpha}(\frac{\delta \Gamma_f}{\Gamma_f})$	$\frac{\delta \alpha}{\alpha}(\frac{\delta \Gamma}{\Gamma})$
34	1.95E-08	3.46E-05	3.58E-05	4.03E-06	5.00E-05
35	1.92E-08	4.22E-05	3.60E-05	5.72E-06	5.58E-05
36	2.18E-08	4.74E-05	5.64E-05	6.21E-06	7.40E-05
37	3.29E-08	5.73E-05	6.08E-05	8.99E-06	8.40E-05
38	5.59E-08	9.13E-05	6.73E-05	6.85E-06	1.13E-04
39	9.29E-08	1.55E-04	1.40E-04	9.32E-06	2.09E-04
40	1.24E-07	2.00E-04	1.55E-04	2.34E-05	2.54E-04
41	1.03E-07	1.90E-04	1.40E-04	1.24E-05	2.37E-04
42	2.45E-07	4.19E-04	2.87E-04	3.17E-05	5.09E-04
43	3.62E-07	6.20E-04	4.76E-04	3.32E-05	7.82E-04
44	8.15E-07	1.45E-03	1.15E-03	6.01E-05	1.85E-03
45	2.83E-07	5.17E-04	4.21E-04	2.05E-05	6.68E-04
46	8.58E-07	1.55E-03	1.09E-03	1.10E-04	1.90E-03
47	8.41E-07	1.51E-03	1.18E-03	1.02E-04	1.92E-03
48	1.32E-06	2.51E-03	4.43E-04	1.21E-04	2.55E-03
49	2.65E-05	4.83E-02	3.45E-02	1.37E-03	5.93E-02
50	8.22E-06	1.46E-02	1.55E-02	2.41E-04	2.13E-02
51	2.75E-07	5.48E-04	6.58E-04	1.22E-06	8.57E-04
52	1.83E-05	3.59E-02	1.08E-02	6.54E-04	3.75E-02
53	4.31E-07	8.40E-04	3.22E-04	1.44E-05	9.00E-04
54	4.21E-05	8.24E-02	3.96E-02	1.17E-03	9.14E-02
55	1.01E-05	2.00E-02	4.60E-03	1.90E-04	2.05E-02
56	0.0	0.0	0.0	0.0	0.0
57	6.81E-06	1.34E-02	3.28E-03	9.75E-06	1.38E-02

Table 8 Uncertainty of $^{240}Pu(n,\gamma)$ Resonance Self-Shielding Factor for Large Fast Breeder Reactor at $\sigma_0 = 37$ barn and $T = 487.5^0$k

IBG	EH (eV)	Uncertainty Components (absolute)				
		$\frac{\delta f}{f}(\frac{\delta Er}{Er})$	$\frac{\delta f}{f}(\frac{\delta \Gamma_n}{\Gamma_n})$	$\frac{\delta f}{f}(\frac{\delta \Gamma_\gamma}{\Gamma_\gamma})$	$\frac{\delta f}{f}(\frac{\delta \Gamma_f}{\Gamma_f})$	$\frac{\delta f}{f}(\frac{\delta \Gamma}{\Gamma})$
32	4.3074E+3	1.21E-04	4.21E-02	5.71E-02	3.20E-02	7.79E-02
33	3.3546E+3	1.09E-04	3.08E-02	6.17E-02	2.22E-02	7.25E-02
34	2.6126E+3	9.84E-05	2.89E-02	5.87E-02	2.66E-02	7.07E-02
35	2.0347E+3	8.47E-05	1.81E-02	6.14E-02	1.91E-02	6.68E-02
36	1.5846E+3	8.12E-05	1.68E-02	6.59E-02	2.02E-02	7.10E-02
37	1.2341E+3	9.06E-05	1.68E-02	5.21E-02	1.40E-02	5.65E-02
38	9.6122E+2	8.40E-05	1.62E-02	5.62E-02	1.72E-02	6.10E-02
39	7.4852E+2	8.14E-05	1.21E-02	7.86E-03	1.83E-02	2.33E-02
40	5.8295E+2	1.49E-04	2.62E-02	1.86E-02	2.96E-02	4.37E-02
41	4.5400E+2	1.72E-04	8.55E-03	8.69E-03	2.03E-02	2.37E-02
42	3.5358E+2	3.60E-04	4.91E-03	1.09E-02	1.17E-02	1.67E-02
43	2.7536E+2	7.37E-04	2.94E-02	2.40E-02	1.43E-02	4.06E-02
44	2.1445E+2	1.11E-04	5.07E-02	9.14E-03	1.11E-01	1.22E-01
45	1.6702E+2	1.52E-04	7.88E-02	2.08E-02	1.43E-02	8.28E-02
46	1.3007E+2	6.43E-04	1.48E-02	1.24E-02	1.38E-03	1.94E-02
47	1.0130E+2	1.75E-05	3.41E-03	3.86E-02	3.91E-02	5.51E-02
48	7.8893E+1	2.27E-04	6.03E-03	9.70E-03	3.63E-02	3.80E-02
49	6.1442E+1	0.0	0.0	0.0	0.0	0.0
50	4.7851E+1	3.75E-04	1.28E-02	4.85E-02	3.00E-03	5.03E-02
51	3.7267E+1	0.0	0.0	0.0	0.0	0.0
52	2.9023E+1	0.0	0.0	0.0	0.0	0.0
53	2.2603E+1	1.89E-03	4.83E-02	5.78E-02	5.78E-05	7.54E-02
54	1.7603E+1	0.0	0.0	0.0	0.0	0.0
55	1.3710E+1	0.0	0.0	0.0	0.0	0.0
56	1.0677E+1	0.0	0.0	0.0	0.0	0.0
57	8.3153E+0	0.0	0.0	0.0	0.0	0.0
58	6.4760E+0	0.0	0.0	0.0	0.0	0.0
59	5.0435E+0	0.0	0.0	0.0	0.0	0.0
60	3.9279E+0	0.0	0.0	0.0	0.0	0.0
61	3.0590E+0	0.0	0.0	0.0	0.0	0.0
62	2.3824E+0	0.0	0.0	0.0	0.0	0.0
63	1.8554E+0	0.0	0.0	0.0	0.0	0.0
64	1.4450E+0	0.0	0.0	0.0	0.0	0.0
65	1.1254E+0	4.98E-04	0.0	2.21E-01	0.0	2.21E-01

Table 9 Uncertainty of The Temperature Gradient α of $^{240}Pu(n,\gamma)$ f-factor for Large Fast Breeder Reactor at $\sigma_0 = 37$ barn and $T = 487.5^0$k

IBG	Uncertainty Components (absolute)				
	$\frac{\delta \alpha}{\alpha}(\frac{\delta Er}{Er})$	$\frac{\delta \alpha}{\alpha}(\frac{\delta \Gamma_n}{\Gamma_n})$	$\frac{\delta \alpha}{\alpha}(\frac{\delta \Gamma_\gamma}{\Gamma_\gamma})$	$\frac{\delta \alpha}{\alpha}(\frac{\delta \Gamma_f}{\Gamma_f})$	$\frac{\delta \alpha}{\alpha}(\frac{\delta \Gamma}{\Gamma})$
32	5.78E-08	4.59E-06	1.48E-06	9.57E-08	4.82E-06
33	1.54E-07	8.31E-06	2.79E-06	2.40E-06	9.09E-06
34	1.49E-07	1.21E-05	3.81E-06	5.50E-07	1.27E-05
35	1.70E-07	6.29E-06	4.31E-06	6.86E-07	7.66E-06
36	3.61E-07	1.22E-05	1.03E-05	6.21E-07	1.60E-05
37	2.37E-07	9.83E-06	1.09E-05	2.74E-07	1.46E-05
38	3.66E-07	1.12E-05	1.46E-05	3.13E-06	1.87E-05
39	6.51E-07	1.96E-05	2.41E-05	4.70E-07	3.11E-05
40	5.21E-07	4.20E-05	7.44E-05	7.40E-08	8.54E-05
41	3.85E-06	9.65E-05	1.46E-04	2.94E-07	1.75E-04
42	1.85E-06	1.85E-05	5.63E-05	6.49E-08	5.93E-05
43	9.91E-07	3.90E-05	2.39E-05	4.44E-08	4.57E-05
44	1.11E-06	1.00E-04	1.73E-05	3.13E-08	1.02E-04
45	2.26E-05	5.08E-03	1.15E-03	7.25E-07	5.21E-03
46	4.85E-06	1.12E-04	4.84E-05	5.59E-08	1.22E-04
47	4.00E-05	1.34E-03	3.68E-03	9.12E-07	3.92E-03
48	4.35E-06	8.22E-05	6.69E-05	4.55E-08	1.06E-04
49	0.0	0.0	0.0	0.0	0.0
50	2.26E-04	8.03E-03	1.69E-02	2.77E-06	1.87E-02
51	0.0	0.0	0.0	0.0	0.0
52	0.0	0.0	0.0	0.0	0.0
53	4.58E-05	1.16E-03	1.29E-03	9.28E-08	1.74E-03
54	0.0	0.0	0.0	0.0	0.0
55	0.0	0.0	0.0	0.0	0.0
56	0.0	0.0	0.0	0.0	0.0
57	0.0	0.0	0.0	0.0	0.0
58	0.0	0.0	0.0	0.0	0.0
59	0.0	0.0	0.0	0.0	0.0
60	0.0	0.0	0.0	0.0	0.0
61	0.0	0.0	0.0	0.0	0.0
62	0.0	0.0	0.0	0.0	0.0
63	0.0	0.0	0.0	0.0	0.0
64	0.0	0.0	0.0	0.0	0.0
65	7.31E-04	0.0	2.39E-01	0.0	2.39E-01

Table 10 Uncertainty of $^{240}Pu(n,f)$ Resonance Self-Shielding Factor for Large Fast Breeder Reactor at $\sigma_0 = 37$ barn and $T = 487.5^0$k

IBG	EH (eV)	Uncertainty Components (absolute)				
		$\frac{\delta f}{f}(\frac{\delta Er}{Er})$	$\frac{\delta f}{f}(\frac{\delta \Gamma_n}{\Gamma_n})$	$\frac{\delta f}{f}(\frac{\delta \Gamma_\gamma}{\Gamma_\gamma})$	$\frac{\delta f}{f}(\frac{\delta \Gamma_f}{\Gamma_f})$	$\frac{\delta f}{f}(\frac{\delta \Gamma}{\Gamma})$
32	4.3074E+3	1.11E-04	6.59E-02	3.75E-02	4.80E-02	8.98E-02
33	3.3546E+3	9.31E-05	5.17E-02	3.61E-02	3.93E-02	7.44E-02
34	2.6126E+3	9.30E-05	1.06E-01	3.31E-02	5.22E-02	1.22E-01
35	2.0347E+3	8.76E-05	5.92E-02	3.12E-02	4.66E-02	8.16E-02
36	1.5846E+3	8.92E-05	5.09E-02	3.32E-02	5.23E-02	8.02E-02
37	1.2341E+3	9.05E-05	5.78E-02	3.11E-02	6.98E-02	9.59E-02
38	9.6122E+2	9.43E-05	4.35E-01	2.99E-02	3.53E-02	4.38E-01
39	7.4852E+2	1.20E-04	5.29E-02	1.22E-02	6.20E-02	8.25E-02
40	5.8295E+2	1.65E-04	7.46E-02	3.15E-02	3.07E-02	8.67E-02
41	4.5400E+2	1.82E-04	2.96E-02	3.62E-02	5.03E-02	6.87E-02
42	3.5358E+2	2.03E-04	1.29E-02	4.84E-02	4.57E-02	6.79E-02
43	2.7536E+2	5.87E-04	4.86E-02	7.57E-02	1.02E-01	1.36E-01
44	2.1445E+2	2.55E-04	6.12E-02	1.14E-02	1.74E-01	1.85E-01
45	1.6702E+2	1.75E-04	7.71E-02	2.02E-02	4.38E-02	9.10E-02
46	1.3007E+2	5.28E-04	1.24E-02	3.45E-02	1.29E-02	3.89E-02
47	1.0130E+2	9.51E-05	3.71E-03	4.58E-02	3.50E-02	5.78E-02
48	7.8893E+1	2.17E-05	3.66E-03	9.22E-03	4.61E-02	4.71E-02
49	6.1442E+1	0.0	0.0	0.0	0.0	0.0
50	4.7851E+1	1.05E-04	5.15E-03	4.19E-02	7.33E-03	4.28E-02
51	3.7267E+1	0.0	0.0	0.0	0.0	0.0
52	2.9023E+1	0.0	0.0	0.0	0.0	0.0
53	2.2603E+1	1.89E-03	4.83E-02	5.78E-02	5.78E-05	7.54E-02
54	1.7603E+1	0.0	0.0	0.0	0.0	0.0
55	1.3710E+1	0.0	0.0	0.0	0.0	0.0
56	1.0677E+1	0.0	0.0	0.0	0.0	0.0
57	8.3153E+0	0.0	0.0	0.0	0.0	0.0
58	6.4760E+0	0.0	0.0	0.0	0.0	0.0
59	5.0435E+0	0.0	0.0	0.0	0.0	0.0
60	3.9279E+0	0.0	0.0	0.0	0.0	0.0
61	3.0590E+0	0.0	0.0	0.0	0.0	0.0
62	2.3824E+0	0.0	0.0	0.0	0.0	0.0
63	1.8554E+0	0.0	0.0	0.0	0.0	0.0
64	1.4450E+0	0.0	0.0	0.0	0.0	0.0
65	1.1254E+0	4.98E-04	0.0	2.21E-01	0.0	2.21E-01

Table 11 Uncertainty of The Temperature Gradient α of $^{240}Pu(n,f)$ f-factor for Large Fast Breeder Reactor at $\sigma_0 = 37$ barn and $T = 487.5^0$k

IBG	Uncertainty Components (absolute)				
	$\frac{\delta \alpha}{\alpha}(\frac{\delta Er}{Er})$	$\frac{\delta \alpha}{\alpha}(\frac{\delta \Gamma_n}{\Gamma_n})$	$\frac{\delta \alpha}{\alpha}(\frac{\delta \Gamma_\gamma}{\Gamma_\gamma})$	$\frac{\delta \alpha}{\alpha}(\frac{\delta \Gamma_f}{\Gamma_f})$	$\frac{\delta \alpha}{\alpha}(\frac{\delta \Gamma}{\Gamma})$
32	5.83E-08	1.33E-05	4.24E-06	1.47E-07	1.40E-05
33	8.18E-08	1.79E-05	6.08E-06	8.36E-07	1.89E-05
34	1.23E-07	6.72E-05	1.48E-05	7.33E-07	6.88E-05
35	1.35E-07	3.99E-05	1.86E-05	7.82E-07	4.40E-05
36	1.67E-07	4.81E-05	3.31E-05	7.70E-07	5.84E-05
37	1.69E-07	4.96E-05	4.21E-05	3.92E-07	6.51E-05
38	1.93E-07	1.33E-04	3.91E-05	1.36E-06	1.39E-04
39	2.77E-07	3.54E-05	4.24E-05	3.46E-07	5.52E-05
40	5.91E-07	1.39E-04	1.46E-04	8.83E-08	2.02E-04
41	8.07E-07	6.19E-05	1.64E-04	8.96E-08	1.75E-04
42	1.21E-06	4.30E-05	2.41E-04	8.52E-08	2.45E-04
43	1.79E-06	1.07E-04	2.57E-04	7.78E-08	2.78E-04
44	6.26E-06	9.36E-04	1.68E-04	1.88E-07	9.51E-04
45	2.80E-06	6.80E-04	1.51E-04	9.26E-08	6.97E-04
46	6.13E-06	1.47E-04	3.66E-04	7.48E-08	3.95E-04
47	4.17E-06	1.38E-04	4.13E-04	9.66E-08	4.36E-04
48	3.24E-06	1.23E-04	7.51E-05	3.79E-08	1.44E-04
49	0.0	0.0	0.0	0.0	0.0
50	2.64E-05	1.19E-03	2.94E-03	3.14E-07	3.17E-03
51	0.0	0.0	0.0	0.0	0.0
52	0.0	0.0	0.0	0.0	0.0
53	2.50E-04	6.37E-03	7.06E-03	5.06E-07	9.52E-03
54	0.0	0.0	0.0	0.0	0.0
55	0.0	0.0	0.0	0.0	0.0
56	0.0	0.0	0.0	0.0	0.0
57	0.0	0.0	0.0	0.0	0.0
58	0.0	0.0	0.0	0.0	0.0
59	0.0	0.0	0.0	0.0	0.0
60	0.0	0.0	0.0	0.0	0.0
61	0.0	0.0	0.0	0.0	0.0
62	0.0	0.0	0.0	0.0	0.0
63	0.0	0.0	0.0	0.0	0.0
64	0.0	0.0	0.0	0.0	0.0
65	7.31E-04	0.0	2.39E-01	0.0	2.39E-01

Table 12 Uncertainty of ^{238}U Doppler Reactivity Worth for Large Fast Breeder Reactor at σ_0 = 37 barn and $T = 487.5^0$k

IBG	Uncertainty Components (absolute)				
	$\frac{\delta\rho}{\rho}(\frac{\delta Er}{Er})$	$\frac{\delta\rho}{\rho}(\frac{\delta\Gamma_n}{\Gamma_n})$	$\frac{\delta\rho}{\rho}(\frac{\delta\Gamma_\gamma}{\Gamma_\gamma})$	$\frac{\delta\rho}{\rho}(\frac{\delta\Gamma_f}{\Gamma_f})$	$\frac{\delta\rho}{\rho}(\frac{\delta\Gamma}{\Gamma})$
28	5.95E-06	2.11E-03	1.40E-03	0.0	2.53E-03
29	5.36E-05	2.65E-03	2.04E-03	0.0	3.35E-03
30	9.26E-05	4.12E-03	3.12E-03	0.0	5.17E-03
31	4.95E-05	4.78E-03	3.89E-03	0.0	6.17E-03
32	3.57E-06	2.15E-03	2.85E-03	0.0	3.57E-03
33	1.78E-06	6.25E-04	1.17E-03	0.0	1.32E-03
34	2.39E-06	1.86E-03	4.45E-03	0.0	4.83E-03
35	6.57E-06	3.21E-03	8.36E-03	0.0	8.96E-03
36	6.74E-06	3.98E-03	1.04E-02	0.0	1.11E-02
37	5.63E-06	2.65E-03	9.54E-03	0.0	9.90E-03
38	1.41E-05	1.50E-02	1.03E-02	0.0	1.82E-02
39	1.05E-05	8.53E-03	8.61E-03	0.0	1.21E-02
40	9.02E-06	6.99E-03	6.80E-03	0.0	9.75E-03
41	5.89E-06	6.28E-03	5.96E-03	0.0	8.66E-03
42	6.07E-06	6.24E-03	9.30E-03	0.0	1.12E-02
43	2.12E-06	1.39E-04	1.00E-03	0.0	1.01E-03
44	9.95E-07	1.60E-05	7.26E-05	0.0	7.44E-05
45	2.10E-06	1.12E-03	1.07E-02	0.0	1.08E-02
46	8.36E-07	2.60E-05	1.36E-04	0.0	1.39E-04
47	2.01E-07	2.83E-05	5.06E-05	0.0	5.80E-05
48	2.20E-08	8.42E-07	3.15E-06	0.0	3.26E-06
49	5.50E-14	3.28E-12	8.67E-13	0.0	3.40E-12
50	8.53E-14	3.98E-11	1.66E-11	0.0	4.32E-11
51	4.32E-09	2.86E-08	1.14E-07	0.0	1.17E-07
52	4.08E-14	9.40E-13	4.06E-13	0.0	1.02E-12
53	1.59E-09	1.44E-08	3.21E-08	0.0	3.52E-08
54	0.0	0.0	0.0	0.0	0.0
55	2.02E-15	1.05E-13	1.24E-13	0.0	1.63E-13
56	1.87E-13	1.90E-11	3.32E-11	0.0	3.83E-11
57	1.40E-10	4.50E-09	5.99E-09	0.0	7.49E-09
58	0.0	0.0	0.0	0.0	0.0
59	1.34E-15	5.72E-14	6.47E-14	0.0	8.64E-14
SUM=	1.20E-04	2.28E-02	2.82E-02	0.0	3.62E-02

Table 13(a) ^{238}U Total Doppler Reactivity Worth Uncertainty for Large Fast Breeder Reactor at σ_0 = 37 barn and $T = 487.5^0$k

$I\sigma_0$ (b)	Temperature in ^{0}k				
	3.000E+02	4.875E+02	6.444e+02	1.273E+03	5.273E+03
1.000E+01	0.0	4.905E+00	3.263E+00	1.918E+00	1.212E+00
3.700E+01	0.0	3.630E+00	2.427E+00	1.447E+00	9.381E-01
1.000E+02	0.0	3.129E+00	2.110E+00	1.282E+00	8.599E-01
1.000E+03	0.0	2.465E+00	1.776E+00	1.214E+00	9.351E-01
1.000E+04	0.0	2.742E+00	2.119E+00	1.542E+00	1.228E+00
1.000E+05	0.0	1.247E+00	1.109E+00	9.423E-01	8.302E-01
1.000E+06	0.0	8.565E-01	8.903E-01	8.583E-01	8.294E-01
1.000E+07	0.0	2.881E-01	2.993E-01	2.806E-01	2.786E-01
1.000E+08	0.0	0.0	0.0	0.0	0.0
1.000E+09	0.0	0.0	0.0	0.0	0.0
1.000E+10	0.0	0.0	0.0	0.0	0.0

Table 13(b) ^{239}Pu Total Doppler Reactivity Worth Uncertainty for Large Fast Breeder Reactor at σ_0 = 37 barn and $T = 487.5^0$k

σ_0 (b)	Temperature in ^{0}k				
	3.000E+02	4.875E+02	6.444E+02	1.273E+03	5.273E+03
1.000E+01	0.0	5.611E-02	3.725E-02	2.169E-02	1.340E-02
3.700E+01	0.0	1.278E-02	8.455E-03	4.890E-03	2.993E-03
1.000E+02	0.0	5.760E-03	3.804E-03	2.193E-03	1.337E-03
1.000E+03	0.0	1.989E-03	1.317E-03	7.620E-04	4.675E-04
1.000E+04	0.0	2.020E-04	1.387E-04	8.234E-05	5.085E-05
1.000E+05	0.0	2.635E-06	2.518E-06	1.551E-06	1.299E-06
1.000E+06	0.0	0.0	0.0	0.0	0.0
1.000E+07	0.0	0.0	0.0	0.0	0.0
1.000E+08	0.0	0.0	0.0	0.0	0.0
1.000E+09	0.0	0.0	0.0	0.0	0.0
1.000E+10	0.0	0.0	0.0	0.0	0.0

Table 13(c) ^{240}Pu Total Doppler Reactivity Worth Uncertainty for Large Fast Breeder Reactor at σ_0 = 37 barn and $T = 487.5^0$k

σ_0 (b)	Temperature in ^{0}k				
	3.000E+02	4.875E+02	6.444E+02	1.273E+03	5.273E+03
1.000E+01	0.0	3.379E-03	2.241E-03	1.306E-03	8.099E-04
3.700E+01	0.0	1.833E-03	1.212E-03	7.010E-04	4.296E-04
1.000E+02	0.0	1.394E-03	9.187E-04	5.286E-04	3.222E-04
1.000E+03	0.0	8.897E-04	5.897E-04	3.416E-04	2.096E-04
1.000E+04	0.0	2.449E-03	1.608E-03	9.191E-04	5.568E-04
1.000E+05	0.0	3.776E-02	2.563E-02	1.533E-02	9.785E-03
1.000E+06	0.0	1.862E-03	1.544E-03	1.164E-03	9.761E-04
1.000E+07	0.0	0.0	0.0	0.0	0.0
1.000E+08	0.0	0.0	0.0	0.0	0.0
1.000E+09	0.0	0.0	0.0	0.0	0.0
1.000E+10	0.0	0.0	0.0	0.0	0.0

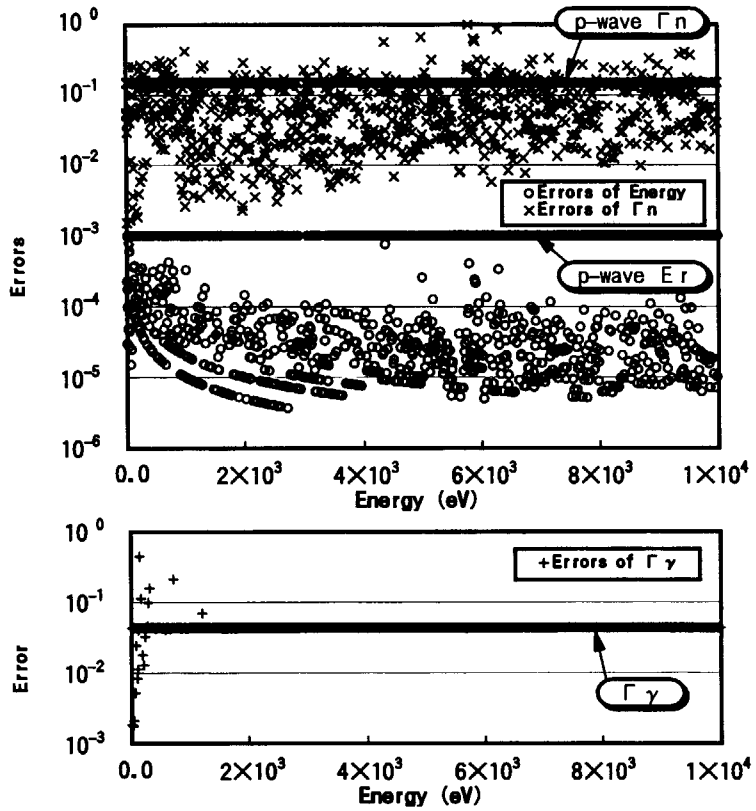

Fig.1 Energy Distribution of the Evaluated Errors of Resolved Resonance Parameters for ^{238}U.

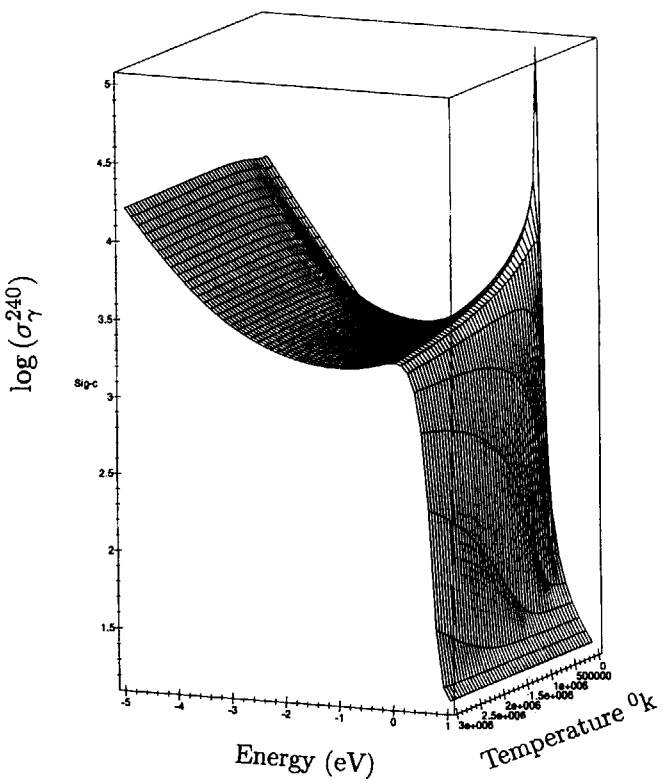

Fig. 2 ^{240}Pu Capture Cross Section σ_γ^{240} as function of Temperature and Energy.

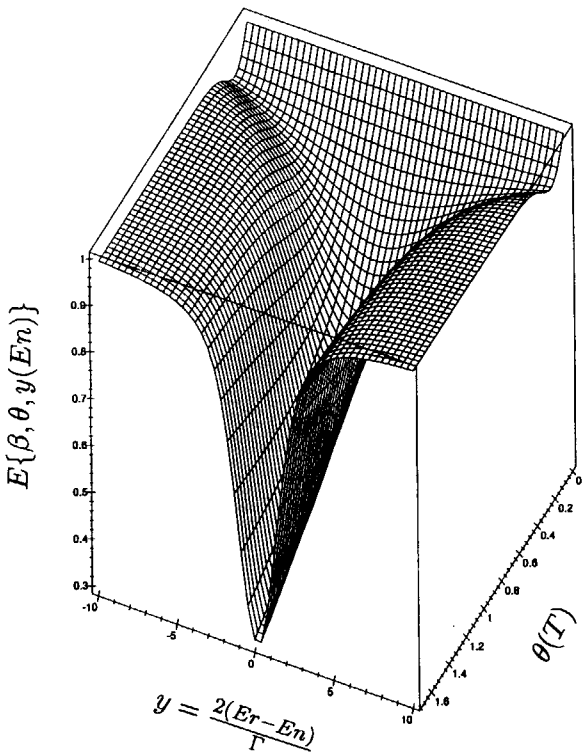

Fig. 3 Criterion Function $E\{\beta,\theta,y(En)\}$ for Power Series Expansion.

2.5 Topics

2.5.1 Present Status of Research on Optical Potential for Neutron

Masaru MATOBA
Department of Nuclear Engineering, Faculty of Engineering,
Kyushu University, Fukuoka, 812-81, Japan
matoba@kune2a.nucl.kyushu-u.ac.jp

Motivations of establishment of the research committee on "Unified Neutron Potential" in the Atomic Energy Society of Japan and results of discussions in the committee are presented.

1.New trends in nuclear data activity

The research on nuclear data started in old time to evaluate the basic nuclear data for nuclear reactor dynamics and operation/management of nuclear plants. These researches have been done quite actively in long-time.

Now, a large number of nuclear plants operate daily and the technical problems are considerably resolved. Present main problems may be the safety in operation of the plants, the decrease of nuclear wastes and the design of the future nuclear energy generation system.

Recently, new applications of nuclear reactions expand widely in several fields, for examples, transmutation of TRU, beam driven power systems, nuclear fusion, nuclear medicine, non-destroyed diagnostics, LSI fabrications, surface and low level analysis, space science and technology, basic sciences and so on.

These applications request, of course, new nuclear data. The region of concerned physical quantity increases widely in incident particles, target nuclei and incident energy.

2.Establishment of a research committee

In this background, a research committee on "Unified Neutron Potential" was established in the Atomic Energy Society of Japan (AESJ) from April 1994 to March 1996. This committee investigated new trends in the research on nuclear data with a focused item "neutron potential" which is the basic quantity in this field. A number of workshops are opened in Kyushu University.

After several discussions, the final report is published from the AESJ at May 1997 [1]. This report reviews the present status of research on neutron potential as follows.

1) Optical model, new basic problems and nuclear data,

2) Present status of optical model analysis
   - low energy
   - medium/high energy
   - unstable and FP nuclei

3) Dispersion relation in optical model analysis

4) Related problems
   - nuclear data
   - neutron induced experiments

- pre-equilibrium model
- topics

3.Proporsals

For future study, general problems to be considered for new nuclear data are remarked as follows.

1) Accelerators
   To measure required nuclear data, many accelerators are needed, while the first purposes to construct these accelerators are different and some are finished. It is impossible to measure all the required data with points-to-points.

2) Data analysis
   Data already measured are not analyzed to obtain double differential cross sections, and then almost all the data should be re-measured.

3) Nuclear models
   The role of nuclear theory and model becomes quite important from reasons 1) and 2).

4) Nuclear data evaluation
   It is important for nuclear data evaluation groups to measure the decisive data with themselves and construct new data-bases.

5) Data from microscopic to macroscopic region
   Nuclear data-bases should be provided to answer various types of requests and the required groups are not always familiar to nuclear interaction. Then, it is important to prepare data-bases as integrated and/or macroscopic shape calculated from microscopic data.

4.Future activity

It is requested strongly to continue the research in this field. Now, some projects are started to realize the next-step activities as,

1) establishment of a new sub-group "accelerator·beam science" in the AESJ,

2) realization of a forum "accelerator·beam science" at next spring meeting of AESJ,

3) application of the science fund to the ministry of education, science and culture, Japan as a fund of review and project, "Medium and high energy nuclear reaction data and the space-time structure", and

4) a plan to open a summer school for young scientists.

5.Conclusion

We propose here for many specialist groups in Japan to conduct this research co-operatively.

Reference

[1] "Present Status of Neutron Potential –Further Development of Optical Potential Research–", the Atomic Energy Society of Japan, 1997.

2.5.2 Evaluation Method of Nuclear Data: Half-Lives, Gamma-Ray Intensities etc.

Yasukazu YOSHIZAWA*, Osamu MIYATAKE+, and Masao TOYAMA++
*Koi-Osako 3-21-10, Nishiku, Hiroshima 733
+Wakamatsudai 1-1, 1-701, Sakai 590-01
++Gakuenminami 2-10-2, Nara 631

The evaluation method has been studied. The basic problem is how to estimate and treat the systematic error. Nuclear decay data were evaluated. Eight practical examples of half-lives are shown in this report.

1. Introduction

Numerical values which are widely used in other fields should be evaluated by using several reliable experimental results. Because scientists and engineers in other fields cannot select the best values, and it is much better for them to use the common numerical values. The basic constants such as the fundamental physical constants, the atomic weights, the melting points and the evaporation points have been evaluated.

Nuclear data, i.e. neutron cross section data, nuclear decay data, etc. have been evaluated. One of the authors (Y.Y.) experienced the IAEA evaluation work of gamma-ray standards and half-lives of 35 nuclides in the 1980's. From this experience, the authors thought that the evaluation theory was not satisfactory.

In this report we first describe the outline of the IAEA evaluation work, and secondly a development of the evaluation theory. Finally some evaluation examples of half-lives are shown.

2. IAEA evaluation work

Ten scientists from 7 countries met and discussed about evaluation for a few days every one or two years at each place in Europe where the ICRM meeting was to be held. The members selected 35 nuclides for gamma-ray intensities per decays and these 35 plus 1 nuclides for half-lives. At the first meeting the work was shared by the members. All half-lives were evaluated by two persons, and gamma-ray intensities per decays were done by ten persons.

The problems which appeared during this work are as follows:

(a) Results with small uncertainties which were not discussed in their paper were not reliable in some cases. In other words, if experimenters analyze error sources in details and then estimate

uncertainties, uncertainties become larger than theirs in some cases. The evaluater calculates the weighted mean of experimental values, where the inverses of squares of uncertainties are usually used for the weights. Thus the smaller uncertainty gives the larger weight for the mean value.

(b) It is difficult for experimenters to estimate systematic errors. Experimental values are often scattered beyond uncertainties. The reason is that estimated systematic errors were too small.

(c) Experimental values often gather in two or three groups. Probably some components of systematic errors are common in each group.

These problems, which are common in other evaluation, were not resolved in this work. Another problem is that experimenters have not discuss about uncertainties in their reports. Referees and editors should understand such kind of problems and recommend authors to write detail about uncertainties in their papers.

There are only a few measurements of gamma-ray intensities per decay evaluated in this work, but many data of relative gamma-ray intensities were available. Relative intensities were thus evaluated in many cases, and intensities per decay were calculated by means of so-called Yoshizawa's method. This method is that one compiles all feedings of the beta decay, internal conversion, gamma rays etc. to the ground state or the first excited state and then calculates the intensities per decay from these feedings. When the decay scheme is constructed, the values of the intensities per decay are more accurate than those by direct measurements.

Finally the evaluated results were published from IAEA. The IAEA evaluation work was fruitful.

3. Theoretical

Evaluation is not only to calculate the average value or the weighted mean of experimental results, but also is to estimate the systematic error and adjust the uncertainty or the weight. The systematic error has an important role in evaluation. The facts mentioned in chapter 2 (b) and (c) originate from the systematic error. One of the basic problems of the evaluation method is how to estimate and treat systematic errors on the basis of the mathematical statistics. First we define the systematic error as the difference between the mean of observed values and the true value, and secondly define the relative systematic error as the systematic error minus its common part with other systematic errors.

We have almost no theory about the evaluation, but only the analysis of variance can be applied to the evaluation. According to this method of the analysis, the distance between an experimental value and the mean of values indicates the relative systematic error. The mean of the distances is called the external error, which corresponds to the relative systematic error of the mean value. The external error is given by

$$U_{ext}^2 = \frac{1}{p}\sum_i (x_i - \bar{x})^2, \qquad (1)$$

where p is the number of the experiments, x_i is an experimental value, $i = 1, 2, \ldots, p$ and $\bar{x}$ is the mean of the experimental values. The distance $|x_i - \bar{x}|$ is approximately equal to the relative systematic error of x_i.

If the systematic error δ_i is independent of the random error σ_i, the error is given by $\varepsilon_i^2=\sigma_i^2+\delta_i^2$. If the systematic error correlate to the random error, the error is usually written by $\varepsilon_i'=\sigma_i+\delta_i$. Then $\varepsilon_i<\varepsilon_i'$. The weighted mean $\bar{x}$ is expressed by

$$\bar{x} = \frac{1}{w}\sum_i w_i x_i, \tag{2}$$

where $w_i=1/\varepsilon_i^2$ and $w=\Sigma w_i$. Then the uncertainty ε of the mean value $\bar{x}$ is written as

$$\varepsilon^2 = \frac{1}{w^2}\sum_i w_i^2 \varepsilon_i^2 . \tag{3}$$

This equation is generally used for calculation of the uncertainty of the mean value. But the weighted mean of the systematic error δ and the total uncertainty ε is not the same as the random error σ^2.

Another problem is grouping of data as mentioned in chapter 2 (c). This grouping suggests that the systematic error does not decrease from each experimental value to the mean value as the random error does. If the systematic error is a variable similar to the variable x, the weighted mean of the systematic errors is given by the same equation (2), that is

$$\delta = \frac{1}{w}\sum w_i \delta_i, \tag{4}$$

where $w_i=1/\varepsilon_i^2$ and $\varepsilon_i^2=\sigma_i^2+\delta_i^2$ or $\varepsilon_i=\sigma_i+\delta_i$. If the equation (2) is correct, the variance of the mean is

$$\sigma^2 = \frac{1}{w^2}\sum_i w_i^2 \sigma_i^2 . \tag{5}$$

The total uncertainty of the mean value is given by

$$\varepsilon^2 = \sigma^2 + \delta^2 \quad \text{or} \quad \varepsilon = \sigma + \delta . \tag{6}$$

Other theoretical methods have been examined for evaluation, for example an idea of the distance of probability distributions has been applied to the evaluation method. Simulation is applied to the evaluation calculation by using random numbers.

4. Examples of half-lives

Purpose of this report is to examine the method of evaluation and the property of the systematic error. Since the half-life evaluation is simple, compared with other nuclear decay data, the typical examples of half-lives were adopted for the evaluation. We selected eight from 35 nuclides in IAEA evaluation work, and evaluated them.

Since the remarkable progress was made in experimental techniques and instruments around 1970, experimental values later than 1970 were adopted for evaluation. One experimental value with a large uncertainty was neglected for most of nuclides. Following points are important: more

than three values are necessary for evaluation, and whether the grouping property exists or not. In the eight nuclides, each of three nuclides has two groups, each of other two has three groups and the rest of three have no grouping property (one group). The grouping property appears in more nuclides than we expected, because many long-lived nuclides longer than a year were selected for this evaluation.

The grouping property means that the systematic errors are much larger than uncertainties estimated by experimenters and have the common component. When one calculates the weighted mean, the systematic error δ of the mean value must be expressed by the equation (4) different from the rule (5) of random error σ, as discussed in chapter 3.

Three examples are shown in figures, where experimental values and both IAEA and present evaluated values are plotted. Fig. 1 shows the half-life of ^{22}Na. The vertical axis indicates the half-life, and the horizontal axis represents the age of publication. Only three data are available between 1970 and 1990, and one is far from two other values beyond the uncertainties. Thus these three form two groups. Fig. 2 shows the half-life of ^{60}Co. A datum with a large uncertainty in 1973 was not adopted. Other eight data separate into two groups of two and six data. We calculated two following cases: the weighted mean of two groups and the weighted mean of the lower group with 6 data. Finally

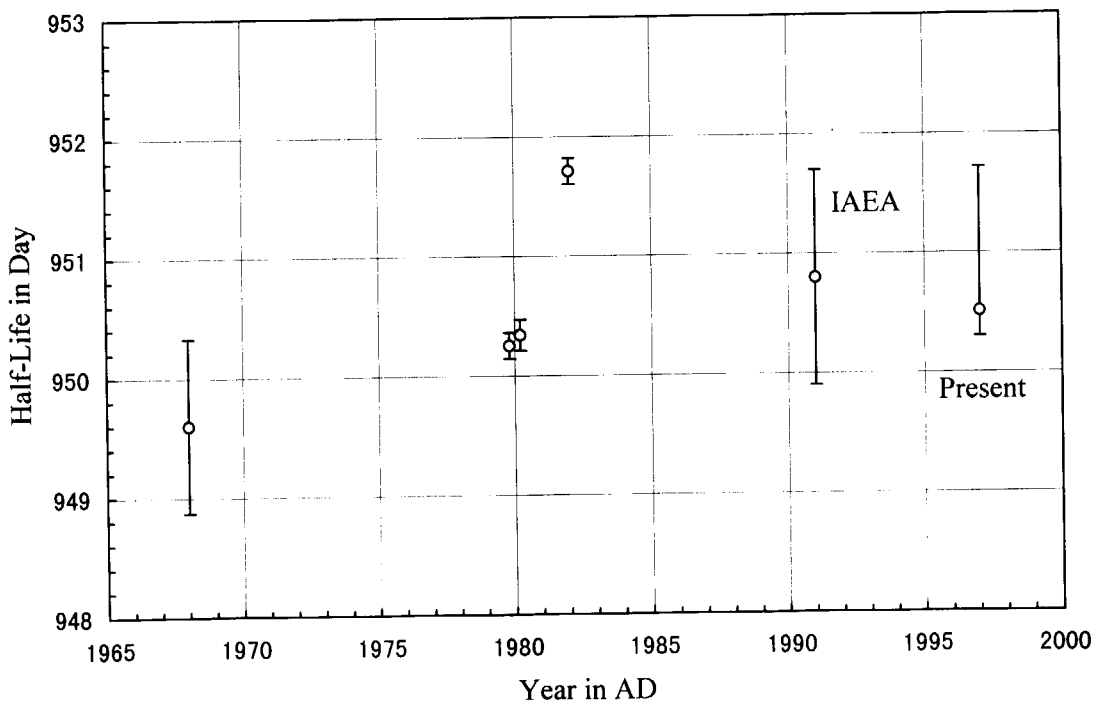

Fig. 1. Experimental and evaluated values of half-life of ^{22}Na. Only three measurements with good uncertainties are available for this nuclide, but one value is far from the other two, compared with their uncertainties, that is, three data form two groups.

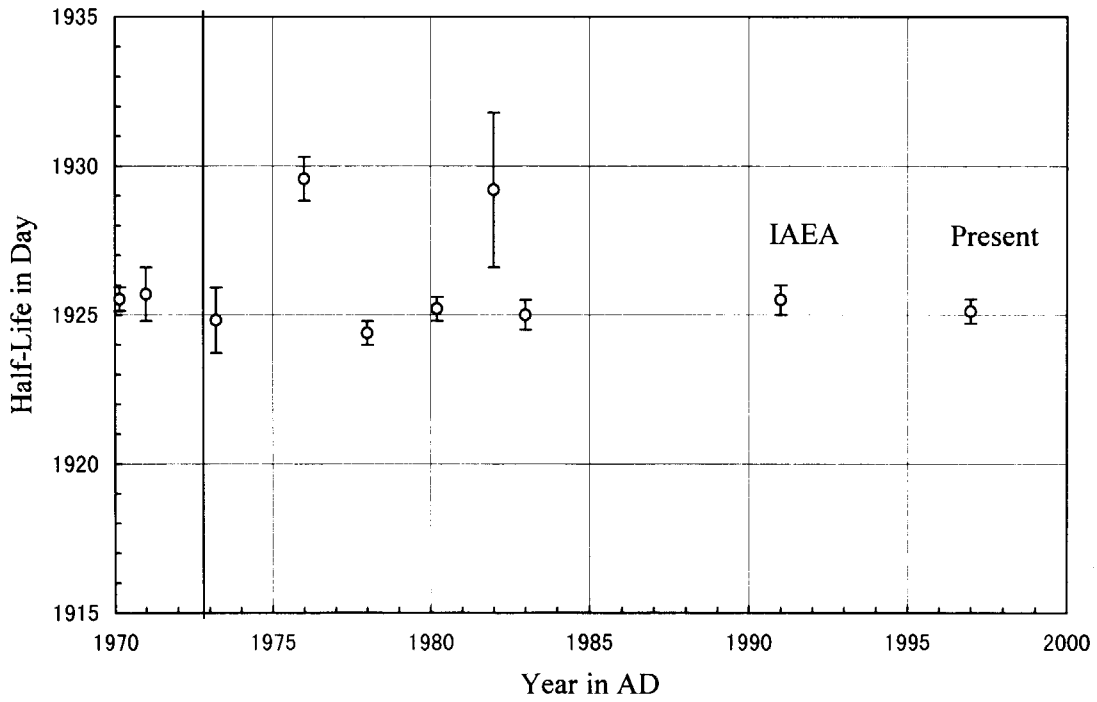

Fig. 2. Experimental and evaluated values of half-life of ^{60}Co. There are nine experimental values for this nuclide, which form two groups. One datum with a large uncertainty was neglected.

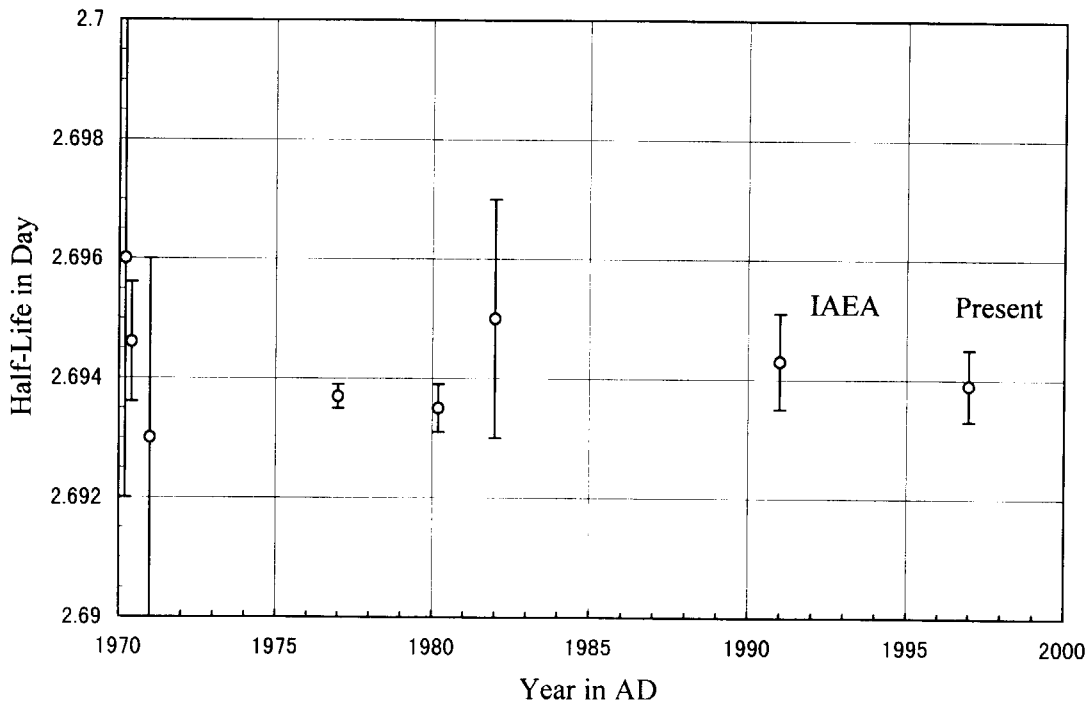

Fig. 3. Experimental and evaluated values of half-life of ^{198}Au. This is a typical example of one group with six data. One with the largest uncertainty was neglected.

Table. 1. Evaluated values of half-lives of eight nuclides.

Nuclide	IAEA evaluation day	Number of data	Number of groups	Present evaluation day	Present year or hour
^{22}Na	950.8 ± 0.9	3	2	$950.51^{+1.21}_{-0.07}$	$2.6024^{+0.0033}_{-0.0002}$ y
^{24}Na	0.62356 ± 0.00017	11	2*	0.62331 ± 0.00007	14.9594 ± 0.017 h
^{54}Mn	312.3 ± 0.4	5	1	312.21 ± 0.03	
^{60}Co	1925.5 ± 0.5	9	2*	1925.12 ± 0.41	5.2708 ± 0.0011 y
^{134}Cs	724.28 ± 0.22	7	1	754.25 ± 0.40	2.0651 ± 0.0011 y
^{137}Cs	11023 ± 0.55	9	3	11004^{+202}_{-91}	$30.13^{+0.55}_{-0.25}$ y
^{152}Eu	4933 ± 11	7	3*	4941^{+8}_{-43}	$13.52^{+0.02}_{-0.12}$ y
^{198}Au	2.6943 ± 0.0008	7	1	2.6937 ± 0.0006	

* means that the mean value of a large group was adopted as the evaluated value.

the latter was adopted, because the uncertainties of data in the higher group are large. Fig. 3 shows the half-life of ^{198}Au. This is a typical example of a single group. An old datum with large uncertainty was not used, and the weighted mean was adopted as the evaluated value.

Half-lives of 8 nuclides are listed in Table 1. The table shows the IAEA evaluated values (1991), the number of data from 1970 to 1989, the number of groups and new evaluated values. The average value of two or three groups is about the same as that of all data. The difference exists in the uncertainties. In some cases we chose one of two groups, when data in the other group are only one or two data and their uncertainties are large. The uncertainty of the mean is asymmetric in the case of two or three groups.

5. Conclusion

Purpose of this report is to study the evaluation method and to examine practical examples. A few evaluation methods were examined, and a method is proposed in chapter 3. Half-lives of 8 nuclides were evaluated by this method. If one plots data and the evaluated values in figures, one understands the method of this evaluation. The present values are not very different from the IAEA values. The IAEA evaluation work was performed without theoretical principle, but now we get a principle mentioned in chapter 3. But the evaluation method is not yet completed from a theoretical point of view. Since new data after 1990 are not included in this evaluation, these evaluated values are not final recommended ones. We think that evaluation works on the nuclear decay data are still necessary.

2.5.3

Energy Distribution of Projectile Fragment Particles in heavy Ion Therapeutic Beam

Naruhiro MATSUFUJI, Hiromi TOMURA, Yasuyuki FUTAMI, Haruo YAMASHITA,
Akifumi FUKUMURA, Tatsuaki KANAI
National Institute of Radiological Sciences (NIRS)
9-1, Anagawa-4, Inage-ku, Chiba-shi, Chiba 263-8555 JAPAN
e-mail : matufuji@nirs.go.jp

Akio HIGASHI, Takashi AKAGI
Hyogo Prefectural Government
5-10-1, Shimoyamatedori, Chuo-ku, Kobe-shi, Hyogo 650-0011 JAPAN

Hideaki KOMAMI, Toshiyuki KOHNO
Tokyo Institute of Technology
4259 Nagatsuda-cho, Midori-ku, Yokohama-shi, Kanagawa 226-0026 JAPAN

Production of fragment particles in a patient's body is one of important problems for heavy charged particle therapy. It is required to know the yield and the energy spectrum for each fragment element - so called 'beam quality' to understand the effect of therapeutic beam precisely. In this study, fragment particles produced by practical therapeutic beam of HIMAC were investigated with using tissue-equivalent material and a detector complex. From the results, fragment particles were well identified by difference of their atomic numbers and the beam quality was derived. Responses of the detectors in this energy region were also researched.

1. Introduction

High energetic heavy charged particles have many desirable characteristics for radiotherapy. What is particularly important in physical point of view is its unique depth-dose distribution known as 'Bragg curve' and less scattering in a matter. These features enable us to localize irradiation dose to tumor in deep body much better than using conventional beams as photon, neutron or even proton. The advantage is highly regarded as important especially when treating tumor grown close to critical normal tissue.

However, the heavy charged particle beam brings its specific physical problem that should be taken into consideration, *i.e.*, production of fragment particles. High energetic heavy charged particle is broken into some fragment particles in a patient's body by spallation reaction. Fig.1 shows the model of fragment reaction. The velocity of projectile fragments is nearly equal to the velocity of primary particle at the reaction point. Therefore, the projectile fragments lighter than primary particles are transported to region deeper than the range of primary particles and cause unwanted exposure to normal tissues there.

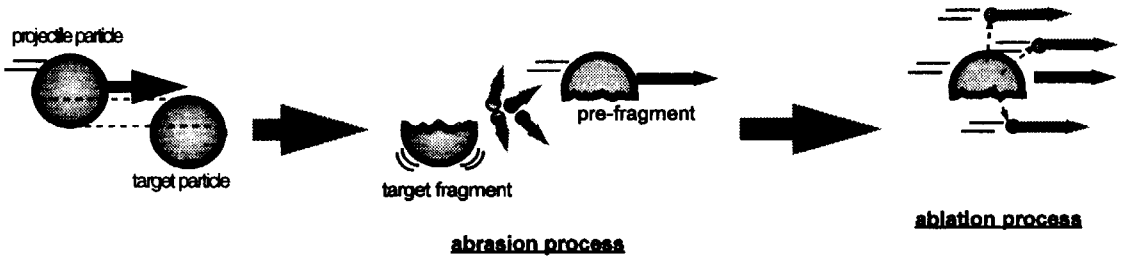

Fig.1 Spallation reaction in abrasion-ablation model [1].

The production of fragment particles also complicates biological effectiveness of the therapeutic beam because relative biological effectiveness (RBE) of radiation is a function of the beam quality: namely the kind of particle and its linear energy transfer (LET) [2]. In our treatment planning, the beam quality has not been fully taken into account yet because of the lack of reliable model and data. The aim of this study is to investigate the beam quality with using experimental methods.

2. Materials and Methods

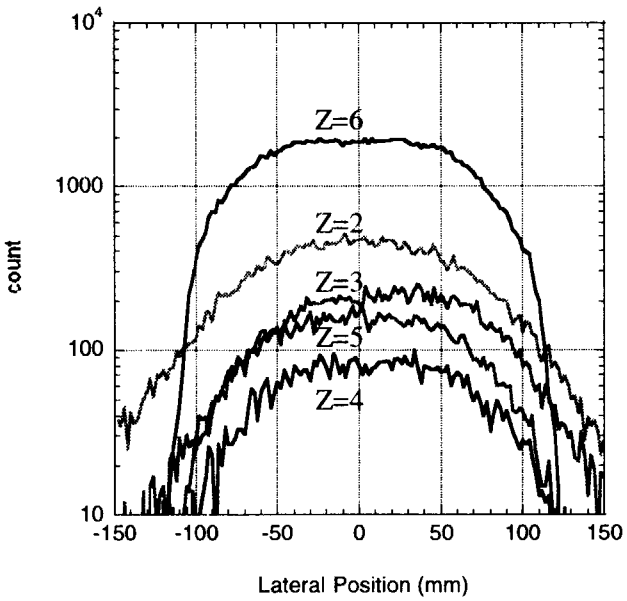

Fig.2 Lateral distribution of fragments for the incidence of 290MeV/nucleon of carbon in PMMA (90.0mm)

Experiments were carried out at biological experiment port at HIMAC (Heavy Ion Medical Accelerator in Chiba) of NIRS. Incident beam was broadened to 100 mm in diameter at iso-center with wobbler magnets and a scatterer. A stack of plates made of PMMA (polymethyl methacrylrate (Lucite), ρ=1.16g/cm^3, $(C_5H_8O_2)_n$) was used as a substitution of human body. The thickness was variously changeable in the range from 0mm to 512mm by 0.5mm step.

Lateral uniformity of the fragment element was checked by using X-ray films and a position sensitive ΔE counter. Fig.2 shows a preliminary result of fragments' lateral distribution measured by the position-sensitive counter for carbon 290 MeV/nucleon beam after passing through 90.0mm of PMMA. The result indicates sufficient uniformity at the center of the beam.

Beam quality was then investigated at the center position for 290 MeV/nucleon of carbon beam that has been used for our clinical trial. Beams of 400 MeV/nucleon of neon, 150 MeV/nucleon of helium and 490 MeV/nucleon of silicon were also used to research the responses of measurement system. These beams have the range of about 150mm in water. Intensity of the beam was drastically reduced than the intensity for therapy: in the level of 10^4 particles/3.3s at the biological port that enables us to count particles one by one.

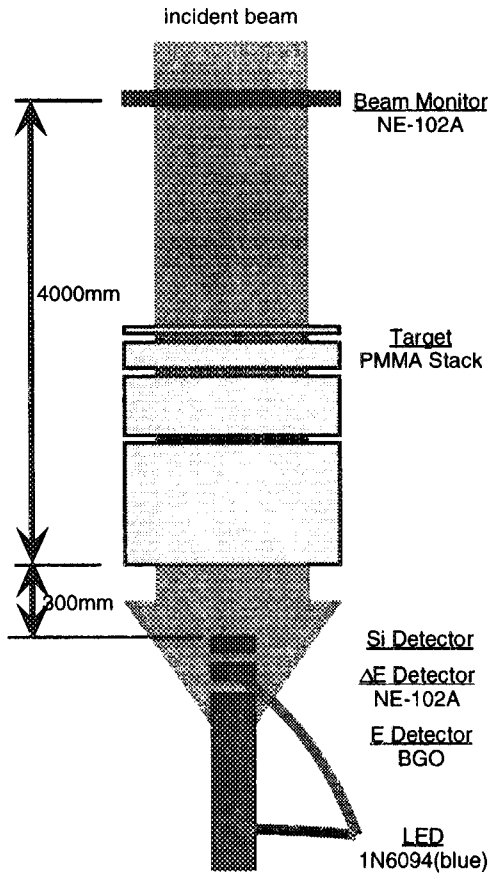

Fig.3 Configulation of beam quality measurement system.

We configured the measurement system of the beam quality based on counter telescope method. The experimental arrangement is illustrated in Fig.3. A NE102A plastic scintillator of 2.0 mm in thickness was served for counting primary particles and located at the upstream position in the experiment room. Another NE102A of 5.0 mm in thickness and 300.0 mm thickness of BGO scintillator were placed at the isocenter, 300mm downstream from PMMA target, and used as ΔE and E detector, respectively. The plastic scintillators were connected with HAMAMATSU photomultipliers while BGO scintillator was connected with HAMAMATSU photo-diode to gain wider dynamic range. A silicon detector of 1.5 mm in thickness was placed in front of ΔE detector to measure energy loss spectra. Stabilized blue light emitted by an LED was guided to the scintillators via optical cables to monitor drift of the gain. Measurements were carried out by changing the thickness of PMMA variously. Outputs from the detectors were processed with NIM modules and stored in a UNIX computer in list mode via Ethernet.

3. Results and Discussion

3-1 Particle Distribution

Fragment particle was well identified down to hydrogen by ΔE-E scatter plot of the NE102A and the BGO scintillator. Fig.4 shows an example of the scatter plot for 400 MeV/nucleon of neon beam after passing through 135.0 mm of PMMA target. The number of particles included in each band were counted and normalized by total number of incident primary particles. Fig.5 and 6 shows the number of primary carbon and fragment particles for each element as a function of PMMA thickness. Lines in the figure represent calculational results of 'hibrac' [3]. They shows good agreement on primary carbon particles, however, discrepancy is also shown on the number of hydrogen or beryllium particles. The reason is considered as an incompleteness of cross section model in the code.

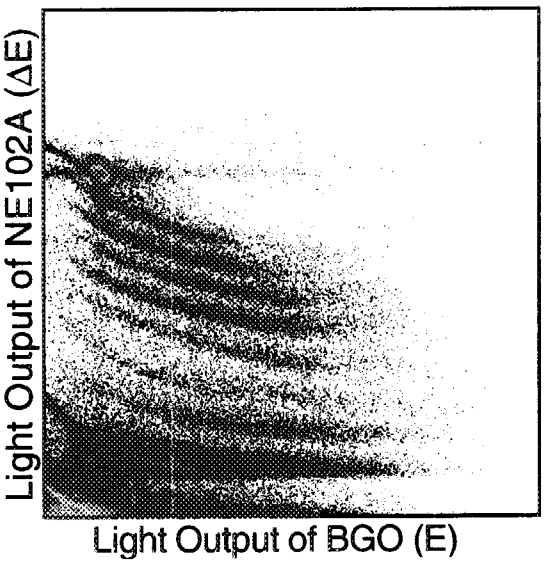

Fig.4 DE-E scatter plot for the incidence of 400MeV/nucleon of neon in PMMA (135.0mm).

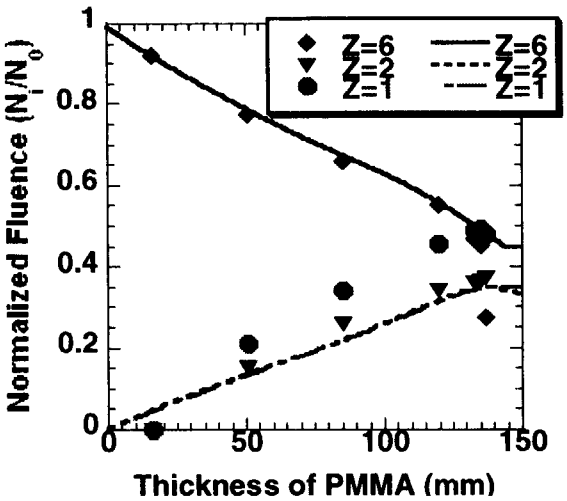

Fig.5 Fluence of primary and fragments (Z=1, 2) as a function of PMMA thickness for the incidence of 290 MeV/nucleon of carbon.

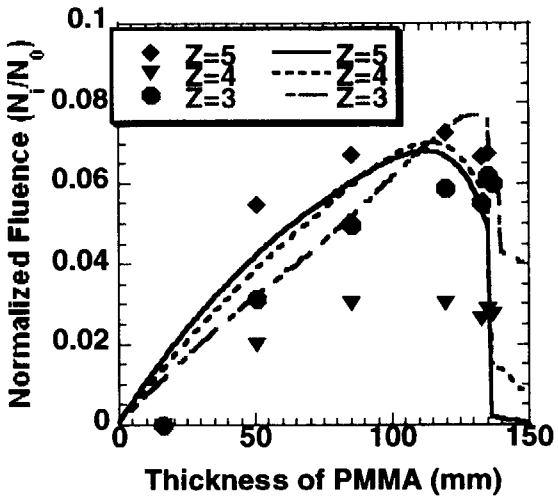

Fig.6 Fluence of fragments (Z=3–5) as a function of PMMA thickness for the incidence of 290 MeV/nucleon of carbon.

3-2 Response Function and Energy Spectra

The responses of silicon detector, NE102A scintillator and BGO scintillator in this energy region were determined as shown in figs. 7-9, respectively. The response of the silicon detector can be regarded as independent of the kind of elements. The characteristic enables us to obtain energy loss in silicon detector in good precision. However, the atomic number of silicon is larger than water that accupies the main component of

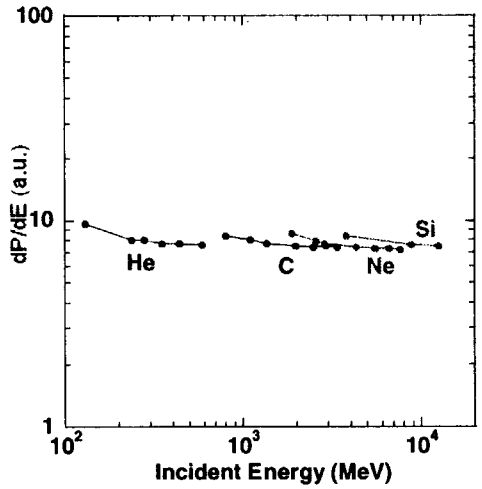

Fig.7 Response function of silicon detector.

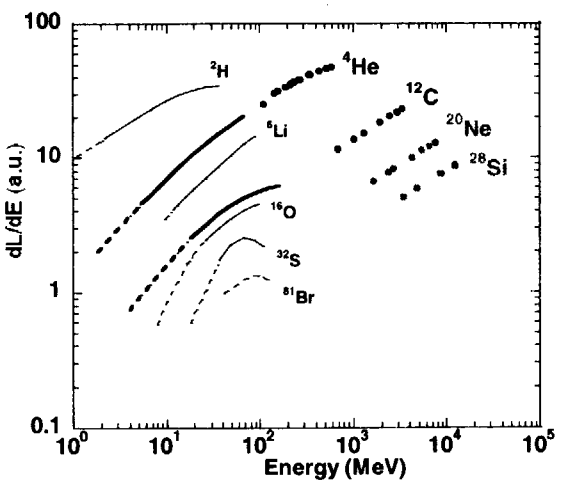

Fig.8 Response function of NE102A detector. lines : Becchetti *et al*[4], dots : this work

human tissue. The large difference of atomic number makes it difficult to deduce energy loss in tissue because the stopping power drastically changes by the difference of atomic number.

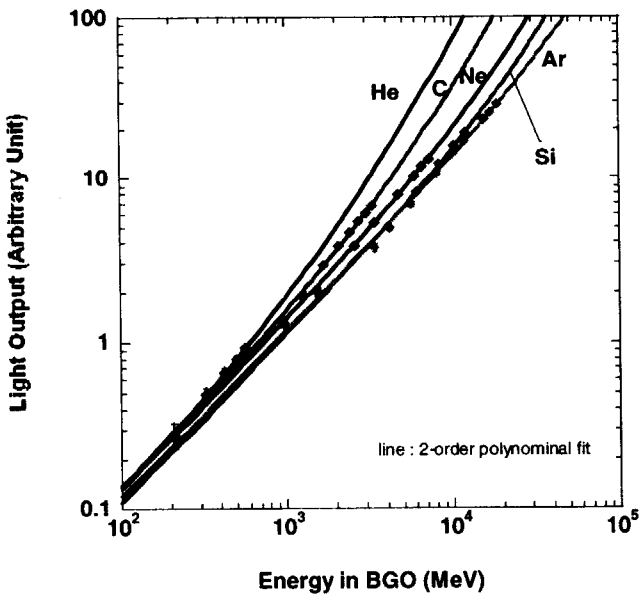

Fig.9 Response function of BGO scintillator.

The responses of NE102A plastic scintillators show obvious element dependency in this energy region. As shown in. fig.5, the yields of lighter elements such as hydrogen or proton in patient's body are very large in comparison with other elements. The response means an advantage to identify these lighter elements by using NE102A scintillator as ΔE detector because the element dependency tends to enlarge the difference of DE/dx of lighter elements.

The response of BGO scintillator also shows element dependency. Here, unlike energy loss spectra in silicon, the residual energy spectra in BGO are independent of the kind of medium. Therefore, the information is directly applicable as basic data to the estimation of biological effect of

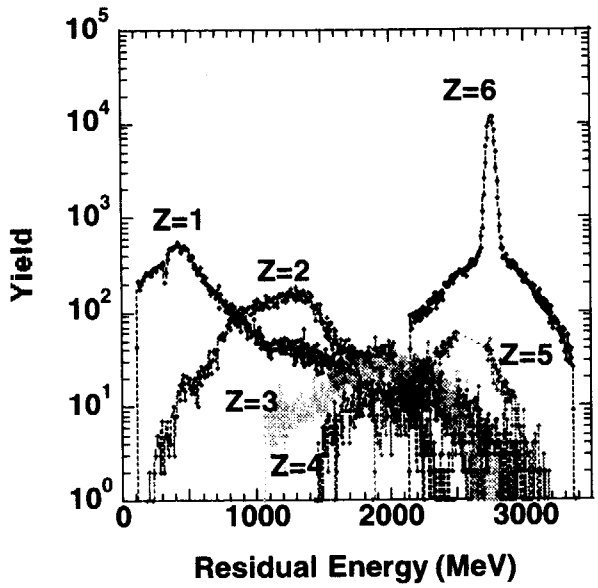

Fig.10 Energy spectra of fragments for the incidence of 290 MeV/nucleon of carboon in PMMA (40.0mm) .

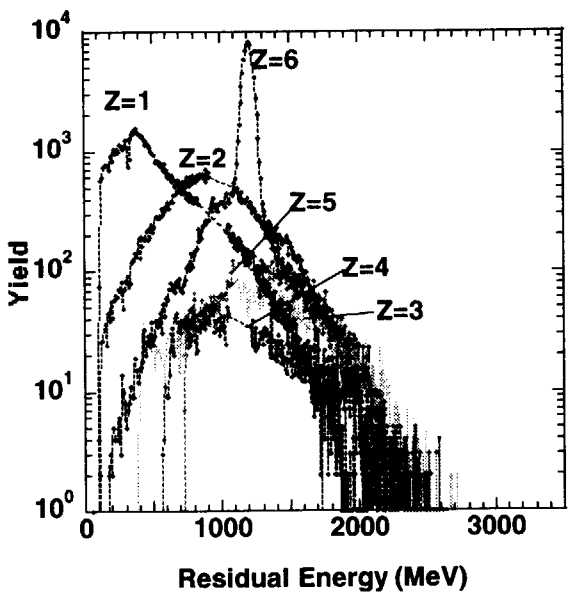

Fig.11 Energy spectra of fragments for the incidence of 290 MeV/nucleon of carboon in PMMA (120.0mm) .

therapeutic beam. Fig.10 and 11 shows preliminary spectra of residual energy of carbon beam deduced from BGO's energy response function.

4. Conclusion

Beam quality measurement system was developed. Through the measurements, fragment particles were well identified by difference of their atomic numbers. The comparison of the yield of fragments with calculational result showed differences on hydrogen and beryllium. It is strongly required to establish reliable simulation code together with experimental data from now on.

Responses of the detectors in this energy region were determined. The results extended existing measured responses. Appropriate usage of each detector for the beam quality measurement was derived based on the each detector's response function.

Acknowledgements

Authors wish to thank to the members of division of accelerator physics and engineering and all the staffs who take part in HIMAC project for their kind supports.

References

[1] Wilson J.W., Townsend L.W. and Badavi F.F., Nucl. Instr. and Meth. Phys. Res. Sect. B, B18, 225(1987)

[2] Kiefer J.: Int'l. J. of Radiat. Biol., 48, 873 (1986)

[3] Sihver L., Tsao C.H., Silberberg R., Barghouty A.F. and Kanai T.: Adv. Space Res., 17, 105 (1995)

[4] Becchetti F.D., Thorn C.E. and Levine M.J.: Nucl. Instr. and Meth., 138, 93 (1976)

2.6 New Facilities and Nuclear Data Needs

2.6.1 Present Status and Future Plan of Neutron Experiments by using TIARA

M.BABA
Quantum Science & Energy Engineering, Tohoku University
Sendai 980-77, Japan
mamoru.baba@qse.tohoku.ac.jp

A brief review is presented on the present status and the future plan of neutron experiments at 40-90 MeV ^{7}Li(p,n) neutron source facility of TIARA cyclotron in JAERI Takasaki.

1. Introduction

Utilization of large accelerators are growing rapidly in various fields, i.e., energy production and waste transmutation, fusion material research, medicine and biology and so on. For the design and efficient utilization of the facilities, basic data and computer codes are required to evaluate the transport and the radiation effects of high energy particles. It is also the case for the development of space technologies.

To promote the study of accelerator shielding and related data, a quasi monoenergetic ^{7}Li(p,n) neutron source was established at the AVF cyclotron (K=110) facility of TIARA (Takasaki Ion Accelerators for Advanced Radiation Application) in Takasaki Establishment of JAERI [1]. This source provides a well collimated neutron beam in 40-90 MeV region where the experimental data are of special importance because of the complexity of the nuclear reaction mechanism and the ambiguity in theoretical calculation.

Using the source, studies on the accelerator shielding and nuclear data have been conducted since 1992 by the members of universities and JAERI under the framework of "Universities-JAERI Joint Research Project". In the 1-st phase program from 1992 to 1996, four experiments were carried out on 1)accelerator shielding benchmark, 2)activation cross section of accelerator materials, 3)neutron cross sections for accelerator shielding, and 4)secondary neutrons and gamma-rays by ion beams. Under the program, measurements of neutron activation and charged-particle production cross sections were carried out as well as shielding experiments. The results have been reported in many publications and complied in Ref.2. In 1997, a new 3-yrs project on " Particle production by energetic neutrons and charged particles" has started and is in progress.

This report describes the status and a future plan of neutron experiments at the TIARA facility focusing on the nuclear data activity.

2. Neutron source and its characterization [1,2,3]

Figure 1 illustrates the layout of the TIARA monoenergetic neutron source. A proton beam provided by the cyclotron bombards a ^{7}Li(99.9% ^{7}Li) target and produces a quasi-monoenergetic neutrons. Neutrons produced are guided to the experimental room (Light Ion Room 3) through a ~3 m thick collimator made of iron and concrete. Protons which transmitted the target are swept into a shielded Faraday cup by a sweep magnet. The intensity of the proton beam is a few μA on the target. The neutron intensity is monitored with a Faraday cup and ^{232}Th, ^{238}U fission chambers placed around the target. Thus far, neutrons were produced and provided for the experiments at eight energy points; 45, 50, 55, 60, 65, 70, 80 and 90 MeV.

The intensity and spectrum of the source neutrons were studied using a proton recoil telescope (PRT; Fig.2) [3] and the TOF technique with organic liquid scintillation detectors [4,5]. The

spectrum data are important for the analysis of the experiment because the p-Li source is not monoenergetic.

Figure 3 shows typical neutron spectra measured by PRT and a BC501 scintillator in a TOF mode. The results by two methods agreed within error if the detection efficiency of BC501 is determined based on the measured response function (cf. Sect.3). The flux of peak neutrons at the experimental room is about 3.5×10^9n sr^{-1} μC^{-1} (Ep=45 MeV) to 5.8×10^9n sr^{-1} μC^{-1} (Ep=90 MeV) for ^{7}Li target of 2 MeV thick. These spectrum data are used to analyze the experimental data obtained by the facility. From the measured data, the $^7Li(p,n_{0,1})$ cross section for the peak neutron production was derived as shown in Fig.4. The spectrum of continuum neutrons were found to be reproduced consistently by the phase space distribution corresponding to the $^7Li(p,n^3He)\alpha$ reaction.

3. Shielding benchmark experiments [2,4-8]

To obtain benchmark data for accelerator shielding calculations, neutron spectra and flux behind concrete, iron and polyethylene slabs and inside a plastic phantom were measured for neutrons produced by 43(45) MeV and 68 (70) MeV protons, using a BC501 scintillator, a Boner ball and various dosimeters. Neutron spectrum data were obtained by unfolding the data of BC501 and Boner.

Prior to the experiments, the response functions of organic scintillation detectors were measured and compared with calculations to examine the validity of the codes [4,5]. Figure 5 shows examples [5]; the response functions calculated by the codes, SCINFUL and CECIL show marked discrepancies from the measurements both in shape and magnitude because of inadequate data for the differential np scattering cross sections and the light output of the scintillator, and so on. The data in the code were revised so as to reproduce the measured ones.

Shielding data were obtained for various thickness up to 200 cm, 230 cm and 180 cm for concrete, iron and polyethylene, respectively [6-8]. Figure 6 illustrates the comparison of the experiment with the calculations by MORSE and DOT3.5 using the data DLC119. For the data on the neutron beam axis, both calculations reproduce the experimental data within a factor of two even in the worst case. However, as shown in Fig.7, the calculation by the cascade model code HETC overestimates largely the flux on the beam axis and underestimates the off axis flux because of too strong forward peaking of differential nucleon scattering cross section. Therefore, the refinement of the cascade code is needed urgently.

4. Neutron cross section measurements [9-11]

Neutron induced activation cross sections were measured for C, Al, Fe, Ni, Cu, and Bi at eight energy points mentioned above [9,10]. In this study, measurements were carried out step by step from low energy to subtract the backgrounds due to the non-monoenergetic component of the source neutrons. Because of the limited neutron flux, samples of 1 to several grams were irradiated around 4 m from the target to increase the activation rate. Measurements were done also at the neutron fields in INS, Univ. of Tokyo and RIKEN to cover the energy range up to 210 MeV. These data can be used directly for assessment of the activation rate of accelerator components and as the benchmark data for nuclear data evaluation. Figures 8 and 9 show examples of the results in comparison with calculations. The $^{209}Bi(n,xn)$ reaction is expected to be useful as a neutron spectrometer in a medium energy region.

Double-differential charged particle emission cross sections were also studied at TIARA for C and Al [11]. The results are presented by Nauch *et al* in this proceedings.

5. Neutron production by charged particles [12,13]

In this experiments, measurements were done for double-differential thick target neutron

yields which are indispensable for the design of accelerator shielding. Measurements were done at the HB beam course of the cyclotron using the TOF method with the BC501 detector previously calibrated. Data were obtained for 68 MeV protons on Be, C, Al, Cu, Nb, Au and Pb, 100 MeV He on C, Fe, Au, 220 MeV C and 460 MeV ^{40}Ar on C, Fe, Zr at seven laboratory angles, 0, 15, 30, 45, 60, 90 and 120°. Gamma-ray spectra were also deduced. Examples of the neutron spectra are shown in Fig.10. Very strong angular dependencies are observed. The experimental data are compared with theoretical calculations by the codes QMD and NMTC/JAERRI (only for protons) to validate and improve the codes.

6 Future plan of neutron experiments at TIARA

Following the achievement mentioned above, a new Joint Research Project "Particle production by the nuclear reaction of neutron and charged-particles" started in 1997 as a three-years project. The project consists of four subjects:

1)Particle production by neutron reactions: (n,xz), (n,xn), (n,xγ)
2)Particle production by charged-particles: (p,xz), (p,xn) etc.
3)Development and characterization of neutron detectors,
3)Particle transport in medium and human-body.

Under the program, measurements of double differential cross sections of charged-particle, gamma-rays and neutron production reactions are in progress as well as the detector development and integral experiments. Measurements will be extended to low energy particles in (n,xz), and (p,xz) experiments using newly developed wide range spectrometers, and new measurements on neutron scattering cross sections are also planned to obtain neutron angular distribution data which are important to improve the cascade model code as discussed in set.3.

Acknowledgment

The above cited works were performed by the members of "Universities-JAERI Joint Research Project (Leader: T.Nakamura (Tohoku Univ), and H.Yasuda (JAERI))". The author would like to thank the members for providing him with the data and information for this review. He also appreciate the operating crew of the cyclotron at TIARA for their cooperation.

References:

1. Su. Tanaka et al.: Proc. 2-nd Int. Sym. On Advanced Nuclear Energy Research -Evolution by accelerators-, (JAERI 1992, Jan.24-26 Mito), p.342
2 T.Nakamura (ed.) : Report of the Research by the Grant-in-Aid for Scientific Research "Study on the behavior and transport of high energy paricles in the matter", CYRIC Tohoku University, 1996 (in Japanese)
3. M.Baba et al.: Proc. Int. Conf. Nucl. Data. (1993, Gatlinburg) p.90. .
4. N.Nakao et al: Nucl. Instrum. Methods, A362 454-465 (1995)
5. S.Meigo et al.: Ref.2 and to be published in Nucl. Instrum. Methods, A
6. N. Nakao et al.: Nucl. Sci. Engi., 124 228 (1996)
7. H.Nakashima et al.: ibid., p.243-257
8. N.Nakao et al.: J. Nucl. Sci. Technol., 34 348 (1997).
9 .E. Kim et al.: JAERI-Conf 96-008 (1997) 236-241
10. E. Kim et al.: Submitted to Nucl. Sci. Eng., .
11. Y. Nauchi. et al.: Proc. Int. Conf. Nucl. Data. (1997, Trieste) to be published ..
12. S.Meigo et al.: JAERI-conf 97-005 81997) p. 205
13. S.Meigo et al: Proc. Int. Conf. Nucl. Data. (1997, Trieste) to be published ..

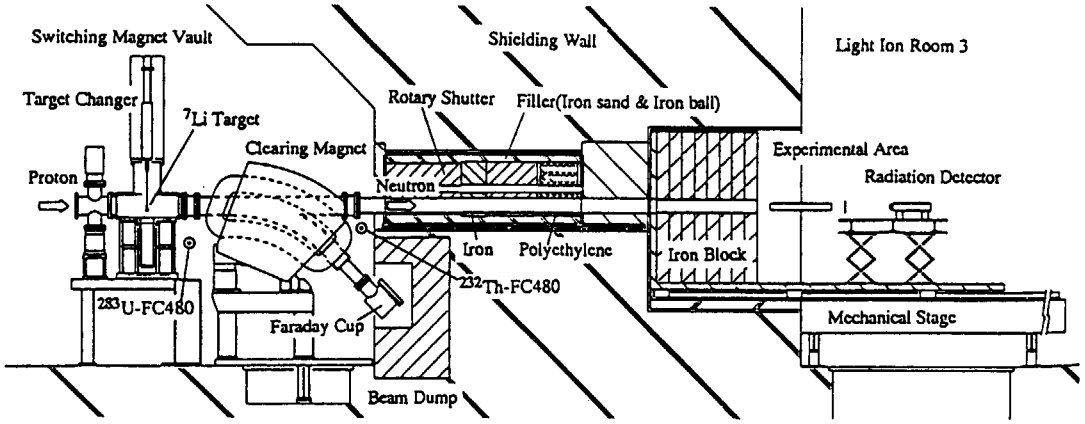

Fig.1: Layout of the TIARA ^{7}Li(p,n) neutron source

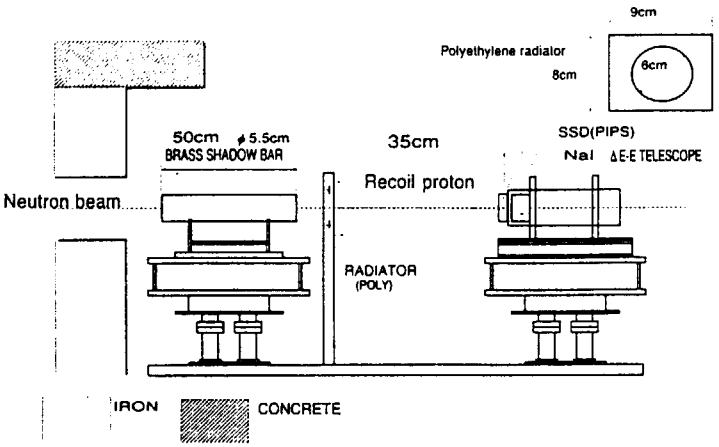

Fig.2: Schematic view of PRT

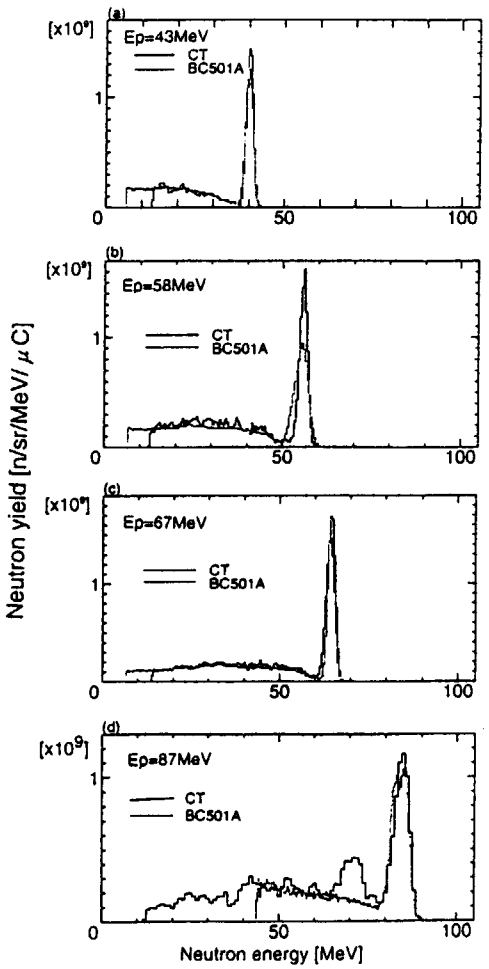

Fig.3: ^{7}Li(p,n) neutron spectra

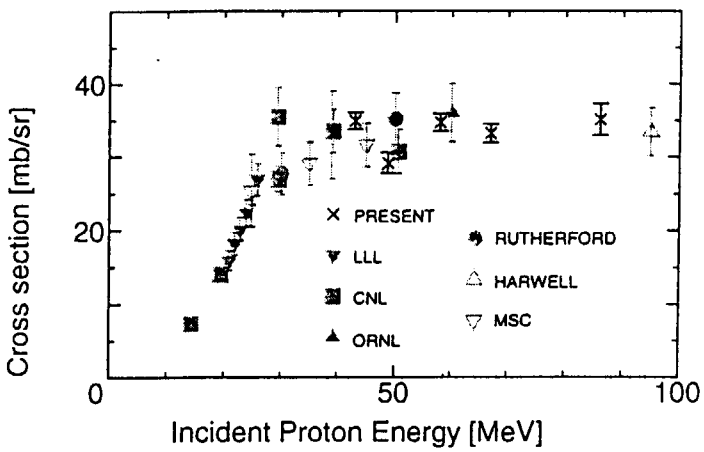

Fig.4: ^{7}Li(p,$n_{0,1}$) cross section

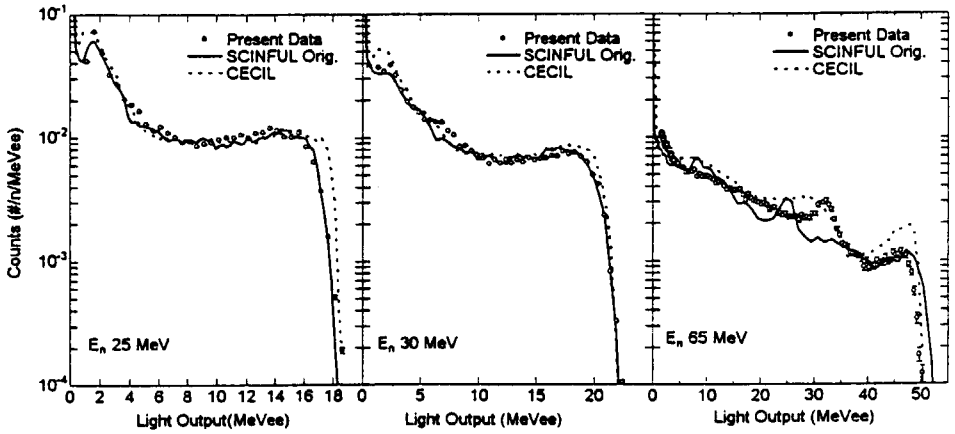

Fig.5: Response functions of NE213 scintillator .

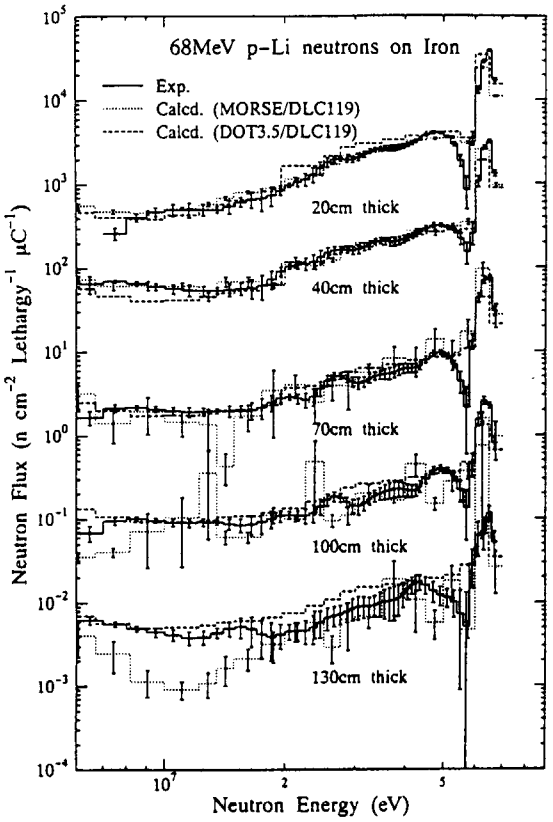

Fig.6: Neutron spectra behind iron slab

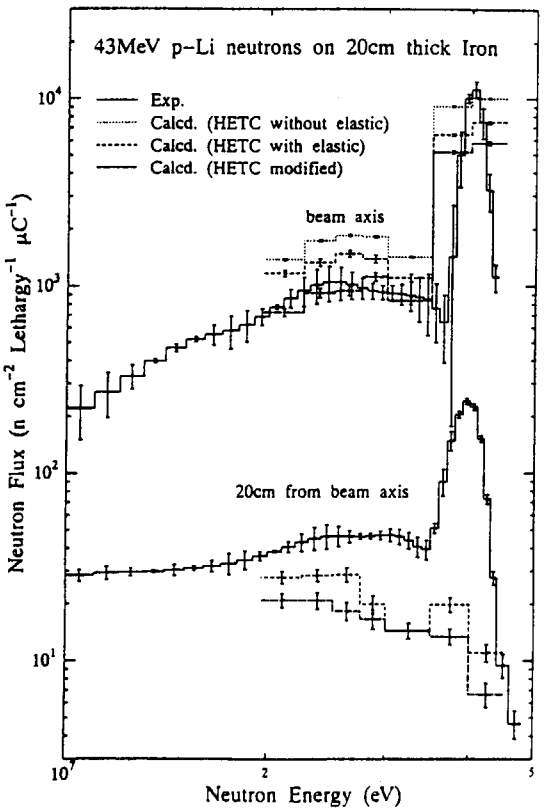

Fig.7: Neutron spectra behind iron slab

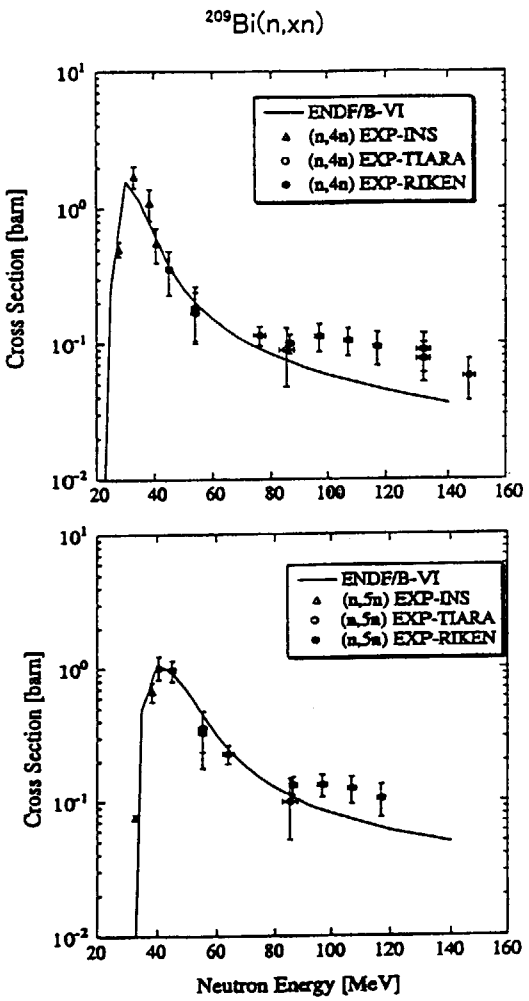

Fig.8: ^{219}Bi(n,xn) cross section

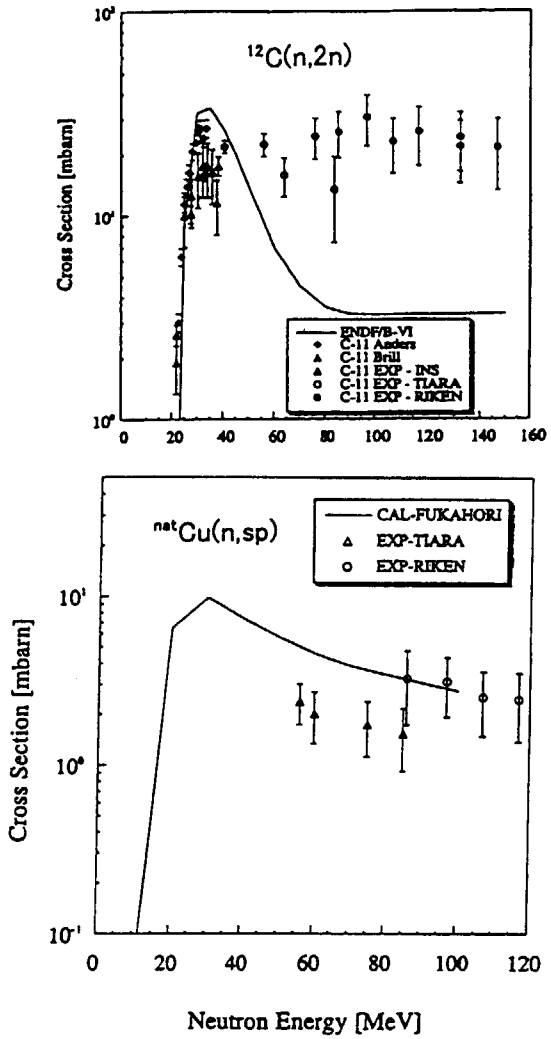

Fig.9 ^{12}C(n,2n), ^{nat}Cu(n,sp) cross section

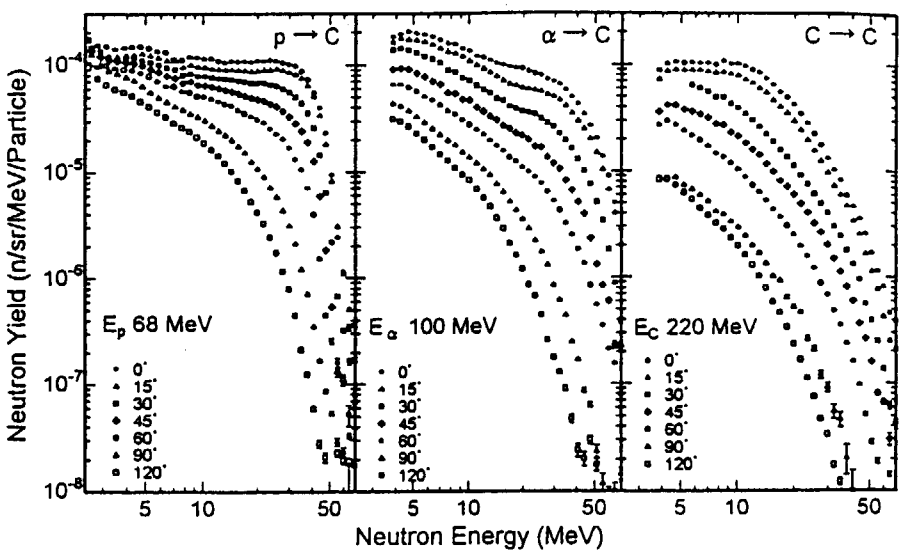

Fig.10. Neutron emission spectra from thick target of carbon bombarded with proton, α and carbon beam.

2.6.2 Neutron Science Project at JAERI

Y. Oyama
Japan Atomic Energy Research Institute
Tokai-mura, Ibaraki-ken, 319-11 Japan
e-mail: oyama@fnshp.tokai.jaeri.go.jp

Japan Atomic Energy Research Institute, JAERI, is proposing the Neutron Science Project which aims at bringing about scientific and technological innovation in the fields of basic science and nuclear technology for the 21st century, using high intense spallation neutron source. The research areas to be promoted by the project are neutron structural biology, material science, nuclear physics and various technology developments for accelerator-driven transmutation of long-lived radio-nuclides which are associated with nuclear power generation. JAERI has been carrying out a R&D program for the partitioning and transmutation with the intention to solve the problem of nuclear fuel cycle backend. The accelerator-driven transmutation study is also covered with this program. In the present stage of the project, a conceptual design is being prepared for a research complex utilizing spallation neutrons, including a high intensity pulsed and steady spallation neutron source with 1.5 GeV and 8MW superconducting proton linac. The idea and facility plan of the project is described, including the status of technological development of the accelerator, target and facilities.

1. Introduction

The Neutron Science Project at JAERI[1], It aims at pushing researches utilizing neutrons for basic science and accelerator transmutation of long-lived nuclides associated with nuclear power generation. The major facilities of the planned Neutron Science Center at Tokai are an 8 MW (1.5GeV,5.3 mA) super-conducting proton linac, a 5 MW target station allowing neutron pulses for neutron scattering research, and research facilities for transmutation engineering, neutron physics, material irradiation, medical isotopes production, spallation RI beam production for exotic nuclei investigation.

Since one of the major technical challenges of a high-current accelerator besides in the low-energy section, JAERI has been carrying out the R&D endeavors for ion source, RFQ, DTL, and RFQ since 1990. In the recent beam test with a 150 mA (peak) ion source and a 2 MeV RFQ, the peak current of 80mA with duty factor of 8 % was achieved. A hot test model of DTL for mockup of low energy portion (2 MeV to 100 MeV) was fabricated and tested for high power and high duty (20 %) operation. Another challenge is a super-conducting proton linac. Since there has been no super-conducting proton linac in the world, an effort has been started from developing a super-conducting cavity. Recently a single cavity was tested at 2.2K and 30MV/m of RF electric field was obtained as a world record. Besides the above, high power RF power supplies are also under developing. In addition, spallation target station for a neutron scattering facility is also being developed. Specially a liquid target concept are developed for thermal-hydraulic and mechanical design. In addition, a target/moderator/reflector optimization study of neutronic performance is extensively carried out using nuclear cascade and high energy Monte Carlo transport codes.

2. Concept and Development of a High Intensity Proton Linac[2,3]

The Neutron Science Project of JAERI comprises very wide fields of basic science which utilizes the neutron as the probe to investigate materials of their structure and dynamics, and of nuclear technology. Various beam modes are required to fulfill the experimental requirements of these wide fields, namely, very short pulse for neutron physics, short pulse for neutron scattering, and steady beam (continuous wave, CW) or long pulse mode for transmutation experiments and material irradiation.

The total beam power of 8MW with pulse mode operation is distributed to the neutron scattering targets by 5MW, transmutation experiments by 2MW and the other experiments by 1MW. In a cw mode operation, several MW is required for the thermo-hydrolic and material tests of a spallation target of a transmutation system. The concept of the accelerator complex is shown in

Fig.1. Two injectors for higher energy DTLs are considered to allow both pulse and cw beam operations, and two ion sources for the pulse mode injector to be able to accelerate positive and negative ions at the same time. A super-conducting cavity linac was chosen for higher energy accelerators from 100MeV. The superconducting option was adopted by the reasons: 1) for large current acceleration with smaller beam hollow, 2) the cost reduction owing to the reduction of length of the linac and savings in operating costs, and 3) the technology path to nuclear energy system.

The R&D efforts are attempted so far to 1) a beam dynamics calculation study including the high energy linac. 2) development of positive and negative ion sources, a radio frequency a quadrupole linac (RFQ) and a drift tube linac (DTL), 3) single cavity test for superconducting cavity development, 4) conceptual design of high intensity proton beam storage ring, and 5) the design optimization of the total system. These status of present development activities is summarized in Table 1.

3. Concept and Development of a Spallation Target[4]

The target system is one of the major facilities and needs extensive efforts to develop. It suffers from severe irradiation of high energy protons and neutrons, and thermal shocks. Two types of the target systems are used corresponding to beam power and development stage. A solid system is used at low power up to 1.5 MW and at the initial stage and a liquid metal system for high power stage. The spallation target material is mercury and the moderators are two cold moderator with premoderator above the target, a thermal moderator and a epithermal moderator beneath the target. A concept of liquid target and moderator system is shown in Fig. 2

The solid target plates are made of Ta or W and will be exposed to high heat flux up to 12 MW/m^2. Thus it is necessary to develop a method of heat transfer augmentation against the high heat flux, especially for coping with anticipated transient phenomena. A test of rib-roughened target surface is under way for augmenting method of heat transfer.

Mercury was selected for a liqud target material as the high power target of 5MW, because it has several advantages compared to solid targets. Those are 1) no radiation damage, 2) work with room temperature in liquid metals, 3) no need for cooling water which act as a neutron absorber and a tritium generator under the spallation source environment. A laboratory-scale mercury-loop of flow rate of 15l/min was constructed to obtain the data on controllability of the electric-magnetic pump, the stability of electric-magnetic flow-meter, the cooling ability of thermal exchanger and so on. Because pressure and stress behaviors of liquid mercury and its container are very crucial to design the target structure, high energy proton injection experiments have been performed using AGS accelerator complex at Brook haven National Laboratory (BNL) of USA by international collaborative work among JAERI, ESS, NSNS and BNL teams.

A series of neutronics analyses are performed for solid and liquid metal target with reflector and moderator systems to optimize the configuration to obtain the maximum neutronics performance. At the same time nuclear heating distribution is evaluated to feed back to design of cryogenic system for moderators. The optimization study of moderator arrangement is also fed back to optimization of neutron beam tube arrangement.

4. Researches and Facilities for Basic Science

Research facilites considered are clasified into three groups on the basis of differece of pulse time duration, namely, a short pulse facility, a very short pulse facility, and a long pulse or continuous beam facility. Also, direct proton beam use of proton energy of 100-200MeV is considered for medical RI production. The concept of the facility complex is shown in Fig. 3.

Neutron scattering facility using 5MW beam covers the fields of structural biology for investigating the structure and dynamics of biological molecules such as protein, advanced material science (e.g., under extreme conditions). A plan of the facility layout is shown in Fig. 4. The thirty neutron beam lines are planned from the target, including hot sample experiment room for a damage

study.

Very short pulse around 1 ns of time duration is required for such experiments with high time resolution as high energy neutron nuclear physics by neutron time-of-flight (TOF) spectrometers (e.g., spallation phenomena) and nuclear cross-section measurements for transmutation study. This short pulse also provides very small current beam less than 10 nA for basic reactor physics experiments for accelerator-driven transmutation system development. In addition, a small current beam is also required for low power experiments as spallation RI beam science in which heavy-ion beam science for utilizing unstable heavy nuclei through spallation nuclear reaction, and synthesis of super heavy of extremely-neutron-rich nuclei. Various radioisotopes are produced by bombarding a target with 1.5 GeV protons through the spallation process. In this facility, the produced radioisotopes are separated with an ISOL (Isotope Separator On-line), and then accelerated by the existing Tandem Van de Graaff acclerator at Tokai site. Extremely-neutron-rich nuclei are produced which change easily into many exotic nuclei, heavy and super-heavy nuclei.

Muon utilization is an option of facility complex The muon intensity may be 2-3 orders higher at our facility than those of the existing muon facilities of LANSCE, TRIUMF and ISIS. The intense muon beam will be useful for the muon catalyzed fusion (μCF) engineering study.

5. Researches and Facilities for Accelerator-driven Transmutation System Development

The program of engineering development for an accelerator-driven nuclear transmutation system is to be proceeded in two steps.[5] The first step will be the feasibility study of the accelerator-driven system concept with a spallation target and a uranium subcritical system[6] at a very low power level at the very short pulse beam line mentioned before as the reactor physics experiment. The experiments will demonstrate the stable operation of an accelerator-driven system and minor actinides (MA) burn-up with use of MA foils. It will provide and verify the database for the development and design of an experimental system in the second step.

In the first step, target hydraulics, target windows and the other components should be tested using relatively high power beam such as in a 1-2MW level. This facility also includes the material irradiation utilizes long pulse beam or continuous beam directly from the linac. The irradiation facility has a slender metal target to obtain high neutron flux of 2×10^{14} n/cm^2/s around the traget by 1MW.

The facilty complex in the Neutron Science Project could be extend to the facility for the second phase. In the second phase, an experimental system will be constructed to perform engineering tests of an integrated target/core system at a thermal power level around 30 MW with a CW beam. Transmutation efficiency of the accelerator-driven system will be tested using MA target pellets or pins. These system level tests will demonstrate the technical viability of accelerator-based transmutation. Technical feasibility of spallation target and beam window will be also tested with a high beam power around 7 MW in the second step experiments. These experiments are expected to give prospect for the development of future nuclear options of accelerator-driven systems.

5 Time Scale

The proton linac is designed to deliver 8MW beam power and at the first stage is constructed at a power of 1.5 MW (1.5 GeV, 1mA), and upgraded to 8MW as experience of high power accelerator operation being accumlated. At the first stage, the accelerator will be operated with the pulsed mode and at the second stage, both with pulse and cw mode. The R&D efforts will continue for another 3 to 4 years. The proposal of the facility construction will be submitted in 2 to 3 years. The first stage construction will be completed by 2005 with the beam power on target of 1.5MW and some of the research facilities. For upgrading the beam power up to 8MW and constructing the transmutation test facility, it will take anther 3 to 4 years.

Acknowledgments

The present work has been performed by the members of Center for Neutron Science and with collaboration by user groups.

References

[1] Mukaiyama T., et al.: "Neutron Science project at JAERI," Proc. ANS Topical Meeting on Nuclear Application of Accelerator Technology (AccApp'97), Nov. 16-20,1997, Albuquerque, USA

[2] Mizumoto, M. et al.: "A High Intensity Proton Linac Development for Neutron Science Project Program", XVIII Intn. Linac Conf. LINAC96, Geneva,Switzerland 26-30 August, 1996, p662-664.

[3] Kinsho, M. et al.: "High Intensity Proton Linac Development for Neutron Science Research " Proc. ANS Topical Meeting on Nuclear Application of Accelerator Technology (AccApp'97), Nov. 16-20,1997, Albuquerque

[4] Hino R., et al.: "Developing Plan and Pre-conceptual Design of Target System for JAERI's High Intensity Neutron Source," Proc. 2nd Workshop of Neutron Science Project, March 13-14, 1997, Tokai , Japan, JAERI-Conf 97-010 (In Japanese)

[5] Takizuka T., et al.: " Research on Accelerator-driven Transmutation and Studies of Experimental Facilities," ibid.

[6] Yasuda H., et al.: " Reactor Physics R&D for Accelerator-based TRU Transmuation," Proc. 1st Workshop of Neutron Science Project, March 12-13, 1996, Tokai , Japan, JAERI-Conf 96-014 (In Japanese)

Table 1 Present status of development activities of accelerator

Item	Goal	Present
Ion Source		
Current	120mA	>140mA
Proton ratio	>90%	80%
R&D subjects	Proton ratio,Stability,Filement life	
RFQ(Beam Test)		
Cuurent	100mA	80mA
Duty	10%	10% (8%for stable op.)
Emittance(rms)	0.2π mm.mrad	0.7-0.8π mm.mrad
R&D subjects	Beam Diagnostics	
DTL High Power Test		
RF Power	128kW (12%)	128 kW (20%)
Superconducting Cavity Test		
Peak Electric Field	16MV/m	20MV/m at 4.2K 30MV/m at 2.1K

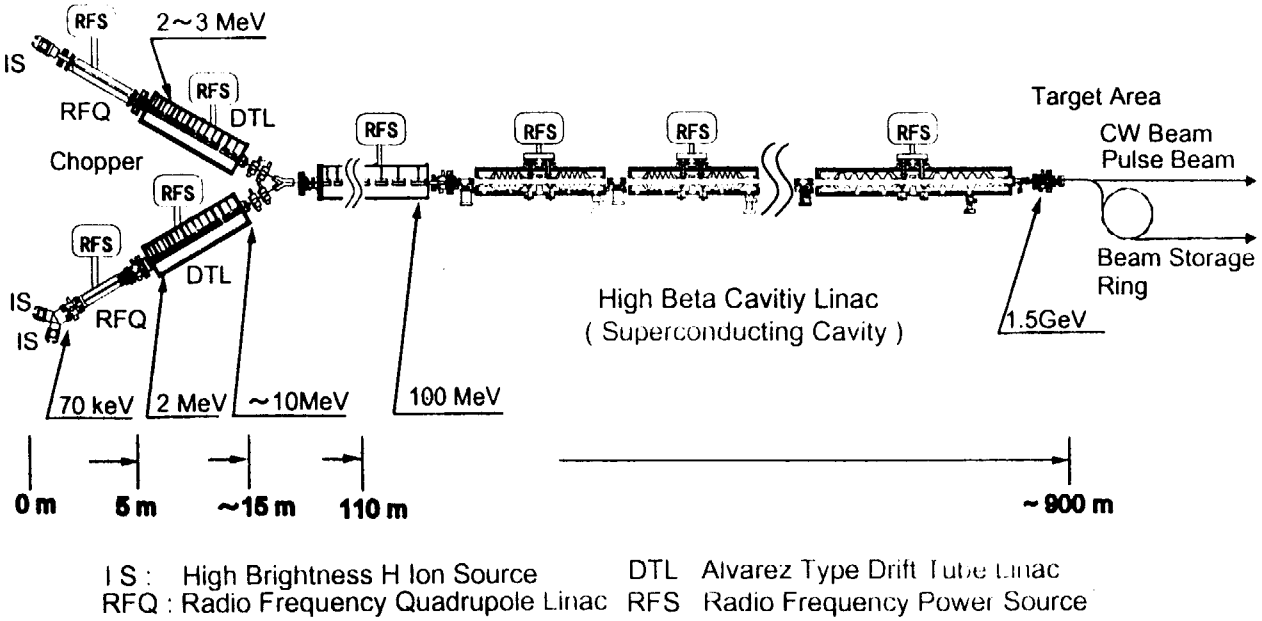

Fig. 1 A concept of the accelerator complex

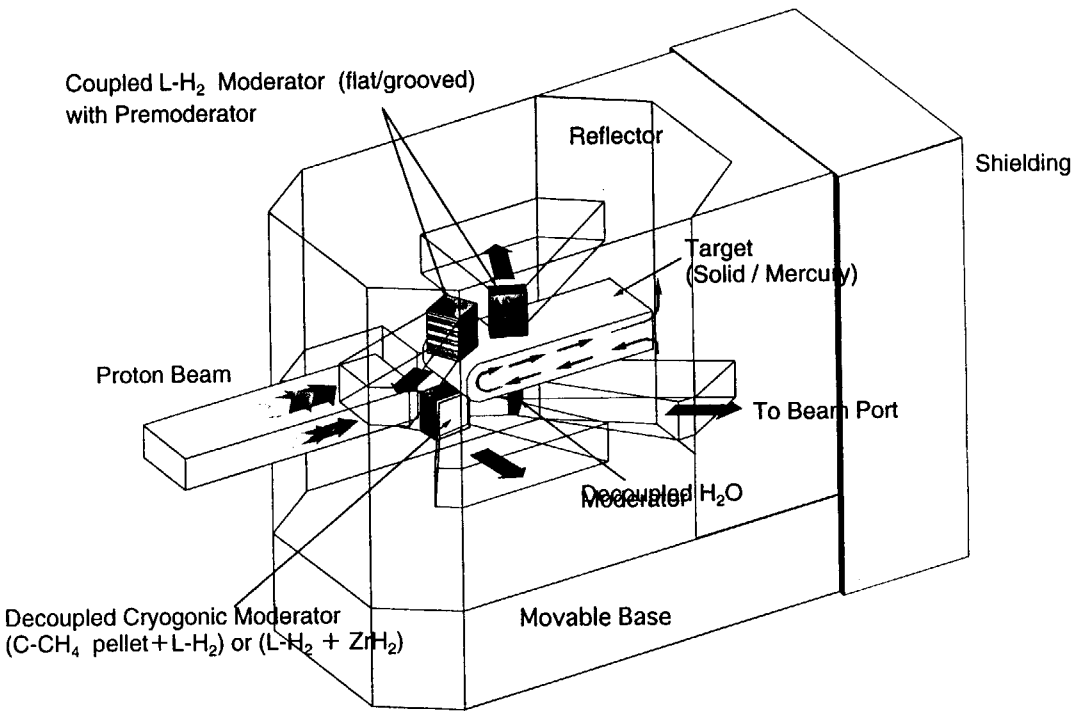

Fig.2 A concept of liquid target and moderator system

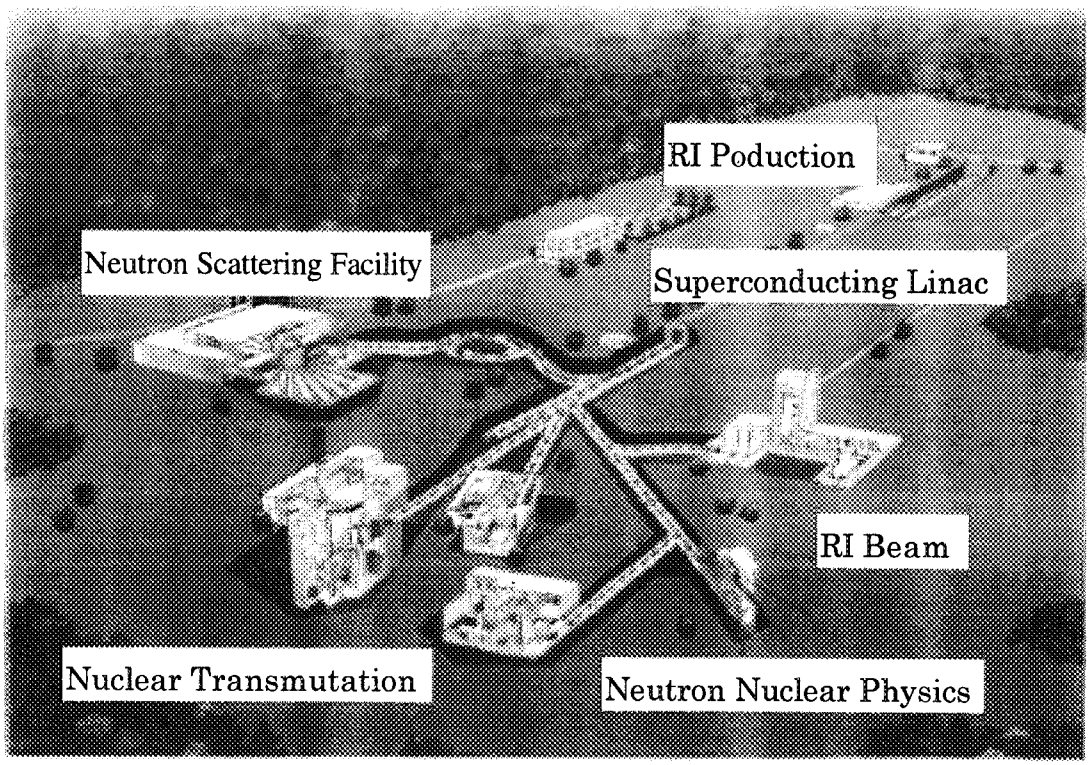

Fig.3 A concept of the facility complex

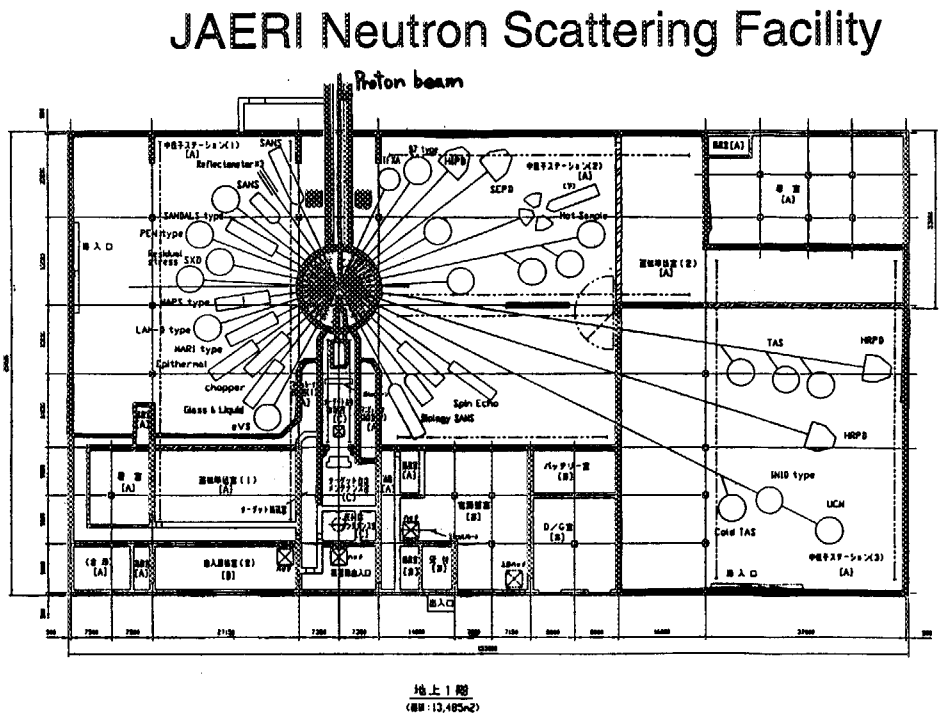

Fig.4 A plan of neutron beam line layout of the neutron scattering facility

2.6.3 Japan Hadron Facility

Tokushi SHIBATA
High Energy Accelerator Research Organization,
Radiation Science Center
1-1 Oho, Tsukuba, Ibaraki 305, Japan
e-mail: tokushi.shibata@kek.jp

JHF aims at promoting the variety of research fields using various secondary beams produced by high-intensity proton beams. The accelerator of JHF will be an accelerator complex of a 200 MeV LINAC, a 3 GeV booster proton synchrotron, and a 50 GeV proton synchrotron. The four main experimental facilities of K-Arena, M-Arena, N-Arena, and E-arena are planed. The outline of the project is presented

1. Accelerator complex

The accelerator complex for JHF[1] consists of three accelerators: a 200 MeV linear accelerator for the injector, a 3 GeV proton synchrotron for the booster ring, and a 50 GeV proton synchrotron for the main ring as shown in Fig.1.

The 200 MeV linear accelerator consists of a 3 MeV RFQ, 50 MeV DTL, and 200 MeV SDTL. The main parameter of the 200 MeV LINAC is given in Table1.

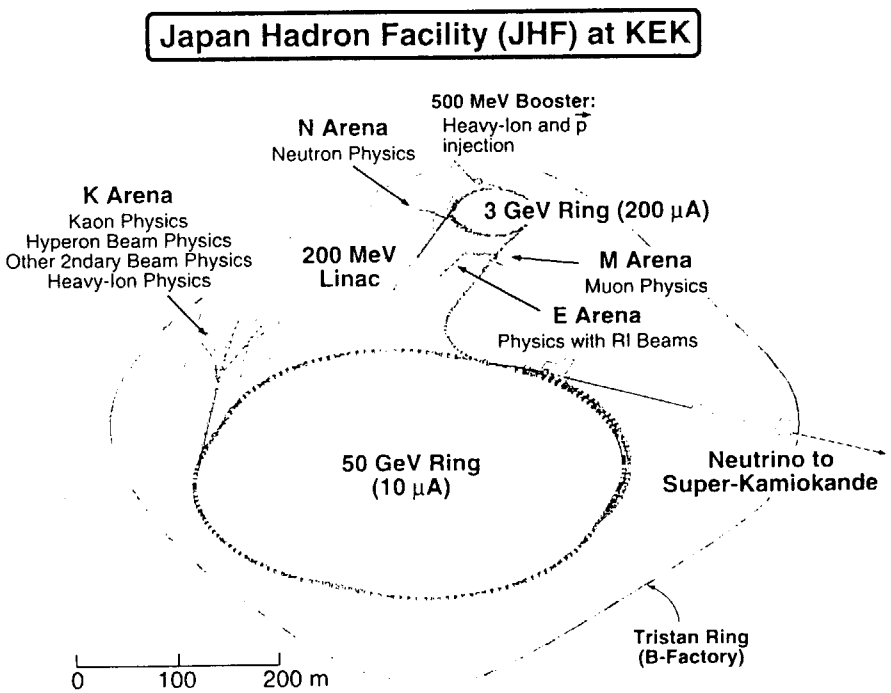

Fig.1. Proposed accelerator complex and experimental areas for JHF

Table 1 Parameter for the 200MeV LINAC

Energy	200 MeV	Average beam current	200 μA
Repetition rate	25 Hz	Peak current	30 mA
Beam width	400 μs	Frequency	324 MHz

The 3 GeV booster synchrotron is constructed in the present 12 GeV proton synchrotron tunnel. The beam extraction is designed for the fast extraction for M, N, E Arenas and the injection to the 50GeV ring. The Main parameter for the 3 GeV booster synchrotron is given in Table 2.

Table 2 Parameter for the 3 GeV booster synchrotron

Energy	3 GeV	Intensity	5×10^{13}ppp
Repetition rate	25 Hz	Beam power	0.6 MW
RF frequency	1.99-3.43 MHz	Circumference	340 m

The 50 GeV proton synchrotron provides the fast extracted beam for the neutrino experiment and the sow extracted beam for K-Arena. The accelerator will be set in a newly constructed tunnel at the beam level of 5 m below the ground surface. The main parameter for the 50 GeV synchrotron is given in Table 3.

Table 3 Parameter for the 50 GeV synchrotron

Energy	50 GeV	Intensity	2×10^{14}ppp
Repetition rate	0.3 Hz	Beam power	0.5 MW
RF frequency	3.43-3.51 MHz	Circumference	1445 m

2. Experimental Facilities

The four main experimental facilities are planed: K-Arena, M-Arena, N-Arena, and E-Arena. The main research topics of the K-Arena are hadrons in nuclear matter, hadron spectroscopy, hyperon-nucleon scattering, high density matter, rare K and μ decays, and neutrino oscillation. The antiproton accumulator ring will be installed in future. The layout of K-Arena is shown in Fig.2.

A precise nuclear spectroscopic investigation of hypernucleus may show an any change in hyperon in the nuclear matter such as mass and magnetic moment. The rare K and μ decays are important for the basic problems in particle physics such as the precision test of the standard model and the determination of the Cabbibo-Kobayashi-Maskawa matrix elements, violation of the fundamental symmetries, and lepton flavor

violation in the μ decay process. An experiment to search for long-baseline neutrino oscillation from KEK 12 GeV PS to Super-Kamiokande(250 km apart) is currently being prepared. Once the neutrino oscillation is observed, the an appearance search for ν_τ is crucial to understand the neutrino oscillation. To observe the ν_τ appearance, 50 GeV protons are needed because the production of τ particle requires high energy neutrinos.

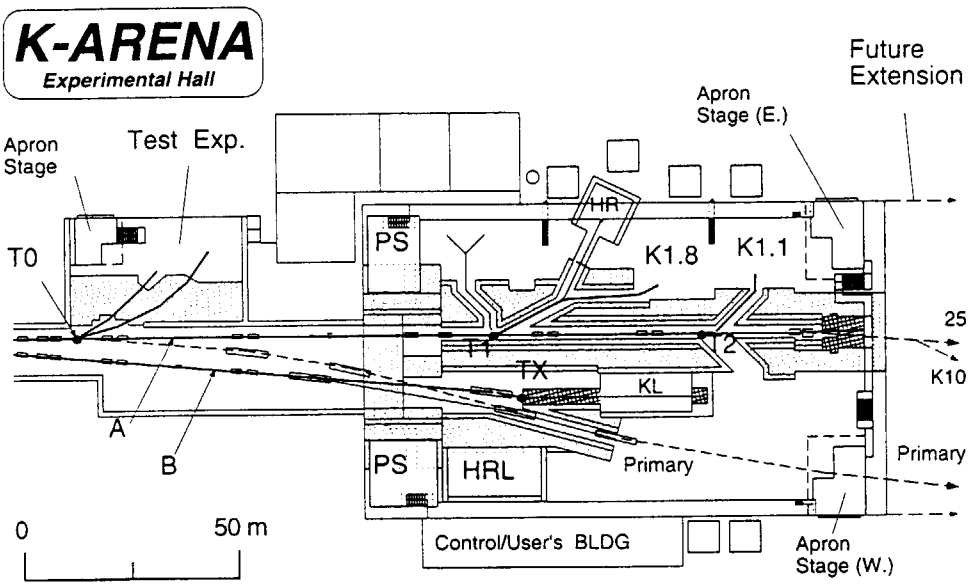

Fig.2 Schematic layout of the K-Arena experimental area

The research plans in the M-Arena are physics using μ spin probe for condensed matter, development of ultra-slow μ source and its applications, muon-catalyzed fusion and related muonic atoms, fundamental muon physics, and rare muon processes. The layout of M-Arena is shown in Fig.3.

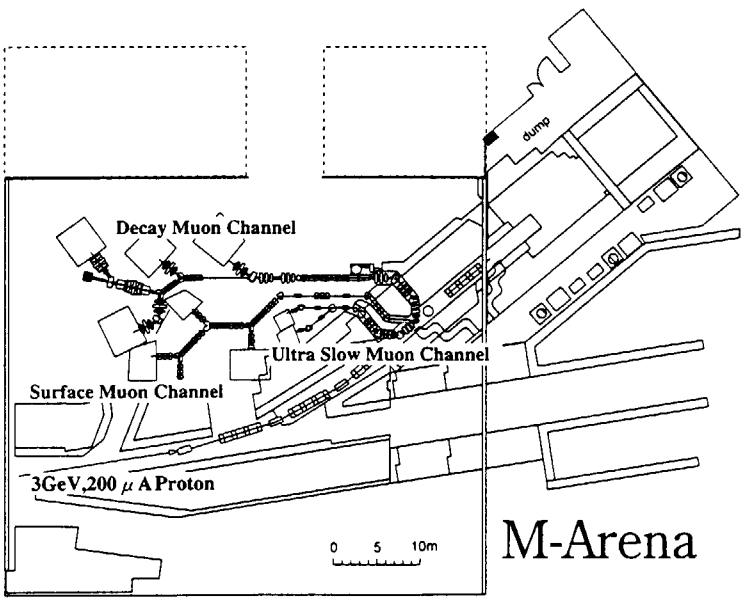

Fig.3 Facility layout of M-Arena

High intensity pulsed μ-beam in JHF enable us to use μSR method for smaller-size samples and time sequential measurements and further experiments under extreme conditions become enable. Muon catalyzed fusion and its related topics such as muon molecule formation in various D_2, DT, T_2 conditions of selected electronic molecular states, muon catalyzed fusion in plasma, and multi-muon contribution for reactions can be investigated by using intense muon-beams. High intensity muon beams can also be used for a precise measurement of the ground state splitting of a μ-atoms to test QED.

The research subjects of the N-Arena are; material science such as physics in condensed matter, earth science, phenomena in liquids and amorphous system, polymer science, biomolecular science studying the molecular structure and dynamics of DNA, RNA, and protein etc., and fundamental physics using polarized neutron such as parity violation and time reversal. The design of the experimental hall of N-Arena is shown in Fig.4.

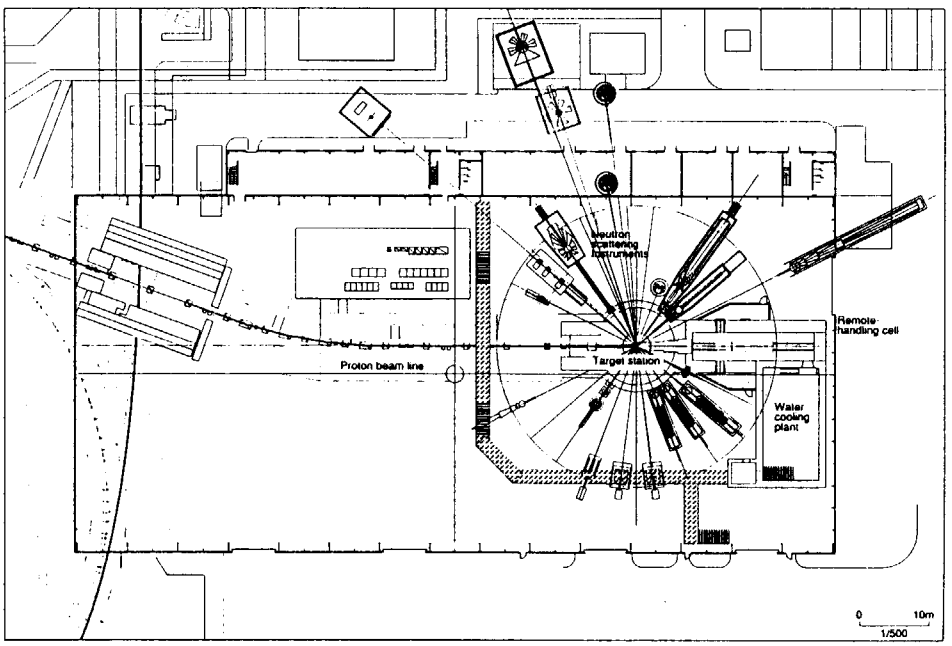

Fig.4 Schematic layout of N-Arena

The neutron flux of the N-Arena will allow sufficiently good resolution of both momentum and energy space, measurements on small system like new materials or stress around a crack tip or more dilute solution etc., very short experiment period which allows real time spectroscopy, wide energy-momentum range, high signal-to-background ratio, and routine use of polarized analysis up to high energy.

The expected typical research fields in E-Arena are surface science, property of exotic nuclei, material science, hot atom chemistry, nuclear astrophysics, non-destructive analysis of material, exotic nuclear physics and medical diagnostics. The plan view of the E-Arena experimental area is shown in fig.5.

Unstable neutron far-rich nucleus reactions make it possible to reach a region in the nuclear chart around the magic numbers of neutron 184 and proton 114 where possible long lived super heavy nuclei exist.

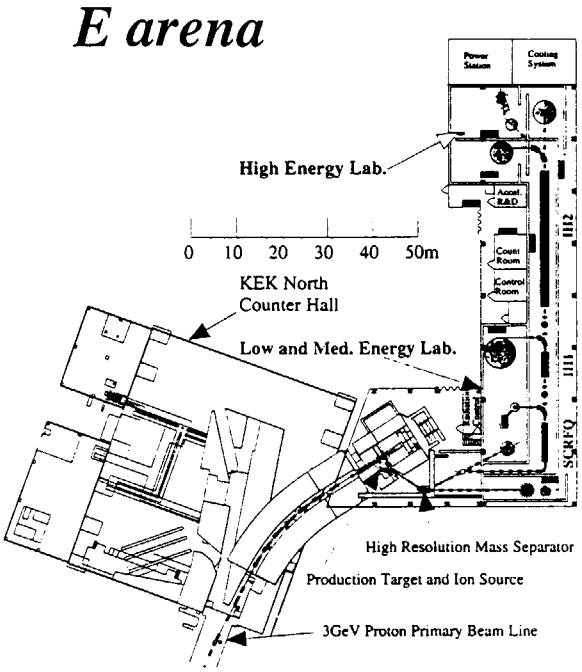

Fig.5 Plan view of E-Arena

The unstable nuclear beam open the new fields of physics such as reaction mechanism of neutron-rich nuclei, chosmochronology and heavy-element synthesis, direct measurement of astrophysical nuclear reaction, extremely high-spin and exotic deformation in nuclei, and physics with spin-oriented radioactive nuclei. Using ion trap technique ultra high precision nuclear spectroscopy will be carried out on unstable nuclei.

3. Remarks

The experimental proposals in each Arena are the extension of the present activities developed at the KEK 12GeV proton synchrotron, the 500 MeV booster synchrotron, and the research and development project of the radioactive beam acceleration at KEK Tanashi Branch.

JHF will be used by not only Japanese researchers but also a number of researchers from abroad. Thus JHF will be an international research facility and the research center of the Asian countries.

References

[1] Proposed for Japan Hadron Project, KEK Report 97-3(1997)

2.6.4 Nuclear Data for Designing the IFMIF Accelerator

Masayoshi SUGIMOTO
Intense Neutron Source Laboratory, Japan Atomic Energy Research Institute
Tokai-mura, Naka-gun, Ibaraki-ken 319-11
e-mail: sugimoto@ifmif.tokai.jaeri.go.jp

The objective of the International Fusion Materials Irradiation Facility (IFMIF) and the design concept of the IFMIF accelerator system are described. The status of the nuclear data, especially for the deuteron-induced reactions, to qualify the system design is reviewed. The requests for the nuclear data compilation and/or evaluation are summarized.

1. Introduction

The International Fusion Materials Irradiation Facility (IFMIF) is an accelerator-based intense neutron source, which give a broad peak around 14 MeV by using the d+Li reaction and adjusting the energy of the incident deuteron beam, similar to FMIT [1] and ESNIT [2]. So far many types of neutron sources are proposed for the irradiation tests of the fusion materials and the two main characteristics, intensity and spectrum, are compared with each other, as shown in
Fig. 1. The d+Li source is the best choice from the viewpoint of the state of the technology for designing the accelerator and target systems. However, it has one undesirable property called "high energy tail", i.e. unknown effects of the neutrons with energy higher than 14 MeV. So the recent designs including IFMIF employ the energy selectivity to tailor the neutron field according to the irradiated materials. The characteristics of the neutron sources with the irradiation volume are also compared in Fig. 2. The most important feature of IFMIF is its irradiation volume over the various intensity levels. The IFMIF Conceptual Design Activity (CDA) in the framework of the international collaboration among Japan, US, EU and Russia under IEA has been completed in early 1997 [3] and the extended design works called Conceptual Design Evaluation (CDE) will be continued for a few years. In Fig. 3, the layout of the principal subsystems of IFMIF is drawn schematically. Two deuteron beams are accelerated in parallel and independently transported to the lithium target station followed by the test cell containing the irradiated materials. The main features of the deuteron linacs for such a facility are given in Table 1.

In Sec. 2, we describe the design concept of the IFMIF accelerator from the viewpoint of the nuclear data related topics. The status of the nuclear data of the deuteron-induced reaction required for designing the accelerator is reviewed and the requests for the data are summarized in Sec. 3.

Source Type	Intensity	Spectrum	Comment
d+t reaction	×	◎	RTNS; VNS (fusion reactor); D_2O, T_2O target proposals
Fission reactor	◎	×	Average energy too low
Proton spallation	○	×	Similar to fission source; Too high energy component
t+p reaction	×	○	Triton accelerator; H_2O target; no high energy tail
(d,n) stripping reaction	○	△ (➔ ○)	High energy tail (using energy selectivity)

US: FMIT* (1978~85)

Japan: ESNIT** (1988~94)

International (Japan,US,EU,Russia): IFMIF (1995~)

*) FMIT: Fusion Materials Irradiation Test facility
**) ESNIT: Energy Selective Neutron Irradiation Test facility

Fig. 1. Proposed neutron sources for fusion materials irradiation tests.

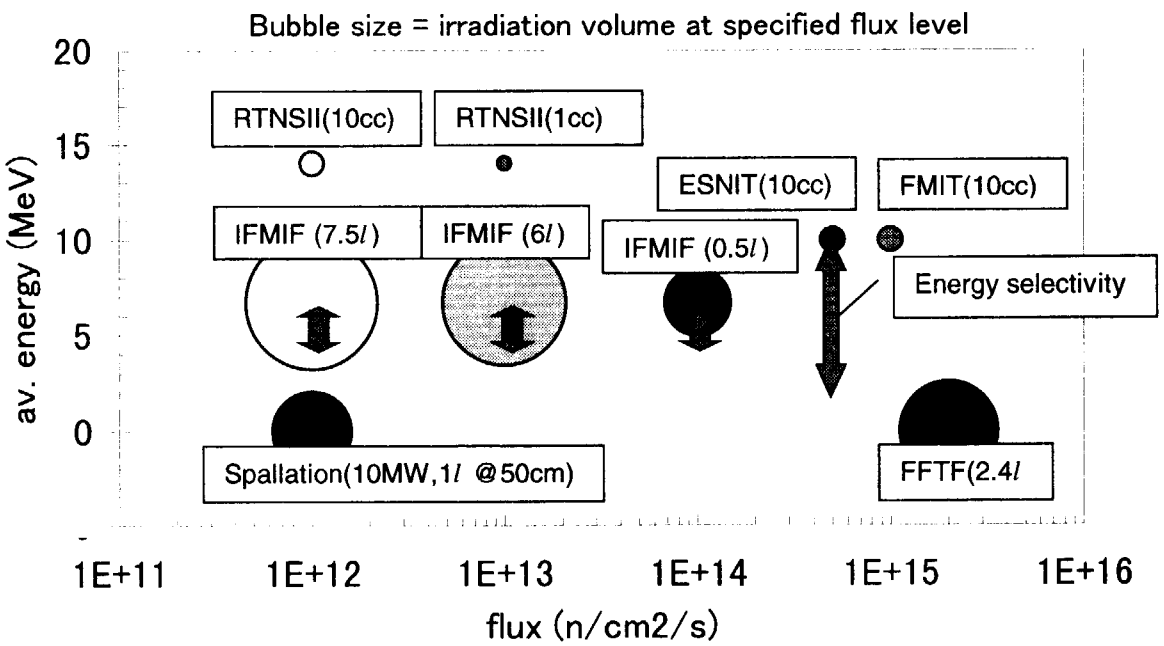

Fig. 2. Characteristics of the neutron sources for fusion materials irradiation tests.

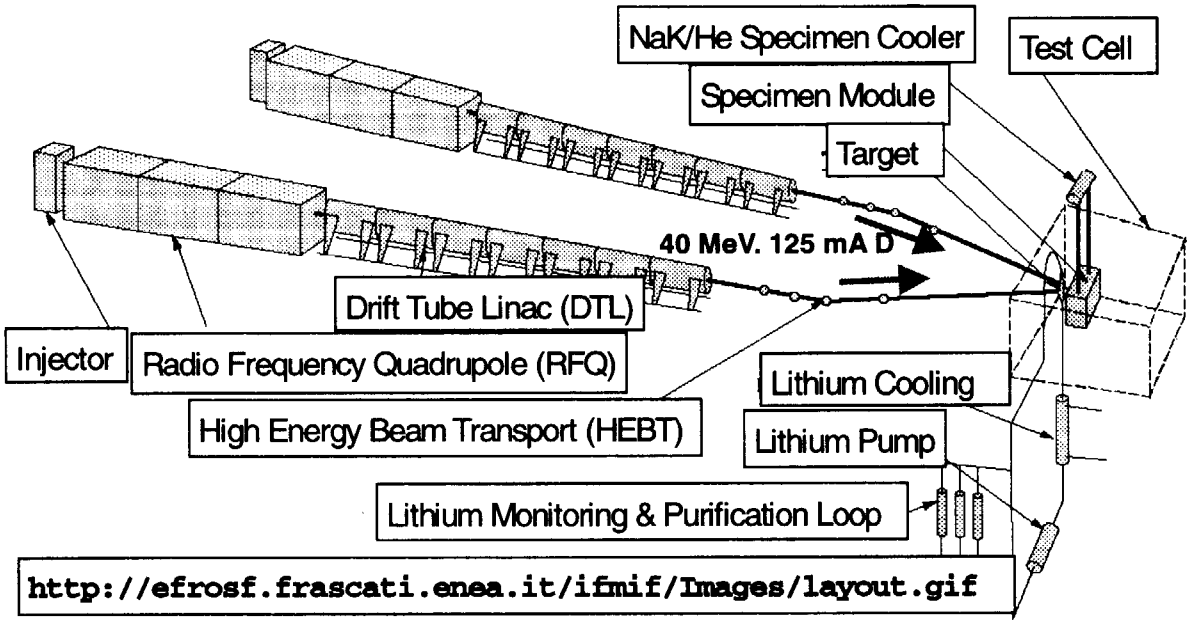

Fig. 3. Schematic layout of the main subsystems in the IFMIF.

Table 1. Requirements for the deuteron linacs of the fusion materials irradiation facilities.

Item	FMIT	ESNIT	**IFMIF**
Frequency	80 MHz	120 MHz	**175 MHz**
Beam current	100 mA	50 mA	**125 mA x 2**
Output energy	35 MeV	10 – 40 MeV, 5 MeV step	**32, 36, 40 MeV**
Beam size on target	3 cm W x 1 cm H, gaussian	5 cm W x 5 cm H, uniform	**20 cm W x 5 cm H, uniform** **1 cm fall off in vertical sides**
Ion species	D^+ (H_2^+ in tests)	D^+, H_2^+, Simultaneous acceleration : D+ and D- , H2+ and D-	**D^+ (H_2^+ in tests)**
Feature	High Flux	Energy Selectivity	**Irradiation Volume**

2. Accelerator design concept

The deuteron beam, 40-MeV and 250-mA CW, is required and achieved by the two identical 125-mA deuteron linac modules. Each of linac consists of a 100-keV, 140-mA ion injector, an 8-MeV, 125-mA Radio Frequency Quadrupole (RFQ), and eight Drift-Tube Linac (DTL) tanks as shown in Fig. 4. The output energy is selectable from 32-, 36-, and 40-MeV by switching on and off the RF power to the last two DTL tanks. The accelerator system contains the RF system and the other support systems, however,

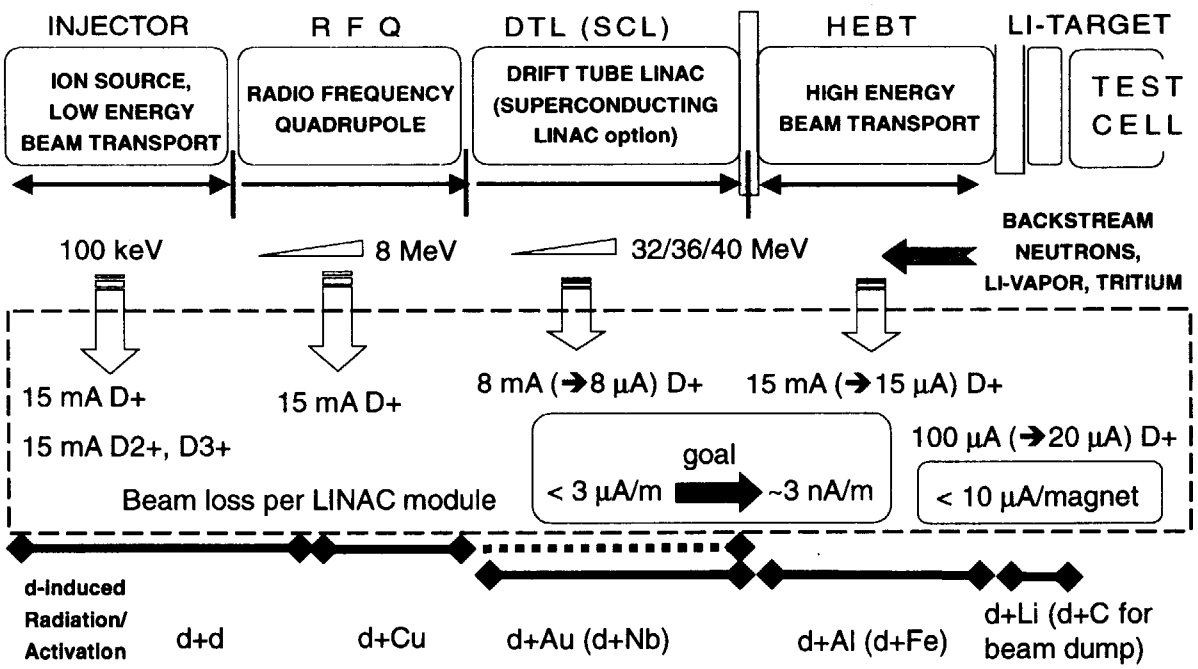

Fig. 4. Layout of the IFMIF accelerator system and associated beam loss/activation issues.

they are out of scope in the viewpoint of the nuclear data related discussion.

Since the availability goal of the accelerator system is 88 %, the machine operation should be extremely stable and the suppression of the beam spill along the accelerator/transport lines is the most important to keep the hands-on maintenance philosophy. The possible sources of radiation and radioactivity due to the beam loss are (1) the primary beam (deuteron) induced neutrons, gamma rays and activity and (2) the secondary beam (neutron, gamma) induced activity. As shown in Fig. 4, the target nuclei are the structural material elements (Al, Fe, Cu, Nb, etc.) and the gasses absorbed in the structure (H, D, He, etc.). In some cases the shielding materials and the coolants also may be activated. To confirm the radiation source terms, the precise analysis of the beam loss during the realistic machine operation schedule. In the present design study we only treated the steady state beam loss in the RFQ channel. The resultant neutron production along the RFQ is 10^6 ~ 10^7 n/cm/sec at the first 5 m due to D+D reaction, and 10^7~ 10^8 n/cm/sec at the last 3 m due to D+Cu reaction. Similar analysis is undergone for the main linac and the transport line where the maximum loss is tentatively set to 3 μA/m and 10 μA per hot spot in the bending or focussing magnets in the conceptual design. However, this exceeds easily the limit of radiation level for hands-on maintenance, and the beam loss should be reduced to 3 nA/m in the actual operation.

As shown in Table 1, the IFMIF accelerator has a capability to accelerate H_2^+ beam for the calibration purpose. So the large amount of proton beam can be lost during the machine calibration time and the similar work as the deuteron-induced reactions is necessary for the proton-induced reactions.

3. Nuclear data needs

The neutron-induced reactions up to 50-MeV are primary concern of the design study of the irradiation field and are investigated intensively. However, the deuteron-induced reactions up to 40-MeV (and proton-induced reactions up to 20-MeV) are also important in the accelerator design study and are rarely discussed in a systematical way through the IFMIF-CDA. The nuclear data of the charged particle-induced reactions are necessary to plan the accelerator system performance during its lifetime. The general needs for the nuclear data are summarized in Table 2 required at the design phase and the operation phase. The (d,n) source reactions and the d-induced activities with half-lives longer than minute have the highest priorities. For the safety analysis, it is important to estimate the d-induced tritium production rate. The status of the typical reactions is surveyed and summarized as follows.

(1) Angular dependence of the neutron production from (d,n) reactions can be described by Serber model [4], however its prediction of the energy spectrum is not satisfactory and the integrated cross sections should be based on the experimental data. Especially, the approach to construct the double differential form by the product of the angular dependence and the energy spectrum terms is misleading. It is preferred to make the direct measurements of the limited number of targets used in the accelerator structure and to conduct the distorted wave analysis instead of the Serber's plane wave formula. It is valuable if the "thin" target measurements can be carried out systematically.

Table 2. General needs for the nuclear data for design and operation phases.

Design Phase	Experiment Planning	Neutron Field, Nuclear Heat	● Li(d,n) neutron source distribution ● neutron cross sections up to 50 MeV
	Safety Analysis	Shield design ---------- Tritium inventory Radiation hazard (Accelerator, Target, Test cell)	● (d,n) source distribution (d+d, d+C, d+Al, d+Cu, d+Nb, d+Au etc.) ● neutron cross sections up to 50 MeV ● d-induced tritium-production ● d-induced radioactivities
Operation Phase	Dosimetry		● dosimetry cross sections
	Maintenance	Cooling time, Local shield, Remote handling	● (d,n) source distribution ● d-induced radioactivities ● n-induced radioactivities
	Start-up	H_2^+ beam	● p-induced radiations/activities

(2) The status of the Li(d,n) reaction as well as Be(d,n) is almost satisfactory to investigate the systematics.

(3) The other cross sections of d-induced reactions are compiled [5], however, its quality is much less than those of p-induced reactions. Only the several reactions are well surveyed for the specific purposes, such as ^{27}Al(d,pα), (d,2nx), (d,4nx). The d-induced inclusive activity was calculated for Ed=40 MeV and at 10 cm distance [6]. The dose rate at 1-h cooling after 168-h irradiation becomes 50 rem/h/μA-D, which is not so different with 20 and 60 for Cu and Fe, respectively. The resultant dose rate was 0.4 rem/h/μA-D for Ta. Such high Z material can be used as a protection from the beam loss and a

collimator to suppress beam halo. Only the use of aluminum beam duct is not effective to reduce the activity immediately after the shut-down.

(4) The tritium production rate during the operation is an important issue in the safety analysis. In the CDA design report, essentially no accumulation of tritium is assumed in the accelerator system, by removing the all tritium escaped from lithium target using the differential pumping system at the accelerator-target interface. In the CDE phase, we must supply a more confident production rate in the target and the accelerator structure due to beam loss. In Ref. [7], the dependence of the inclusive t-production is suggested as $A^{1/3}/Z$. The production rate along the Al-transport line is estimated to be 1500 (or 120) μCi/day at the beam loss of 3 μA/m (or for case of 3 nA/m goal).

4. Conclusion

The deuteron accelerator based neutron source is the best choice for the fusion materials irradiation tests to satisfy the requirements of the neutron flux/fluence and the irradiation volume. In the accelerator design the beam loss consideration is the most important issue, and the nuclear data for d-induced reactions and activities are required. The current status of the (d,n) source reaction data is satisfactory compared with the other reaction data. However, the application of the Serber model to predict the neutron energy distribution is not so confident opposed to the angular distribution case. More precise approach using the distorted wave analysis may be helpful and the "thin" target measurements are valuable for direct application and theoretical study. Other nuclear data are poorer than those for p-induced nuclear data. It is indicative that activity of aluminum immediately after the shut-down is comparable to Fe and Cu, and some high-Z materials should be used where the beam loss is expected. The inclusive tritium-production rate is important for the safety analysis but large ambiguity exists in the estimation and more accurate cross sections are desired.

Acknowledgements

The technical contributions provided by all the participant members of the IFMIF-CDA are gratefully acknowledged.

References

[1] Pottmeyer Jr. E.W. et al.: J. of Nucl. Materials, 85 & 86, 463 (1979).

[2] Noda K.et al.: J. of Nucl. Materials, 191 & 194, 1367 (1992).

[3] IFMIF CDA Team: "IFMIF International Fusion Materials Irradiation Facility Conceptual Design Activity Final Report", edited by Martone M., ENEA RT/ERG/FUS/96/11, Dec. 1996.

[4] Serber R.: Phys. Rev. 72, 1008 (1947).

[5] Barbier M.: "Induced Raioactivity", North-Holland Pub. Co. Amsterdam, 1969.

[6] Fulmer C.B. and Kindred G.: ORNL TM-2834, Aug. 1970.

[7] Mann F.M.: private communication.

This is a blank page.

3. Papers Presented at Poster Session

This is a blank page.

3.1 Critical Experiments Analyses by Using 70 Energy Group Library Based on ENDF/B-VI

Yoshihisa TAHARA, Hideki MATSUMOTO
Nuclear Energy Systems Engineering Center, Mitsubishi Heavy Industries, Ltd.
3-1, Minatomirai 3-chome, Nishi-ku Yokohama 220-8401 Japan
tahara@atom.hq.mhi.co.jp, matsu@atom.hq.mhi.co.jp

Harish C.HURIA, Mohamed OUISLOUMEN
Westinghouse Electric Corporation
P.O. Box355, Pittsburgh, PA-15230, USA
harish.huria@cnfd.pgh.wec.com, mohamed.ouisloumen@cnfd.pgh.wec.com

ABSTRACT

The newly developed 70-group library has been validated by comparing kinf from a continuous energy Monte-Carlo code MCNP and a two dimensional spectrum calculation code PHOENIX-CP. The code employs Discrete Angular Flux Method based on Collision Probability. The library has been also validated against a large number of critical experiments and numerical benchmarks for assemblies with MOX and Gd fuels.

1. Introduction

A 70-energy group library based on the basic nuclear data of ENDF/B-VI has been developed to improve calculation accuracy of high burnup and MOX fueled cores[1, 2]. The NJOY code was used to covert the point-wise data to the specified multigroup structure. The creation and processing of the library is discussed in detail in Ref.1. The library has been validated against a large number of criticals and numerical benchmarks using the PHOENIX-P code. PHOENIX-P uses a nodal coupling method followed by a 2-D S_4 solution for the assembly spectrum calculation[3]. A new 2-D spectrum calculation code PHOENIX-CP[4] has been developed in the Joint Development Program between MHI and WH. This is a revised version of PHOENIX-P with a different neutronic solution method. The transport equation is solved using the collision probability method.

The validity and accuracy of our new 70-group library have been shown by comparing infinite multiplication factor (kinf) between PHOENIX-CP and MCNP[5]

Gd rod worths experiments and KRITZ high-temperature experiments have also been analyzed to show the adequacy of the combination of PHOENIX-CP and the new 70-group library as a nuclear core design tool.

2. The new cross-section library and Resonance treatment

The 70-energy group structure is a modified form of the WIMS library group boundaries so as to have better treatment of Pu resonance. Thermal cut-off energy is chosen at 2.1eV to optimize upscattering effect and resonance treatment. The Pu^{240} resonance at 1.06 eV is treated through multigroup shielding factors built within PHOENIX-CP. The library has the following broad group structure :

Fast range :	14 groups	10.0MeV-9.118MeV
Resonance range :	17 groups	9.118KeV-2.1eV
Thermal range :	39 groups	2.1eV-0.0eV.

3. Validation and results

This paper describes the re-analyses of the cold critical experiments included in Ref.1. Besides those,

some more experiments have been added to the list as part of final qualification of the library and the newly developed spectrum calculation code PHOENIX-CP. All these calculations have been done with a special version of the library wherein the important nuclides used in these experiments have been weighted with a spectrum typical of cold conditions. The following experiments and benchmarks were selected for the analyses:

(1) TCA critical experiments with UO_2 and MOX fuel[6]
(2) SAXTON and ESADA MOX/UO_2 two-region criticals[7,8]
(3) CSEWG recommended TRX and BAPL critical experiments[9]
(4) Strawbridge and Barry 101criticals[10]
(5) Numerical benchmarks with high plutonium contents and high U^{235} enrichment
(6) 17*17 PWR assembly benchmarks
(7) 14*14 PWR assembly benchmarks
(8) TCA Critical experiments with gadolinium burnable absorber rods[11]
(9) B&W critical experiments[12,13]
(10) KRITZ high-temperature critical experiments[14]

Monte-Carlo models for the first seven sets of experiments were set up. Most of the MCNP values are quoted from Ref.1. However, no Monte-Carlo models were developed for TCA Gd, B&W and KRITZ criticals since the objectives are to compare the Gd reactivity worths, measured power distributions and effective multiplication factors (keff), respectively. Comparisons of kinf's between PHOENIX-CP and MCNP are shown in **Table 1** through **Table 4** for critical experiments. Strawbridge and Barry 101 critical experiments were analyzed with PHOENIX-CP and MCNP. The ratio of kinf between the two codes are processed statistically and the average ratio of 1.00062 and the standard deviation of 0.00226 were obtained as shown in **Table 5.**

Table 1 TCA Critical Experiments

Core	kinf PH-CP(2D)	kinf MCNP(2D)
TCA150U	1.36418	1.36362 ± 0.00045
TCA183U	1.37535	1.37568 ± 0.00049
TCA248U	1.37193	1.37217 ± 0.00054
TCA300U	1.35608	1.35558 ± 0.00044
TCA242Pu	1.34768	1.34806 ± 0.00054
TCA298Pu	1.34033	1.34303 ± 0.00061
TCA424Pu	1.30050	1.30126 ± 0.00046
TCA555Pu	1.24294	1.24446 ± 0.00048

Table 2 SAXTON Critical Experiments

Core	kinf PH-CP(2D)	kinf MCNP(2D)
1b	1.46037	1.46517 ± 0.00068
2	1.30960	1.30902 ± 0.00080
3	1.31161	1.31134 ± 0.00068
4	1.45832	1.46225 ± 0.00060
5	1.32880	1.32929 ± 0.00085

Table 3 ESADA Critical Experiments

Core	kinf PH-CP(2D)	kinf MCNP(2D)
13	1.36268	1.36499 ± 0.00055
14	1.32876	1.33080 ± 0.00052
15	1.27105	1.27212 ± 0.00064
16	1.27803	1.28065 ± 0.00045
17	1.35008	1.35124 ± 0.00051

We have also performed the analysis of numerical benchmarks with high Plutonium contents and high U^{235} enrichment using the cell proposed by OECD/ NEA[15]. Isotopic composition of 6.1w/o Pu case is a

typical one assumed in PWR MOX recycling study[1 6]. The results are shown in **Table 6**.

We prepared the 17*17 PWR assembly benchmarks for the qualification calculation. The brief description of the 17*17 assembly is given below:

1) MOX assembly with typical Pu isotopic composition(6.1w/o Pu-fissile enrichment)
2) MOX assembly with worst Pu isotopic composition(6.0w/o Pu-fissile enrichment)
3) UO_2 assembly with 4.1w/o U^{235} 16 6w/o Gd_2O_3 fuel rods
1) UO_2 assembly with 4.8w/o U^{235} 24 9w/o Gd_2O_3 fuel rods

The typical Pu isotopic composition corresponds to the following Pu vector(w/o) :
Typical : Pu^{238} : Pu^{239} : Pu^{240} : Pu^{241} : Pu^{242} : Am^{241}
= 1.9 : 57.5 : 23.3 : 10.0 : 5.4 : 1.9
The Pu^{240} content of the worst Pu isotopic composition is about 2 times lager than that of the typical Pu. The results are shown in **Table 7**.

A 14*14 OFA assembly was also modeled using PHOENIX-CP and MCNP. The result is shown in **Table 8**. This has an enrichment of 4.0w/o U^{235}

TCA Critical experiments with gadolinium burnable absorber rods were analyzed. Geometrical and material specifications of TCA gadolinium critical experiments were taken from Ref.11. The core model consists of a 21*21 fuel lattice configuration followed by water reflector of 15 cell pitches on all the sides. Experimental axial buckling has also been used to get effective multiplication factor. However, here, the emphasis is to derive the Gd reactivity worth and not to get the absolute eigen values.

Eight different core configurations were included in the present analysis. The Gd reactivity worth was calculated as the reactivity equivalent of the assembly with Gd rods with references

Table 4 TRX/BAPL Critical Experiments

Core	kinf	
	PH-CP(2D)	MCNP(2D)
TRX-1	1.18461	1.18402 ± 0.00043
TRX-2	1.16831	1.16897 ± 0.00041
BAPL-1	1.14724	1.14629 ± 0.00058
BAPL-2	1.15057	1.15083 ± 0.00046
BAPL-3	1.13583	1.13615 ± 0.00053

Table 5 Strawbridge & Barry 101 Criticals

	Ave.±std.Deviation
$\frac{k_{inf}^{PH-CP}}{k_{inf}^{MCNP}}$	1.00062 ± 0.00226

Table 6 Additional cell benchmarks

Cell	kinf	
	PH-CP(2D)	MCNP(2D)
Better Pu	1.22415	1.22281 ± 0.00082[a]
Dirty Pu	1.17441	1.17384 ± 0.00075[a]
6.1w/o Pu	1.20832	1.20975 ± 0.00071[a]
4.1w/o U	1.36890	1.37152 ± 0.00060

a :These values are recalculated and different from those in Ref.1.

Table 7 Benchmarks for 17*17 assembly

Assembly	kinf		
17*17 Type	PH-CP(2D)	MCNP(2D)	Dif.(pcm)
6.1w/o Pu (Typical)	1.20074	1.20088 ± 0.00065	14
6.0w/o Pu (Worst)	1.14038	1.14117 ± 0.00064	79
UO_2 with 6w/o Gd_2O_3	1.17886	1.18117 ± 0.00058	231
UO_2 with 9w/o Gd_2O_3	1.13703	1.14065 ± 0.00066	362

Table 8 Benchmarks for 14*14 assembly

Assembly	kinf		
14*14type	PH-CP(2D)	MCNP(2D)	Dif.(pcm)
UO_2 4.0w/oU^{235}	1.29520	1.29659 ± 0.00059	139

to the assembly without Gd rods. The results are shown in **Table 9**. The difference of Gd reactivity worths between calculation and measurement is less than 4%.

Table 9 TCA Gd Critical Experiments

Core name	Gd Fuel Gd w/o	Gd Fuel Number	Gd Worth (%) PH-CP	Gd Worth (%) Mea.	Dif.(%)
S-A	0.00	1		.....	.....
S-B	0.25	1	0.565	0.587	3.89
S-D	1.50	1	0.764	0.779	1.96
S-E	3.00	1	0.825	0.841	1.94
D-a-D	1.50	2	1.423	1.433	0.70
D-b-D	1.50	2	1.466	1.455	-0.75
D-e-D	1.50	2	1.371	1.319	-3.79
T-a-D	1.50	3	1.916	1.862	-2.82

The Core XI and Core XIV of B&W Critical Experiments were analyzed by PHOENIX-CP and the results are summarized together with the core configuration and conditions in **Table 10**.

Measured relative power distributions for the B&W critical experiments were compared with the PHOENIX-CP predictions. The calculated rod powers were renormalized to the total measured power of the center assembly in the test region. The comparison of rod power distribution between calculation and measurement is shown in Fig.1 for the Loading Pattern No.4 of Core XIV, where 24 Pyrex absorber rods are loaded. The maximum error of 2.6 % appears at the fuel cell which is on the diagonal and next to a water cell and the standard deviation is 0.92%.

Table 10 Experimental Configurations and results for Core XI and XIV

Core	Loading Pattern	Fuel Rods	Water Holes	Pyrex Rods	Soluble Boron (ppm)	keff
XI	2	4808	153	0	1334	0.99883
	3	4808	153	0	1337	0.99935
	4	4808	117	36	1183	0.99774
	5	4808	117	36	1181	0.99737
	6	4808	81	72	1034	0.99700
	7	4808	81	72	1031	0.99631
	8	4808	9	144	794	0.99480
	9	4808	9	144	779	0.99508
XIV	4	4736	201	24	1246	0.99972
	5	4736	201	24	1204	0.99987

The critical facility KRITZ has a pressure tank and is operated up to a maximum temperature of 245 °C. The twelve high-temperature critical experiments were analyzed using PHOENIX-CP and 3-D nodal code ANC[17]. The core configuration and conditions are summarized in **Table-11**.

A fuel bundle with water reflector model was employed to take account for spectrum effect on the peripheral fuel due to water reflector. Two-group homogenized cross-sections of fuel and water from

PHOENIX-CP were used in the ANC calculation. The results of keff are listed in the **Table-11**. The mean keff of the 12 experiments is 1.00015 and the standard deviation is 0.00190.

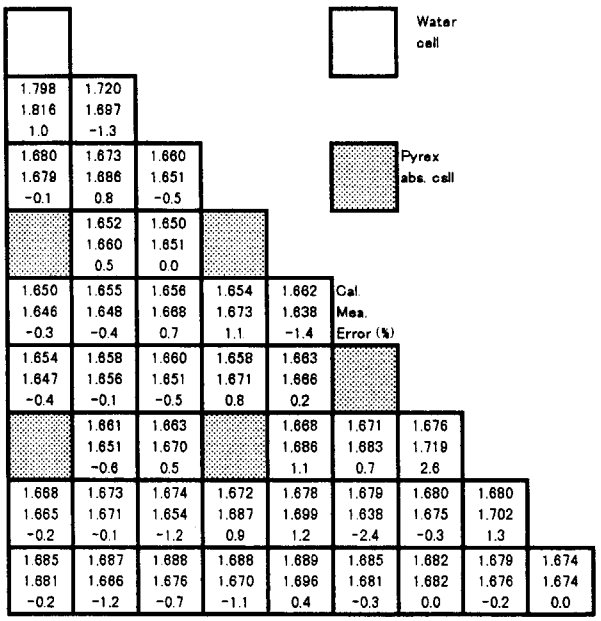

Fig. 1 Power distribution for Loading pattern-4 of core XIV

Table 11 Core conditions and results for KRITZ experiments

Case	Lattice	Boron (ppm)	Temp. (°C)	keff
01	39*39	0.8	41.2	0.99984
02	39*39	0.8	90.0	1.00155
03	39*39	0.8	216.6	1.00079
04	39*39	0.8	225.6	1.00080
05	46*46	46.3	90.4	0.99594
06	46*46	46.3	206.0	0.99820
07	46*46	46.3	227.3	0.99777
08	46*46	46.3	245.8	0.99994
09	46*46	175.0	22.4	1.00080
10	46*46	175.0	89.1	1.00318
11	46*46	175.0	201.3	1.00149
12	46*46	175.05	205.3	1.00153

Discussions

Good agreement in Kinf has been obtained for all the critical experiments - TCA, SAXTON, ESADA, Strawbridge & Barry, TRX, and BAPL. PHOENIX-CP and MCNP calculated eigenvalues for the numerical benchmarks agree quite well not only for UO_2 but for MOX cells as well. However, for the assembly benchmarks, PHOENIX-CP underpredicts kinf by about 140 pcm to 360 pcm compared to MCNP for UO_2 assembly cases. The maximum difference occurs in the case of assembly with 9 w/o Gd content. This small reactivity underprediction is due to the cell model. A six-region subdivision and coupling order of 3 has been used in the calculations ; the diagonal splitting of moderator, one region each for fuel and cladding. Ouisloumen shows that PHOENIX-CP underpredicts kinf by about 240 pcm compared to MCNP for a control rod inserted UO_2 fuel assembly like 17*17 array if such a cell model is employed[4]. Considering the fact and the standard deviation of about 60pcm in MCNP calculation, it can be said that the library gives really accurate results for UO_2 assembly cases.

We will do further investigation on resonance treatment for UO_2 and MOX assembly calculations because the reactivity difference between the two codes has different tendency for UO_2 and MOX assembly calculations.

The agreement of Gd worth is excellent. The difference is less than 4%. B&W analyses show good agreement in keff with experiment and the maximum difference between measured and calculated rod power is only 2.6%. KRITZ analysis also shows a good agreement of keff .

Conclusions

Kinf's of PHOENIX -CP with the new 70-group library and MCNP agree very well and the predictions of criticality of the KRITZ High-temperature experiments are excellent. These results validate the developed library and PHOENIX-CP methodology.

Acknowledgments

One of the authors(Y.T) would like to thank Dr. Chao and Dr. Casadei for their helpful suggestions

and valuable advice.

References

1 H.C.Huria,Y.Tahara, "New Multigroup Library for PHOENIX-P," PHYSOR96(1996).

2 H.Huria, M.Ouisloumen, "ENDF/B-VI : U^{238} Resonance Integral Reduction-A Closer Look," Trans. Am. Nucl. Soc., 76,329(1997).

3 R.J.J.Stamm'ler, M.J.Abbate, "Method of Steady-State Reactor Physics in Nuclear Design," ACADEMIC PRESS(1983).

4 M.Ouisloumen, S.Aoki, "The Two-Dimensional Collision Probability Calculation in Westinghouse Lattice Code: Methodology and Benchmarking," PHYSOR96(1996).

5 "MCNP 4A Monte Carlo N-Particle Transport Code System," CCC-200,RSIC,ORNL(1993).

6 H.Tsuruta,et al., "Critical Sizes of Light-Water Moderated UO_2 and PuO_2-UO_2 Lattices." JAERI1254(1978).

7 R.D.Leamer, "PuO_2-UO_2 Fueled Critical Experiments," WCAP-3726-1(1967).

8 W.L.Orr, "Saxton Plutonium Program Progress and Topical Reports," WCAP-3385-57(1974).

9 "Cross Section Evaluation Working Group Benchmark Specifications," BNL-19302(ENDF-202), (1974).

10 L.E.Strawbridge, R.F.Barry, "Criticality Calculations for Uniform Water-moderated lattices." Nucl. Sci. Eng., 23, 58(1965).

11 S.Matsuura et al., "Physical characteristics of Gd_2O_3-UO_2 fuel in LWR," JAERI-M 9844(1981).

12 M.N.Baldwin, M.E.Stern, "Physics Verification Program Part III, Task 4 Summary Report," BAW- 3647-20, March 1971.

13 M.N.Baldwin, "Physics Verification Program Part III, Task 11 Quarterly Technical Report July-September 1974," BAW- 3647-32, February 1975.

14 R.Persson et al., "High-temperature critical experiments with H_2O-moderated fuel assemblies in KRITZ," Technical Meeting No.2/11, NUCLEX72(1972).

15 J.Vergens,et al., "Working Party on PHYSICS of Plutonium Recycling-Benchmark Specifications for Plutonium Recycling in PWRs," OECD NUCLEAR ENERGY AGENCY Nuclear Science Committee, NSC/DOC(93)19, August 1993.

16 K.Yamate, et al., "MOX Fuel Design and Development Consideration," International Atomic Energy Agency, Technical Committee Meeting on Recycling of Plutonium in Water Reactor Fuel, Newby Bridge, Windermere, U.K., July 1995.

17 Y.S.Liu, et al., "ANC: A Westinghouse Advanced Nodal Computer Code," WCAP-0965, December 1985.

3.2 Measurement of Neutron Inelastic Scattering Cross Section of ^{238}U

Takako MIURA, Mamoru BABA, Masanobu IBARAKI, Toshiya SANAMI,
Than Win, Yoshitaka HIRASAWA, Shigeo MATSUYAMA, Naohiro HIRAKAWA
Department of Quantum Science and Energy Engineering, Tohoku University
Aramaki-Aza-Aoba, Aoba-ku, Sendai, 980-77, Japan
email : takako@rpl.qse.tohoku.ac.jp

Neutron scattering from the 0^+, 2^+ (1-st) and 4^+ (2nd) levels of ^{238}U was measured for incident energies between 0.4 and 0.85MeV at the Tohoku University 4.5MV Dynamitron facility, using the time-of-flight (TOF) method with monoenergetic pulsed neutrons by the ^{7}Li(p,n) reaction. The results are presented in comparison with other experimental data and evaluated data.

1. Introduction

^{238}U is one of the main constituent element in fast and accelerator-based reactors. The inelastic scattering cross section of ^{238}U, therefore, is of great importance in the design of the reactors. However, experimental data of neutron inelastic scattering cross section and secondary neutron spectra of ^{238}U are discrepant largely in spite of the significance. Then large differences exist among the evaluated values of the inelastic scattering cross section of ^{238}U. Cooperation for the improvement of the data status is in progress in OECD NEA.

In this study, following our previous works on the double differential neutron emission cross sections of ^{238}U[1], we have studied the excitation of low lying levels of ^{238}U for hundreds keV incident neutrons that is important as the basis for the evaluation of the ^{238}U nuclear data .

2. Experiment

The experiment was carried out at the Tohoku University 4.5MV Dynamitron facility, using the-time-of flight (TOF) method with mono-energetic pulsed neutrons by the ^{7}Li(p,n) reaction. Figure1 shows the experimental set up. The sample is a metallic cylinder of elemental uranium, 2cm diameter and 5cm long, and packed in an aluminum can, 0.5mm thick. The same size aluminum can was used for the background measurement. In addition we employed a lead sample with the same size as the uranium sample, to simulate the shape of the elastic peak of uranium (cf. section 3). The main detector is a 5" diameter and 2" thick NE213 scintillation detector. It was heavily shielded in a massive collimator made of water and paraffin. Data were acquired by 3-paramerer list mode for pulse height, pulse shape, and TOF.

The detector efficiency was determined from the measurement of well-known angular distributions of the ^{7}Li(p,n) neutrons.

In the present experiment, the separation between peaks are essential. To separate clearly the elastic and 1-st inelastic peaks, therefore, we optimized the experimental conditions as follows. The lithium target

was made thin to make the energy spread ~10keV, the flight path was long enough, 4~6m, and the target-sample distance was ~12cm to narrow the incident neutron energy width caused by the solid angle. Besides, the measurement was made at backward emission angles (120° and 135°) to minimize the effect of the elastic peak.

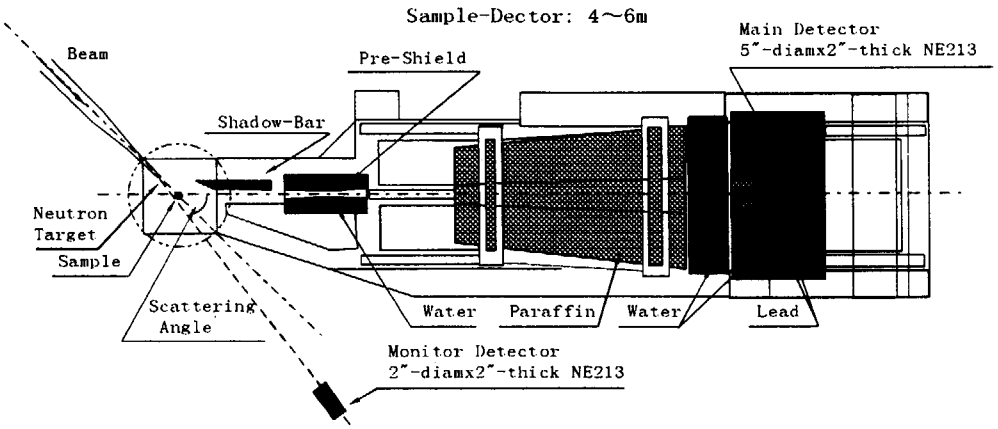

Fig.1 experimental arrangement

Data Reduction

The TOF spectra were transformed into energy spectra after subtracting the sample independent background and gamma-rays from the active sample. In fig.2, typical TOF spectra are shown. The peaks are separated fairly well, but the tail of the elastic peak extends down to the first inelastic peak.

Then we carried out peak fitting to separate the first inelastic peak from the elastic peak by the following way. The shape of the elastic peak of lead was used to simulate the elastic peak of ^{238}U, and the inelastic peak of the 2^+ level (excitation energy 44.9keV) was deduced by subtracting the appropriately normalized elastic peak of lead from the spectrum of ^{238}U. The spectrum fitted is shown in fig.3.

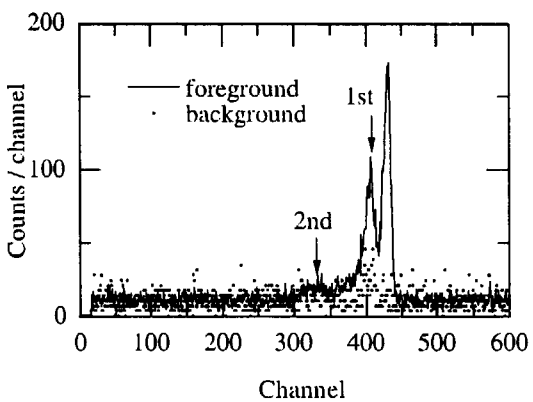

Fig.2 ^{238}U scattered neutron TOF spectrum at 120° for En=465 keV

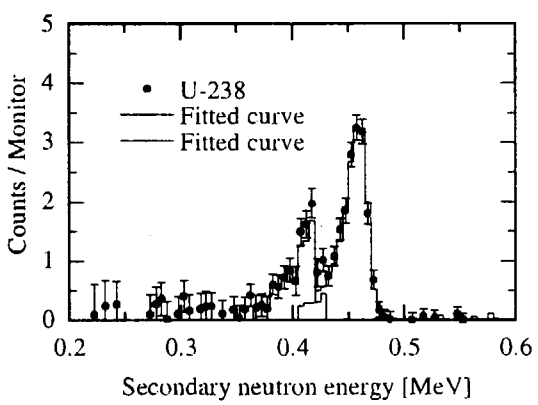

Fig.3 Fitted curve for the elastic peak and inelastic peak of ^{238}U

The absolute value of the cross section was determined by taking the ratio of scattered neutron yields to the source neutron yield measured at 0°. Differential cross sections were derived by the following equation.

$$\frac{d\sigma}{d\Omega}(E_0, E, \theta) = \frac{Y(E_0, E, \theta)}{Y(E_0, 0)} \cdot \frac{d^2}{N} \cdot \frac{D^2(\theta)}{D^2(0)} \cdot \frac{\varepsilon(E_0)}{\varepsilon(E)} \cdot f \cdot A(E_0, E, \theta) \quad ,$$

where

$Y(E_0, E, \theta)$, $Y(E_0, 0)$	=	the monitor-normalized yields of the scattered neutrons of energy E at angle θ and of the incident neutrons of energy E_0 at 0°, respectively
d	=	the target-sample distance
N	=	the number of atoms of the sample
$D^2(\theta)$, $D^2(0)$	=	the sample-detector distance at θ and at 0°, respectively
$\varepsilon(E_0)$, $\varepsilon(E)$	=	the relative detector efficiency for incident and scattered neutron, respectively
f	=	the correction factor for the effects of source neutron anisotropy and the geometry in the source-sample arrangement
A	=	the correction factor for finite size effects in the sample.

The correction factor f is given by the following expression [2]

$$f = \left[1 - \frac{1}{8d^2}\left(kR^2 + \frac{k+2}{3}H^2\right)\right]^{-1} \quad , \qquad k = \sum_i \frac{i(i+1)}{2} a_i \quad ,$$

where R and H are the radius and the height of the sample, respectively, a_i is the coefficient of Legendre polynomial expansion for the angular distribution of source neutrons.

The correction factor A was deduced by using a Monte Carlo code SYNTHIA[3]. In this work, this factor was 1.1~1.2, 0.95~1.1 and 0.9~1.0 for the 0^+, 2^+(1-st) and 4^+(2nd) levels of ^{238}U, respectively.

The experimental error was estimated considering the error sources of (1) counting statistics, (2) detector efficiency 5%, (3) integration of the peak yield 10%, (4) data correction 10%

3. Results and Discussion

The experimental angular differential cross sections of the 0^+ level (ground state) of ^{238}U at 120° are shown in fig.4. The present values are close to the values of JENDL-3.2.

Figure 5 and fig.6 show the preliminary values of angle-integrated cross sections of 2^+ and 4^+ levels of ^{238}U, respectively, deduced by multiplying the data at 120° by 4π.

For the 1-st level, several experimental data have been reported in the energy range of the present study. However, their values are different up to 50% or more, and the evaluated values of JENDL-3.2 and ENDF/B-VI are close to the lowest experimental values. The present results at 700keV and 850keV are lower than the data by Haouat et al.[2] and by Beghian et al.[4], but close to the evaluated values in the angle-integrated values. However, the differential cross section by the present experiment (120°) is in good agreement with that by Haouat et al.(125°). Therefore the angular distribution should be taken into account in the data comparison. The present data at 465keV and 550keV are also close to the evaluations and lower than those by Guenther et al.[5]. However, the values in this region are sensitive to the detector threshold, and further studies will be made. The present values of 2nd level are close to the data by Haouat et al. and Begian et al., while the experimental errors are relatively large.

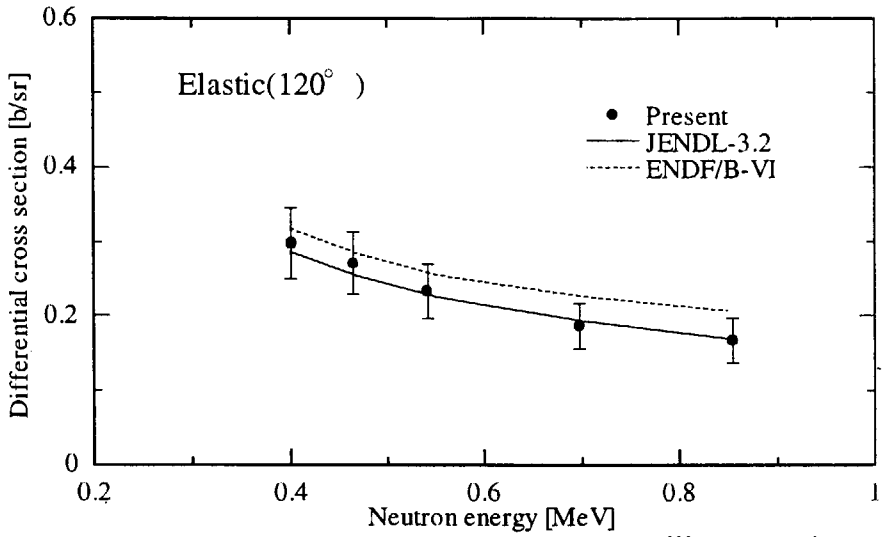

Fig.4 Elastic scattering cross section of ^{238}U at 120°

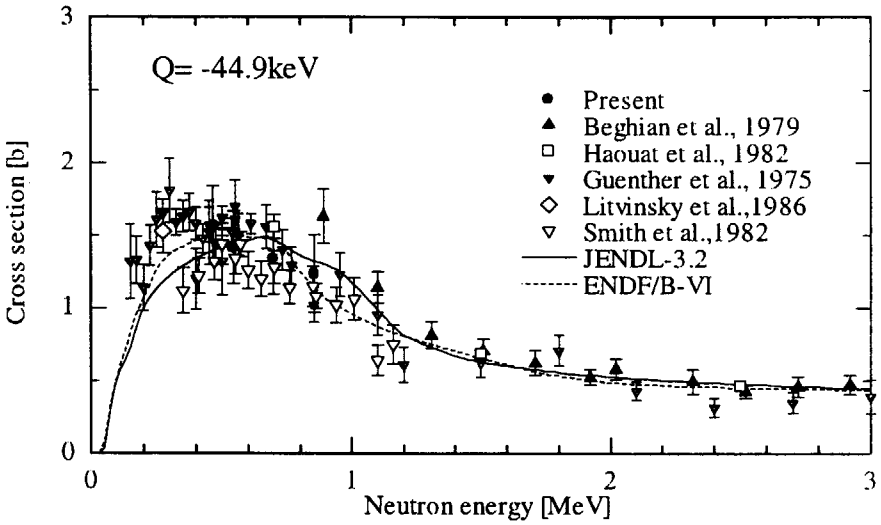

Fig.5 Inelastic scattering of 1-st level of ^{238}U

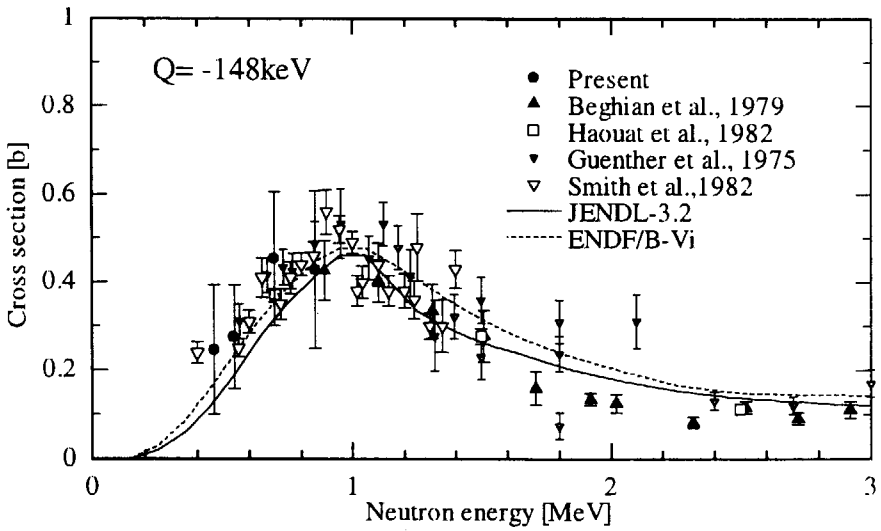

Fig.6 Inelastic scattering of 2nd level of ^{238}U

4. Summary

By using the TOF technique, neutron scattering cross sections of low-lying levels of ^{238}U were measured for 0.4 -0.85 MeV incident neutrons. The peaks by the elastic and inelastic scattering could be separated fairly well, and the cross sections of the 0^+, 2^+ and 4^+ levels were deduced. Further data analysis and experiment, however, will be needed to reduce the experimental error and to confirm the data consistency.

References

[1] M. Baba et al., J. Nucl. Sci. and Technol., 27(7), 601-616(1990)

[2] G. Haouat et al., Nucl. Sci. and Eng., 81, 491-511(1982)

[3] M. Baba et al., Nucl. Inst. and Meth., A366,354 -365(1995)

[4] L. E. Beghian et al., Nucl. Sci. and Eng., 69, 191(1979)

[5] P. Guenther et al., ANL-NDM-16

[6] A. B. Smith et al., Proc. Int. Conf. Nucl. Data for Sci. and Technol., Antwerpen, Belguim, September 6- 10, p39 (1982)

3.3 Accuracy of Helium Accumulation Fluence Monitor for Fast Reactor Dosimetry

Chikara ITO and Takafumi AOYAMA
Reactor Technology Section, Experimental Reactor Division, Oarai Engineering Center
Power Reactor and Nuclear Fuel Development Corporation
4002 Narita-cho, Oarai-machi, Ibaraki-ken 311-1393 JAPAN
E-mail: ito@oec.pnc.go.jp

A helium (He) accumulation fluence monitor (HAFM) has been developed for fast reactor dosimetry. In order to evaluate the measurement accuracy of neutron fluence by the HAFM method, the HAFMs of enriched boron (B) and beryllium (Be) were irradiated in the Fast Neutron Source Reactor "YAYOI". The number of He atoms produced in the HAFMs were measured and compared with the calculated values. As a result of this study, it was confirmed that the neutron fluence could be measured within 5 % by the HAFM method, and that met the required accuracy for fast reactor dosimetry.

1. Introduction

A He accumulation fluence monitor[1] (HAFM) has been developed for fast reactor dosimetry in various irradiation tests and material surveillance tests. The He production rate is measured by counting He atoms accumulated in the HAFM and the neutron fluence is then obtained using measured He production rates in the same way as employed for the foil activation method. Another application of the HAFM is expected for the direct measurement of He production in the structural component materials of fast reactors.

The calibration of the HAFM measurement system as to counting He atoms in the HAFM materials was carried out using the He ions implanted samples in the previous study, and the counting error was evaluated to be approximately 5 %[2].

Based on the last study, the accuracy of measuring neutron fluence by the HAFM method was evaluated. As the measurement accuracy of neutron fluence was determined by that of He production rates during irradiation, HAFMs were irradiated in the well characterized fast neutron spectrum field of the Fast Neutron Source Reactor "YAYOI"[3] of the University of Tokyo. The accuracy of measuring neutron fluence was evaluated by comparing the measured He production with calculated values using the neutron flux and He production cross section.

2. HAFM Measurement System

2.1 System Outline

The HAFM measurement system is illustrated in Fig. 1. An electric furnace is used to melt the HAFM materials, and the released He atoms were counted by means of a magnetic type gas mass spectrometer. The number of He atoms which can be measured in this system ranged $10^{12} \sim 10^{19}$. This range covers the expected number of He atoms when the HAFM is used in a typical fast reactor irradiation field.

2.2 Calibration

The calibration of the HAFM measurement system has already been performed using the He implanted samples. The samples of copper, aluminum and vanadium chips contained He ions of $10^{13} \sim 10^{15}$ which had been implanted by the ion source and the accelerator of Kyushu University. The relation between the number of He atoms and the mass spectrometer output indicated good linearity as shown in Fig. 1. The counting error of He atoms was evaluated to be approximately 5 % in this system.

3. Experiments

3.1 Irradiation

The specifications of HAFMs and their irradiation conditions are summarized in Table 3. The HAFMs of 93 % enriched B were irradiated at three locations: those are reactor core center (Glory hole: Gy), under the leakage neutron field from the reactor core (Fast column: FC) and at an experimental hole through the blanket surrounding the core (BLK) to total fluences of $10^{15} \sim 10^{17}$ n/cm^2. At BLK, the HAFMs of Be were also irradiated to test the applicability for fast neutron monitoring.

The He production rate spectra in each irradiation position are shown in Fig. 3. Considering each neutron spectrum, the He production in B type HAFM occurred with neutron of which energy ranged 10 keV $\sim$ 1 MeV at Gy and BLK, and with neutron less than 10 keV at FC. As to Be type HAFM, the He was produced with neutron over 1 MeV at BLK.

3.2 Measurement and Calculation

The number of He atoms produced in the irradiated HAFMs was counted by the HAFM measurement system. Some of the irradiated HAFMs were measured independently by the system[4] of Kyushu University to secure the reliability of this experiments.

The He production rate was calculated with the neutron flux and He production cross sections processed from the JENDL-3.2 cross section library[5] [6]. The neutron spectra were determined based on the foil activation method.

4. Results

The measured (M) and calculated (C) number of He atoms are shown in Figs. 4 to 7. The average value of M/C ranged 0.98 $\sim$ 1.03 for the B type HAFMs and was 0.96 for the Be type HAFMs as shown in Table 2.

It was found that the differences of He production between the calculated and measured values were as follows: it was less than 5 % for the B type HAFM at Gy, BLK and FC, and it was also less than 5 % for the Be type HAFM at BLK. This result indicated that the Be type HAFM could be applied for fast neutron measurement over 1 MeV.

The differences of the measured values between our results and those by Kyushu University were less than the experimental error, that means the measured values were reliable.

5. Conclusion

In order to evaluate the measurement accuracy of neutron fluence by the HAFM method, the B and Be type HAFMs were irradiated in "YAYOI". The number of He atoms in the irradiated HAFMs were measured and compared with the calculated values. As a result, it was confirmed that the neutron fluence could be measured within 5 % by the HAFM method, and that met the required accuracy for fast reactor dosimetry. This result indicates that the HAFM can be applicable to monitor neutron fluences for various irradiation tests and material surveillance tests conducted in fast reactors.

Acknowledgements

The authors wish to thank Dr. T. IGUCHI of Nagoya University for the irradiation of HAFMs in "YAYOI" and the characterization of irradiation fields. We also would like to thank Dr. Y. TAKAO of Kyushu University for the measurement of HAFMs and for his valuable comments regarding the He measuring technique. And, we would like to thank Mr. K. YOSHIKAWA of Inspection Development Company for his assistance of measurement of HAFMs using the HAFM measurement system.

References

[1] R. STORER, *et al.*: *1994 Annual Books of ASTM Standards* **12.02**, E910-89 (1994)

[2] C. ITO: "Calibration of a He Accumulation Fluence Monitor for Fast Reactor Dosimetry," *JAERI-Conf* 97-005, 96 (1997)

[3] M. NAKAZAWA and A. SEKIGUCHI: "Dosimetry Data Collection in the Fast Neutron Source Reactor YAYOI," *UTNL*-R0037 (1976)

[4] Y. TAKAO and Y. KANDA: "A system for measurement of sub-parts-per-trillion helium in solids," *Review of Scientific Instruments* **67** [1], 198 (1996)

[5] Y. KIKUCHI, *et al.*: "JENDL-3 Revision-2 (JENDL-3.2)," *Proceedings of International Conference of Nuclear Data for Science and Technology, Gatlinburg, May 1994* (1994)

[6] T. NAKAGAWA, *et al.*: "Japanese Evaluated Nuclear Data Library Version 3 Revision-2: JENDL-3.2," *Journal of Nuclear Science and Technology* **32** [12], 1259 (1995)

Table 1 Irradiation Condition of HAFMs

Irradiation Position	HAFM*1	Integrated Reactor Power [kWh]	Total Neutron Fluence [10^{15} n/cm^2]
Glory Hole (Gy)	93 % Enriched Boron 1 mg	192	313
Fast Column (FC)	93 % Enriched Boron 1 mg	239 ~ 269	2.08 ~ 2.54
Experimental Hole through the Blanket (BLK)	Enriched Boron 40 mg	93.2	33.7 ~ 53.9
	Beryllium 100 mg	193	72.9 ~ 102

*1 HAFM materials are enclosed in vanadium capsules.

Table 2 Comparison of Measured and Calculated He Production

HAFM	Irradiation Position	Measurement / Caluclation	
		PNC	Kyushu Univ.
Enriched Boron	Glory Hole	1.03±0.03	1.05±0.05
	Fast Column	0.98±0.05	1.06±0.07
	Experimental Hole through the Blanket	1.00±0.05	0.95±0.08
Beryllium		0.96±0.04	———

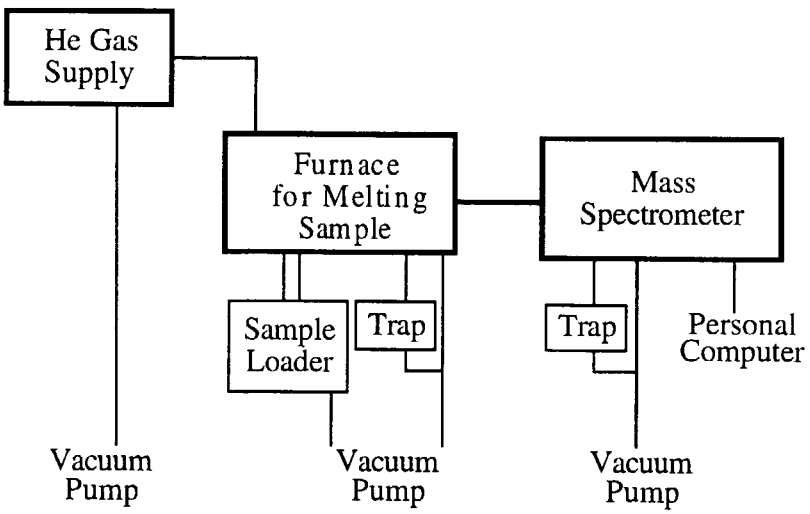

Fig. 1 HAFM Measurement System

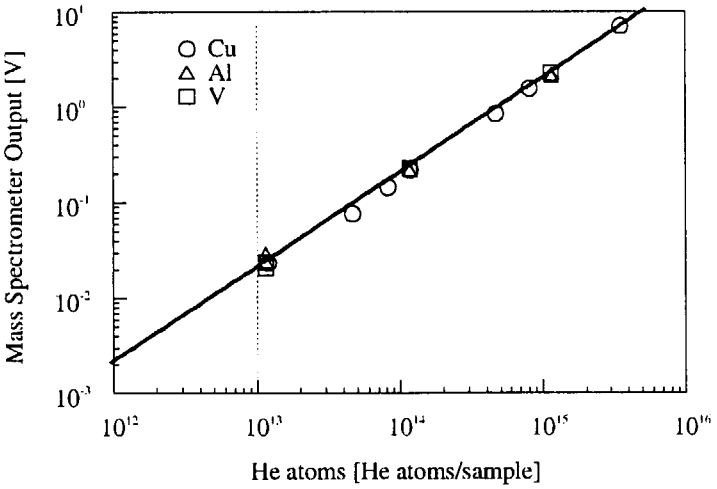

Fig. 2 Calibration Curve

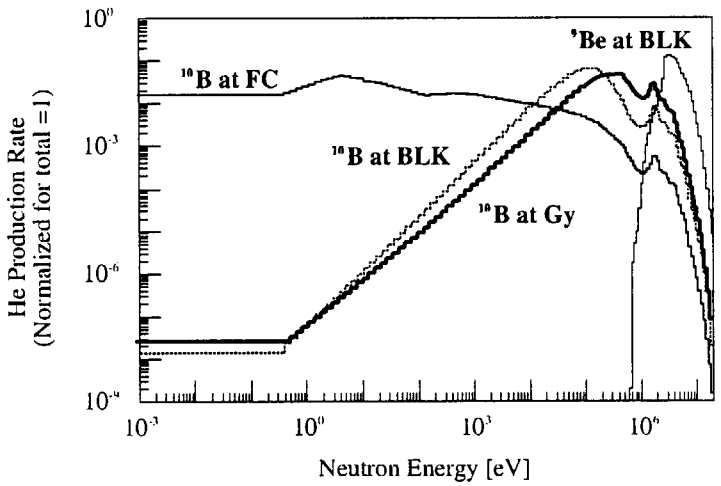

Fig. 3 He Production Rate Spectra

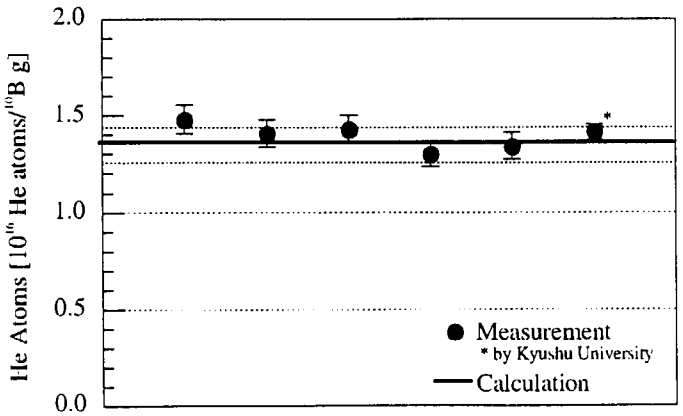

Fig. 4 He Production of B at Glory Hole

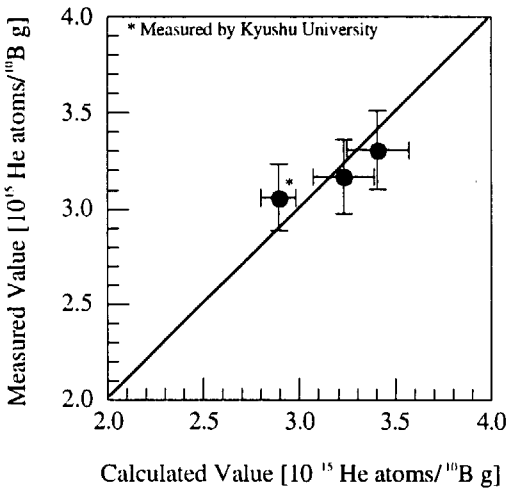

Fig. 5 He Production of B at Fast Column

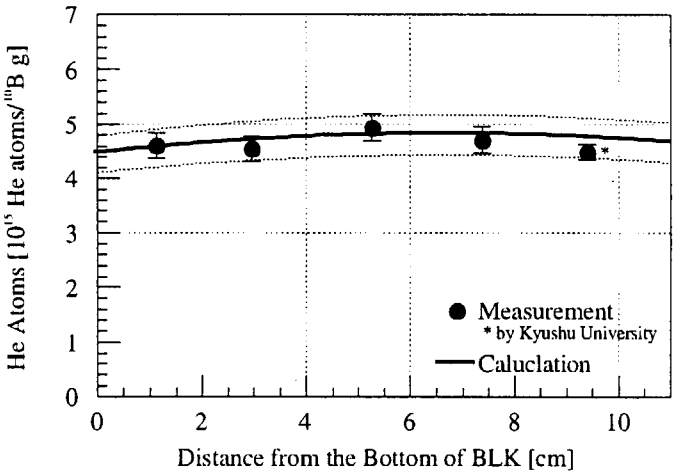

Fig. 6 He Production of B at BLK

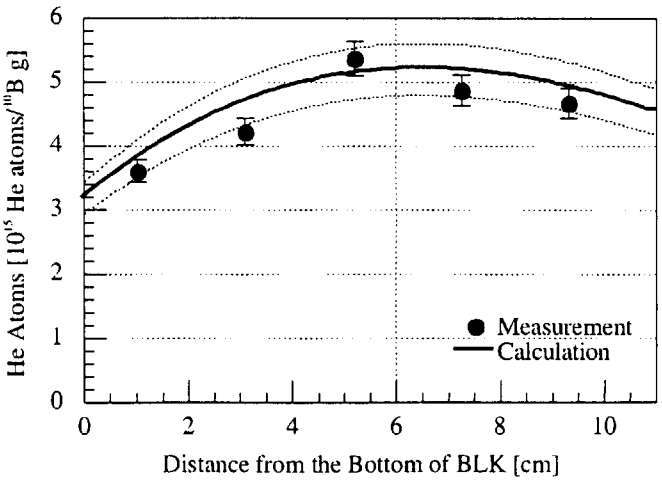

Fig. 7 He Production of Be at BLK

3.4 Recommended Evaluation Procedure for Photonuclear Cross Section

Young-Ouk LEE*
Jonghwa Chang
Tokio FUKAHORI
Nuclear Data Center, Japan Atomic Energy Research Institute
Tokai-mura, Naka-gun, Ibaraki-ken 319-11
e-mail: lee@cracker.tokai.jaeri.go.jp
Japan Atomic Energy Research Institute
*Permanent Address: Korea Atomic Energy Research Institute

ABSTRACT

In order to generate photonuclear cross section library for the necessary applications, data evaluation is combined with theoretical evaluation, since photonuclear cross sections measured cannot provide all necessary data. This report recommends a procedure consisting of four steps: (1) analysis of experimental data, (2) data evaluation, (3) theoretical evaluation and, if necessary, (4) modification of results. In the stage of analysis, data obtained by different measurements are reprocessed through the analysis of their discrepancies to a representative data set. In the data evaluation, photonuclear absorption cross sections are evaluated via giant dipole resonance and quasi-deutron mechanism. With photoabsorption cross sections from the data evaluation, theoretical evaluation is applied to determine various decay channel cross sections and emission spectra using equilibrium and preequilibrium mechanism. After this, the calculated results are compared with measured data, and in some cases the results are modified to better describe measurements.

1. INTRODUCTION

Evaluated libraries of photonuclear cross sections are expected to be utilized in the some fields such as:

- Radiation protection and dosimetry of photoneutrons produced by electron/photon accelerators in medical applications
- Calculations of absorbed does in human body during radiotherapy
- Physics and technology of fission reactors and fusion reactors
- Activation analysis, safetyguards and inspection technologies
- Nuclear waste transmutation
- Astrophysics
- Design of photon induced neutron source

The most important data needed are photoabsorption cross sections and neutron yields (neutron production cross sections), followed by neutron spectra and their angular distributions. Unfortunately photonuclear cross sections measured cannot provide all

necessary data since both excitation functions of the photoabsorption cross sections and energy spectra of emitted particles have been scarcely measured in the entire energy region. In order to generate libraries for such applications, data evaluation is combined with theoretical evaluation and, if necessary, some systematics. In this report, we recommend a procedure to evaluate photonuclear data.

The evaluation procedure of photonuclear data can be divided into four steps (1) analysis of experimental data, (2) data evaluation, (3) theoretical evaluation and, if necessary, (4) modification of results. In the stage of analysis, the data obtained by different measurements are reprocessed using independent analysis of their discrepancies to a representative data set. In the data evaluation, photonuclear absorption cross sections are evaluated via giant dipole resonance and quasi-deutron mechanism. With photoabsorption cross sections from the data evaluation, theoretical evaluation is applied to determine various decay channel cross sections and emission spectra using equilibrium and preequilibrium mechanism. After this, the results from theoretical evaluation are compared with reference data, and in some cases the results are modified to better describe measurements.

Following chapters explain each step with results of actual evaluation for Ta-181 up to 140 MeV[1].

2 Analysis of measurements.

A recent study by Sao Paulo laboratory[2,3] showed that the differences between the Saclay and Livermore photoneutron cross sections (Fig. 1) arose from the separation of the partial cross section from the total neutron counts (neutron multiplicities sorting). Based on this results, new reference experimental data for (γ,n) and (γ,2n) can be constructed from the measurements of Saclay[4] and Livermore[5] by applying the neutron multiplicity of the Livermore measurement, based on the analysis of Sao Paulo. The (γ,abs) data of Saclay measurements are consequently modified according to the reconstructed (γ,n) and (γ,2n) data.

In actual evaluation work for Ta-181 photonuclear cross sections, followings steps are applied to produce representative data set.

A. Remove differences of absolute cross sections (Fig. 2)

$$\sigma^{L*}_{\gamma,n} = \frac{\sigma^{S}_{\gamma,Tn}}{\sigma^{L}_{\gamma,Tn}} \sigma^{L}_{\gamma,n}$$

B. Re-construct (γ,2n) cross section (Fig. 3)

$$\sigma^{S*}_{\gamma,2n} = \sigma^{S}_{\gamma,2n} + \frac{1}{2}(\sigma^{S}_{\gamma,n} - \sigma^{L*}_{\gamma,n}),$$

C. Re-construct (γ,n) cross section (Fig. 4)

$$\sigma^{S*}_{\gamma,n} = \sigma^{S}_{\gamma,Tn} - 2\sigma^{S*}_{\gamma,2n} - 3\sigma^{S}_{\gamma,3n}$$

D. Re-construct (γ,abs) cross section (Fig. 5)

$$\sigma^{S*}_{\gamma,abs} = \sum_{x} \sigma_{\gamma,x} \approx \sigma^{S*}_{\gamma,n} + \sigma^{S*}_{\gamma,2n} + \sigma^{S}_{\gamma,3n} + ..$$

E. Re-construct (γ,Tn) cross section

$$\sigma^{S*}_{\gamma,Tn} = \sigma^{S*}_{\gamma,n} + 2\sigma^{S*}_{\gamma,2n} + 3\sigma^{S}_{\gamma,3n} \text{ (Fig. 13)}$$

where superscripts S and L refer to measurement of Saclay and Livermore, respectively, and * refers re-constructed data.

3 Data Evaluation

For the data evaluation of the photoabsorption cross sections, a fitting function is used for the photoabsorption data as

$$\sigma_{abs}(E) = \sigma_{abs}^{GDR}(E) + \sigma_{abs}^{QDM}(E),$$

where the notation of "GDR" and "QDM" are Giant Dipole Resonance Model and Quasi Deutron Model, respectively. In the GDR region, a Laurentian approximation is used:

$$\sigma_{abs}^{GDR}(E) = \sum_{i=1}^{2} \frac{\sigma_i}{1+[\frac{(E^2-E_i^2)^2}{E^2\Gamma_i^2}]}, \text{ (Fig. 6)}$$

where σ_i , E_i and Γ_i denote the peak cross sections, energies at which the maxima in the cross sections occur, and widths at half-maximum of component where fitted.

In the energy range above 40 MeV up to 140 MeV, the QDM describes the dominant mechanism for photoabsorption reaction. This model was first proposed by Levinger[6-8] as

$$\sigma_{abs}^{QDM}(\varepsilon_\gamma) = \frac{L}{A} NZ\sigma_d(\varepsilon_\gamma) f(\varepsilon_\gamma), \text{ (Fig.7)}$$

where L is Levinger parameter, $\sigma_d(\varepsilon_\gamma)$ photodisintegration cross sections of free deutron, $f(\varepsilon_\gamma)$ Pauli-blocking function. The factor NZ is the total number of neutron-proton pairs inside the nucleus, which is multiplied by a reduction factor L/A to account for the fact that it is only correlated pairs that can be considered to be quasideutrons. The function $f(\varepsilon_\gamma)$ accounts for those excitations of neutron-proton pairs that cannot occur since the Pauli-exclusion principle allows only final particle states which lie above the Fermi level.

4. Theoretical Evaluation

From the microscopic view point of nuclear theory, the excitation process of the GDR through photoabsorption is considered as production of a particle-hole excited state. On the other hand, the quasideutron model assumes that the incident photon excites two-particle cluster rather than a single particle above the Fermi energy. It is therefore expected that the precompound(exciton) plus evaporation model can describe the de-excitation process of the photonuclear reaction. With the photoabsorption cross sections given, statistic+preequilibrium model is adopted using ALICE-F[9] to calculate decaying processes including neutron, proton, deutron and alpha emission cross sections (Fig. 8 - 13). The initial exciton number is shifted to 3 (two-particle one-hole state) at the energy where the QDM component of photoabsorption become larger than the GDR's. The neutron/proton fraction of initial exciton number is chosen as neutron/proton fraction of target nuclide.

5. modification of results

When the model calculation for the decaying process does not reproduce measured data, such as photoneutron cross sections which are considered more important quantities, photoabsorption cross section is is renormalized as :

$$\sigma_{abs}^{eval} = \sigma_{abs} \frac{\sigma_{Tn}^{fit}}{\sigma_{Tn}}$$

To reproduce measured photoneutron emission cross sections, non-neutron emission cross

sections also can be renormalized as:

$$\sigma_{non-nx}^{eval.} = \frac{\sigma_{abs} - \sigma_{nx}^{fit}}{\sigma_{abs} - \sigma_{nx}} \sigma_{non-nx}$$

References

(1) Lee Y.O., Chang J. and Fukahori T. :"Evaluation of photoneutron cross sections for Ta-181 in the giant dipole resonance region", Fall Conf. of Korean Physical Society, Oct. 24 - 25, 1997, Kyungki Univ. Suwon, Korea

(2) Wolfen, E., Martinez, A. R. V., Gouffon, P., Miyao, Y., Serrao, V.A., Martins, M. N.: Phys. Rev. **C29**, 1137 (1984)

(3) Martins, M. N.: "Discrepancies between Saclay and Livermore photoneutron cross sections", Summary Report of the 1st Research Co-ordination Meeting on Compilation and Evaluation of Photonuclear Data for Applications, Obnisk, Russia, 3-6 December 1996, INDC(NDS)-364 (1997).

(4) Bergere, R., Beil, H., Veyssiere, A.: Nucl. Phys. A121, 463 (1968).

(5) Bramblett, R. L., et al.: Phys. Rev. **129**, 2723 (1963).

(6) Levinger, J. S.: Phys. Lett. **82B**, 181 (1979)

(7) Chadwick, M. B., et al.: Phys. Rev. **C44**, 814 (1991)

(8) Lepretre, A., et al.: Nucl. Phys. **A367** 237 (1881)

(9) Fukahori, T.,: "ALICE-F Calculation of Nuclear Data up to 1 GeV", Proc. Specialists' Meeting on High Energy Nuclear Data, Tokai, Ibaraki, Oct. 3-4, 1991, JAERI-M 92-039 (1992)

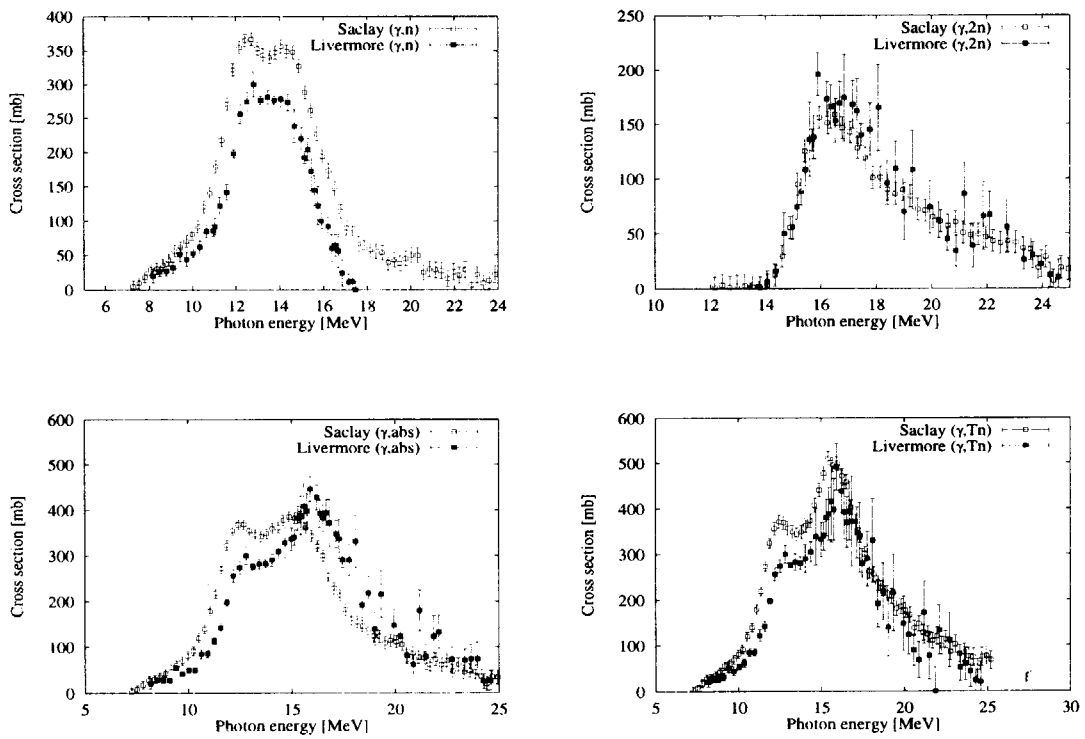

Figure . 1 Discrepancies between two measurements

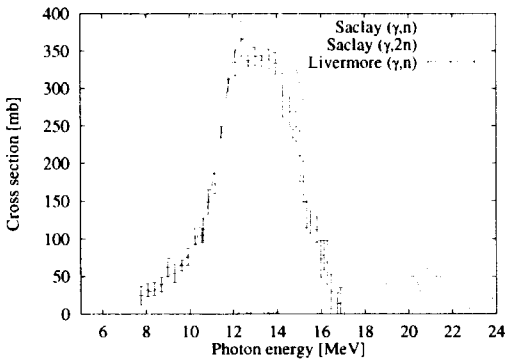

Fig. 2. Measurements of Ta-181 (γ,n), (γ,2n) cross sections from Saclay and modified (γ,n) cross sections from Livermore

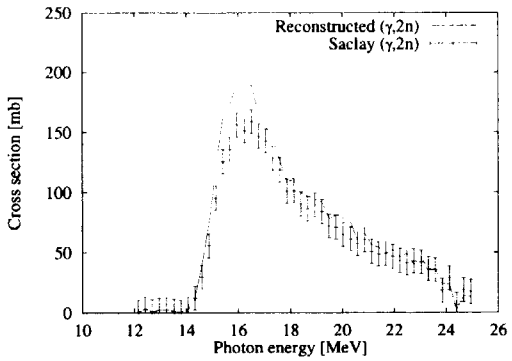

Fig. 3. Reconstructed Ta-181 (γ,2n) cross section and measurements from Saclay

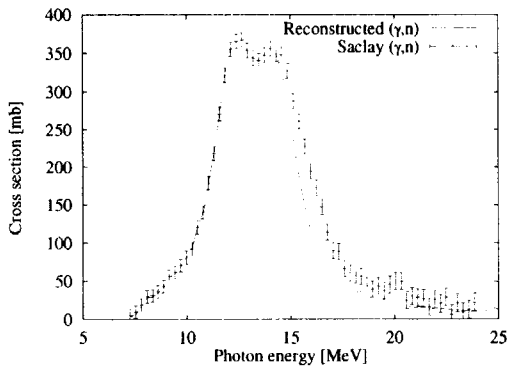

Fig. 4. Reconstructed Ta-181 (γ,n) cross section and measurements from Saclay

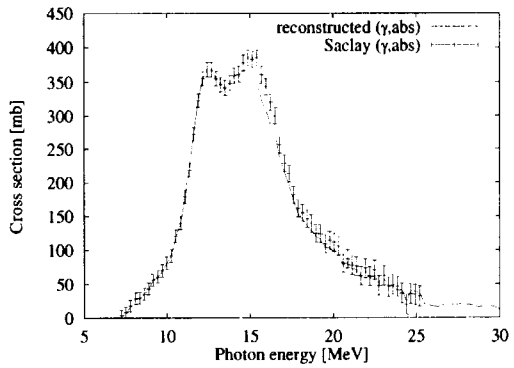

Fig. 5. Reconstructed Ta-181 (γ,abs) cross section and measurements from Saclay

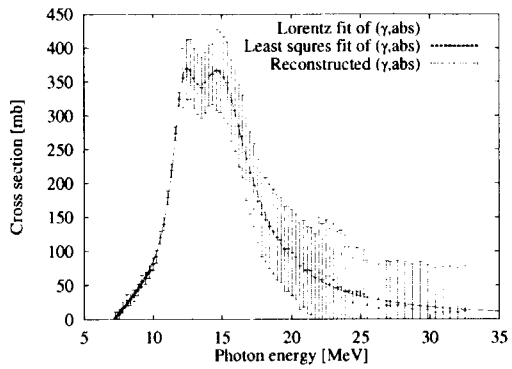

Fig. 6. Fitting of Ta-181 (γ,abs) cross section from the reconstructed data in GDR region

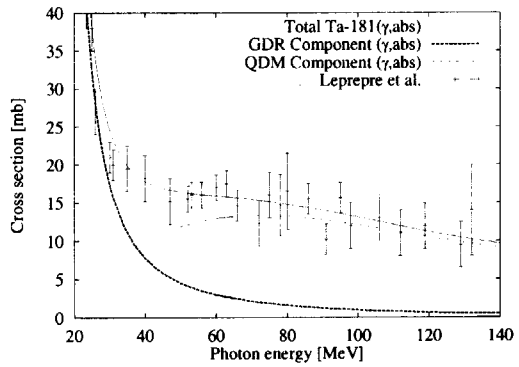

Fig. 7. QDM and GDR components of Ta-181 (γ,abs) cross section and experiment data up to 140 MeV

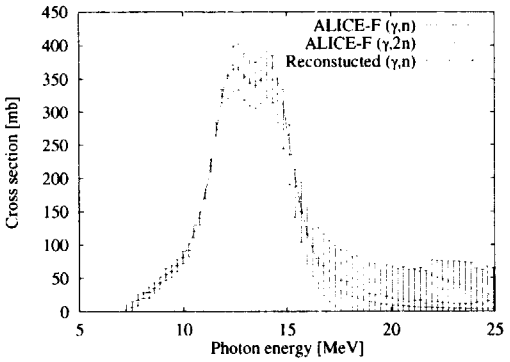

Fig. 8. ALICE-F Results for Ta-181 (γ,n) cross section with reconstructed data

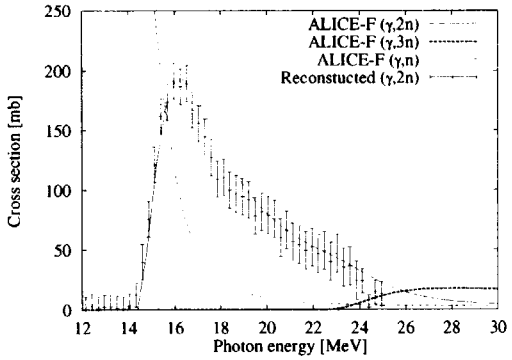

Fig. 9. ALICE-F Results for Ta-181 (γ,2n) cross section with reconstructed data

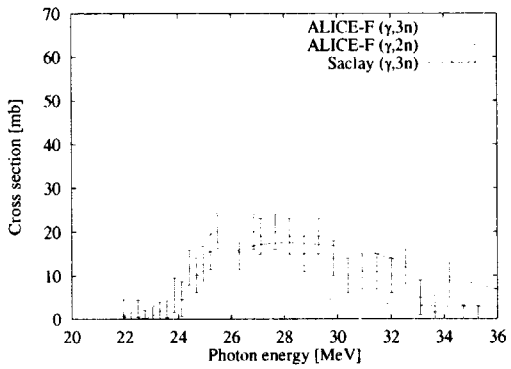

Fig. 10. ALICE-F results for Ta-181 (γ,3n) cross section with reconstructed data

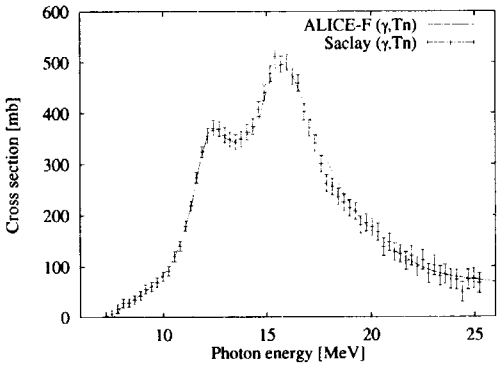

Fig. 11. ALICE-F results for Ta-181 (γ,Tn) cross section with Saclay data up to 40 MeV

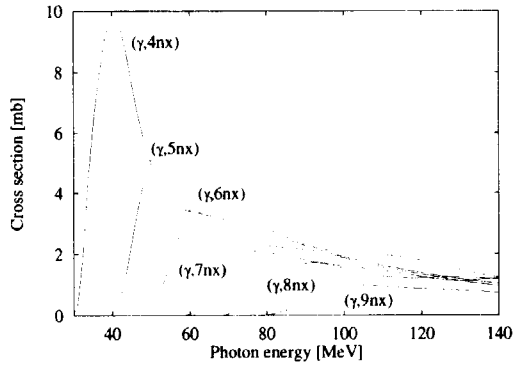

Fig. 12. ALICE-F Results for Ta-181 (γ,4nx) - (γ,9nx) cross section up to 140 MeV

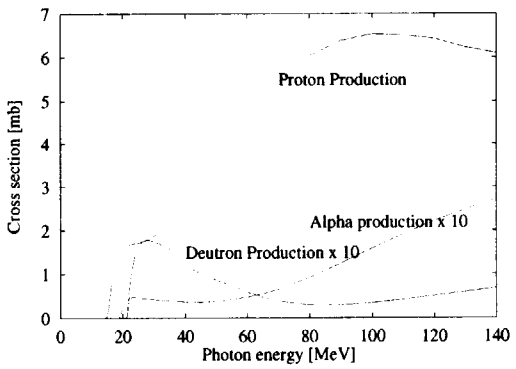

Fig. 13. ALICE-F results for photon induced Proton, Deutron and Alpha production cross sections for Ta-181

3.5 Systematics in Delayed Neutron Yields

Takaaki OHSAWA
Atomic Energy Research Institute, Kinki University
3-4-1 Kowakae, Higashi-osaka, Osaka 577

Abstract: An attempt was made to reproduce the systematic trend observed in the delayed neutron yields for actinides on the basis of the five-Gaussian representation of the fission yield together with available data sets for delayed neutron emission probability. It was found that systematic decrease in DNY for heavier actinides is mainly due to decrease of fission yields of precursors in the lighter side of the light fragment region.

1. Introduction

Recent interest in incineration of long-lived actinides by nuclear reactors necessitates exact nuclear data for relevant reactions and fission-related quantities. The delayed neutron data, among others, are important in assessment of kinetics of reactors fueled with transuranium nuclides, due to their small delayed neutron yields (DNY). It has been common practice to use Tuttle's systematics[1] to infer DNYs for nuclei for which no experimental data are available. However, the physical basis for the systematics were not evident. In this study, an attempt was made to reproduce the systematic trend observed in the delayed neutron yields for a wide range of actinides by summation method.

2. Method of Calculation

The absolute DNY is given as a sum of contributions of each precursor nucleus :

$$\nu_d = \sum_i Y_i P_{ni} \qquad (1)$$

where Y_i and P_{ni} stand for the fission yield (FY) and the delayed neutron emission probability of the precursor i, respectively.

2.1 Fission Yield Data

In the present analysis, the five-Gaussian representations by Moriyama and Ohnishi[2] (abbreviated as MO model hereafter) and Dickens[3] were used to obtain the FYs of precursors. These models, however, do not account for the even-odd effects in the FY.

As is known, the fission yields for even-Z FPs are generally higher than those for odd-Z FPs. In contrast, it is known that major part (~95%) of the contribution to the total DNY comes from odd-Z precursors[4]. This is because odd-Z precursors have larger *energy*

window for subsequent neutron emission after β-decay due to larger Qβ-value for β-decay, thus leading to higher *Pn*- values. Accordingly, it is of vital importance to take into account the even-off effects on FY of precursors. The proton and neutron odd-even effects are defined as

$$X = [Y_{(e\text{-}Z)} - Y_{(o\text{-}Z)}] / [Y_{(e\text{-}Z)} + Y_{(o\text{-}Z)}], \qquad Y = [Y_{(e\text{-}N)} - Y_{(o\text{-}N)}] / [Y_{(e\text{-}N)} + Y_{(o\text{-}N)}], \tag{2}$$

respectively. In this study, a new fitting to the existing data for proton odd-even effect was made by least-squared method to obtain the following equation:

$$X = -0.1033 + 0.6907(Z^2/A - 33.8486) \tag{3}$$

The neutron odd-even effect was calculated with the relation[5]:

$$Y = (0.193 \pm 0.152)X \tag{4}$$

2.2 Delayed Neutron Emission Probability

For *Pn*-data, use was made of the evaluated data by Wahl[6] and theoretical calculation on the basis of the gross theory of beta decay by Tachibana *et al.*[7].

3. Results

Four combinations of two FY models and two *Pn*-data sets were attempted. The results are shown in **Figs.1** to **3**. It was observed that the overall trend of ν_d as a function of the parameter $(3Zc\text{-}Ac)(Ac/Zc)$ was roughly reproduced by the summation calculation, where *Zc* and *A*c are the charge and mass numbers of the fissioning nucleus. The combination of MO model (with and without odd-even effects) and Wahl's *Pn*- data set (**Fig.1**) led to values that are higher than the Tuttle systematics shown with a straight line. In contrast, the combination of MO model with the gross theory (**Fig.2**) led to values lower than the Tuttle systematics. This originated from generally lower *Pn*-values of gross theory than those of Wahl's evaluation, as can be seen from **Table 1**, where the *Pn*-values of main precursors in the two sets are compared. Wahl's evaluation is based on the measured data, partly supplemented with the Kratz-Herrmann systematics[8], while Tachibana's data are purely theoretical calculation by the gross theory of bata decay. At the present stage of accuracy of theoretical calculation of *Pn*, the realistic choice of the *Pn*-values for the purpose of DNY calculation would be an evaluation based on the empirical data supplemented with those from theoretical calculation for precursors for which experimental data are not available.

The results of calculation for Dickens' model for FY are shown in **Fig.3** for different choice of the *Pn*-data sets. In this case, the calculated data are generally higher than the Tuttle systematics both for Wahl's and Tachibana's *Pn*-data sets, with the Wahl results tending to be a bit higher than the Tachibana results. This implies that exact evaluation of the FY data are also important as well as *Pn*-data.

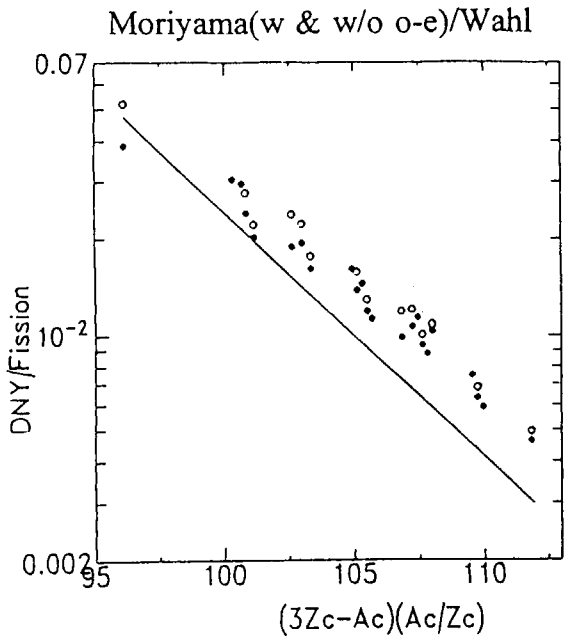

Fig.1 The results of summation calculation by use of MO model and Wahl's evaluation of *Pn*-values. The open symbols show the results without odd-even effect, the closed symbols with inclusion of the odd-even effect.

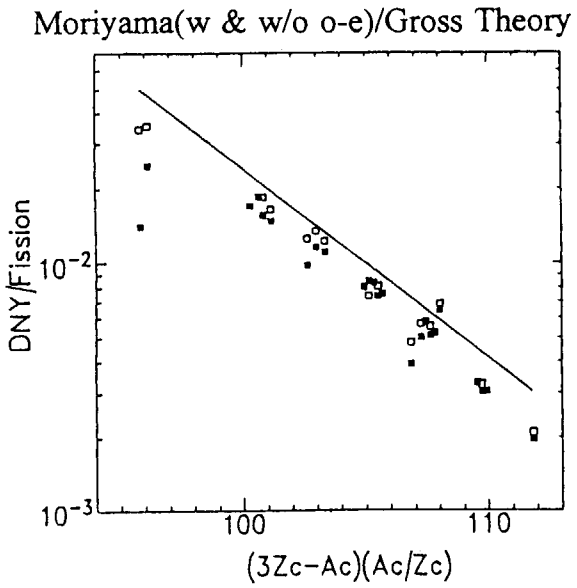

Fig.2 The same as Fig.1 except that Tachibana's *Pn*-data were used instead of Wahl's data.

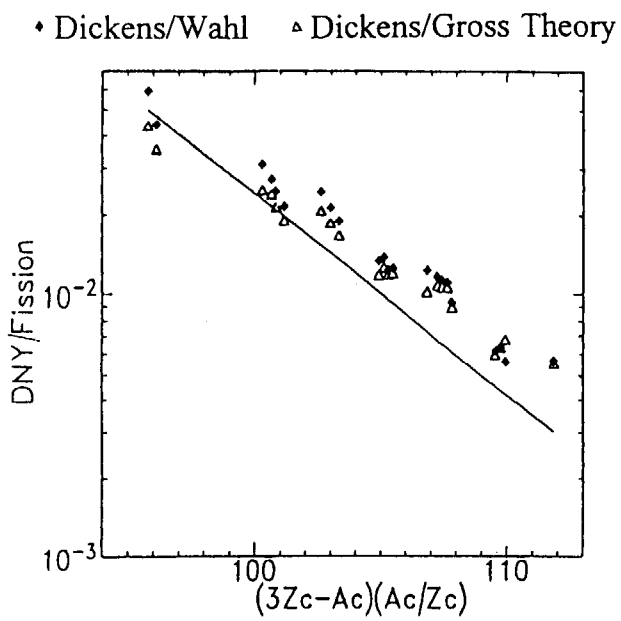

Fig.3 Similar results for the case of Dickens' five-Gaussian model. The open symbols here stand for the results for *Pn*-data from the gross theory, the closed symbols the results for Wahl's *Pn*-data.

Table 1. Comparison of *Pn*-values from the evaluation of Wahl and the calculation from gross theory for important precursors.

Group	Precursor	Wahl	Gross theory
1	Br-87	2.54%	0.111%
2	Br-88	6.26	1.102
	I-137	6.97	2.035
3	Br-89	14.0	4.552
	I-138	5.38	4.396
4	Br-90	24.6	6.584
	Rb-94	10.0	2.027
	I-139	9.81	11.465
5 & 6	Rb-95	6.62	8.213
	Y -98	0.228	0.057

The reason for the decreasing tendency of ν_d-values for heavier actinides can be interpreted as due to decrease of FY for precursors located in the left side of the light fragment peak. This can be better seen by plotting the FY of precursors as a function of nuclides (**Fig.4 - 8**). As can be seen from these figures, the FYs for precursors in the left side of the light fragment region, such as Br-87, -88, -89 and -90, show apparent decrease for heavy actinides, while the precursor yields in the heavy fragment region do not show such a steep decrease. This is because the light fragment peak shifts to heavier side as the mass of the fissioning nucleus increases, while the heavy fragment peak remains essentially fixed because of the double shell effects of 82-neutron and 50-proton shells near the mass number 132.

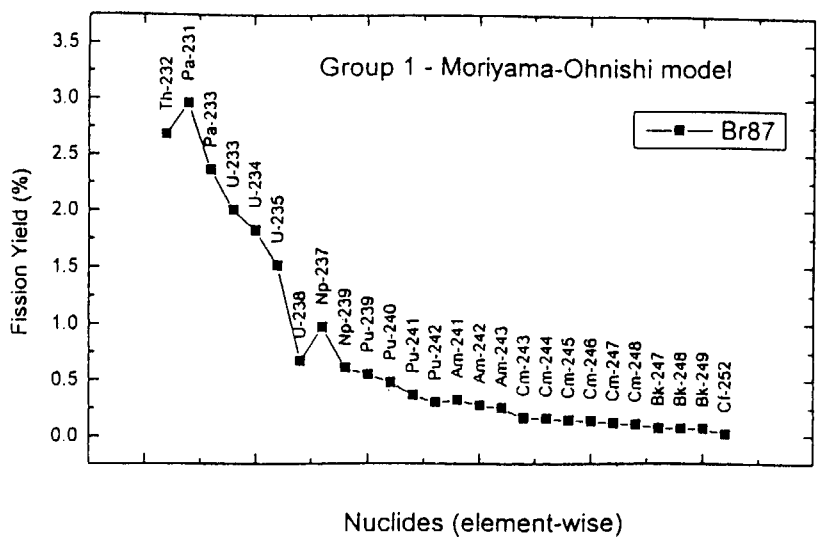

Fig.4 Systematic trend of FYs for the precursor of Group 1 (Br-87), as calculated with the MO model.

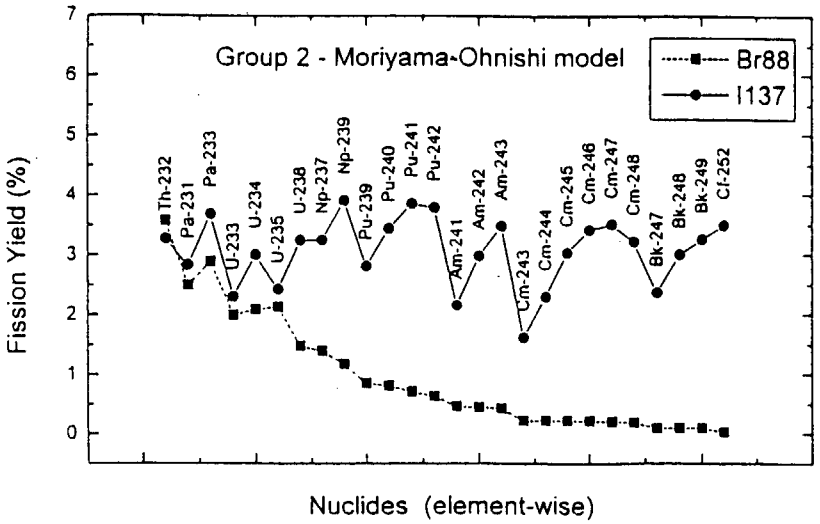

Fig.5 Similar results for Group 2 (Br-88, I-137).

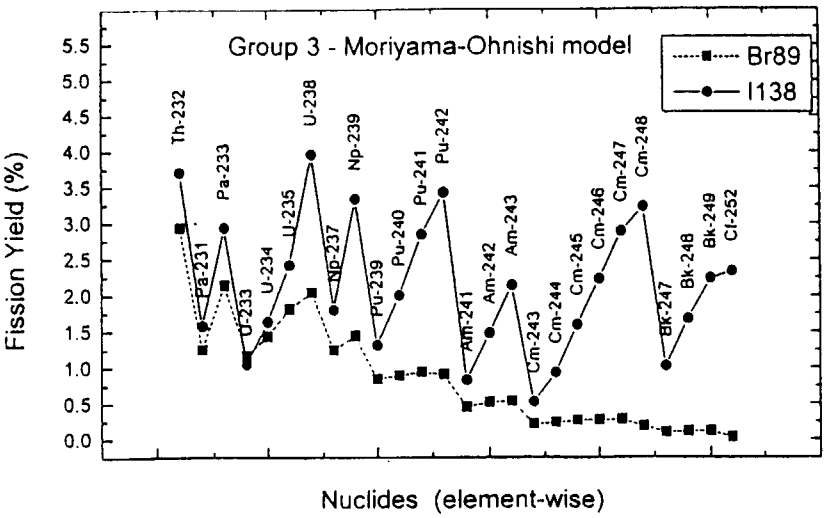

Fig.6 Similar results for Group 3 (Br-89, I-138).

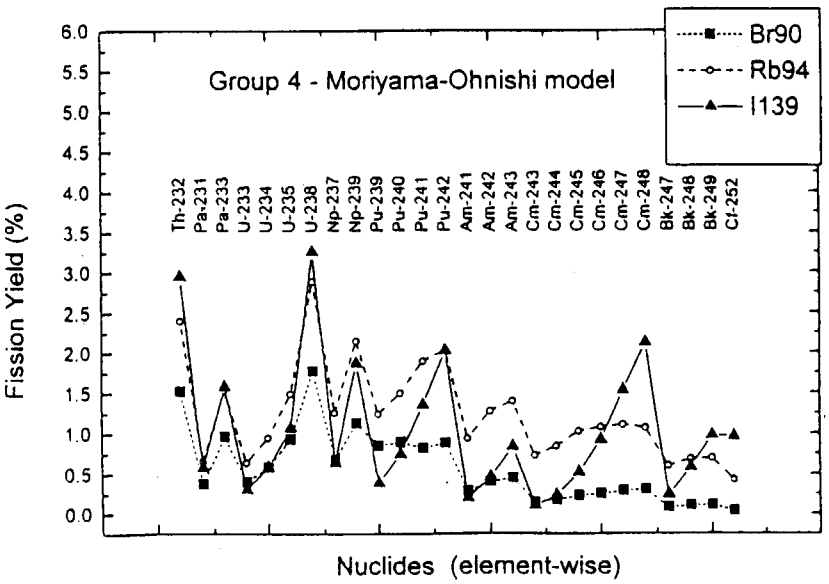

Fig.7 Similar results for Group 4 (Br-90, Rb-94, I-139).

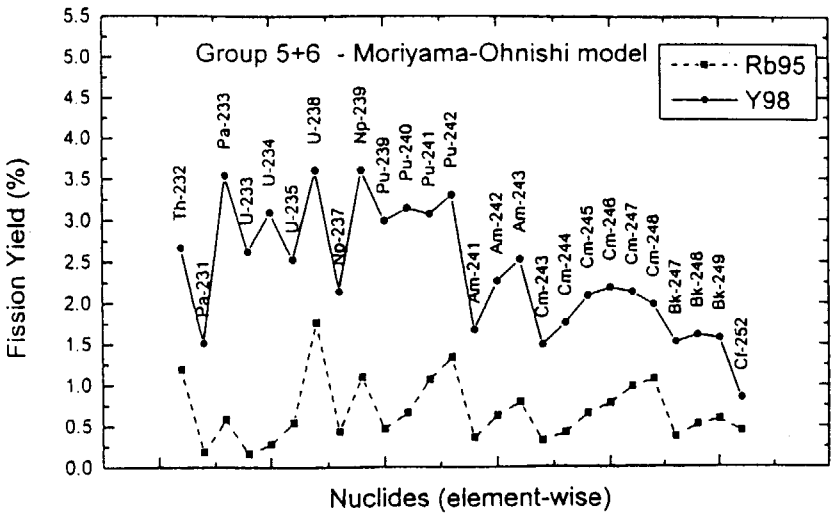

Fig.8 Similar results for Group 5-6 (Rb-95, Y-98).

4. Conclusions

1) The systematic decrease of DNY for heavier actinides is mainly due to the decrease of the FYs for precursors in the lighter side if the light fragment peak.

2) The summation calculation approximately reproduced the systematic behavior of DNY, but still suffered from ambiguities due to uncertainties both in FY and *Pn*.

Acknowledgments

This work is a part of the study performed under the contract between Kinki University and the Nuclear Data Center of Japan Atomic Energy Research Institute.

References

[1] Tuttle, R.J., INDC(NDS)-107/G (1979)

[2] Moriyama, H., and T.Ohnishi, *Technical Reports of the Institute of Atomic Energy, Kyoto University*, **No.166**, Sept. 1974

[3] Dickens, J.K., *Nucl. Sci. Eng.* **96**, 8 (1987)

[4] Reeder, P.L., and R.A.Warner, *Nucl. Sci. Eng.* **87**, 181 (1984)

[5] Madland,D.G, and T.R.England, LA-6430-MS (1976)

[6] Wahl, A.C., *Atomic and Nuclear Data Tables*, **39**, 1 (1988)

[7] Tachibana, T., *et al.* *Proc. Int. Conf. on Nuclear Data for Science and Technology*, Mito, 1988, p.885 (1989)

[8] Kratz, K.L. and G.Herrmann, *Z. Phys.* **263**, 435 (1973)

3.6 Decay Heat Measurement on Fusion Reactor Materials and Validation of Calculation Code System

Fujio MAEKAWA, Yujiro IKEDA and Masayuki WADA
High Energy Neutron Laboratory, Japan Atomic Energy Research Institute
Tokai-mura, Naka-gun, Ibaraki-ken 319-11 JAPAN
e-mail: fujio@fnshp.tokai.jaeri.go.jp

Decay heat rates for 32 fusion reactor relevant materials irradiated with 14-MeV neutrons were measured for the cooling time period between 1 minute and 400 days. With using the experimental data base, validity of decay heat calculation systems for fusion reactors were investigated.

1. Introduction

Very accurate prediction of decay heat is required for safety designs of fusion reactors. In the latest design of the International Thermonuclear Experimental Reactor (ITER), 40 % increase of decay heat results in approximately 10 times increase of hydrogen generation via the beryllium-steam chemical reactions to induce a hydrogen explosion.[1] Hence, uncertainties associated with the decay heat prediction less than 15 % are strongly requested by the designers of ITER. Comparisons of calculated decay heat with experimental data are the most straightforward way for validating decay heat calculation systems. There had however been no experimental decay heat data for fusion applications. In this work, a systematic decay heat measurement on fusion reactor relevant materials was conducted, and validity of several decay heat calculation systems was investigated with the experimental data base.

2. Experiment

Thirty-two fusion relevant sample materials shown in Table 1 were used for the experiment. About a half of them were metallic thin foils with an area of 25 x 25 mm^2 while the rest were powder sandwiched by two thin plastic tapes of 24 x 24 mm^2. Metallic powder and chemical compound powder samples were used because of their physical and chemical stability, respectively. An aluminum foil of 50 μm in thickness with the same size as the sample was attached to the sample for determination of D-T neutron fluence with using the $^{27}Al(n,\alpha)^{24}Na$ reaction rate.

The samples were irradiated in a D-T neutron field provided by the Fusion Neutronics Source (FNS) facility in JAERI. Decay heat associated with the radioactive nuclides disintegrated in the sample was measured with the Whole Energy Absorption Spectrometer (WEAS)[2, 3]. To

Table 1. Sample materials for the decay heat measurement.

Metallic Foil Sample		Powder Sample	
Al	Mo	B_4C	Y_2O_3
Ti	Ta	Na_2CO_3	SnO
V	W	SiO_2	$BaCO_3$
Fe	Pb	S	Re
Co	SS304	K_2CO_3	Bi
Ni	SS316	CaO	
Cu	Inconel-600	Cr	
Zr	NiChrom	Mn	
Nb	CF_2	$SrCO_3$	

obtain decay heat data for a wide range of cooling time, two combinations of irradiation and cooling time were adopted: 5 minutes irradiation for 1 ~ 60 minutes cooling time and 7 hours irradiation for cooling time more than 0.6 days. All the data were normalized at the D-T neutron flux of 10^{10} [n/s/cm^2]. Owing to the simple principle of the measurement, high sensitivity and wide dynamic range of WEAS, a comprehensive data base of decay heat for 32 fusion reactor relevant materials has been obtained for a wide cooling time from 1 minute up to 400 days.

3. Calculation

To investigate validity of decay heat calculation systems, the experimental analyses were performed with two Japanese calculation codes and three activation cross section libraries, as shown in Table 2. The ACT4 code is the main calculation module of the THIDA code system [4]. The CINAC code [5] is the same as the ACT4 code in principle, and its calculation algorithm is refined to achieve much faster computation speed. The FENDL/A-2.0 [6] and JENDL Activation File [7] are comprehensive activation cross section libraries which have been available since 1996. The Lib90 is a library developed for the THIDA code system in 1990, and has been used by

Table 2. Calculation codes and nuclear data bases.

Code	Cross Section Library	Decay Data Library
ACT4	FENDL/A-2.0	ENSDF & Table of Radioactive Isotopes
ACT4	JENDL Activation File	
CINAC-V4	FENDL/A-2.0	
CINAC-V4	1990's Library (Lib90)	Table of Isotopes (7th Edition)

Japanese fusion reactor designers with combination with the ACT4 and CINAC-V4 code for a long time.

4. Results and Discussions

As a result of preliminary comparisons of the experimental and calculated decay heat, several serious errors were found in either the codes and nuclear data libraries. Errors found in the codes and decay data libraries except Lib90 were corrected. The activation cross sections were untouched. And then, the experimental and calculated decay heat for all the 32 materials were compared in the manner shown in Fig. 1, as an example for the most important structural material of ITER, type 316 stainless steel (SS316). Agreements between the experiment and calculations, and dominant nuclei to the decay heat are explicitly indicated in Fig. 1. By examining the figures for all the materials, validity of the decay heat calculation systems was investigated. The following remarks were pointed out.

(1) Results by ACT4 and CINAC with the same FENDL library are almost identical, and in general, the calculated results show very good agreements with the experimental data, as shown in Fig. 1. Both codes are valid for calculating decay heat if adequate nuclear data bases are provided.

(2) The ACT4+JENDL calculations also give good results in many cases, but they sometimes give considerably smaller results compared to the experimental data due to lack of cross section data. Figure 2 shows an example for the zirconium sample. The $^{90}Zr(n,2n)^{89m}Zr$ reaction cross section is not included in JENDL.

(3) In many cases, CINAC+Lib90 calculations give smaller results compared with the experimental data due to systematically smaller beta-ray energies in Lib90, typically by a few tens of percentages. Figure 3 shows an example for the iron sample.

(4) When discrepancies are found between the experiment and calculation with FENDL, most of them can be attributed to inadequate cross sections in FENDL. Several crucial information on cross section data at 14-MeV can be extracted from the comparisons. For example, Fig. 4 shows decay heat for the copper sample irradiated for 7 hours. The discrepancy found in the cooling time more than 10 days suggests that the $^{63}Cu(n,\alpha)^{60m+g}Co$ cross section is given smaller in both FENDL. In fact, as shown in Fig. 5, those evaluated cross sections are smaller than the experimental cross section[8] measured at FNS. JENDL also gives smaller cross section in this case.

For two important materials for ITER, i.e., copper and SS316, the ACT4 and CINAC calculations with FENDL/A-2.0 and JENDL Activation File agreed within ± 10 % with the experimental data for a cooling time period up to 3 days. This result demonstrates that the required accuracy of ± 15 % for prediction of decay heat for ITER can be satisfied by those calculation systems.

5. International Benchmark

The experimental data base obtained in this work was provided as an international benchmark problem of decay heat calculation systems at the end of July, 1997. On October 2-3, 1997, a workshop on decay heat validation for fusion reactors was held at San Diego, U.S., and six international organizations from four countries attended to show their results. This is the first experimental validation work of decay heat calculation systems for fusion reactors.

6. Summary

Decay heat data for 32 fusion reactor relevant materials were measured for the cooling time period between 1 minute and 400 days. With using the experimental data base, validity of decay heat calculation systems for fusion reactors were investigated. Since decay heat calculation systems for fusion reactors had not been validated due to lack of experimental data, this work has contributed significantly to the safety aspect of ITER.

References

[1] Bartels H. -W., et al.: Fusion Eng. Des., 31, pp. 203-219 (1996).

[2] Maekawa F. and Ikeda Y.: "Whole Energy Absorption Spectrometer for Decay Heat Measurement of Fusion Reactor Materials and Application for Beta-Ray Spectrum Measurement", Proc. International Conference on Nucl. Data for Science and Technology, Trieste, Italy, May 19-24, 1997, to be published (1997).

[3] Maekawa F. and Ikeda Y.: "Development of Whole Energy Absorption Spectrometer for Decay Heat Measurement on Fusion Reactor Materials", Proc. '96 Symposium on Nuclear Data, JAERI-Conf 97-005, pp. 182-186 (1997).

[4] Seki Y., et al.: "THIDA-2: An Advanced Code System fro Calculation of Transmutation, Activation, Decay Heat and Dose Rate", JAERI 1301 (1986).

[5] Fukumoto H.: J. Nucl. Sci. Technol., 23, pp. 97-109 (1986).

[6] Pashchenko A. B.: "Summary Report for IAEA Consultants' Meeting on Selection of Evaluations for the FENDL/A-2 Activation Cross Section Library", INDC(NDS)-341, International Atomic Energy Agency (1996).

[7] Nakajima Y.: "Status of the JENDL Activation File", JAERI-Conf 96-008, pp. 50-55 (1996).

[8] Konno C., et al.: "Activation Cross Section Measurement at Neutron Energy from 13.3 to 14.9 MeV Using the FNS Facility", JAERI 1329 (1993).

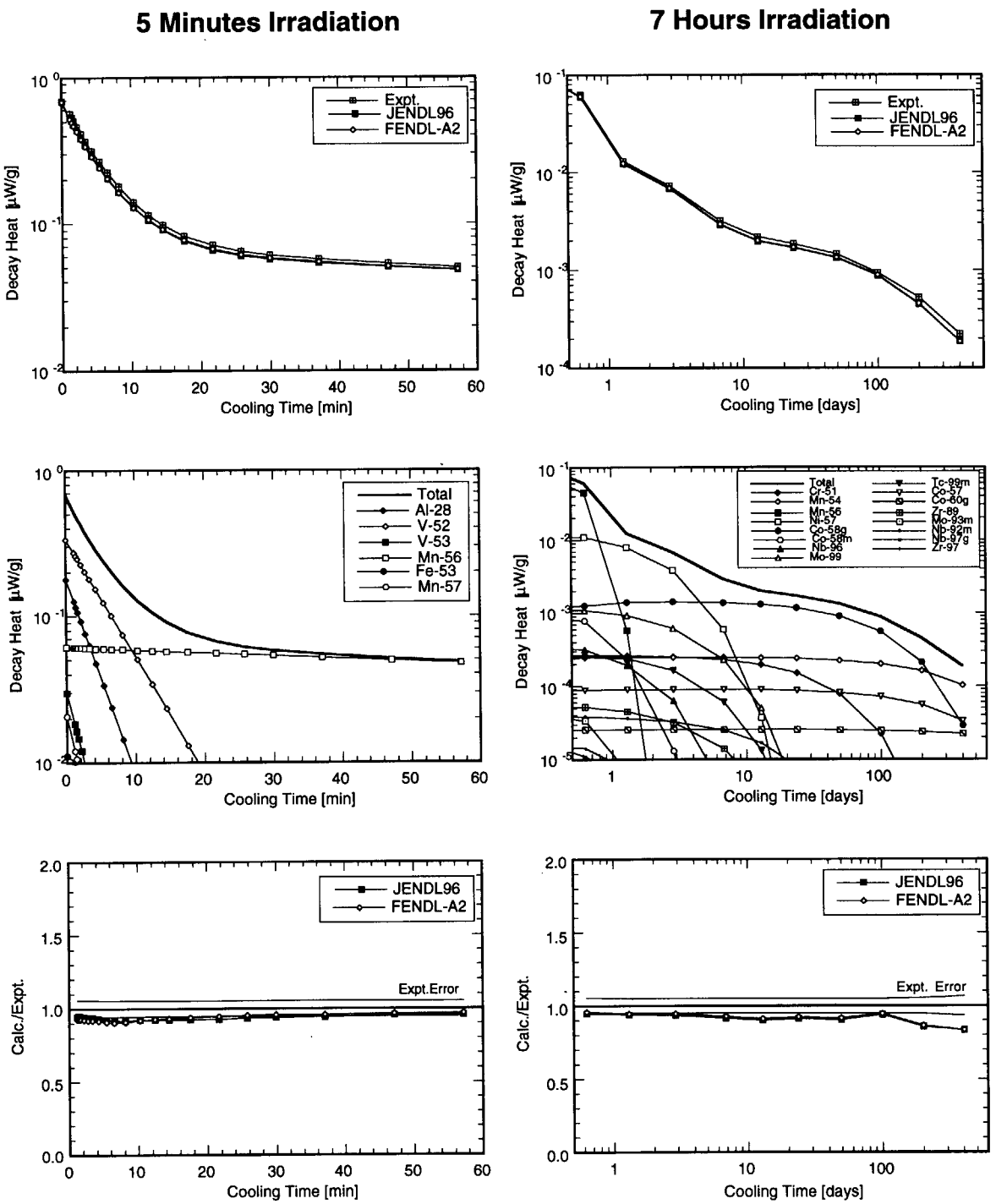

Fig. 1 Results for the SS316 sample with the ACT4 code. The left and right hand side figures correspond to the 5 minutes and 7 hours irradiations, respectively. The upper two figures are direct comparisons of the experimental and calculated decay heat. The middle two figures indicate predominantly contributing nuclei based on the ACT4+FENDL calculations. The lower two figures are calculated to experimental ratios.

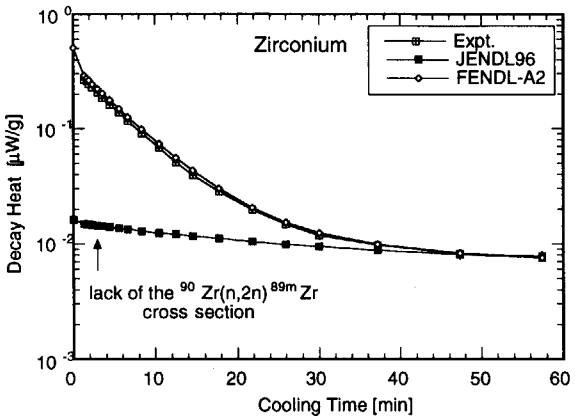

Fig. 2 Calculated decay heat of zirconium by theACT4 code with two cross section librariescompared with the measured data.

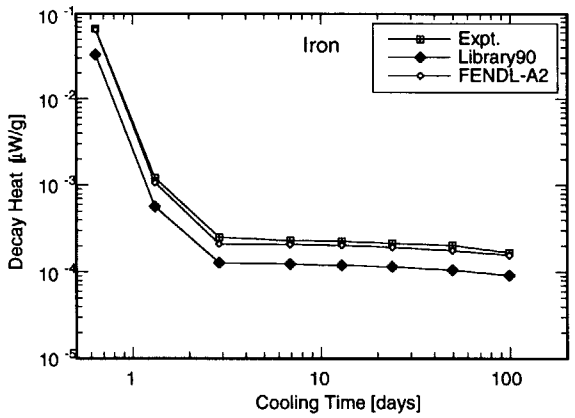

Fig. 3 Calculated decay heat of iron by the CINAC code with two cross section libraries compared with the measured data.

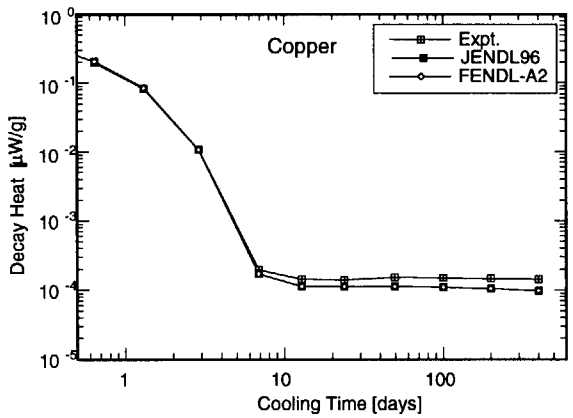

Fig. 4 Calculated decay heat of copper by the ACT4 code with two cross section librariescompared with the measured data.

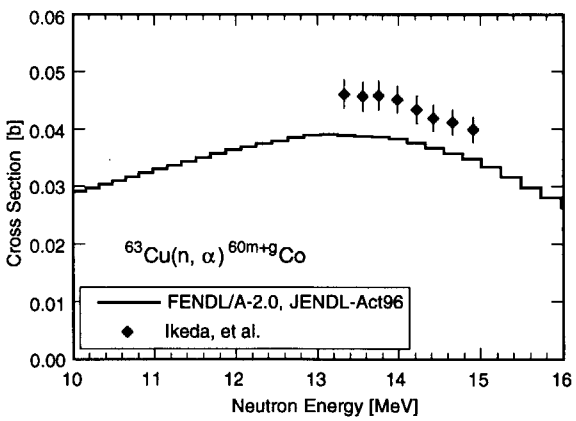

Fig. 5 The $^{63}Cu(n,\alpha)^{60m+g}Co$ cross section in FENDL/A-2.0 and JENDL Activation File compared with the measured data.

3.7 Benchmark Experiment on Vanadium Assembly with D-T Neutrons - In-situ Measurement -

Fujio MAEKAWA, Yoshimi KASUGAI, Chikara KONNO,
Masayuki WADA, Yukio OYAMA and Yujiro IKEDA
High Energy Neutron Laboratory, Japan Atomic Energy Research Institute
Tokai-mura, Naka-gun, Ibaraki-ken 319-11 JAPAN
e-mail: fujio@fnshp.tokai.jaeri.go.jp

Isao MURATA, KOKOOO and Akito TAKAHASHI
Department of Nuclear Engineering, Osaka University
Yamada-oka 2-1, Suita-si, Osaka-fu 565 JAPAN

Fusion neutronics benchmark experimental data on vanadium were obtained for neutrons in almost entire energies as well as secondary gamma-rays. Benchmark calculations for the experiment were performed to investigate validity of recent nuclear data files, i.e., JENDL Fusion File, FENDL/E-1.0 and EFF-3.

1. Introduction

Vanadium-alloy is one of advanced low-activation structural materials for fusion reactors. As vanadium is the major constituent of the vanadium-alloy, benchmark experiments on vanadium are strongly required to validate evaluated nuclear data files used for fusion reactor designs. The leakage neutron spectrum measurement from spherical vanadium shells of 35 and 105 mm in thickness in the energy range above 0.07 MeV done by Möllendorff et al. had been the unique existing benchmark experiment on vanadium. [1] For validation of low energy neutron cross sections and secondary gamma-ray data for vanadium, there are, however, no benchmark experimental data. To provide supplementary experimental data on vanadium, a benchmark experiment was conducted at the Fusion Neutronics Source (FNS) facility in JAERI. This report deals with the in-situ measurement. The leakage neutron spectrum measurement is also reported in this symposium.

2. Experiment

A cubic experimental assembly of 254 mm made of pure vanadium was placed at a 200 mm distance from the D-T neutron source. Four side surfaces and a rear surface of the assembly were covered with a graphite reflector of 51 mm in thickness to reduce leakage neutrons out of

the assembly and incoming background neutrons from the outside. Two experimental channels to insert detectors into the assembly were located at 76 and 178 mm depths measured from the front surface.

The following nuclear parameters were measured at the front surface of the assembly and in the two experimental channels during D-T neutron irradiations; (i) neutron spectra (> 1.5 MeV) by a 14 mm in diameter sphere NE213 liquid organic scintillation spectrometer, (ii) neutron spectra (20 keV ~ 1 MeV) by proton recoil gas proportional counters, (iii) neutron spectra (1 eV - 300 eV) by the slowing down time method, (iv) dosimetry reaction rates of the $^{27}Al(n,\alpha)^{24}Na$, $^{93}Nb(n,2n)^{92m}Nb$, $^{115}In(n,n')^{115m}In$ and $^{197}Au(n,\gamma)^{198}Au$ reactions by the foil activation method, (v) gamma-ray spectra by a 40 mm in diameter sphere BC537 liquid organic scintillation spectrometer and (vi) gamma-ray heating rates by TLD.

3. Benchmark Calculation

Transport calculations were performed by the continuous energy Monte Carlo code MCNP-4A [2] with evaluated nuclear data files, i.e., JENDL Fusion File (JENDL-FF)[3], FENDL/E-1.0 (FENDL-1) [4] and European Fusion File version-3 (EFF-3)[5]. The cross section data of vanadium in JENDL Fusion File are selected for FENDL/E-2.0. Those in FENDL/E-1.0 are taken from ENDF/B-VI.

A calculation with JENDL-3.2 [6] was also performed. Cross section data in JENDL-FF and JENDL-3.2 are completely the same as each other except for the expression of secondary neutrons, i.e., DDX and EDX+ADX, respectively. Influences of the difference of the cross section on results of the calculations are very small, and both calculations are almost identical. Hence, the results of JENDL-3.2 are excluded in this report.

4. Results for Neutron

Figure 1 shows the measured and calculated neutron spectra. Figure 2 shows calculated to experimental (C/E) ratios for (a) the $^{93}Nb(n,2n)^{92m}Nb$ and (b) the $^{115}In(n,n')^{115m}In$ reactions which are mainly sensitive to neutrons > 10 MeV and 1-10 MeV, respectively, (c) the integral neutron flux in the energy range of 0.1~1 MeV, and the $^{197}Au(n,\gamma)^{198}Au$ reaction sensitive to low energy neutrons. As shown in these figures, all the three calculations adequately predict the experimental data as far as the energy region above 20 keV is concerned. Although scatters of the C/Es by JENDL are the largest among the three, no serious problem is found in all the three nuclear data files for the high energy neutrons.

In the energy region below 300 eV, as shown in Fig. 1, the calculated spectra with EFF-3 and FENDL-1 follow the measured spectrum while the calculated spectrum flux with JENDL-FF is about a half of the measured data. This trend is also found in reaction rates of gold which is sensitive to low energy neutrons, as shown in Fig. 2 (d). The reason of the large underestimation of the low energy neutron flux by JENDL-FF is attributable to the smaller total cross section at ~ 2 keV. Figure 3 compares experimental and evaluated total cross section of vanadium. Apparently,

JENDL gives smaller total cross compared with the experimental data. Around this energy, the total cross section is almost equivalent to the elastic scattering cross section. The smaller elastic scattering cross section reduces slowing down of neutrons at ~ 2 keV, and also, enhances leakage of neutrons outside the experimental assembly due to the longer mean free path. Accordingly, neutron spectrum fluxes below ~ 2 keV are predicted smaller by the smaller total cross section. The present integral experiment is consistent with the differential cross section measurements at this point.

5. Results for Secondary Gamma-Ray

Figure 4 shows the measured and calculated gamma-ray spectra. The spectrum by JENDL-FF agrees very well with the measured spectrum. EFF-3 gives a rather larger spectrum flux over the entire energies. The spectrum by FENDL-1 is smaller than the measured one. Especially, the prominent peak at ~ 1.6 MeV observed in the measured spectrum is not so clear in the spectrum calculated by FENDL-1. Figure 5 shows measured [7] and evaluated energy-differential gamma-ray production cross sections at En= 14.5 MeV. The present experimental results for secondary gamma-rays are fairly consistent with the results for the differential gamma-ray production cross sections. Secondary gamma-ray data of JENDL-FF is evaluated [8] by considering the secondary gamma-ray spectra measured at ORNL[9], therefore, accurate secondary gamma-ray data are given in JENDL-FF.

Neutron KERMA factors of vanadium calculated by the energy-balance method are shown in Fig. 6. Secondary neutron and gamma-ray energies are subtracted from the total available energy to deduce the KERMA factors in the energy-balance method. This method is sometimes not so accurate for calculating KERMA factors when cross sections for both neutrons and gamma-rays are not evaluated consistently from the viewpoint of energy-balance. The KERMA factors are, therefore, good indices for testing the evaluated nuclear data in the point whether they are energetically consistent or not. In Fig. 6, the KERMA factors of JENDL-FF and ENDF/B-VI (FENDL-1) seem to be adequate while those of EFF-3 are apparently inadequate because of unreasonable negative KERMA factors above 4 MeV. Since accurate neutron cross sections are given in EFF-3 according to the neutron results, the negative KERMA factors of EFF-3 also implies too large gamma-ray production cross sections.

6. Summary

Benchmark experimental data on vanadium were obtained for neutrons in almost entire energies as well as secondary gamma-rays. As a result of benchmark calculations, several problems were pointed out in the evaluated nuclear data files. Although adequate neutron cross sections are given in FENDL-1 and EFF-3, secondary gamma-ray data in these libraries should be modified. Especially, gamma-ray production cross section of EFF-3 should be reduced over the entire energy range. As for JENDL-FF, secondary gamma-ray data are good while neutron total cross section around 2 keV is too small. Modification of the total cross section in JENDL-FF is

strongly recommended because the low energy part of the cross section is very important for structural materials for shielding calculations. As JENDL-FF has been selected for FENDL/E-2.0, the revision is urgent

References

[1] Möllendorff U., et al.: "A 14-MeV Neutron Transmission Experiment on Vanadium", Proc. 19th Symposium on Fusion Technology, Lisbon, September 16-21, 1996, pp. 1575-1578 (1997).

[2] Briesmeister J. F. (Ed.): "MCNP - A General Monte Carlo N-Particle Transport Code, Version 4A", LA-12625-M, Los Alamos National Laboratory (1993).

[3] Chiba S., et al.: "Evaluation of the Double-Differential Cross Sections of Medium-Heavy Nuclei for JENDL Fusion File", JAERI-Conf 96-005, 45 (1996).

[4] Ganesan S. and McLaughin P. K., IAEA-NDS-128 (1995).

[5] Gruppelaar H. and Kopecky J.: Proc. International Conference on Nucl. Data for Science and Technology, Gatlinburg, Tennessee, USA, May 9-13, 1994, pp. 699-701 (1994).

[6] Nakagawa T., et al.: J. Nucl. Sci. Technol., 32, pp. 1259-1271 (1995).

[7] Takayama T., et al.: "Gamma-ray Production Cross Sections with 14 MeV Neutrons for 8 Elements fro Z=22 to 29", JAERI-M 91-032, pp. 255-264 (1991).

[8] Shibata K., et al.: J. Nucl. Sci. Technol., 34, pp. 503-509 (1997).

[9] Newman E. and Morgan G. L.: "The V(n,xγ) Reaction Cross Section for Incident Neutron Energies between 0.2 and 20 MeV", ORNL/TM-5299 (1976).

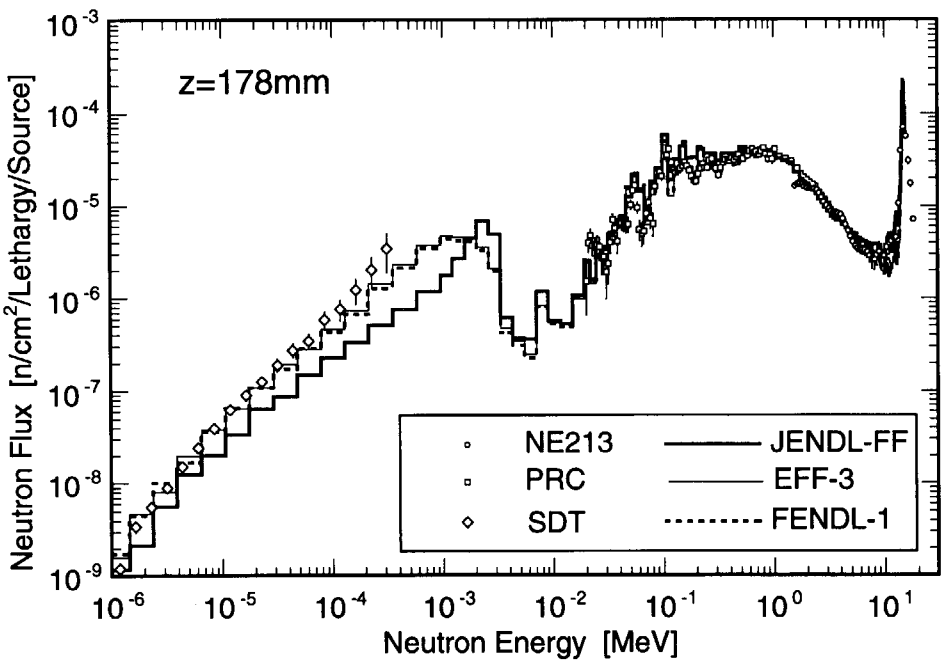

Fig. 1 Comparison of the measured and calculated neutron energy spectrum.

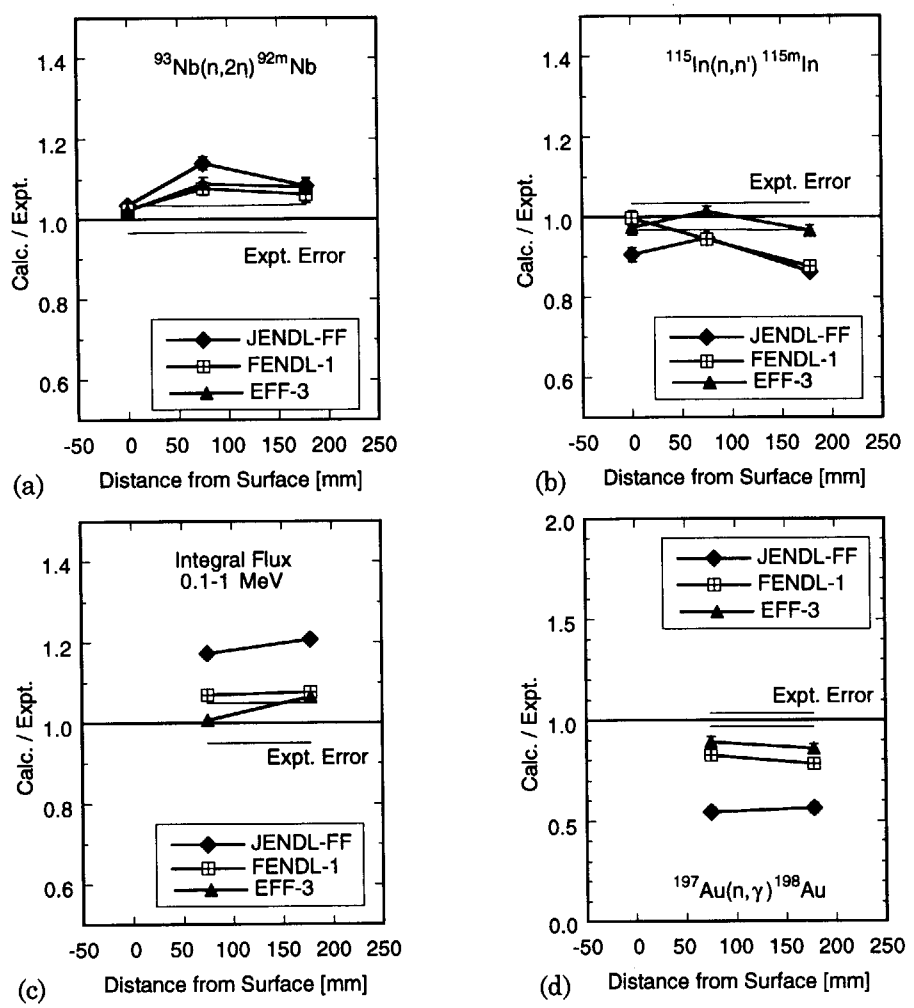

Fig. 2 C/E ratios for (a) the $^{93}Nb(n,2n)^{92m}Nb$, (b) $^{115}In(n,n')^{115m}In$ and (d) $^{197}Au(n,\gamma)^{198}Au$ reaction rate and (c) the integral flux of 0.1 ~ 1 MeV.

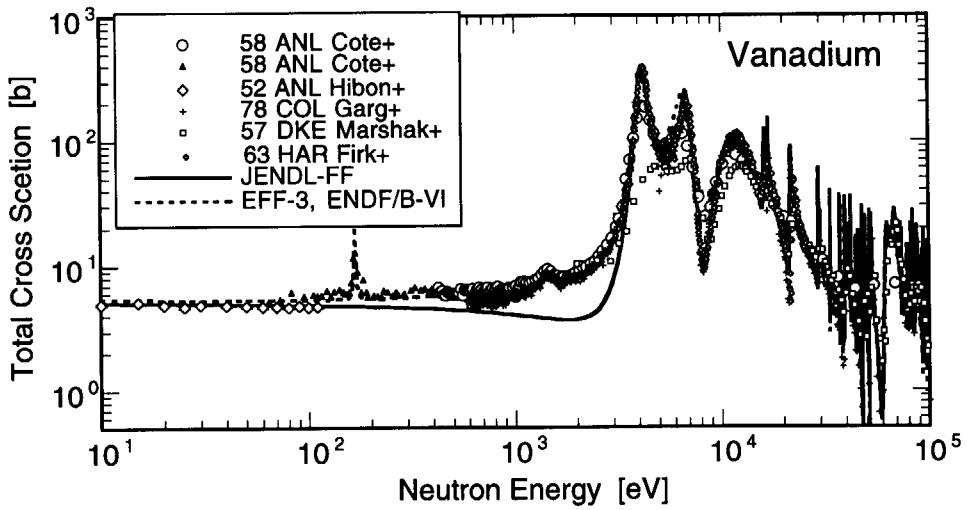

Fig. 3 Experimental and evaluated total cross section of vanadium.

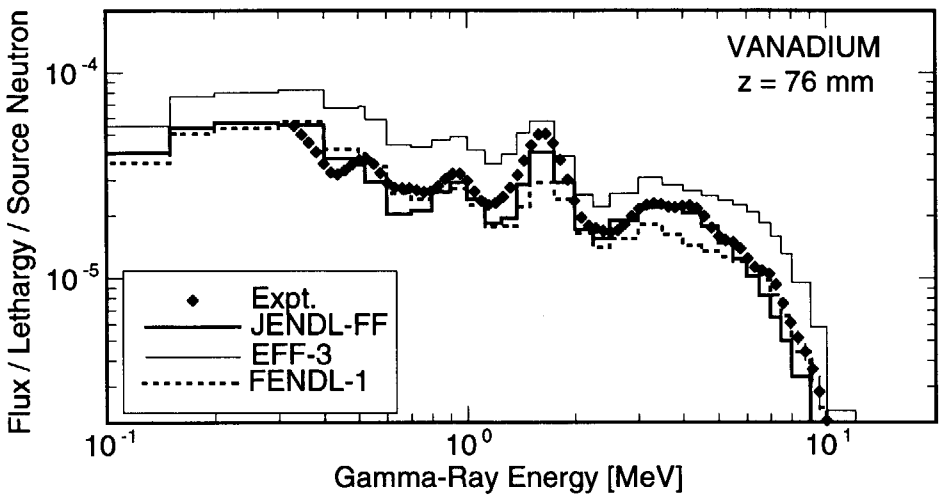

Fig. 4 Comparison of the measured and calculated gamma-ray energy spectrum.

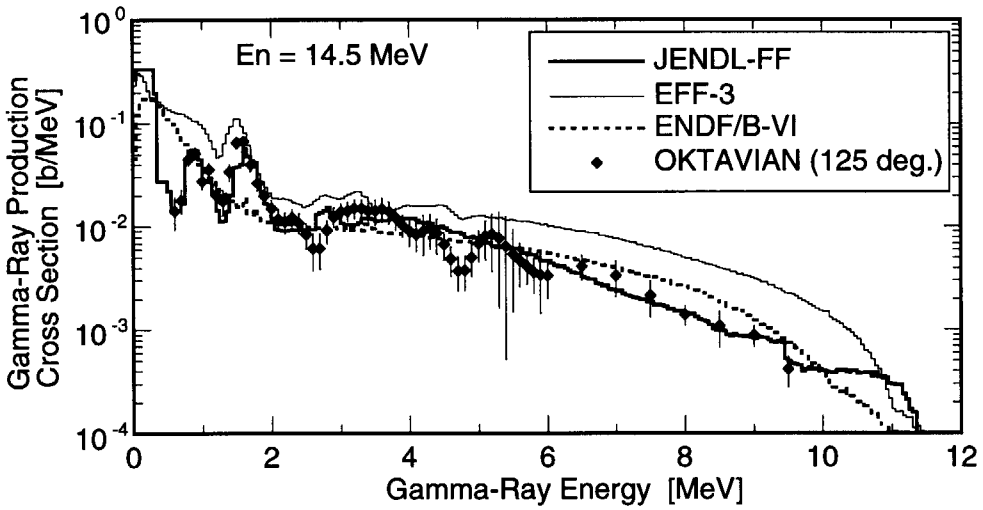

Fig. 5 Comparison of the measured and calculated gamma-ray production cross section for neutron incident energy at 14.5 MeV.

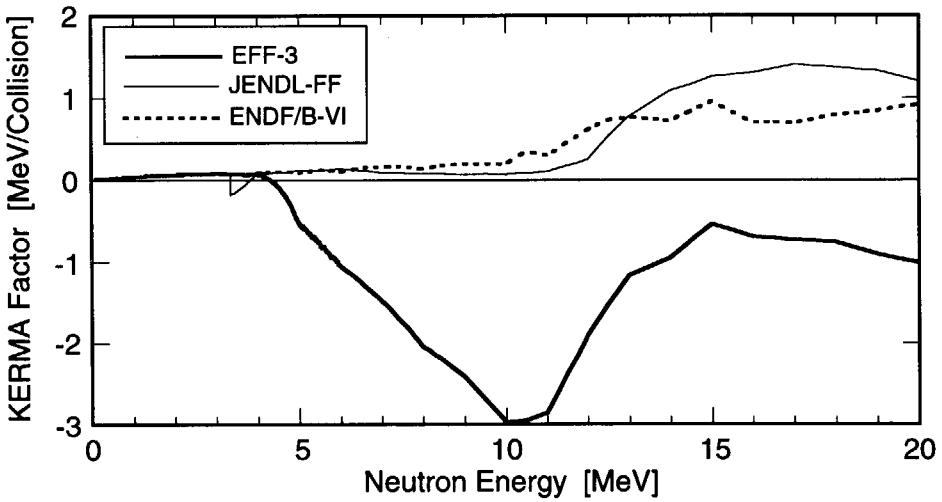

Fig. 6 Neutron KERMA factors of vanadium calculated by the energy-balance method.

3.8

Benchmark Validation by means of Pulsed Sphere Experiment at OKTAVIAN

Chihiro ICHIHARA, Research Reactor Institute, Kyoto University*
Shu A. HAYASHI, Institute for Atomic Energy, Rikkyo University,
Itsuro KIMURA, Department of Nuclear Engineering, Kyoto University,
Junji YAMAMOTO, Department of Electrical Engineering, Setsunan University,
Akito TAKAHASHI, Department of Nuclear Engineering, Osaka University,
*e-mail address: chihiro@kuca.rri.kyoto-u.ac.jp

In order to make benchmark validation of the existing evaluated nuclear data for fusion related material, neutron leakage spectra from spherical piles were measured with a time-of-flight technique using the intense 14 MeV neutron source, OKTAVIAN in the energy range from 0.1 to 15 MeV. The neutron energy spectra were obtained as the absolute value normalized per the source neutron. The measured spectra were compared with those by theoretical calculation using a Monte Carlo neutron transport code, MCNP with several libraries processed from the evaluated nuclear data files. Comparison has been made with the spectrum shape, the C/E values of neutron numbers integrated in 4 energy regions and the calculated spectra unfolded by the number of collisions, especially those after a single collision.

The new libraries predicted the experiment fairly well for Li, Cr, Mn, Cu and Mo. For Al, Si, Zr, Nb and W, new data files could give fair prediction. However, C/E differed more than 20 % for several regions. For LiF, CF_2, Ti and Co, no calculation could predict the experiment. The detailed discussion has been given for Cr, Mn and Cu samples. EFF-2 calculation overestimated by 24 % for the Cr experiment between 1 and 5-MeV neutron energy region, presumably because of overestimation of inelastic cross section and ^{52}Cr(n,2n) cross section and the problem in energy and angular distribution of secondary neutrons in EFF-2. For Cu, ENDF/B-VI and EFF-2 overestimated the experiment by about 20 to 30-% in the energy range between 5 and 12-MeV, presumably from the problem in inelastic scattering cross section.

1. INTRODUCTION

In a D-T fusion reactor, intense 14-MeV neutrons from plasma bombard a first wall, and enter a blanket to generate heat by various reactions and to produce tritium by the ^{6}Li(n, α) T and Li ($n,n\,\alpha$) T reactions. Some neutrons hit superconducting magnets and other important devices around the blanket. Therefore, neutron transport calculation is of essential importance for the design of the D-T fusion reactors.

More reaction channels, such as (n,n) open and angular distributions of scattered neutrons become anisotropic with the neutrons above 10-MeV compared with those of fission reactors. Also, the structure of D-T fusion rectors is usually very complicated. For these reasons, the neutron transport calculation in the blanket for a D-T fusion reactor has more ambiguity than that in a fission reactor. This ambiguity is mainly due to simplified modeling of the real geometry and to large uncertainty in nuclear data for higher energy neutrons. Recently the ambiguity from the former can be drastically reduced by using Monte Carlo calculation, but that caused by the latter has not yet been improved for obtaining sufficient accuracy.

In several countries and international organizations, great effort have been made to prepare nuclear data files for the design of D-T fusion reactors by adopting newly measured data, such as double differential cross section (DDX), and by using more sophisticated neutron reaction theory. Such new nuclear data files have to be validated through benchmark experiment for the actual application to the design work.

The purpose of this work is to validate currently available modern nuclear data libraries for D-T fusion reactors by carrying out pulsed sphere experiment. By making use of the intense 14-MeV neutron source,

OKTAVIAN, a series of pulsed sphere experiments including 15 elements and compounds systematically, but the results for the Cr, Mn and Cu piles are given in this paper. We tried to measure the absolute value of neutron spectra by making use of the activation method of a Nb cover foil which surrounded the D-T target. In the comparison of calculated spectra with measured ones, not only the spectrum shape, but also the C/E values of neutron numbers integrated in 4 energy regions were considered. In order to analyze the effects of different reactions and their secondary neutrons, the calculated spectra unfolded by the number of collisions, especially those after a single collision were examined. As the nuclear data for D-T fusion reactors, adopted were two working libraries attached with MCNP-4A[1] code (BMCCS, ENDL-85), and the libraries processed from nuclear data files - JENDL-3.1[2], JENDL-3.2[3], JENDL Fusion file[3], FENDL/E-1.0[4], EFF-2[5]. Some detailed discussion for Cr, Mn and Cu sample piles are given.

2. EXPERIMENTAL FACILITY AND PROCEDURE

1) Neutron Source

The experiment was performed at OKTAVIAN[6], which is an intense 14-MeV neutron source facility of Osaka University. This consists of a 400 kV high voltage generator and a duoplasmatron ion source capable of 25 mA of deuteron beam. We used the pulsed beam line which was capable of neutron pulse of few ns of pulse width. In this experiment, the deuteron beam pulsed width and the repetition rate was 2 ns and 250 kHz or 500 kHz, respectively. The deuteron beam was introduced to the center of the spherical sample pile through a beam hole and bombarded the tritium target to generate 14-MeV neutrons by the $^{3}T(d,n)^{4}He$ reactions. A 370-GBq tritium target of "gas-in-metal" type of 3.18 cm diameter and 0.05 cm thickness copper backing plate. The average neutron yield was about 10^{9} n/sec.

2) Experimental Arrangement

The neutrons leaking from the outer surface of the spherical sample piles were detected with a liquid scintillation counter composed of a NE-218 scintillator of 12.7 cm-diam. × 5.08 cm-long and a RCA8854 photo multiplier tube. This detector was located 11 m apart from the center of the pile and 55 degrees horizontally and -5 degrees vertically with respect to the deuteron beam axis.

The pre-collimator was placed between the sample pile and the detector to reduce the background neutrons scattered by the walls and other structural materials in the measurement room of OKTAVIAN. This consisted of mufti-layers of polyethylene and iron with outer diameter of 1.2 m and an inner aperture diameter of 0.3 m. The aperture size was decided so that all neutrons leaking from the surface within 2-π solid angle to the detector could go through this aperture.

The trigger signals were taken from a beam pick-up ring. The neutron signals from the NE-218 liquid scintillation counter were discriminated from gamma-ray signals by using the pulse shape discrimination technique. To cover neutron energy down to 0.1-MeV, two identical shape discriminating circuits were used in parallel with different gain settings of the delay-line amplifiers.

3) Sample Piles

As all the materials were powder or small pellets, they were packed in spherical shells made of stainless steel or mild steel. Li, CF_2 , Al, Si, Ti, Cr, Co and W were contained in 40-cm diameter shells made of stainless steel, the outer diameter and the thickness of which were 40-cm and 0.2-cm, respectively. The shell of this type was equipped with a central void section of 20-cm in diameter to accommodate the tritium target and with a reentrant hole, the diameter of which was 11-cm. LiF, Mn, Cu, Zr and Mo sample were contained in 61-cm diameter shells, the outer diameter and the wall thickness of which were 61-cm, and 0.5-cm, respectively. The shell of this type had a 5-cm diameter reentrant hole for introducing the tritium target but no central void was equipped. Nb sample was contained in the similar shell to 61-cm one except for the outer diameter which was 28-cm for this shell. We used 60 cm diameter shell for another Si sample pile. This was similar to 40-cm shell except that the diameter and wall thickness were 60-cm and 0.5-cm, respectively. In the Table-1, shown are the diameters, packing density (kg/cm^3) and the sample thickness measured by the mean free path for 14-MeV neutrons calculated from the total neutron cross section at 14-MeV of each material.

3. DATA PROCESSING

The absolute values of the neutron spectra were determined by combining a relative detector efficiency, a run-to-run neutron fluence monitor with a Nb activation foil covering the target, and a D-T source

neutron detection with the time-of-flight measurement circuit, according to the following procedure.
1) The relative efficiency of the neutron detector between 0.83 and 8.2 MeV was determined from the time-of-flight measurement of the neutrons from a ^{252}Cf spontaneous fission source. The prompt gamma-rays from the spontaneous fission of ^{252}Cf were used as the trigger signals for utilizing the same counting circuit as the main experiment.
2) The relative efficiency between 0.05-MeV and 0.83-MeV was determined by the time-of-flight measurement of the leaking spectrum from 30 cm-diam. spherical pile.
3) The absolute efficiency above 0.1-MeV was calculated by using a Monte Carlo code OS5.
4) The efficiency determined from graphite measurement and the calculated efficiency were normalized between 0.3 and 0.8-MeV. The efficiency determined from ^{252}Cf measurement and the calculated efficiency were normalized between 4 and 8-MeV. The efficiency curve was obtained by combining the above values.
5) The total leakage neutron current was obtained by combining the efficiency curve and the integrated count of the D-T neutron source measurement with the TOF counting circuit. The detailed description of this method is given elsewhere[7].

4. CALCULATIONS

The theoretical calculations were performed using a three-dimensional continuous energy Monte Carlo transport code, MCNP-4A. Used working libraries were BMCCS, ENDL-85, FENDL/MC-1[8], EFF-2 and three JENDL-3 based libraries- FSXLIB-J3[9], FSXLIB-J3R2[10] and FSXLIB-J3FF[11]. BMCCS is an attached library with MCNP4A, which consists of ENDF/B-IV[12], ENDL-73[13] and so on. ENDL-85 was also attached with MCNP code and was processed from the 1985 version of LLNL evaluations[15]. FENDL/MC-1 was processed from FENDL/E-1.0 data file, which consisted of ENDF/B-VI[16], JENDL-3.1, EFF-2, BROND-2[17]. FSXLIB-J32, FSXLIB-J3R2 and FSXLIB-JFF were processed from JENDL-3.1, JENDL-3.2 and JENDL Fusion File by Kosako, respectively.

The source neutrons were treated as an isotropic point source and the measured energy distributions was given as the neutron source. As the experimental results were reduced as the total leakage current per source neutron, the neutron tally adopted was a surface crossing tally. The neutron histories were taken as 10^7 in most cases and the statistic error of less than 1 % for each energy bin was obtained.

5. RESULT AND DISCUSSION

In the Table-1, given are the calculated-to-experimental (C/E) values of the spectra integrated over 4 energy regions for the sample piles. The spectrum in the highest energy region (>10 MeV) is reflected by the direct neutrons from the target, neutrons elastically scattered in the sample pile and neutrons after inelastically scattered to the discrete levels few times. The next energy region $5<E_n<10$-MeV is reflected by the neutrons after inelastically scattered to continuum regions and secondary neutrons generated by threshold reactions. The third region ($1<E_n<5$-MeV) is reflected by the spectrum component formed by various interactions such as inelastic scattering and (n,2n) reactions. The lowest region is reflected by the resonance structures of the cross sections of each element. The calculations with new nuclear data- three JENDL data files, FENDL-1, EFF-2 could predicted the experiment fairly well in general. Especially, for Li, Cr, Mn, Cu and Mo, all data files could calculate nearly perfect spectra giving less than 10 % disagreement between experiment and calculation. For Al, Si, Zr, Nb and W, the C/E values for whole energy region were less than 10 %. However, disagreement as large as 20- 40 % was obtained partly for these samples, which implicated some problem in the nuclear data files. For LiF, CF_2, Ti, and Co, the calculations with all libraries had large disagreement from the experiment.
In the Cr, Mn and Cu result, the old nuclear data files, ENDF/B-IV for Cr and Cu and ENDL-73 for Mn did not predict the experiment satisfactorily, especially in the energy region between 5- and 10-MeV as shown in Figs. -1,-2 and -3. At the period when these data files were dominantly used, the idea of applying the direct process theory to the neutron-nuclear interaction was not necessary. The inelastic cross sections mainly bear the problem caused by the ignorance of the direct process. In the Table-2, total inelastic cross section values for Cr, Mn and Cu are listed. The severe overestimation and underestimation of the

Table-1 Sample list and the C/E values of the spectra integrated over 4 energy regions

Table 1

	Energy	JENDL-3.2	JENDL-FF	JENDL-3.1	EFF-2	FENDL-1	BMCCS
Li	10<En<20	0.961	0.961	0.960		0.968	0.955
40cm	5<En<10	0.751	0.752	0.744		0.675	0.758
ρ=0.534	1<En<5	0.975	0.973	0.982	NA	0.981	0.958
1.3 MFP	.1<En<1	1.012	1.013	1.017		0.972	1.053
	total	0.948	0.948	0.948		0.944	0.945
LiF	10<En<20	1.137	1.141	0.900		1.076	0.891
60cm	5<En<10	0.932	0.970	0.632		0.834	0.769
ρ=1.79	1<En<5	0.856	0.858	0.862	NA	0.856	0.881
3.5 MFP	.1<En<1	0.597	0.590	0.658		0.680	0.719
	total	0.861	0.864	0.781		0.860	0.819
CF	10<En<20	0.767	0.768	0.709		0.761	0.724
40cm	5<En<10	0.545	0.555	0.521		0.606	0.578
ρ=1.30	1<En<5	0.625	0.624	0.804	NA	0.617	0.770
0.7 MFP	.1<En<1	0.611	0.605	0.726		0.645	0.704
	total	0.713	0.714	0.711		0.715	0.719
Al	10<En<20	1.060	1.062	1.051	1.052	1.051	1.020
40cm	5<En<10	0.792	0.819	0.644	0.814	0.644	0.916
ρ=1.22	1<En<5	0.893	0.889	1.010	0.992	1.010	1.006
0.5 MFP	.1<En<1	1.260	1.244	1.217	1.147	1.217	1.357
	total	1.034	1.035	1.036	1.037	1.036	1.037
Si	10<En<20	0.974	0.936	0.974	0.974	0.861	0.966
40cm	5<En<10	0.685	0.648	0.689	0.707	0.655	0.579
ρ=1.30	1<En<5	0.776	0.857	0.774	0.735	0.741	0.646
0.55 MFP	.1<En<1	0.847	1.101	0.853	0.728	1.797	1.018
	total	0.927	0.922	0.927	0.915	0.891	0.909
Si	10<En<20	1.096	1.104	1.095	0.888	0.920	1.073
60cm	5<En<10	0.764	0.789	0.755	0.887	0.712	0.607
ρ=1.30	1<En<5	0.976	0.995	0.975	1.069	0.791	0.755
1.1 MFP	.1<En<1	1.163	1.045	1.171	1.170	1.931	1.387
	total	1.058	1.055	1.058	0.961	0.999	1.013
Ti	10<En<20	1.193	1.195	1.154	1.155	1.186	1.207
40 cm	5<En<10	1.006	1.023	0.993	1.008	0.970	0.856
ρ=1.54	1<En<5	1.160	1.154	1.414	1.418	1.377	1.342
0.5 MFP	.1<En<1	1.560	1.562	1.508	1.469	1.408	1.279
	total	1.216	1.216	1.227	1.225	1.232	1.222
Cr	10<En<20	0.993	1.025	1.024	0.972	0.987	1.040
40cm	5<En<10	0.998	1.014	0.998	0.965	1.127	2.171
ρ=3.72	1<En<5	1.080	1.056	1.053	1.236	1.118	0.969
0.7 MFP	.1<En<1	1.131	1.062	1.072	1.069	1.068	0.897
	total	1.041	1.039	1.039	1.040	1.037	1.041
Mn	10<En<20	0.982	0.985	0.936	0.749	0.942	0.955
60cm	5<En<10	1.104	1.085	0.880	0.967	0.982	0.501
ρ=4.37	1<En<5	1.097	1.111	1.116	1.121	1.127	0.685
3.4 MFP	.1<En<1	1.080	1.077	1.088	1.079	1.072	1.135
	total	1.071	1.073	1.068	1.041	1.065	0.985
Co	10<En<20	0.982	0.969	0.959	0.998	0.986	0.997
40cm	5<En<10	0.694	0.667	0.751	0.516	0.529	0.458
ρ=1.94	1<En<5	0.650	0.677	0.670	0.637	0.650	0.658
0.5 MFP	.1<En<1	0.650	0.678	0.707	0.643	0.681	0.606
	total	0.834	0.838	0.839	0.831	0.835	0.827
Cu	10<En<20	1.074	1.165	1.064	1.034	1.127	0.938
60cm	5<En<10	0.993	1.082	0.915	1.263	1.365	0.533
ρ=6.01	1<En<5	0.974	1.050	0.964	1.067	1.133	0.870
4.7 MFP	.1<En<1	1.088	1.060	1.074	1.085	1.094	1.076
	total	1.067	1.068	1.053	1.080	1.107	1.023
Zr	10<En<20	1.149	1.153	0.961	1.129	1.200	1.132
60cm	5<En<10	0.965	0.986	1.374	1.636	1.196	1.644
ρ=2.84	1<En<5	1.087	1.071	1.238	1.545	1.217	1.541
2.0 MFP	.1<En<1	1.245	1.233	1.223	0.998	1.107	0.992
	total	1.165	1.157	1.157	1.209	1.167	1.206
Nb	10<En<20	1.040	1.039	1.051	1.040	1.038	1.056
28cm	5<En<10	0.930	0.954	1.187	1.163	1.110	0.904
ρ=4.39	1<En<5	1.035	1.041	1.035	1.450	1.244	0.996
1.1 MFP	.1<En<1	1.340	1.350	1.256	1.110	1.244	1.304
	total	1.127	1.132	1.115	1.147	1.144	1.114
Mo	10<En<20	0.857	0.859	0.890	0.889	0.894	0.824
60cm	5<En<10	0.835	0.854	0.664	0.809	0.709	0.688
ρ=2.15	1<En<5	0.918	0.921	0.991	1.015	0.993	1.296
1.5 MFP	.1<En<1	0.937	0.933	0.940	0.866	0.928	0.945
	total	0.899	0.900	0.923	0.904	0.922	0.965

W	10<En<20	0.906	0.908	0.920	0.920	0.920	0.902
40cm	5<En<10	0.604	0.614	0.643	0.656	0.720	0.740
ρ =4.43	1<En<5	0.788	0.786	0.876	0.882	0.879	1.106
0.8 MFP	.1<En<1	1.003	0.992	0.878	0.869	0.843	0.717
	total	0.901	0.900	0.892	0.891	0.886	0.884

experiment were observed for Cr and Cu, respectively. This could be explained by the difference of the total inelastic cross section values from those of JENDL-3.2. Though the cross section values of Mn in both JENDL-3.2 and BMCCS are similar, it turned out that BMCCS had no inelastic level inelastic cross section, ie, all the inelastic scattering cross section was considered as continuum. This should be a dominant cause for the odd shape in the calculated Mn spectrum.

EFF-2 calculation for Cr overestimated the experiment by about 24 %, whereas the other data files could predicted the experiment within about 10 %. As the difference between EFF-2 and other calculations mostly found in the spectra after single collision or 2 collisions as shown in Fig-4, the cause for this difference could be considered as the difference of the (n,2n) reaction of EFF-2.

6. CONCLUSION

Benchmark study to validate existing nuclear data files between 0.1 and 15 MeV neutron energy. The new data files could predict the experiment well in general for Li, Cr, Mn, Cu and Mo. For Al, Si, Zr, Nb and W, 10-20 % disagreement was The old libraries, i.e. ENDF/B-IV and ENDL-73 do not predict the experiment for Cr, Mn and Cu around 10 MeV neutron energy. This may be mainly caused by the problem in the discrete inelastic cross sections. However, the prediction is almost satisfactory in the other energy region. The new libraries-JENDL-3.2, JENDL Fusion file, EFF-2 and ENDF/B-VI could predict the experiment within 3 to 10 %.

	JENDL-3.2	BMCCS
Cr	707	808
Mn	526	520
Cu	560	456

Table-2 Total elastic cross section values at 14-MeV (mb)

REFERENCES

1) BRIESMEISTER, J.F. (ed.): LA-1265-M (1993)
2) SHIBATA, T., et al.: JAERI 1319, (1990)
3) NAKAJIMA, T., et al.: J. Nuclear Science and Technology, 32[12], 1259 (1995).
4) PASHCHENCO, A.B., et al.: FENDL/E-1.0, IAEA-NDS-128 Rev 2., (1995
5) LEMMEL, H.D., et al.: IAEA-NDS-170, (1995)
6) SUMITA ,K., et al.: Nuclear Science and Engineering., 106, 249 (1990).
7) TAKAHASHI, et al.,: OKTAVIAN Report C-83-02, (1983)
8) MACFARLANE, R.E. et al.: IAEA-NDS-169, (1995).
9) KOSAKO, K., et al.: JAERI-M 91-187, (1991).
10) KOSAKO, K., et al.: JAERI-Data/Code 94-020, (1994).
11) KOSAKO, K., et al.: JAERI-Conf 96-005, (1996)
12) BNL-NCS-17541, (1975)
13) HOWERTON, R.J., et al.: UCRL-50400, vol-15, (1975)
14) HOWERTON, R.J., et al.: UCRL-50400, vol-15, (1986)
15) ROSE, P.F. (ed.): 4th Edition of BNL-NCS-17541, (1991).
16) MANOKHIN, V.N. et al.: IAEA-NDS-90 Rev. 8, (1994)

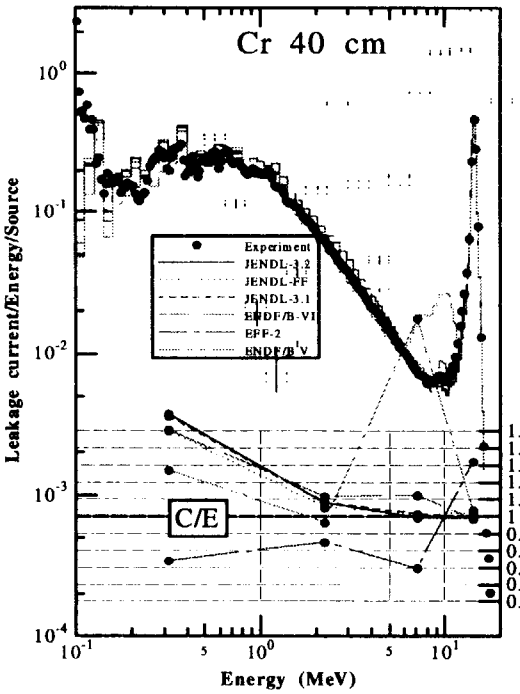

Fig.1 Cr Spectra and C/E

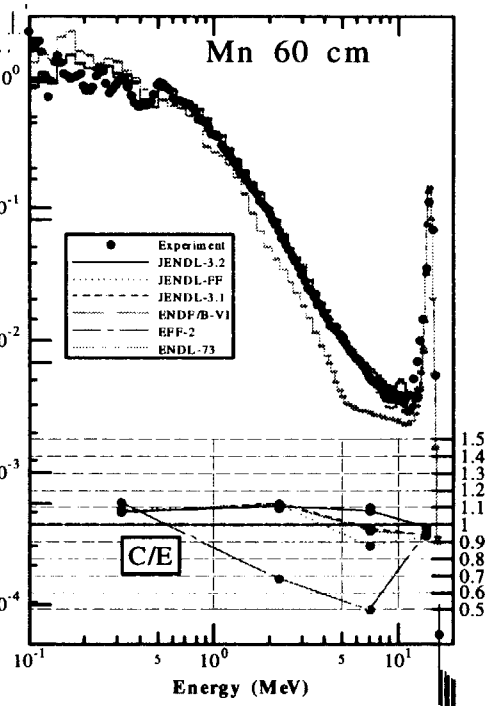

Fig.2 Mn Spectra and C/E

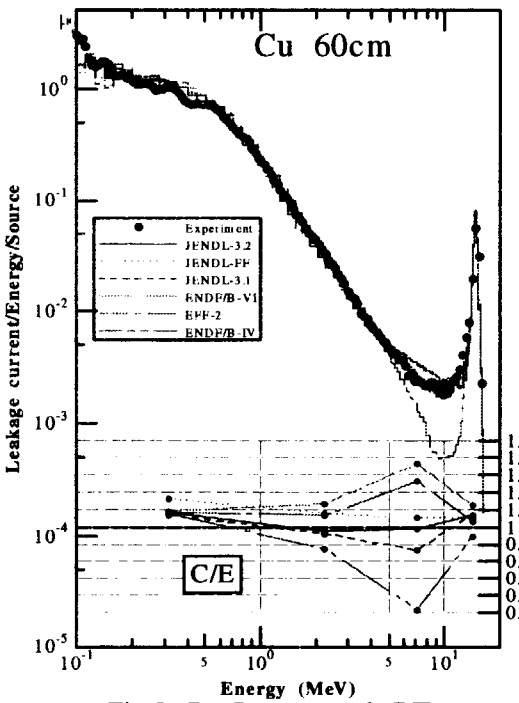

Fig.3 Cu Spectra and C/E

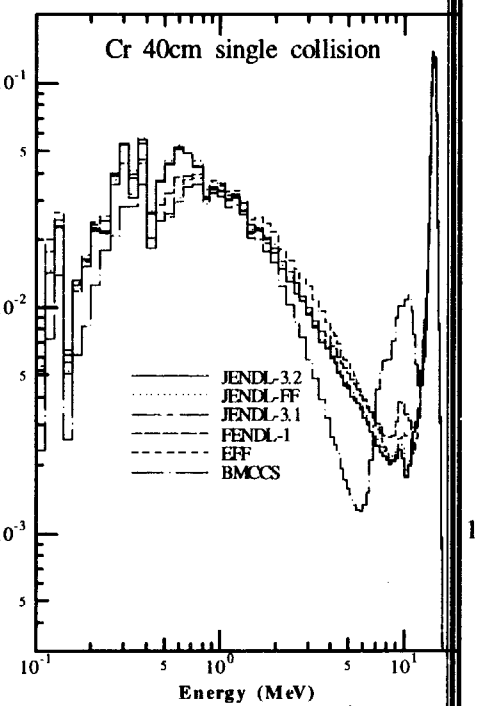

Fig.4 Cr Spectra after single collision

3.9 Helium Production Cross Section Measurement of Pb and Sn for 14.9MeV Neutrons

Yoshiyuki TAKAO, Toshihiro FUJIMOTO, Shuji OZAKI,
Masatomo MURAMASU and Hideki NAKASHIMA
Department of Energy Conversion Engineering, Kyushu University
6-1 Kasuga-Kouen, Kasuga-Shi, Fukuoka 816, Japan
E-mail: takao@ence.kyushu-u.ac.jp

Yukinori KANDA
Oita National College of Technology
1666 Maki, Oita, 870-01, Japan

Yujiro IKEDA
Department of Reactor Engineering, Japan Atomic Energy Research Institute,
Tokai-mura, Naka-gun, Ibaraki-ken 319-11, Japan

Helium production cross sections of lead and tin for 14.9MeV neutrons were measured by helium accumulation method. Lead and tin samples were irradiated with FNS, an intense d-T neutron source of JAERI. The amount of helium produced in the samples by the neutron irradiation was measured with the Helium Atoms Measurement System (HAMS) at Kyushu University. As the samples contained a small amount of helium because of their small helium production cross sections at 14.9MeV, the samples were evaporated by radiation from a tungsten filament to decrease background gases at helium measurement. Uncertainties of the present results were less than $\pm 4.4\%$. The results were compared with other experimental data in the literature and also compared with the evaluated values in JENDL-3.2.

1. Introduction

In design for structural materials of fusion reactors, helium production cross sections are required to predict the property changes and the life of the fusion materials. The structural materials such as a first wall are exposed to heavy irradiation of high-energy neutrons and are damaged by gas production reactions induced by neutrons. Helium production reaction is especially important, because the produced helium causes mechanical property changes and embrittlement of the structural materials. Although helium production cross sections are important by these reasons, the experimentally measured ones are few.

Helium accumulation method is one of the useful techniques to measure helium production cross sections, because helium production cross sections are directly determined from the amount of helium produced in samples by neutron irradiation. We have been measured helium production cross sections by this method and by using the Helium Atoms Measurement System (HAMS)[1].

In the present study, Lead and tin samples were irradiated with 14.9MeV neutrons with FNS, an intense d-T neutron source of JAERI. The amount of helium produced in

the samples by the neutron irradiation was measured with the HAMS at Kyushu University and helium production cross sections of lead: Pb(n,He) cross section, and tin: Sn(n,He) cross section, were determined. Lead and tin are minor constituents of stainless steels; however, helium production cross sections for many elements are required in detailed structural material design. The irradiated lead and tin samples contained very few helium atoms ($<10^{10}$ He atoms) because of their small helium production cross sections, so the samples were vaporized with using a special furnace of a radiant heat type. The furnace is available for a sample, which has a low melting point, to evaporate it without producing a large amount of background gases.

2. Experimental

2.1. Sample Preparation

Pb samples had a size of $12\times8\times0.5mm^3$ and a nominal chemical purity of 99.999%. Sn samples had a size of $12\times8\times1mm^3$ and a nominal chemical purity of 99.999%.The samples were cut out of as-given plates of natural material. Three Pb samples were covered with a Pb plate (thickness of 0.5mm, a nominal chemical purity of 99.999%). Three Sn ones were also done with a Sn plate (thickness of 0.5mm, a nominal chemical purity of 99.999%). This structure of the covered samples got rid of the outgoing phenomenon of energetic α-particles produced by nuclear reactions from the sample surface. The incoming α-particles from the cover plate canceled out the outgoing ones from the samples. These samples and covers were cleaned ultrasonically in an acetone bath for 20 minutes and were then heated at a pressure of less than 7×10^{-4}Pa for an hour of outgassing at 553K(Pb) and 473K(Sn). The covered samples and Nb foils for neutron fluence monitors were assembled into a sample set. We measured the produced He atoms in the samples after removing the cover plates from the covered samples.

2.2. Neutron Irradiation

The sample set were irradiated by d-T neutrons at Fusion Neutronics Source (FNS) of an intense d-T neutron source at Japan Atomic Energy Research Institute (JAERI). The sample set was set at the neutron emission angles of 20° and the distance of 3cm from the neutron source. Neutron energy was 14.9MeV at the positon. The arrangement of the sample set in the neutron irradiation field and the arrangement of the samples in the sample set are shown in Fig.1. Neutron energy was determined with MORSE-DD of a Monte Carlo code. The neutron fluence decided by referring to the $^{93}Nb(n,2n)^{92m}Nb$ cross section of 455mb$\pm$2%[2] and was ranged from 4.2×10^{15} to 7.5×10^{15} n/cm^2.

2.3. Helium Atom Measurement

The amount of He atoms accumulated in the samples were measured with the HAMS. Figure 2 shows the block diagram of the HAMS. The HAMS consisted of three blocks: a gas releaser, a mass spectrometer, and a standard He supply. Each block was evacuated with a turbo-molecular pump to keep it at an ultra-high vacuum. We used the special furnace of a radiant heat type (Fig.3), because the samples contained very few helium atoms. By using it, very low level helium can be detected because of low level background gas. In the case of a resist heat type furnace, a sample was heated on a evaporating boat and the boat was damaged by alloying with molten sample. The damaged evaporating boat produced a large amount of background gases from itself and from the inside wall, heated unexpectedly, of the furnace. In the case of a radiant heat

type one, a sample was put on a Cu boat under a W filament and was evaporated by the radiation from the electrically heated filament. The filament was not damaged by alloying. The gas released from the sample was purified with the trap of Ti-getter pump. The purified gas was then admitted into the quadrupole mass spectrometer (QMS), controlled by a personal computer (PC), and was analyzed to determine the mass distribution. The obtained mass distribution was converted into the numerical data. The data was stored in the PC and was displayed on the CRT of the PC. The number of He atoms was calculated from the integration of the mass 4 current in the mass distribution.

The efficiency of the HAMS in He measurement was calibrated by a series of measurements of standard He gases: a known amount of He gas prepared with the standard He supply.

2.4. Experimental Errors

The overall errors for the measurement of individual samples were estimated to be 4.3%(Pb) and 4.4%(Sn). Major errors were 2% for the ^{93}Nb(n,2n) cross section[2], ~1.5% for the γ-ray counting efficiency, 2~2.5% for the γ-ray counting statistical uncertainty, 1.5% for the fluctuation of He measuring efficiency of the QMS, 2.3% for the calibration of the HAMS, and 0.7%(Pb) for the fluctuation of the mass-4 background and 1.2%(Sn) for it. The measurement uncertainties are summarized in Table 1.

3. Results and Discussion

The results of this measurement are shown in Fig.4 and 5 together with cross sections measured in available experiments and the most recent evaluations (JENDL-3.2) of the Pb(n,He) and Sn(n,He) excitation function from 13.5 to 15MeV.

Pb(n,He) cross section has been measured by Kneff et al.[3]. The Kneff et al. is in good agreement with the present measurement. Yu et al.[4] and Maslov et al. [5] measured ^{206}Pb(n,α)^{203}Hg cross sections by activation method. Both the results are discrepant. Coleman et al.[6] measured ^{208}Pb(n,α)^{205}Hg with activation measurement. Those results by activation method cannot compared with our result directly, but the results supports our result for the Pb(n,He) cross section.

Sn(n,He) cross section has been measured by Kneff et al.[3]. The kneff et al.; their value is higher than our measurement. Activation measurements have been made for (n, α) reactions in two of the ten stable tin isotopes. Yu[7] measured ^{120}Sn(n,α)^{117}Cd cross section. Ikeda et al.[8] measured ^{120}Sn(n,α)^{117m}Cd and ^{120}Sn(n,α)^{117g}Cd cross sections. Both results agree with in the error. ^{118}Sn(n,α)^{115g}Cd cross sections were measured by Levkovskii et al.[9] and Bayhurst et al.[10]. These results by activation measurements cannot be compared with our results, but support our measured result.

The comparison with the evaluated values of JENDL-3.2 indicates that the JENDL-3.2 values are almost higher than the present measurements.

References

[1] TAKAO,Y., KANDA,Y.: *Rev. Sci. Instrum.*, **67**[1], 198(1996).

[2] IKEDA,Y., KONNO,C., OYAMA,Y., KOSAKO,K., OISHI,K., MAEKAWA,H.: Absolute Measurements of Activation Cross Sections of ^{27}Al(n,p)^{27}Mg, ^{27}Al(n,α)^{24}Na, ^{56}Fe(n,p)^{56}Mn, ^{90}Zr(n,2n)$^{89m+g}$Zr and ^{93}Nb(n,2n)^{92m}Nb at Energy Range of 13.3~14.9 MeV, *J. Nucl. Sci. Technol.*, **30**[9], 870(1993).

[3] KNEFF,D.W., OLIVER,B.M., FARRAR IV,H., GREENWOOD,L.R.: *Nucl. Sci. Eng.*, **92**, 491(1986).

[4] YU,Y.W., GARDNER,D.G.: *Nucl.Phys.*, **A98**, 451(1967).

[5] MASLOV,G.N., NASYROV,F., PASHKIN,N.F.: Experimental Cross-Sections for Nuclear Reactions Involving Neutrons with Energies of About 14 MeV, Report YK-9, p.50, Jadernye Konstanty, Obninsk, USSR(1972); Nuclear Constants No.9, INDC(CCP)-42U,p. 10, International Nuclear Data Committee, Vienna (1974) (English translation).
[6] COLEMAN,R.F., HAWKER,B.E., O'CONNOR,L.P., PERKIN,J.L.: *Proc :Phys. Soc. (London)*, **73**, 215(1959).
[7] YU,Y.W.: *Diss. Abst. Int. B*, **27**, 4267(1967).
[8] IKEDA,Y., KONNO,C., OISHI,K., NAKAMURA,T., MIYADE,H., KAWASE,K., YAMAMOTO,H., KATOH,T.: Activation Cross Section Measurements for Fusion Reactor Structural Materials at Neutron Energy from 13.3 to 15.0 MeV Using FNS Facility, *JAERI 1312*, (1988).
[9] LEVKOVSKII,V.N., VINITSKAYA,G.P., KOVEL'SKAYA,G.E., STEPANOV,M.: *Yad. Fiz.*, **10**, 44(1969); *Sov. J. Nucl. Phys.*, **10**,25 (1970) (English translation).
[10]BAYHURST,B.P., PRESTWOOD,R.J.: *J. Inorg. Nucl. Chem.*, **23**, 173 (1961).

Table 1. Sources of uncertainty and uncertainties in the measured Pb(n,He) and Sn(n,He) cross sections.

	Sources of uncertainty	uncertainty (%)
Determination of neutron fluence	γ-ray counting statistics	±2.0~2.5
	Reference cross section of $^{93}Nb(n,2n)^{92m}Nb$	±2.0
	Efficiency of γ-ray counting	±1.0~1.5
Helium atoms measurement	Fluctuation of ^{4}He background	±0.7 (Pb) ±1.2 (Sn)
	HAMS absolute calibration (Uncertainty of Standard Gas and fluctuation of QMS efficiency)	±2.3
Combined uncertainty		±4.3 (Pb) ±4.4 (Sn)

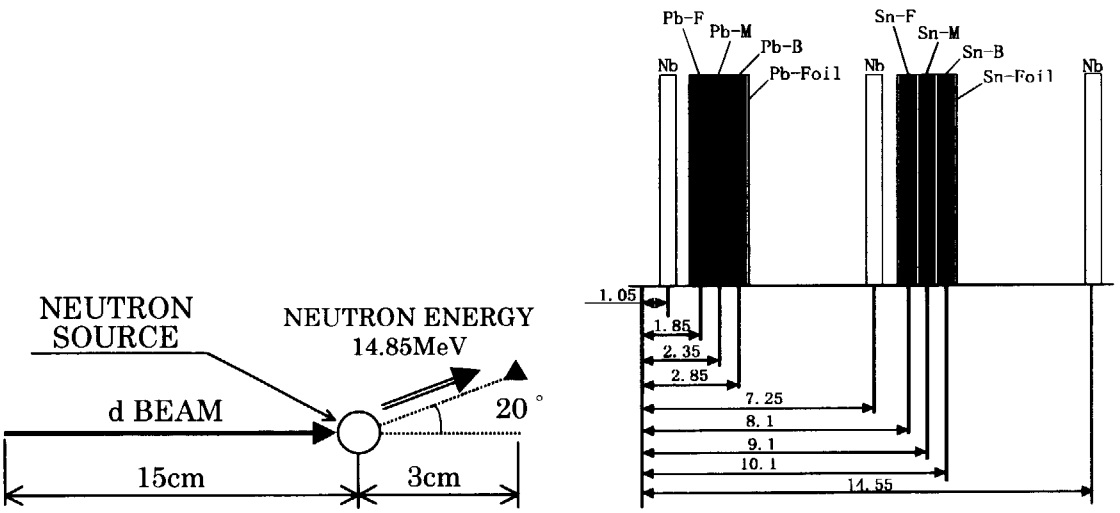

Fig.1. The sample setting position in the neutron field and the sample arrangement in the sample set.

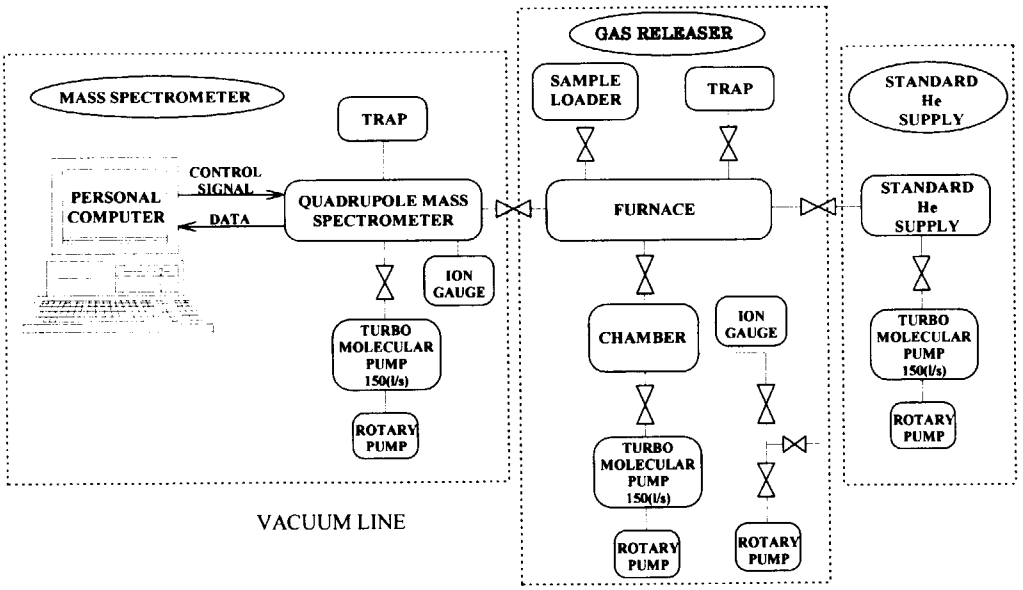

Fig.2. Block diagram of the helium atoms measurement system (HAMS).

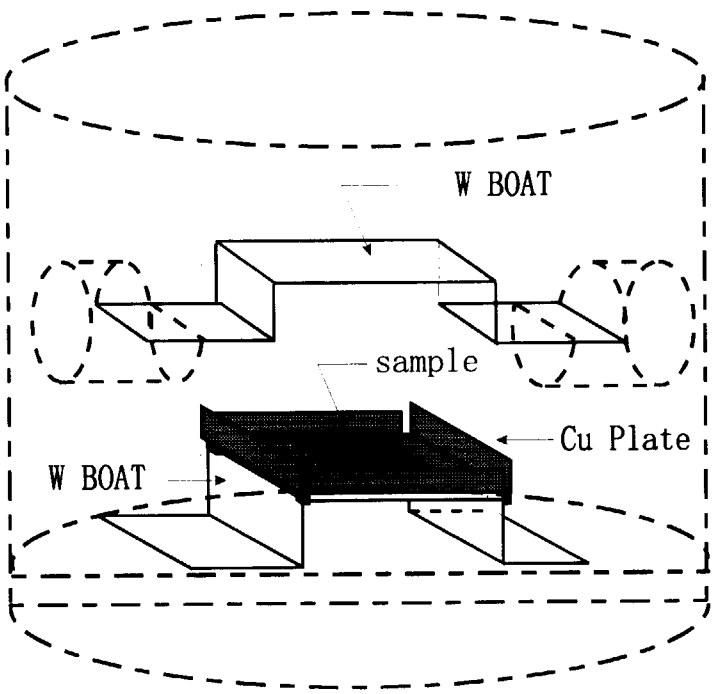

Fig.3. Arrangement of heating devices and a sample in the furnace.

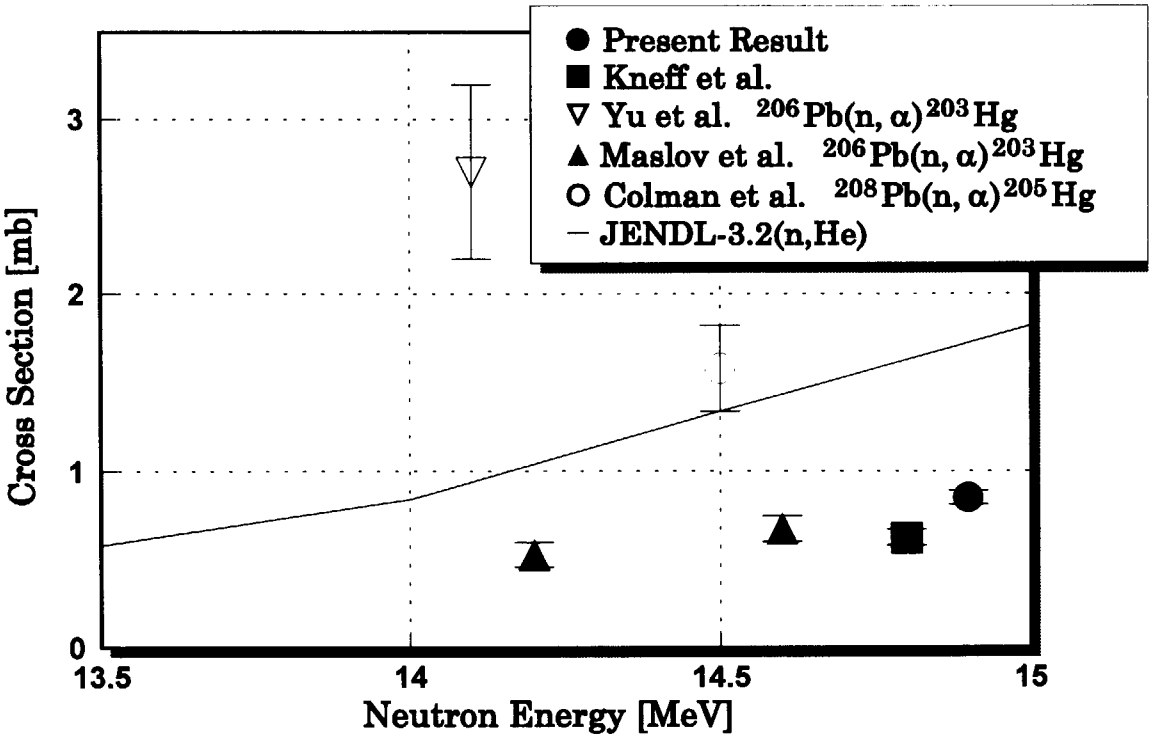

Fig.4. The measured result of Pb(n,He) cross section.

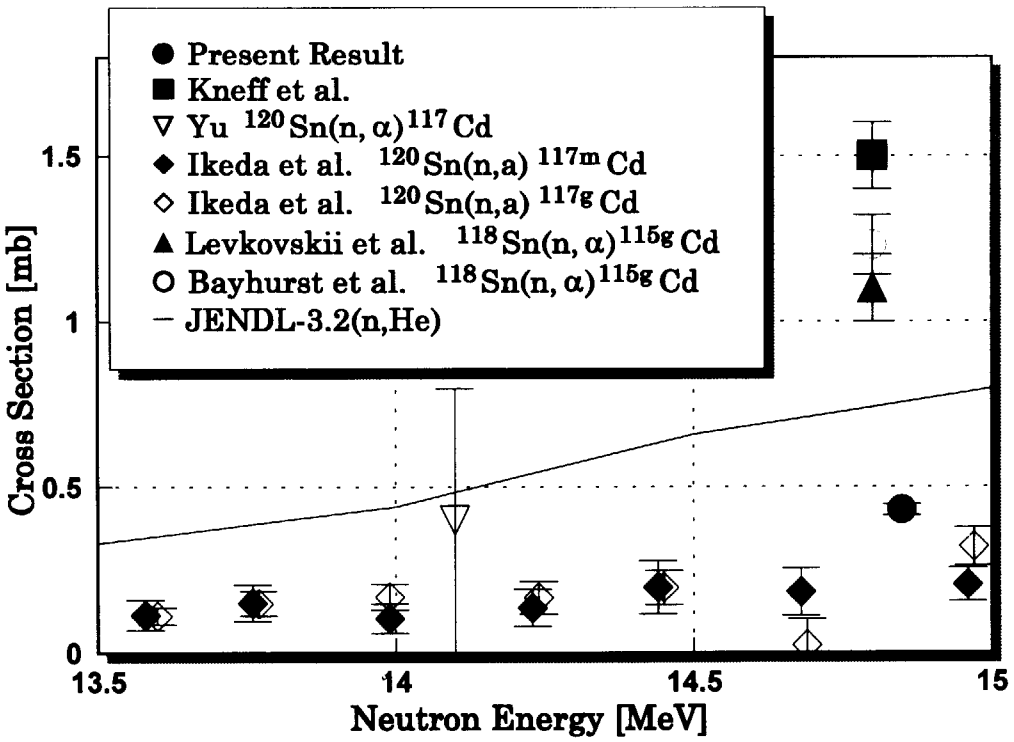

Fig.5. The measured result of Sn(n,He) cross section.

3.10 Apparatus to Measure Low Level Helium for Neutron Dosimetry

Shuji OZAKI, Yoshiyuki TAKAO, Masatomo MURAMASU, Tomoya HIDA,
Hirofumi SOU, and Hideki NAKASHIMA
Department of Energy Conversion Engineering, Kyushu University
6-1 Kasuga-Kouen, Kasuga-Shi, Fukuoka 816 Japan
E-mail: zacky@ence.kyushu-u.ac.jp

Yukinori KANDA
Oita National College of Technology
1666 Maki, Oita, 870-01, Japan

An apparatus to measure low level helium in a solid sample for neutron dosimetry in the practical use such as area monitoring in the long-term and reactor surveillance was reported. In our previous work, the helium atoms measurement system (HAMS) was developed. A sample was evaporated in the furnace and the released gas from the sample was analyzed with the mass spectrometer of the system to determine the amount of helium contained in it. The system has been improved to advance the lower helium measurement limit in a solid sample for its application to an area monitoring system. The mass of a solid is up to 100mg. Two important points should be considered to advance the lower limit. One was to produce a high quality vacuum in the system chamber for suppressing background gases during the sample measurement. The other important point was to detect very small output from the mass spectrometer. A pulse counting system was used to get high sensitivity in the mass 4 analyzing.

1. Introduction

The helium atoms measurement system (HAMS) was developed to measure He production cross sections in our previous work[1]. We obtained He production cross sections for several elements by measuring He atoms down to 10^{10} He atoms in a solid sample[2, 3] by using the system. The purpose of this work is to advance the lower helium measurement limit of the HAMS to less than 10^7 He atoms in a solid sample. The improvement is for applying this system to a new type of area monitoring system to which a He gas measurement method is employed. In the method, the amount of He produced in a dosimeter by neutron irradiation is measured with the absolutely calibrated mass spectrometer. The amount of He is in proportion to neutron fluence at the dosimeter-setting position and is independent of variation in neutron flux. The only He production cross section is, moreover, required to obtain absolute neutron fluence value.

Two important points should be considered to achieve the lower limit described above. One is to produce a high quality vacuum in the system chambers to decrease the background gas during the sample measurement. The other is to detect very small output from the mass spectrometer. A pulse counting system is applied to get high sensitivity in the mass 4 analyzing. This paper presents the detail description of architecture of the improved HAMS and preliminary results of performance tests.

2. Apparatus

A block diagram of the HAMS is shown in Fig.1. The HAMS is composed of three blocks, which are a gas releaser, a mass spectrometer, and a standard He supply. The measurement procedure is described briefly as follows. A solid sample containing He is set in the furnace of the gas releaser and is evaporated. The released gases are purified with a trap of the gas releaser and then are introduced into the mass spectrometer to measure the amount of He in the sample. The mass spectrometer has a quadrupole mass spectrometer (QMS), a digital electrometer, a multichannel analyzer and a personal computer which controls the QMS and stores data from the digital electrometer or the multichannel analyzer, and additional information. The sensitivity of HAMS to He is calibrated by measuring standard He. The standard He is produced by using the standard He supply.

2.1. Vacuum evacuation

Vacuum vessels of the HAMS are redesigned to decrease background gases at the He measurement. They are made by welding their parts at the inside of the parts and their inside walls are cleaned by emery polishing and electric polishing. The total volume of the HAMS vessels is decreased and the pumping speed from the vessels is increased. The three blocks (the gas releaser, the QMS, and the standard He supply) have individual turbo-molecular pumps to keep them at the high quality vacuum. The QMS block, especially, has tandem jointed turbo-molecular pumps and is evacuated to lower than 1.2×10^{-8} Pa. The tandem jointed pumps also pump the gas releaser. Two Ti-getter pumps cooled by liquid nitrogen are attached to the gas releaser and the QMS to trap the background gases and purify the released gas. Valves employed in this system are metal seal valves to prevent He permeation.

2.2. Gas releaser

The gas releaser is composed of a furnace, a sample loader, and a trap. The furnace is a device for releasing He from the solid sample by vaporizing it. The furnace has a pair of electrodes and a shield. An evaporating boat which is heated electrically is located between the electrodes which are made of stainless steel 304. The material of the evaporating boat is selected from tungsten, molybdenum, tantalum and graphite and is chosen according to the melting point and the element of the sample.

2.3. Mass spectrometer

The mass spectrometer is composed of a quadrupole-type mass spectrometer (QMS), a personal computer, a digital electrometer, a multichannel analyzer, and a trap. The QMS is adjusted to be able to measure the mass from 1 to 6 in atomic mass units with the mass analyzing power of 0.025amu(10% valley).

The released gas is introduced into the QMS from the furnace, is purified again with the trap in the QMS, and is then analyzed. The output current is amplified by a pulse counting type of secondary electron multiplier (gain: $<1 \times 10^{8}$) with which the QMS is equipped, and led to the digital electrometer or the multichannel analyzer. The improved HAMS operates in the current measurement mode or the pulse counting mode. The pulse counting by a multichannel analyzer is applied to measure the very small amount of He of less than 10^{10}. The computer code for these procedures can control and compute the timing for measurements and the processing for preparations of the standard He gas when we input the operating conditions.

2.4. Traps

The traps are Ti-getter pumps cooled with liquid nitrogen, which have a nominal total pumping speed of 11.5 l/s, and have two kinds of roles to purify the sample gas and to keep the devices at an ultra-high vacuum during He measurement. When we operate HAMS, the QMS and the furnace are isolated from the turbo-molecular pumps in order to increase the sensitivity to gases.

The Ti-getter pump works in either a dynamic mode or a static mode. In the dynamic mode, the Ti-filament is emitting Ti vapor and is producing new Ti-film on the inside wall of its vessel all through the He measurement. In the static mode, a fresh Ti-film is produced once just before isolating the pump and is used throughout the operation. The dynamic mode is preferable because the pumping speed is expected to be steady. The flashing of the Ti-filament, however, generates the background of the mass-4 equivalent to about $1x10^8$ He atoms. Therefore, The static mode is used in He measurement of less than $1x10^{10}$ He atoms. In this mode, we must pay attention to the amount of gases released from a sample because excess sample gases sometimes can not be pumped out and then saturate the QMS.

2.5. Standard He supply

Figure 2 shows a block diagram of the standard He supply producing the standard He which is used to calibrate HAMS absolutely. Standard He in the range of 1×10^9 to 5×10^{15} He atoms can be produced in a routine manner described below.

The standard He supply comprises four vessels: the glass standard volume vessel (V1), the sub-standard vessel (V2), the inlet vessel (V3), and the dilution vessel (V4) and three absolute pressure gauges. The furnace is used as the fifth vessel in producing the standard He, so it is called V5. These vessels are made of stainless steel and connected with all metal-sealed valves and flanges except the glass standard vessel and its cock valve, which are made of Pyrex glass. Farrar IV et al.[4] used aluminosilicate glass for their vessels which are long-term storage vessels for standard He instead of Pyrex glass to prevent He contained in the atmosphere from permeating through the vessel wall. The permeating He increases the amount of the standard He and causes undesirable uncertainty. In our apparatus, Pyrex glass is employed only for the glass standard volume vessel, which is not used in preparing the standard He but just in determining the volume of the other vessels.

To prepare the standard He, we must know the volumes of the five vessels, V1 ~ V5, whose volumes are also represented as V1 ~V5, respectively. The volume of V1 is 20.254 cm^3 determined by measuring the net weight when it is filled with distilled water. The volumes of V2 ~ V5 are determined by comparing the pressure of filled He and that after expanding the He into the relating volume and referring to the volume of V1 with Boyle's law. It can be assumed that the experimental conditions about the temperature are the same. The absolute pressure gauges are two diaphragm-type gauges and a spinning-rotor gauge. One of the diaphragm-type gauges has a measurable maximum range of ~ 1330 Pa with the uncertainty of 0.3% and the other has a range of ~ 13.3 Pa with 0.1%. They are suitably used to prepare the standard He so as to decrease the uncertainty for the resultant standard He. The spinning-rotor gauge is used to calibrate other gauges because of its good long-term stability.

3. Performance

Many standard He gases in the range of 1×10^{10} ~1×10^{13} He atoms were produced with the standard He supply and were measured with the HAMS in the current measurement mode. These results with a regression curve are shown in Fig.3. QMS output is converted into the real number of He atoms by this curve. The curve indicates a good linearity and fluctuation of the He measurement efficiency of the HAMS is improved.

Figure 4 shows a result of background measurement in the pulse counting mode at mass number of 4.000amu. The result contains both pulses caused by electric noise and ones by background gases. The total number of pulses corresponds less than $1x10^9$ He atoms. It is important to eliminate the electric noise and to optimize some parameters such as SEM gain and time constants of pulse shaping, for achieving reliable measurement.

References

[1] Takao Y., Kanda Y.: Rev. Sci. Instrum., **67** 198(1996).
[2] Takao Y., Kanda Y., Uenohara Y., Takahashi T., Itadani S., Iida T., Takahashi A.: J. Nucl. Sci. Technol., **34**[1], 1(1997).
[3] Takao Y., Kanda Y., Hashimoto H., Yamasaki K., Yamaguchi K., Yonemoto T., Miwa M., Etoh H., Nagae K.: J. Nucl. Sci. Technol., **34**[2], 109 (1997).
[4] Farrar IV H. and Oliver B. M.: J. Vac. Sci. Technol. A **4**, 1740(1986).

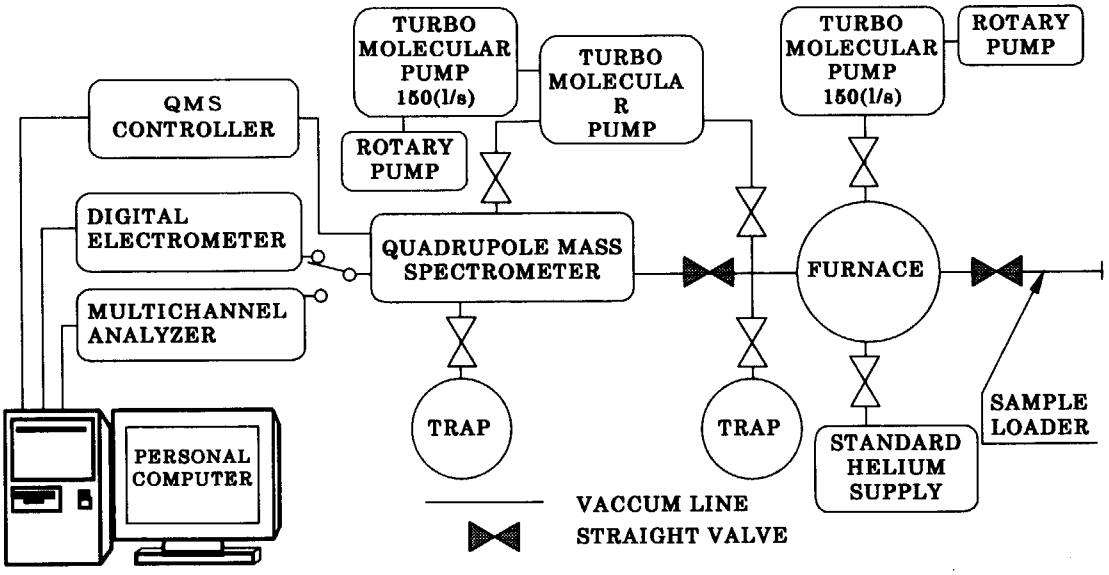

Fig.1 A block diagram of the Helium Atoms Measurement System

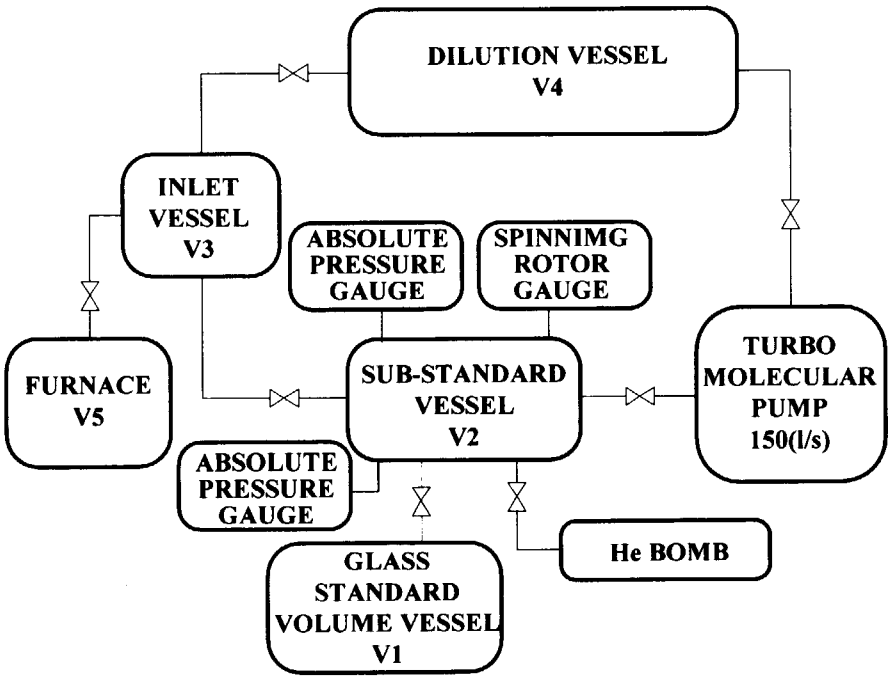

Fig.2 A block diagram of Standard He Gas Supply

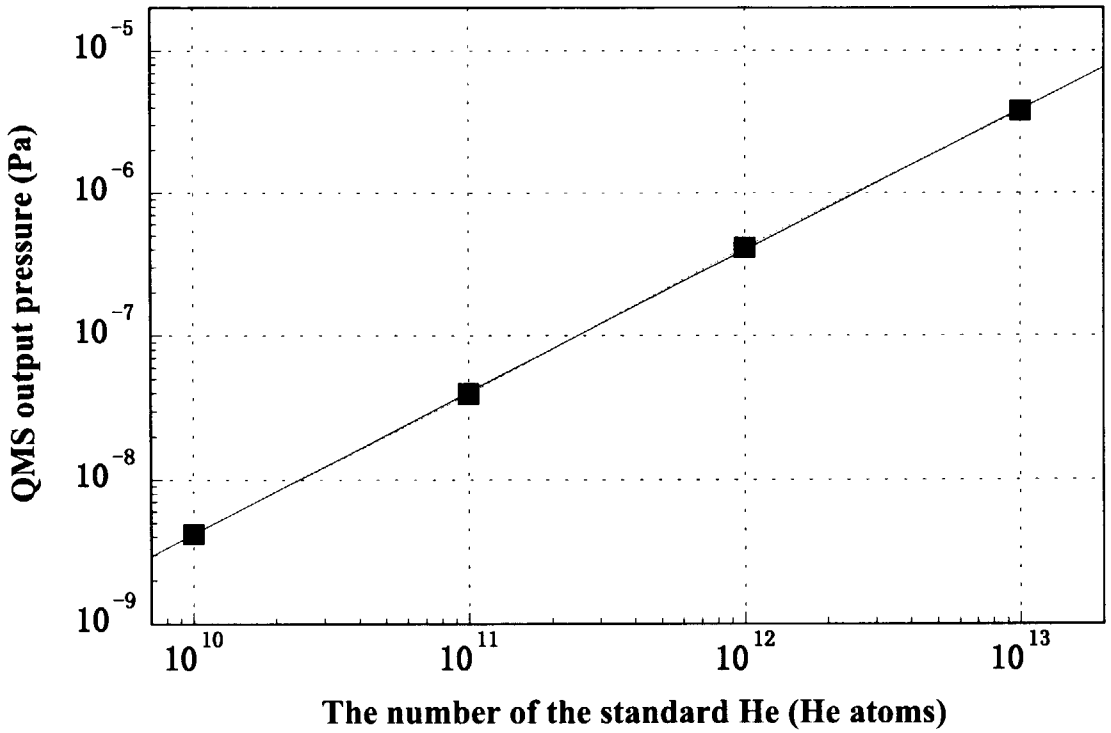

Fig.3 The results of standard He measurement in the range of $1\times10^{10}\sim1\times10^{13}$ He atoms

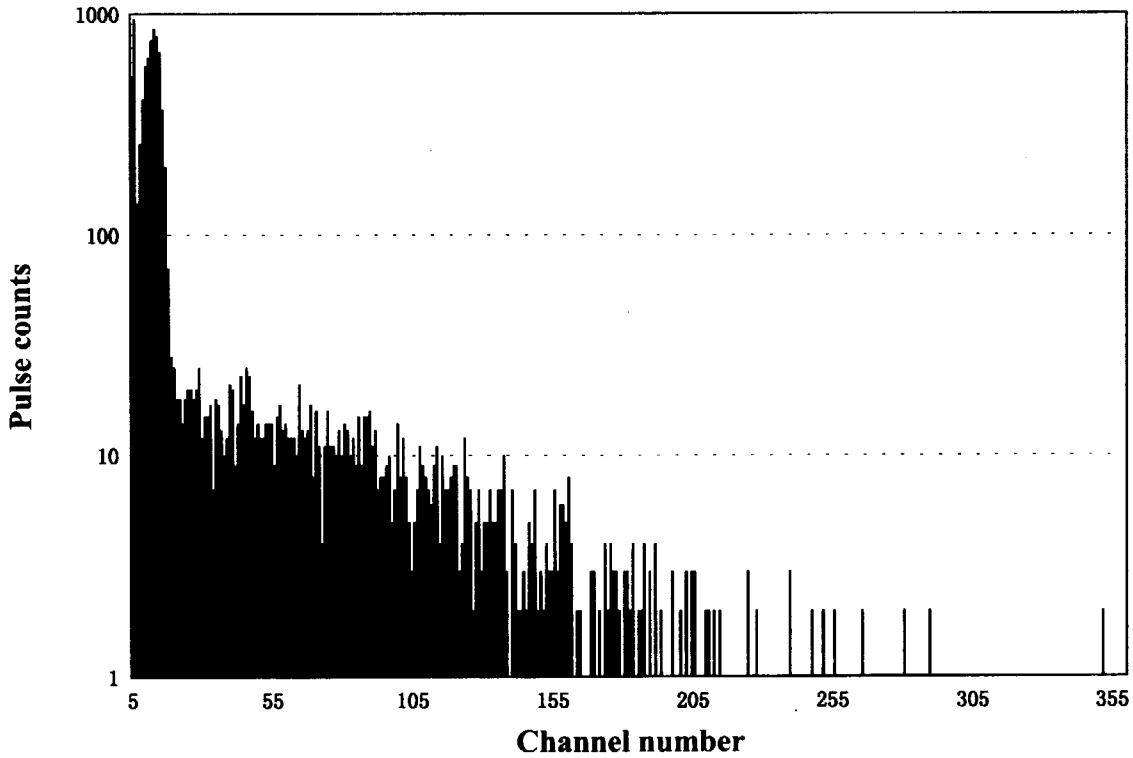

Fig.4 The result of a background measurement in the pulse counting mode

3.11 (n,α) cross section measurement of light nuclei using gridded ionization chamber and gaseous sample

Toshiya Sanami, Mamoru Baba, Keiichiro Saito, Yasutaka Ibara*,
Tetsuro Yamazaki, Jun Sato, Naohiro Hirakawa
Quantum Science and Energy Engineering, Tohoku University, Sendai 980-77

e-mail : toshi@rpl.qse.tohoku.ac.jp, mamoru.baba@qse.tohoku.ac.jp

We have developed a measuring method of (n,α) cross section by using gaseous sample in a gidded ionization chamber. In this study, we measured the $^{12}C(n,\alpha_0)$ and the $^{16}O(n,\alpha_0)$, (n,α_{123}) cross sections for En=11.5 and 12.8 MeV neutrons. We also deduced the $^{12}C(n,x\alpha)$ spectrum and analyzed the data by a kinematic calculation combined with the reaction data of the $^{12}C(n,n'3\alpha)$.

1. Introduction

Neutron induced α production cross section data of light nuclei are required in various fields, i.e, nuclear engineering, biological and medical fields. In spite of the importance of the data, there are few experimental data, even for C, O and N, in En=10-20 MeV region, probably because of experimental difficulty and the unavailability of an appropriate foil sample of ^{16}O and ^{14}N. In addition, theoretical calculations are ambiguous in estimation of the cross section. This condition causes large uncertainty in experimental data and evaluations.

We have conducted the measurements of (n,xα) cross sections of Fe, Ni, Cr and Cu by a gridded ionization chamber (GIC) and foil samples [**1,2**]. Recently, we have extended the measurements to light nuclei by using gaseous samples. This method enables cross section measurements in a very large solid angle without distortion by the energy loss in samples, but requires a method to estimate the effective number of sample atoms and the magnitude of the wall effects [**3**]. We found the method to eliminate the effects by using GIC signals and a tight neutron collimation. In this study, we describe the recent results of the $^{12}C(n,\alpha_0)$ and the $^{16}O(n,\alpha_0)$, (n,α_{123}) cross sections for 11.5 and 12.8 MeV neutrons. We also present the analysis of the $^{12}C(n,x\alpha)$ spectrum for 14.1 MeV neutrons to estimate the $^{12}C(n,n'3\alpha)$ reaction process.

2. Experimental method

The experiments were carried out at Tohoku University 4.5MV Dynamitoron accelerator laboratory.

---

* Present address : Kandenko co.,ltd.

Experimental method is same as in the former experiments in Ref. 3. Neutrons of 11.5 and 12.8 MeV were produced via the $^{15}N(d,n)^{16}O$ reaction in a $^{15}N_2$ gas target. The neutrons are quasi mono-energetic, but the 11.5 and 12.8 MeV neutrons are apart about 6 MeV from contaminate neutrons feeding to the excited states of residual nuclei ^{16}O [4]. Therefore, we can treat the source neutron to be monoenergy for the $^{12}C(n,\alpha)$ and the $^{16}O(n,\alpha_0)$, (n,α_{123}) reactions with high threshold energy. The neutrons were collimated with a 15 cm long Cu collimator to irradiate sample gases contained in a counting gas of GIC. The counting gas is $Kr+CH_4$ and $Kr+CO_2$ mixtures to measure the $^{12}C(n,x\alpha)$ and $^{16}O(n,x\alpha)$, respectively. Alpha particles from the sample gas ionize the counting gas and produce two output signals, Pa and Pc (anode and cathode, respectively). If alpha particles are produced and stopped between the cathode and the grid electrode, Pa and Pc are represented by the following equations,

$$Pa=Ca\cdot(E+\sigma Pc) \quad \text{and} \quad Pc=Cc\cdot E(1-x/d), \qquad (1),(2)$$

where, Ca and Cc are the amplitude factor of the anode and the cathode, respectively, E is the particle energy, σ is the grid inefficiency (5.9%), x is the distance between the cathode plate and the center-of-gravity of electrons (detection position). By choosing an appropriate gas pressure and combining Pa and Pc, we can find the detection position (x) of each event to pick up the events that give full energies to GIC.

$$x=d\cdot(1-Ca\cdot Pc/(Ca\cdot Pa+\sigma\cdot Ca\cdot Cc\cdot Pc)) \qquad (3)$$

By this method and the tight neutron collimation, we can determine the number of sample atoms irradiated by neutrons.

The running time was about 3 and 9 hours with 4μA beam current of D^+ ion for 11.5 and 12.8 MeV measurement, respectively. Alpha yields in a central volume of GIC were selected by using the anode and the cathode signals according to eq.3. The number of sample atoms was determined from the neutron beam profile and the volume of the sample region. The neutron profile was measured with an imaging plate [5], and the neutron flux was measured with a recoil-proton counter telescope [6].

3. Data reduction and error estimation

Fig. 1 shows a two-dimensional spectrum of the 3.0 kgf/cm^2 $Kr+CH_4$ gas for 14.1MeV neutrons. The events from the $^{12}C(n,\alpha_0)^9Be$ reaction forms the vertical strip because the anode signal shows sum energy of the α_0 and the ^9Be particle. The $^{12}C(n,n'3\alpha)$ events show continuous distribution because neutrons do not deposite an energy in GIC. The background events from H(n,p) and Kr(n,α) were also observed, but H(n,p) events exist only in the low energy region and Kr(n,α) events are negligibly few. Cross sections were deduced by

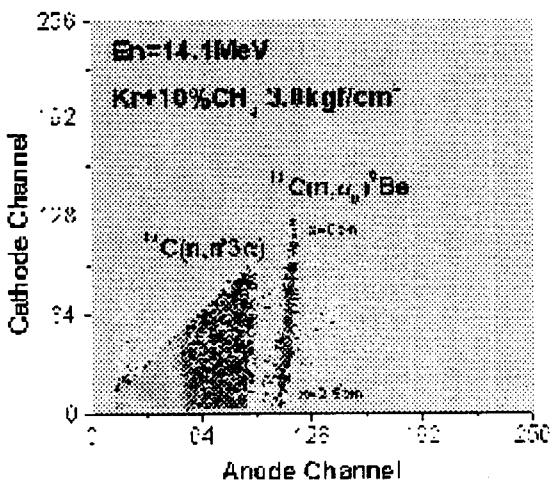

Fig. 1 Two dimensional spectrum of $Kr+10\%CH_4$

the relation,

$$Y=N\cdot\sigma\cdot\phi, \tag{4}$$

where Y is the yield in the center of GIC, N is the number of sample atom, σ is the reaction cross section, ϕ is the neutron flux measured by counter telescope. For the $^{12}C(n,\alpha_0)$ reaction, Y is obtained from the peak yield of the $Kr+CH_4$ spectrum. In the case of the $^{16}O(n,\alpha)$, it is obtained from the difference between the spectra for $Kr+CH_4$ and $Kr+CO_2$ [3]. We estimate errors from the counting statistics, the effective area and the normalization by the neutron flux. The total error is about 12% in the worst case.

4. Results and discussion

4-1.The $^{12}C(n,\alpha_0)$ cross sections

Fig. 2 shows the $^{12}C(n,\alpha_0)$ cross sections in comparison with other experimental results [7] and evaluations. There is no other experimental $^{12}C(n,\alpha_0)$ data around 12 MeV, but our data are consistent with evaluations and connects smoothly between the results in low and high energy. As shown later, the $^{12}C(n,\alpha_0)$ reaction is not a dominant process of the $^{12}C(n,x\alpha)$ above 10 MeV region. Therefore, the $^{12}C(n,n'3\alpha)$ process is important for the $^{12}C(n,x\alpha)$ cross section in this region.

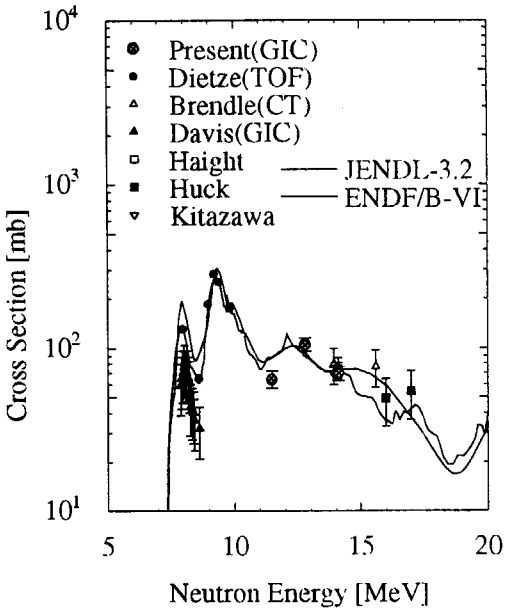

Fig. 2 $^{12}C(n,\alpha_0)$ cross sections

4-2. $^{12}C(n,n'3\alpha)$ spectrum

The $^{12}C(n,n'3\alpha)$ reaction has many reaction process [10][11]. In this study, we deduce a total energy spectrum of the $^{12}C(n,x\alpha)$ reaction and compare with a simple calculation. Figure 3 shows the energy spectrum of $Kr+CH_4$ gas for 14.1 MeV neutrons at various counting gas pressure. From high-pressure result, the $^{12}C(n,\alpha_0)$ peak and the $^{12}C(n,n'3\alpha)$ edge could be observed clearly, but low energy α events are hidden by protons form H(n,p) reaction. On the other hand, the peak and the edge disappear in the low-pressure result, but details of structures in low energy region can still be observed. Therefore, by the combining these two results, we can obtain the energy spectrum with little proton contamination. This spectrum also contains the recoil

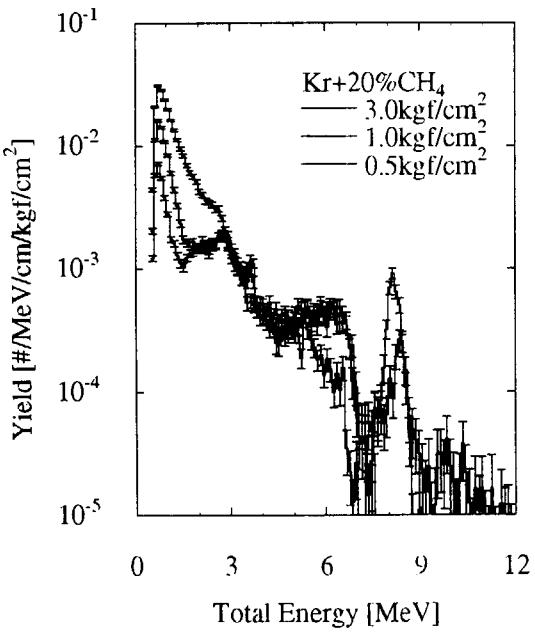

Fig. 3 $Kr+CH_4$ spectrum in various pressures

particles from the $^{12}C(n,n')^{12}C$ reaction.

To simulate the spectrum, we calculate the contributions of each reaction. The recoil ^{12}C from $^{12}C(n,n_{el})$ and $^{12}C(n,n_1)$ reaction, and α_0 energy spectrum are obtained by the kinematics calculation using the cross section data by JENDL-3.2 with the Gaussian smearing (0.5 MeV FWHM). About the $^{12}C(n,n'3\alpha)$ channel, dominant channels are as follows **[10,11]**.

(1) 2body + 3 body simultaneous decay : $^{12}C(n,n')\,^{12}C^*_{Ex}$, $^{12}C^*_{Ex} \rightarrow 3\alpha$

(2) 2body + 3body simultaneous decay : $^{12}C(n,\alpha)\,^{9}Be_{Ex}$, $^{9}Be_{Ex} \rightarrow 2\alpha+n$

(3) 3body + 2body sequential decay : $^{12}C(n,n'\alpha)^{8}Be$, $^{8}Be \rightarrow 2\alpha$

The sum energy of 3α, $E_{3\alpha}$, is the calculated by following equation,

$$E_{3\alpha}=E_{in}+Q_{(n,n'3\alpha)}-E_n\,,$$

where, E_{in} is the incident neutron energy, $Q_{(n,n'3\alpha)}$ is the Q-value of the $^{12}C(n,n'3\alpha)$ reaction and E_n is the ejected neutron energy. The calculation for process (1) was done by 2-body kinematics using the (n,n') data in JENDL-3.2. The 3-body simultaneous decay (2) and (3) was calculated based on a 3-body phase space model **[8]**,

$$d\sigma/dE=C_0^2\cdot(E_{cm}\cdot(E_{max}-E_{cm}))^{1/2}\,, \qquad (4)$$

where, $d\sigma/dE$ is the energy spectrum of the center-of-mass system and E_{max} is the maximum kinematically allowed energy of the ejectile particle. The relationship of the two sequential process was considered by an analytical method **[9]**.

Fig. 4 and 5 shows the comparison between experimental results and calculation using the branching ratio in Refs. 9 and 10, respectively. In figure 4, the calculation considering the process (1) [only for Ex=9.63 MeV state] and (3) underestimates the high energy edge of the $^{12}C(n,n'3\alpha)$ reaction. In contrast, in Fig. 5, the calculation taking account of (1) [Ex is 7.66, 9.63, 10.1, 10.8, 11.1, 12.7 MeV] and (2) [Ex=2.43MeV] processes, are in fair agreement with the experiment around the edge. In the low energy part, the experimental data would still contain the proton contaminant by H(n,p).

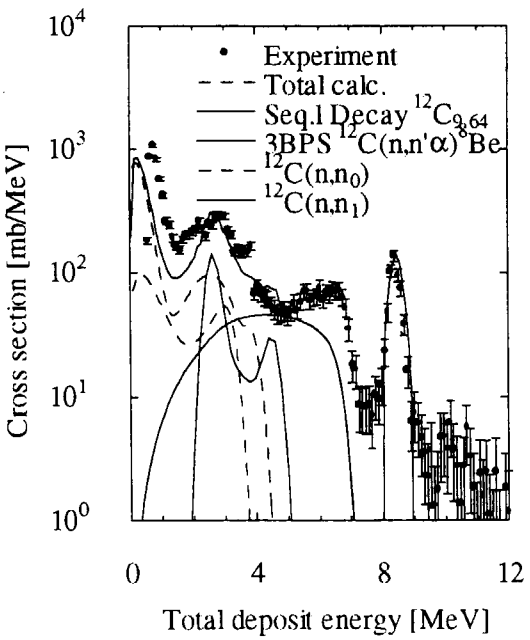

Fig. 4 $^{12}C(n,x\alpha)$ spectrum with calculation **[9]**

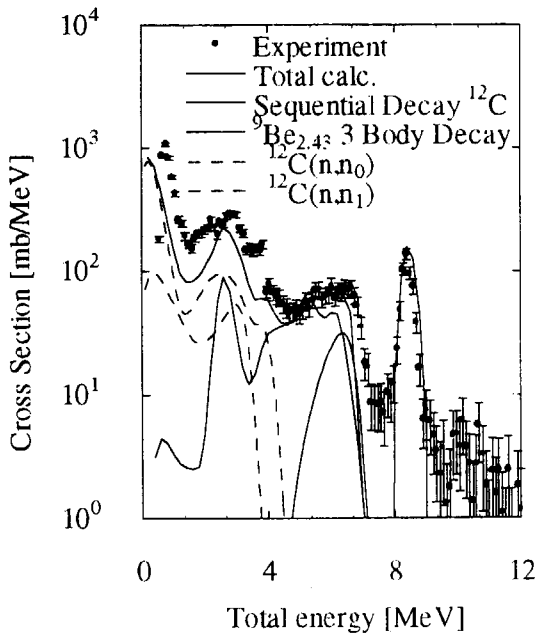

Fig. 5 $^{12}C(n,x\alpha)$ spectrum with calculation **[10]**

4-3. $^{16}O(n,\alpha)$ cross section

Fig. 6 and 7 show the $^{16}O(n,\alpha_0)$ and the $^{16}O(n,\alpha_{1,2,3})$ cross sections together with evaluations and other experimental results **[12-16]** by γ-detection and the counter telescope method. In Fig. 6, the present results are in fair agreement with others, but, about the $^{16}O(n,\alpha_{1,2,3})$ cross sections, there is some difference between present and orphan data.

Fig. 8 shows the result of the $^{16}O(n,x\alpha)$ cross section in comparison with the evaluations and other experimental results **[16-18]** by the emulsion, cloud chamber and scintillator method. In the case of ENDF/B-VI, the $^{16}O(n,x\alpha)$ cross section is given by the sum of the $^{16}O(n,\alpha_0)$, the $^{16}O(n,\alpha_{1,2,3})$ and some neutron inelastic scattering cross section. In the case of JENDL-3.2, the cross section is given by the sum of the $^{16}O(n,\alpha)$ and the $^{16}O(n,n'\alpha)$. In comparison between experimental data, the present value at 14.1 and 15.0 MeV are slightly smaller. The reason is that the $^{16}O(n,n'\alpha)$ cross section was obtained by summing the α events with channel energy below 4 MeV. Then, our values do not include the α events with low channel energy and might result in underestimation of the cross section.

From these results, the difference between the experimental values and JENDL can not be explained only by the difference in the $^{16}O(n,\alpha_0)$ and the $^{16}O(n,\alpha_{123})$ branch. Therefore, we can conclude that the key of the $^{16}O(n,x\alpha)$ cross section determination is the $^{16}O(n,n'\alpha)$ value.

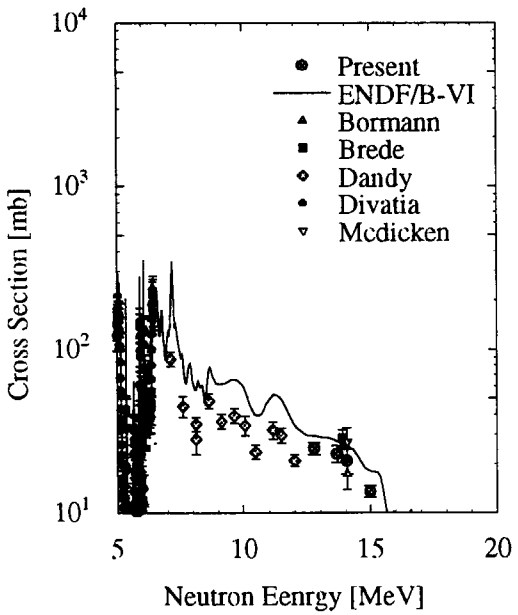

Fig. 6 $^{16}O(n,\alpha_0)$ cross sections

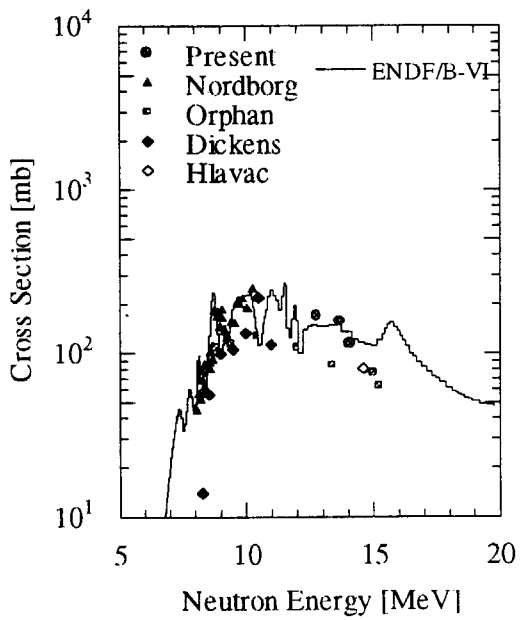

Fig. 7 $^{16}O(n,\alpha_{1,2,3})$ cross sections

5. Conclusion

In this study, we described the results of the $^{12}C(n,\alpha_0)$ and the $^{16}O(n,\alpha_0)$, (n,α_{123}) cross section for En=11.5

and 12.8 MeV by a measuring method using gaseous sample and GIC, and the analysis of $^{12}C(n,n'3\alpha)$ reaction. We should note that the method is useful for light nuclei cross section measurement.

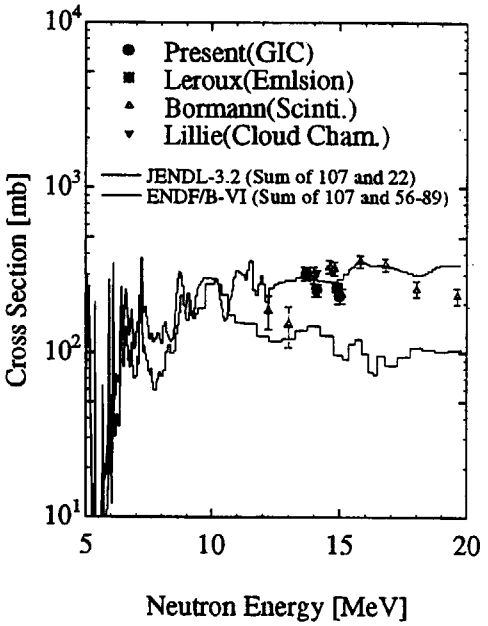

Fig. 8 $^{16}O(n,\alpha)$ cross sections

References

1. N.Ito, M.Baba, S.Matsuyama, I.Matsuyama and N.Hirakawa, *Nucle.Instrm. Methods*, **A337**, 474 (1994)
2. M.Baba, N.Ito, I.Matsuyama, S.Matsuyama, N.Hirakwa, S.Chiba, T.Fukahori, M.Mizumoto, Kazuo.Hasegawa and S.Meigo, *J.Nucl.Sci.Technol.*, **31**, 745 (1994)
3. T.Sanami, M.Baba, K.Saito, Y.Ibara and N.Hirakawa, *Proc.Int.Conf. on nucle Data for Sci. and Technol.* (Trieste, Italy 1997), to be published
4. J.L.Weil and K.W.Jones, *Phys.Rev.*, **112** 1775 (1985)
5. T. Sanami, M.Baba, K.Saito, Y.Ibara, A.Yamadera, S.Taniguchi, T.Nakamura and N.Hirakawa, *Proc. of 10th workshop on radiation detectors and their uses*, (KEK, Tukuba, 1997), p74
6. M.Baba, M.Takada, T.Iwasaki, S.Matsuyama, T.Nakamura, H.Ohguchi, T.Nakao, T.Sanami and N.Hirakawa, *Nucle.Instrm.Meth.*, **A376**, 115 (1996)
7. R.C.Haight, S.M.Grims, R.G.Johnson and H.H.Barschall, *Nucl.Sci.Eng.* **87**, 41 (1984)
8. G.G.Olsen, *Nucl.Instrm.Meth.*, **37**, 240 (1965)
9. M.D.Baker, H.D.Knox and E.reitenberger, *Nucl.Sci.Eng.*, **96**, 39 (1987)
10. B.Antolkovic, I.Slaus, D.Plenkovic, P.Maco and J.P.Meulders, *Nucl.Phys.*, **A394**, 87 (1983)
11. B.Antolkovic, G.Dietze and H.Klein, *Nucl.Sci.Eng.*, **107**, 1 (1991)
12. C.Nordborg and L.Nilsson: ,*Nucl.Sci.Eng.*, **66**, 75 (1978)
13. V.J.Orphan, C.G.Hoot and Joseph John, *Nucl.Sci.Eng.*, **42**, 352 (1970)
14. J.K.Dickens and F.G.Perey : *Nucl.Sci.Eng.*, **40**, 283 (1970)
15. S.Hlavac, P. Oblozinsky, I. Turzo, Ľ. Dostal and J. Kliman, private communication
16. B.Leroux, K.El-Hammami, J.Dalmas, R.Chastel, G.Lamot, C.Fayard and J.H.Boutros: *Nucl.Phys* **A116**. 196 (1968)
17. M.Bormann, S.Cierjacks, E.Fretwurst, K.-J.Giesecke, H.Neuert and H.Pollehn:*Z.Phys* **174**, 1 (1963)
18. A.B.Lillie, *Phys.Rev.* **87**, 716 (1952)

3.12 Some Remarks on Multigroup Library

Chikara KONNO, Fujio MAEKAWA and Masayuki WADA
High Energy Neutron Laboratory, Japan Atomic Energy Research Institute
Tokai-mura, Naka-gun, Ibaraki-ken 319-11
e-mail: konno@fnshp.tokai.jaeri.go.jp

Some remarks on the multigroup library were found from the comparison of the DORT calculations with the MCNP calculation for the benchmark experiment on a copper slab.

1. Introduction

The new analysis by two-dimensional Sn transport code DORT3.1[1] with JENDL-3.2[2] was performed for the benchmark experiment[3,4] on a copper slab assembly of 630 mm in effective diameter and 608 mm in thickness bombarded by D-T neutrons. Some remarks on the multigroup library were found from the comparison of the DORT calculations with the calculation by continuous energy Monte Carlo code MCNP-4A[5].

2. Calculation Procedure

Two multigroup libraries (neutron 125 groups, γ 40 groups and P_5 Legendre expansion with self-shielding correction) were made from JSSTDL-295n-104γ[6] of JENDL-3.2 and matxs files newly processed from JENDL-3.2 by the NJOY94.66[7] code. The DORT calculations with these two libraries will be presented as DORT(JSSTDL) and DORT(NJOY) in this section, respectively. The angular quadrature of S_{16} and theta-weighted (theta : 0.9) were adopted in the DORT calculations. The FSXLIB-J3R2[8] library processed from JENDL-3.2 was used for the MCNP-4A calculation.

3. Insufficient self-shielding correction in JSSTDL system

Figure 1 shows the measured and calculated neutron spectra at the depths of 228 and 532 mm. The MCNP calculation overestimates neutrons from 10 keV to 1 MeV by 10 - 40 % and underestimates neutrons below 1 keV by a factor of 2 - 3. Probably some improvement of the copper data in JENDL-3.2 will be required. Here we focus our attentions on the difference among the calculations. All the calculations agree each other in the neutron energy above 40 keV. On the contrary, the discrepancy among the calculations appears in the neutron energy

below 40 keV. of the discrepancy was due to the incomplete self-shielding correction for the scattering matrix. The f-table (self-shielding correction coefficient) for elastic scattering cross section is used for the scattering matrices in the JSSTDL system, while the f-table for the scattering matrix in the NJOY system is appropriately prepared. As a result, the factors of Legendre expansion of the scattering matrices in the JSSTDL system are different from those in the NJOY system as shown in Fig. 3, which shows the P_0 factors of the in-group scattering matrices of copper in JENDL-3.2 multigroup libraries processed from JSSTDL and NJOY system. Since this insufficient self-shielding correction method is adopted not only for copper but also for all nuclei in the JSSTDL system, it should be noted that Sn calculations with the JSSTDL library sometimes give incorrect results.

4. Overcorrection of self-shielding for the resonance around 500 eV in copper

From Fig. 1 it is also noted that the neutron spectra of MCNP and DORT(NJOY) are different below 500 eV, while they are the almost same above 500 eV. This reason is probably the overcorrection of the self-shielding of the large sharp resonance around 500 eV in copper as shown in Fig. 2. In order to confirm this idea, we performed DORT calculation with the multigroup library (neutron 138 groups) of the finer group structure around 500 eV. This DORT calculation agrees with the MCNP calculation better as shown in Fig. 4. It is considered that the self-shielding correction in the multigroup library is not so perfect for a large sharp resonance even in the NJOY system.

5. Self-shielding correction for multigroup dosimetry cross section

The agreement of the DOT3.5[9] calculation and measurement in the reaction rate of $Cu(n,x)^{64}Cu$, which is sum of $^{63}Cu(n,\gamma)^{64}Cu$ and $^{65}Cu(n,2n)^{64}Cu$, was very poor (the ratio of the calculation to the experiment was 2.5 at the depth of 532 mm) compared with the MCNP calculation in the previous paper[3] for this benchmark experiment. The reaction rate of $Cu(n,x)^{64}Cu$ was given by using the multigroup dosimetry cross section of $Cu(n,x)^{64}Cu$ without self-shielding correction in the DOT calculation, while it was obtained by using the continuous energy dosimetry cross section of $Cu(n,x)^{64}Cu$ in the MCNP calculation. We thought out that the reason of the discrepancy between the DOT and MCNP calculations was due to the multigroup dosimetry cross section of $Cu(n,x)^{64}Cu$ without self-shielding correction. In order to test this idea, we made the 125-group dosimetry cross sections of $Cu(n,x)^{64}Cu$ with and without self-shielding correction, which are shown in Fig. 5, by the TRANSX2.5[10] code from the ^{63}Cu and ^{65}Cu data in ENDF/B-VI[11], which were used since isotope libraries in JENDL-3.2 are incomplete. Figure 6 shows the ratio of the calculation to the experiment (C/E) for the reaction rate of $Cu(n,x)^{64}Cu$. The DORT calculation is almost the same as the MCNP calculation if the self-shielding corrected multigroup dosimetry cross section is adopted. The self-shielding correc-

tion for multigroup dosimetry cross section is essential for the precise activation calculations including (n,γ) reactions for principal material with DORT, e.g. the activation estimation of type 316 stainless steel in International Thermonuclear Experimental Reactor.

6. Concluding Remarks

The following remarks were deduced through the DORT analysis of the benchmark experiment on a copper slab.

1) The self-shielding correction for the scattering matrix in the JSSTDL system is inadequate. It should be noted that Sn calculations with the JSSTDL library sometimes give incorrect results.
2) The self-shielding correction in the multigroup library is not so perfect for a large sharp resonance, e.g. a resonance around 500 eV in copper, even in the NJOY system.
3) The self-shielding correction for multigroup dosimetry cross section is essential for the precise activation calculations including (n,γ) reactions for principal material with DORT.

Acknowledgment

The authors would like to thank Mr. K. Kosako, Sumitomo Atomic Energy Industories, Ltd., for his fruitful discussion.

References

[1] Rhodes W.A. and Mynatt F.R. : Nucl. Sci. Eng., 99, 88 (1988).
[2] Nakagawa T. et al. : J. Nucl. Sci. Technol., 32, 1259 (1995).
[3] Konno C., et al. : Fusion Engineering and Design, 28, 745 (1995).
[4] Maekawa F., et al. : Fusion Engineering and Design, 28, 753 (1995).
[5] Briesmeister J.F. (edited): LA-12625-M, Los Alamos National Laboratory, (1993).
[6] Nakagawa T. : private communication (1995).
[7] MacFarlane R.E. and Muir D.W.: LA-12740-M (1994).
[8] Kosako K., et al. : JAERI-Data/Code 94-20 (1994).
[9] Rhodes W.A. and Mynatt F.R. : ORNL-TM-4280 (1973).
[10] MacFarlane R.E. : LA-12312-MS (1992).
[11] Rose P.F. (edited) : BNL-NCS-17541 (1991).

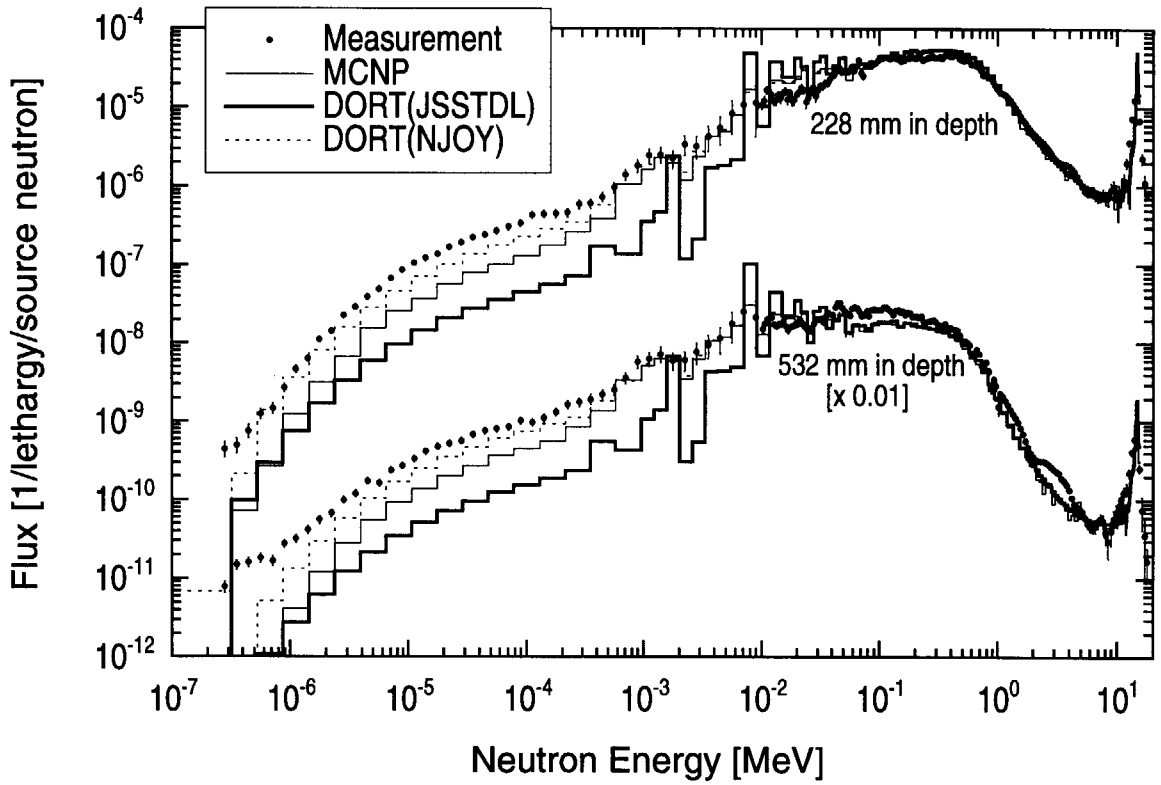

Fig. 1 Measured and calculated neutron spectra at the depths of 228 and 532 mm.

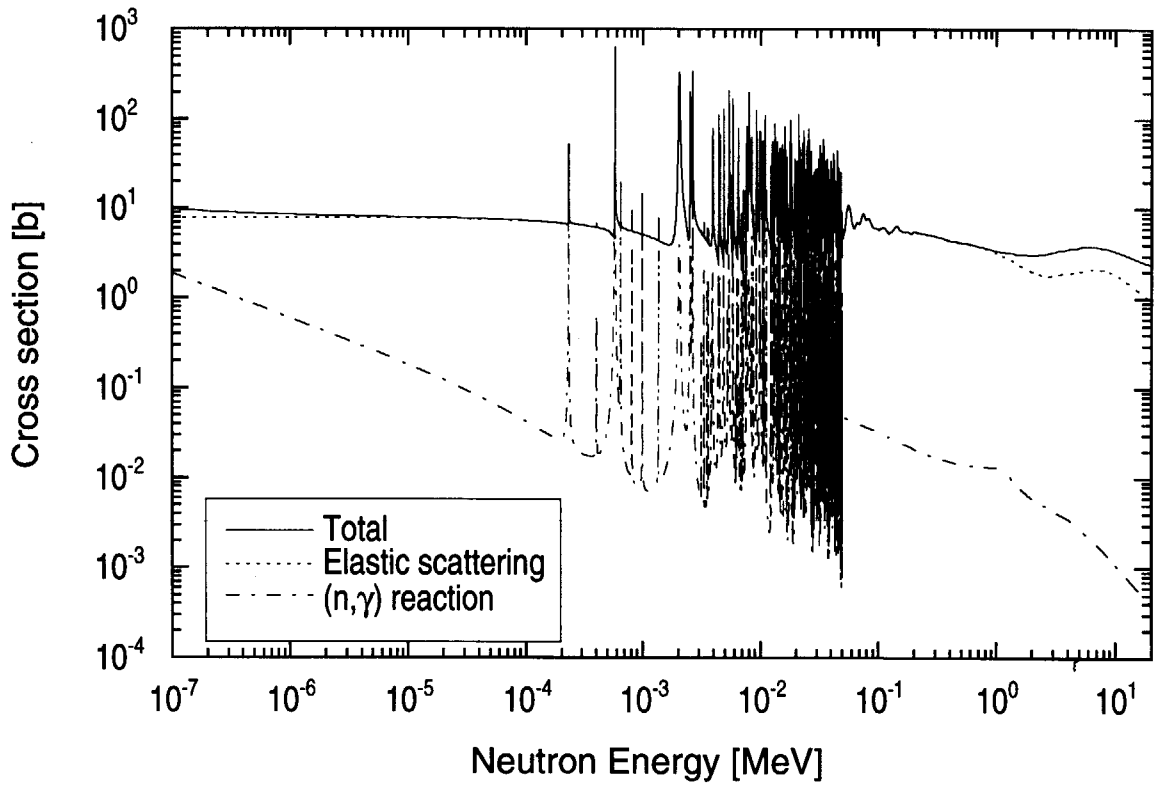

Fig. 2 Cross sections of copper in JENDL-3.2.

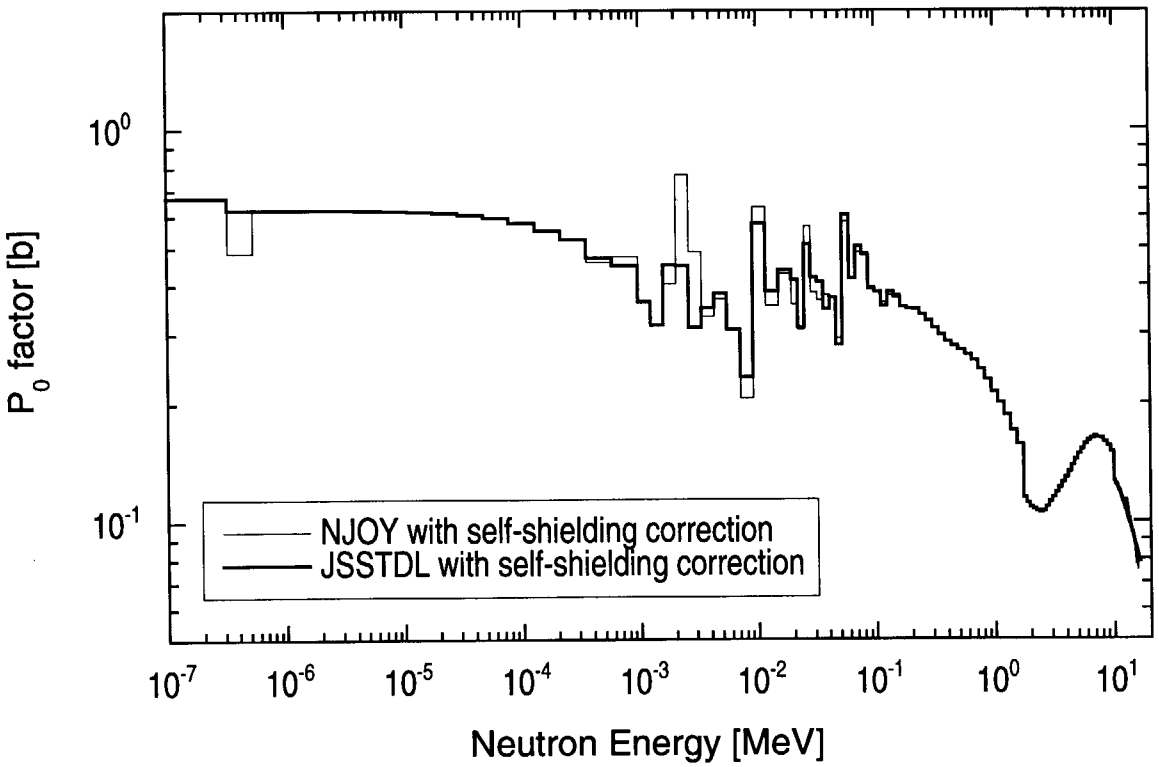

Fig. 3 P_0 factors of the in-group scattering matrices of copper in JENDL-3.2 multigroup libraries processed from JSSTDL and NJOY system.

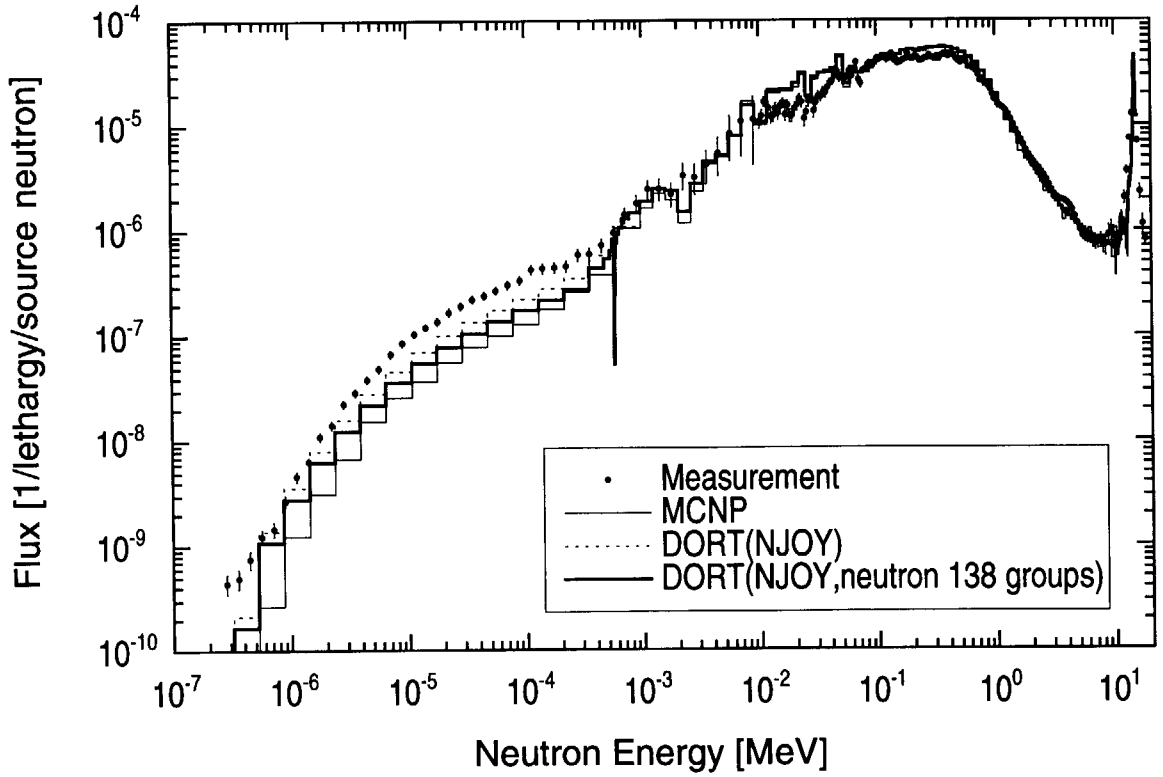

Fig. 4 Measured and calculated neutron spectra at the depth of 228 mm.

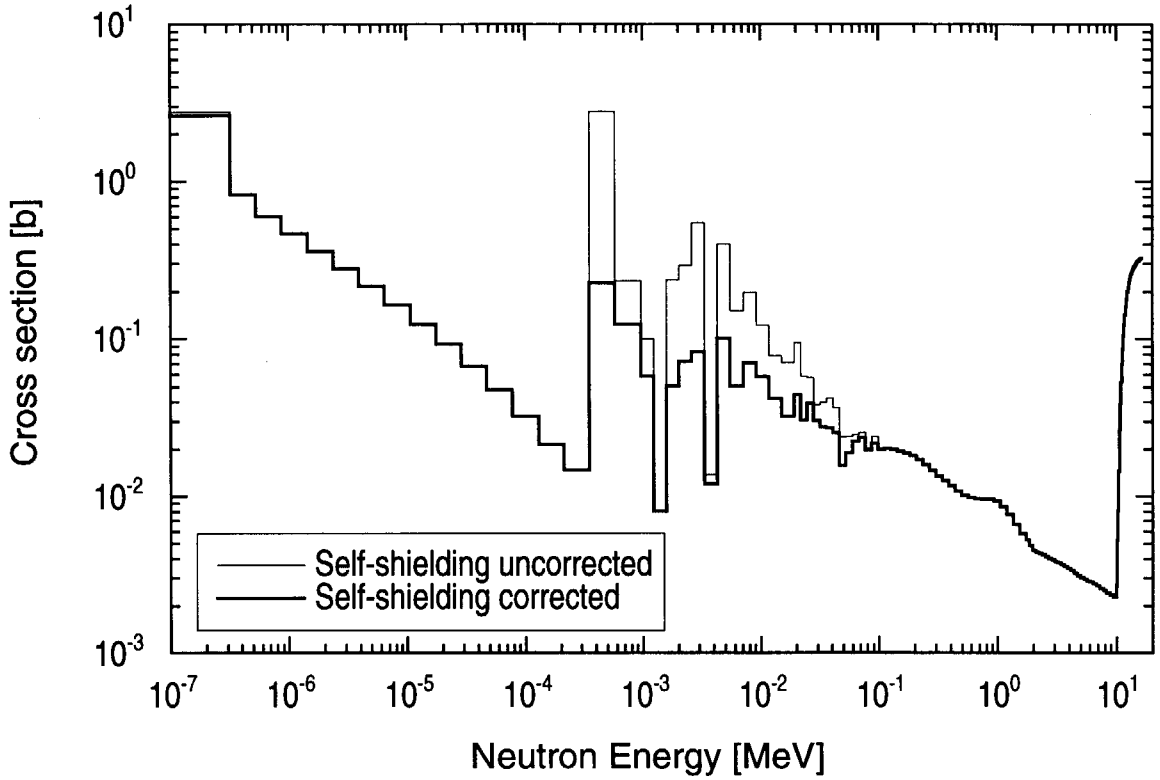

Fig. 5 Multigroup dosimetry cross sections of Cu(n,x)^{64}Cu with and without self-shielding correction.

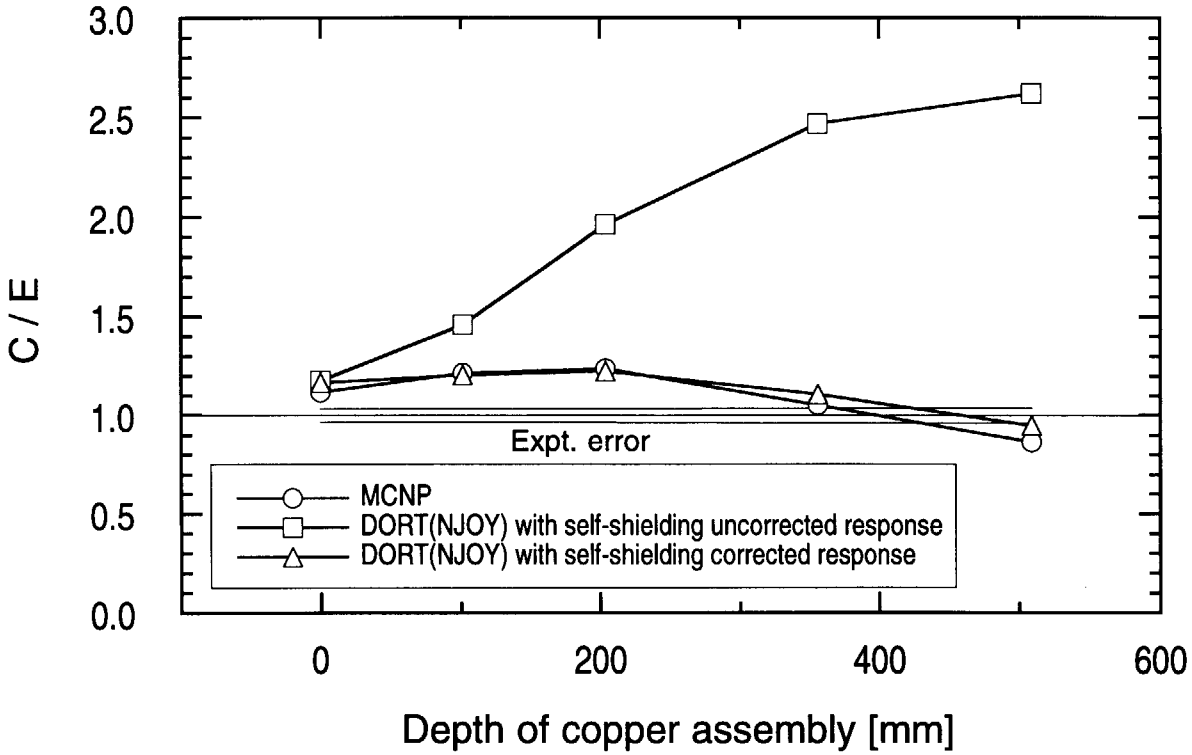

Fig. 6 C/E of the reaction rate of Cu(n,x)^{64}Cu.

3.13

Benchmark Experiment on Vanadium Assembly with D-T Neutrons -Leakage Neutron Spectrum Measurement

Kokooo, I.Murata, D.Nakano, A.Takahashi
Department of Nuclear Engineering, Osaka University
Yamadaoka 2-1, Suita, Osaka 565

F.Maekawa, Y.Ikeda
High Energy Neutron Laboratory, Japan Atomic Energy Research Institute
Tokai-mura, Naka-gun, Ibaraki-ken 319-11

The fusion neutronics benchmark experiments have been done for vanadium and vanadium alloy by using the slab assembly and time-of-flight (TOF) method. The leakage neutron spectra were measured from 50 keV to 15 MeV and comparison were done with MCNP-4A calculations which was made by using evaluated nuclear data of JENDL-3.2, JENDL-Fusion File and FENDL/E-1.0.

1. Introduction

Vanadium has a high potential to use as a structural material for fusion power reactors because of its low activation property. The accuracy of fusion reactor design depends on the evaluated nuclear data libraries. The leakage neutron spectrum measurement done by U. von Moellendorff et al. at IPPE, Obninsk, Russia is the only existing benchmark experiment for vanadium[1]. Therefore, benchmark experiments on Vanadium are strongly required to validate the evaluated nuclear data libraries. Under the IEA collaboration, fusion neutronics benchmark experiments for vanadium and vanadium alloy(V 92% Cr 4% and Ti 4%) were performed at Fusion Neutronics Source (FNS) in JAERI. In this symposium, In-situ measurement experiment performed at FNS for vanadium [2] was also presented together with the present paper.

2. Experiment

2.1. Experimental Arrangement

The Leakage spectrum measurements from the slab assembly by using the time-of-flight (TOF) method[3,4] were done at FNS/JAERI with the water cooled tritium target (3.7×10^{11} Bq) of the 80 degree beam line. As for the pulse neutron conditions, pulse width, pulse repetition frequency and average deuteron beam current were ~2 ns, ~4 μs and ~20 μA, respectively. The average neutron yield is about 2×10^9 n/s. We have measured the neutron spectrum for vanadium of 5 cm, 15 cm and 25 cm thickness and vanadium alloy assembly of 10 cm thickness at two

detecting angle positions, 0 degree and 24.9 degree. The experimental arrangement is shown in Fig.1. The 5.08 cm diameter and 5.08 cm thick NE-213 liquid scintillation detector was used to measure the neutron spectrum. The source neutron monitor count was measured by detecting the associated α particles with a silicon surface barrier detector (SSD). The block diagram of measuring system is shown in Fig. 2. Background measurements were done by blocking the collimator hole with a plug of type 304 stainless steel of 0.6 m length and acryl of 0.4 m length.[4] The foreground and background TOF spectrum for the 15 cm thick vanadium assembly measurement at the detector position of 0 degree is shown in Fig.3.

2.2. Efficiency Determination

For the efficiency determination, SCINFUL calculation and the neutron spectrum measurements for beryllium assembly, ^{252}Cf source and polyethylene (CH_2) were done. The MCNP-4A calculations have been done with the nuclear data of JENDL-FF for efficiency determination of Be and CH_2. The Be assembly of 20 cm (35 x 35 x 20 cm^3) thickness was used rather than graphite pile because the better data could be acquired for the low energy region. The detector position in Be measurement is 0 degree. The raw neutron spectrum of Be measurement is shown in Fig.4. The neutron spectra at the emission angles of 30°, 40°, 50° and 60° were measured in CH_2 measurement. The size of CH_2 is 1 cm ϕ x 5 cm. The flight path for these two measurements is about 7 m. We also measured the fission spectrum of ^{252}Cf and compared it with the Watt spectrum to make a relative detector efficiency. The flight path in ^{252}Cf measurement is about 3.6 m. The efficiency can be derived from the measurement by using the equation,

$$\varepsilon(E_n) = \frac{C(E_n)}{\phi(E_n)}$$

where, $\varepsilon(E_n)$ = efficiency, $C(E_n)$=measured data and $\phi(E_n)$=calculated data. The comparison were made among the efficiencies of the measured data and SCINFUL calculation. In Fig.5, the comparison of efficiency of Be measurement, SCINFUL calculation and the determined efficiency are shown. The SCINFUL calculation and the measured efficiency of Be agree well in the energy region larger than 0.7 MeV. The discrepancies were found for the energy region smaller than 0.7 MeV because the energy distribution of the neutron source was neglected in the SCINFUL calculation. Only Be efficiency has been used for data reduction in the energy region smaller than 0.7 MeV.

2.3. Data Reduction

The measured time of flight spectra have been transformed into energy spectrum by using the equation,

$$E_n = \frac{72.3 L_{eff}^{\ 2}}{t^2}$$

where, E_n is neutron energy in MeV, L_{eff} is effective flight path in meter and t is the time of flight in nanosecond. L_{eff} is the sum of the effective emission depth and the distance between the rear surface of the assembly and the detector. The MCNP-4A calculation has been done to determine the effective emission depth. From the raw TOF spectrum, the neutron flux at the detector position can be deduced by the following expression.

$$\phi(E_n) = \frac{C(E_n)}{\varepsilon(E_n) \cdot A_d \cdot S_n}$$

where, $\phi(E_n)$ = the neutron flux at the detector position (n/cm^2/Lethargy/Source)

$C(E_n)$ = the net counts (FG-BG) (n/Lethargy/Source)

$\varepsilon(E_n)$ = the efficiency of the detector

A_d = surface area of the detector and

S_n = number of source D-T neutrons.

The data were obtained as low as 50 keV to perform the precise comparison with the evaluated nuclear data.

3. Calculations

The three dimensional Monte-Carlo neutron transport calculation has been done by using MCNP-4A code and the evaluated nuclear data of JENDL-3.2, JENDL-Fusion File and FENDL/E-1.0. The neutron source was modeled as a point source and the measured source spectrum was used in the calculation. The source spectrum can be seen in Fig. 6. The ideal collimator was modeled by the cylinder of 5 cm diameter surrounded by a zero importance region. The point detector is used in the calculations.

4. Results

The measured spectra were compared with the calculations in Figs. 7~10. The calculated spectra with JENDL-3.2 and JENDL-Fusion File agree well with the measured spectra, however, the calculated flux with FENDL/E-1.0 underestimated the measured data in the high energy region.

References

(1)Moellendorff U., et. al.," A 14-MeV Neutron Transmission Experiment on Vanadium", Proc. 19th Symposium on Fusion Technology, Lisbon, September 16-21, 1996,pp.1575-1578 (1997).

(2)F. Maekawa, et.al.," Benchmark Experiment on Vanadium Assembly with D-T Neutrons –In-situ Measurement –", Contribution to this Symposium (1998).

(3)A. Takahashi, et. al., J. Nucl. Sci. and Tech. 21, 577(1984)

(4)Y. Oyama, H. Maekawa, Nucl. Instrum. Meth.,A245, 173(1986)

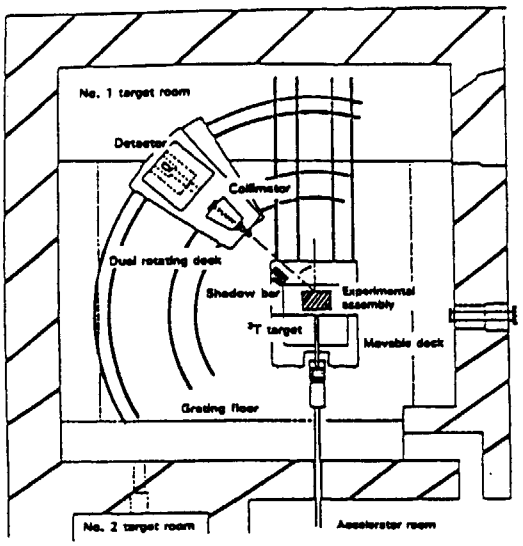

Fig. 1. Experimental arrangement and target room

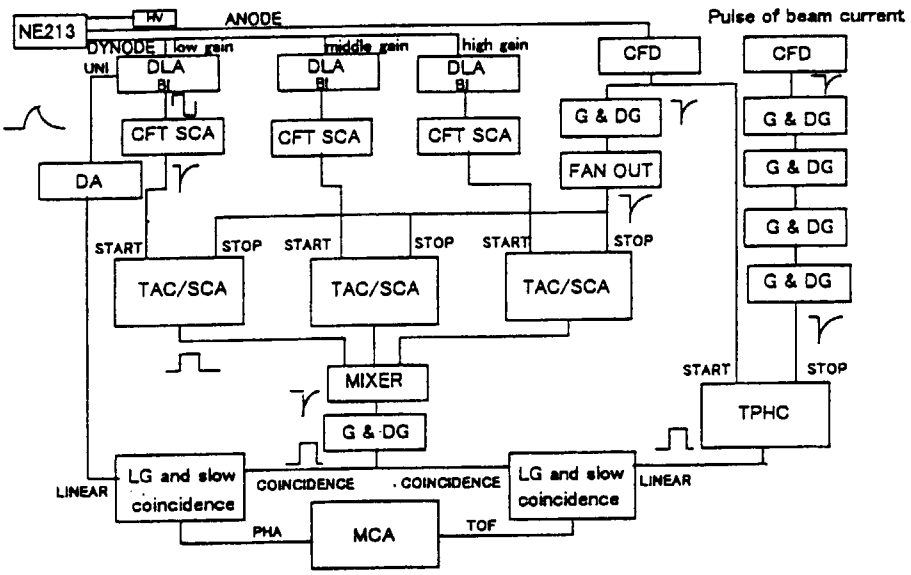

Fig. 2. The Block Diagram of the measuring system

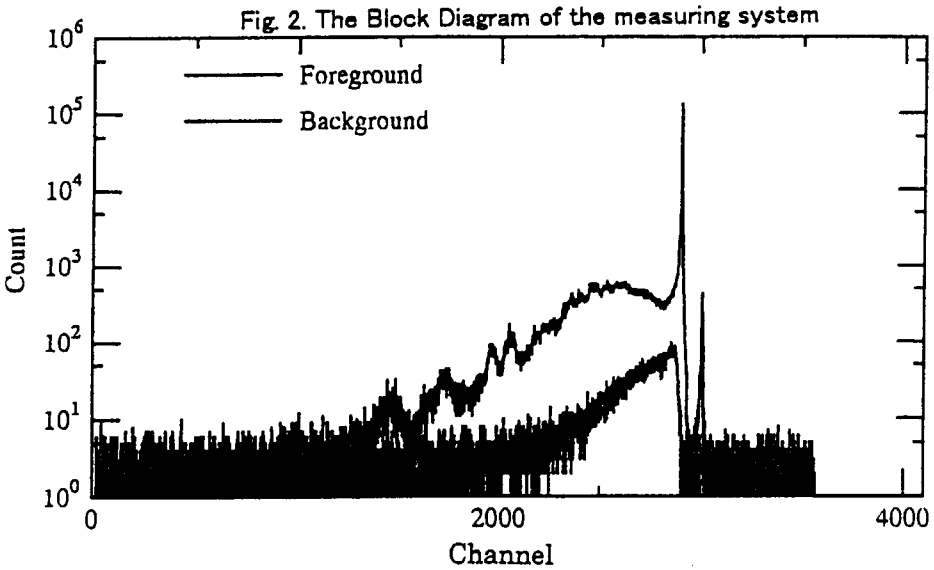

Fig. 3. Foreground and Background spectrum at 0 degree for 15 cm thick Vanadium measurement

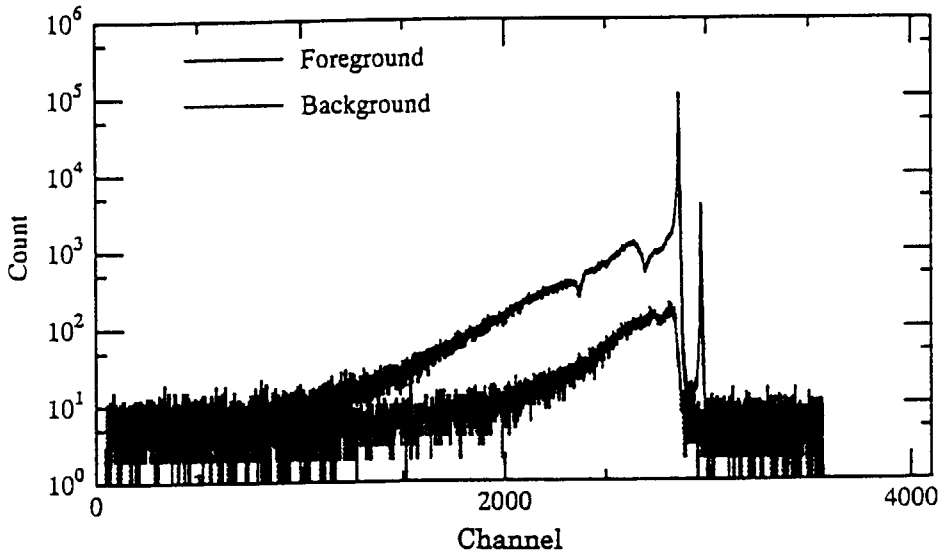

Fig. 4. The Foreground and Background counts in Be measurement

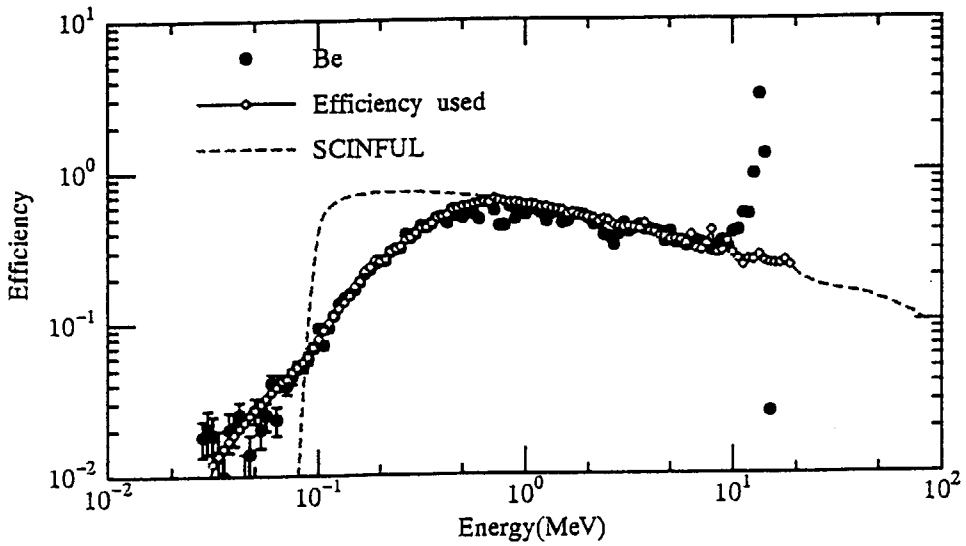

Fig. 5. The comparison of the Efficiency determinations

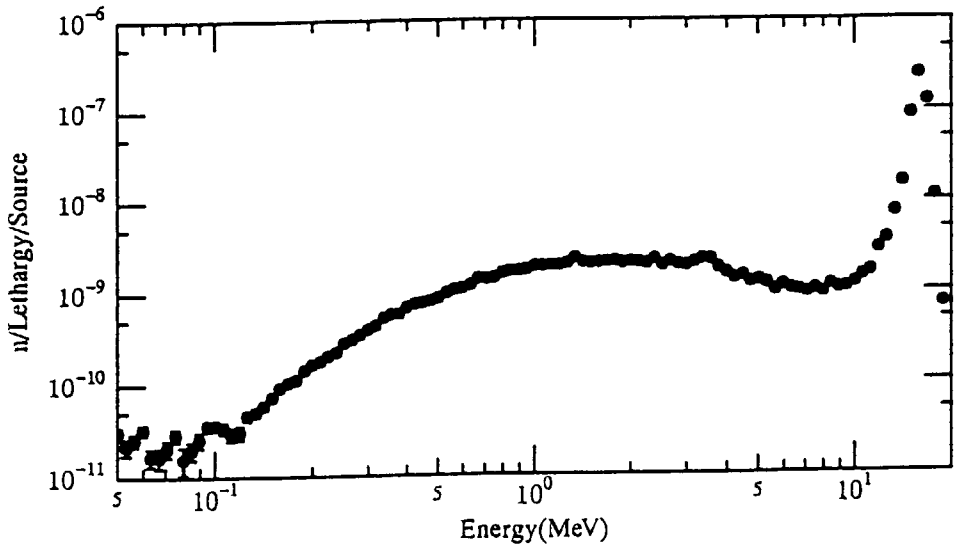

Fig. 6. The source neutron spectrum

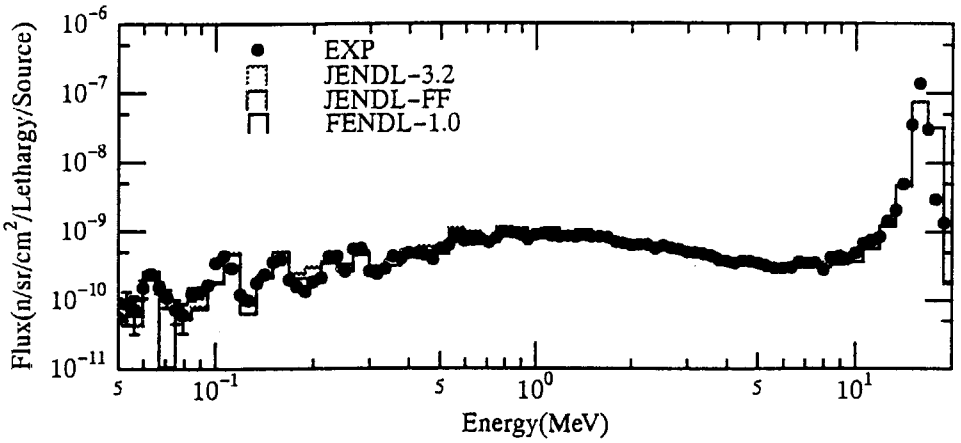

Fig. 7. The neutron flux spectrum at 0 degree for Vanadium Assembly of 15 cm thickness

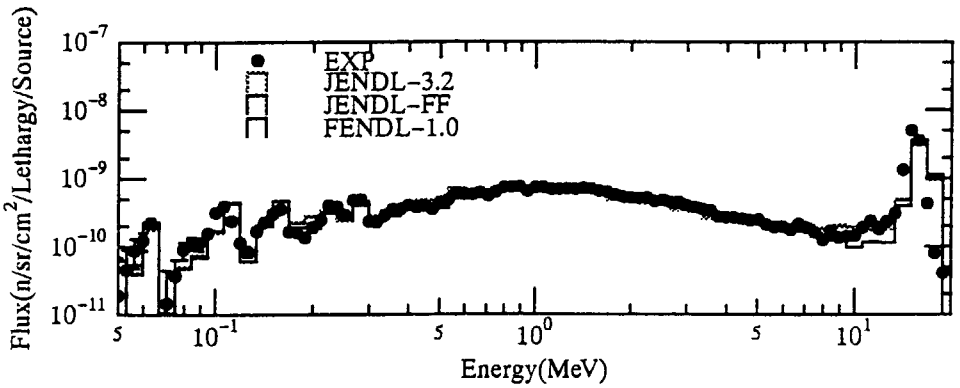

Fig. 8. The neutron flux spectrum at 25 degree for Vanadium Assembly of 15 cm thickness

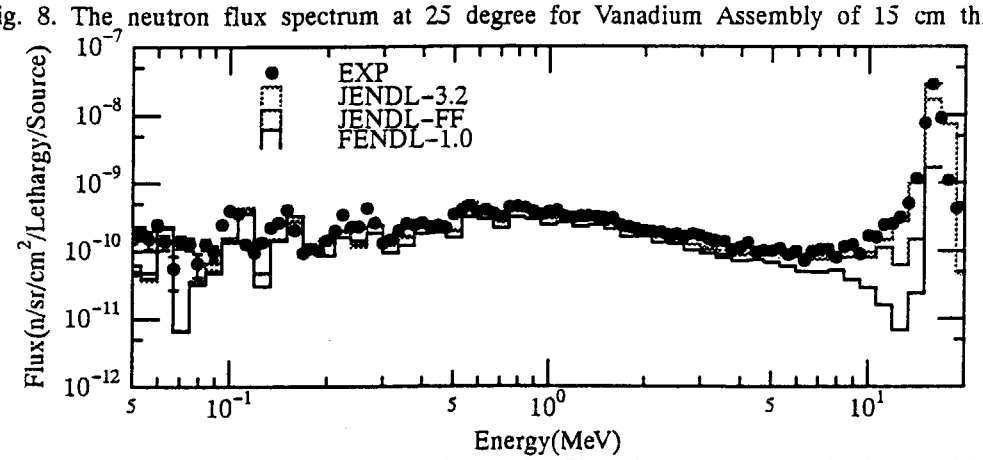

Fig. 9. The neutron flux spectrum at 0 degree for Vanadium Assembly of 25 cm thickness

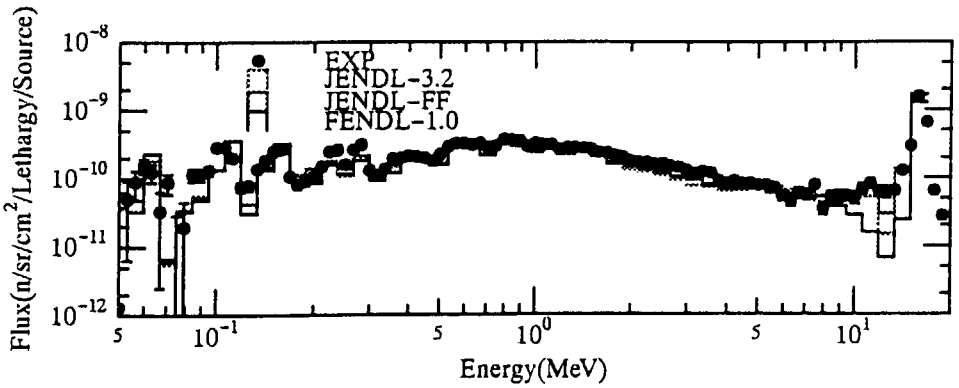

Fig. 10. The neutron spectrum at 25 degree for Vanadium Assembly of 25 cm thickness

3.14 Measurement of Reaction Cross Sections of Fission Products Induced by DT Neutrons

Daisuke NAKANO, Isao MURATA and Akito TAKAHASHI
Department of Nuclear Engineering, Osaka University
Yamada-oka, 2-1, Suita 565, Japan
e-mail: daisuke@newjapan.nucl.eng.osaka-u.ac.jp

With the view of future application of fusion reactor to incineration of fission products, we have measured the $^{129}I(n,2n)^{128}I$ reaction cross section by DT neutrons with the activation method. The measured cross section was compared with the evaluated nuclear data of JENDL-3.2. From the result, it was confirmed that the evaluation overestimated the cross section by about 20~40 %.

1. Introduction

The incineration methods of nuclear wastes, i.e., minor actinide (MA) and fission product (FP), have been widely investigated.(1) It is generally considered that the incineration is performed by using fission reactor, fusion reactor, proton accelerator and so on. Recently, for the incineration of FPs using fission reactor, the neutron capture cross sections of some FPs induced by thermal neutrons have been measured.(2)-(6) However, there exist few measured nuclear data to estimate the feasibility to incinerate FPs with fusion reactor.

In this study, ^{129}I as one of the most famous FPs was selected as a target sample due to its extremely long half life as shown in Table 1. The DT neutron induced cross section of the $^{129}I(n,2n)^{128}I$ reaction, which has a relative large cross section in comparison with other reactions, was measured to give basic data for estimation of incineration performance, nuclear data evaluation and nuclear physics of unstable nuclide. The experimental result was compared with the evaluated nuclear data of JENDL-3.2.

2. Experimental

2.1 Sample and Neutron Source

In the cross section measurement, a massive sample cannot be treated because

^{129}I is originally radioactive. Therefore we adopted the activation method, with which we could obtain the information of reaction products of an irradiated sample by gamma-ray measurement, even if the amount of the sample is quite small. ^{129}I has the following advantages of the measurement: (1) Its long half life (1.57×10^7 years) increases the applicable amount of sample in the measurement. (2) Since energy of gamma-ray emitted following its beta decay is so low that the gamma-ray cannot transmit the detector window, the background from sample itself can be suppressed. (3) The radioactive nuclide ^{128}I produced by (n,2n) reaction has an appropriate half live (24.99 minutes) for the measurement. The sample for irradiation is a sealed source of 37.9 kBq, in which about 3×10^{19} nuclei are contained.

The measurement was carried out using a continuous DT neutron source of the DC line of OKTAVIAN facility of Osaka University. The sample was set up on the front surface of the rotating tritium target assembly and in the end section of a pneumatic tube of the irradiation and sample transport system. The effective neutron energy was determined by experiment with the Zr/Nb reaction activation ratio method.[7] As for neutron flux monitor, the reaction $^{27}Al(n,\alpha)^{24}Na$ was used as an activation detector. Time dependence relative neutron intensity was measured with a MCS system using BF_3 proportional counter. The obtained neutron flux was about $10^8 \sim 10^9$ n/cm^2/s at the sample position.

2.2 Neutron Irradiation and Activity Measurement

In the measurement, irradiating, cooling and counting periods are 60 minutes, 2 minutes and 75 minutes, respectively. After retrieving the sample by the pneumatic sample transport system, the gamma-rays from an irradiated sample were measured with a 180 cc high purity germanium detector.

3. Results and Discussion

From the measured pulse height spectrum in Fig. 1, three gamma-ray peaks were observed to be identified as the transitions from the excited states of ^{128}I. We confirmed that these peaks corresponded to those of ^{128}I through ascertaining each peak energy and its corresponding half life. In the determination of the cross section, corrections for neutron multiple scattering and gamma-ray attenuation in the sample were taken into account. The measured cross sections of $^{129}I(n,2n)^{128}I$ reaction at 13.5, 14.2 and 14.7 MeV are shown in Table 2. From the comparison with the evaluated nuclear data of JENDL-3.2, the evaluation overestimates the cross section by about 20~40 %. Figure 2 shows the measured cross section compared with other data. The error estimation of the results is summarized in Table 3.

4. Conclusion

This paper has reported the results of the measurement of the $^{129}I(n,2n)^{128}I$ reaction cross section for the neutron energy at 13.5, 14.2 and 14.7 MeV. From the result, it was confirmed that the evaluated nuclear data of JENDL-3.2 overestimated the cross section by 20~40 %.

References

(1) H. Sekimoto and T. Osawa (Ed.), J. At. Energy Soc. Japan, 37[3], 159 (1995)
(2) T. Sekine, et al., J. Nucl. Sci. Technol., 30[11], 1099 (1993).
(3) H. Harada, et al., ibid., 31[3], 173 (1994).
(4) T. Katoh, et al., Proc. Int. Conf. on Nuclear Data for Science and Technology, Gatlinburg, 230 (1994), ORNL.
(5) S. Nakamura, et al., J. Nucl. Sci. Technol., 33[4], 283 (1996).
(6) T. Katoh, et al., ibid., 34[5], 431 (1997).
(7) V. E. Lewis and K. J. Zieba, Nucl. Instrum. Methods, 174, 141 (1980)

Table 1 Main incineration target FPs

Nuclide	Half life (year)	Eγ (keV)	Atom/μCi	Key issue
^{137}Cs	30.07	662	~10^{14}	Heat source
^{90}Sr	28.78	-		
^{99}Tc	2.11×10^{5}	-	~10^{18}	Inherent risk
^{135}Cs	2.3×10^{6}	-		
^{129}I	1.57×10^{7}	39.6		

Table 2 Measured cross sections with evaluation

	$^{129}I(n,2n)^{128}I$ reaction cross section		
	13.5 MeV	14.2 MeV	14.7 MeV
Present experiment*	1.02±0.14	1.26±0.17	1.13±0.15
JENDL-3.2	1.44	1.48	1.52

* Errors in the measurement are summarized in Table 3

Table 3 Error estimation

Item		Error (%)
Sample	Activity	10
	Half life	2.6
	Measurement	2
Position of the sample and foil		5
Activation foil	Weight	2.5
	Measurement	3
Standard source	Activity	5
	Half life	<1.4
Total error		<14

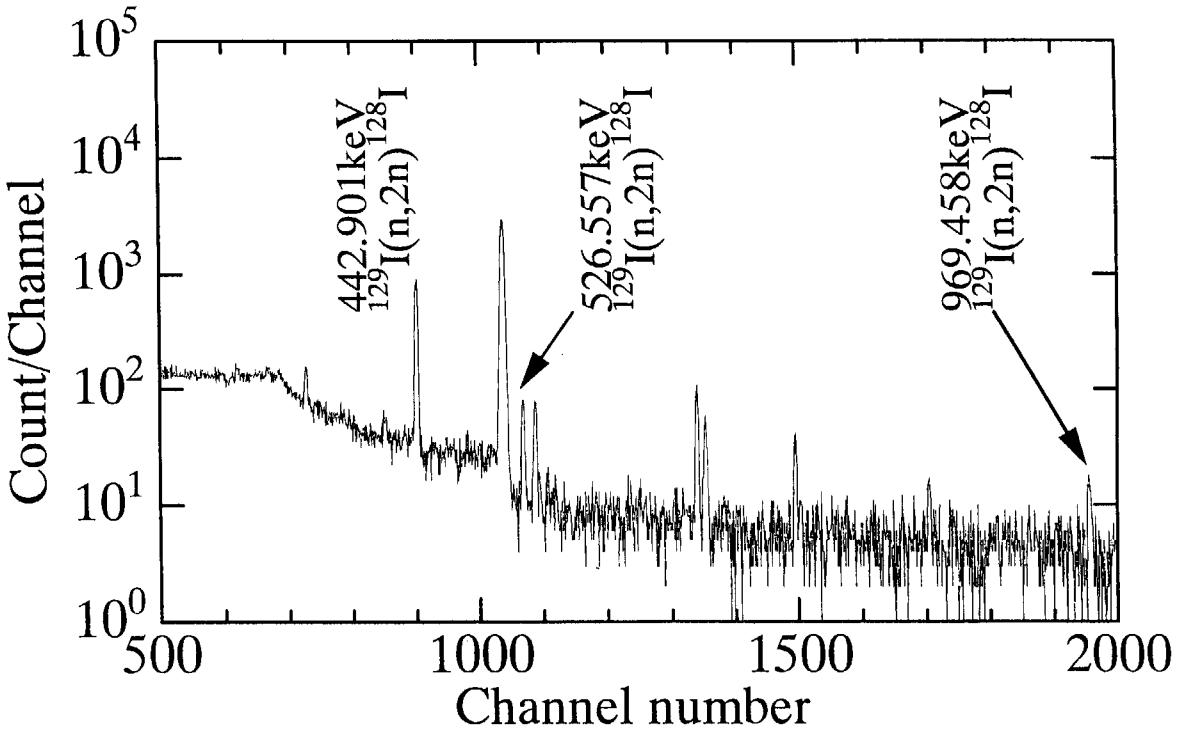

Fig. 1 Pulse height spectrum of gamma-rays from ^{128}I

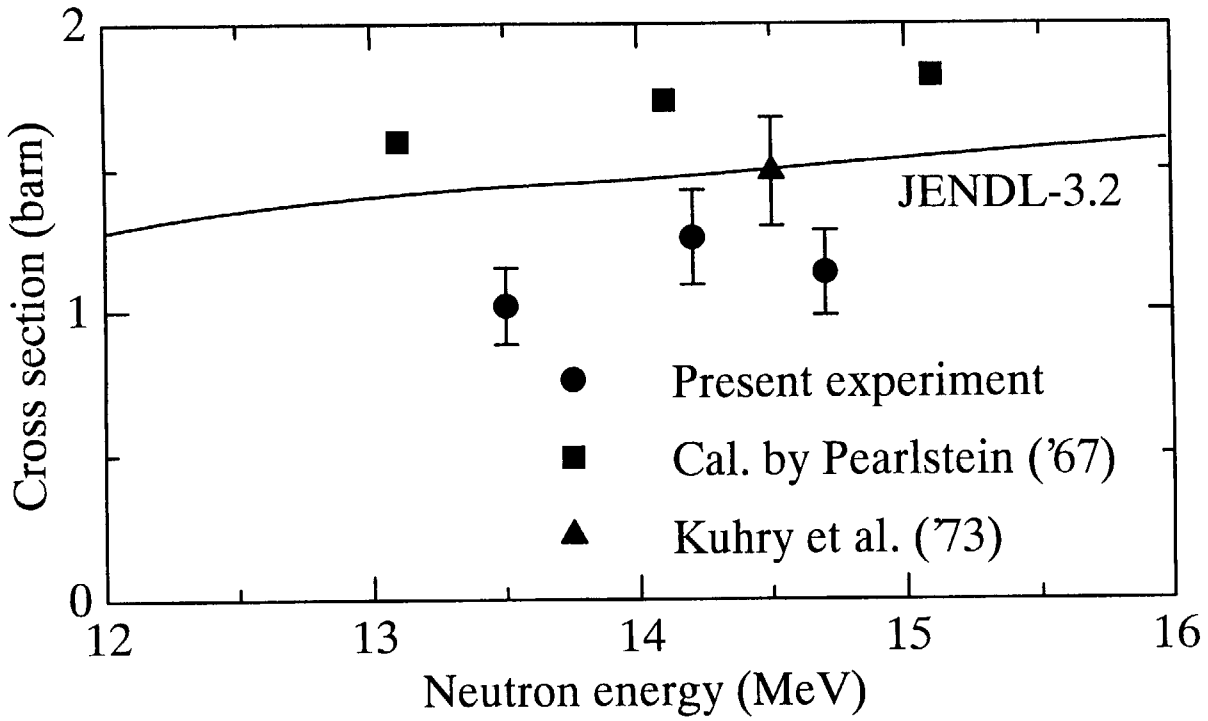

Fig.2 $^{129}I(n,2n)^{128}I$ reaction cross section

3.15 Resonance Analysis of the $^{12}C,^{13}C(\alpha,n)$ Reactions and Evaluation of Neutron Yield Data of the Reaction

Toru MURATA
AITEL corporation
1-18-16 Shinbashi,Nihon-Seimei BLDG,Minato-ku,Tokyo
e-mail:murata@aitel.toshiba.co.jp

The $^{12}C(\alpha, n)^{15}O$ reaction and the $^{13}C(\alpha, n)^{16}O$ reaction were analyzed with a resonance formula in the incident α-particle energy range of 1.0 to 16.0 MeV. With the obtained resonance parameters, branching ratios of the emitted neutrons to the several levels of the residual nucleus and their angular distributions were calculated to obtain the energy spectrum of emitted neutrons. Thick target neutron yield of carbon were also calculated and compared with the experimental data.

1. Introduction

Neutron yield data of alpha-particle induced reactions are required in the fields of particle accelerator shielding design, design and operation of some nuclear fuel facilities and also that of some medical therapy facilities. Evaluation of the data are now being performed in Japan by the Working Group on Charged Particle Nuclear Data, JNDC. Alpha-particle energy range of the evaluation is set below 15 MeV. The present work was performed as a part of the working group activities. The (α,n) reaction cross section of light nuclei, such as carbon shows resonance structures in the present energy region. So, the experimental cross sections were analyzed with an approximate R-matrix formula and using the determined resonance parameters, branching ratios and angular distributions of the emitted neutrons were calculated. Thick target neutron yield of carbon were also calculated and compared with the experimental data.

2. Resonance Analysis

Resonance analysis were made with the following ordinary cross section formula using the collision matrix Ucc' of an approximate R-matrix theory which was derived assuming that the same spin-parity resonance levels have same ratios of reduced width among the relevant reaction channels[1].

$$\sigma_{cc'} = \frac{\pi}{k_c^2} \sum_{Jll'ss'} \frac{2J+1}{(2I_1+1)(2I_2+1)} |T_{c's'l'csl}^{\ J}|^2 \quad ,$$

$$T_{c's'l'csl}^{\ J} = \exp(2i\omega_{c'l'})\delta_{c's'l',csl} - U_{c's'l'csl}^{\ J} \quad ,$$

$$U_{cc'}^{\ J} = \exp i(\omega_c - \phi_c)[\delta_{cc'} + \frac{\sum_\lambda i\Gamma_{\lambda c}^{1/2}\Gamma_{\lambda c'}^{1/2} / (E_\lambda - E)}{1 + \sum_\lambda (\Delta_\lambda - i\Gamma_\lambda / 2) / (E_\lambda - E)}]\exp i(\omega_{c'} - \phi_{c'})$$

where nomenclature follows that of Lane and Thomas[2]. As an initial guess of the resonance parameters, the compound nucleus level schemes given in the compilation of Ajzenberg-Selove [3] were adopted and modified to fit the available experimental cross sections.

For ^{12}C, the threshold energy of the (α,n) reaction is 11.34 Mev. Analysis was made for the experimental cross sections measured by Black et al.[4]. The result of the analysis is shown in Fig.1 and the resonance parameters are summarized in Table 1.

For ^{13}C, the reaction Q-value is 2.216 MeV, exothermic. Experimental cross sections measured by Sekharan et al.[5] and measured by Bair and Haas[6] were analyzed in the incident energy range below about 6.0 MeV . At higher energy region, no experimental cross sections were available, but West and Sherwood [7] measured thick target neutron yield data up to 10 Mev and Matsunobu [8] converted them into cross sections. No spin-parity assignments were given in the above-mentioned compilation. To infer the resonance parameters, the optical model reaction cross section was calculated using Igo's potential [9] with small imaginary potential (2.0 MeV). Structure correspondence between the converted cross section and the calculated reaction cross section was fairly good as is shown in Fig.2 . Analysis of the converted cross sections and extrapolation up to 16 MeV were made with the parameters inferred from the optical model reaction cross section structure. The result of the analysis is shown in Fig. 3a and Fig.3b, and the resonance parameters are given in Table 2.

3. Neutron Yield Data Evaluation

3.1) Thick Target Neutron Yield

Neutron yield by alpha particle bombardment of natural carbon thick target was calculated using the analyzed cross sections and alpha-particle stopping power given by Ziegler [10]. Figure 4 shows the calculated thick target neutron yield comparing with the experimental yield data measured by Bair [11] and West and Sherwood [8].

3.2) Neutron Energy Spectrum Data

To evaluate neutron energy spectrum, neutron emission branching ratios to each level of the residual nucleus and angular distributions of emitted neutrons are required.

The branching ratios: For ^{12}C, neutrons feed only to the ground state of ^{15}O in the present alpha-particle energy range. For ^{13}C, neutron feeding was assumed to be continuous above 5th excited levels of ^{16}O and discrete to the levels below that. The branching ratio to level I from resonance level J was calculated using the barrier penetration factor $P_l(E_n)$ and level density $\rho_I(E_x)$ of continuum states, as follows,

$$\frac{\Gamma_{nIJ}}{\Gamma_{nJ}} = \frac{\sum_{sl} P_{I(sl)J}(E_n)}{\sum_{I'}\sum_{sl'} P_{I'(sl')J}(E_n) + \sum_{I'} \int P_{I'(sl')J}(E_n)\rho_{I'}(E_X)dE_X} ,$$

$$\rho_I(E_X) = \rho_0(2I+1)\exp\{-I(I+1)/I_0(I_0+1)\}\exp\sqrt{2aE_X}\,/\,E_X^{5/4}$$

where the parameters ρ_0=1.15x10^{-3}/MeV, a=1.90/MeV and I_0=2 were determined to reproduce the stair-case plot of the ^{16}O level scheme. The calculated branching ratios are given in Table 3.

Angular Distributions: Emitted neutron energy depends strongly on emission angle for light nuclei. So, angular distributions of emitted neutrons are necessary for evaluation of neutron energy spectrum and calculated with Blatt - Biedenharn formalism [2] using the resonance parameters obtained by the present analysis. As examples of the angular distribution, Fig.5 shows those of the $^{12}C(\alpha,n)^{15}O$(ground state) reaction.

4. Conclusion

The $^{12}C(\alpha, n)^{15}O$ reaction and the $^{13}C(\alpha, n)^{16}O$ reaction were analyzed with a resonance formula. With the resonance parameters, evaluation was made for the neutron yield data of natural carbon, such as thick target neutron yield , branching ratios of emitted neutrons and their angular distributions.

References

[1] Murata,T.: Proc.Int.Conf. on Nuclear Data for Sci.and Tech.(Mito,1988),p.557

[2] Lane,A.M. and Thomas,R.G.: Rev.Mod.Phys.30,257(1958)

[3] Ajzenberg-Selove,F.:Nucl.Phys.A268,1(1976), ibid.A460,1(1986)

[4] Black,J.L. et al.: Nucl.Phys.A115,683(1968)

[5] Sekharan,K.K. et al.: Phys.Rev.156,1187(1967)

[6] Bair,J.K. and Haas,F.X.: Phys.Rev.C7,1356(1973)

[7] West,D. and Sherwood,A.C.: Ann.Nucl.Energy 9,551(1982)

[8] Matsunobu,H.: private communication

[9] Igo,G.J.: Phys.Rev.115,1665(1960), ibid.117,1079(1960)

[10]Ziegler,J.F.(edit.):"HELIUM:stopping power and ranges in all elements"(Pergamon,1977)
[11] Bair,J.K.: Nucl.Sci.Eng.51,83(1973)

Table 1 Resonance parameters of the $^{12}C(\alpha,n)^{15}O$ reaction

ER(MeV)	SPIN	PARITY	TOT.WIDTH(keV)	INC.WIDTH(keV)	OUT.WIDTH(keV)
11.540	0.0	1	6.00E+02	1.50E+02	4.20E+01
11.540	3.0	-1	6.00E+02	1.20E+02	1.00E+00
12.000	2.0	1	6.00E+02	4.00E+02	2.10E+00
12.380	1.0	-1	3.00E+01	7.00E+00	2.50E+00
12.730	4.0	1	5.00E+02	9.00E+01	1.60E+01
13.300	1.0	-1	9.00E+01	5.50E+01	3.50E+00
13.860	1.0	-1	1.70E+02	5.50E+01	1.50E+01
14.270	4.0	1	4.00E+02	1.10E+02	1.30E+01
14.680	0.0	1	3.00E+02	1.45E+02	1.50E+02
15.330	0.0	1	3.80E+02	3.60E+02	1.20E+01
15.800	0.0	1	3.00E+02	1.50E+02	2.00E+00

Table 2 Resonance parameters of the $^{13}C(\alpha,n)^{16}O$ reaction

ER(MeV)	SPIN	PARITY	TOT.WIDTH(keV)	INC.WIDTH(keV)	OUT.WIDTH(keV)
1.056	2.5	-1	1.50E+00	3.00E-03	1.50E+00
1.337	2.5	-1	1.00E+00	5.00E-03	9.95E-01
1.591	3.5	-1	5.00E+00	1.00E-02	4.99E+00
1.745	3.5	-1	1.50E+01	3.00E-02	1.50E+01
2.083	0.5	1	1.00E+02	1.20E+01	8.80E+01
2.250	1.5	1	1.00E+02	1.00E+01	9.00E+01
2.410	1.5	-1	8.00E+01	8.00E+00	7.20E+01
2.602	0.5	1	1.50E+01	3.50E+00	1.15E+01
2.680	2.5	1	8.00E+00	8.00E-01	7.20E+00
2.700	0.5	-1	3.00E+02	1.00E+01	2.90E+02
2.765	3.5	1	4.00E+00	1.20E+00	2.80E+00
2.809	2.5	-1	1.00E+01	3.00E+00	7.00E+00
3.065	1.5	-1	1.20E+02	9.60E+00	1.10E+02
3.280	1.5	1	1.20E+02	1.80E+01	1.02E+02
3.415	3.5	-1	2.00E+01	1.50E+00	1.85E+01
3.645	0.5	-1	8.00E+00	7.00E-01	7.30E+00
3.714	2.5	1	6.00E+00	1.20E+00	4.80E+00
3.700	1.5	1	5.00E+02	5.00E-01	5.00E+02
4.096	2.5	-1	1.60E+01	7.00E-01	1.53E+01
4.394	3.5	1	2.00E+01	2.70E+00	1.73E+01
4.460	1.5	1	1.40E+01	1.38E+01	2.00E-01
4.583	2.5	-1	6.00E+00	2.10E+00	3.90E+00
4.730	2.5	1	1.00E+02	2.60E+00	9.74E+01
4.800	0.5	1	8.00E+01	1.20E+01	6.80E+01
4.987	3.5	-1	4.00E+01	5.80E+00	3.42E+01
5.220	2.5	1	2.40E+02	7.00E+01	1.70E+02
5.325	1.5	-1	1.00E+01	3.00E+00	7.00E+00
5.460	4.5	1	1.20E+02	1.10E+01	1.09E+02
6.000	5.5	-1	7.00E+02	1.96E+02	5.04E+02
7.000	6.5	1	3.60E+02	8.50E+01	2.75E+02
7.780	7.5	-1	6.70E+02	1.95E+02	4.80E+02
8.700	7.5	1	5.00E+02	3.00E+01	3.70E+02
10.200	8.5	-1	7.00E+02	1.25E+02	5.75E+02
11.500	8.5	1	7.00E+02	1.25E+02	5.75E+02
14.200	9.5	1	8.00E+02	5.00E+01	7.50E+02

Table 3 Neutron emission branching ratios of the $^{13}C(\alpha,n)^{16}O$ reaction resonance levels

ER(MeV)	ground	1st	2nd	3rd	4th	continuum
4.987	1.00E+00	0.00E+00	0.00E+00	0.00E+00	0.00E+00	0.00E+00
5.220	8.50E-01	1.10E-01	4.03E-02	0.00E+00	0.00E+00	0.00E+00
5.325	8.67E-01	1.28E-01	4.83E-03	0.00E+00	0.00E+00	0.00E+00
5.450	8.06E-01	1.83E-01	1.21E-02	0.00E+00	0.00E+00	0.00E+00
6.000	7.49E-01	2.49E-01	2.46E-03	0.00E+00	0.00E+00	0.00E+00
7.000	6.90E-01	3.09E-01	5.49E-04	3.57E-07	2.71E-10	0.00E+00
7.780	6.63E-01	3.37E-01	4.91E-05	6.39E-08	1.51E-10	0.00E+00
8.700	6.39E-01	3.61E-01	1.62E-04	6.58E-07	3.77E-09	0.00E+00
10.200	6.09E-01	3.84E-01	2.26E-05	1.28E-07	1.02E-09	7.14E-03
11.500	5.78E-01	3.88E-01	6.66E-05	6.64E-07	8.02E-09	3.35E-02
14.200	4.57E-01	3.35E-01	1.26E-05	1.61E-07	2.43E-09	2.09E-01

RESONANCE LEVELS BELOW 4.987 MeV FEED ONLY TO THE GROUND STATE OF O-16

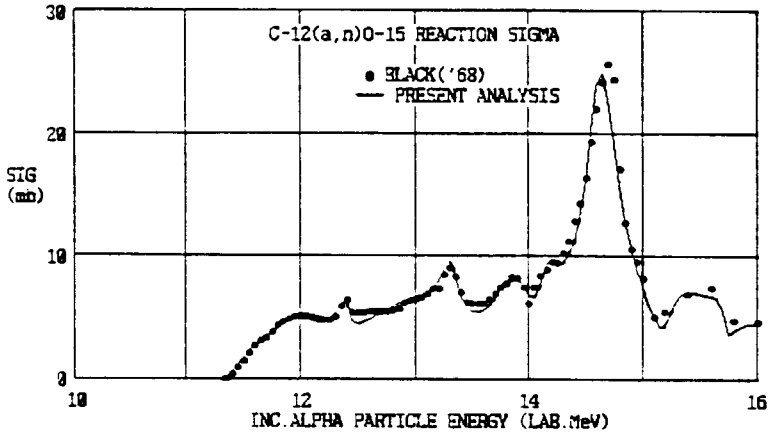

Fig. 1 The $^{12}C(\alpha,n)^{15}O$ reaction cross section

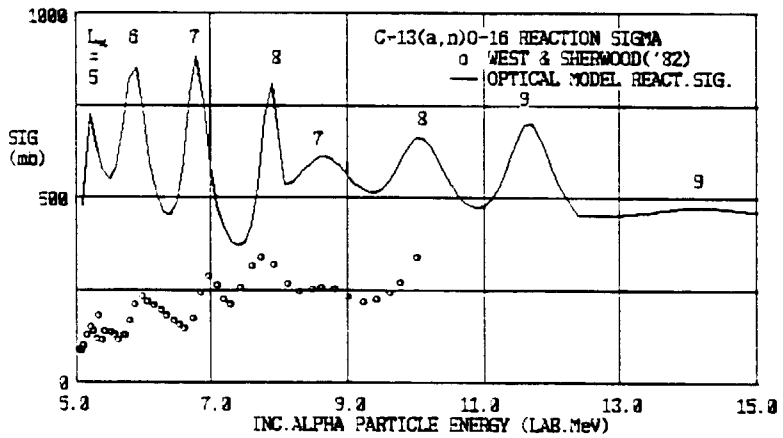

Fig. 2 Comparison of the experimental $^{13}C(\alpha,n)^{16}O$ reaction cross section[9] and the optical model reaction cross section (solid line) in high energy part.

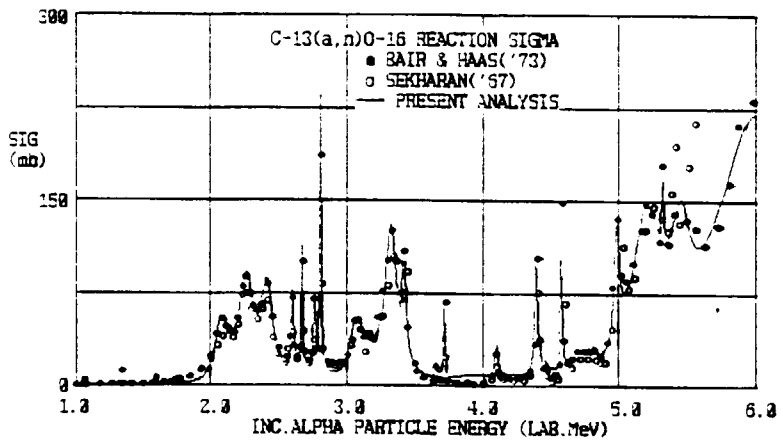

Fig. 3a The $^{13}C(\alpha,n)^{16}O$ reaction cross section (Low energy part)

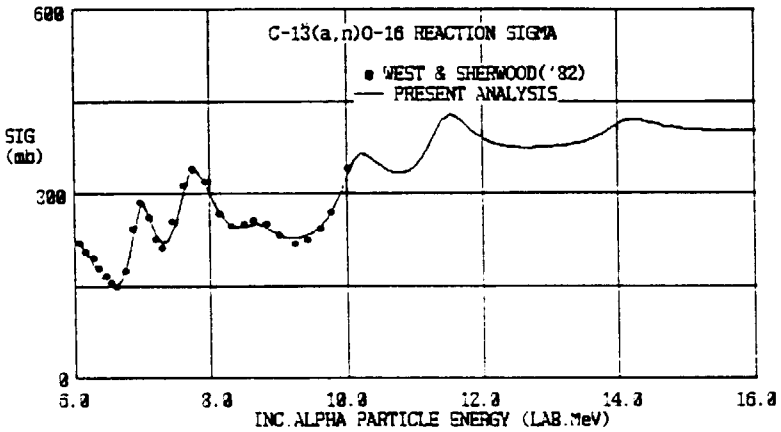

Fig. 3b The $^{13}C(\alpha,n)^{16}O$ reaction cross section (High energy part)

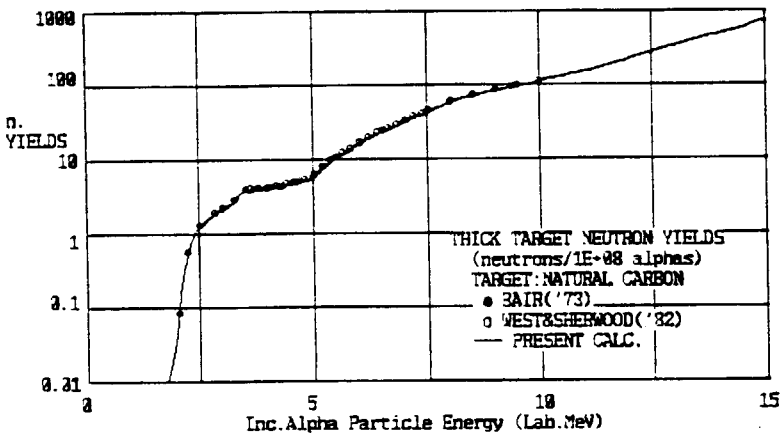

Fig. 4 Natural carbon thick target neutron yield by alpha-particle bombardment

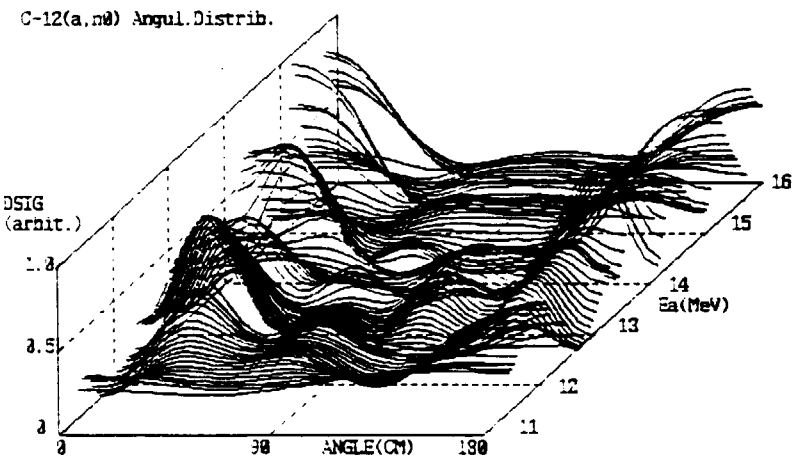

Fig. 5 Angular distribution of neutrons emitted by the $^{12}C(\alpha,n_0)^{15}O$ reaction

3.16

Measurements of Neutron Cross Section of the $^{243}Am(n,\gamma)^{244}Am$ Reaction

Yuichi HATSUKAWA, Nobuo SHINOHARA, Kentaro HATA
Nuclear Chemistry Laboratory
Tokai-mura, Naka-gun, Ibaraki-ken 319-11
e-mail: hatsu@popsvr.tokai.jaeri.go.jp

The effective thermal neutron cross section of $^{243}Am(n,\gamma)^{244}Am$ reaction was measured by the activation method. Highly-purified ^{243}Am target was irradiated in an aluminum capsule by using a research reactor JRR-3M. The tentative effective thermal neutron cross sections are 3.92 b, and 84.44 b for the production of ^{244g}Am and ^{244m}Am, respectively.

1. Introduction

Minor actinides are produced by successive neutron capture reactions of nuclear fuel and accumulated in a high burn up reactor. The minor actinides caused severe problems in nuclear waste management. The nuclide ^{243}Am is one of the important minor actinides, because of this alpha emitter has long half-life(7380 year), a large amount of its activity remains in waste a long period. To reduce such radioactivity, nuclear transmutation system by reactor or proton accelerator has been actively investigated(1,2). It is necessary for the system to obtain the accurate neutron cross sections for determining the transmutation rate of the nuclide ^{243}Am. In this study, the effective thermal neutron cross section of $^{243}Am(n,\gamma)^{244}Am$ reaction was measured by the activation method

2. Experiment

For target preparation, 1 μl of highly-purified americium solution containing 3 kBq of ^{243}Am was put into a small quartz tube and evaporated to dryness. The tube was heat-sealed and housed in an aluminum capsule together with a flux-monitor wire of Co/Al-alloy.

The target contained in an alminum capsule shown in **Fig.1** was irradiated during a 10 hour period in the HR-pipe of the JRR-3M reactor at JAERI. The irradiation position is characterized with a thermal neutron flux of 1 x 10^{14} n/cm^2 s.

After the irradiation, the quartz tube was measured by using a HP Ge detector with 1.8

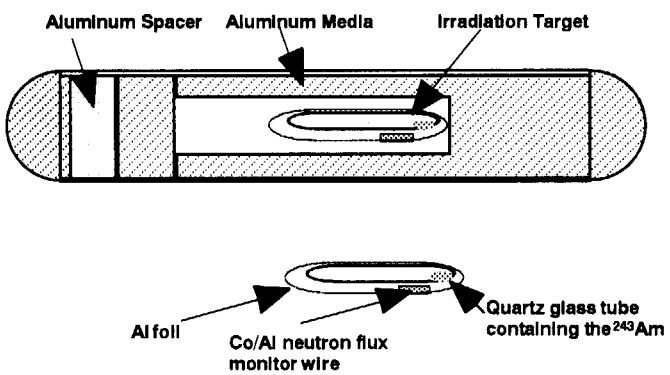

Fig. 1 Hydraulic type capsule of the ^{243}Am target irradiated in JRR-3M.

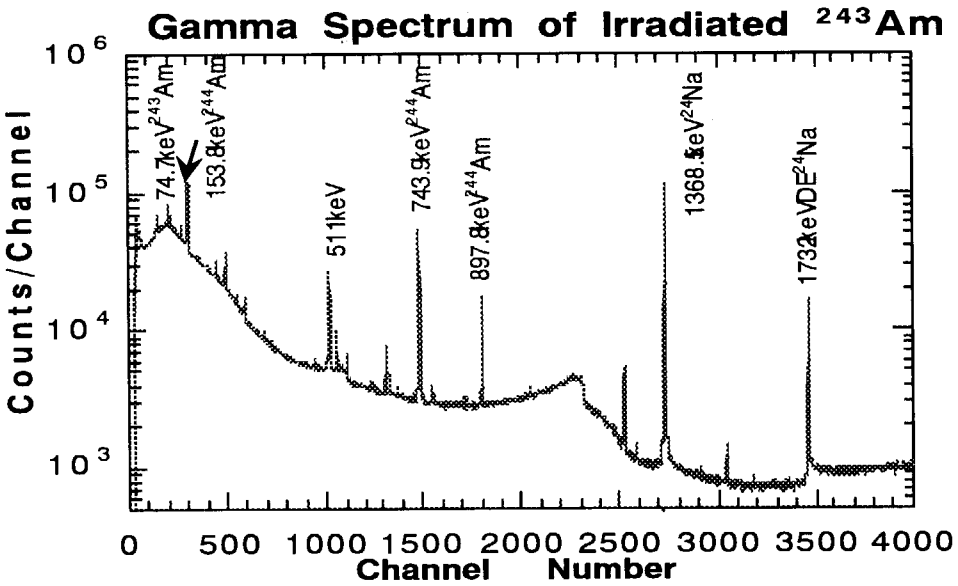

Fig. 2 Gamma spectrum of the irradiated ^{243}Am target.

keV energy resolution at 1.3 MeV. After γ-ray measurements, the target was dissolved in water and a radiometric source for alpha spectroscopy was prepared by dropping the americium solution onto a tantalum disk and evaporating it. The alpha particle spectrum of the source was measured with a silicon surface barrier detector.

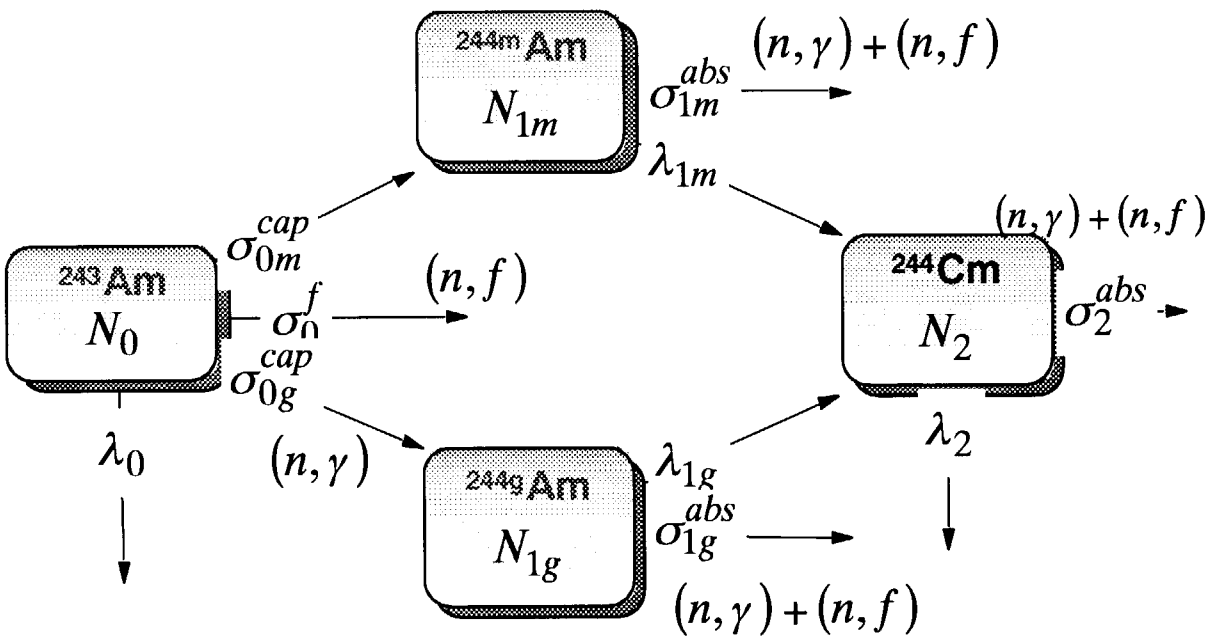

Fig. 3 Decay and growth of Am and Cm isotopes in neutron irradiation of the ^{243}Am target.

3. Results and Discussions

Figure 2 shows a γ-ray spectrum obtained from the irradiated ^{243}Am targets, where the γ-rays of ^{244g}Am can be seen at 154, 744 and 898 keV. The cross section for the ^{243}Am(n,γ)^{244g}Am reaction was deduced from the intensities of ^{244g}Am γ-rays and determined to be 3.92 b.

The ^{244}Cm nuclide is formed by the decays of the nuclides ^{244m}Am and ^{244g}Am that are produced by the neutron capture reaction of ^{243}Am as given in **Fig. 4.** In order to obtain the cross section of the ^{243}Am(n,γ)^{244m}Am, the α-particle spectrum of the irradiated target shown in Fig.4 was analyzed and determined the activity of 5.80 MeV peak of ^{244}Cm. The cross section for the formation of ^{244m}Am was calculated according to the following formulas:

We define that $N_i(t)$, σ_i^{abs} and σ_i^{cap} are the atom number, the absorption cross section and the capture cross section for the nuclide i at irradiation time t, respsctively. The time-derivatives of atom numbers of the actinide nuclides during irradiation are given by

$$\frac{dN_0(t)}{dt} = -N_0(t)\left(\lambda_0 + \phi\sigma_{0t}^{abs}\right) \quad (1)$$

$$\frac{dN_{1m}(t)}{dt} = N_0(t)\phi\sigma_{0m}^{cap} - N_{1m}(t)\left(\lambda_{1m} + \phi\sigma_{1m}^{abs}\right) \quad (2)$$

$$\frac{dN_{1g}(t)}{dt} = N_0(t)\phi\sigma_{0g}^{cap} - N_{1g}(t)\left(\lambda_{1g} + \phi\sigma_{1g}^{abs}\right) \quad (3)$$

$$\frac{dN_{2m}(t)}{dt} = \lambda_{1m}N_{1m}(t) - N_{2m}(t)\left(\lambda_2 + \phi\sigma_2^{abs}\right) \quad (4)$$

$$\frac{dN_{2g}(t)}{dt} = \lambda_{1g}N_{1g}(t) - N_{2g}(t)\left(\lambda_2 + \phi\sigma_2^{abs}\right) \quad (5)$$

$$N_2(t) = N_{2m}(t) + N_{2g}(t) \quad (6)$$

where the notation of each nuclide i is given in **Fig.3**. ϕ and λ_i are the netron flux and the decay constant, respectively. The solution of these differential equations are

$$N_0(t) = N_0 e^{-A_0 t} \quad (7)$$

$$N_{1m}(t) = \frac{N_0(0)\phi\sigma_{0m}^{cap}\left(e^{-A_0 t} - e^{-A_{1m} t}\right)}{-A_0 + A_{1m}} \quad (8)$$

$$N_{2m}(t) = \frac{N_0(0)\phi\lambda_{1m}\sigma_{0m}^{cap}\left[-A_0\left(e^{-A_{1m} t} - e^{-A_2 t}\right) + A_{1m}\left(e^{-A_0 t} - e^{-A_2 t}\right) - A_2\left(e^{-A_0 t} - e^{-A_{1m} t}\right)\right]}{\left(A_0 - A_{1m}\right)\left(-A_0 + A_2\right)\left(-A_{1m} + A_2\right)} \quad (9)$$

$$N_{2g}(t) = \frac{N_0(0)\phi\lambda_{1g}\sigma_{0g}^{cap}\left[-A_0\left(e^{-A_{1g} t} - e^{-A_2 t}\right) + A_{1g}\left(e^{-A_0 t} - e^{-A_2 t}\right) - A_2\left(e^{-A_0 t} - e^{-A_{1g} t}\right)\right]}{\left(A_0 - A_{1g}\right)\left(-A_0 + A_2\right)\left(-A_{1g} + A_2\right)} \quad (10)$$

where A_i is

$A_i = r_i + \phi\,\sigma_i^{abs}$.

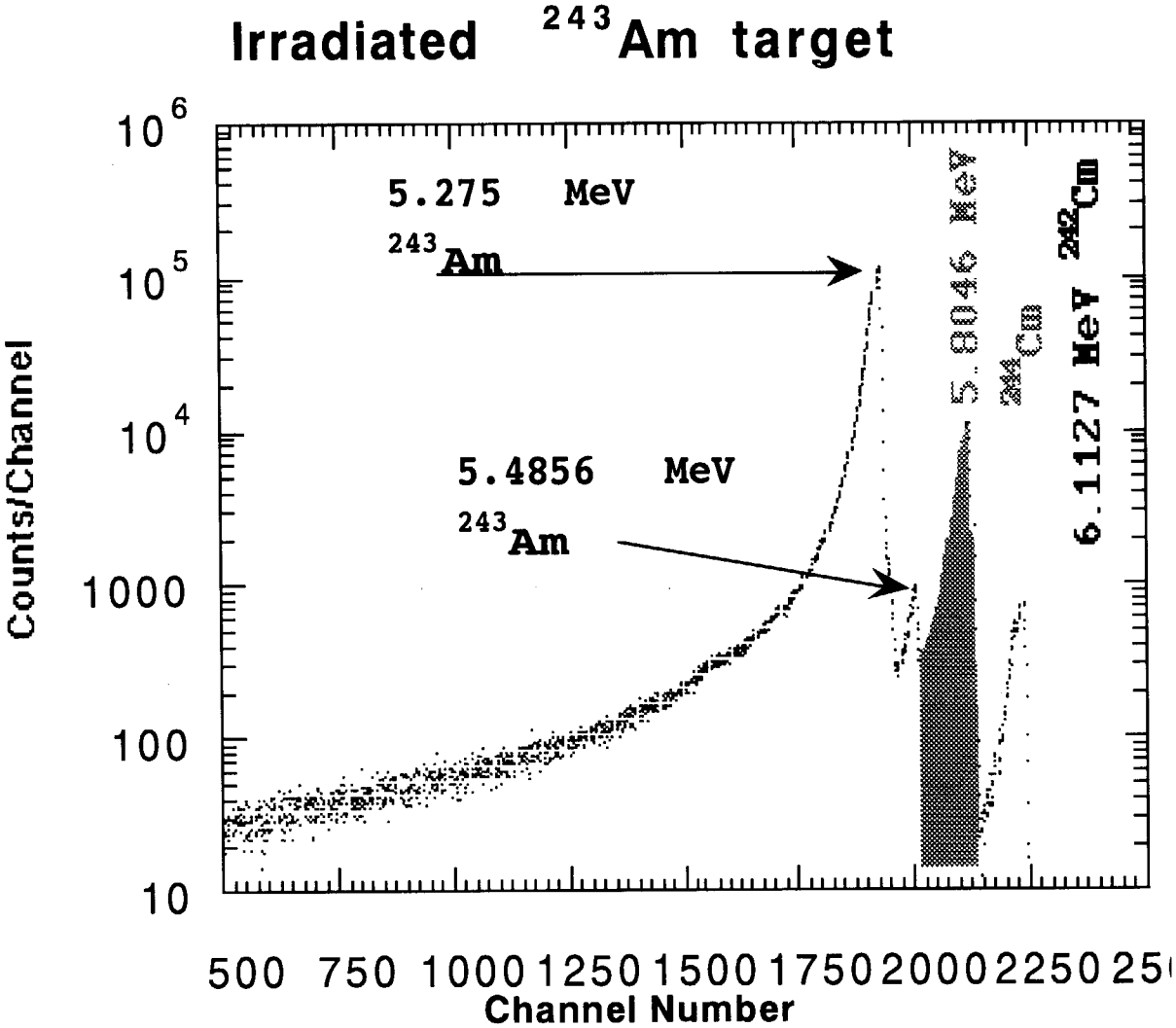

Fig. 4 Alpha spectrum of the irradiated ^{243}Am target

The cross sections of ^{243}Am(n,γ)^{244}Am reaction obtained from the calculated atom number of ^{244m}Am is 84.4 b.

The present value of 3.92 b for ^{243}Am(n,γ)^{244g}Am reaction is good agreement with the previous one of 3.8 ± 0.4 b[4]. On the other hand, the cross section of the ^{243}Am(n,γ) ^{244m}Am reaction measured in this study (84.4 b) is not consistent with the value of 75.1 ± 1.8 b[4] but agree with that of 83 ± 6 b measured by Garrilov et al.[5] The neutron cross sections for ^{243}Am in JENDEL-3-2 should be evaluated newly on the basis of these results.

References

(1) Taube, M: Nucl. Sci. Eng., **61**, 212(1976)
(2)Bowman, C.D., Lisowski, P.W., Arthur, E.D.,: Proc. of 2nd Int. Symp. Advanced Nuclear Energy Research-Evolution by Accelerator-, Jan. 24, 1990, Mito, Japan, p. 149, JAERI.
(3)Kocherov, N., McLaughlin, P.K.(eds.): INDC(SEC)-104, (1993).
(4)Lederer, C.M., Shirley, V.S.: Table of Isotopes, (8th ed.) (1996), John Wiley & Sons, New York
(5)Garrilov, V.D., Goncharov, V.A., Ivanenko, V.V., Kustov, V.N., and Smirnov, V.P.: Atomnaya Energiya, **41**, 185 (1976)

3.17 Fission Cross Section Measurement of Am-242m using Lead Slowing-down Spectrometer

Tetsuya Kai[1], Katsuhei Kobayashi[1], Shuji Yamamoto[1], Yoshiaki Fujita[1], Itsuro Kimura[2], Yasushi Ohkawachi[3] and Toshio Wakabayashi[3]

1 *Research Reactor Institute, Kyoto University*
Kumatori-cho, Sennan-gun, Osaka 590-04, Japan

2 *Department of Nuclear Engineering, Kyoto University*
Yoshidahonmachi, Sakyo-ku, Kyoto 606-01, Japan

3 *Power Reactor and Nuclear Fuel Development Corporation*
4002 Narita, O-arai machi, Ibaraki, 311-13, Japan
e-mail:tkai@post3.rri.kyoto-u.ac.jp

By making use of double fission chamber and lead slowing-down spectrometer coupled to an electron linear accelerator, fission cross section for the ^{242m}Am(n,f) reaction has been measured relative to that for the ^{235}U(n,f) reaction in the energy range from 0.1 eV to 10 keV. The measured result was compared with the evaluated nuclear data appeared in ENDF/B-VI and JENDL-3.2, of which evaluated data were broadened by the energy resolution function of the spectrometer. Although the JENDL-3.2 data seem to be a little smaller than the present measurement, good agreement can be seen in the general shape and the absolute values. The ENDF/B-VI data are larger more than 50 % than the present values above 3 eV.

1. Introduction

Americium(Am) isotopes are burdensome minor actinides which are abundantly produced in power reactors. The nuclear data for them are of great importance for the design of reactors with mixed oxide or plutonium fuels and the system design of spent fuel reprocessing. In addition, the fission cross sections are also of interest for its transmutation from the standpoint of the disposal of radioactive waste.[1]-[5] Recently, the authors have measured the fission cross section of ^{237}Np, ^{241}Am and ^{243}Am in the resonance energy region[6]-[8]. As well as these isotopes, the ^{242m}Am isotope is also interesting because of its large fission cross section at lower energies (the thermal neutron cross section is about 6,500 b, which is more than ten times comparing to that of ^{235}U). But there exist large discrepancies among the evaluated fission cross sections of ^{242m}Am in JENDL-3.2[9] and ENDF/B-VI[10] data files, especially at resonance energies.

The fission cross section for the ^{242m}Am(n,f) reaction was measured at energies between 0.1 eV and 10 keV relative to that for the ^{235}U(n,f) reaction by making use of back-to-back(BTB) type double fission chamber and lead slowing-down spectrometer coupled to the 46-MeV electron linear accelerator (linac) of Research Reactor Institute, Kyoto University (KURRI). To avoid the interference between the ^{242m}Am and the ^{235}U resonances, the ^{242m}Am fission cross section was also measured relative to the ^{10}B(n,α) reaction using a BF_3 counter below 1 keV, and the result was normalized to that measured with the BTB chamber at energies between 200 eV and 1 keV. The experimental technique is the same as before[6]-[8]. The measured result is compared with the evaluated nuclear data in JENDL-3.2 and ENDF/B-VI.

2. Experimental Methods

2.1. Lead Slowing-down Spectrometer

The lead slowing-down spectrometer is coupled to the 46 MeV electron linac at KURRI. The Kyoto University Lead Slowing-down Spectrometer (KULS) is composed of 1600 blocks (each is 10 ×10 ×20 cm^3, and purity is 99.9%), and these are piled up to make a cube of 1.5 ×1.5 ×1.5 m^3 (~ 40t) without any other structural materials. At the center of the KULS, we have placed an air-cooled photoneutron target of tantalum to produce pulsed fast neutrons. Thermocouples were attached on the surface of the target case to monitor the temperature. The linac was operated in such a way as to keep the temperature less than 300°C. The KULS has eight experimental/irradiation holes (10 ×10 cm^2, 55 or 45 cm in depth), and one of the holes is covered by bismuth layers of 10 to 15 cm in thickness to shield high energy gamma-rays (6 to 7 MeV) produced by the Pb(n,γ) reaction in the spectrometer.[11]

Characteristic behavior of neutrons in the KULS was studied by calculations with the continuous energy Monte Carlo Code MCNP[12] and by experiments with resonance filter method[11]. There exists the relation of $E=K/t^2$ between the neutron slowing-down time t and the energy E, where K is the slowing-down constant.[14][15] The constant K for the Bi hole was determined to be 190 ± 2 keV μs^2, making use of resonance filers of In, Te, Ta, Au, Cd, Mo, and Mn. It was also found that the energy resolution was around 40 % for the experimental hole at energies from a few eV to about 500 eV and was larger in the lower and the higher energy regions. More detailed characteristics of the KULS are given in other literature.[7][11]

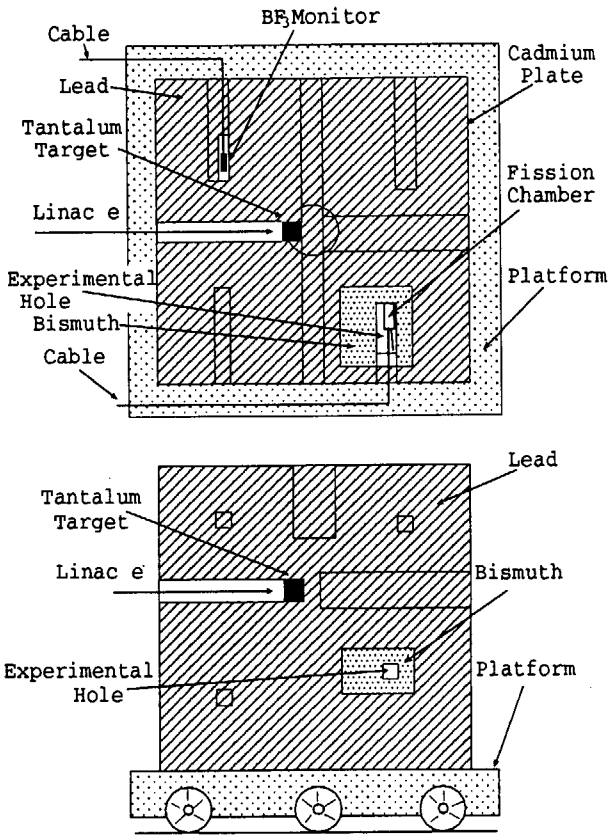

Fig. 1 Cross sectional view of the KULS.

2.2. The ^{242m}Am and ^{235}U Samples

The ^{242m}Am deposit was purchased from Chemotrade GMBH, and the ^{242m}Am was electrodeposited (radioactive area of 20 mm in diameter) on the stainless steel disk (28 mm in diameter and 0.2 mm in thickness). The purity of the ^{242m}Am was 85.25 %, and the major impurities were 14.22 % for ^{241}Am and 0.53 % for 243Am. The number of ^{242m}Am atoms was determined by alpha and gamma-ray spectroscopies. The alpha-rays having energies in the range 5.1416 to 5.2078 MeV were measured with a silicon surface barrier detector, and the 49.367 keV gamma-ray from ^{242m}Am was measured with a high-purity germanium detector. The pulse height distribution of ^{242m}Am was shown in Fig. 2 and Fig. 3. As the result of both analyses,

the number of ^{242m}Am atoms was determined to be $(2.039 \pm 0.042) \times 10^{16}$, as shown in Table I.

Highly enriched uranium oxide (99.91 % of ^{235}U) was got from ORNL. The uranium was also electrodeposited on the stainless steel disk at KURRI. This ^{235}U sample was used to monitor the neutron flux in this study as the well-known reference cross section of the ^{235}U(n,f) reaction. As well as the americium sample, the number of the ^{235}U atoms was determined by the analyses of the alpha-rays with 4.152 to 4.597 MeV and of the 185.7 keV gamma-ray, and was determined to be $(2.81 \pm 0.030) \times 10^{16}$, as seen in Table I.

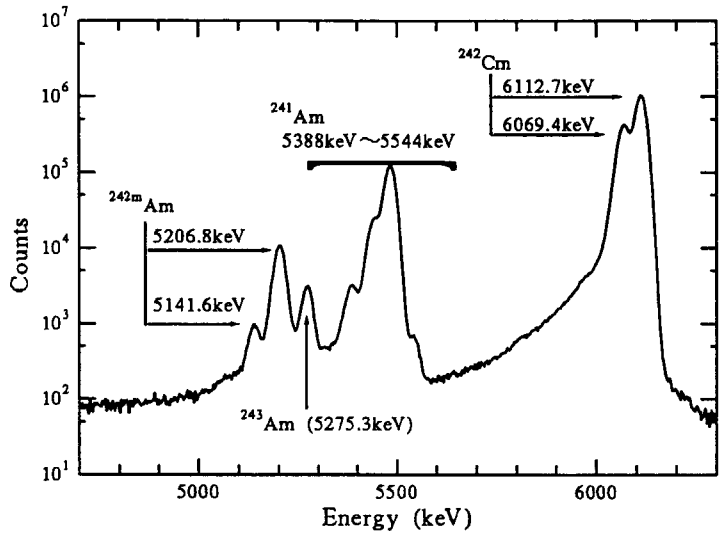

Fig. 2 Alpha-ray Spectrum of ^{242m}Am

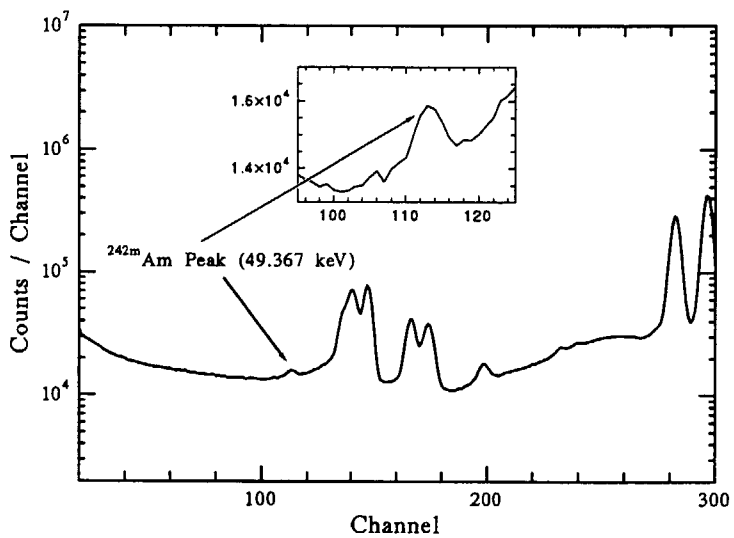

Fig. 3 Gamma-ray Spectrum of ^{242m}Am

Table I. Determination of the Number of Atoms for the ^{242m}Am and ^{235}U Oxide Deposits

Method	^{242m}Am Deposit	^{235}U Deposit
Alpha spectroscopy	$(2.047 \pm 0.053) \times 10^{16}$	$(2.757 \pm 0.042) \times 10^{16}$
Gamma spectroscopy	$(2.026 \pm 0.070) \times 10^{16}$	$(2.856 \pm 0.043) \times 10^{16}$
Weighted mean value	$(2.039 \pm 0.042) \times 10^{16}$	$(2.805 \pm 0.030) \times 10^{16}$

2.3. Fission Chamber

The fission chamber is composed of two identical parallel plate-type ionization chambers, as shown in Fig.2.3.. As the back sides of the sample deposit(^{242m}Am) and the reference one(^{235}U) are face each other, it is called back-to-back(BTB) type. This chamber was originally designed for in-core fission ratio measurements.[13] The double fission chamber was made of aluminum and filled with a mixed gas of 97 % Ar and 3 % N_2 at the pressure of 1 atm. Fission pulses were clearly discriminated from background ones caused by the alpha-rays since we used the thin electrodeposited layers of Am and U.

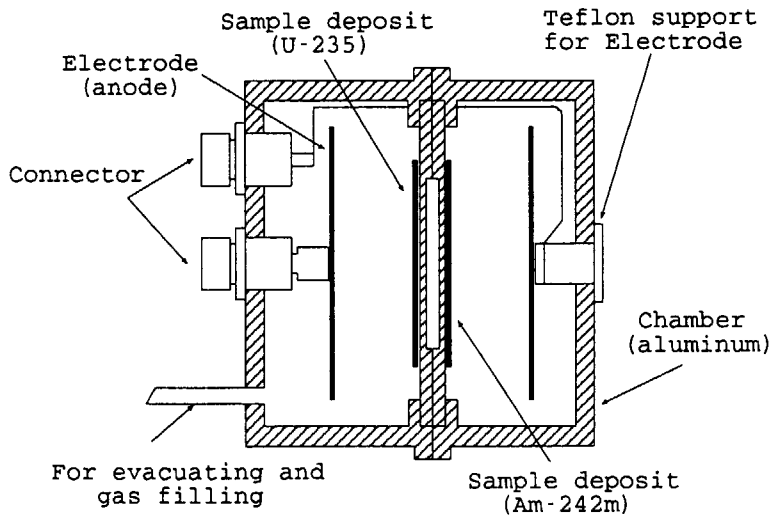

Fig. 4 Cross sectional view of the BTB chamber

2.4. The BF_3 Counter

The ^{10}B(n, α) reaction is well known to be one of the standard cross sections and is often applied to cross section measurements as a reference. Instead of the ^{235}U(n,f) reaction, the ^{10}B(n, α)reaction was applied to the measurement of the ^{242m}Am(n,f) cross section using a BF_3 counter in order to avoid the resonance interference between ^{242m}Am and ^{235}U fission cross sections. The BF_3 counter was of a cylindrical type, 50 mm in effective length, 12 mm in diameter and 1 atm, and high-voltage bias was 1100 V.

2.5. Data Taking and Fission Ratio Measurement

The lead slowing-down spectrometer KULS was driven by the 46-MeV electron linac at KURRI, and the typical operating conditions during the experiments were as follows: pulse repetition rate of 200 Hz, pulse width of 22 ns, electron peak current of ~1.5 A, and the electron energy of about 30 MeV.

The fission cross section of ^{242m}Am has been measured relative to that of ^{235}U by making use of the BTB chamber in the bismuth hole. We have employed not only the BTB chamber but also the BF_3 counter that is well known as a good $1/v$ detector in the energy range for the current measurement, for the reason that there may be interference between ^{242m}Am and ^{235}U resonaces in the relevant energy region. The relative fission cross section of ^{242m}Am , which was measured with the BF_3 counter below 1 keV, was normalized to the fission cross section between 200 eV and 1 keV obtained relative to the ^{235}U(n,f) reaction using the BTB chamber. Two identical electronic circuits were employed for the ^{242m}Am and ^{235}U chambers. Through the amplifiers and the discriminators, signals from the fission chambers were fed into the respective 4096-channel time-analyzer with 62.5 or 500 ns/channel, which was initiated by the linac electron burst, and the slowing-down time data of fission counts were stored for each measurement of 4-5 hour duration in a data acquisition system. From the fission counts of the ^{242m}Am and the ^{235}U deposits, the energy dependent cross section for the ^{242m}Am(n,f) reaction is obtained by

$$\sigma_{Am}(E) = \frac{C_{Am}(E)}{C_U(E)} \frac{N_U}{N_{Am}} \sigma_U(E)$$

where

$C_{Am}(E)$: fission counts of ^{242m}Am at energy E,
$C_U(E)$: fission counts of ^{235}U at energy E,
N_{Am} : number of ^{242m}Am atoms in the ^{242m}Am deposit,
N_U : number of ^{235}U atoms in the ^{235}U deposit,
$\sigma_U(E)$: energy dependent fission cross section of ^{235}U .

The reference cross section $\sigma_U(E)$ was used from ENDF/B-VI[10], whose data were broadened by the energy resolution of the KULS.

3. Results and Discussion

The present result is shown in Fig.5 and compared with the evaluated cross section in ENDF/B-VI[10] and the JENDL-3.2[9], which are broadened by the energy resolution of about 40 % of the KULS. The experimental uncertainties are considered to be mainly due to (1)the statistical error in fission counts, (2)assignment of fission counts, (3)number of atoms for the ^{242m}Am and the ^{235}U deposits, and (4)the reference fission cross section for the ^{235}U(n,f) reaction. Total amount of the experimental uncertainties is 3.5 to 4.5 %.

It is seen in Fig.5 that both of the evaluated data show good agreement with the present result below 3 eV. Above 3 eV, although the JENDL-3.2 data seems to be a little smaller than the measurement, good agreement can be seen in general. Hpowever, the ENDF/B-VI data are larger more than 50 % than the present values.

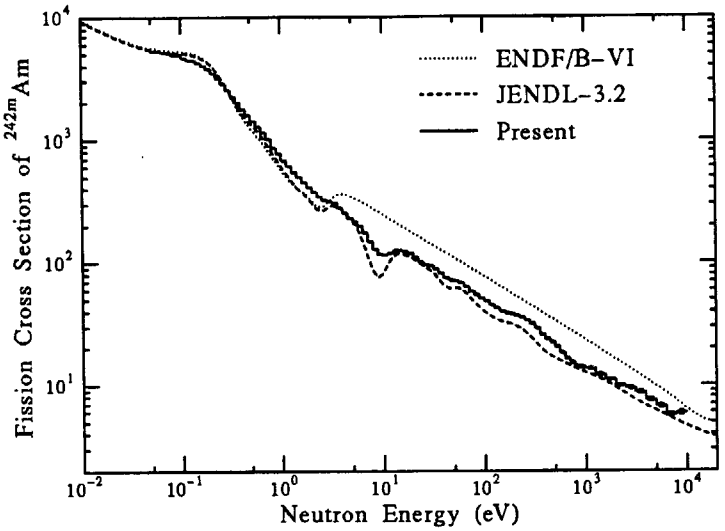

Fig. 5 Comparison of the measured fission cross section of ^{242m}Am with those in the evaluated data.

References

[1] Lancaster, D.: *Proc. of the Int. Conf. and Technol. Exposition on Future Nucl. Systems: Global '93"*, ANS, La Grange Park, Illinois, p.609 (1993).

[2] Tommasi, J., *et al.*: *ibid.*, p.1252 (1993).

[3] Wakabayashi, T., *et al.*: *Proc. of the Int. Conf. of Evaluation of Emerging Nuclear Fuel Cycle systems: Global '95"*, CEA, p.800 (1995).

[4] Kloosterman, J. L., Li, J. M.: *ibid.*, p.1106 (1995).

[5] Mukaiyama, T., *et al.*: *J. At. Energy Soc. Japan*, **37**, 3, p.159 (1995).

[6] Yamanaka, A., *et al.*: *J. Nucl. Sci. Technol.*, **30**, 9, 863 (1993).

[7] Yamamoto, S., *et al.*: *Nucl. Sci. Eng.*, **126**, 201-212 (1997).

[8] Kobayashi, K., *et al.*: *Proc. of Int. Conf. on Future Nuclear Systems, Global '97"*, Yokohama, Japan, pp784-788 (1997).

[9] Nakagawa, T., *et al.*: *J. Nucl. Sci. Technol.*, **32**, No.12, 1259 (1995).

[10] Rose, R. F.(Ed.): *BNL-NCS*-17541, 4th Ed. (ENDF/B-VI) (1991).

[11] Kobayashi,K., *et al.*: *Nucl. Instrum. and Methods in Phys. Res. A* **385**, 145-156 (1997).

[12] "MCNP - A General Monte Carlo for Neutron and Photon Transport, Version 3A", LA-7396-M, Rev. 2, Los Alamos National Laboratory (1986).

[13] Obu, M.: *JAERI-M* 9757 (1981).

[14] Bergman, A. A., *et al.*: *Proc. 1st Int. Conf. on the Peaceful Uses of Atomic Energy*, United Nations, 4, 135 (1955).

[15] Beckurts, K. H., Wirtz, K.: *"Neutron Physics"*, Springer-Verlag, New York, p.167 (1964).

3.18 Measurements of Fast Neutron-Induced Fission Data of Np-237

Than Win, Keiichiro SAITO, Mamoru BABA, Tomohiko IWASAKI,
Masanobu IBARAKI, Takako MIURA, Toshiya SANAMI, Yasushi NAUCHI,
Naohiro HIRAKAWA
Department of Quantum Science and Energy Engineering, Tohoku University
Aoba-Ku, Sendai 980-77, Japan
E-mail: thanwin@rpl.qse.tohoku.ac.jp
ksaito@rpl.qse.tohoku.ac.jp

We have performed the following measurements for ^{237}Np using the 4.5 MV Dynamitron accelerator of Tohoku University as the pulsed neutron source:

(1) Prompt fission neutron spectrum for 0.62 MeV incident neutrons, and

(2) Neutron-Induced fission cross-section between 10 and 100 keV.

The prompt fission neutron spectrum was measured using TOF method with a heavily shielded NE213 scintillation detector. The Maxwellian temperature T_m derived is 1.28MeV, which is lower than that of 1.38MeV in JENDL-3.2.

The fission cross sections were measured between 10 ~ 100 keV. The results are between JENDL-3.2 and ENDF/B-VI.

I. Introduction

The nuclear data for ^{237}Np are important for the transmutation problem since it is a major waste material of reactors. The data of the prompt fission neutron spectrum and the fission cross-section play an important role in the design of transmutation systems.

The fission spectrum is the source term in a Np-loaded system, and is important for the analysis of the performance and the design of the system. It is also important for the evaluation of the inelastically scattered neutron spectra and inelastic cross sections. But, only a few data are existing and more information for the fission spectrum is required in the present condition.

Fission cross sections directly dominate the transmutation rate and play an important role in the design of a transmutation system and high burn-up reactors. However, the database available is not sufficient to meet the required accuracy, especially between 10 ~ 100 keV. The results of four measurements reported since 1970 in this energy range but have discrepancies far beyond the quoted experimental errors. For example, the discrepancy is more than 100% between the measurements by Hoffman et al. and these by White et al. As a result, nuclear data files also show large discrepancy. Therefore, new measurements are expected for the fission cross sections between 10 ~ 100 keV.

For the reasons mentioned above, we have carried out the following measurements using the 4.5 MV Dynamitron accelerator of Tohoku University as a pulsed neutron source[1,2].

(1) Prompt fission neutron spectrum of ^{237}Np for 0.62 MeV incident neutrons, and

(2) Neutron-Induced fission cross section of ^{237}Np between 10 and 100 keV, relative to ^{235}U. In this measurement, to reduce the experimental uncertainty, we have developed a fast timing back-to-back fission chamber and a water-cooled Li metal target.

II. Prompt Fission Neutron Spectrum Measurement

II (A) Experimental Method

Incident neutrons of 0.62MeV were produced by bombarding a ^{7}Li metal target with a pulsed proton beam provided by the Dynamitron. The fission spectrum was measured by the Time-of-Flight (TOF) method.

Fig. 1 shows the experimental set up of the present work. The sample used was NpO_2 powder, 19.99g in weight. It was enclosed in a cylindrical-shaped and two-layered stainless steel container having a 13.8mm-diam and 120mm long outer layer, and a 12.8mm-diam and 107mm long inner layer.

Fission neutrons were detected by a NE213 scintillation detector, 14cm in diameter and 10cm thick. To reduce the effect of background, the detector was mounted on a shield made of paraffin containing Li_2Co_3. Moreover, a slab of lead, 2cm thick, was placed at the entrance of the shield to reduce the effect of the sample activity. The detector was placed at an angle of 90-deg to the incident neutron beam. The flight path was chosen to be 2.45m as a compromise among the energy resolution, S/N and a counting rate.

As the monitor detector, a small NE213 scintillation detector, 5.08cm in diameter and 5.08cm thick, was used to measure the spectrum and the intensity of the source neutrons. It is shadowed from the Np sample to avoid the effect of the sample activity.

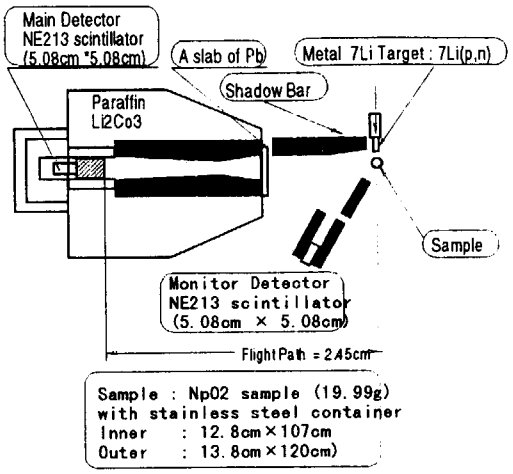

Figure 1 Experimental set up

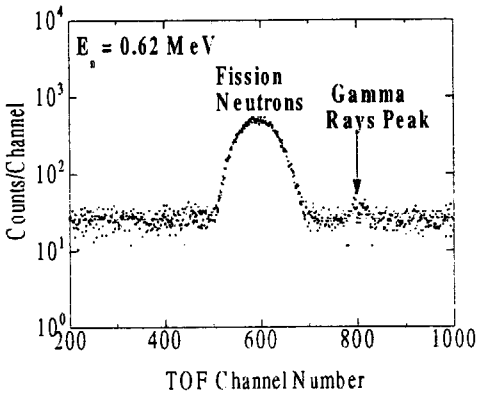

Fig.2 TOF spectrum of ^{237}Np

Three parameter data were collected for TOF, pulse-height and n-γ as the form of list data.

II (B) Data Processing

At first, we transformed three parameter data into TOF spectrum by making pulse-height biasing and n-γ discrimination. In pulse-height biasing, not only low pulse-height bias data but also high pulse-height bias data were deduced separately. The TOF spectrum for high pulse-height biasing is shown in Fig. 2. Next, we transformed the TOF spectrum of each bias into an energy spectrum, and joined these two energy spectra. The detector efficiency was determined using TOF measurement of the spontaneous fission neutrons of ^{252}Cf for <3MeV, and using the SCINFUL efficiency code for >3MeV.

The data were corrected for the effects of (1) backgrounds, (2) detector efficiency, (3) neutron attenuation due to the lead slab and (4) the multiple scattering inside the sample.

Finally, the Maxwellian temperature T_m was derived from the energy spectrum.

II(C) Results and Discussion

The Maxwellain spectrum is frequently employed for conventional expression of the prompt fission neutron spectrum. Its spectrum and average energy are given by the following

equations:

$$\chi(E) = C_m \sqrt{E} \exp\left(-E/T_m\right) \quad (1) \qquad \langle E \rangle = 3T_m/2 \quad (2)$$

Fig. 3 shows the plot of ln N (E)/$\sqrt{E}$ *vs* E for the experimental spectrum N (E). Since the data lie on the straight line, one can conclude that the data are described well by the Maxwellian spectrum. Fig. 4 shows the present result fitted with the Maxwellian spectrum. The Maxwellian temperature T_m derived by fitting the experimental result is (1.28±0.04) MeV.

Table 1 shows the result of the present work in comparison with other results. In this table, the value of T_m of the present work is compared with Howerton-Doyas evaluation based on the average number of the prompt neutrons $\bar{\nu}_f(E)$ [4]:

$$T_m = 0.997 + 0.125\bar{\nu}_f(E) \qquad (3)$$

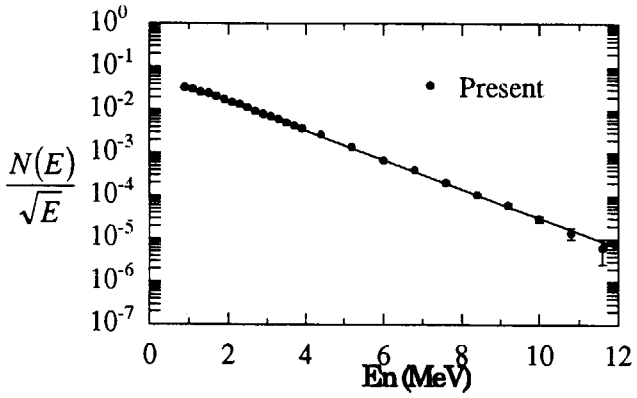

Fig.3 $\frac{N(E)}{\sqrt{E}}$ Vs E_n

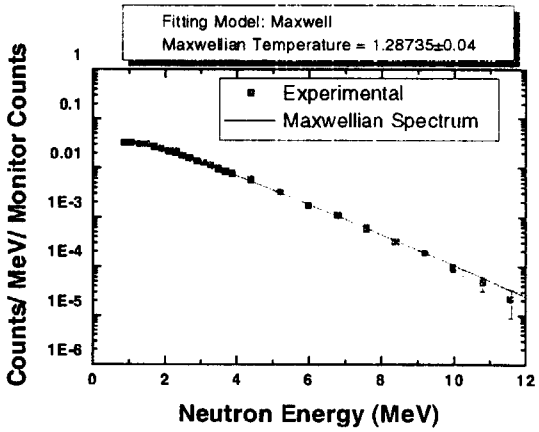

Fig. 4 ^{237}Np fission neutron spectrum

In JENDL-3.2, the Maxwellian temperature is given as 1.38MeV independently with neutron energy. As a conclusion, one can conclude that the value of T_m of the present work agrees fairly with that of Kornilov [3], and the value of T_m given by JENDL-3.2 is higher than the results of the experimental data.

Table 1 Comparison of ^{237}Np fission spectrum data

Authors	E_n (MeV)	T_m (MeV)	<E> (MeV)
Present(Exp)	0.62	1.28±0.04	1.93±0.06 (Eq (2))
Kornilov[3] (Exp)	0.52	1.31 (Eq (2))	1.966
Trufanov[4] (Exp)	4.9±0.1	-	2.186±0.04
	7.8±0.2	-	2.03 ±0.08
Boikov[5] (Exp)	2.9	1.369±0.015	2.054±0.023
	14.7	-	2.114±0.029
JENDL- 3.2	-	1.38	2.07 (Eq (2))
Howerton-Doyas[6] (Evaluation)	0.62	1.324	-

III. Fission Cross Section Measurement

III (A) Experimental Method

The experiment was performed using a pulsed white neutron source. Figure 5 shows the arrangement of the present measurement. A ^{237}Np sample was loaded with a ^{235}U standard sample within a back-to-back type chamber.

Both samples were electroplated on a Pt plate of 0.3 mm thick and 36 mm in diameter. The diameter of the deposit is 25 mm. Table 2 shows the details of the samples.

Pulsed white neutrons were produced via the ^{7}Li(p,n) reaction using a thick Li-metal target. The energy spectrum of the neutrons was measured with TOF method by a ^{6}Li-glass scintilator at 0-deg to the beam line. In fig.6, the energy spectrum is shown. The highest energy was 120.1 keV.

Based on this energy spectrum, the energy scale of TOF was calibrated. The energy scale was confirmed by measuring the known resonance of ^{NAT}Fe as shown in fig. 6.

The present fission rate measurement was composed of two runs. In the first run, the sample of ^{237}Np was faced to the target. In the second run, the standard sample of ^{235}U was faced to the target by rotating the fission chamber by 180-deg at the same position. This operation eliminates the necessity of some corrections for the anisotropic behavior of the fission fragment, the neutron attenuation in the backing plates and the small difference of the solid angles of the samples between two runs.

The data accumulation was carried out using two-sets of two-parameter pulse height analyzer. Figure 7 shows a typical two-dimensional spectrum for ^{237}Np. The vertical and horizontal axes represent the TOF and the pulse height scale respectively. Alpha particle events are seen in the low pulse-height region. The overall counts about 2000 of fission events were accumulated for 20 hours. To check the stability of neutron generation, a BF_3 counter was placed at 90-deg to the beam line.

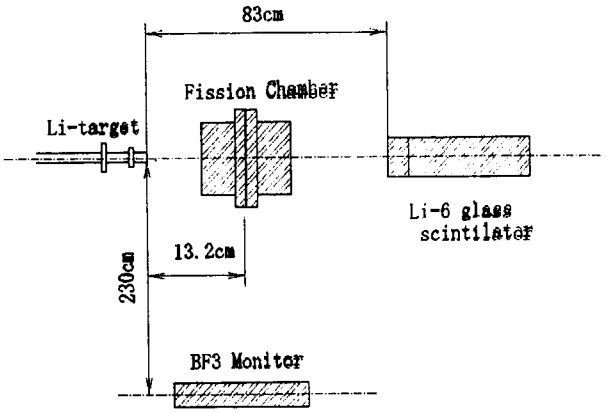

Fig. 5 Experimental setup

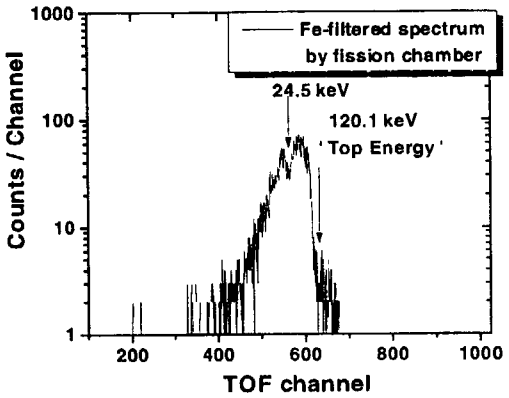

Fig. 6 Energy confirmation by Fe resonance

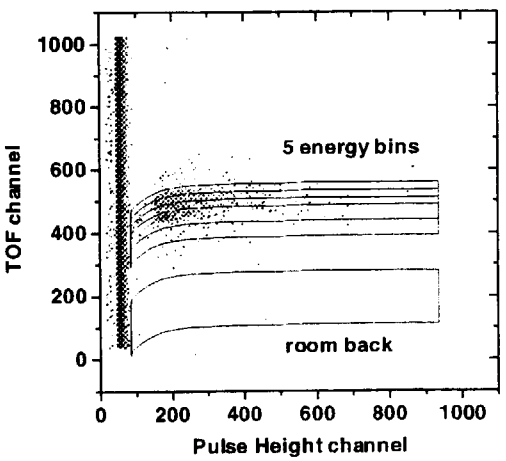

Fig 7 Typical 2-D spectrum of ^{237}Np

Table 2 Sample used

Sample	Mass (mg)	Purity (%)	Uniformity (%)
^{237}Np	1.051	100	1
^{235}U	0.406	99.9	4

III (B) Results

The TOF data were divided into five energy bins for obtaining fission counts as shown in fig.7. The shape of curving in the low pulse-height region is due to an effect of "time walk". The "walk" shape in the pulse height spectrum was determined experimentally by using a mono energetic neutron source.

The fission count obtained was corrected for (1) the background fission's by room returned neutrons, (2) the pulse-height discrimination and (3) the self-absorption in the fission sample. Table 3 shows the correction values.

The fission cross section ratio was derived by Eqn. (4)

$$R = \sqrt{\frac{C^{f}_{237} \cdot C^{b}_{237}}{C^{f}_{235} \cdot C^{b}_{235}}} \cdot \frac{N_{235}}{N_{237}} \qquad (4)$$

237: ^{237}Np 235: ^{235}U
f: forward run b : backward run
N: number of atom

Figure 8 shows the cross section ratios measured by two separate runs in comparison with JENDL-3.2 and ENDF/B6. The 1-st and 2nd results agree within experimental errors except for the highest energy point. Figure 9 shows the fission cross section of ^{237}Np deduced from the fission cross section of ^{235}U given by JENDL-3.2. The errors were 20% and 8% at 8.4 keV and 83.5 keV, respectively. The present result shows good agreement with the result of Hoffman et al. below ~ 100 keV and consistent with that of Yamanaka et al. in low energy region.

Table 3 Correction values

	α-decay	Self-absorption	Room back	Scattered neutrons	Total
^{235}U	0.8%	0.74%	0.4 ~ 3.4%	1.3%	~ 6.4%
^{237}Np	1.0%	1.4%	0.6 ~ 5.4%		~ 9.3%

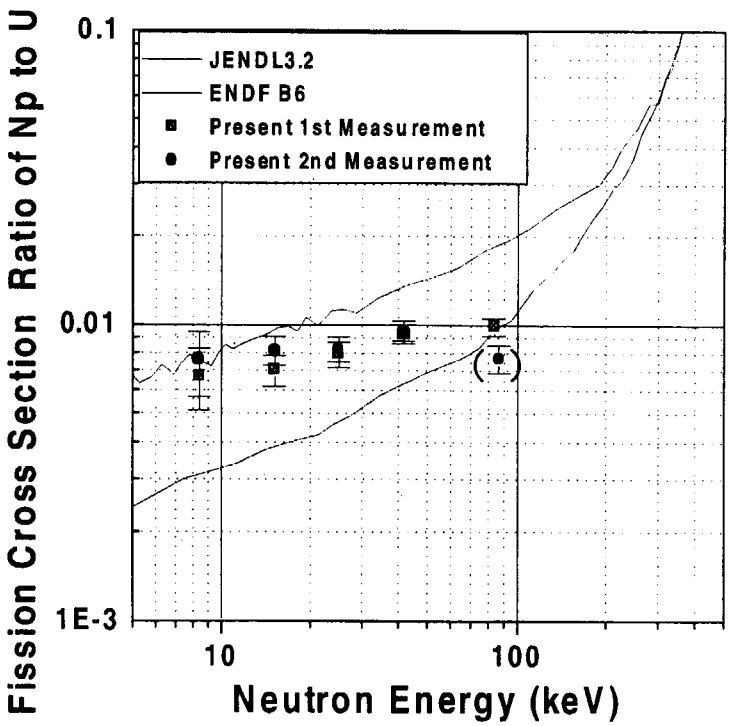

Fig 8 Measured fission cross section ratios of ^{237}Np

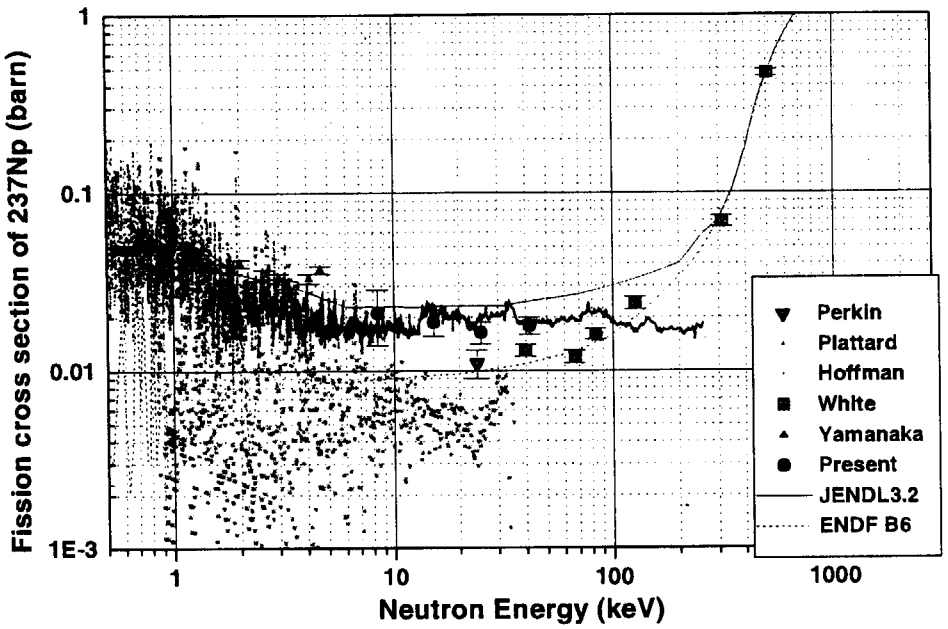

Figure 9 Obtained fission cross section of ^{237}Np

Acknowledgement

We would like to express our thanks to Drs Ando and Ohsugi of FCA, JAREI, for lending us the ^{237}Np sample used in the fission neutron spectrum measurement.

Fission cross section measurement was partly supported by the Power Reactor and Nuclear Fuel Development Corporation (PNC).

References

[1]Baba M., Hirakawa N., Iwasaki T., Kanda T., Nucl. Sci. Technol., 26, 11 (1989)
[2]Iwasaki T. et al., J. Nucl. Sci. Technol., 27, 885 (1990)
[3]Kornilov N.V., ISINN-5, Dubna, 1997
[4]Trufanov A.M., Yader. Fyz., **55** 298 (1992)
[5]Boikov G. S., *Phys. of Atomic Nucl.*, **57** (12), 1240 (1994)
[6]Howerton R. J., *Nucl. Sci. Eng.*,**46**,414 (1971)

3.19 Measurement of the Effective Thermal Cross Section of ^{134}Cs by Triple Neutron Capture Reaction

Shoji NAKAMURA[1)], Hideo HARADA[1)], Toshio KATOH[1),2)], Yuichi HATSUKAWA[3)], Nobuo SHINOHARA[3)], Kentaro HATA[3)], Katsutoshi KOBAYASHI[3)], Shoji MOTOISHI[3)] and Masakazu TANASE[3)]

1) Power Reactor and Nuclear Fuel Development Corp., Tokai-mura, Naka-gun, Ibaraki-ken 319-11

2) Visiting staff at Gifu College of Medical Technology, Nagamine, Ichihiraga, Seki, Gifu-ken 501-3822

3) Japan Atomic Energy Research Institute, Tokai-mura, Naka-gun, Ibaraki-ken 319-11

E-mail: rgm@tokai.pnc.go.jp

The effective thermal cross section (σ_{eff}) of the $^{134}Cs(n,\gamma)^{135}Cs$ reaction was measured by the activation method and the γ-ray spectroscopic method in order to obtain fundamental data for research on the transmutation of nuclear wastes. The effective thermal cross section of the reaction $^{134}Cs(n,\gamma)^{135}Cs$ was found to be 140.6±8.5 barns.

1. Introduction

The effective thermal cross section (σ_{eff}) of the reaction $^{134}Cs(n,\gamma)^{135}Cs$ was measured by the activation method and the γ-ray spectroscopic method in order to obtain fundamental data for research on the transmutation of nuclear wastes.

It was also designed to show the effectiveness of a triple neutron capture reaction method used in this measurement.

2. Experiment

The pure natural CsCl (purity 99.99%) samples were used for the targets, and then the ^{134}Cs induced by the triple neutron irradiation of ^{133}Cs was utilized for the $^{134}Cs(n,g)^{135}$ reaction, since ^{134}Cs solution available commercially contains natural ^{133}Cs and this causes ambiguity of amount of target nuclide ^{134}Cs due to the production of ^{134}Cs through the neutron capture of ^{133}Cs. The amount of ^{135}Cs was estimated by the activity measurement of the ^{136}Cs induced from the $^{135}Cs(n,\gamma)^{136}Cs$ reaction, since the ^{135}Cs decays by a β-transition, does not emit γ-rays.

It was aimed to measure the cross section of ^{134}Cs by utilizing the triple neutron capture reaction, i.e.

$$^{133}Cs(n,\gamma)^{134}Cs(n,\gamma)^{135}Cs(n,\gamma)^{136}Cs.$$

2.1 Neutron Irradiation

The target of Cs was irradiated for 24 days in a HR-1 pipe of the swimming pool type reactor JRR-3, which has a 1/E spectrum, at Japan Atomic Energy Research Institute (JAERI).

In order to monitor the neutron flux, the wires of Au/Al and Co/Al alloy were used as activation detectors. The irradiation position was characterized as having a thermal neutron flux of 8.68×10^{13} n/cm^{2}s, and the epithermal index of Westcott's convention[1] of 0.01.

2.2 Activity Measurement

The counts of γ-rays emitted from the irradiated targets were measured using a high purity Ge detector with a 90% relative efficiency and an energy resolution of 2.1 keV FWHM at 1.33 MeV of ^{60}Co. The details of the data taking system were described elsewhere[2].

Figure 1 shows the γ-ray spectrum emitted from the irradiated Cs target. The γ-rays, originated from the ^{134}Cs and ^{136}Cs nuclides induced by the one- and triple-neutron capture reaction of ^{133}Cs, were seen at the energies of 802, 796, 819, 1039, 1048, 1168 and 1235 keV.

3. Analysis

3.1 Neutron Flux Analysis

We used the following equations obtained by modifying Westcott's convention[1] for the analysis of neutron flux at the irradiation position.

$$\frac{R}{\sigma_0} = \phi_1 + \phi_2 s_0 G_{epi}, \tag{1}$$

for irradiation without a Cd shield capsule.

$$\frac{R'}{\sigma_0} = \phi_1' + \phi_2' s_0 G_{epi}, \tag{2}$$

for irradiation with a Cd shield capsule. The s_0 is defined by

$$s_0 = \frac{2}{\sqrt{\pi}} \frac{I_0'}{\sigma_0}, \tag{3}$$

with I_0', the resonance integral after subtracting the 1/υ component.

The value of the flux factors, $\phi_{1,2}$ and $\phi'_{1,2}$ were determined with the R and R' values of the flux monitor wires, namely Au/Al and Co/Al alloy wires. The $\phi_{1,2}$ and $\phi'_{1,2}$ were summarized in **Table 1**.

3.2 Triple Neutron Capture Reaction

The number of the each nuclide induced by the triple neutron capture reaction of ^{133}Cs were estimated by the following process and equations:

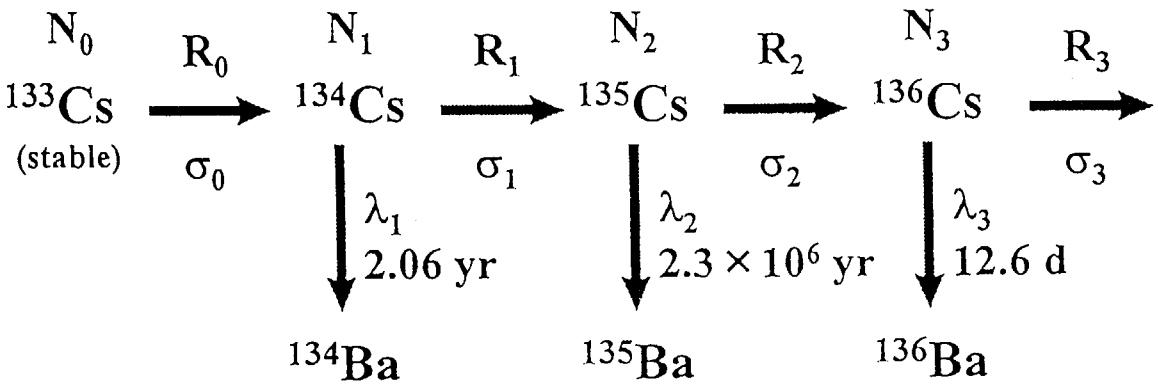

$$N_1 = N_0(0) R_0 \cdot \left[\frac{\exp(-R_0 t) - \exp\{-(R_1+\lambda_1)t\}}{(R_1+\lambda_1) - R_0} \right], \tag{4}$$

$$N_3 = N_0(0) R_0 R_1 R_2 \cdot \left[\frac{\exp(-R_0 t) - \exp\{-(R_3+\lambda_3)t\}}{\{(R_1+\lambda_1)-R_0\}\{(R_2+\lambda_2)-R_0\}\{(R_3+\lambda_3)-R_0\}} \right.$$

$$+ \frac{\exp\{-(R_1+\lambda_1)t\} - \exp\{-(R_3+\lambda_3)t\}}{\{R_0-(R_1+\lambda_1)\}\{(R_2+\lambda_2)-(R_1+\lambda_1)\}\{(R_3+\lambda_3)-(R_1+\lambda_1)\}}$$

$$\left. + \frac{\exp\{-(R_2+\lambda_2)t\} - \exp\{-(R_3+\lambda_3)t\}}{\{R_0-(R_2+\lambda_2)\}\{(R_1+\lambda_1)-(R_2+\lambda_2)\}\{(R_3+\lambda_3)-(R_2+\lambda_2)\}} \right] \tag{5}$$

where N_0 is the number of ^{133}Cs nucleus contained in the target, N the number of nucleus induced by the reaction, λ the decay constant, t the irradiation period, R the reaction rates. The subscripts of number 1,2 and 3 denotes the ^{134}Cs ^{135}Cs and ^{136}Cs nucleus.

The analysis was performed by using the values of the cross sections for the $^{135}Cs(n,\gamma)^{136}Cs$ reaction, which were previously measured by present authors[3]. The effective cross section of ^{134}Cs was deduced from comparing the measured values of the activity ratio with the calculated one by Eqs. (4) and (5).

4. Result

The results of the effective cross section of ^{134}Cs is shown in **Table 2** together with the previously reported data[4] by the activation and the mass-spectrometric methods.

5. Conclusion

The effective cross section of $^{134}Cs(n,\gamma)^{135}Cs$ reaction was found to be 140.6±8.5 barns. The present data agrees with the reported value within the limits of error.

The triple neutron capture reaction method was also demonstrated to be effective for the measurement of (n,γ) cross section for radioactive nuclei.

Acknowledgments

The authors wish to acknowledge their indebtedness to the crew of JRR-3 reactor at Japan Atomic Energy Research Institute (JAERI) for their cooperation. This work was supported by PNC, JAERI and the Inter-University Program for the Joint Use of JAERI Reactors.

References

[1] C.H.Westcott et al.: Proc. 2nd Int. Conf. Peaceful Uses of Atomic Energy, Geneva, Vol.**16**, 70 (1958).

[2] H. Harada et al.: J. Nucl. Sci. Technol., Vol.**32**, No.5, 395 (1995).

[3] T. Katoh et al.: J. Nucl. Sci. Technol., Vol.**34**, No.5, 431 (1997).

[4] J. G. Bayly et al.: J. Inorg. Nucl. Chem., Vol.**5**, 259 (1958).

[5] Kawai, M., Iijima, S., Nakagawa, T., Nakajima, Y., Sugi, T., Watanabe, T., Matsunobu, H., Sasaki, M., Zukeran, A.: J. Nucl. Sci. Technol., Vol.**29**, 195 (1992).

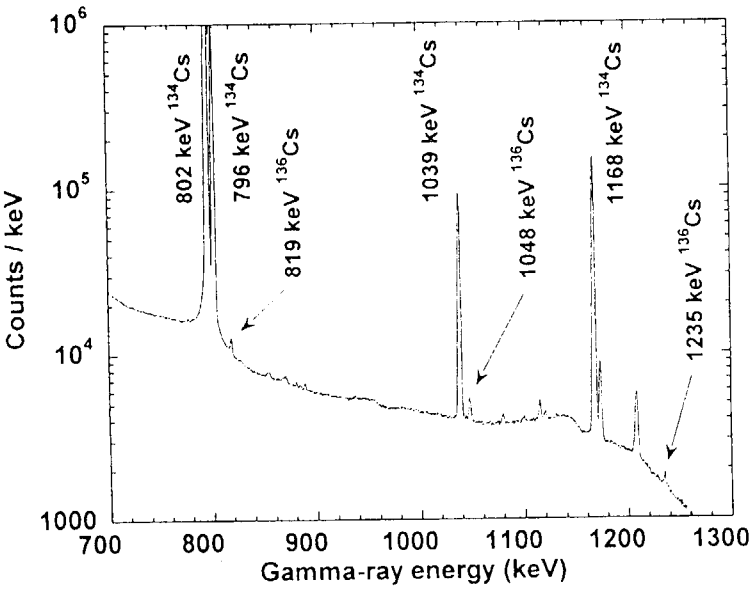

Fig.1 Gamma-ray spectrum of the irradiated Cs target

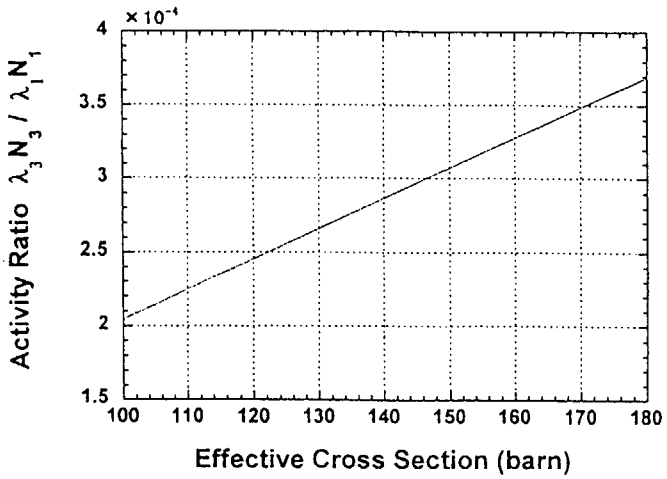

Fig. 2 Ratio of the activity of ^{136}Cs to that of ^{134}Cs calculated with Eqs.(4) and (5)

Table 1 Results of neutron flux in HR-1 pipe of JRR-3

Irradiation Type	Irradiation Period	ϕ_1 or ϕ'_1	ϕ_2 or ϕ'_2
		($\times 10^{13}$ n/cm^{2}s)	
no Cd	10 min	8.68 ±0.21	0.081±0.018
with Cd	50 min	0.0249±0.0066	0.109±0.003

Table 2 Results of the effective cross section

	σ_{eff} (barn)	Ref.
This work	140.6±8.5	
Bayly et al.('58)	134 ±12	[4]
JENDL-3.2	139.7*	[5]

* thermal neutron cross section

3.20 Measurement of MA Fission Cross Sections at YAYOI

Yasushi Ohkawachi, Shigeo Ohki, Toshio Wakabayashi,

Oarai Engineering Center, Power Reactor and Nuclear Fuel Development corporation

4002 Narita, Oarai-machi, Ibaraki, 311-13, JAPAN

Tel:81-29-267-4141 (ex.2393) FAX:81-29-267-0579 E-mail:okawachi@oec.pnc.go.jp

ABSTRACT

Fission cross section ratios of minor actinide nuclides (Am-241,Am-243) relative to U-235 in the fast neutron energy region have been measured using a back-to-back (BTB) fission chamber at YAYOI fast neutron source reactor. A small BTB fission chamber was developed to measure the fission cross section ratios in the center of the core at YAYOI reactor. Dependence of the fission cross section ratios on neutron spectra was investigated by changing the position of the detector in the reactor core.

The measurement results were compared with the fission cross sections in the JENDL-3.2, ENDF/B-VI and JEF-2.2 libraries. It was found that calculated values of Am-241 using the JENDL-3.2, ENDF/B-VI and JEF-2.2 data are lower by about 15% than the measured value in the center of the core (the neutron average energy is 1.44E+6 [eV]). And, good agreement can be seen the measured value and calculated value of Am-243 using the JENDL-3.2 data in the center of the core (the neutron average energy is 1.44E+6 [eV]), but calculated values of Am-243 using the ENDF/B-VI and JEF-2.2 data are lower by 11% and 13% than the measured value.

I. INTRODUCTION

Some of the minor actinide nucledes (MA:Np,Am and Cm) produced by the operation of nuclear power plants have extremely long-term radiotoxicity and their management is one of the key issues for nuclear power to be accepted by public. Fast breeder reactors (FBRs) are considered to have the potentiality of transmuting MA nuclides effectively because of their hard neutron specta. In MA burner core analyses[1], nuclear data for MA nuclides and fission products are of primary importance. However, nuclear data for many MA nuclides are still unknown to the desired accuracy. Accurate experimental data of neutron cross section for MA are indispensable to establish MA transmutation technology by FBRs.

So fission cross section ratios of minor actinide nuclides (Am-241,Am-243) relative to U-235 in the fast neutron energy region have been measured to evaluate the accuracy of MA nuclear data using a back-to-back (BTB) fission chamber at YAYOI fast neutron source reactor.

II. EXPERIMENTAL METHOD AND MEASUREMENT

A. Outline of YAYOI and measurement position

YAYOI is the cylindrical small fast reactor. The Cross-sectional view of YAYOI is shown in Fig.1. The core of YAYOI is made of pure metallic uranium surrounded by a piece of depleted uranium annular blanket. The core is located inside a hollow lead reflector. The core has 2kW power and is cooled by air. YAYOI has various experimental holes. The experimental hole which pierces through the center of the core is called the glory hole (Gy). And the experimental hole which pierces through the blanket is called the glazing hole (Gz).

Dependence of the fission cross section ratios on neutron spectra was investigated by changing the axial position of the BTB fission chamber in the glory hole. Three axial positions in the glory hole were selected for the measurement of the fission cross section ratios. The irradiation of the BTB fission chamber with MA nuclide was performed in the power level of 100W.

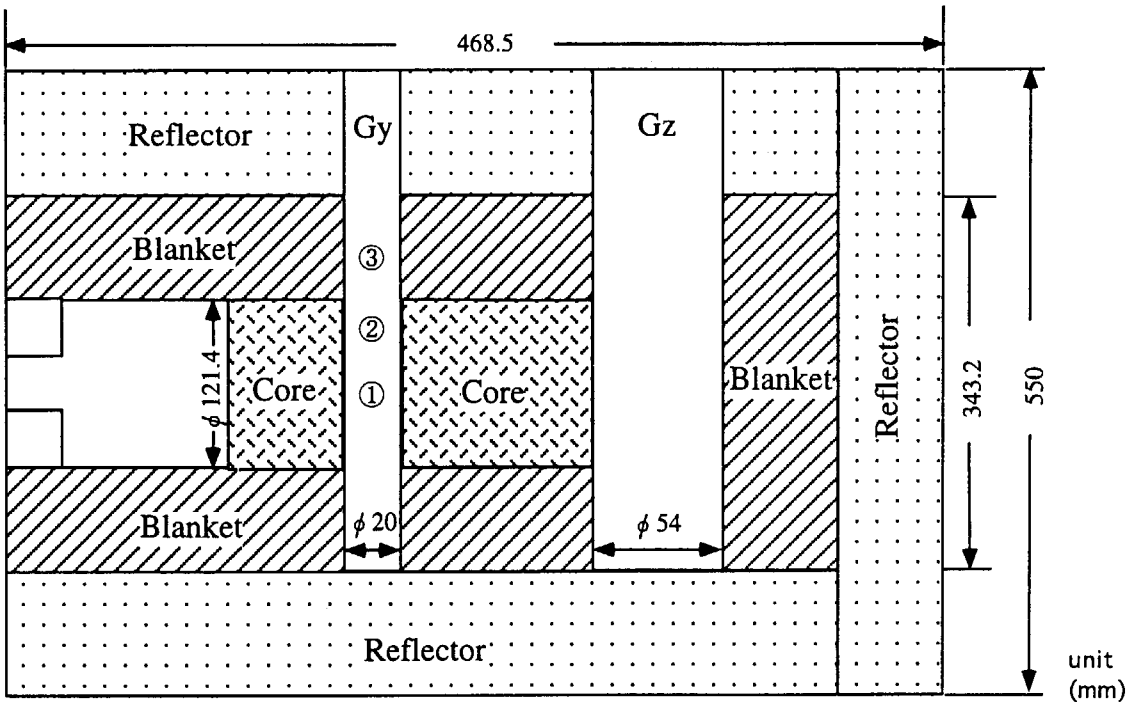

Gy:Glory Hole Gz:Glazing Hole

Measurement position:①The center of the core, ②50mm up to the center, ③100mm up to the center

Fig.1 Cross-sectional view of YAYOI and measurement position

B. BTB fission chamber

The fission chamber employed for the present experiment have two identical parallel ionization chambers. It is shown in Fig.2. And block diagram of electronic circuits to measure fission counts with the fission chamber is shown in Fig.3. As the back sides of a sample deposit (MA:Am-241,Am-243) on a stainless steel plate and a reference one (U-235) are faced each other,it is called back-to-back (BTB) type.

The chambers were made of stainless steel and filled with a PR gas (Ar:90v/o, CH4:10v/o). The operation voltage was 500V. The glory hole diameter is 20mm, so a small BTB fission chamber was developed to insert into the glory hole. The BTB fission chamber is a cylinder with 16mm in diameter and 53mm in height. The distance between the two electrodes was 6mm.

Each sample of MA nuclides was electroplated on a platinum plate of 0.3mm and 8mm in diameter. The sample (Am-241,Am-243) was put into the fission chamber together with a platinum plate with the layer of U-235.

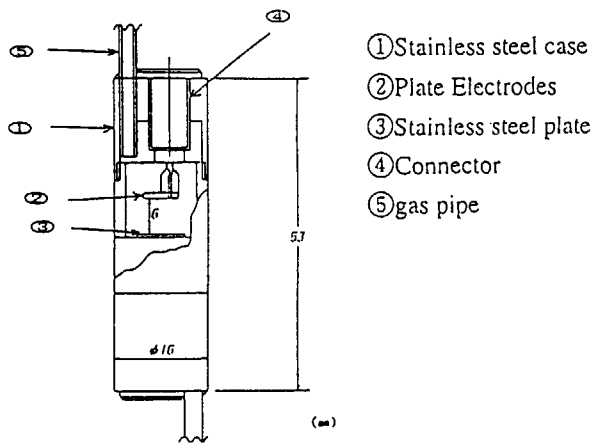

Fig.2 Cross-sectional view of BTB fission chamber

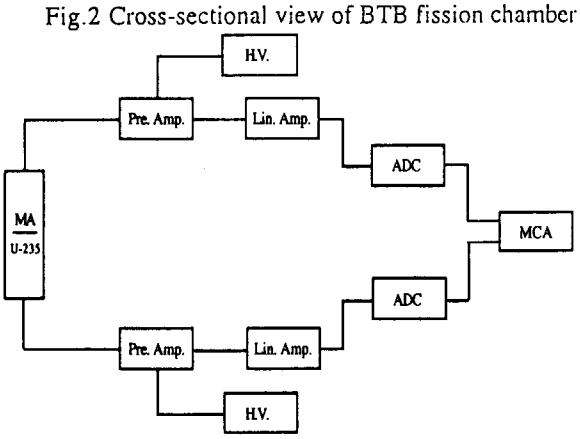

Fig.3. Block diagram of electronic circuits to measure fission counts from BTB fission chamber

C. Calculation of the neutron spectrum

The neutron spectrum of the measurement position was calculated using the continuous energy Monte-Carlo code MVP.[6] The following are simulated in as bilut : on the core is fuel which is covered with SUS ,knocking pin, experimental hole, hole for the thermocouple. And, control rod and main experimental hole were considered in the blanket. On the reflector,the detailed structure was disregarded. Still, used cross-section library is JENDL-3.2. The comparison of neutron spectrum calculated value by the MVP code and experimental value measured by the activation foil in a past is shown Fig.4. Good agreement can be seen between the calculated value by MVP code and experimental value measured by the activation foil. The comparison of the neutron spectrum by the three measurement positions obtained by the MVP code is shown Fig.5. The average energy for each measurement position is 1.44E+6 [eV] (the center of the core), 1.30E+6 [eV] (axial upper on 50mm from the center of the core), 8.24E+5 [eV] (axial upper on 100mm from the center of the core).

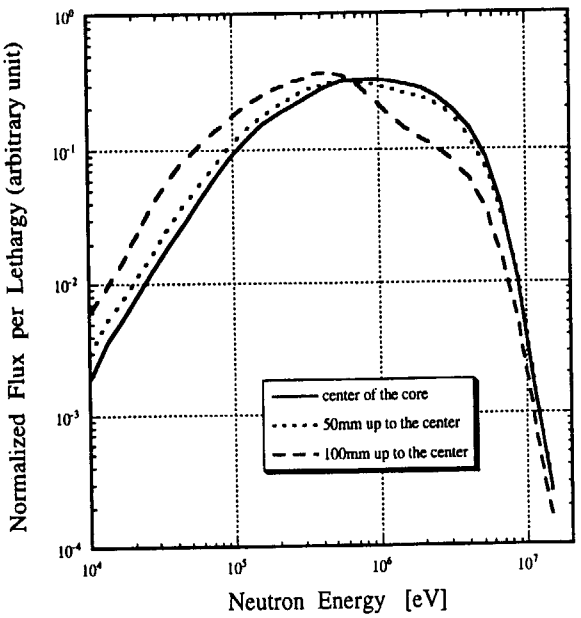

Fig.5 Comparision of the neutron spectra by the three measurement positions obtained by the MVP code

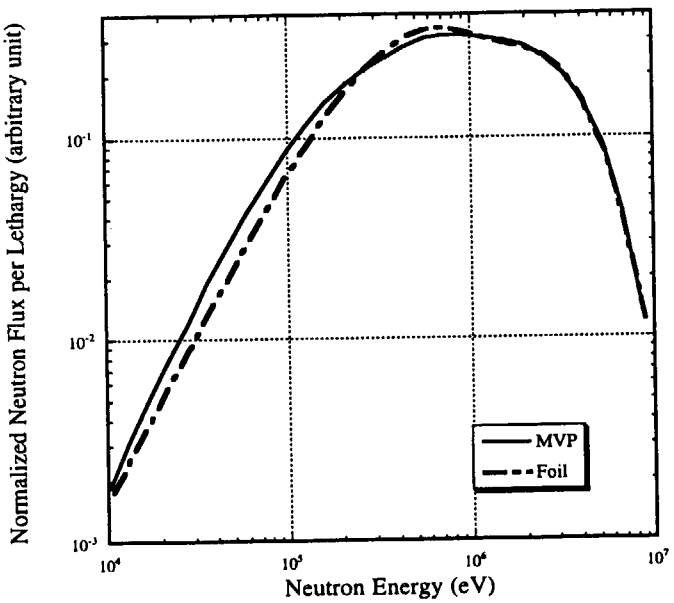

Fig.4 Comparison of neutron spectra calculated values by the MVP code and experimental values measured by the activation foil

D. Fission Cross Section Measurement

From the fission counts of the MA (Am-241, Am-243) and the U-235 deposits, the fission cross section for MA (Am-241, Am-243) is obtained by[2) 3) 4) 5) 6) 7) 8) 9)]

$$\langle \sigma_{MA} \rangle = \frac{C_{MA}}{C_U} \frac{N_U}{N_{MA}} \langle \sigma_U \rangle$$

where, C_{MA} : fission counts of MA

C_U : fission counts of U-235

N_U: number of U-235 atoms

N_{MA} : number of MA atoms

$\langle \sigma_U \rangle$: collaps fission cross section of U-235

The number of atoms in MA and U samples were determined by the 2π ionization chamber and the alpha-spectrometry using a Si semiconductor detector. Systematic difference between the MA and U-235 deposit positions in the BTB chambers was experimentally investigated by exchanging the positions each other.

III. RESULTS AND DISCUSSION

Using the spectrum obtained by the MVP code, fission cross section ratios of MA (Am-241,Am-243) to U-235 (Am-241/U-235, Am-243/U-235) in the JENDL-3.2, ENDF/B-VI and JEF-2.2 libraries were calculated. The experimental results were compared with the calculated values.The comparison of fission cross section ratios (Am-241/U-235, Am-243/U-235) by the difference the neutron average energy is shown Fig.6. and Fig.7. And, the comparision of C/E by the difference the neutron average energy is shown Fig.8 and Fig.9.

It was found that calculated values of Am-241 using the JENDL-3.2, ENDF/B-VI and JEF-2.2 data are lower by 15%, 14% and 16% than the measured value in the center of the core (the neutron average energy is 1.44E+6 [eV]). The other measured values (the neutron average energy is 1.30E+6[eV] and 8.24E+5[eV]), good agreement can be seen between the measured value and calculated value of Am-241 using the JENDL-3.2, ENDF/B-VI and JEF-2.2 data. And, it was found that good agreement can be seen the measured value and calculated value of Am-243 using the JENDL-3.2 data in the center of the core (the neutron average energy is 1.44E+6 [eV]), but calculated values of Am-243 using the ENDF/B-VI and JEF-2.2 data are lower by 11% and 13% than the measured value. The other measured values (the neutron average energy is 1.30E+6[eV] and 8.24E+5[eV]), good agreement can be seen between the measured value and calculated value except for calculated values of Am-243 using the JENDL-3.2 data is higher by 20% than the measured value for the neutron average energy is 8.24E+5[eV].

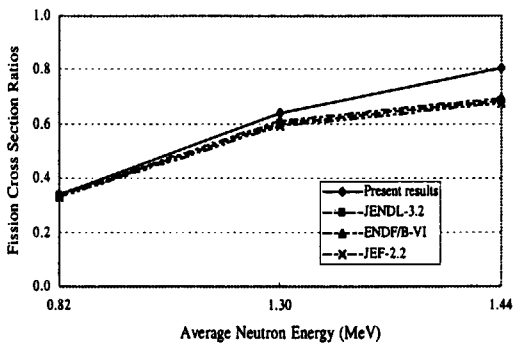

Fig.6 Comparison of fission cross section ratios (Am-241/U-235) depending on the average neutron energy

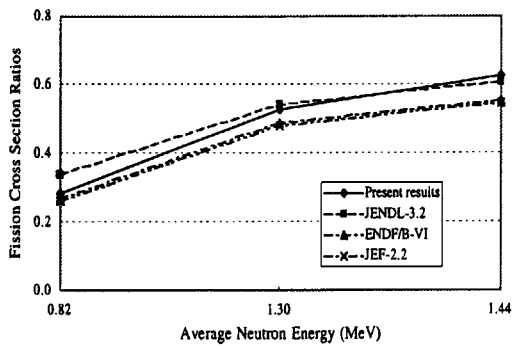

Fig.7 Comparison of fission cross section ratios (Am-243/U-235) depending on the average neutron energy

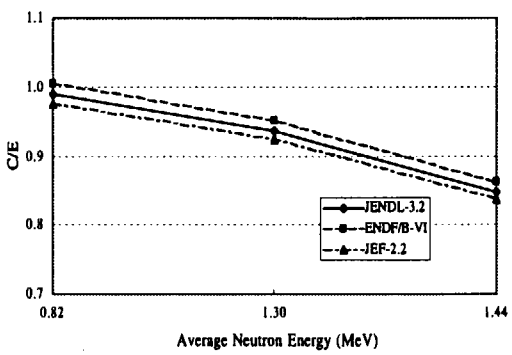

Fig.8 Comparison of C/E (Am-241/U-235) depending on the average neutron energy

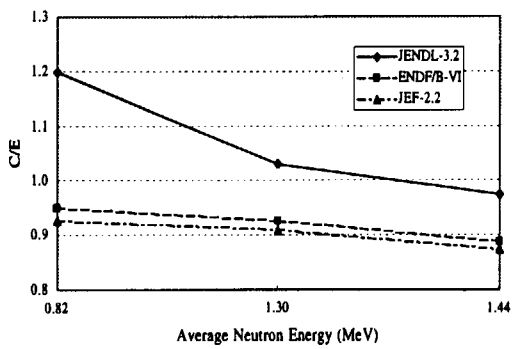

Fig.9 Comparison of C/E (Am-243/U-235) depending on the average neutron energy

IV. CONCLUSION

(1) Present experimental result is obtained at an accuracy within 5%.

(2) For Am-241, calculated values of using the JENDL-3.2, ENDF/B-VI and JEF-2.2 data are lower by about 15% than the measured value in the center of the core (the neutron average energy is 1.44E+6 [eV]). The other measured values (the neutron average energy is 1.30E+6[eV] and 8.24E+5[eV]), good agreement can be seen between the measured value and calculated value.

(3) For Am-243, good agreement can be seen the measured value and calculated value of using the JENDL-3.2 data in the center of the core (the neutron average energy is 1.44E+6 [eV]), but calculated values of using the ENDF/B-VI and JEF-2.2 data are lower by about 12% than the measured value. The other measured values (the neutron average energy is 1.30E+6[eV] and 8.24E+5[eV]), good agreement can be seen between the measured value and calculated value except for calculated values of using the JENDL-3.2 data is higher by 20% than the measured value for the neutron average energy is 8.24E+5[eV].

REFERENCE

1. T. Wakabayashi, et al., "Feasibility Studies of an Optimized Fast Reactor Core for MA and FP Transmutation", Proc. of the Int'l Conf. on Evaluation of Emerging Nuclear Fuel Cycle Systems: Global'95", Sept. 11-14, 1995, p.800, CEA, 1995.

2. P.W.Frank, "Recoil Range of Fission Fragments", Bettis Technical Review, WAPD-BT-30 (1964)

3. F. Manabe et al., "Measurements of Neutron Induced Fission Cross Section Ratios of 232Th, 233U, 234U, 236U, 238U, 237Np, 242Pu and 243Am Relative to 235U around 14MeV", The Technology Reports of the Tohoku University, Vol.52 (1988) No.2, March pp 97-126

4. K.Kanda et al.,J.Nucl.Sci.Technol.,24,423(1987).

5. M.Baba et al.,J.Nucl.Sci.Technol.,26,11(1989).

6. M. Obu, "Preparation and Characteristics of Fission Chambers with Actinide Nuclides", JAERI-M 9757(1981).

7. A. Yamanaka, et al., J.Nucl.Sci.Technol.,30,863(1993).

8.K.Kobayashi, et al., J.Nucl.Sci.Technol.,31,1239(1994).

9. K. Kobayashi, et al., "Fission Cross Section Measurement of Am-241 between 0.1 eV and 10 keV with Lead Slowing-down Spectrometer", Gatlinburg, Tenn., May 1994, J.K.Dickens(Ed.), ORNL, Vol.1, p.242(1994).

10. T. Mori and M. Nakagawa, "MVP/GMVP: General Purpose Monte Carlo Codes for Neutron and Photon Transport Calculations based on Continuous Energy and Multigroup Methods", JAERI-Data/Code 94-007.

3.21 Multiplicity and Energy of Neutrons from $^{233}U(n_{th},f)$ Fission Fragments

Katsuhisa NISHIO*†, Itsuro KIMURA*, Yoshihiro NAKAGOME**

* *Department of Nuclear Engineering, Kyoto University*

** *Research Reactor Institute, Kyoto University*

† e-mail : nishio@n-grp.nucleng.kyoto-u.ac.jp

Abstract

The correlation between fission fragments and prompt neutrons from the reaction $^{233}U(n_{th},f)$ was measured with improved accuracy. The results determined the neutron multiplicity and emission energy as a function of fragment mass and total kinetic energy. The average energy as a function of fragment mass followed a nearly symmetric distribution centered about the equal mass-split and formed a remarkable contrast with the saw-tooth distribution of the average neutron multiplicity. The neutron multiplicity from the specified fragment decreases linearly with total kinetic energy, and the slope of multiplicity with kinetic energy had the minimum value at about 130 u. The level density parameter versus mass determined from the neutron data showed a saw-tooth structure with the pronounced minimum at about 128 and generally followed the formula by Gilbert and Cameron, suggesting that the neutron emission process was very much affected by the shell-effect of the fission fragment.

1. Introduction

Simultaneous measurement of prompt neutrons with fission fragments supplies important information to understand the nuclear fission process. It is assumed that the excitation energy of a fully accelerated fission fragment has its origin in the deformation energy at the scission point. As the excitation energy is dissipated largely by neutrons, the measurement of the neutron multiplicity (ν) and energy (η) allows us to determine the scission configuration when the total kinetic energy is incorporated in the analysis to fix the charge-center distance. But the multiplicity and energy of neutrons as a function of fragment mass ($m*$) and/or total kinetic energy (TKE) measured so far are limited only two reactions, $^{252}Cf(s.f)$ [1] and $^{235}U(n_{th},f)$ [2]. Therefore, in the present work, we aimed to obtain the similar data for the $^{233}U(n_{th},f)$ system.

The average neutron energy versus mass, $\overline{\eta}(m*)$, shows approximately symmetric distribution about the equal mass division and forms a remarkable contrast with the saw-tooth shape of $\overline{\nu}(m*)$ [1][2]. The $\overline{\nu}$ and $\overline{\eta}$ should be nearly proportional to the average fragment excitation energy, $\overline{E}_{ex}$, and the nuclear temperature, T, respectively. Since the $\overline{E}_{ex}$ is correlated to T by the level density parameter, a, as $\overline{E}_{ex} = aT^2$, the shape difference between $\overline{\eta}(m*)$ and $\overline{\nu}(m*)$ attributes to the distribution of $a(m*)$. The actually obtained $a(m*)$ for the reaction of $^{252}Cf(s.f)$ [1] shows saw-tooth trend with the minimum dip at about 130u and does not follow the relation, $a(m*) = m*/K$, where K is a constant. As the level density parameter is phenomenologically expressed by using

the shell-energy correction [3], we can explain the the shape difference between $\overline{\eta}(m^*)$ and $\overline{\nu}(m^*)$ by the shell-effect of the fragment. The same experimental results of $\overline{\eta}(m^*)$ and $\overline{\nu}(m^*)$ would be expected also for $^{233}U(n_{th},f)$. Furthermore, the $a(m^*)$ is determined by using the present data and is compared to the formula [3].

2. Experiment

The measurement was carried out by using the slow neutrons from the Kyoto University Reactor. The system used in this measurement is shown in Fig. 1. The ^{233}U target was fabricated by the electrodeposition of $UO_2(NO_3)_2$ on a 90 μ g/cm^2 thick nickel foil, and the target thickness was about 30 μ g/cm^2. On both sides of the target, a silicon surface barrier detector (SSBD), having sensitive area of 900 mm^2, and a position sensitive parallel plate avalanche counter (PPAC) with active diameter of 22 cm were mounted to detect fission fragments. By recording the pulse height induced by the fission fragment 1 (FF1) and the time difference between the signal from the both detectors, masses and energies of the fragments were determined. The incident position of the FF2 on the PPAC determined the fission axis, θ, relative to the axis of the apparatus, which was equivalent to the emission angle of the neutron from FF1.

The neutrons were detected with a liquid organic scintilator (NE213) in a 12.8 cm diameter container that was 5 cm thick. The neutron energy was determined from the time-of-flight technique over a flight path of 76.5 cm. The start time was triggered by the FF1 too. The pulse-shape was recorded to separate the prompt neutron and background γ –ray event. The pulse-height was also recorded to check the gain stability. The signals were stored in a computer in a list mode for off-line analysis.

The neutron energy was transformed to the center-of-mass (c.m.) system of the respective fragment in a conventional manner using the fragment velocity and the neutron emission angle, θ. The neutron multiplicity versus mass and total kinetic energy was obtained from the number of the fragment-neutron coincidences divided by the number of the two-fragment coincidences with a normalization of 2.495 per fission [4]. The data analysis method is given elsewhere [2][5].

3. Experimental results

3.1 Neutron energy

The spectra of neutron energy in the c.m. system are shown in Fig. 2 by solid circles in the form of $\phi(\eta)/\eta^{1/2}$. The mass number of the neutron emitter is noted in each section of the figure. The solid lines are the results of the fitting the data with the Maxwellian shape of

$$\phi(\eta) = const.\eta^{1/2}\exp\left(-\eta/T_{eff}\right), \tag{1}$$

where T_{eff} is the effective nuclear temperature. It is found that the equation provides a good representation of the measred value for $\eta < 3$ MeV. The average value of the neutron energy, $\overline{\eta}$, are plotted as a function of fragment mass in Fig. 3, together with the statistical error bars. In this figure, the mass yield curve obtained in this measurement

is shown by open circles. It is found in Fig. 3 that (1) the $\overline{\eta}(m^*)$ is approximately symmetrically distributed about the equal mass-division of the fissioning nucleus, and the minimum values apprear at 95 and 145u, and (2) the neutron energies from the symmetric fission fragments and very asymmetric fission fragments reaches to about 1.8 MeV.

3.2 Neutron multiplicity

The average neutron multiplicity from the fission fragment, $\overline{\nu}(m^*)$, is shown in Fig. 4(a) as a function of fragment mass together with statistical error bars. The multiplicities emitted from the light and heavy fragment group are 1.49 and 1.01, respectively, meaning that 60 % of the fission neutrons have its origin in the light fragments. In the same figiure, the data by Milton and Fraser [6] and Apalin *et al.* [7] are shown for comparison. The present data as well as the other two shows a 'step' at 100 to 105 u. The pronounced minimum at 129 u is observed in the present measurement as well as in ref. [7]. The average toal neutron multiplicity, $\overline{\nu}^{tot}(m^*)$, which is the sum of neutrons from both fragments, is plotted in Fig. 4(b). The data in ref.[7] is shown for comparison. It is found that ; (1) the present $\overline{\nu}^{tot}$ in $125 < m^* < 150$ u lies between 2.3 and 2.6, and is approximately constant against the mass number, and (2) the minimum value appear at 130 u. The minimum position is close to 132 u seen in ref. [7], however their data in the typical mass region is discrepant from the present results and increases with increasing the mass asymmetry. The interesting aspect is the enhanced neutron emission in the symmetric fission. The current data displays that the system emits about 1.5 times more neutrons than the typical asymmetric fission. The neutron enhancement is also observed in the results in ref. [7]. The present data suggests that the system around the symmetric fission has considerably large total deformation energy at the scission point.

The neutron multiplicity is plotted in Fig. 5 as a function of TKE for the selected fragment mass. In every fragment, the linear relation is observed between ν and TKE. The data points in each mass window are fitted to a linear function, and the results displayed by the solid line. In this process the slope, $-d\nu/dTKE$, is determined and the result is shown in Fig. 6. The distribution has the minimum at about 130 u. The $-d\nu/dTKE$ reflects the scission configuration as follows. If we make an image that two deformed fragments are nearly touching at the scission point, the deviation of TKE, which is equivalent to that of the charge-center distance, CCD, is caused by the elongation or shrinkage of the fragments. Since the deformation energy is nearly proportional to the neutron multiplicity, the fragment with larger $-d\nu/dTKE$ value contributes more largely to the shift of CCD. Figure 6 suggests that the fragment with 130 u resists to deformation at the scission point, whereas the complementary fragment with 104 u accepts large deformation.

4. Level density parameter

The level density parameter relates the excitation energy and temperature of the fragment by

$$\overline{E}_{ex} = aT^2 . \qquad (2)$$

Since the neutron spectrum in the c.m. system is approximately expressed by eq. (1), the following relation can be applied to estimate the nuclear temperature, T.

$$T = (3/4)\overline{\eta} \ . \tag{3}$$

The average excitation energy of the fragment is determined by

$$\overline{E}_{ex} = \overline{\nu}\left(\overline{\eta} + \overline{B}_n\right) + 0.6\overline{B}_n \ , \tag{4}$$

where the first and second term in the right hand side are the energies dissipated by the neutrons and γ-rays, respectively. The neutron binding energy, $\overline{B}_n$, is determined by the mass table in ref. [8]. The resulting $a(m^*)$ for ^{233}U(n_{th},f) fission fragments is shown in Fig. 7 by solid circles with associated statistical error bars. It is evident that $a(m^*)$ shows a saw-tooth trend with the pronounced minimum at about 126 u.

The level density parameter of a nucleus having N-neutrons and Z-protons is phenomenologically expressed by using the shell-energy correction [3] as

$$a/m^* = 0.00917\left(S(N) + S(Z)\right) + 0.120 \ [\mathrm{MeV}^{-1}], \tag{5}$$

$$S = S(N) + S(Z) \ \ [\mathrm{MeV}], \tag{6}$$

where $S(N)$ and $S(Z)$ are the neuron and proton shell-energy correction, respectively. The solid curve is the result when eq.(5) and (6) is applied to the fragment for ^{233}U(n_{th},f). Here, the Z/N value of the fragment was set to that of ^{234}U. It is seen that the resulting $a(m^*)$ generally agrees with that determined from the neutron data. Especially the minimum at about 130 u is well reproduced. No shell-energy correction ($S = 0$) gives the linear relation shown by the dotted line. When the formula is applied to the stable nucleus, the broken curve is obtained and cannot reproduce the measured $a(m^*)$ at about 130 u. It indicates that the fission fragment near 130 u has large negative shell-energy correction compared to the stable nucleus. The Segrè chart [9] shown in Fig. 8 is useful to explain the anomalous value of $a(m^*)$ for ^{233}U(n_{th},f). The fission fragments produced in this reaction positions approximately on the solid line, $Z/N = 92/142$. The solid and open circles correspond to the heavy and light fragment, respectively. The magic-numbers are indicated by the dashed lines. Since the fission fragments are neutron rich nucleus, the fragment with 130 u approaches to the double-magic nucleus ^{132}Sn, and hence the fragment have large negative shell-energy correction, S, compared to the stable nuclei.

5. Conclusions

The correlation between fission fragments and neutrons for the reaction of ^{233}U(n_{th},f) have been investigated. The spectra of neutrons emitted from the specified show the Maxwellian shape below 3MeV. The average neutron multiplicity in the c.m. system correlated with the fragment mass distributes approximately symmetrical shape centered about the equal mass division. Neutron multiplicity from a specified fragment is determined as a function of total kinetic energy. The slope of neutron multiplicity with kinetic energy, $-d\nu/dTKE$, has the minimum value at 130 u, suggesting that the fragment near the double-magic numbers resists to deformation at the scission point. The level density parameter of the fragment, $a(m^*)$, determined from the neutron data shows a saw-tooth structure and has a pronounced minimum at about 126 u. The formula by Gilbert and Cameron reproduces the $a(m^*)$ in general. From the analysis, it is demonstrated that the neutron rich fragment with ~130 u, produced by ^{233}U(n_{th},f), has large negative shell-energy correction compared to the stable nucleus having the same mass number.

References

[1] Budtz-Jørgensen and H.-H. Knitter, Nucl. Phys. **A490** (1988) 307.

[2] K. Nishio, *et al.* submitted to Nucl. Phys. A

[3] A. Gilbert and A.G.W. Cameron, Can. J. Phys. **43**, 1446 (1965).

[4] C. Wagemans, "The Nuclear Fission Process", CRC Press, p.514 (1991).

[5] K. Nishio *et al.*, Nucl. Instrum. Meth. **A385**, 171 (1997).

[6] J.C.D. Miltion and J.S. Fraser, Symposium on the Physics and Chemistry of Fission, Vol.2, p.39 (1965).

[7] V.F. Apalin *et al.*, Nucl. Phys., **71**, 553 (1965).

[8] P. Möller and J.R. Nix, At. Data and Nucl. Data Tables. **26**, 165 (1981).

[9] T. Horiguchi *et al.*, 'Chart of The Nuclides', (1992).

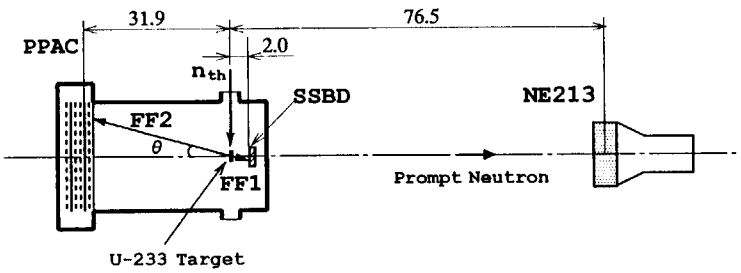

Fig. 1 Experimental arrangement. The distance is designated with cm unit.

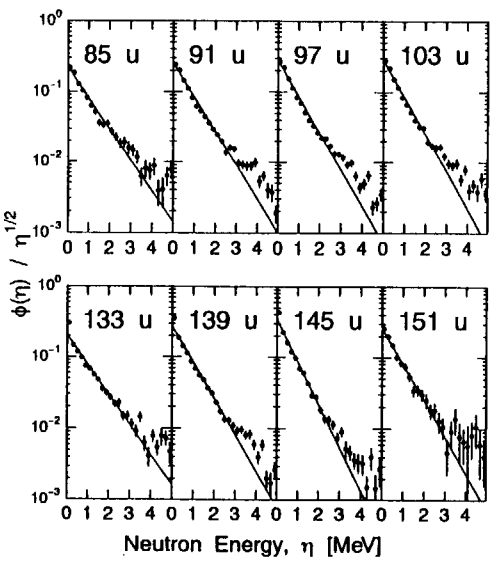

Fig. 2 Neutron spectra in the center-of-mass system for $^{233}U(n_{th},f)$.

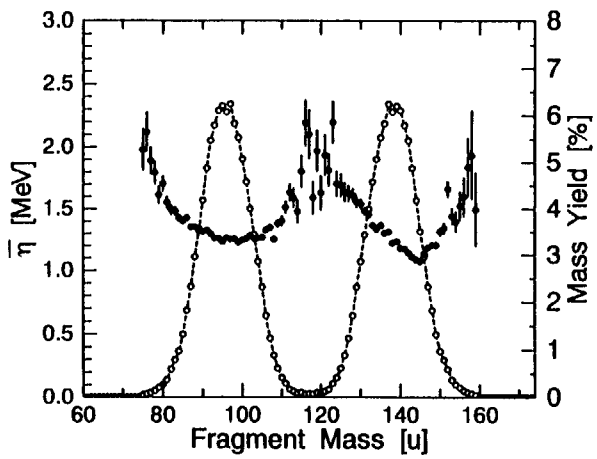

Fig. 3 Average neutron energy plotted as a function of fragment mass (left side) and mass yield curve (right side).

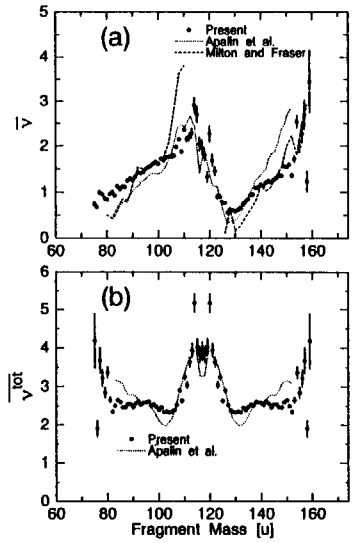

Fig. 4 (a) Average neutron multiplicity. (b) Average total neutron multiplicity.

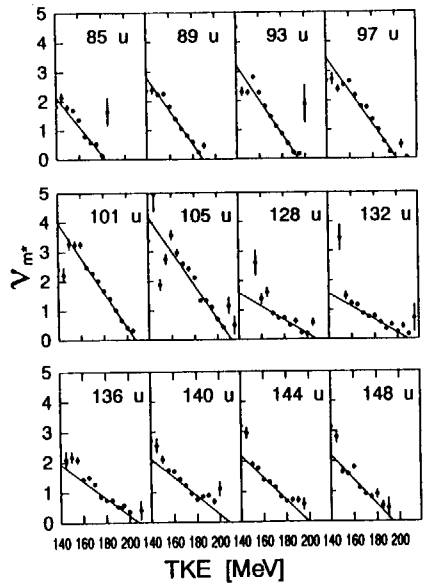

Fig. 5 Neutron multiplicity from specified fragment plotted as a function of total kinetic energy.

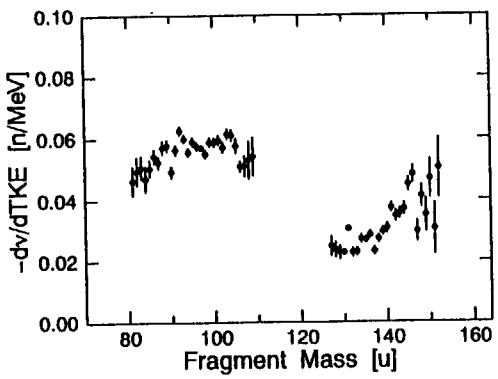

Fig. 6 Slope of neutron multiplicity with mass plotted as a function of fragment mass.

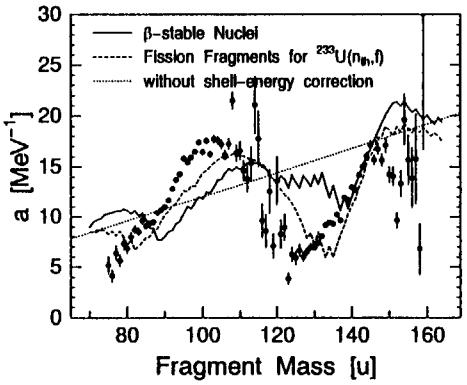

Fig. 7 Level density parameter of fission fragment for $^{233}U(n_{th},f)$.

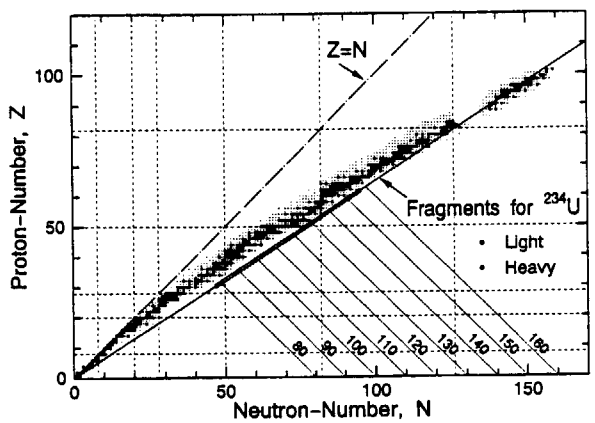

Fig. 8 Segrè chart.

3.22 Measurements of Gamma Rays from keV-Neutron Resonance Capture by Odd-Z Nuclei in the 2s-1d Shell Region

Masayuki IGASHIRA, Sam Yol LEE, Satoshi MIZUNO, Jun-ichi HORI
Research Laboratory for Nuclear Reactors, Tokyo Institute of Technology
2-12-1 O-okayama, Meguro-ku, Tokyo 152-8550, Japan
e-mail:iga@nr.titech.ac.jp

Hideo KITAZAWA
Department of Energy Sciences, Interdisciplinary Graduate School of Science and Engineering, Tokyo Institute of Technology
4259 Nagatsuta-cho, Midori-ku, Yokohama 226-8502,Japan

Measurements of gamma rays from keV-neutron resonance capture by ^{19}F, ^{23}Na, and ^{27}Al, which are odd-Z nuclei in the 2s-1d shell region, were performed, using an anti-Compton HPGe spectrometer and a pulsed neutron source by the ^{7}Li(p,n)^{7}Be reaction. Capture gamma rays from the 27-, 49-, and 97-keV resonances of ^{19}F, the 35- and 53-keV resonances of ^{23}Na, and the 35-keV resonance of ^{27}Al were observed. Some results are presented.

1. Introduction

For the last decade, we measured capture gamma rays from broad keV-neutron resonances of 1p shell and 2s-1d shell nuclei to study resonance capture mechanisms[1], using an anti-Compton NaI(Tl) gamma-ray spectrometer because the detection efficiency of NaI(Tl) was much larger than that of Ge(Li) or HPGe detector. For odd-Z nuclei, however, the energy resolution of NaI(Tl) is not enough because the level spacing of residual nucleus is so small that some gamma rays cannot be resolved.

Large HPGe detectors are available at present, and it becomes possible to apply a large HPGe detector to our resonance experiment. Therefore, we have constructed an anti-Compton HPGe spectrometer with 100% relative efficiency[2], and started systematic measurements of keV-neutron resonance capture gamma rays for odd-Z nuclei in the 2s-1d shell region.

A series of measurements for ^{19}F, ^{23}Na and ^{27}Al has been performed, and capture gamma rays from the 27-, 49-, and 97-keV resonances of ^{19}F, the 35- and 53-keV resonances of ^{23}Na, and the 35-keV resonance of ^{27}Al were observed. Some results are presented in this contribution.

2. Experimental Procedure

The experimental arrangement is shown in Fig.1. Pulsed keV-neutrons were produced from the ^{7}Li(p,n)^{7}Be reaction by bombarding a Li-evaporated copper disk with a 1.5-ns bunched proton beam from the 3-MV Pelletron accelerator of the Research Laboratory for Nuclear Reactors at the Tokyo Institute of Technology. The incident neutron spectrum on a

capture sample was measured by means of a Time-of-Flight(TOF) method, employing a ^{6}Li-glass scintillation detector. Capture samples and a standard Au sample were disks with a diameter of 90 mm and a thickness of 5 mm or 1 mm. The sample was located 12 cm away from the neutron source at an angle of 0° with respect to the proton beam direction. Resonance capture gamma rays were detected with the anti-Compton HPGe spectrometer at 125° . The spectrometer was placed in a heavy shield consisted of borated polyethylene, cadmium, lead, and lithium-6 hydride. The distance between the capture sample and the spectrometer was about 80 cm. The signals from the spectrometer were stored in a workstation as two dimensional data of Pulse-Height(PH) and TOF.

3. Data Processing

The TOF spectra observed with the HPGe spectrometer were corrected for the time walk of timing signals from the spectrometer, employing an experimentally obtained relation between PH and time walk. Figure 2 shows the corrected TOF spectrum for the ^{19}F measurement in the lower neutron energy region of 5 to 70 keV. The peak around 4,500 channel is due to the neutron resonance capture gamma rays and that around 5,300 channel is due to the gamma rays from the ^{7}Li(p,γ)^{8}Be reaction. Digital windows were set in the TOF spectum to obtain foreground and background PH spectra. The net capture gamma-ray PH spectra were extracted by subtracting a background PH spectrum from the foreground PH spectra.

The net PH spectra for the 27-keV resonance of ^{19}F and the 35-keV resonance of ^{27}Al are shown in Figs.3 and 4, respectively. Many peaks due to the primary- and secondary-transition gamma rays are seen in the figures. The intensity of each peak was obtained from the peak area and the corresponding gamma-ray detection efficiency.

A PH weighting technique[3] with experimentally obtained response functions of the HPGe spectrometer was applied to the net PH spectrum of standard Au sample to obtain its capture yield. The relative energy spectrum of neutrons incident on the capture sample or the standard Au sample was extracted from the TOF spectrum observed by the ^{6}Li-glass scintillation detector and its relative neutron detection efficiency. Then, the absolute number of neutrons incident on the standard Au sample was obtained from the capture yield of Au sample, the standard capture cross sections of Au[4], and the relative neutron spectrum. Finally, the absolute number of neutrons incident on each capture sample was calculated from that incident on the standard Au sample and the ratio of monitor counts by the ^{6}Li-glass scintillation detector.

Partial radiative widths were derived from the peak intensities and the absolute number of incident neutrons, neglecting the gamma rays from non-resonant capture.

Corrections were made for the self-shielding and multiple-scattering of neutrons in the sample, for the absorption of capture gamma rays in the sample, and for the dependence of gamma-ray detection efficiency on the position in the sample.

4. Results and Discussion

Relative intensities of primary transitions from the 27-, 49-, and 97-keV p-wave resonances of ^{19}F are shown in Table 1 and compared with our previous results[5,6] with an anti-Compton NaI(Tl) spectrometer and the results of Kenny et al.[7] with a Ge(Li) detector. The

present 27- and 49-keV resonance results are in good agreement with those of Kenny et al. except for the transitions from the 27-keV resonance to the 0.0- and 1.971-MeV states. In our previous measurement for the 27-keV resonance, the transitions to the 1.843-, 1.971-, and 2.044-MeV states, those to the 3.488-, 3.587-, and 3.680-MeV states, and those to the 3.965- and 4.082-MeV states were not resolved in the PH spectrum, so we extracted the intensities by using information on the branching ratios of the related states and observed secondary-transition intensities. Therefore, some discrepancies are seen for those transition intensities. From a comparison between the present and our previous results for the 49- and 97-keV resonances, discrepancies are also seen for some transitions, especially those to the 1.309- and 2.044-MeV states.

Relative intensities of primary transitions from the 35-keV s-wave resonance of ^{27}Al are shown in Table 2 and compared with other experimental results[7,8]. Intensities by other experiments were renormalized so that the sum of them are equal to that of the corresponding present intensities, and the renormalized values are shown in parentheses. The present results are in good agreement with our previous results[8] and in reasonable agreement with those of Kenny et al.[7] The strong M1 transition to the ground state and the rare E2 transition to the 1.014-MeV state are the characteristics of the 35-keV s-wave resonance of ^{27}Al.

References

[1]H. Kitazawa and M. Igashira, Proc. Specialists' Meeting on Measurement, Calculation and Evaluation of Photon Production Data, NEA/NSC/DOC(95)1 (1995) 169.

[2]M. Igashira et al., Proc. the 8th Int. Symp. on Capture Gamma-Ray Spectroscopy and Related Topics, 1993, p.992.

[3]R.L. Macklin and J.H. Gibons, Phys. Rev. **159** (1967) 1007.

[4]ENDF/B-VI data file for ^{197}Au (MAT=7925), evaluated by P.G. Young (1984).

[5]M. Igashira et al., Proc. Int. Conf. on Nuclear Data for Science and Technology, 1994, p.1045.

[6]M. Kato, Bachelor Thesis, Tokyo Institute of Technology, 1994.

[7]M.J. Kenny et al., Aust. J. Phys. **27** (1974) 759.

[8]M. Igashira et al., AIP Conference Proceedings 238, Capture Gamma-Ray Spectroscopy, 1990, p.624; J. Hori, Master Thesis, Tokyo Institute of Technology, 1997.

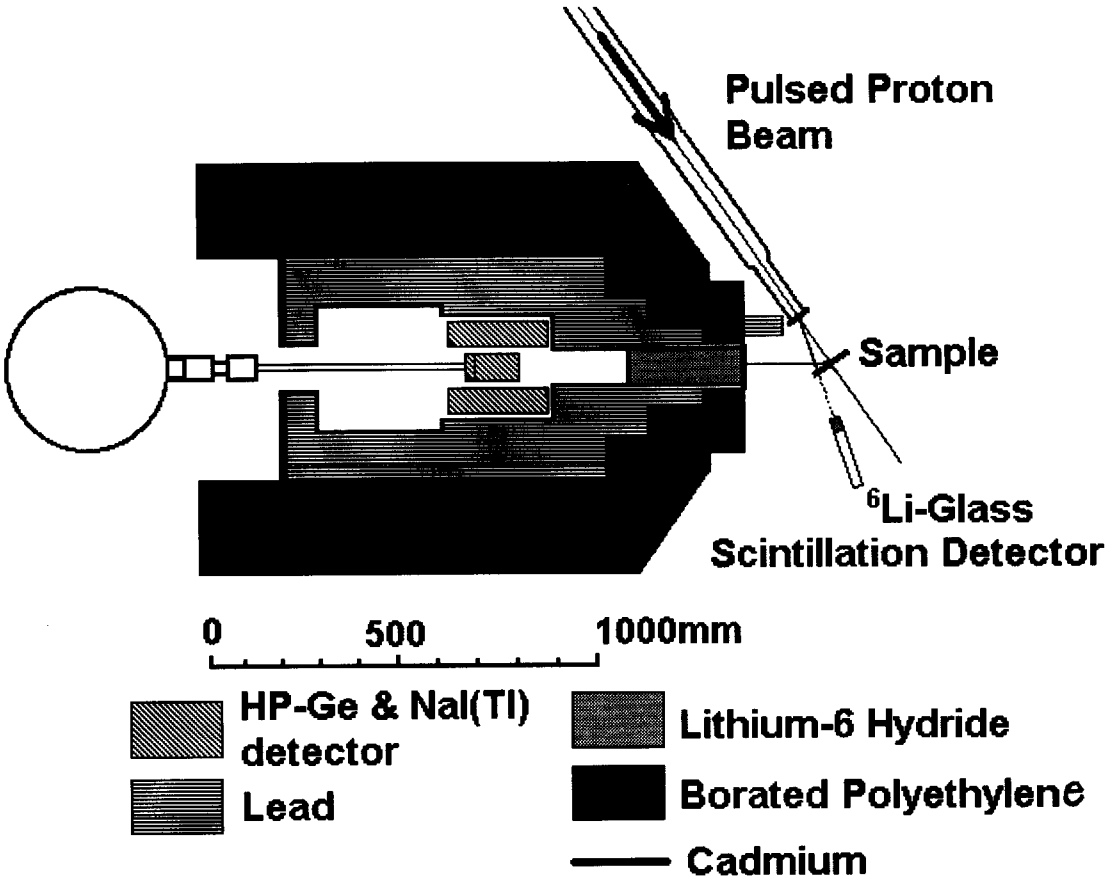

Fig. 1. Experimental arrangement

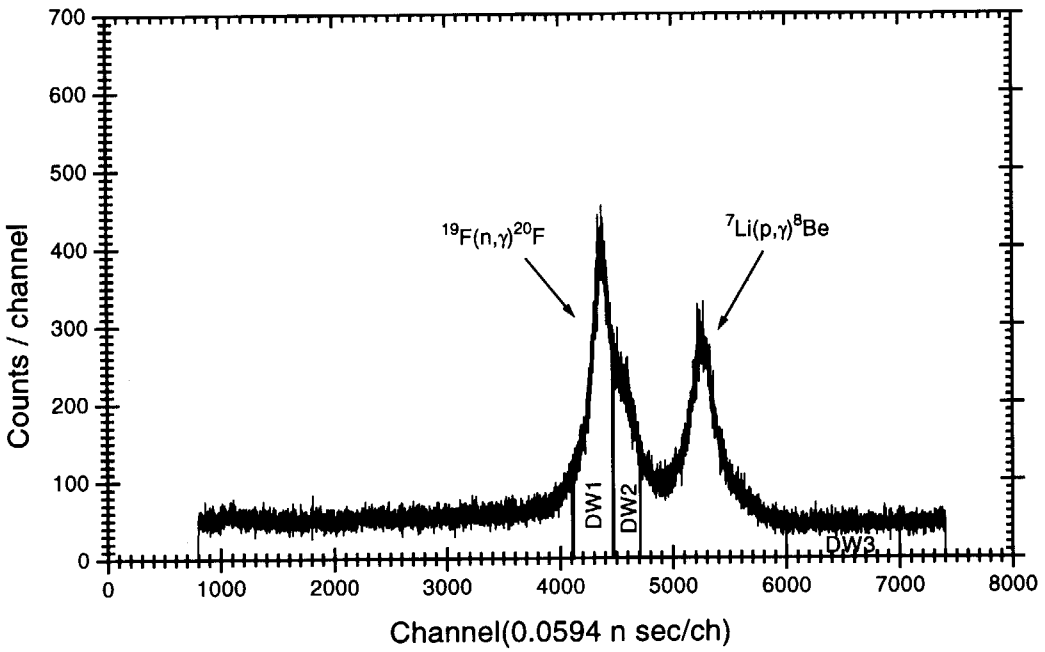

Fig. 2. Corrected TOF spectrum for the ^{19}F measurement

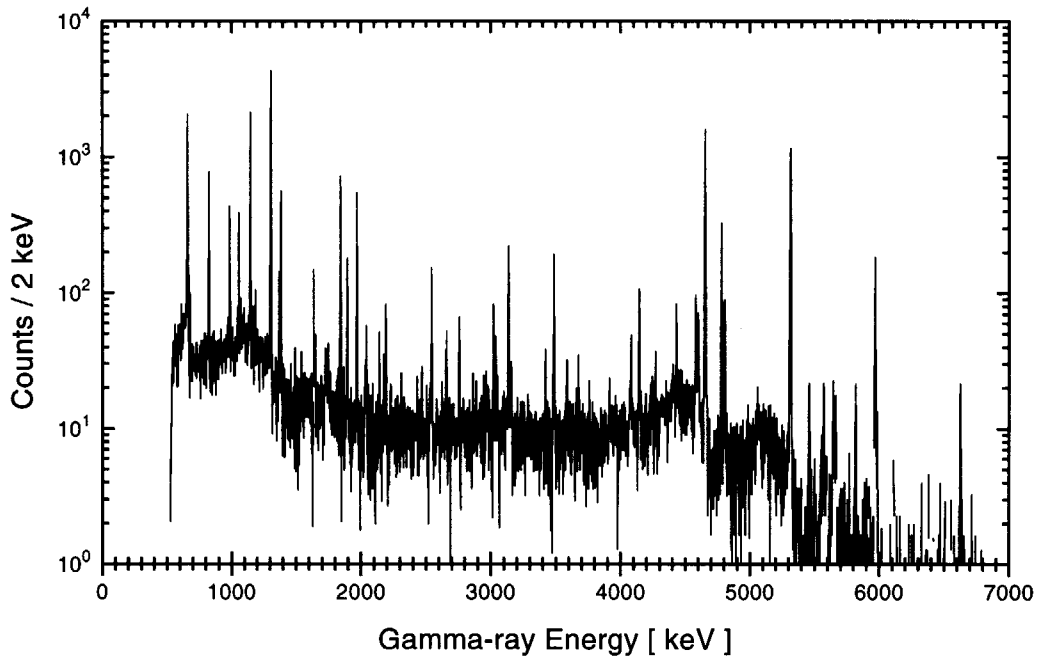

Fig. 3. Net PH spectrum for the 27-keV resonance of ^{19}F

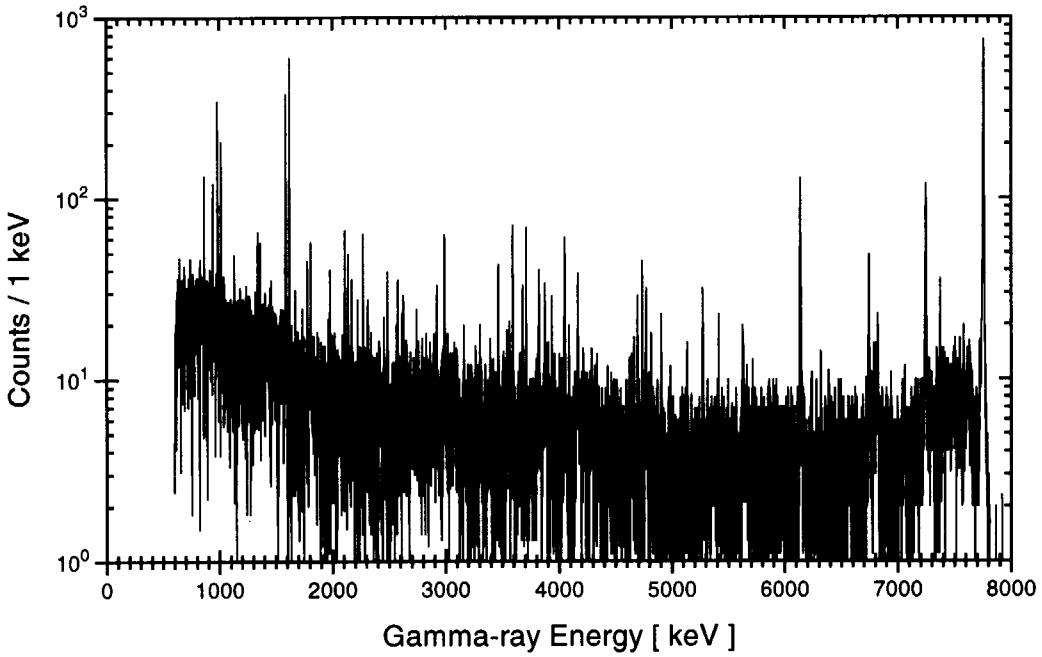

Fig. 4. Net PH spectrum for the 35-keV resonance of ^{27}Al

Table 1. Relative intensities of primary transitions from the resonances of ^{19}F

Final States (MeV)	J^{π}	Relative Intensities (%) 27-keV resonance 2^- Present	Ref[5]	Ref[7]	49-keV resonance 1^- Present	Ref[6]	Ref[7]	97-keV resonance 1^- Present	Ref[6]
0.000	2^+	1.2±0.1	0.9±0.1	2.0±0.5	2.0±0.2	2.4±0.04	----	22.5±1.2	18.3±1.2
0.656	3^+	5.5±0.3	6.0±0.2	6±1	----	----	----	----	----
0.984	1^-	0.5±0.1	1.9±0.1	----	17.1±1.0		18±4	17.1±1.0	14.5±0.94
1.057	1^+	0.7±0.1		----	9.3±0.6	25.8±0.77	9±4	----	----
1.309	2^-	32.7±1.6	34±0.5	31±2	1.2±0.2	7.0±0.5	----	23.0±1.3	21.8±1.2
1.824	5^+	3.1±0.2	----	----	----	----	----	----	----
1.843	2^-	7.8±0.6	6.8±0.1	8±2	----	----	----	----	----
1.971	(3^-)	34.1±2.8	38±0.5	46±4	----	----	----	----	----
2.044	2^+	2.1±0.2	2.0±0.02	1.5±1	54.4±4.6	43.2±0.52	59±6	5.1±0.5	13.0±0.99
2.194	(3^+)	1.8±0.2	2.0±0.3	----	----	2.9±0.8	----	----	----
3.488	1^+	3.0±0.1	5.6±0.3	3±1	14.9±0.71	18.9±0.72	14±5	7.4±0.4	
3.526	0^+	0.2±0.02	----	----	----	----	----	15.0±0.72	30.0±1.4
3.587	$(1, 2^+)$	1.0±0.1	----	----	----	----	----	----	----
3.680	1, 2	0.4±0.03	----	----	----	----	----	----	----
3.965	1^+	0.5±0.04	1.4±0.1	----	----	----	----	----	----
4.082	$(1)^+$	2.1±0.1	1.6±0.2	2.5±1	1.1±0.1	----	----	----	----
4.315	$(0, 1)^+$	0.6±0.1	----	----	----	----	----	9.8±0.7	----
4.731	$(3^-, 4, 5^+)$	1.5±0.1	----	----	----	----	----	----	----
4.766		0.3±0.02	----	----	----	----	----	----	----
5.131	$(2^-, 3, 4^+)$	0.5±0.1	----	----	----	----	----	----	----
5.555	$1, 2^+$	0.8±0.04	----	----	----	----	----	----	----

Table 2. Relative intensities of primary transitions from the 35-keV resonance $(2^+)$of ^{27}Al

Final States (MeV)	J^{π}	Relative Intensities (%) Present	Ref[8]	Ref[7]
0.000	3^+	70.5±2.3	83.2±8.4(71.2)	79±5(70.5)
0.031	2^+	0.7±0.2		2.5±1(2.2)
1.014	0^+	4.2±0.3	4.1±1(3.5)	3±1(2.6)
1.373	1^+	0.8±0.1		----
1.620	1^+	3.0±0.2	12.6±1.8(10.8)	10±2(8.7)
1.623	2^+	6.3±0.5		
2.139	2^+	0.7±0.2	----	1.5±1(1.3)
2.272	4^+	----	----	2±1(1.7)
2.486	2^+	2.0±0.2	----	----
2.988	$(1, 3)^+$	1.5±0.2	----	----
3.591	3^-	0.8±0.1	----	----
3.671	3^+	0.4±0.1	----	----
3.709	$(2, 3)^+$	2.9±0.2	----	----
3.876	2^-	0.4±0.1	----	----
3.935	2^+	1.5±0.1	----	----
4.597	1^+	0.7±0.1	----	----
4.765	2^-	1.9±0.2	----	2±1(1.7)
4.846	1^+	0.3±0.1	----	----
5.015	3^+	0.4±0.1	----	----
5.135	3^-	0.5±0.1	----	----
5.442	2^-	0.8±0.1	----	----

3.23 Direct Capture of Low-Energy Neutrons by ^{16}O

Hideo KITAZAWA
Department of Energy Sciences, Interdisciplinary Graduate School of Science and Engineering, Tokyo Institute of Technology, 4259 Nagatsuta-cho, Midori-ku, Yokohama 226
e-mail: kitazawa@es.titech.ac.jp

Masayuki IGASHIRA
Research Laboratory for Nuclear Reactors, Tokyo Institute of Technology, 2-12-1 O-okayama, Meguro-ku, Tokyo 152

A dispersive optical potential for the interaction between low-energy neutrons and ^{16}O-nuclei is derived from a dispersion relation based on the Feshbach generalized optical model. This potential is applied to direct-capture model calculations in explaining the observed off-resonance capture transitions to the ground ($5/2^+$) and 871 keV($1/2^+$) levels in ^{17}O at neutron energies of 20-70 keV. The model calculations take account of the spatial nonlocality of the neutron-nucleus interaction potential.

1. Introduction

Low-energy neutron capture reactions on light nuclei play an important role in the nucleosynthesis on the inhomogeneous big-bang model as well as in the s-process nucleosynthesis in red giant stars. Furthermore, drip-line light nuclei were found to have radii much larger than those of other neighboring nuclei [1]. This suggests the existence of a neutron-halo structure in the nuclei. A neutron halo is basically characterized by the presence of a weakly-bound state which has an appreciable single-particle component of low angular momentum. The combination of the low neutron-separation energy and the low angular momentum allows neutrons to remain at distances much larger than the normal nuclear radius. Therefore, the neutron-halo wave function could be probed by observing low-energy neutron direct-capture reactions on light nuclei.

Stimulated by the above findings, a lot of experimental work has recently been performed to obtain off-resonance neutron-capture cross sections of light nuclei in the steller energy region [2-4]. Simultaneously, these cross sections have been evaluated by Mengoni *et al.* [5], Otsuka *et al.* [6], and Kitazawa *et al.* [7] in the framework of a direct-capture model, because the reactions may be decoupled from resonance excitation. In particular, Kitazawa *et al.* have used a dispersive optical model to achieve consistency between capture and scattering. In the present study, we intend to describe low-energy neutron direct-capture reactions on ^{16}O, following our previous work [7]. The results are compared to recently-observed off-resonance capture cross sections of ^{16}O at 20-70 keV neutron energies [8].

2. Dispersion Potential

In this section, we determine a dispersive optical potential to explain off-resonance capture of low-energy neutrons by ^{16}O using the direct-capture model. The optical potential is described as the sum of a Hartree-Fock component and a dispersive component [9]. The Hartree-Fock component is theoretically approximated by a local potential, whose strength decreases linearly

with increasing incident neutron energy. While, the dispersive component is represented by a dispersion relation that connects the real part of an optical potential with the imaginary absorptive part. The real central part of this potential is then expressed as [10,11]

$$V(r,E) = V_H(r,E) + \frac{P}{\pi}\int_{-\infty}^{\infty} \frac{W_s(r,E')}{E'-E}dE'$$

$$= V_H(r,E) + \frac{2}{\pi}(E-E_F)P\int_{E_F}^{\infty} \frac{W_s(r,E')}{(E'-E_F)^2-(E-E_F)^2}dE'$$

$$= V_H(r,E) + \Delta V_s(r,E), \tag{1}$$

where P indicates a principal value. The potential $V_H(r,E)$ is the Hartree-Fock component, and $\Delta V_s(r,E)$ is the dispersive component due to the surface absorption $W_s(r,E)$, which is assumed to be symmetric about the Fermi energy E_F. Equation (1) shows how much of the energy dependence of empirical optical potentials arises from the nonlocality and how much from the dispersive nature of nuclear matter.

As an initial guess of the Hartree-Fock potential strength $V_H(E)$, we use the central part of the neutron optical potential of ^{16}O (called DG-potential) obtained by Dave and Gould at 7-15 MeV [12]:

$$V_H(E) = -48.25 + 0.053E, \tag{2}$$

where E is the center-of-mass energy in MeV. The absorption potential strength linearly increases with increasing neutron energy: $W_S(E) = -4.418 - 0.556E$. However, no information is given on the dependence of the absorption potential upon neutron energies below 7 MeV. Watson *et al.* [13] have proposed a global neutron optical potential for 1p-shell nuclei, in which the absorption potential strength decreases linearly with decreasing neutron energy and becomes zero at $E = 0$. Above E=13.8 MeV, the energy dependence is much weaker than that of the DG-potential. From these facts, we assume the absorption potential as follows: $W_S(E) = 0$ at $E_F \le E \le 0$, $W_S(E) = -0.942E$ MeV at $0 \le E \le 13.8$ MeV, and $W_S(E) = -13.0$ MeV at $E \ge 13.8$ MeV. Using this potential, the dispersion potential $\Delta V_s(r,E)$ is obtained from the principal-value integral in Eq. (1). The Fermi energy E_F is defined as an average of the minimum energy E_F^+ of particle states and the maximum energy E_F^- of hole states in ^{16}O:

$$E_F = \left(E_F^+ + E_F^-\right)/2 = -9.91\text{MeV}. \tag{3}$$

The dispersive optical potential reproduces the ENDF/B-V ^{16}O+n total cross sections at neutron energies of 10-300 keV. Then, the potential form factors and spin-orbit potential depth are taken to be the same as those of the DG-potential, except increasing only slightly the radius parameter r_0 of the Hartree-Fock potential. On the other hand, the potential with $\Delta V_s(E)= 0$

overestimates the total cross sections, and the discrepancy between the calculated and ENDF/B-V values greatly increases with decreasing neutron energy. In other words, the dispersion correction is important for reproducing the total cross sections, in particular at lower neutron energies.

3. Model Calculations and Discussion

In the direct-capture model calculation, the radial wave functions of initial and final neutron single-particle states are calculated using the dispersive optical potential obtained in Section 2. The bound-state wave function is calculated so as to reproduce the observed neutron binding energy. Moreover, in order to take account of the spatial nonlocality of the microscopic mean field of nucleon-nucleon interaction, the bound-state wave function is modified as [14]

$$U_{nlj}(r) = C_{nlj} P(r) u_{nlj}(r), \tag{4}$$

where $u_{nlj}(r)$ is the radial wave function of a bound state in $V(r,E)$, C_{nlj} is introduced for normalizing $U_{nlj}(r)$, and $P(r)$ is a Perey damping factor [15]. When the Hartree-Fock potential has a linear energy dependence of Eq. (2) for negative energies, the damping factor is given by

$$P(r) = \left[1 - \alpha f_H(r)\right]^{1/2}, \tag{5}$$

where α is 0.053 and $f_H(r)$ is the Hartree-Fock potential form factor.

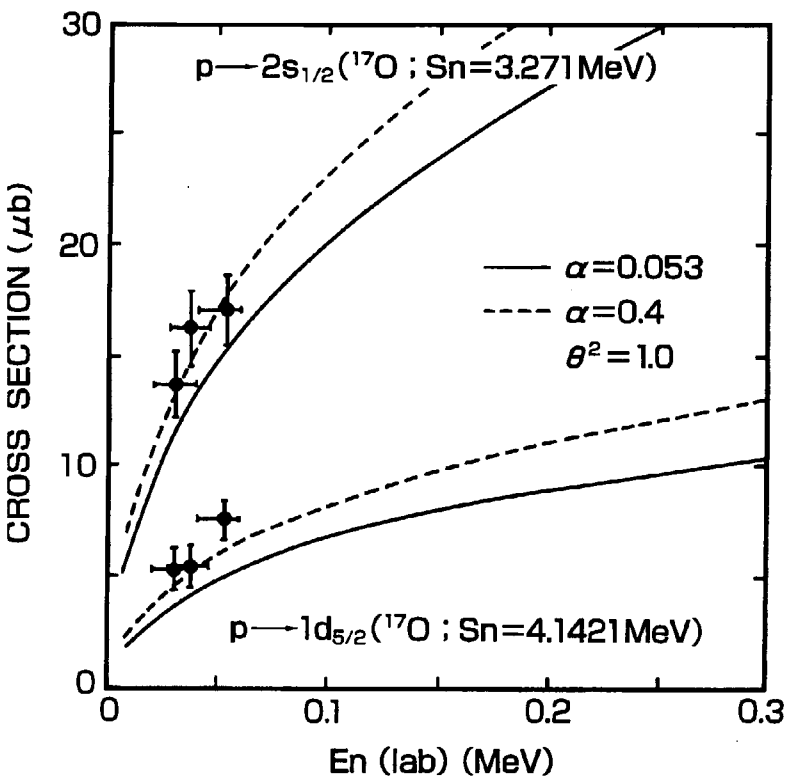

Fig. 1 Cross sections for neutron capture to the ground ($5/2^+$) and 871 keV($1/2^+$) levels in ^{17}O.

In Fig. 1 the observed cross sections for neutron capture to the ground ($5/2^+$) and 871 keV($1/2^+$) levels in ^{17}O are compared to the direct-capture cross sections for the transitions to the $1d_{5/2}$ and $2s_{1/2}$ pure single-particle states (θ^2=1.0). As well known, both levels are of strong single-particle character. The model calculations with α = 0.053, shown by the solid lines, predict the cross sections to be 20 % smaller than those observed for the ground ($5/2^+$) level transition and 12 % smaller for the 871 keV($1/2^+$) level transition.

For the dominant $p_{3/2}$-wave capture to the $1d_{5/2}$ state, the contribution of the nuclear-interior overlap integrand to the transition amplitude is minor, as compared to that of the nuclear exterior, and therefore the direct-capture cross sections are not so sensitive to the Hartree-Fock potential depth. But, the coupling between the direct-capture transition and the excitation of the giant-dipole resonance (GDR) and nearby resonances would not be negligible. On the other hand, for the p-wave capture to the $2s_{1/2}$ state, the negative and positive parts of the overlap integrand are completely canceled out in the nuclear interior, which makes the direct-capture cross sections rather insensitive to the Hartree-Fock potential depth [7]. And also, the direct-capture transition would be decoupled by this cancellation from excitation of the GDR and nearby resonances, because the transition amplitude in the nuclear interior is responsible for the coupling between the single-particle and resonance transitions. Therefore, it is inconceivable that the above discrepancy between the calculated and observed values is caused by an unsuitable choice of the Hartree-Fock potential strength.

The broken lines in Fig. 1 show the direct-capture cross sections calculated using α = 0.4, which is determined so as to reproduce the observed cross sections. The large α value might be produced by the nearby resonances. However, it should be noteworthy that the energy dependence of the real volume integral of the Jeukenne-Lejeune-Mahaux potential derived from a realistic nucleon-nucleon interaction is much stronger than that of the DG-potential [12,16].

4. Conclusions

We determined the dispersive optical potential for the interaction between low-energy neutrons and ^{16}O-nuclei, using the optical potential obtained by Dave and Gould from neutron scattering experiments. As a result, it was found that the dispersive optical potential reproduces the total cross sections at neutron energies of 10-300 keV. But, the direct-capture model calculations taking account of the spatial nonlocality of the neutron-nucleus interaction potential for negative energies indicate a strong energy dependence of the local Hartree-Fock potential depth, which is in striking contrast to the weak energy dependence of the Hartree-Fock potential assumed in Section 2.

References

[1] Tanihata I., Hamagaki H., Hashimoto O., Shida Y., Yoshikawa N., Sugimoto K., Yamakawa O., and Kobayashi T.: Phys. Rev. Lett., 55, 2676 (1985).

[2] Nagai Y., Igashira M., Takeda K., Mukai N., Motoyama S., Uesawa F., Kitazawa H., and Fukuda T.: Astrophys. J., 372, 683 (1991).

[3] Ohsaki T., Nagai Y., Igashira M., Shima T., Takeda K., Seino S., and Irie T: Astrophys. J., 422, 912 (1994).

[4] Igashira M., Nagai Y., Masuda K., Ohsaki T., and Kitazawa H.: Astrophys. J.,441, L89 (1995).

[5] Mengoni A., Otsuka T., and Ishihara M.: Phys. Rev., C52, R2334 (1995).

[6] Otsuka T., Ishihara M., Fukunishi N., Nakamura T., and Yokoyama M.: Phys. Rev., C49, R2289 (1994).

[7] Kitazawa H., Go K., and Igashira M.: Proc. 9th Int. Symp. on Capture Gamma-ray Spectroscopy and Related Topics, Budapest, Hungary, October 8-12, 1996; to be published in Phys. Rev. C.
[8] Nagai Y.: private communication.
[9] Feshbach H.: Ann. Phys., 5, 357 (1958).
[10] Mahaux C. and Ngô H.: Nucl. Phys., A378, 205 (1982)
[11] Mahaux C., Ngô H., and Satchler G. R.: Nucl. Phys., A449, 354 (1986).
[12] Dave J. H. and Gould C. R.: Phys. Rev., C28, 2212 (1983).
[13] Watson B. A., Singh P. P., and Segel R. E.: Phys. Rev., 182, 977(1969).
[14] Dover C. B. and Giai N. V.: Nucl. Phys., A190, 373 (1972).
[15] Perey F. G. and Saruis A. M.: Nucl. Phys., 70, 225 (1965).
[16] Jeukenne J. -P., Lejeune A., and Mahaux C.: Phys. Rev. C16, 80 (1977).

3.24 Measurements of Effective Total Macroscopic Cross Sections and Effective Energy of Continuum Beam.

KOBAYASHI, Hisao

Institute for Atomic Energy, Rikkyo University
e-mail: j00343@sinet.ad.jp

ABSTRACT

Two practically useful quantities are introduced in this study to characterize a continuum neutron beam and to describe transmission phenomena of the beam in field of quantitative neutron radiography: an *effective energy* instead of a peak energy or a mean energy of the spectrum and an *effective total macroscopic* (ETM) cross section instead of a total macroscopic (TM) cross section defined at the monochromatic energy.

The effective energy was evaluated by means of energy dependence of ETM cross section. To realize the method a beam quality indicator (BQI) has been proposed recently. Several effective energies were measured for non-filtered, filtered neutron beams, and outputs of neutron guide tubes in world by the BQI.

A thermal neutron beam and three beams modulated by Pb filters with different thicknesses are studied to measure ETM cross sections for various materials and summarized in a table. Validity of the effective energy determined by the BQI is discussed relating with ETM cross sections of materials.

1. INTRODUCTION

A beam having a continuum spectrum has to be used in the ordinary neutron radiography. A precise analysis of neutron transmission phenomenon using nuclear data and a neutron spectrum is not necessarily valuable in the practical field. One of reasons is that given nuclear data have not be covered completely and be finished to compile for arbitrary materials, for various solid state characteristics of all elements, and for arbitrary chemical compound. An arbitrary inhomogeneous materials with arbitrary shape of objects are also expected. In addition to these reasons, neutron spectra are not always known for every facility.

If a practically useful quantity can be introduced and can describe the transmission characteristics of materials, it is valuable for quantitative analysis of neutron radiography images. An ETM cross section was defined to be an average logarithmic decreasing rate (removal rate) of transmittance for an individual continuum neutron beam instead of TM cross section at an interesting depth [1]. The new quantity is practically useful as a parameter to describe actual neutron transmission phenomena approximately within a limited thickness of an object. Of course some materials having a deep Bragg cutoff such as Be are not suitable to describe such unique parameter. However, Oda et al. [2] proved in the case that transmission characters of such materials are still able to describe with sufficiently good approximation by a thickness dependent ETM cross section.

Since ETM cross sections for many materials depend on the energy spectrum of neutron beam, it is required to know a beam qualified quantity which is able to describe the ETM cross

Table I Effective Energies for Various Neutron Breams

Facility (country)	Filter (moderator/reflector)	R_{Cd}	[1]E_{mean}	[2]t_{Pb}/t_{Ti}	[3]E_{eff} (meV)
(Without filter)					
Rikkyo RUR-N2(Japan)	none (graphite)	2	meV	1.67 ± 0.01	28.9 ± 0.2
JAERI JRR3M-TF2(Japan)	none (D_2O)	130	47.2	1.73 ± 0.03	27.3 ± 0.9
PML-FNR-V(USA)	none (D_2O)	47		1.76 ± 0.12	26.7 ± 2.8
Kyoto U. KUR-E2(Japan)	none (D_2O)	400		1.78 ± 0.04	26.6 ± 0.8
Kinki U. UTR(Japan)	none (graphite)	4.3		1.93 ± 0.17	22.8 ± 1.2
(With non-cooled filter)					
JSW-Cyclotron (Japan)	Pb 0.5 cm+Poly 4cm (poly)			1.72 ± 0.01	27.7 ± 0.3
JSW-Cyclotron (Japan)	Pb 0.5 cm+Poly 4cm +C 2cm (poly)			1.77 ± 0.01	26.6 ± 0.3
AECL-NRU(Canada)	quartz/sapphire (graphite)	>1000		1.82 ± 0.04	25.7 ± 0.9
JSW-Cyclotron (Japan)	Pb 0.5 cm+Poly 4cm+Bi 3cm (poly)			1.84 ± 0.02	25.3 ± 0.4
McMaster U.MNR(Canada)	Bi 15cm			1.91 ± 0.06	24.2 ± 1.2
PSI-SINQ (Swiss)	Bi 10 cm (D_2O)			1.98 ± 0.02	18.6 ± 0.3
Rikkyo RUR-N2(Japan)	Pb 5 cm (graphite)			2.03 ± 0.01	17.2 ± 0.2
PSI-SAPHIR(Swiss)	Bi 10cm+Si 6cm (graphite)			2.24 ± 0.01	13.1 ± 0.1
HFR-HB8-T(Netherlands)	Si 25cm+Bi 25cm (50K) (graphite)			2.25 ± 0.04	13.0 ± 0.4
PML-FNR-E(USA)	Pb 12.7cm (D_2O)	200		2.27 ± 0.10	12.6 ± 0.9
AUR (Austria)	Bi 14 cm (graphite)			2.47 ± 0.14	10.6 ± 0.9
Rikkyo RUR-N2(Japan)	Pb 10 cm (graphite)			2.58 ± 0.03	9.8 ± 0.2
Rikkyo RUR-N2(Japan)	Pb 15 cm (graphite)			3.33 ± 0.07	7.1 ± 0.2
Rikkyo RUR-N2(Japan)	Pb 20 cm (graphite)			3.87 ± 0.09	6.2 ± 0.2
U. Virginia MTR(USA)	Pb 6.7cm+Bi 25 cm			7.00 ± 0.40	5.0 ± 0.5
(With cooled filter)					
HFR-HB8-C(Netherlands)	Be30(50K)+Bi25(50K) (grph)	560		11.60 ± 1.20	3.23 ± 0.53
(Neutron guide tube)					
Kyoto U. KUR-CN3(Jpn)	Characteristic w.l.λ_c=1.8Å (lq.D_2)		12.	11.05 ± 0.31	3.24 ± 0.14
Kyoto U. KUR-CN2(Jpn)	Characteristic w.l.λ_c=2.6Å (liq.D_2)		7.2	12.05 ± 0.77	3.20 ± 0.33
JAERI JRR3M-C2-3(Jpn)	Characteristic w.l.λ_c=4.0Å (lq.H_2)		4.6	17.58 ± 0.50	2.63 ± 0.11

(Revised Nov. 20, 1997)

1 Mean value from TOF measured spectrum.

2 This work: Estimated thickness t_{Pb}/t_{Ti} ratio from the BQI image.

3 This work: Results of analyses from BQI image.

section. To solve this requirement, an effective energy was proposed and estimated using two different transmission characters of materials, Pb and Ti [3].

After a concept of beam quality indicator (BQI) is described, estimated effective energies will be shown for various beams having different beam spectra. Secondly, measured ETM cross sections of 28 materials for four different beams are summarized in a table. Where transmission data were obtained with an ordinary direct-film method and a neutron-sensitized imaging plate (NIP).

2. ETM CROSS SECTION AND EFFECTIVE ENRGY DETERMINATION

The ETM cross section for continuum beams, $\langle\Sigma\rangle$, has been defined instead of TM cross sections for neutrons of monochromatic energy by Kobayashi et al. [1] as

$$\langle\Sigma\rangle = \langle[\ln\{I(t)\}]/\mathrm{d}t\rangle \approx \ln[I_0/I(t)]/t. \qquad (1)$$

The concept of the effective energy determination is simple and easily to understand. It is based on a monotonic relation between energy and cross section ratio of two materials whose cross sections have both monotonical within an interesting energy range and also have an opposite tendency of energy dependence. Ti and Pb are suitable for this purpose. Where Ti has a typical $1/v$ energy dependent cross section and Pb made of an extruding process has a complex character but depends on energy monotonically up to 0.1 eV. If thicknesses of the two materials, t_{Ti} and t_{Pb}, corresponds to give the same transmittance, the cross section ratio is immediately replaced by the thickness ratio by

$$R(E_{eff}) = \langle\Sigma_{Ti}(E_{eff})\rangle / \langle\Sigma_{Pb}(E_{eff})\rangle = t_{Pb}/t_{Ti}, \quad \text{and then} \quad E_{eff} = R^{-1}(t_{Pb}/t_{Ti}), \qquad (2)$$

where $\langle\Sigma_{Ti}(E_{eff})\rangle$ and $\langle\Sigma_{Pb}(E_{eff})\rangle$ are ETM cross section for continuum neutron defined by eq.(1) for Ti and Pb, respectively. Thus, E_{eff} is given by the inverse function in eq. 2. The beam quality indicator (BQI) was designed based on the concept. If Ti and Pb are used in this purpose, the BQI are varied in the energy range E_{eff}<0.1 eV. More detailed explanations and discussions have been described elsewhere [3].

3. EXPERIMENTAL AND RESULTS

3.1 Effective Energies of Various Facilities

Various neutron beams have been examined to estimate effective energies using the BQI and summarized [4]. Some results including output of a cyclotron neutron generator and some filtered beams are added in this report and are summarized in table I. The 24 beams are classified into five non-filtered neutron beams, fifteen beams with various non-cooled filter, one cooled filtered beam, and three outputs of neutron guide tubes.

3.2 Beam Modulation using Filters

As shown in Table I, effective energies of all filtered beam were much or less lowered from expected thermal energies. Effective energy modulation by use of filters have been studied theoretically and experimentally for Be, Bi, and Pb [5]. It is also proved that the effective energy of continuum thermal neutron beams are easily lowered to sub-thermal region by use of

Table II Effective Total Macroscopic Cross Sections of Various Materials for Four Neutron Beams with Different Effective Energies from 9.68 meV to1.45 eV(unit: 1/cm)

Beam Filter E_{eff}	Sub-thermal Pb = 10 cm 9.68 meV	Sub-thermal Pb = 5 cm 17.0 meV	Thermal none 28.9 meV	In Epi-thermal Cd = 1 mm 1.46 eV	Comment
Al	0.095 ± 0.001	*** ± ***	0.102 ± 0.001	*** ± ***	
Au	6.98 ± 0.13	6.09 ± 0.09	5.62 ± 0.11	1.93 ± 0.02	Dental
Ag	4.55 ± 0.11	4.07 ± 0.13	3.60 ± 0.10	1.05 ± 0.03	Dental
Cd	114.6 ± 2.8	109.6 ± 3.8	96.7 ± 3.0	0.593 ± 0.011	Dental
Cu	0.921 ± 0.016	0.899 ± 0.009	0.849 ± 0.014	0.586 ± 0.011	Dental
Dy	35.6 ± 1.0	31.4 ± 0.9	28.0 ± 0.6	7.64 ± 0.33	
Graphite	0.380 ± 0.008	0.398 ± 0.009	0.389 ± 0.007	0.317 ± 0.004	
Fe	1.02 ± 0.03	1.04 ± 0.02	1.04 ± 0.02	0.531 ± 0.016	
In	9.42 ± 0.31	8.23 ± 0.33	7.45 ± 0.22	46.8 ± 6.2	t<0.28 mm
Ni	1.648 ± 0.072	1.592 ± 0.048	1.604 ± 0.040	0.932 ± 0.010	
Pb	0.259 ± 0.011	0.293 ± 0.008	0.312 ± 0.006	0.262 ± 0.006	Pure
Pb(Te)	0.236 ± 0.005	0.274 ± 0.004	0.304 ± 0.004	0.304 ± 0.005	
Rh	11.2± 0.3	9.86 ± 0.18	9.11 ± 0.16	10.5 ± 2.7	
Ti	0.637 ± 0.010	0.553 ± 0.010	0.517 ± 0.005	0.209 ± 0.003	
Zn	0.356 ± 0.005	0.346 ± 0.006	0.331 ± 0.004	0.230 ± 0.003	
Ag-alloy	4.184 ± 0.064	3.814 ± 0.037	3.416 ± 0.06	5.70 ± 1.12	Dental
Au-Pd	3.81 ± 0.09	3.24 ± 0.06	2.97± 0.077	3.26 ± 0.25	Dental
Brass	0.724 ± 0.011	0.670 ± 0.007	0.652 ± 0.008	0.348 ± 0.008	
LiF	*** ± ***	*** ± ***	*** ± ***	0.771 ± ***	
PBN	30.2 ± 1.6	28.2 ± 1.2	19.8 ± 1.4	5.40 ± 0.05	
SUS	1.01 ± 0.02	1.02 ± 0.01	1.01 ± 0.01	0.521 ± 0.009	
H_2O	3.56 ± 0.03	3.38 ± 0.05	2.80 ± 0.02	0.489 ± 0.053	
D_2O	0.666 ± 0.008	*** ± ***	0.503 ± 0.004	*** ± ***	
Teflon	0.318 ± 0.006	0.321 ± 0.004	0.323 ± 0.003	0.217 ± 0.005	
Poly	4.73 ± 0.12	4.40 ± 0.05	3.54 ± 0.09	1.33 ± 0.05	t=<0.6cm
Acryl	3.54 ± 0.03	3.25 ± 0.04	2.72 ± 0.04	1.052± 0.03	t=<0.6cm
Tissue	3.50 ± 0.06	3.18 ± 0.07	2.25 ± 0.13	0.865 ± 0.042	t=<1.19cm
Bone	2.73 ± 0.08	2.11 ± 0.14	1.66 ± 0.13	0.606 ± 0.057	t=<2.07cm

Neutron beam: Rikkyo TRIGA-II (100kW) – Beam port No.2 with Pb filter (0, 5 and 10 cm).
Measurements of effective energies: BQI with Imaging Plate for neutron detection (BAS NR2025).
Measurements of ETM cross sections: Average slopes of transmission curves after scattered component corrections.

*** : Not measured to date.

those filters. In this experiment, two Pb filters with thickness of 5 cm and 10 cm were inserted into the tangential beam port of TRIGA-II (100kW) reactor in Rikkyo University. To study efficacy and reliability of the filter effect, effective energies were estimated for each beams by the BQI. It was found that the effective energy was lowered from 29 meV for non-filtered beam to 17 meV for 5 cm-thick Pb filter and 9.7 meV for 10 cm.

In addition to those three beams, an epi-thermal beam was obtained after filtered the thermal neutrons less than ~0.4 eV by a Cd plate with thickness of 1 mm. An In metal foil of 20 cm x 20 cm x 0.3 mm-*t* is applied to detect mainly 1.46 eV resonance neutrons.

The five non-filtered and filtered beams from Rikkyo TRIGA II are used to measure ETM cross sections for various materials.

3.3 Transmission Measurements

An imaging plate IP(N) for neutron detection (BAS-NR2025) is made of a mixture of a photo stimulated luminescence material ($BaFBr:Eu^{2+}$) and a Gd_2O_3. A simple imaging plate for X/gamma-ray detection (BAS-SR2505) is also used with In foil for 1.46 eV neutron detection by means of transfer method. Photo stimulated luminescent (PSL) signals from all IP's were measured and analyzed by the *bio-imaging analyzer* (BAS5000: Fuji Photo Film Co. Ltd.) which can be analyzed the PSL signals with 16-bit-length covering four or five decade of the PSL value and with 25 μm of maximum spatial resolution within the maximum area of 20 x 25 cm^2.

Step shapes of 28 materials were imaged by the IP. After scattering neutrons and gamma-ray background signals were corrected by use of the *shadow method** [1], transmittance were analyzed to found ETM cross sections for the four neutron beams. Results are summarized in Table II. Where uncertainties shows the 95% confidence interval of regression analysis when the transmittance curve is assumed to be an exponential form. As results, almost of ETM cross sections were determined with uncertainty of 2%. However, a few uncertainties for the case of In-resonance epi-thermal became over 10% but less than 20% for In, Rh, Ag-alloy, H_2O and Bone phantom. This is because of non-exponential transmission character such as discussed by Oda et al. [2].

4. DISCUSSIONS

Naturally, ETM cross sections for materials with finite thicknesses are lower than total macroscopic (TM) cross sections for monochromatic energy neutrons except for some energy independent materials. For thermal and sub-thermal neutrons, measured ETM cross sections shown in Table II are 10% to 30% lower than the TM cross sections given by elsewhere such as BNL-325 [6]. Where the TM cross sections were compared with energies the same as the effective energies determined by the BQI. The discrepancy should be mainly due to a beam *softening* or a *hardening* effect and to a difference of atomic density from that of the comparing data source, and to deformation of neutron spectrum from that of the Maxwell neutron beam. Much serious discrepancies are observed for some materials in the In epi-thermal case. One of

---

* In the method, Cd strips with thickness of 1 mm were used for thermal and sub-thermal neutron stoppers, and a stack of an 1mm Cd plus a 3 mm In strips for In resonant epi-thermal neutrons.

additive reason may be understandable by complex shapes of the filtered spectra and insufficient estimation of scattered background radiation.

It is shown that the effective energy defined by the BQI is well characterized direct and filtered continuum beams and well correlated with the ETM cross sections. The result lead to great advantage in a quantitative study comparing with the traditional estimations at the 2200 m/s for thermal neutron beam. Further studies will be extend to confirmation of validity of the study including estimations of systematic errors in near future.

ACKNOWLEDGEMENT

Author would like to acknowledge following scientists in Institutes, Universities and the company shown in Table I who kindly permitted to use facilities, operated their neutron beams and assisted to make radiography images:

Akira Tsuruno and Masahito Matsubayashi (Tokai, JAERI - TOKAI - Japan)
Kenji Yoneda and Shigenori Fujine (KURI - KUMATORI - Japan)
Takeo Niwa and Takao Tsuruta (Atomic Energy Res. Inst., Kinki Univ. - OSAKA - Japan)
Koji Yoshii (Nucl. Eng. Res. Lab., Univ. of Tokyo, TOKAI - Japan)
Yuujiro Toda and Hyougo Yoshida (Japan Steel Works Ltd. - MURORAN - Japan)
H. P. Leeflang (HFR Dept., ECN Petten - PETTEN - The Netherlands)
J. F. W. Markgraf (HFR Div., JRC Petten - PETTEN - The Netherlands)
J. Hammer and E. Lehmann (SAPHIR/SINQ, Paul Scherrer Inst. - VILLIGEN - Switzerland)
G. M. MacGillivray (AECL Res., Chalk River Lab. - CHALK RIVER - Canada)
M. P. Butler (McMaster Nuclear Reactor, McMaster Univ., HAMILTON - Canada)
J. S. Brenizer Jr., R. Johnson, and D. Raine (Univ. of Virginia, Reactor Facility, CHARLOTTESVILLE - USA)
J. T. Lindsay (Phoenix Memorial Lab., Univ. of Michigan, ANN ARBOR - USA)

Also author wish to extend his gratitude to Mr. S. Iwai, Fuji Photo Film Co. Ltd., for his kind permission to use the BAS5000 bio-analyzing system. He also express his thanks to Dr. H. Wakao and Mr. S. Watanabe for huge amount of film readings and analyses.

[1] H. Kobayashi, *et al.*, J. Nucl. Sci. Technol. 29 (1992) 1045.
[2] M. Oda, *et al*, Nucl. Instr. Methods, A377 (1996) 72-75.
[3] H. Kobayashi and Y. Kiyanagi, Nucl. Instr. Methods, A377 (1996) 52-57.
[4] H. Kobayashi, Proc. Int. Conf. on Nucl. Data for Science and Tech. (Trieste, May 19-24, 1997) (to be published)
[5] H. Kobayashi, *et al.*, Nucl. Instr. Methods, A377 (1996) 37-40.
[6] D. I. Garber and R. R. Kinsey, Neutron Cross sections Vol. I & II, BNL-325 (1976).

3.25 Measurements of (n,xp), (n,xd) Double Differential Cross Sections of Al and C for neutrons at 75 and 65MeV

Yasushi NAUCHI[1], Mamoru BABA[1], Tomohiko IWASAKI[1], Toshiya SANAMI[1], Takashi TABEI[1], Takanori SUZUKI[1], Masanobu IBARAKI[1], Susumu TANAKA[2], Hiroshi NAKASHIMA[3], Shin-ichiro Meigo[3], Hiroshi TAKADA[3], Noriaki NAKAO[4], Takashi NAKAMURA[5], Yukinobu WATANABE[6], Masahide HARADA[6], Tomoya NUNOMIYA[1],Naohiro HIRAKAWA[1]

[1]Dept. Quantum Sci. and Energy Eng., Tohoku Univ., Sendai 980-77
[2]Takasaki Establishment, Japan Atomic Energy Research Institute, Takasaki 370-123
[3]Tokai Establishment, Japan Atomic Energy research Institute, Tokai-Mura319-11
[4]Tanashi Branch, High Energy Accelerator Research Organization, 3-2-1, Midori-Cho, Tanashi-Shi
[5]Cyclotron Radioisotope Center, Tohoku Univ., Sendai 980-77
[6]Dept. Energy Conversion Eng., Kyushu Univ., Kasuga 816

Abstract

The (n,xp) and (n,xd) double differential cross sections (DDXs) of Al and C were measured at 6 angles (12°, 17°, 25°, 40°, 55° and 70 °) for neutrons En=65 and 75MeV. These data are compared with theoretical calculations of ISOBAR and GNASH. A new wide range spectrometer under fabrication to down the detection threshold is also described.

1 introduction

Charged particles emission reaction data induced by ten's MeV neutrons are essential for accelerator applications, such as the accelerator therapy, the high intensity neutron sources for material research, and the accelerator driven transmutation systems. For the purpose, not only the total amount of the secondary charged particles, but also energy spectra and angular distributions of those particles (i. e. DDXs) are requested.

Experimental data are very limited and discrepant even if there are experimental data. The data for carbon reported by U. C. Davis [1] and U. C. Louvain[2] show marked differences in low energy region. As for the DDX data of structural materials, (n,xα) DDXs for neutrons up to 50MeV at carried out at LANL/WNR[3], but no proton and deuteron data have been reported.

Theoretical calculation codes as GNASH, QMD, ISOBAR etc. have been developed to describe spectra in the intermediate energy region. However, the validations have not been done sufficiently for the neutron induced reactions because of the lack of experimental data.

For this reason, we have been conducting the measurements of (n,xp), (n,xd) DDXs for ten's MeV neutrons at the ^{7}Li(p,n) mono-energetic neutron source facility in TIARA (Takasaki Establishment, JAERI) [4]. In the present work, we report the proton and deuteron spectra of Al and C for 75MeV and 65MeV neutrons measured at 6 angles from 12° to 70°. The comparisons of the experiments with calculations of ISOBAR and GNASH are also presented.

The detection threshold of the present measurements is, however, still high(11MeV for protons). In order to obtain low energy spectra, a new low threshold spectrometer is now under fabrication. It consists of a vacuum chamber and three telescopes, consisting of a low pressure gas proportional counter and a BaF_2 scintillator. Recent results of the gas counter and the BaF_2 are also mentioned.

2 Experiment and Data Processing

The experiments were done at the ^{7}Li(p,n) quasi mono-energetic neutron source facility at TIARA[1]. The facility and the measured spectra of ^{7}Li(p,n) neutrons were previously described in detail[6]. The important parameter in the present work are shown in the table below.

Table: Energy and flux of the ^{7}Li(p,n$_{0,1}$) neutrons

E_p(MeV)	E_n (MeV)	Resolution (MeV)	^{7}Li(p,n$_{0,1}$) flux(n/sr/μC)
67.5	64.5	2.6	4.3×10^9
78.	75.	3.4	4.8×10^9

Experiments were done using two different geometry, namely, "inclined geometry" and "annuler geometry". Figure 1 shows the experimental set-up of the usual inclined geometry. Neutrons from a ^{7}Li(99%) metal target, defined by a concrete and iron collimator (3m long, 11cm in diameter), were guided to a disk shape sample (7cm in diameter, thickness was 160mg/cm^2 for Al, 110mg/cm^2 for C) located ~5.5m from the ^{7}Li target. Emitted protons and deuterons were detected by two $\Delta E - E$ counter telescopes which consists of a SSD(900mm^2, 150μm in thickness) a NaI(Tl)(5.08cm in diam.,3cm thick). The detection angles are 25°, 40°, 55°, 70°. For the measurements at angles below 25°, the counters were exposed by direct neutrons. To overcome the problem, we employed an 'annular' geometry, in which an annular shape sample (inner diam. =6cm, outer diam. =9.6cm) was employed, and one telescope was located on the 0° axis being shadowed by a 50cm long brass shadow-bar(5.5cm in diam.) as shown in fig. 2. The sample thickness was 60mg/cm^2 for C and 80mg/cm^2 for Al. By using the annular geometry, we obtained the DDXs at 12° and 17°.

The pulse height data of the SSD and NaI were taken event by event together with the time of flight (TOF) data relative to cyclotron RF that indicate the flight time of the incident neutron. Protons and deuterons were identified using the ΔE-E method, then the event induced by the peak neutrons were selected using the TOF information. The spectra from the sample were obtained by subtracting sample-out spectra from sample-in spectra. Although triton components can be seen in ΔE-E spectra, the counting statistics and S/N were too poor to deduce the triton spectra.

The energy scale of the spectra was determined by the recoil proton peak corresponding to the ^{7}Li(p,n$_{0,1}$) neutrons and the linear response of NaI(Tl)[8]. The correction for the energy loss in the sample, air, Al window (0.115mm) and SSD were done assuming that all particles are generated in the middle plane of the sample, and transported to the NaI on the same path. The detection threshold is $E_p = 11MeV$ for protons.

Finally, DDXs are obtained by normalizing the spectra with neutron flux, the number of the sample atoms and the solid angle.

3 Results and Discussion

3.1 Aluminum spectra

The Al(n,xp) DDXs are shown in fig. 3 together with calculations by GNASH[7] and by the modified versions of ISOBAR[5]. The experimental spectra (dot) show continuum-like

[1]Takasaki Ion Accelerator facility for advanced Radiation Application, JAERI

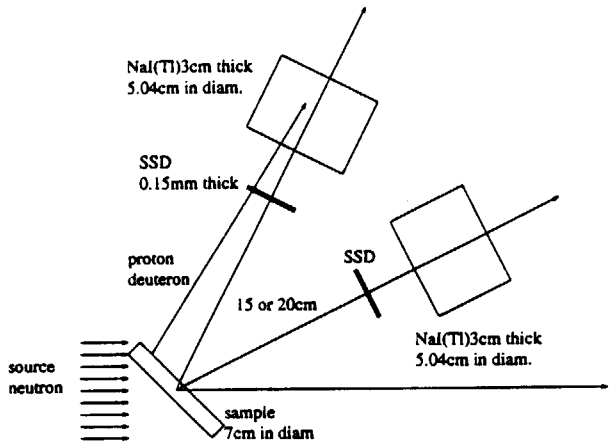

Figure 1: inclined geometry

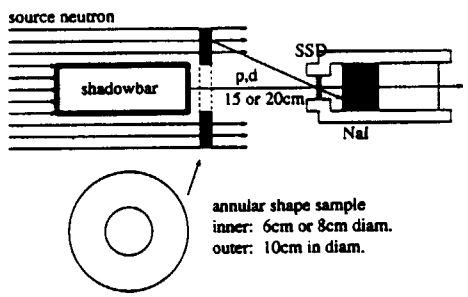

Figure 2: annular geometry

structure having forward peaking angular distribution. No peaks can be seen even in the high energy regions, because the level spacing of residual nucleus(^{27}Mg) is narrower than the width of the source neutron. Both ISOBAR (solid line) and GNASH (dashed line) reproduce the experiments fairly well in spectral shape, although they underestimate the magnitude at very forward angle (12°). ISOBAR systematically underestimates the spectra than GNASH, and the differences between the two codes are large below the detection threshold. To validate the codes, new experiments with low threshold should be done.

Figure 4 shows the Al(n,xd) DDXs (dot) with calculations by GNASH (solid line). The high energy parts of the spectra vary rapidly with detection angles, and the GNASH does not follow the angular dependence satisfactorily. The data in low energy continuum show milder angular dependence which will be due to multi-step reactions, but are not traced by GNASH again. The amount of the low energy components is significant, so the (n,xd) whole spectra are required to study nuclear heating and particle accumulation effects in materials.

3.2 Carbon spectra

Proton spectra (dot) of C for 65MeV are shown in fig.5 together with ISOBAR calculations(solid line). In contrast to the Al(n,xp)DDXs, prominent peaks are observed at foreword angles corresponding to the ground state and the low-lying levels of the residual nucleus ^{12}B. The low energy parts of the spectra show milder angular dependence, and ISOBAR traces the spectral shape fairly well but under estimates the magnitude as in the Al(n,xp) case.

C(n,xd) DDXs are shown in fig. 6. A prominent peak corresponding to the ^{11}B ground state appears on the continuum. The peaks rapidly decreases as angle goes backward, and will be due to the pick-up reaction. The continuum show milder angular dependencies and the amounts of the continuum is smaller than that of the Al(n,xd) case.

4 Developments of new spectrometer

The detection threshold of the present spectrometer was too high to obtain low energy proton spectra. Besides, it cannot be applied to detect the (n,α) DDXs which are also essential

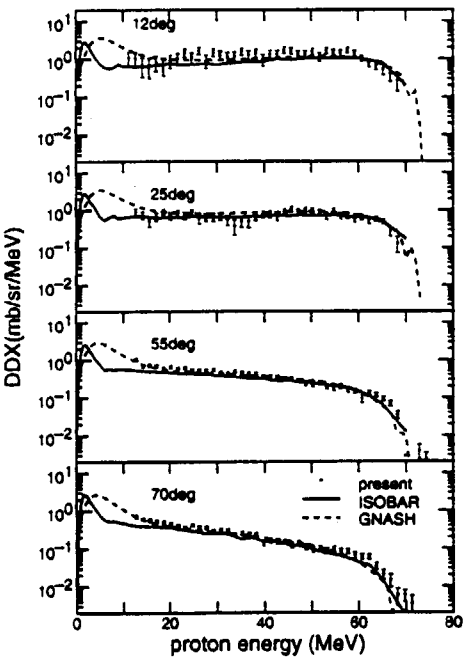

Figure 3: Al(n,xp)DDXs for 75MeV neutrons

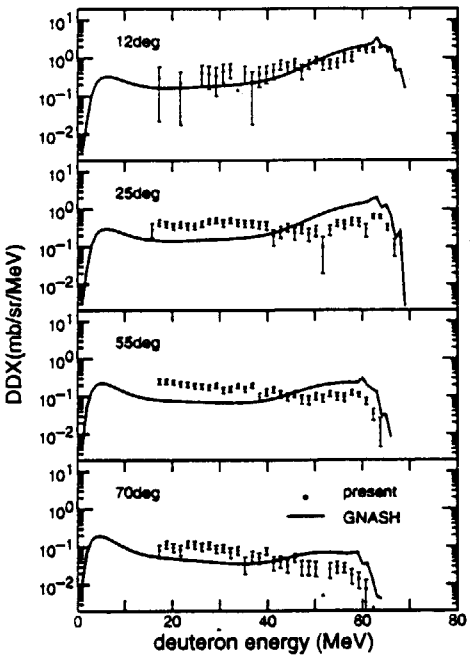

Figure 4: Al(n,xd)DDXs for 75MeV neutrons

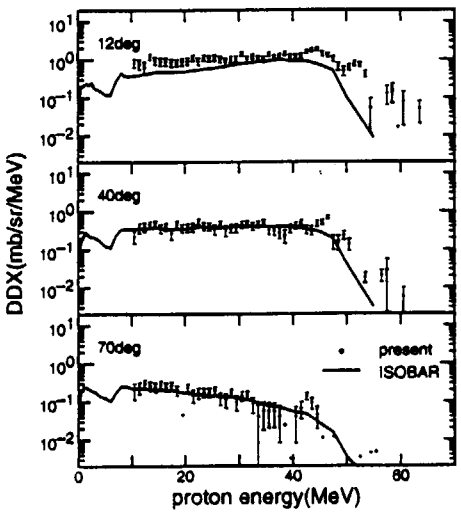

Figure 5: C(n,xp)DDXs for 65MeV neutrons

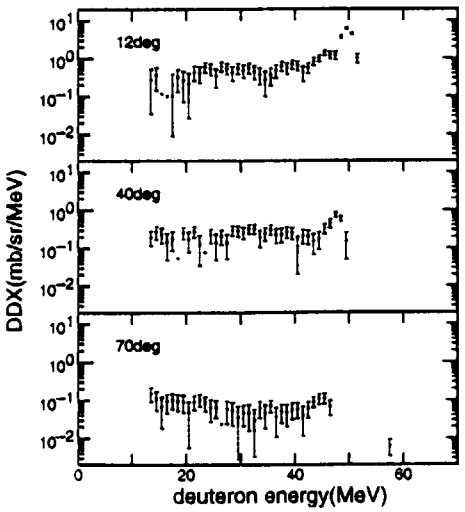

Figure 6: C(n,xd)DDXs for 65MeV neutrons

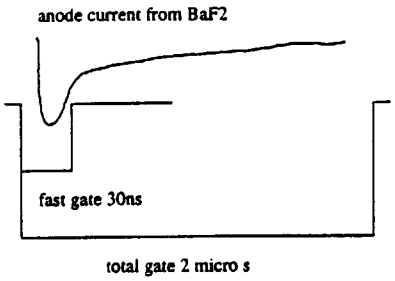

Figure 7: gate condition

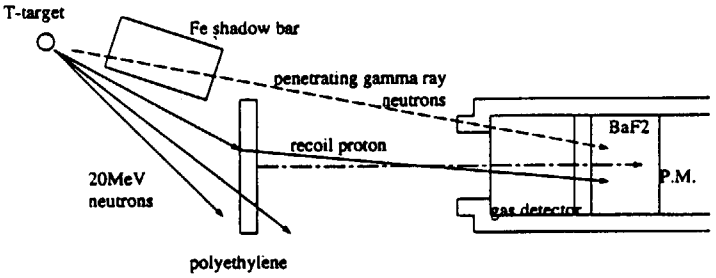

Figure 8: P.I. test experiments set up

for the material damage by fast neutrons, because α particles lose too large energy in the air, the aluminum window and the SSD.

In the present experiments, there was another problem of high backgrounds from nitrogen and oxygen in the air, because the number of atoms between the sample and the detector was comparable with that of the sample.

To overcome those problem, a new spectrometer which consists of a vacuum chamber and ΔE-E counter telescopes is now under fabrication as reported in the previous symposium[4].

To lower the energy loss in front of the E-detector, low pressure (0.1atm P-10) gas counters (4.2cm in diam., 5.4cm long) with thin windows (3.4μm thick mylar) are adopted as ΔE detectors. By using the vacuum chamber and the gas counter, the detection threshold can be as low as 4MeV for α particles. However, 80MeV protons deposit so small energy (< 30keV) in the gas counter that particle identifications (PI) by the ΔE-E method will be difficult. To solve the problem, we adopt a BaF_2 scintillator (4cm in diam., 2.2cm thick) as the E-detector of the telescopes, because of its PI capability by pulse shape discrimination method (PSD). PI by PSD is done by the gate-integration method using CAMAC module[9]. The gate condition used is shown in fig. 7.

Uniformity of the gas multiplication over the large scale ($\sim$10cm^2) were confirmed recently by the test experiments using ^{241}Am α source. Besides, some modifications were also tried to improve the PI of the BaF_2. 1) Silicon-oil with low attenuation coefficient for fast components (λ =310nm, T_{decay} =600ps[10]) of the light output was adopted to couple the BaF_2 and the photo-multiplier, and 2) delay times to adjust the timing in the gate integration method were carefully examined.

Test experiments of the PI by the ΔE-E method and by the PSD method were done using T(d,n) 20MeV neutrons at 4.5MV Dynamitron facility in Tohoku university. The experimental set up is shown in fig. 8. Neutrons from a tritium target bombarded a sheet of polyethylene sample (1mm in thickness), then recoil protons were detected by a Gas-BaF_2 telescopes at 30°. The BaF_2 were shadowed by a 10cm long iron shadow bar from the T target but was exposed by neutrons and γ rays penetrating the shadow bar. The pulse height data of the two detectors were acquired event by event for the ΔE-E method requiring coincidence. For the test of PSD of the BaF_2, the anode current data were acquired in single-detector mode.

The ΔE-E spectrum measured by the detectors are shown in fig. 9. Proton events are clearly separated from noize or electron events.

The PSD spectra of BaF_2 is shown in fig. 10. The horizontal axis indicates the energy, and the vertical axis indicates the amount of the fast components. γ-rays, protons, deuterons and α particles are separated fairly clearly even for several MeV region.

As the results, the PI to identify H and He isotopes will be achieved using the gas-BaF_2

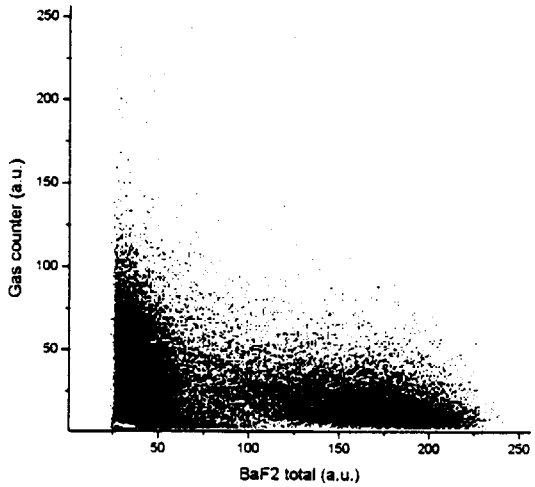

Figure 9: ΔE-E spectra of recoil proton

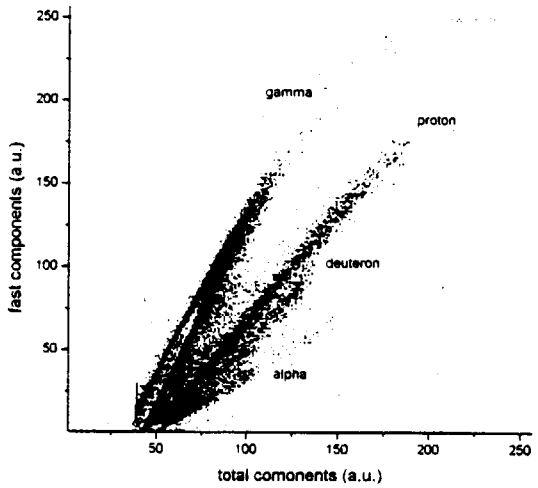

Figure 10: P.I. by P.S.D method

telecopes over wide energy range from 5MeV α particles up to 80MeV protons.

Acknowledgement

The present work was undertaken as part of the special project research between universities and JAERI. The authors would like to thanks the operating crew of JAERI TAKASAKI cyclotron for their collabolation.

The authors express their thanks to Dr. M. Chadwick of LANL for his GNASH calculations.

References

[1] T. S. Sabramanian et. al.,*Nucl. Instr. Meth.* **174** 475 1980

[2] I. Slypen et. al., *Phys. Rev.* **C51** 1303 1995

[3] S. M. Greims et. al., *Nucl. Sci. Eng.* **124** 271 1996

[4] Y. Nauchi et. al., *JAERI-Conf 97-005 proc. 1996 sympo. Nucl. Data* p. 126

[5] H. Takada et. al., *J. Nucl. Sci. Technol.* **33** 275 1996

[6] M. Baba et. al., *Proc. Int. Conf. on Nucl. Data for Sci. Technol.* (1994, Gatlinburg) p. 90

[7] M. Chadwick, *Private Comunications*

[8] J. L. Romero et. al., *Nucl. Instr. Meth.* **A301** 241 1991

[9] G. Lanzano et. al., *Nucl. Instr. Meth.* **A312** 515 1992

[10] C. Agodi et. al., *Nucl. Instr. Meth.* **A269** 595 1988

3.26 Study of the p+^{12}C reaction at energies up to 30 MeV

M. Harada[a)], A. Yamamoto, S. Yoshioka, K. Sato, T. Nakashima, H. Ijiri, Y. Watanabe,
H. Yoshida[*], Y. Uozumi[*], S. Chiba[**], T. Fukahori[**], S. Meigo[**] and O. Iwamoto[**]
Department of Energy Conversion Engineering, Kyushu University, Kasuga,Fukuoka 816, Japan
[*]Department of Nuclear Engineering, Kyushu University, Fukuoka 812, Japan
[**]Japan Atomic Energy Research Institute, Tokai, Ibaraki 319-11, Japan
[a)]e-mail : harada@ence.kyushu-u.ac.jp

Double differential cross sections of charged-particles emitted in the p+^{12}C reaction were measured in the energy region from 14 to 26 MeV. The observed continuous components of emitted protons and α-particles were analyzed by assuming sequential decay of intermediate reaction products and/or simultaneous breakup process. It was found that the three body simultaneous decay, p+α+^{8}Be, and the sequential decay via p+^{12}C*$_{3-}$ and α+^{9}B$_{g.s.}$ are most important in the proton-induced breakup of ^{12}C for energies up to 30 MeV.

1. Introduction

Intermediate energy nuclear data of neutron- and proton-induced reactions on ^{12}C are required for various applications, e.g., dose evaluation in proton radiotherapy. Some of the authors have recently evaluated the neutron nuclear data of ^{12}C for energies up to 80 MeV[1]. In the work, it was found that α-particle production cross sections for the n+^{12}C reaction become large at energies around 20 MeV. They assumed that α-particle emission occurs mainly via the sequential and simultaneous breakup of intermediate excited nuclei such as ^{12}C and ^{9}B and evaluated double-differential cross sections (DDXs) for neutron and α-particle emission. To understand the detail of such many-body breakup processes, measurements of DDXs for all particles emitted at the same incident energy and simultaneous analysis are helpful. However, there is few experimental data not only for the n+^{12}C reactions, but also for the p+^{12}C reaction in the energy region of interest. Thus, we have started to study the nucleon-induced breakup processes for ^{12}C through proton experiments which can provide the data with better statistics than neutron experiments. The result is expected to be useful for intermediate energy proton and neutron nuclear data evaluation.

In the present work, we have measured the DDXs of protons and α-particles emitted in the p+^{12}C reaction at energies of 14, 18 and 26 MeV by using two type of ΔE-E counter telescopes and analyzed the continuum components observed in proton and α-particle emission spectra. In this report, preliminary results of our analyses are reported.

2. Measurement

2.1.Counter telescopes

We have developed two counter telescopes for the present experiments. One was a ΔE-E counter telescope having three stacked Si-SSD detectors as ΔE-E detector and an NE102A plastic scintillator as active collimator (AC). The details have been reported in Refs. [2,3,4,5]. A schematic side-view of the counter telescope is illustrated in Fig. 1 and their thickness are also tabulated. The AC played a role of a veto detector to reduce the continuum background component due to the edge-penetration which makes it difficult to measure continuum (p,p') spectra at very forward angles.

The other was a ΔE-E counter telescope with a gas proportional counter as ΔE-detector and a Si-SSD as E-counter. A side-view of the counter telescope is shown with the specification in Fig. 2. The details have been described in Ref.[6]. We chose the gas proportional counter as the ΔE-detector because

we make the detectable threshold energy as low as possible. Note that the threshold energy obtained in the present measurement was 1 MeV for α-particles and 0.5 MeV for protons.

2.2.Outline of the experiments

Two experiments have been carried out using (i) the Kyushu University Tandem accelerator for 14 and 18 MeV and (ii) the JAERI Tandem accelerator for 26 MeV. The above-mentioned two counter telescopes were used in the experiment (i), however only the ΔE-E counter telescope with the AC was used in the experiment (ii). A natural carbon foil of 100 $\mu g/cm^2$ thick was used for both measurements. Signals from each detector were processed using commercially available NIM modules and were stored as even-by-event data using PC-based multi-parameter data acquisition system. Proton and α-particle emission spectra were measured at angles from 20° to 150° in step of 10° in the laboratory system for the 14 MeV and 26 MeV and at 20°, 30°, 40°, 60°, 90°, 120° and 150° in the laboratory system for 18 MeV.

3. Analysis

3.1. Simulation code for breakup processes

The SCINFUL/DDX code[1] developed for the neutron nuclear data evaluation for ^{12}C was revised partly for the analysis of continuous spectra of emitted protons and α-particles. In the revised code, we took account of ten sequential decay processes and one three-body simultaneous break-up (3BSB) as listed in Table I. This code calculates DDXs of particles emitted via these many-body breakup processes by using a Monte Carlo method. The cross sections and angular distributions necessary as the input data are summarized in Table II. The angular distributions of particles emitted at the second stage and afterwards were assumed to be isotropic in the c.m. system. In the addition, the finite lifetime for levels of excited states of ^{12}C, ^{9}B, ^{8}Be were considered by using the decay width of a Lorentzian or Gaussian shape. Finally, the calculated results were smoothed using a Gaussian distribution with the experimental energy resolution (200 keV FWHM) for comparisons with the experiments.

3.2.Results and discussion

Figures 3 to 5 show comparisons of the measured DDXs of $^{12}C(p,xp)$ and $^{12}C(p,x\alpha)$ with the calculated ones for 14, 18 and 26 MeV, respectively. Open circles and open triangles stand for the experimental data taken using the counter telescope with AC and those taken using of the counter telescope with the gas counter. The calculated spectra show overall good agreement with the experimental data.

From the analysis, it was found that the continuous spectra observed in the lower emission energy region are formed mainly via the sequential decay processes denoted by (1) to (10) in Table I. It should be remarked that the present detector system succeeded in observing low energy protons emitted via the sequential decay processes (3) in Table I for 14 and 18 MeV. The component of sequential proton decay of $^{9}B_{g.s.}$ deduced from the experimental cross section of $^{12}C(p,\alpha)^{9}B_{g.s.}$ reproduces satisfactorily the bump structure observed in the low energy part of the proton spectra measured at small angles for 14 and 18 MeV. Also, α-particles decaying chain via $^{9}B_{g.s.}$((3) in Table I) form the small bump observed in the experimental data for 14 and 18 MeV as shown in Figs. 3 and 4. Discrepancies seen in Fig. 4 is attributable to ignoring (p,np) reaction and $(p,\alpha)^{9}B^{*}_{7MeV}$ reaction in the present version of our simulation code.

On the other hand, the 3BSB process becomes predominant with increasing emission energy. The ratios of the 3BSB to the total continuum component extracted from the present analysis amount to 23 % for 14 MeV, 50 % for 18 MeV and 71 % for 26 MeV. This indicates that the 3BSB process has the most dominant contribution to the many-body breakup process of ^{12}C induced by proton with 14 to 26 MeV. However, the 3BSB components near the threshold energy underestimate both the experimental (p,xp) and (p,xα) spectra for any incident energies. It is expected that a possible reason is why the $p+\alpha+^{8}Be_{g.s.}$ process was neglected in the calculation. According to Antolkovic et al., the fraction of the total cross section of the $n+^{12}C \rightarrow n+3\alpha$ amounts to 12.5% for 18 MeV[7]. Our preliminary calculation for the $p+^{12}C$ reaction at 18 MeV with this value showed that the agreement was improved at small angles, but the calculated cross sections overestimated the experimental ones at large angles. This might be due

to some differences between the n+^{12}C and p+^{12}C reactions at the same energy. Further study the 3BSB process in nucleon-induced breakup reactions on ^{12}C will be necessary to know the detail of the mechanism.

4.Conclusion

The DDXs of emitted charged particles in the p+^{12}C reaction were measured at three incident energies of 14, 18 and 26 MeV. The continuum components in proton and α-particle emission spectra were analyzed by assuming the many-body breakup processes. It was found that the sequential decay via p+^{12}C$^*_{3-}$ and α+^{9}B$_{g.s.}$ are dominant in the low emission energy region component and the 3BSB process becomes large with increasing emission energy. There appear some discrepancies between the calculated and measured continuous spectra. Further detailed analysis will be necessary to resolve them and to enhance the understanding of nucleon-induced breakup of ^{12}C over the wide incident energy region.

Acknowledgments

We wish to thank Drs. K. Sagara and H. Nakamura, Department of Physics, Kyushu University, for their kind help during the experiment. We are also grateful to the staff of the JAERI Tandem accelerator for their assistance in operating the accelerator. This work is partly supported by Grand-in-Aid Scientific Research of the Ministry of Education, Science and Culture (No.09558059).

[Reference]

[1] M. Harada et al., J. of Nucl. & Technol. **34**, p.116 (1997).
[2] M. Hayashi et al., Proc. of the 1994 Symp. on Nuclear Data, November 17-18, 1994, JAERI, Tokai, JAERI-Conf. 95-008, p.225 (1995).
[3] Y. Nakao et al., Kyushu University Tandem Laboratory, KUTL report-5, p.115 (1995).
[4] S. Yoshioka, Master thesis, Kyushu Univ. (unpublished) (1997).
[5] Y. Watanabe et al., Int. Conf. on Nuclear Data for Science and Technology, Trieste, Italy, May 1997.
[6] A. Yamamto, Bachelor thesis, Kyushu Univ. (unpublished) (1997).
[7] B. Antolkovic and M. Turk, Nucl. Phys. **A524**, p.285 (1991).
[8] H. Hane, Master thesis, Kyushu Univ. (unpublished) (1992).
[9] R. W. Peelle et al., Phys. Rev. **105**, No.4, p.1311 (1957).
[10] H. Kashimoto, Master thesis, Kyushu Univ. (unpublished) (1993).
[11] M. Q. Makino et al., Nucl. Phys. **68**, p.378 (1965).

Table I : Reaction processes considered in the present analysis

1, p + ^{12}C → p' + ^{12}C* (0$^+$, ex.=7.65MeV)	5, p + ^{12}C → p' + ^{12}C* (1$^-$, ex.=10.8MeV)
2, p + ^{12}C → p' + ^{12}C* (3$^-$, ex.=9.64MeV)	6, p + ^{12}C → p' + ^{12}C* (2$^-$, ex.=11.8MeV)
→ α + ^{8}Be$_{g.s.}$	7, p + ^{12}C → p' + ^{12}C* (1$^+$, ex.=12.7MeV)
→ α + α	8, p + ^{12}C → p' + ^{12}C* (4$^+$, ex.=14.1MeV)
3, p + ^{12}C → α + ^{9}B$_{g.s.}$	9, p + ^{12}C → p' + ^{12}C* (1$^+$, ex.=15.1MeV)
→ p + ^{8}Be$_{g.s.}$	10, p + ^{12}C → p' + ^{12}C* (2$^+$, ex.=16.1MeV)
→ α + α	→ α + ^{8}Be* (2$^+$, ex.=2.94MeV)
4, p + ^{12}C → α + ^{9}B*(5/2$^-$, ex.=2.36MeV)	→ α + α
→ α + ^{5}Li	11, p + ^{12}C → p + α + ^{8}Be* (2$^+$, ex.=2.94MeV)
→ p + α	→ α + α [3BSB]

Table II : Input data used in the simulation code

Reaction	Cross Section	Angular distribution
1, 2	14MeV : Hane (1992)[8] 18MeV : Peelle(1957)[9] 26MeV : Kashimoto(1993)[10]	14MeV : Hane (1992) 18MeV : Peelle(1957) 26MeV : Kashimoto(1993)
3, 4	14MeV&18MeV : *Present work* 26MeV : Kashimoto(1993)	14MeV&18MeV : *Present work* 26MeV : Kashimoto(1993)
5 - 10	14MeV&18MeV : *Present work* 26MeV : Kashimoto(1993)	14MeV&18MeV : *Present work* 26MeV : Kashimoto(1993)
11	14MeV&18MeV : $\sigma_{reac.}$[a)] - σ_{2+}[b)] - $\Sigma_{1-10}\sigma_n$ 26MeV : $\sigma_{p+3\alpha}$[c)] - $\Sigma_{1-10}\sigma_n$	isotropic

[a)]Total reaction cross section : Makino(1965)[11]
[b)]Inelastic 2^+ cross section : Peelle(1957)
[c)]p+3α reaction cross section : Kashimoto(1993)

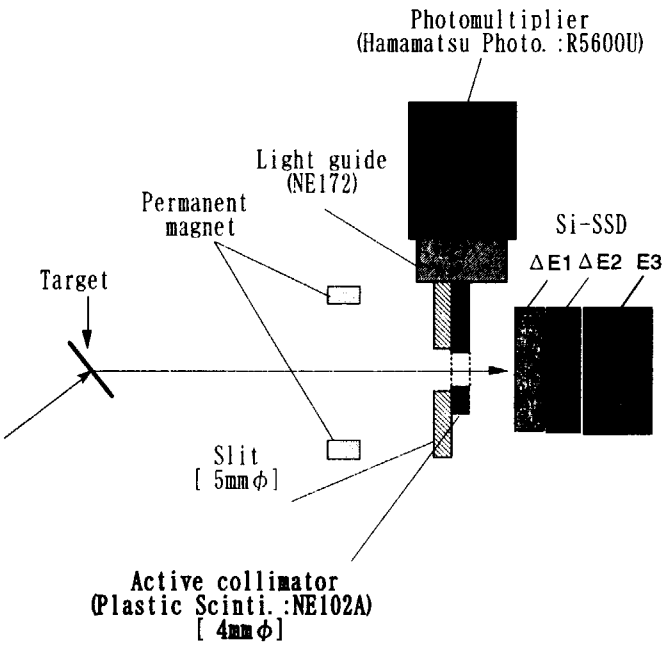

[Thickness of each detector]

	Kyushu-Univ. Exp.	JAERI Exp.
AC	0.5 mm	2 mm
ΔE1	25 μm	30 μm
ΔE2	100 μm	200 μm
E3	2000 μm	5000 μm

Fig. 1 : Side view of counter telescope with active collimator

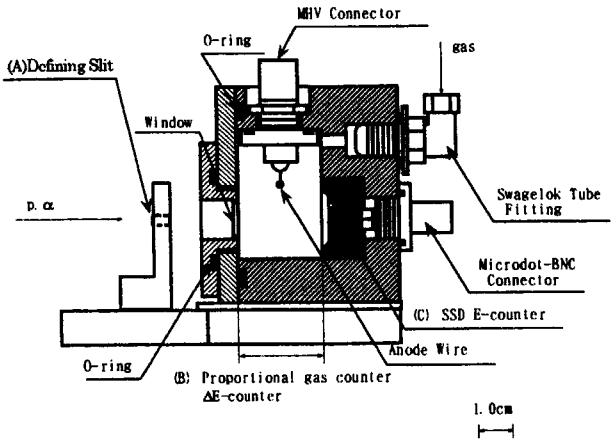

[Detail of defining slit and each detector]

defining silt	3mmϕ	
ΔE-detector	proportional gas counter	
	anode wire	nichrome, 20μmϕ
	window	mylar foil, 1.6μm
	gas	P-10 gas
E-detector	300μm Si-SSD	

Fig. 2 : Side view of low threshold energy counter telescope

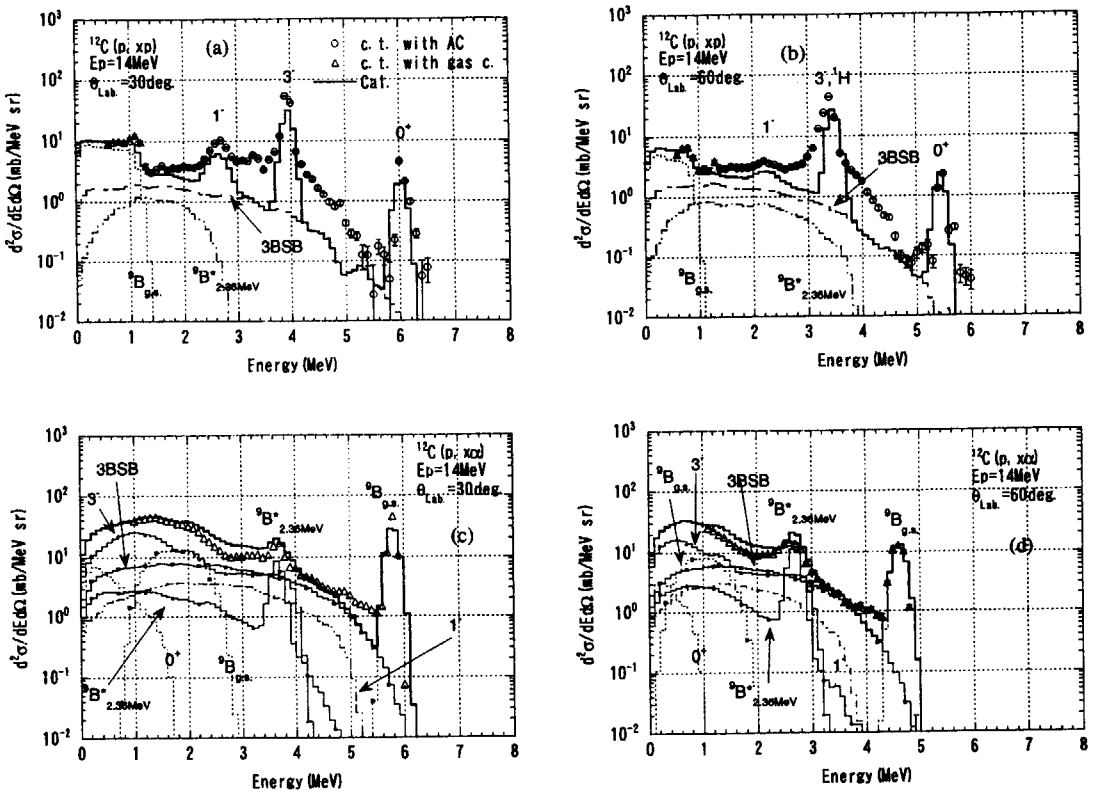

Fig. 3 : Measured and calculated DDXs for 14 MeV (p,xp) and (p,xα) for laboratory angles of 30° and 60°

The peak of the contamination (Hydrogen-1) is denoted by the symbol ^{1}H.

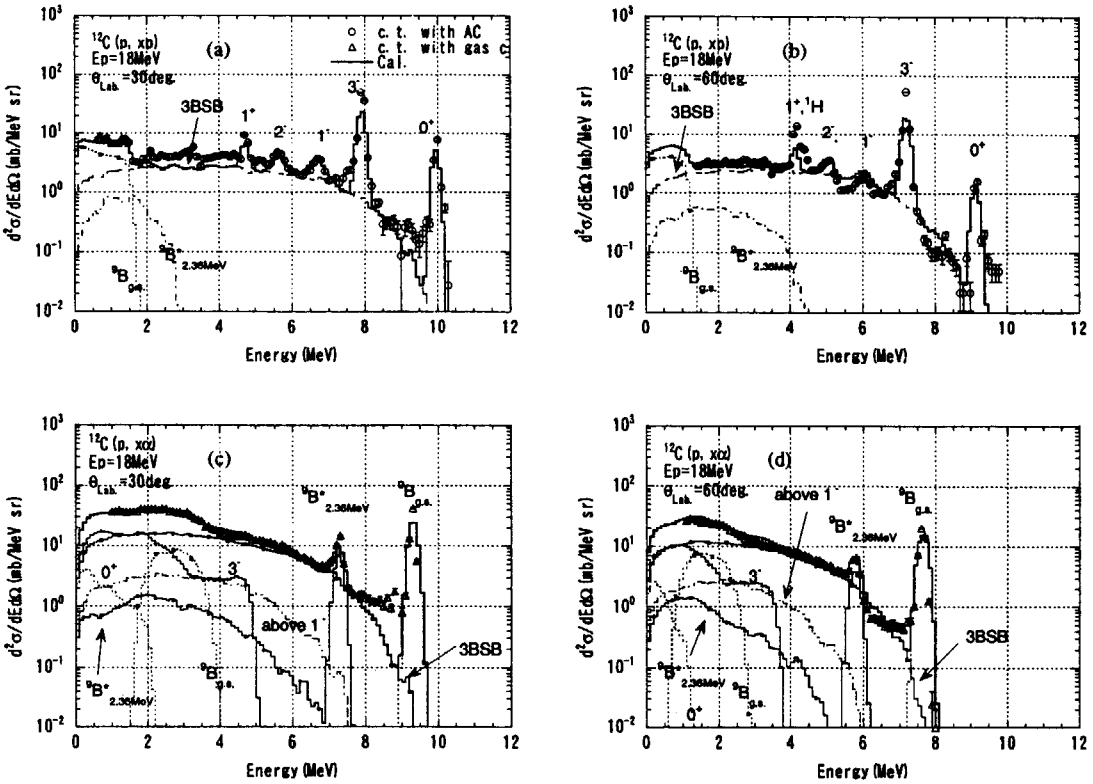

Fig. 4 : Same as in Fig. 3, but for 18 MeV

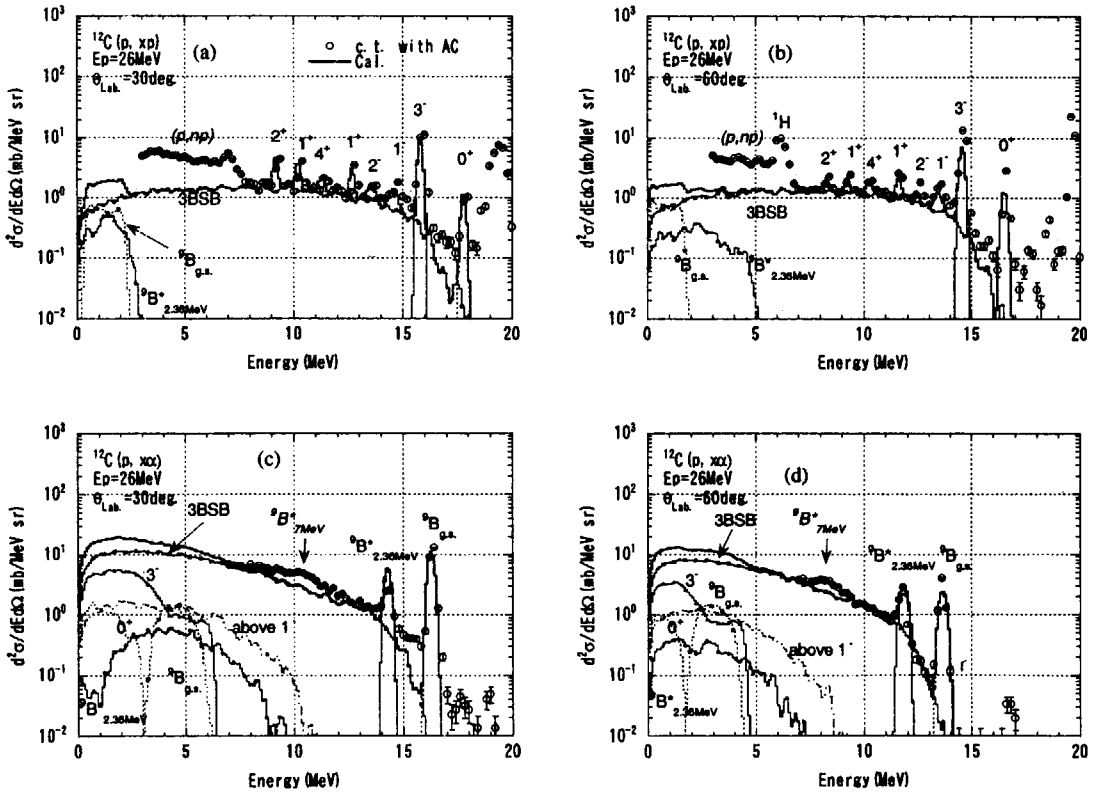

Fig. 5 : Same as in Fig. 3, but for 26 MeV

3.27 IMPROVEMENTS ON SEMI-CLASSICAL DISTORTED-WAVE MODEL

Sun Weili [a),*], Y. Watanabe [a)], R. Kuwata [a)], M. Kohno [b)], K. Ogata [c)], and M. Kawai [c)]
[a)]Dept. of Energy Conversion Engineering, Kyushu University, Kasuga 816, Fukuoka, Japan
[b)] Physics Division, Kyushu Dental College, Kitakyushu 803, Japan
[c)] Dept. of Physics, Kyushu University, Hakozaki, Fukuoka 812, Japan
*email: sun@ence.kyushu-u.ac.jp

Abstract A method of improving the Semi-Classical Distorted Wave (SCDW) model in terms of the Wigner transform of the one-body density matrix is presented. Finite size effect of atomic nuclei can be taken into account by using the single particle wave functions for harmonic oscillator or Wood-Saxon potential, instead of those based on the local Fermi-gas model which were incorporated into previous SCDW model. We carried out a preliminary SCDW calculation of 160 MeV (p,p'x) reaction on ^{90}Zr with the Wigner transform of harmonic oscillator wave functions. It is shown that the present calculation of angular distributions increase remarkably at backward angles than the previous ones and the agreement with the experimental data is improved.

1. Introduction

Dynamical nuclear processes, such as multistep direct (MSD) processes, become dominant in nuclear reactions at intermediate energies more than several tens of MeV. The semi-classical distorted wave (SCDW) model [1,2,3] had been proposed to describe the MSD processes and applied to analyze (p,p'x) reactions on medium-heavy nuclei for incident energies of 65 to 200 MeV. Previous calculations showed that this model succeeded in giving overall good agreement with the experimental angular distributions in the intermediate angular region, but failed to reproduce them at very forward and backward angles. Based on the consideration that the shape of MSD angular distributions is sensitive to the momentum distribution of target nucleons[4], it is supposed that the failure is due to the incorporation of a simple local Fermi-gas (LFG) model into SCDW model to describe the nuclear states, rather than the semi-classical approximations made in the SCDW model.

The LFG model can not properly take into account higher momentum components above the Fermi momentum. In ref. [5], it was indicated that the 1-step cross section drops steeply at the very forward and backward angles if no higher momentum component of nucleons is considered. This situation is similar to the above-mentioned SCDW results. To take into account the higher momentum components, one needs to use more realistic single-particle wave functions, such as that of the shell-

model potential. The Wigner transform of one body density matrix [6] is a proper tool of taking account of such single wave functions, while the characteristic features of the SCDW model keep unchanged, *i.e.*, a closed formed expression in coordinate representation which allows an intuitive interpretation of the MSD reaction. In this present work, we have reformulated the SCDW model in terms of the Wigner transform on the basis of the discussions in ref. [4], and carried out a preliminary calculation of ^{90}Zr(p,p'x) angular distributions at 160 MeV by using the Wigner transform of harmonic oscillator wave functions.

2. Formulation and methods of calculation

2.1 Wigner Transforms

We start from the Wigner transform $f(\mathbf{k},\mathbf{r})$ of one-body mixed density for a j-j coupling single particle model with the wave functions $\phi_{n\ell jm}(\mathbf{x},\sigma)$:

$$f(\mathbf{k},\mathbf{r}) = \sum_{n\ell j} f_{n\ell j}(\mathbf{k},\mathbf{r}), \tag{1}$$

where **k** denotes the momentum of nucleon, **r** the radius, and the sum is over all single particle orbits of target nucleons. The partial Wigner transform is

$$f_{n\ell j}(\mathbf{k},\mathbf{r}) = \sum_m \int d\sigma \int_0^\infty ds \exp(-i\mathbf{k}\mathbf{s}) \sum \phi_{n\ell jm}(\mathbf{r}+\mathbf{s}/2,\sigma)\phi^*_{n\ell jm}(\mathbf{r}-\mathbf{s}/2,\sigma), \tag{2}$$

where

$$\phi_{n\ell jm}(\mathbf{x},\sigma) = x^\ell u_{n\ell j}(x)[Y_\ell(\hat{\mathbf{x}}),\psi_{1/2}(\sigma)]_{jm}, \tag{3}$$

where σ represents the spin of nucleon and $\psi_{1/2}(\sigma)$ the spin function. The radical part $u_{n\ell j}(\mathrm{x})$ is expanded in terms of Gaussian basis:

$$u_{n\ell j}(\mathrm{x}) = \sum_{\upsilon=1}^{N} a_\upsilon^{(n\ell j)} \exp(-\kappa_\upsilon^2 x^2). \tag{4}$$

The expansion coefficients $a_\upsilon^{(n\ell j)}$ is obtained by solving the Schrödinger equation with a finite potential, such as a harmonic oscillator (h.o.) potential or a Woods-Saxon potential through a variation method.

Using the above definitions, the final expression of the partial Wigner transform for a filled j-subshell is given:

$$f_{n\ell j}(\mathbf{k},\mathbf{r}) = (-)^\ell (2j+1) \sum_{\upsilon,\upsilon'=1}^{N} a_\upsilon^{(n\ell j)} a_{\upsilon'}^{(n\ell j)*} \exp(-(\kappa_\upsilon^2+\kappa_{\upsilon'}^2)r^2) \sum_{L=even}^{\infty} i^L P_L(\cos\vartheta)$$
$$\times \sum_{\lambda_1=0}^{\ell} \binom{2\ell+1}{2\lambda_1}^{1/2} r^{\ell-\lambda_1} \sum_{\lambda_2=0}^{\ell} \binom{2\ell+1}{2\lambda_2}^{1/2} r^{\ell-\lambda_2} (\ell\hat{-}\lambda_1)(\ell\hat{-}\lambda_2)$$

$$\times \sum_{M=even}^{\infty}(2M+1)\sum_{\lambda}(-)^{\lambda+\lambda_1}(\lambda 0 M 0|L0)^2 W(\ell-\lambda_1\lambda_1\ell-\lambda_2\lambda_2;\ell\lambda)$$

$$\times(\ell-\lambda_1 0\ell-\lambda_2 0|\lambda 0)(\lambda_1 0\lambda_2 0|\lambda 0)\, I(\upsilon,\upsilon',L,M,\lambda_1,\lambda_2;\kappa_\upsilon,\kappa_{\upsilon'}k,r), \tag{5}$$

where: $I(\upsilon,\upsilon',L,M,\lambda_1,\lambda_2;\kappa_\upsilon,\kappa_{\upsilon'},k,r)$

$$= \int_0^\infty s^2 ds\,[\exp(-(\kappa_\upsilon^2+\kappa_{\upsilon'}^2)\frac{s^2}{4})\, j_L(ks)\,(\frac{s}{2})^{\lambda_1+\lambda_2}\, i_M((\kappa_\upsilon^2-\kappa_{\upsilon'}^2)rs)], \tag{6}$$

where $P_L(\cos\vartheta)$ is Legendre function, ϑ represents the angle between momentum **k** and radius **r**. $j_L(x)$ and $i_M(x)$ are spherical Bessel and modified spherical Bessel functions, respectively, $(\lambda_1 0\lambda_2 0|\lambda 0)$ is Clebsh -Gorden coefficient and W the Racah coefficient.

It should be noted that the above derivation of Wigner transform is general. The sum over orbits in eq. (1) includes two parts, the contributions of all proton orbits and that of all neutron orbits, respectively. In present work, however, the distinction between proton and neutron is not considered, because the Coulomb potential for proton is neglected. In this situation the contribution of proton orbits with the same quantum numbers $n\ell jm$ as neutrons orbits is equal to that of neutron orbits.

2.2 SCDW model with Wigner transform:

The SCDW model and its related formulae had been given in detail elsewhere [1-3]. The Wigner transform can be incorporated into the SCDW model through the kernel $K^{(c)}(\mathbf{r},\mathbf{r}')$ (c denotes proton or neutron shell) as discussed in ref. [4]:

$$K^{(c)}(\mathbf{r},\mathbf{r}') \approx \frac{1}{(2\pi)^6}\int d\mathbf{k}d\mathbf{k}' e^{i\mathbf{q}(\mathbf{r}-\mathbf{r}')} f^{(c)}(\mathbf{k},\mathbf{R})(1-f^{(c)}(\mathbf{k}',\mathbf{R}))\delta(\hbar^2k'^2/2\mu-\hbar^2k^2/2\mu-\omega), \tag{7}$$

$$f^{(c)}(\mathbf{k},\mathbf{R}) = \frac{1}{2}\sum_{n\ell j}{}^{(c)} f_{n\ell j}(\mathbf{k},\mathbf{R}), \tag{8}$$

where $\mathbf{R}=(\mathbf{r}+\mathbf{r}')/2$. The factor $1/2$ in eq.(8) comes from the consideration of spin of nucleon. As a result, the expression of the local average scattering cross section contains only an additional factor $f^{(c)}(\mathbf{k},\mathbf{R})(1-f^{(c)}(\mathbf{k}',\mathbf{R}))$ which stands for the probability of the state with momentum **k** being occupied and the one with **k'** being unoccupied. The other quantities used in the final SCDW expressions keep same. Thus, the present SCDW model with the Wigner transform still gives a simple closed-form expression of cross sections as before.

3. Results and Discussions

As an example, we calculated the Wigner transform and momentum distribution at harmonic oscillator (h. o.) and Woods-Saxon potential for ^{90}Zr. The number of Gaussian basis was taken as 10 which was enough to ensure the stability of Wigner transform against an increase in the number of

basis. The Clebsh-Gorden and Racah coefficients were calculated by standard subroutines. The h. o. parameter is $\hbar\omega_0$ =10 and the depth is -55 MeV. The Woods-Saxon potential is of global type [7].

The calculated Wigner transforms for both potentials are shown in the three-dimensional plot in Figs. 1 and 2. It is found that each Wigner transform varies smoothly with increasing radius r or momentum k when ϑ is fixed. Note that the present numerical results of Wigner transform for h. o. potential is identical to the analytical results given in ref. [8].

In Figs. 3 and 4, the momentum distributions n(k) = $1/(2\pi)^3 \int d\mathbf{r} f(\mathbf{k},\mathbf{r})$ for both potentials are compared with those given by the simple Fermi-gas (FG) model, the LFG model and the QMD calculations[5]. The momentum distributions for both potentials contain a higher momentum tail and converge at k=0. Thus, it was found that the finite size effect of a nucleus improves remarkably the momentum distribution given by the LFG model which is divergent at k=0 and has no higher momentum components above the Fermi momentum. It is interesting to note that, as can be seen in Fig.4, there appears a difference between the momentum distributions for the h.o. potential and the Woods-Saxon potential in the high momentum region above the Fermi momentum: the former drops steeply, but the latter includes a tail extended towards the higher momentum region.

In terms of the Wigner transform, the higher momentum component of target nucleons caused by the finite size effect can be incorporated into the SCDW model. A preliminary calculation of angular distributions of the 160MeV(p,p'x) reaction on ^{90}Zr was carried out using the Wigner transform of h. o. wave functions. The basic input physical quantities, such as the distorting potentials, the N-N scattering cross sections, were kept same as the previous calculations [2].

Figs. 5 and 6 show comparisons of the present results with the previous calculations made with the LFG model. The calculation with the LFG model is in overall agreement with the experimental data in the intermediate angular region from about 30 to 60 degree, but the 1-step cross sections are almost zero at very small angles and drops steeply at backward angles. It can be seen that the use of the h.o. single-particle wave functions leads to remarkable increase not only in the 1-step cross section but also in the 2- and 3-step cross section at backward angles. Although the sum underestimates the experimental data for the lower emission energy, the result is very promising. Thus, it can be concluded that the finite size effect is one of the reasons why the angular distributions underestimate the experimental data at backward angles. We expect that the above calculations will be improved further if the Woods-Saxon potential is used because the higher momentum tail is contained as shown in Fig.4.

4. Summary

We have presented a method of improving the SCDW model in terms of the Wigner transform of the one-body density matrix. The improved SCDW model was applied to the calculation for the 160 MeV (p,p'x) reaction on ^{90}Zr. The preliminary result was very promising and indicated that the finite size effect is important to improve the agreement with the experimental data at backward angles.

However, there still appears somewhat underestimation at backward angles. This would require us to consider either higher order contributions above 3-step process or higher momentum components of target nucleons. SCDW calculations using the Woods-Saxon potential are now in progress in order to investigate the latter effect before time-consuming calculations for higher order contributions above 3-step process are carried out. Also, we intend to investigate how the single-particle wave functions in the surface region of nucleus affect nucleon emission to very small angles in order to give a satisfactory explanation for the rapid fall-off of the 1-step cross section seen around zero degree.

Acknowledgment

This work is partly supported by Grand-in-Aid Scientific Research of the Ministry of Education, Science and Culture (No. 07640416).

References

[1] Y.L.Luo and M.Kawai, Phys.Rev. C 43, 2367 (1991)

[2] Y. Watanabe and M.K.Kawai, Nucl. Phys. A 560, 43(1993)

[3] M.Kawai and H.A.Weidenmuller, Phys.Rev. C 45, 1856 (1992)

[4] M.Kawai, Y.Watanabe,H.Shinohara, M.Higashi, and M.Kohno, *Proceedings of the Fifteenth International Workshop on Nuclear Theory*, Rila mountains, Sofia, Bulgaria, 10-16 June, 1996

[5] S.Chiba, M.B.Chadwick. K. Niita, T.Maruyama and A. Iwamoto, Phys. Rev. C 53, 1824(1996)

[6] See, for example, H.Feshbash, *Theoretical Nuclear Physics, Nuclear Reactions* (John Wiley and Sons, 1992)

[7] A. Bohr and B.R.Mottelson, *Nuclear Structure*, Vol.1, (W.A. Benjamin, Inc. New York, 1969), p.238

[8] J. Martorell and E.Moya De Guerra, Annual of Physics 158, 1 (1984)

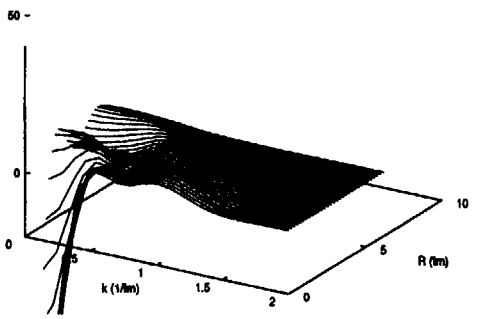

Fig.1 Wigner transform f (k,r) at ϑ =0 for Woods-Saxon potential

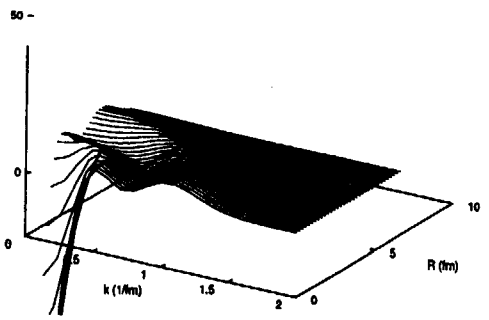

Fig.2 . Wigner transform f (k, r) at $\vartheta = 0$ for h. o. potential

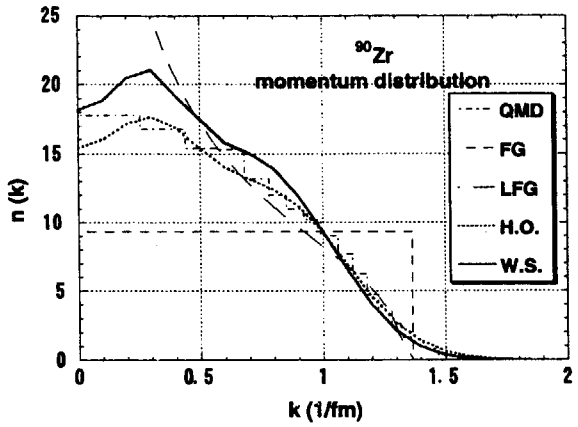

Fig.3 Momentum distribution for ^{90}Zr, (linear)

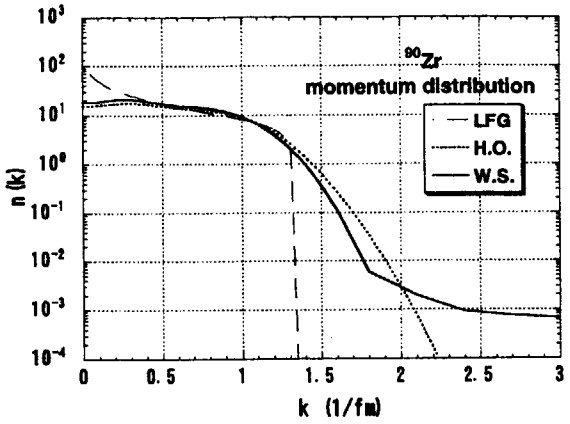

Fig.4 Momentum distribution for ^{90}Zr (logarithmic)

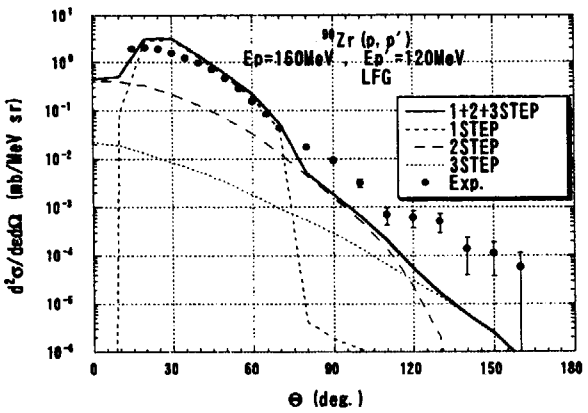

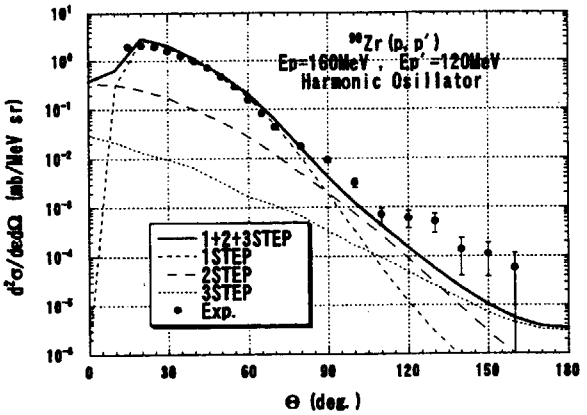

Fig.5 Comparison of calculated angular distributions with experimental data for ^{90}Zr(p,p'x) reaction at an incident energy of 160 MeV and an outgoing energy of 120 MeV. The left and right ones are calculated by SCDW model with LFG model and that with the Wigner transform for the harmonic oscillator potential, respectively.

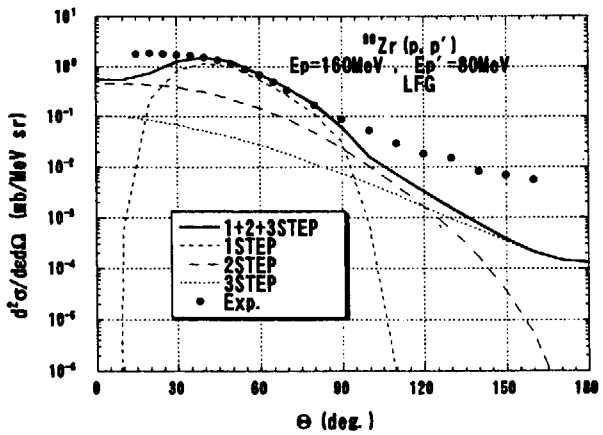

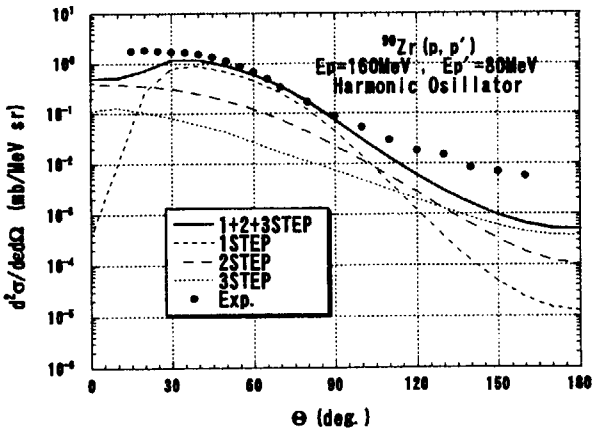

Fig.6 Same as in Fig.5,but for an outgoing energy of 80 MeV

3.28 Neutron and Gamma-ray Emission Double Differential Cross Sections for the Nuclear Reaction by 1.5 GeV π^+ Incidence

Kiminori IGA*1, Kenji ISHIBASHI*1, Nobuhiro SHIGYO*1, Naruhiro MATSUFUJI*1,+1, Tatsushi NAKAMOTO*1,+2, Keisuke MAEHATA*1, Masaharu NUMAJIRI*2, Shin-ichirou MEIGO*3, Hiroshi TAKADA*3, Satoshi CHIBA*3, Takashi NAKAMURA*4, and Yukinobu WATANABE*5

*1 *Department of Nuclear Engineering, Kyushu University, Hakozaki, Higashi-ku, Fukuoka-shi 812-81.*
*2 *High Energy Accelerator Research Organization, Oho, Tsukuba-shi 305.*
*3 *Japan Atomic Energy Research Institute, Tokai-mura, Ibaraki-ken 319-11.*
*4 *Cyclotron-RI Center, Tohoku University, Aramaki, Aoba-ku, Sendai-shi 980-77.*
*5 *Energy Conversion Engineering, Kyushu University, Kasuga-koen, Kasuga-shi 816.*
Present address
+1 *National Institute of Radiological Sciences, Anagawa, Inage-ku, Chiba 263.*
+2 *High Energy Accelerator Research Organization, Oho, Tsukuba-shi 305.*
e-mail: iga@kune2a.nucl.kyushu-u.ac.jp

Neutron and gamma-ray production double differential cross sections were measured for iron by the use of 1.5 GeV π^+ mesons. The measured cross sections were compared with the calculated values by HETC-KFA2. For the neutrons, the calculated results deviate from the experimental data in the neutron energy region below 30 MeV. The calculated values of gamma-ray production agree with the experimental data at gamma-ray energies from 1 to 7 MeV within a factor of three.

I. INTRODUCTION

The proton incident spallation reaction has been investigated for such application as spallation neutron source and accelerator-driven transmutation system. Nuclear data at energies around GeV are necessary for designing such systems. Especially, the neutron production cross sections are important. We measured double differential cross sections on production of spallation neutrons before [1,2]. However, neutron production cross sections by pion incidence are also important, because the secondary pions which are made by the proton-nucleus reaction produce neutrons. Gamma-ray production cross sections are required of researches on shielding of these systems. The neutron and gamma-ray production cross sections by pion incidece, however, have not been taken so far. In this study, we present neutron and gamma-ray production double cross sections by 1.5 GeV π^+ mesons incident on iron. The experimental data are compared with the results calculated by HETC-KFA2 [3].

II. EXPERIMENT AND DATA ANALYSIS

The experiment was carried out at the $\pi 2$ beam line of the 12 GeV proton synchrotron at National Laboratory for High Energy Physics (at present, High Energy Accelerator Research Organization). The experimental method was written in Refs. [1], [2], and [4] and described briefly here. Protons with energies around GeV produces pions having energies of several hundred MeV, but we chose an incident π^+ energy of 1.5 GeV for ease of performing the experiment.

An iron target 4.9 cm in diameter and 3.0 cm thick was located at the beam line height of 1.7 m. The experimental arrangement is illustrated in Fig. 1. Tow different sizes of NE213 detectors were placed at directions of 30, 90 and 150 deg relative to the beam. The larger NE213 detectors 12.7 cm in diameter and 12.7 cm thick were placed at a distance of 1 m from a target, while the smaller NE213 detectors 5.08 cm in diameter and 5.08 cm thick were put at a distance of 0.6 m. The scintillators were used for simultaneous measurement of neutrons and prompt gamma-rays. The time-of-flight (TOF) and photomultiplier-charge data were taken. All data were analyzed with an off-line method.

In the experiment, both target-in and -out measurements were performed. Fig. 2 shows an example of TOF spectra in the target-in and -out measurements. The target-in spectra have a broad peak at a time of 30 ns. Target-out results gives flash gamma-rays, which were produced by upstream plastic scintillators, and slightly prior to those emitted from the target in the target-in measurement. Neutron and gamma-ray spectra were obtained by subtracting the results of the target-out measurement from those of the target-in. Neutron spectra were separated from gamma-ray ones by the pulse-shape discrimination based on a two-gate integration method [5]. The discrimination results are shown in Fig. 3.

The neutron energy was determined by the TOF measurement. The neutron TOF spectrum is plotted in Fig. 4. The flash gamma-ray peak was taken as the time reference for the neutron TOF. The broad peak indicates neutrons from the evaporation process. The neutron detection efficiencies were obtained from calculation results of SCINFUL [6] and SECIL [7] codes. The results of SCINFUL were utilized for neutron detection efficiencies below 80 MeV. The results of CECIL were adjusted to smoothly connect with those of SCINFUL at 80 MeV and were employed above 80 MeV.

The data analysis of gamma-ray was restricted to the prompt gamma-ray production. A TOF time window of 2.8 ns on both sides of prompt gamma-peak was chosen. A charge sensitive Analog-to-Digital Converter spectrum of gamma-rays is shown in Fig. 5. The counts of gamma-ray event decrease rapidly with increasing ADC channel. The gamma-ray energy calibration of the charge spectra was made by the use of checking sources of ^{137}Cs and ^{60}Co, and 4.4 MeV gamma-ray from interaction of Am-Be source neutrons with C. Measured charge spectra were unfolded to obtain gamma-ray emission spectra. Unfolding was carried out by a FERDo-U [8] code. The response function and gamma-ray detection efficiencies of NE213 were calculated by an EGS4 [9] code.

A correction for the effect of multiple-scattering in the target was required for the data analysis because the target thickness of 3.0 cm was not so thin. The effects of multiple-scattering neutrons and gamma-rays were quantitatively checked by the calculation with combination of NMTC/JAERI [10] and MCNP4A [11] codes. The MCNP4A code was adopted to take into consideration the interaction of secondary neutrons and gamma-rays below 20 MeV. The cross section obtained for the ideal thin target was divided by the apparent cross section calculated for the actual thick target. In addition, the effect of gamma-ray attenuation was corrected by using the EGS4 code.

III. RESULTS AND DISCUSSION

The measured and computed results are shown in Figs. 6 and 7. In Fig. 6, the dashed lines show the calculation results of the standard HETC code which employs the free nucleon-nucleon (NN) collision cross sections in the cascade process. The dashed lines generally reproduce the experiment in the neutron energy region from 30 to 200 MeV. In contrast, the calculations overestimate the cross sections below 30 MeV. Solid lines indicate the computation results by the HETC code with modified NN collision cross sections presented by Li and Machleidt [12,13]. They

took account of the in-medium effect for NN elastic scattering in target nuclei. The solid lines are lower than the dashed ones at energies below 30 MeV, and closer to the experimental data. Adoption of the in-medium NN cross sections increases the mean free path of nucleons, so that it enhances the neutron emission from the cascade process in the high energy region roughly above 100 MeV. The enhancement of nucleon emission in the cascade process decreases the excitation energy of remnant nucleuses and suppresses the neutron emission from the evaporation process.

In Fig. 7, the solid lines show the calculation results of HETC-KFA2. These lines agree with the experimental data in the gamma-ray energy region from 1 to 7 MeV within a factor of three. Cross marks present calculated cross sections of the gamma-ray production from the π^0 decay, and dashed lines show the influence of the gamma-rays. The π^0 decay gamma-rays were mistreated in the unfolding, because the response function for gamma-rays above 60 MeV has no clear peak and is almost independent of the incident energy. The influence of π^0 decay gamma-rays was obtained in Monte Carlo simulation. The cross sections in the energy range above 20 MeV were mainly ascribed to the mistreated events, since they were comparable to the evaluated influence of the π^0 decay gamma-rays.

IV. CONCLUSION

The neutron and gamma-ray production double differential cross sections were measured for 1.5 GeV π^+ mesons incident on the iron target. For the neutron production cross sections, the experimental data are not reproduced by the standard HETC code particularly at the neutron energies below 30 MeV. The adoption of in-medium NN cross sections leading to the larger mean free path improves the agreement between the calculations and the experiments. For gamma-ray results, the calculation results agree with the experimental ones in the gamma-ray energy region from 1 to 7 MeV within a factor of three.

ACKNOWLEDGMENTS

The authors express their gratitude to the beam channel staff of KEK for their continuous encouragement and generous support of this experiment. We also acknowledge Prof. H. Hirayama and Dr. Y. Namito for use of the EGS4 code, and Prof. S. Ban for that of the FERDo-U code. We gratefully acknowledge Mr. F. Maekawa of JAERI and Mr. K. Kosako of Sumitomo Atomic Energy Industries, Ltd. for use of the MCNP4A code.

REFERENCES

[1] Nakamoto, T., *et al.*: *J. Nucl. Sci. Technol.*, **32**, 827 (1995).

[2] Ishibashi, K., *et al.*: *J. Nucl. Sci. Technol.*, **34**, 529 (1997).

[3] Cloth, P., *et al.*: HERMES, High Energy Radiation Monte Carlo Elaborate System, *KFA-IRE-E.* AN/12/88 (1988).

[4] Nakamoto, T., *et al.*: *J. Nucl. Sci. Technol.*, **34**, 860 (1997).

[5] Zucker, M. S. and Tsoupas, N.: *Nucl. Instrum. Methods*, **A299**, 281 (1990).

[6] Dickens, J. K.: *ORNL*-6452 (1988).

[7] Cecil, R. A., *et al.*: *Nucl. Instrum. Methods*, **161**, 439 (1979).

[8] Burrus, W. R., :*ORNL-Report*-3743 (1995).

[9] Nelson, W. R., *et al.*: *SLAC-Report*-265 (1995).

[10] Nakahara, Y., *et al.*: *JAERI-M* 82-198 (1982).

[11] Briesmeister, J. F., *et al.*: *LA*-12625 (1993).

[12] Li, G. Q. and Machleidt, R.: *Phys. Rev.*, **C48**, 1702 (1993).

[13] Li, G. Q. and Machleidt, R.: *Phys. Rev.*, **C49**, 566 (1994).

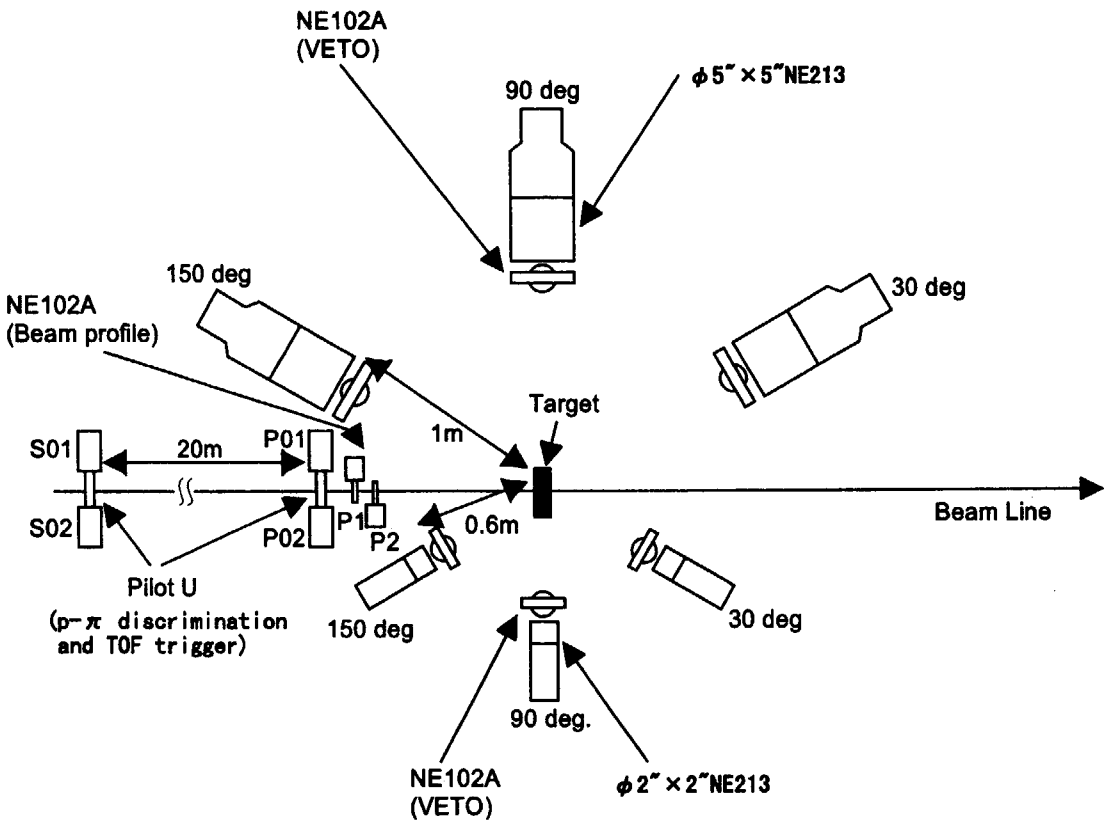

Fig. 1 Illustration of experiment arrangement.

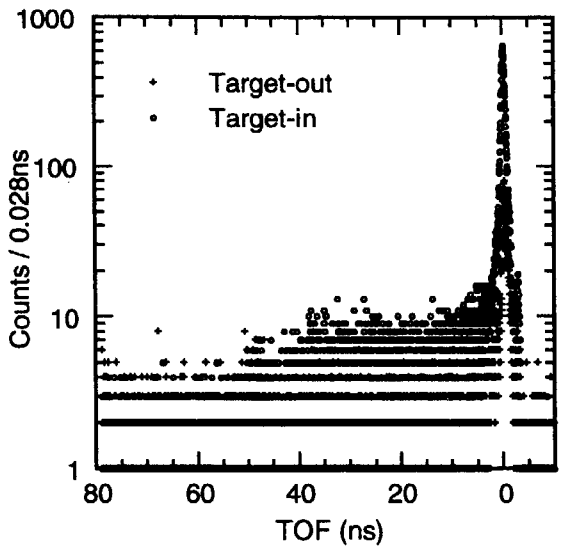

Fig. 2 TOF spectra of the target-in and -out measurements with the 12.7 (dia.) × 12.7 (thick) cm NE213 at 30 deg. The spectra includes both neutron and gamma-rays.

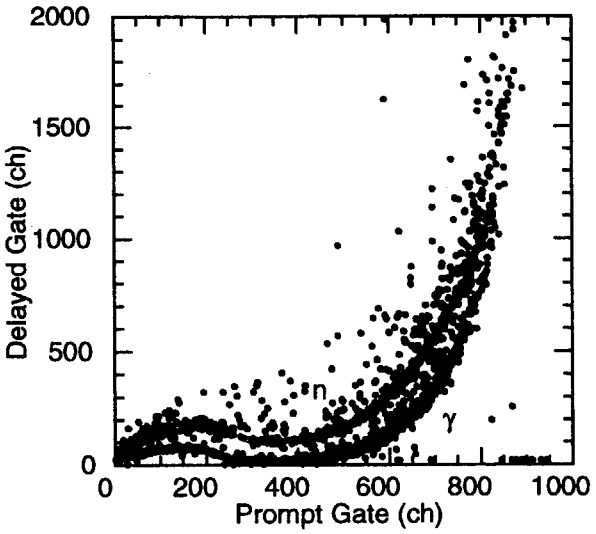

Fig. 3 Neutron and gamma-ray pulse-shape discrimination by two-gate integration method.

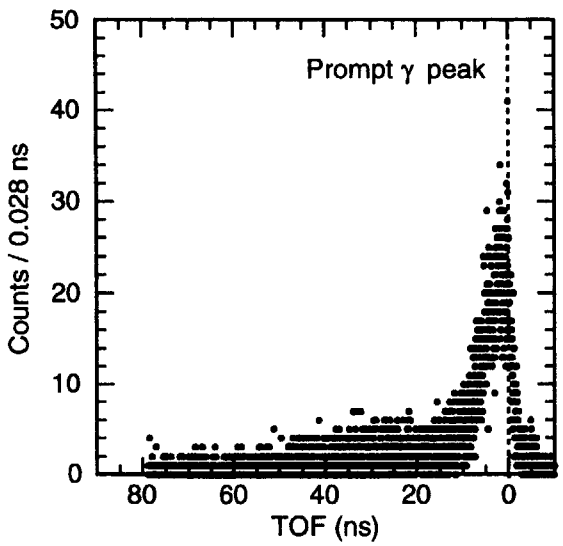

Fig. 4 TOF spectra of neutrons measured with the 12.7 (dia.) × 12.7 (thick) cm NE213 at 30 deg.

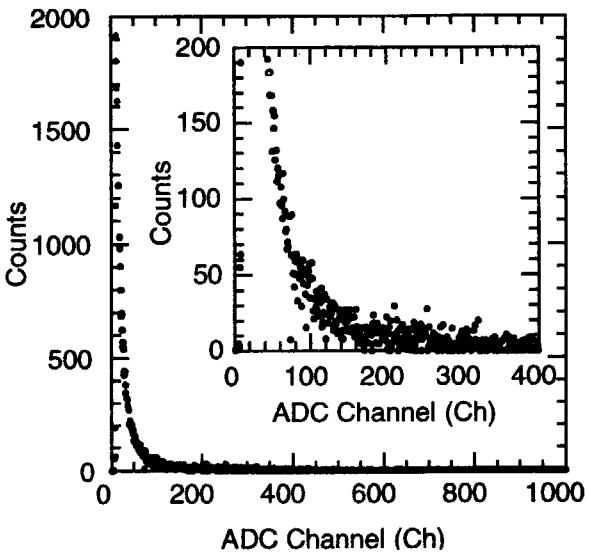

Fig. 5 Charge sensitive ADC spectrum of gamma-ray measured with the 12.7 (dia.) × 12.7 (thick) cm NE213 at 30 deg. The inset is displayed in a magnified scale.

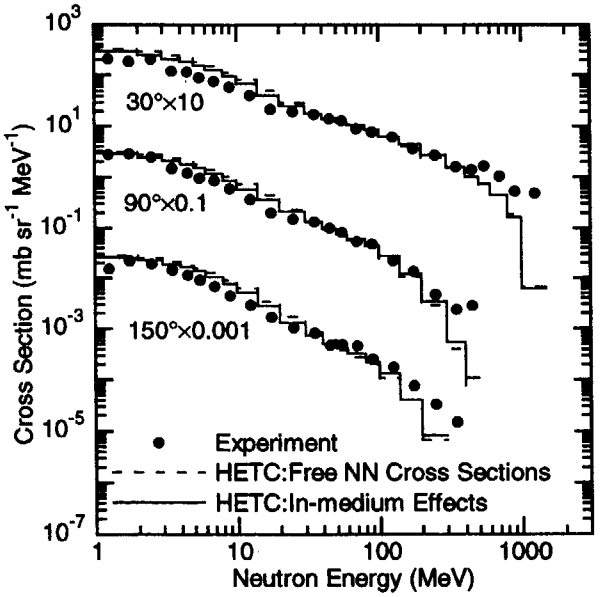

Fig. 6 Neutron production double differential cross sections for 1.5 GeV π^+ on Fe. Dots show the experimental results. Dashed and solid lines show the HETC results with NN cross sections in the free space and in nuclear medium, respectively.

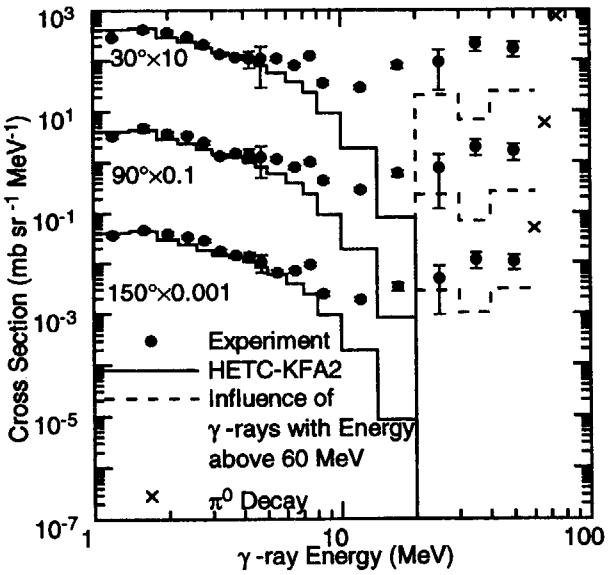

Fig. 7 Unfolded results on gamma-ray production double differential cross sections for 1.5 GeV π^+ on Fe. Dots show the experimental results. Solid lines indicate calculation results by HETC-KFA2. Cross marks present calculated cross sections of the gamma-ray production from the π^0 decay, and dashed lines show the influence of the π^0 gamma-rays.

3.29 Calculations for Nuclear Data Evaluation for Nb, Zr and W in The High Energy Region

Hirohiko Kitsuki, Shin-ichi Maruyama and Kenji Ishibashi
Department of Nuclear Engineering, Kyushu University
Hakozaki, Higashi-ku, Fukuoka 812-81
e-mail:kituki@meteor.nucl.kyushu-u.ac.jp

Neutron total cross sections on Nb, Zr and W were calculated in the high energy region. In this calculation, we used the neutron optical-moodel potentials derived from those for proton incidence with introducing the symmetry term. Proton-induced activation yields for Nb and Zr was calculated by means of HETC/KFA2 and QMD plus SDM at incident energies up to 5 GeV.

1. Introduction

Evaluated nuclear data covering incident energies up to several GeV are required in applications of the spallation reaction to such facilities as an actinide transmutation system and an intense neutron source. The nuclear data libraries, for instance, ENDF/B-VI and JENDL-3.2 cover the energy range up to 20 MeV. Nuclear data evaluation is required in the high energy region. In this study, comparisons between results of experiments and calculations have been made in the high energy region for targets of Nb, Zr and W.

For elastic-scattering and total-reaction cross sections, a number of proton-incident data have been published on in the high energy region. In contrast, there is a limitation on neutron-incident data, because neutron incident experiments on elastic scattering are more difficult than proton ones. We introduced the symmetry terms depending on (N-A)/Z into the proton incident optical-model potentials.

For calculations of proton-incident activation yields, HETC/KFA2[1] and QMD plus SDM code[2] were employed in the energy region up to 5 GeV. We compared the calculation results with various experimental data[3,4].

2. Neutron total cross section

In the high energy region, the optical-model potential is based on the sum of interactions between incident nucleon and individual nucleons in the nucleus. From this point of view, the optical-model potential consists of interaction of proton-proton and proton-neutron. When a proton is incident on the target of Z protons and N neutrons, a local value of potential V has the following dependence :

$$V = U_0 + b\,\frac{(N-Z)}{A},$$

since the symmetry of nuclear force on iso-spin gives the equivalence of nuclear interactions of proton-proton and neutron-neutron.The first term in the right side is the average term, and the second the symmetry term. When a neutron is incident on the same target, the potential becomes

$$V = U_0 - b\,\frac{(N-Z)}{A}.$$

This coincides with the proton potential having the changed sign of the symmetry term. As the first approach, the symmetry terms were simply derived from the proton-incident potentials, on the basis of their dependence on (N-Z)/A of targets. After changing the sign of the symmetry terms, the total cross sections for neutron incidence were calculated. Fig.1 presents the experimental data on neutron total cross sections for Nb, Zr and W by solid marks. The lines below energies of 80 MeV indicate the

calculation values with the potential by Walter and Guss[5]. The results computed with the neutron-converted potentials are plotted by dashed lines in Fig.1 at energies above 80 MeV. The dashed lines reproduce the experimental data[3] for each nucleus only at energies around 200 MeV. The lines underestimate the cross sections in the incident energy region particularly above 300 MeV

To find the influence of the symmetry terms, a quantity of

$$f = (\sigma_1 - \sigma_0) / (\sigma_e - \sigma_0)$$

was evaluated for each nucleus. In this equation, σ_0 is the cross section calculated with proton potentials without the Coulomb ones, σ_1 that with the first-guess neutron potentials after the sign change of the symmetry terms, and σ_e that the experimental cross section. The results for Nb and Zr are plotted in Fig.2 by marks. Then the values of f were fitted over various nuclei by a smooth function as

$$f = \frac{1}{1 + e^{-(T - T_1)/a_1}} \frac{1}{1 + e^{(T - T_2)/a_2}}, \quad T: \text{incident energy (MeV)}$$

$$T_i, a_i = c_1 + c_2 \frac{(N - Z)}{A}, \quad c_i: \text{adjustment parameter } (i = 1,2)$$

The values by fitting are given in Fig.2 by solid lines. The symmetry term was thus adjusted by multiplying the values by f. The solid lines in Fig.1 show the calculated cross sections by the use of the symmetry terms after this adjustment. The solid lines are in good agreement with the experimental data in the whole energy region. Results for ^{63}Cu and ^{208}Pb are also shown in Fig.1. Calculation results for Cu or heavier nuclei are in good agreement with the experimental data.

3. Activation Yield

HETC/KFA2 is based on the intranuclear-cascade(INC) model[6] and evaporation model[7]. In the INC model, the nuclear reaction is treated classically as a sequence of a two-body collision of free nucleons in a Fermi sea in which the Pauli-blocking is taken into account. The evaporation model includes the high energy fission process. In the QMD plus SDM, dynamical process is calculated by the QMD and the contribution from the statistical process is obtained by the SDM. The QMD codes takes a semiclassical simulation method in which each nucleon state is represented by a Gaussian wave function. The SDM code considers n, p, d, t, 3He and α evaporation.

Proton-induced activation yields on Nb and Zr were calculated with both HETC/KFA2 and QMD plus SDM codes for incident proton energies up to 5 GeV. Fig.3(a) and (b) show production cross sections of various nuclei from Nb target, and figs.4(a)-(h) gives these from Zr target. In these figures, marks indicate the experimental data[3,4], solid lines stand for the cross sections calculated by HETC/KFA2, and dashed lines for those by QMD plus SDM. In Fig.4(a), the results calculated with HETC/KFA2 are apart from the experimental data for ^{86}Y at proton energies below 600 MeV. Fig.4(b) shows that both codes reproduce the production yield of ^{83}Sr with a factor of two in the energy region above 100 MeV. In Fig.4(d), HETC/KFA2 reproduces the experimental data over the whole energy range.

4. Conclusion

Neutron-incident optical model potentials were obtained by introduction of the symmetry term into proton-incident ones, and used for the calculation of neutron total cross sections for Zr, Nb and W. The potentials obtained for neutron incidence with some adjustment reproduce the total cross sections for Fe or heavier nuclei in a whole energy region.

The activation yields for Nb and Zr for proton incidence in the energy region up to several GeV were calculated by the use of HETC/KFA2 and QMD plus SDM models. Each code reproduces the experimental yields mostly with the same accuracy.

5. Reference

[1] Cloth, P., et al. : HERMES, High Energy Radiation Monte Calro Elaborate System, KFA-IRE, AN/12/88 (1988).

[2] Niita, K., et al. : Phys. Rev,. C52, 2620 (1995).

[3] Michel, R., et al. : Nucl. Inst. Meth., B113, 434 (1996)

[4] OECD/NEA Experimental Database (EXFOR).

[5] Walter, R.L and Guss, P.P : Proc. Int. Conf., Santa Fe, 1075 (1985).

[6] Bertini, H.W. : Phys. Rev., 188, 1711 (1969).

[7] Dresner, L.W. : ORNL-TM-196, "EVAP-A Fortran Program for Calculating the Evaporation of Various Particles from Excited Compound Nuclei", (1962).

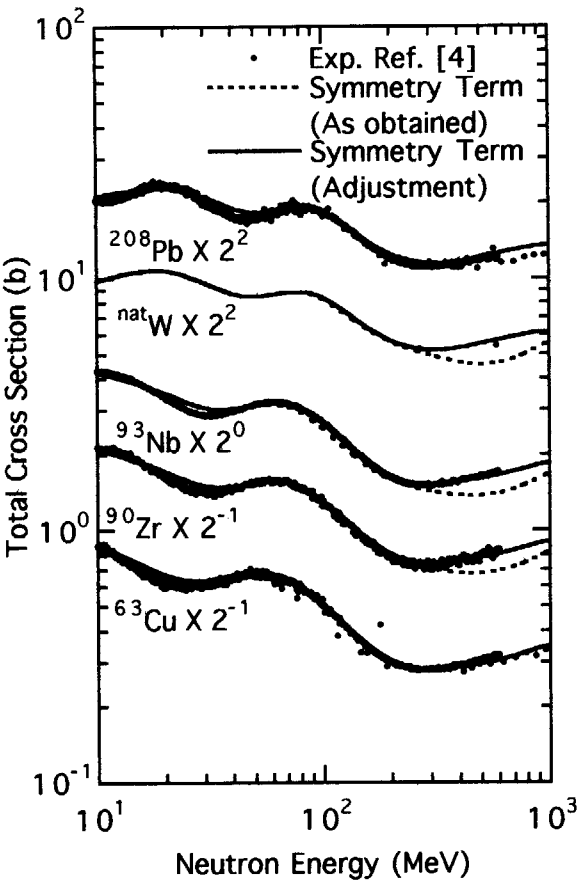

Fig.1 Neutron total cross section

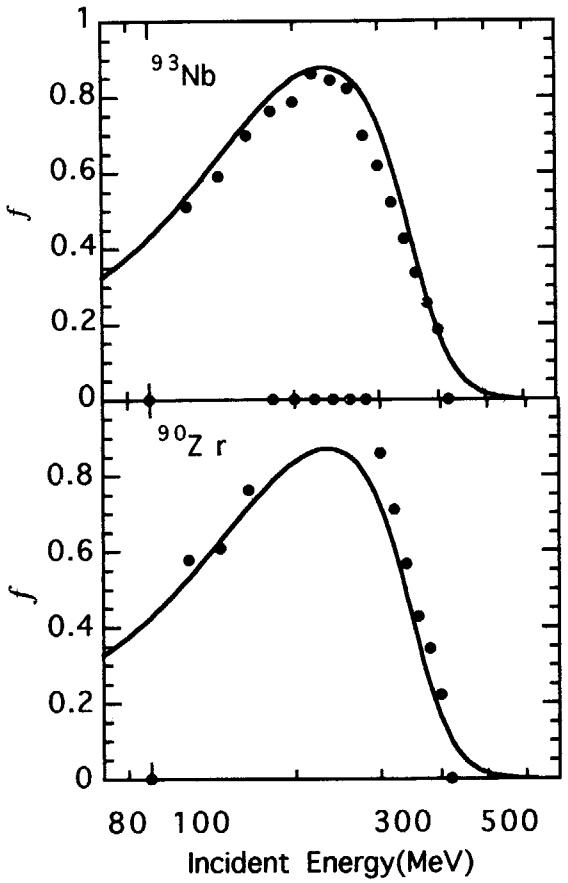

Fig.2 Values of the adjustment factor f.
Marks indicate values for individual nuclei.
Solid lines show results by the smooth function.

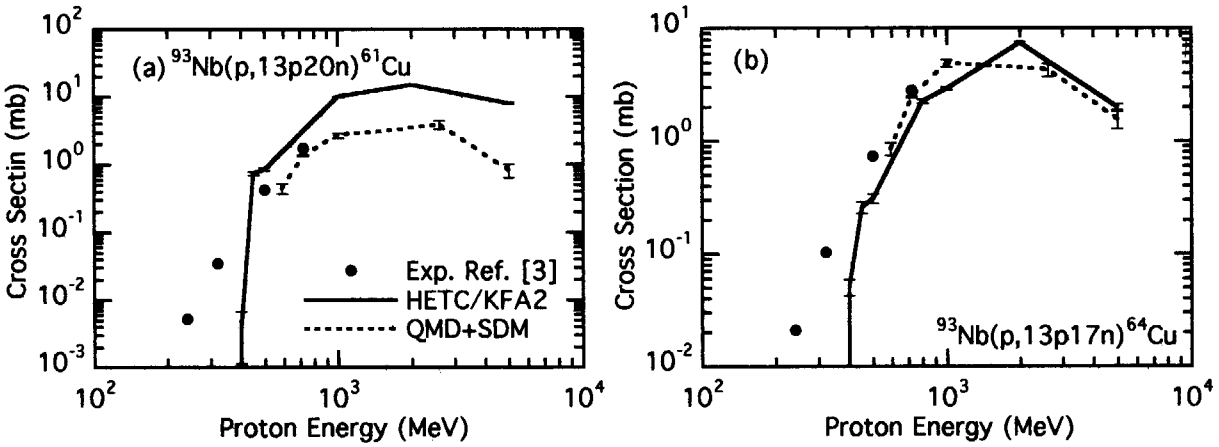

Fig.3 Production cross section from Cu

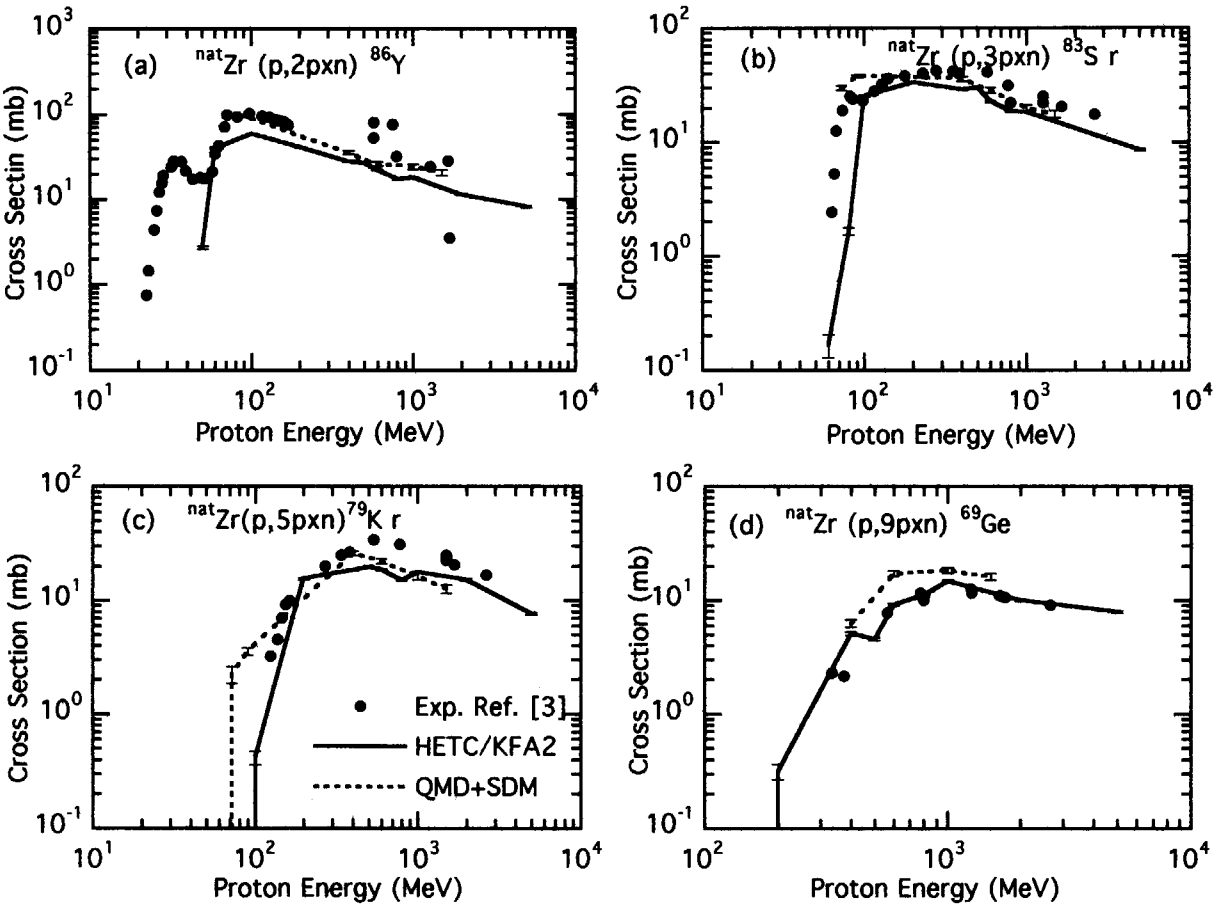

Fig.4(a)-(d) Production cross section from Zr

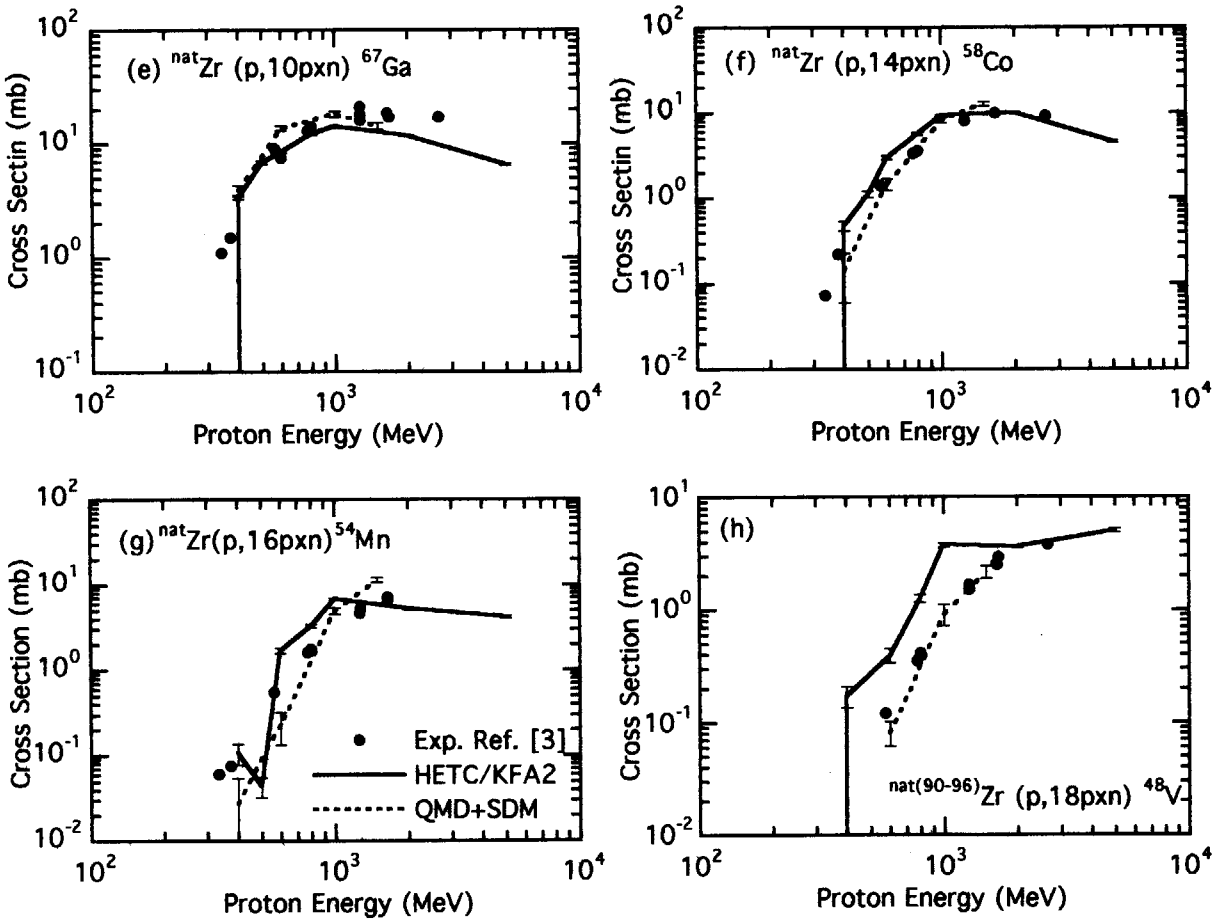

Fig.4(e)-(h) Production cross section from Zr

3.30

Measurement of Continuum Spectrum from $^{12}C(p,p'x)$ at Energy of 392 MeV

Hiroki YOSHIDA, Daisuke KONISHI, Yusuke UOZUMI, Genichiro WAKABAYASHI, Takeji SAKAE, Masaru MATOBA, Akihiro NOHTOMI*, Takashi MAKI** and Norihiko KOORI***

Department of Nuclear Engineering, Kyushu University, Fukuoka 812-81

**Institute of Applied Physics, University of Tsukuba, Tsukuba 305*

***University of Occupational and Environmental Health, Kitakyushu 807*

****College of General Education, University of Tokushima, Tokushima 770*

e-mail : yoshida@nucl.kyushu-u.ac.jp

Continuum spectra from $^{12}C(p,p'x)$ reaction at 392 MeV were measured by using plastic and GSO(Ce) scintillators. The spectra of energy-angle double differential cross sections are compared with that of Quantum Molecular Dynamics (QMD) simulation. Significant differences were found in the results at the forward angles.

1. Introduction

Intermediate energy nuclear data are useful to many applications such as accelerator shield design, radiotherapy and spallation neutron sources. However, there are a few nuclear data of $(p,p'x)$ reactions above 200 MeV. Therefore, it is desired to measure the continuum spectra from $(p,p'x)$ reactions in this energy region.

Stopping detectors, such as scintillator detectors are useful for measurements of proton spectra over a wide energy range. Especially, stacked spectrometers are suitable for these measurements in the intermediate energy region[1]. The cerium doped gadolinium orthosilicate, Gd_2SiO_5(Ce) - GSO(Ce), has several advantages[2] such as a relatively high density and a high radiation hardness, and is suitable for experiments in this energy region. A stacked GSO(Ce) spectrometer was designed[3] to measure continuum spectra from $(p,p'x)$ reactions at incident energies of 200 - 400 MeV.

In the present paper, we show a result of inclusive measurement of $^{12}C(p,p'x)$ reaction at 392 MeV. The spectra of energy-angle double differential cross sections are compared with that of QMD simulation[4].

2. Experiment

The experiment was performed at the Research Center for Nuclear Physics (RCNP), Osaka university. A sketch of the experimental setup is shown in Fig.1. The protons were accelerated up to 392 MeV by the ring-cyclotron and bombarded a polyethylene plate of 1.2 mm thick. The protons scattered off the target nucleus were detected with a stacked spectrometer made up of three 43 mm cubic and a cylindrical GSO(Ce) scintillation crystals. The cylindrical crystal was

of 62 mm in diameter by 120 mm in length. Three plastic scintillators of 5 mm thickness were set in front of the GSO(Ce) scintillators. One of them had an aperture of 15 mm diameter and played as an active slit to determine the solid angle of the spectrometer. The scattering chamber was so small that the spectrometer was placed out of vacuum and about 1 m away from the chamber. A coincidence detector which consisted of a plastic scintillator of 10 mm thickness and a 43 mm cubic GSO(Ce) crystal was placed on the same scattering plane, and on the opposite side of the spectrometer with respect to the beam transport line. This detector was used to identify proton events whether from the $H(p,2p)$ or from the $^{12}C(p,p'x)$ scattering.

In the experiment, $H(p,2p)$ and $^{12}C(p,p'x)$ were measured simultaneously in one run. The $H(p,2p)$ data were used to investigate the light output of GSO(Ce) scintillators[5] and the peak-to-total ratio of the spectrometer[6] and to correct the absolute cross section. The angular distribution of $^{12}C(p,p'x)$ reactions was measured at angles of 30°, 35°, 40°, 45°, 50° and 60°.

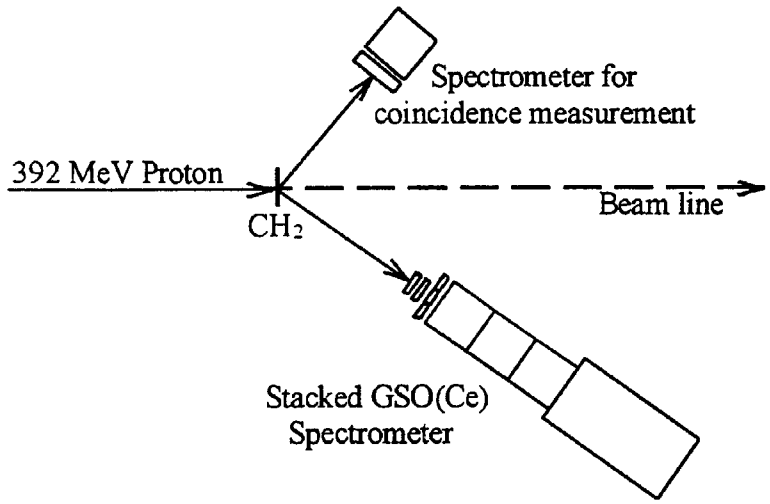

Fig. 1 Sketch of experimental setup.

3. Data Analysis

The energy calibration of each scintillator was made by using monoenergetic protons from $H(p,2p)$. The non-linearity of light output of scintillators was corrected by using an empirical relation[5]. The integral value of beam current was corrected so as to reproduce the pp scattering cross section, because of a systematic error in reading beam current due to the spread of beam after passing through the target foil. The double differential cross sections were determined by means of a tail-subtraction procedure[1] and the correction for the peak-to-total ratio.[6]

4. Result and Discussion

Figure 2 shows the spectral double differential cross sections for $^{12}C(p,p'x)$ reaction for the 392 MeV projectile energy at laboratory angles 30°, 35°, 40° 45°, 50° and 60°. The closed circles are the experimental values for 10 MeV energy bins. The high energy part of the spectra decreases significantly with increasing laboratory angle. This tendency is explained in terms of the kinematics of the quasi-free NN scattering in the nucleus. The QMD calculation which are

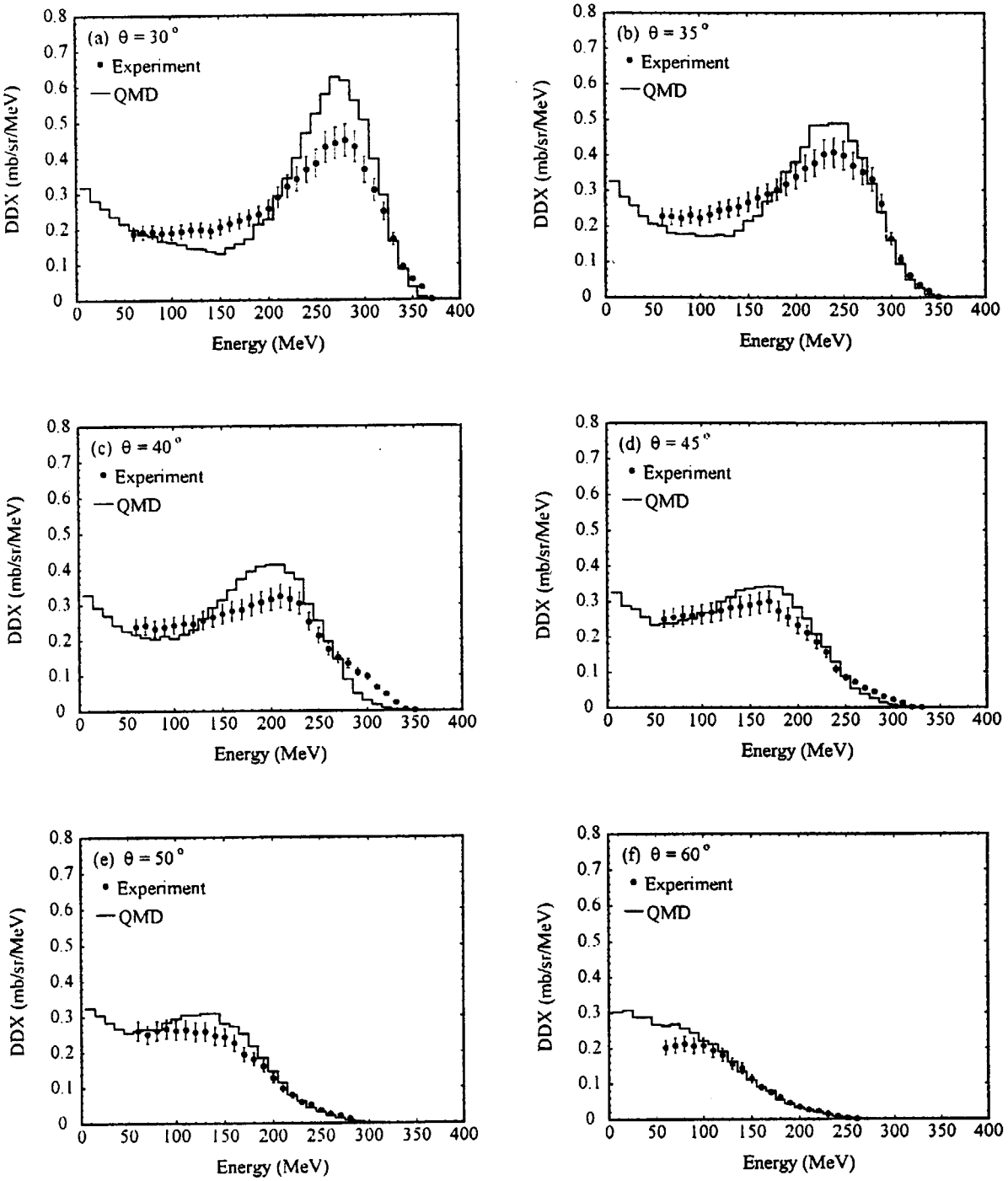

Fig. 2 Double differential cross section of $^{12}C(p, p'x)$ reaction at 392 MeV.

presented by solid lines show higher values than the experiment in this energy part, especially at the forward angles. In rather low energy region where the multiple NN scattering in the nucleus is dominant, the QMD calculation shows lower values than the experiment at the forward angles. At the angle of 45°, 50° and 60°, however, the experimental values are in rather good agreement with the QMD calculation over a wide energy range.

5. Conclusion

The inclusive measurements of the $(p, p'x)$ reaction on ^{12}C have been carried out for a projectile energy of 392 MeV at the RCNP ring cyclotron facility. Proton spectral continua above 60 MeV were obtained for laboratory angles 30°, 35°, 40° 45°, 50° and 60°. The double differential cross section were determined by referring to proton-proton scattering in a polyethylene target. The results were in rather good agreement with the QMD calculation at angle of 45°, 50° and 60°. However, significant differences were found in the results at the forward angles.

Acknowledgment

The authors wish to thank Prof. Hatanaka, Prof. Noro, Dr. Togawa (RCNP) and other cyclotron staff of the RCNP for their support for our experiment. The present work was carried out under the program number E88. The authors are also grateful to Dr. Niita for his agreement with us to use his QMD code.

References

[1] H. Murohka, H. Yoshida, Y. Uozumi, A. Nohtomi, T. Sakae, M. Matoba, O. Iwamoto, T. Maki, N. Koori, *J. Nucl. Sci. and Tech.* **Vol. 34 No. 7** (1997) 708.

[2] M. Kobayashi, K. Takamatsu, S. Ide, K. Mori, S. Sugimoto, H. Takaki and M. Yuasa, *Nucl. Inst. and Meth.* **A306** (1991) 139.

[3] K. Anami, H. Murohka, H. Yoshida, G. Wakabayashi, A. Nohtomi, Y. Uozumi, T. Sakae, M. Matoba, T. Maki and N. Koori, *1996 IEEE NSS Conf. Rec.* (1997) 713.

[4] K. Niita, S. Chiba, T. Maruyama, T. Maruyama, H. Takada, T. Fukahori, Y. Nakahara and A. Iwamoto, *Phys. Rev.* **C Vol. 52, No. 5** (1995) 2620.

[5] K. Anami, H. Yoshida, D. Konishi, H. Murohka, Y. Uozumi, G. Wakabayashi, A. Nohtomi, T. Sakae, M. Matoba, T. Maki and N. Koori, in printing for *Nucl. Inst. and Meth.*

[6] H. Yoshida, D. Konishi, K. Anami, H. Murohka, Y. Uozumi, S. Aoki, T. Yamamoto, G. Wakabayashi, A. Nohtomi, T. Sakae, M. Matoba, T. Maki and N. Koori, in printing for *Nucl. Inst. and Meth.*

3.31 Proton Induced Nuclide Production Cross Section by HETC-3STEP/FRG-R

Nobuhiro SHIGYO, Kenji ISHIBASHI, Nobuaki YOSHIZAWA* and Hiroshi TAKADA**
Department of Nuclear Engineering, Kyushu University
Hakozaki, Higashi-ku, Fukuoka-shi 812-81, Japan
** Mitsubishi Research Institute, Inc.*
2-3-6 Otemachi, Chiyoda-ku, Tokyo 100, Japan
*** Japan Atomic Energy Research Institute*
Tokai-mura, Ibaraki-ken 319-11, Japan
mailto:shigyo@kune2a.nucl.kyushu-u.ac.jp

High Energy Transport Code (HETC) based on the intranuclear-cascade-evaporation model is modified to calculate the fragmentation cross section. The exciton model is adopted for improvement of backward nucleon-emission cross section for low-energy nucleon-incident events. The level density parameter depending on the excitation energy is taken in the evaporation process. The fragmentation reaction is incorporated into HETC as a subroutine set by the use of the systematics of the reaction. The modified HETC (HETC-3STEP/FRG-R) reproduces experimental fragment yields to a reasonable degree.

1. Introduction

Reliable high-energy nuclear data are necessary for application of the spallation reaction to facilities such as the high intensity neutron source [2] and the accelerator based transmutation [1]. Cross sections of the fragmentation reaction which is induced by incident nucleons of energies above several hundred MeV are required for engineering design. Since it is difficult to obtain the whole fragmentation data by experiments, calculation models need to be developed.

High Energy Transport Code (HETC) [3] is currently often used for engineering purposes at intermediate energies. The code mainly considers the intranuclear-cascade and evaporation processes in the nuclear-reaction part. The production yields of the fragments such as ^{7}Be and ^{24}Na are not represented by HETC, since the fragmentation process is not taken into consideration. We, therefore, have modified this code as HETC-FRG to calculate the intermediate-energy proton-incidence fragmentation cross sections. The nuclear in-medium correction is taken into account in the intranuclear-cascade process.

For further improvement of the code, the exciton model is adopted for better reproduction of the nucleon emission cross sections for nucleon-incidence at low energies. This code is named as HETC-3STEP/FRG. To improve production cross sections of the nuclei near the target nucleus, the level density parameter depending on the excitation energy is used in in the evaporation process. This code is designated HETC-3STEP/FRG-R.

2. Fragmentation Process

Before incorporation of the proton-incident fragmentation process into HETC, systematics on the mass yields and the kinetic energy spectra of the process have been constructed [6]. The former was obtained on the basis of a liquid-gas phase transition model [7], and was parameterized by the incident proton energy, the target and the fragment mass numbers and the fragmentation nuclear temperature. For the latter, a formula was devised to have a simple expression considering the Coulomb barrier. The kinetic energy spectra were represented by the parameters of the fragmentation nuclear temperature, the fragment and the target mass numbers and the incident proton energy. The nuclear temperature of the fragmentation was determined in average by the incident proton energy.

For the calculation in HETC, it is assumed that the fragmentation process occurs between the cascade and evaporation processes. The systematics are incorporated with some modification as a subroutine set into HETC [8]. The probability of the fragmentation occurrence is evaluated by the excitation energy after the cascade process, instead of the use of incident proton energy. The nuclear temperature is at first obtained by the fermi gas model after the cascade process without considering a degree of freedom

of the fragmentation: The temperature is given by the excitation energy and the mass number of the nucleus after the cascade process. Then, this temperature is converted into that of the fragmentation. The method takes into account information on the nucleus after the cascade process such as excitation energy and mass number.

The free-space nucleon-nucleon (*NN*) cross sections are used in the intranuclear-cascade process of HETC. Since the *NN* collisions occur in the nuclear medium, however, it is important to consider the in-medium correction of *NN* cross sections [4]. The *NN* cross sections in the intranuclear-cascade process of HETC are modified for this reason. The cross sections in the medium are obtained by simple and practical parameterization [5]. This parameterization is applicable to energies up to 300 MeV. Above 300 MeV, the *NN* cross sections in the medium are postulated to increase linearly, and to equal the free-space *NN* cross sections at the energy of 500 MeV.

3. Exciton Model

The original HETC based on the cascade and evaporation processes is known to underestimate the nucleon emission cross section in the backward direction when incident nucleon energy is around or below 100 MeV. To solve this problem, the exciton model [9] has been adopted as the preequilibrium process between the intranuclear-cascade and the evaporation ones. The model considers the mass and atomic numbers, the excitation energy and the number of the excitons after the intranuclear-cascade process.

The exciton model is effective only in the case that the number of excitons is small, i.e., relatively low excitation energy after the intranuclear-cascade process. On the contrary, the fragmentation tends to occur in a high excitation state, where the number of excitons is larger. At a number of excitons of 15, the calculation is determined to be switched from the process of fragmentation to exciton model. If the number of exciton is below 15, the exciton model calculation follows to the cascade process, whereas the fragmentation process is run if it exceeds 15.

4. Level Density Parameter

The level density parameter independent of the excitation energy is used in the evaporation process of the original HETC. The level density parameter depending on the excitation energy [10] is used in HETC-3STEP/FRG to consider the variation of with the excitation energy.

5. Calculation Results

Figures 1 to 8 show the production cross sections for ^{27}Al, ^{nat}Fe, ^{nat}Zr and ^{197}Au targets. In these figures • marks indicate the experimental data [11]. Long-dashed, short-dashed and solid lines stand for the results of HETC-FRG, HETC-3STEP/FRG and HETC-3STEP/FRG-R, respectively. Since the level density parameter dependent on the excitation energy is adopted, HETC-3STEP/FRG-R reproduces the ^{7}Be production cross section around 80 MeV region better than HETC-FRG and HETC-3STEP/FRG as shown in Fig. 1. For the reaction of ^{27}Al(p, 3pn)^{24}Na in Fig. 2, the cross sections by HETC-3STEP/FRG-R are similar to those by HETC-3STEP/FRG at energies above 40 MeV.

In Fig. 3, each code underestimates the cross sections by a factor of three at proton energies above 400 MeV. The fragmentation process is dominant in the reaction. For the reaction of ^{nat}Fe(p, 4pxn)^{48}V in Fig. 4, the cross sections by the three codes are close to the experimental data for the proton incidence above 400 MeV. HETC-3STEP/FRG-R overestimates the cross sections around 20 MeV. The discrepancy indicates the necessity of checking Q-value in the preequilibrium and evaporation processes.

In Fig. 5, the cross sections by the three codes agree with the experimental data because the fragmentation process is dominant in the reaction. For the reaction of ^{nat}Zr(p, 4pxn)^{84}Rb in Fig. 6, the cross sections by HETC-3STEP/FRG-R are located between values by HETC-3STEP/FRG and HETC-FRG. This is because the level density parameter depending on the excitation energy is used in the evaporation process of HETC-3STEP/FRG-R. HETC-3STEP/FRG-R overestimates the cross sections around 20 MeV as the reaction of ^{nat}Fe(p, 4pxn)^{48}V. The discrepancy also indicates the necessity of checking Q-value in the preequilibrium and evaporation processes.

As shown in Fig. 7, each code represents the production cross section of ^{7}Be within a factor of two. The fragmentation process is dominant as in the reactions of ^{nat}Fe(p, 23pxn)^{7}Be and ^{nat}Zr(p, 37pxn)^{7}Be. For the reaction of ^{197}Au(p, p3n)^{194}Au in Fig. 8, the results by all codes agree with the experimental data.

6. Summary

HETC was modified to calculate the cross section of the proton-incidence fragmentation reaction. The nucleon-nucleon cross sections in the intranuclear-cascade process were changed from free-space to in-medium values. The fragmentation reaction was incorporated into the code as a subroutine set on the basis of the systematics of the proton-induced reaction. The exciton model was taken to improve the nucleon emission cross section in the backward direction. The level density parameter depending on the excitation energy in the evaporation process was adopted. The resultant HETC-3STEP/FRG-R are appropriate to obtain the fragmentation cross sections in the wide target mass range at incident proton energies above several hundred MeV. Although the original HETC is incapable of reproducing the experimental production yields of the light mass fragments like ^{7}Be, HETC-FRG, HETC-3STEP/FRG, HETC-3STEP/FRG-R represent them to a considerable degree. HETC-3STEP/FRG-R reproduces the ^{7}Be production cross section around 80 MeV region better than HETC-FRG and HETC-3STEP/FRG.

References

[1] Carpenter, J.M., *et al.*: *Proceedings of the twelfth Meeting of International Collaboration on Advanced Neutron Sources 24 - 28 May 1993*, Rutherford Appleton Laboratory Report, 94-025, T-95 (1994).

[2] Bowman, C.D., *et al.*: *Nucl. Instr. and Meth.*, **A320**, 336 (1992).

[3] Chandler, K.C., and Armstrong, T.W.: *ORNL* 4744 (1972).

[4] Suetomi, E. *et al.*: *Phys. Lett.*, **B333**, 22 (1994).

[5] Li, G.Q., and Machleidt, R.: *Phys. Rev.*, **C48**, 1702 (1993); Li, G.Q., and Machleidt, R.: *ibid*, **C49**, 566 (1994).

[6] Shigyo, N., *et al.*: *J. Nucl. Sci. Technol.*, **32**, 1 (1995).

[7] Panagiotou, A.D., *et al.*: *Phys. Rev.*, **C31**, 55 (1985).

[8] Shigyo, N., *et al.*: *JAERI-Conf.*, **95-008**, 217 (1995); Shigyo, N., *et al.*: *ibid*, **96-008**, 272 (1995).

[9] Gudima, K.K., *et al.*: *Nucl. Phys.*, **A401**, 329 (1983).

[10] Ignatyuk, A.V.,*et al.*: *Sov. J. Nucl. Phys.*, **29**, 375 (1979).

[11] Iljinov, A.S., *et al.*: "*Production of Radionucleids at Intermediate Energies* ", Springer Verlag, Landolt-Bornstein, New Series, subvolumes I/13a (1991), I/13b (1992), I/13c (1993), I/14d (1994).

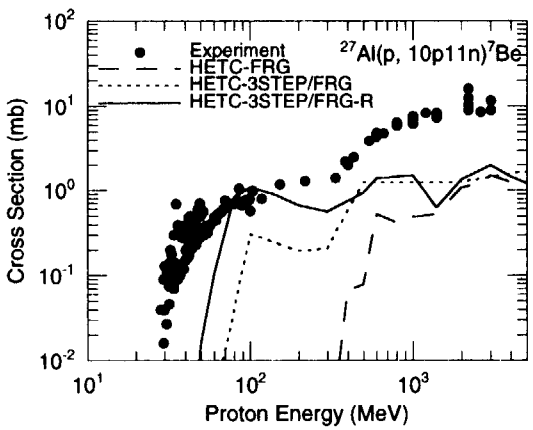

Fig. 1: Production cross section of ^{7}Be from an Al target.

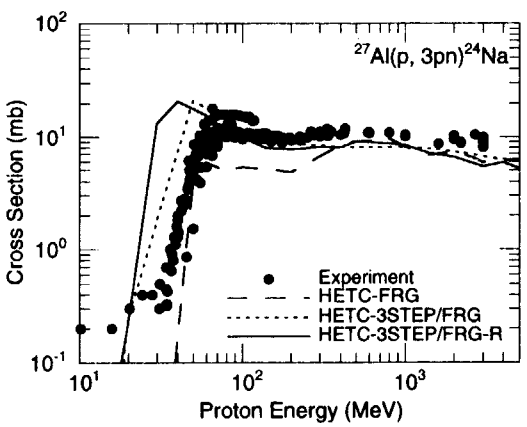

Fig. 2: Production cross section of ^{24}Na from an Al target.

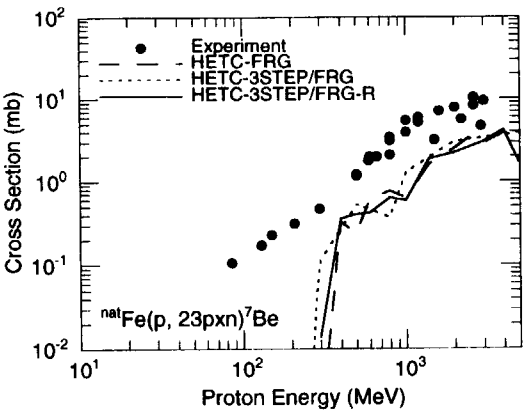

Fig. 3: Production cross section of ^{7}Be from an Fe target.

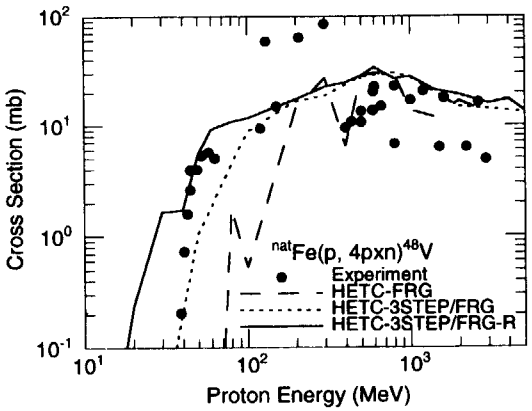

Fig. 4: Production cross section of ^{48}V from an Fe target.

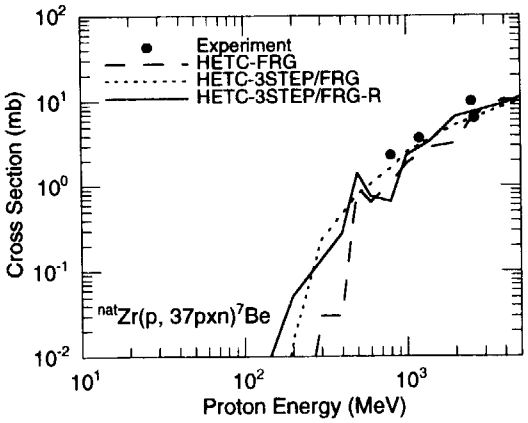

Fig. 5: Production cross section of ^{7}Be from a Zr target.

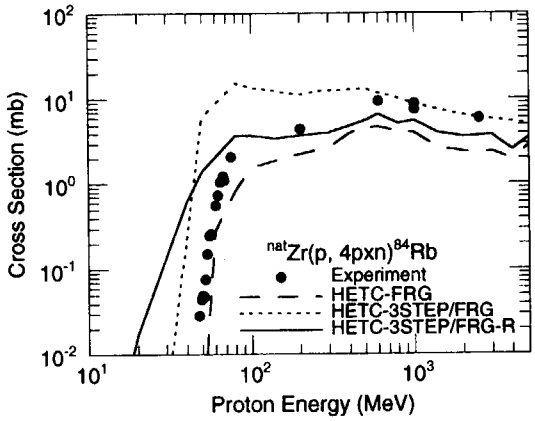

Fig. 6: Production cross section of ^{84}Rb from a Zr target.

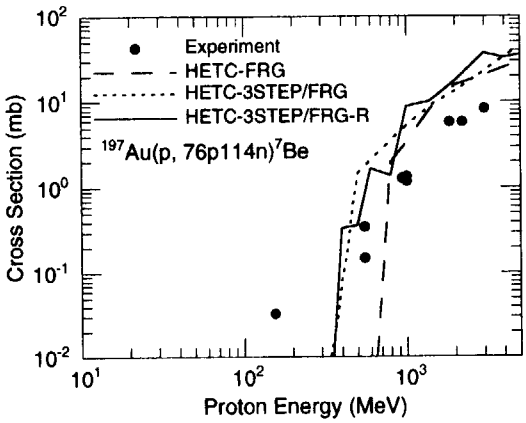

Fig. 7: Production cross section of ^{7}Be from a Au target.

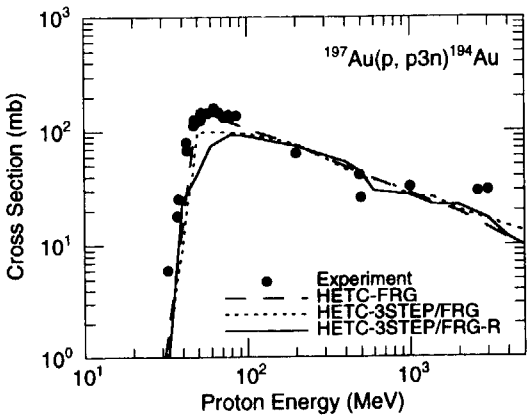

Fig. 8: Production cross section of ^{194}Au from a Au target.

3.32 Development of Twin Ge Detector for High Energy Photon Measurement and Its Performance

Yoshiaki Shigetome and Hideo Harada
Power Reactor and Nuclear Fuel Development Corporation, Tokai Works
Tokai-mura, Naka-gun, Ibaraki-ken, 319-11
e-mail : tomesan@tokai.pnc.go.jp

Prototype twin HPGe detector composed of two large HPGe crystals was developed to obtain better detection efficiency (ε) and *P/T* ratio, which was required for high energy photon spectroscopy. In this work, the performances of the twin HPGe detector were evaluated by computer simulation employing EGS4 code.

1. Introduction

High-purity germanium (HPGe) detectors are useful in variety of photon spectroscopy for their high energy resolution. Despite this advantage, their utilization was limited to relatively low energy region because of their small full energy detection efficiency for high energy photons. To overcome this disadvantage, large volume Ge crystals are necessary.

Recently, large volume Ge detectors which have comparable efficiencies of the commonly used 3 in. by 3 in. NaI(Tl) scintillation detectors became available [1]. Fothermore, the technology of housing several Ge crystals in a detector enabled to obtain better full energy peak efficiency and peak to total ratio (*P/T*)[2][3]. By summing signal outputs of the crystals, HPGe detector composed of plural crystals is equivalent to a detector which has a larger volume crystal. Therefore, a HPGe detector composed of plural large volume crystals is expected to achieve much better full energy peak efficiency than usual HPGe detectors, especially for high energy photons, and to open the door of the high-resolution high-energy photon spectroscopy.

We developed the prototype twin HPGe detector composed of two large HPGe crystals of n-type enclosed in an aluminum housing to obtain larger detection efficiency and *P/T* ratio for high energy photons[4]. Both of crystals are closed ended coaxial and have 95% relative efficiency. They are arranged like twins along the housing axis. In this work, we predict the performances of the twin HPGe detector such as full energy peak efficiency and *P/T* ratio for high energy photons by computer simulation.

2. Description of the detectors

The twin HPGe detector consists of two large volume HPGe crystals. Both of them are closed ended coaxial and have 95% relative efficiency. Their sizes are 80 mm in diameter and 70 mm in length.

They are arranged like twins along the axis and packed in an aluminum housing. The housing is 105 mm in diameter and 200 mm in length. The detector was produced by Eurysis Mesures. Figure 1 gives an overview of the detector. We name the crystal located in the entrance side of photons "Front Ge", the other "Back Ge".

3. Performances of the twin HPGe detector

We show the main characteristics of the twin HPGe detector. In particular, full-energy peak detection efficiency (ε) and peak-to-total ratio (P/T) are examined. In addition, we compare these data of the twin HPGe detector (twin HPGe) with a single 95% HPGe detector (single HPGe) to evaluate the effectiveness of the twin HPGe detector. The detection efficiencies and P/Ts of twin HPGe and single HPGe are expressed as ε_{twin} , ε_{single} , P/T_{twin} and P/T_{single}. In order to evaluate the effectiveness of the twin HPGe, the effective factors R_ε and $R_{P/T}$ are defined as follows

$$R_\varepsilon = \frac{\varepsilon_{Twin}}{\varepsilon_{Single}} \ldots (1)$$

$$R_{P/T} = \frac{(P/T)_{Twin}}{(P/T)_{Single}} \cdots (2).$$

First, we show the experimental values for low energy photons as well as the calculated ones in order to check the reliability of the calculation. After that, the performances in the high energy region are examined.

3.1 Performances in low energy region

Throughout this work, performances of the twin HPGe detector are evaluated by computer simulation employing EGS4 code[5]. In this subsection, the results are compared with the experimental values in order to show the accuracy of the calculation. The energy dependence of the full energy detection efficiency has been measured with the standard sources, such as ^{60}Co and ^{152}Eu, placed at 25 cm from the front surface of Front Ge crystal. Figure 2 shows the calculated and measured efficiencies that compares the twin Ge with the single Ge. From this figure, the effectiveness of twin crystals is larger for higher energy photons. As most of low energy photons are absorbed in Front Ge, the contribution of Back Ge is little. Therefore difference of the efficiency between the twin HPGe and the single HPGe is small in low energy region. The R_εs for E_γ below 0.5MeV is almost equal to one. On the contrary, the effective factors become larger in high energy region since amounts of the energy being absorbed in Front Ge become smaller. The R_ε at 1.33MeV reaches 1.26.

Another main performance of Ge detectors is their peak-to-total (P/T) ratio. Table 1 shows the calculated and experimental P/T ratios about ^{60}Co. As can be deduced from Table 1, the $R_{P/T}$s are about 1.15. According to the results of ε and P/T, the calculated values agree within the error of 10% for ε and 5% for P/T.

3.2 Performances in high energy region

To predict the performances of twin HPGe detector for high energy photons (E_γ is from 5MeV to 30MeV), computer simulation employing EGS4 was performed. In this energy region, we often measure pencil photons generated by accelerators. Therefore, three types of photons are considered, which are as followings.

(1) Isotropic photon sources placed at 25cm from the front surface.

(2) Pencil photons which go along the axis of the detector cylinder and hit the center of the front surface.

(3) Pencil photons which go along the axis of the detector cylinder and hit the front surface at 1cm from the center.

Figurers 3 and 4 show the results. In each case, higher $R\varepsilon$s and $R_{P/T}$s are given for higher energy photons in the same way as in low energy region. In order to explain this result, we define partial full energy detection efficiencies ε_F, ε_B, ε_{FB} and the ratio of ε_{FB} to ε_{twin}, C_{FB}, as followings

ε_F : Efficiency of full energy deposition in Front Ge

ε_B : Efficiency of full energy deposition in Back Ge

$$\varepsilon_{FB} = \varepsilon_{twin} - (\varepsilon_F + \varepsilon_B) \cdots (3)$$

$$C_{FB} = \frac{\varepsilon_{FB}}{\varepsilon_{twin}} \cdots (4)$$

, where ε_{FB} means the efficiency that the full energy is divided into Front Ge and Back Ge.

Figure 5 shows C_{FB}s. According to this result, the C_{FB}s are larger for higher energy photons and C_{FB}s for pencil photons are much larger than for isotropic and off centered pencil photons. In the case of higher energy photons, as the ratios that incident photons absorbed in Front Ge is smaller and the ratios that the photons scattered to the Back Ge are larger, the contribution of Back Ge becomes more important. This means the volume of single crystal is not large enough for high energy photon counting. Therefore, the twin HPGe is more effective for high energy photons.

Comparing the types of incident photons, much higher $R\varepsilon$s, $R_{P/T}$s and C_{FB}s are given for pencil photons than for the others. The reason is as following. Incident pencil photons go through the cylindrical cavity in the front crystal along the axis of it and hit the thin part of Front Ge. Therefore the effective volume of Front Ge is small and it becomes difficult to absorb all photon energy with only Front Ge. In order to perform photon spectroscopy with pencil photons efficiently, it is necessary to arrange the detector so that the photons hit the thick part of Front Ge.

4. Conclusion

Performances of twin HPGe detector are evaluated with Monte Calro simulation code EGS4. The accuracy of the simulation is checked by the experiment with standard photon sources. This detector is developed to achieve large full energy detection efficiency and peak-to-total ratio. These performances

given by the twin HPGe detector are almost same as by usual 95% single HPGe detector at energies below 0.5MeV. However, the advantage of using the twin HPGe detector is remarkable at energies as high as 10MeV and the twin HPGe exhibits around twice larger full energy detection efficiency and *P/T* ratios than the single HPGe.

[1] G. Bellia, et. al. ; Nucl. Instr. and Meth. A 284, 399(1989).
[2] C. Michel, et. al. ; Nucl. Instr. and Meth. A 251, 119(1986).
[3] E. Mauerhofer, et. al. ; Nucl. Instr. and Meth. A 371, 465(1996).
[4] H. Harada and Y. Shigetome, J. Nucl. Sci. Tech., 32, 1189(1995).
[5] W. R. Nelson, et. al. , SLAC-Report-265(1985).

Table 1 *P/T* ratios about ^{60}Co source

		P/T		
		experiment	calculation	C/E
Single	1.17MeV	1.52	1.44	0.95
	1.33MeV	1.37	1.32	0.96
	1.17MeV+1.33MeV	2.89	2.76	0.96
Twin	1.17MeV	1.69	1.64	0.97
	1.33MeV	1.57	1.55	0.99
	1.17MeV+1.33MeV	3.27	3.19	0.98

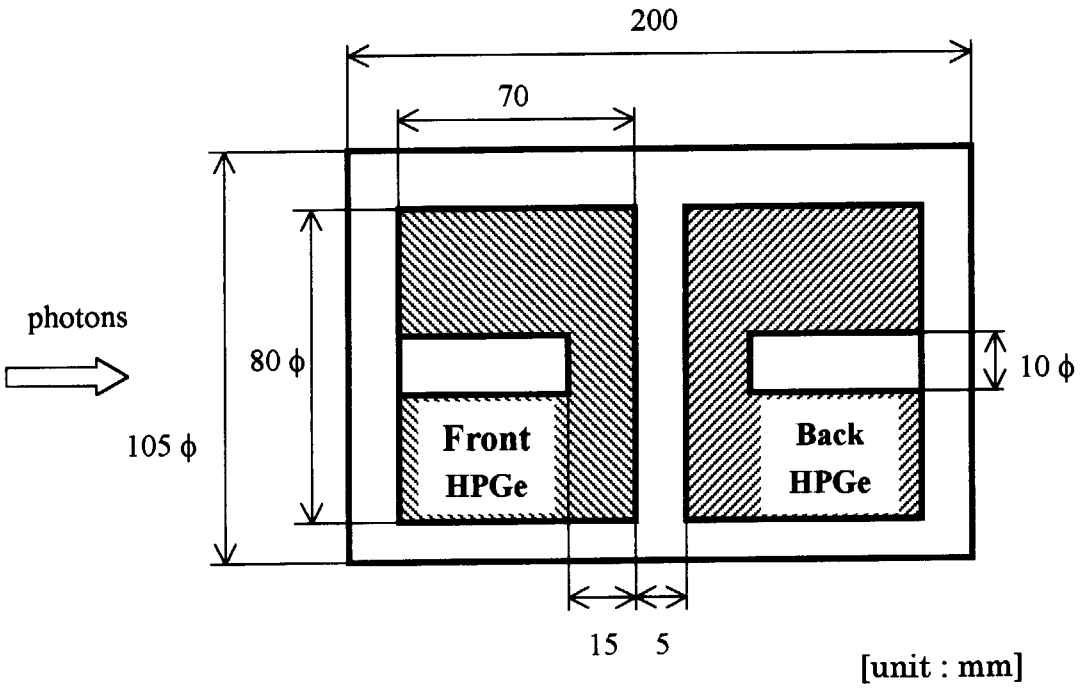

Fig. 1 Overview of twin HPGe detector

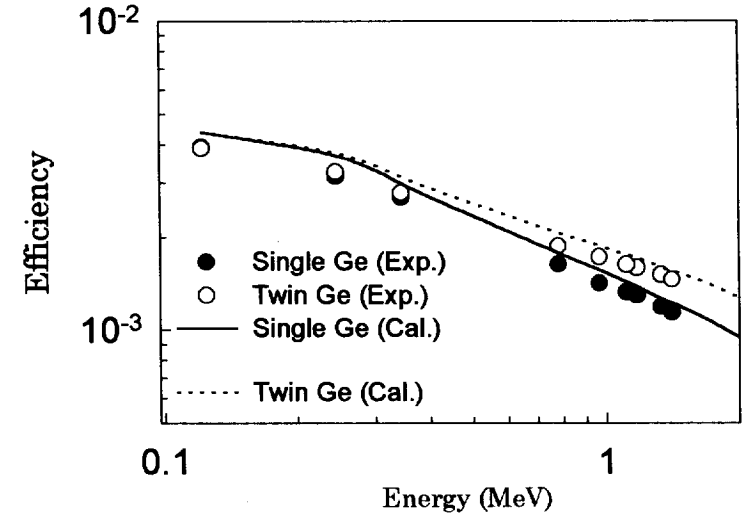

Fig.2 Efficiency of HPGe detector in low energy region

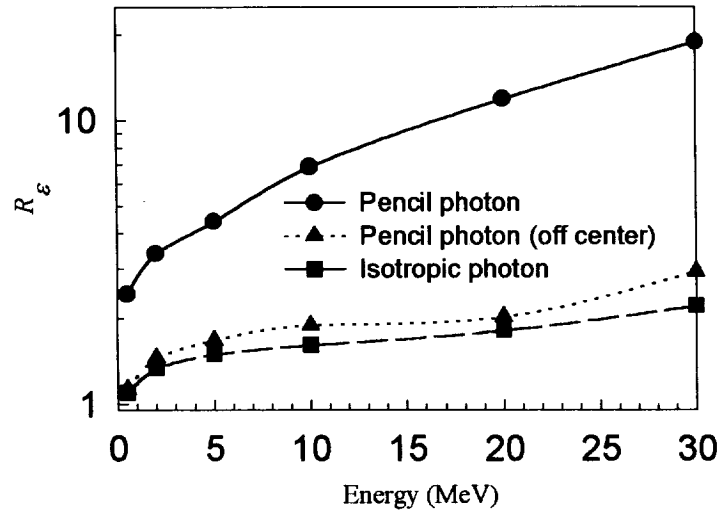

Fig 3 Results of R_ε

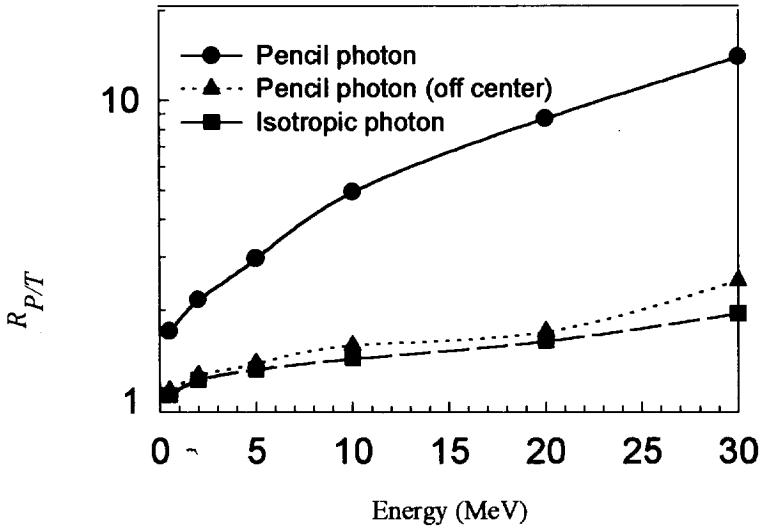

Fig. 4 Results of $R_{P/T}$

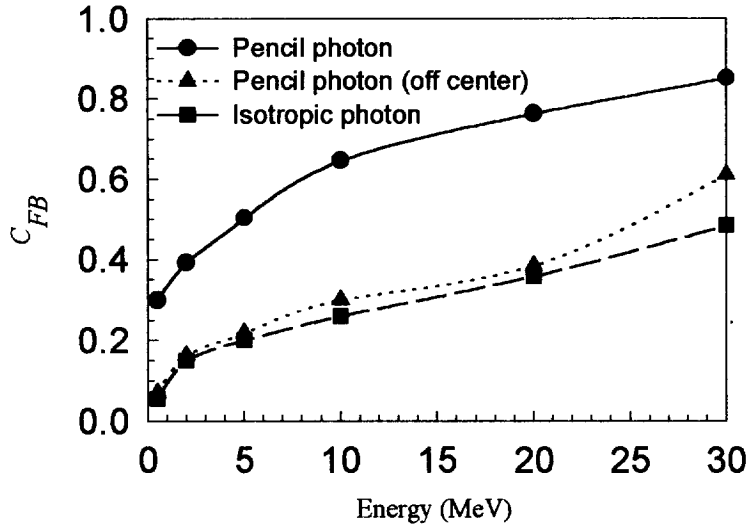

Fig. 5 Ratio of partial full energy detection efficiency

3.33 Development of the Multistep Compound Process Calculation Code

Toshihiko KAWANO
Energy Conversion Engineering, Kyushu University
6-1 Kasuga-kouen, Kasuga 816, Japan
e-mail: kawano@ence.kyushu-u.ac.jp

A program "cmc" has been developed to calculate the multistep compound (MSC) process by Feshbach-Kerman-Koonin. A radial overlap integral in the transition matrix element is calculated microscopically, and comparisons are made for neutron induced ^{93}Nb reactions. Strengths of the two-body interaction V_0 are estimated from the total MSC cross sections.

1. Introduction

The quantum-mechanical theory of the pre-equilibrium nuclear reaction by Feshbach, Kerman, and Koonin[1] (FKK) has a rather simple and feasible formulation, and it has been applied to analyses of medium and high energy nuclear reactions. The theory distinguishes two types of the pre-equilibrium emission — the multistep direct (MSD) and the multistep compound (MSC).

To calculate the MSC process, the original FKK assumes constant wave functions within a nucleus because it has a great advantage to evaluate a transition matrix element easily. Milan university group[2] adopted more realistic wave functions for a bound and an unbound states, and they have developed a MSC code GAMME[3] which calculates the transition matrix elements microscopically. However open questions still exist. The calculated MSC cross section depends on an assumption of the single-particle bound states, normalization of the unbound wave functions, and a limited number of partial waves[4].

A program "cmc" was designed to show the difference between the calculations with the constant wave assumption and without it. It calculates the transition matrix element microscopically too. The bound state wave function is calculated with a harmonic oscillator or a Woods-Saxon potential, and quantum numbers of the single particle states are determined according to the shell model. The unbound state wave function is a distorted wave by a spherical optical potential.

2. The Overlap Integral

The MSC energy spectrum is given by[1]

$$\frac{d\sigma}{dU} = \frac{\pi}{k^2}\sum_J (2J+1)2\pi\frac{\langle\Gamma_{1J}\rangle}{\langle D_{1J}\rangle}\sum_{N=1}^{\infty}\sum_{\nu j}\frac{\langle\Gamma^{\uparrow\nu j}_{NJ}\rho^{\nu}(U)\rangle}{\langle\Gamma_{NJ}\rangle}\prod_{M=1}^{N-1}\frac{\langle\Gamma^{\downarrow}_{MJ}\rangle}{\langle\Gamma_{MJ}\rangle}, \tag{1}$$

where N is the class of the pre-equilibrium states, j is the angular momentum of the emitted particle, $2\pi\langle\Gamma_{1J}\rangle/\langle D_{1J}\rangle$ is the entrance strength for producing bound $2p$-$1h$ states of spin J, $\langle\Gamma^{\uparrow\nu j}_{NJ}\rho^{\nu}(U)\rangle$ is the escape width, $\langle\Gamma^{\downarrow}_{MJ}\rangle$ is the damping width, and $\langle\Gamma_{NJ}\rangle$ is the total width. The

escape and the damping widths are factorized by X and Y functions, $\langle\Gamma_{NJ}\rangle = X_{NJ}Y_N(E)$, where the Y function contains possible phase space for the transition, and the X function contains the possible angular momentum coupling and a radial overlap integral $I(j_1, j_2, j_3, j)$ between initial and final states of interaction. The overlap integral with a zero-range interaction is defined as

$$I(j_1, j_2, j_3, j) = \frac{4}{3}\pi r_0^3 V_0 \frac{1}{4\pi}\int_0^\infty u_{j_1}(r)u_{j_2}(r)u_{j_3}(r)u_j(r)\frac{dr}{r^2}, \tag{2}$$

where $u_{j_1}(r)$ and $u_{j_2}(r)$ are the single particle radial wave functions for the initial states, $u_{j_3}(r)$ and $u_j(r)$ for the final states, r_0 the radius parameter taken to be 1.2 fm, V_0 the strength of residual interaction.

When a Yukawa type residual interaction is taken into account[5], the overlap integral is given by

$$I(j_1, j_2, j_3, j) = V_0 \int_0^\infty\int_0^\infty u_{j_1}(r)u_{j_2}(r)g_L(r,r')u_{j_3}(r')u_j(r')\frac{dr'}{r'^2}\frac{dr}{r^2}, \tag{3}$$

where g_L is calculated from the modified Bessel functions[6],

$$g_L(r,r') = \begin{cases} (\mu r \mu r')^{-1/2} K_{L+\frac{1}{2}}(\mu r) I_{L+\frac{1}{2}}(\mu r') & (r \geq r') \\ (\mu r \mu r')^{-1/2} I_{L+\frac{1}{2}}(\mu r) K_{L+\frac{1}{2}}(\mu r') & (r < r') \end{cases}, \tag{4}$$

where μ^{-1} is the range of interaction.

According to the assumption made by the FKK, the radial wave functions for the bound and the unbound states are constant within the nuclear volume, so that

$$u_B(r) = \sqrt{\frac{3}{R^3}}r, \qquad (r < R) \tag{5}$$

and

$$u_j(r) = \frac{4\pi}{(2\pi)^{3/2}}\frac{\sqrt{\mu k T_j}}{\hbar}r, \tag{6}$$

where $R = r_0 A^{1/3}$, μ is the reduced mass, k is the wave number of the emitted particle, and T_j is the transmission coefficient. The unbound wave function carries the single particle state density of free particles inside the nuclear volume $\mathcal{V} = 4\pi R^3/3$,

$$\int_0^R |u_j(r)|^2 dr = \frac{4\pi}{(2\pi)^3}\mathcal{V}\frac{\mu k}{\hbar^2}T_j \equiv \rho_c(E_c)T_j. \tag{7}$$

To calculate the overlap integral with realistic wave functions, the unbound wave function is replaced by a distorted wave[7] normalized in unit energy,

$$\chi_j(r) = \frac{4\pi}{(2\pi)^{3/2}}\frac{\sqrt{\mu k}}{\hbar}\frac{i}{2k}\left\{H_j^*(r) - S_j H_j(r)\right\}\exp i\delta_\ell, \tag{8}$$

where $H_j(r) = G_j(r) + iF_j(r)$ is the outgoing-wave Coulomb function, S_j the scattering matrix element, and δ_ℓ the Coulomb phase shift.

The bound wave function is calculated with a harmonic oscillator or a Woods-Saxon potential. The quantum numbers and the binding energies of the bound states are determined according to the spherical Nilsson model. These wave functions for $\ell = 0$, 1, 2 and 3, are shown in Fig.1. They are the radial wave functions of $2s_{1/2}$, $1p_{1/2}$, $0d_{5/2}$, and $1f_{7/2}$ states in the Woods-Saxon potential of $V = 50$ MeV, $V_{so} = 7$ MeV, $r = 1.2$ fm, and $a = 0.7$ fm, and the harmonic oscillator with $\hbar\omega = 41A^{-1/3}$. Usually there are several configurations for a possible transition for a given angular momentum transfer. For example, both $I(s_{1/2}, p_{1/2}, d_{5/2}, f_{7/2})$

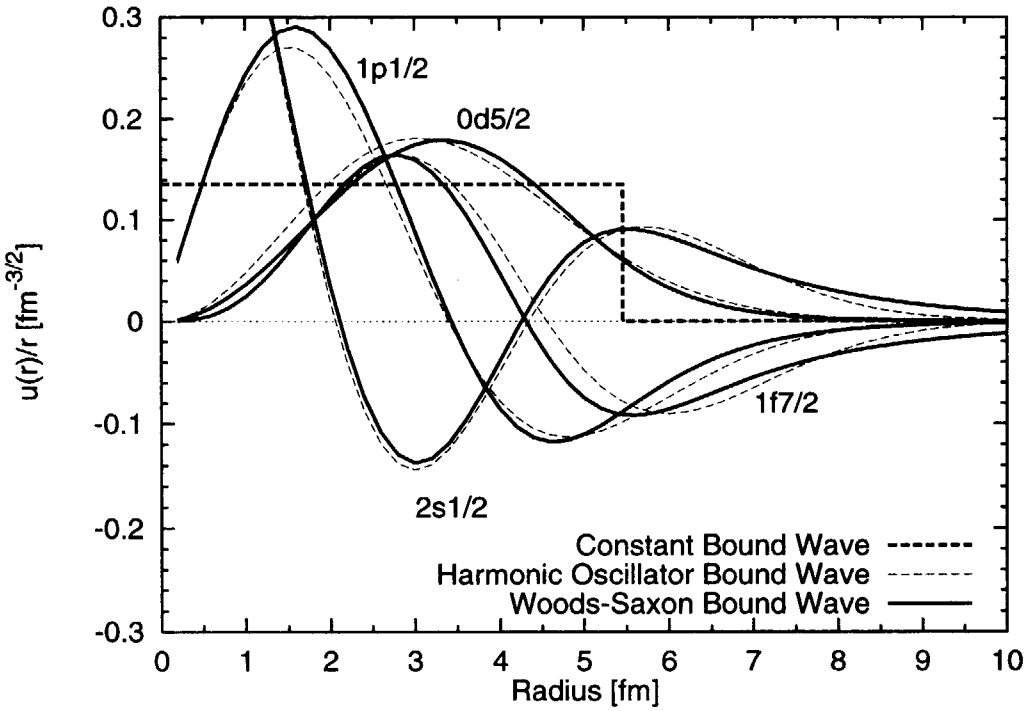

Fig.1: Comparison of the shell model wave functions and the constant wave

and $I(s_{1/2}, p_{1/2}, d_{3/2}, f_{7/2})$ are possible for the case above. These overlap integrals are averaged to give an appropriately averaged matrix element.

The overlap integrals for this configuration are, $I_B/V_0 = 0.0106$ for the constant wave, 3.38×10^{-5} for the harmonic oscillator, and 1.21×10^{-5} for the Woods-Saxon potential. These values strongly depend on a choice of the interacting particles and holes, but the averaged values over various configurations are almost independent. The averaged overlap integrals are, $\bar{I}_B/V_0 = 5.80 \times 10^{-3}$ for the harmonic oscillator, and 7.07×10^{-3} for the Woods-Saxon.

The constant wave function approximation generally overestimates the overlap integrals of not only a bound/bound configuration but also a bound/unbound configuration. This overestimate cancels in the ratio of the widths $\langle \Gamma^{\uparrow \nu j}_{NJ} \rho^{\nu}(U) \rangle$ and $\langle \Gamma^{\downarrow}_{MJ} \rangle$ to the total width $\langle \Gamma_{NJ} \rangle$, and one obtains simple estimates for the ratio regardless of details of the interaction[8]. The approximation has an advantage for the calculation of a composite system decay rate because it contains the ratio only, however it is invalid if one calculates the entrance strength microscopically because it is proportional to the width of the $2p$-$1h$ doorway state.

3. The Entrance Strength Function

From Eq.(1), the emission and the damping probabilities can be calculated regardless to the two-body residual interaction V_0, since V_0 cancels in the ratio of the emission and damping widths to the total width. The entrance strength still holds V_0 and one can estimate the strength of V_0 if the entrance strength is calculated microscopically[9],

$$2\pi \frac{\langle \Gamma_{1J} \rangle}{\langle D_{1J} \rangle} = (2\pi)^2 \omega(2,1,E) \sum_{Qj_3} (2Q+1)(2j_3+1) F(Q) R_1(j_3) \begin{pmatrix} j & j_3 & Q \\ 0 & 0 & 0 \end{pmatrix}^2 I^2(j_1, j_2, j_3, j), \quad (9)$$

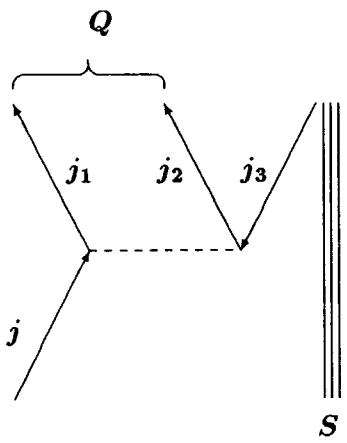

Fig.2: The angular momentum coupling scheme for the entrance channel. The incident particle j is captured in the single particle orbit j_1, creating the particle-hole pair j_2 and j_3

where the angular momentum coupling scheme is defined in Fig.2, $\omega(2,1,E)$ is the $2p$-$1h$ state density at the excitation energy E, and $F(Q)$ is the angular momentum density:

$$F(Q) = \sum_{j_1}\sum_{j_2}(2j_1+1)(2j_2+1)R_1(j_1)R_2(j_2)\begin{pmatrix} j_1 & j_2 & Q \\ 0 & 0 & 0 \end{pmatrix}^2, \tag{10}$$

where $R(j)$ is the spin distribution of the state.

Chadwick and Young[10] found that the entrance strength can be evaluated by the optical model transmission coefficients corrected by a factor $R^{\mathrm{MSC}} = \omega^B(2,1,E)/\omega(2,1,E)$, which is the fraction of flux into the bound $2p$-$1h$ state. The entrance strength becomes

$$2\pi\frac{\langle\Gamma_{1J}\rangle}{\langle D_{1J}\rangle} = R^{\mathrm{MSC}}T_J. \tag{11}$$

Figure 3 shows the calculated strengths for 14 MeV neutron-induced ^{93}Nb reactions (multiplied by $(2J+1)\pi/k^2$ to give an initial $2p$-$1h$ state formation cross section). The distorted wave and the transmission coefficient are calculated with the Walter-Guss' global optical potential[11]. The single-particle state density parameter g is taken as $g = A/13$ MeV^{-1}, and the pairing energy correction $\Delta = 0$. The solid line is calculated according to the coupling scheme in Fig.2, and the total reaction cross section is normalized to the value given by Eq.(11). At the microscopic calculation, the particle and the hole states which obey angular momentum and energy conservation are included. It restricts the possible final states, and results in small cross sections for large J.

The initial $2p$-$1h$ state formation cross section is proportional to V_0^2 when Eq.(9) is employed, and it is possible to estimate V_0 roughly if one compares the cross sections given by Eq.(9) and those by Eq.(11). Figure 4 shows the $2p$-$1h$ state formation cross sections for neutron-induced ^{93}Nb reactions as functions of the incident energy. The solid line is calculated from Eq.(9) with $V_0 = 10.4$ MeV, and the dotted line is Eq.(11). The value of V_0 was chosen to give the same cross section at 14 MeV, and it is larger than the value of 5 MeV obtained by Bonetti, *et al.*[4].

If one assumes the constant wave for the entrance strength calculation[12], it yields large overlap integrals as indicated in the previous section, and results in small V_0. Only 450 keV of V_0 gives the same strength at 14 MeV.

The $2p$-$1h$ formation cross section with the range of 1 fm is shown in Fig.4 by the dashed line. The effect of inclusion of the finite-range correction is very large, but it can be compensated if one adjusts V_0 appropriately. The calculated cross sections are about 30% of the zero-range results, and 19 MeV of V_0 gives almost the same cross sections.

4. Conclusion

A multistep compound process calculation program "cmc" has been developed to calculate an overlap integral microscopically. An entrance strength of the initial MSC process was calculated for ^{93}Nb+n(14 MeV), and it gave a rough estimation for V_0 of about 10.4 MeV for a zero-range interaction, and 19 MeV for a Yukawa interaction with the range of 1 fm.

References

[1] H. Feshbach, A. Kerman, and S. Koonin, *Ann. Phys.*, **125**, 429 (1980).

[2] R. Bonetti, L. Colli-Milazzo, and M. Melanotte, *Nuovo Cimento* **31**, 33 (1981).

[3] R. Bonetti, and M. B. Chadwick, "A computer code to calculate multistep compound reaction cross sections according to the theory of Feshbach, Kerman and Koonin," unpublished, Oxford (1991).

[4] R. Bonetti, L. Colli-Milazzo, and M. Melanotte, *Phys. Rev.*, **C27**, 1003 (1983).

[5] R. Bonetti and L. Colombo, *Phys. Rev.*, **C28**, 980 (1983).

[6] M. B. Johnson, L. W. Owen, and G. R. Satchler, *Phys. Rev.*, **142**, 1 (1966).

[7] G. R. Satchler, *Nucl. Phys.*, **55**, 1 (1964).

[8] E. V. Lee and J. J. Griffin, *Phys. Rev.*, **C5**, 1713 (1972).

[9] R. Bonetti, M. B. Chadwick, P. E. Hodgson, B. V. Carlson, and M. S. Hussein, *Phys. Rep.*, **202**, 171 (1991).

[10] M. B. Chadwick and P. G. Young, *Phys. Rev.*, **C47**, 2255 (1993).

[11] R. L. Walter and P. P. Guss, *Proc. Int. Conf. Nuclear Data for Basic and Applied Science*, Santa Fe, p.1079 (1985).

[12] G. Arbanas, M. B. Chadwick, F. S. Dietrich, and A. K. Kerman, *Phys. Rev.*, **C51**, R1078 (1995).

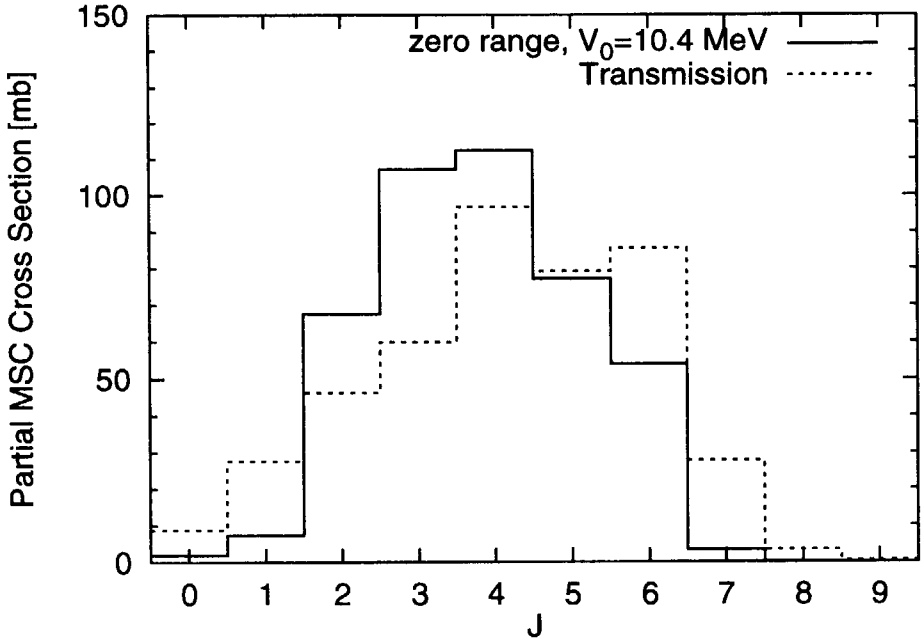

Fig.3: Comparison of the partial cross sections calculated from Eq.(9) and Eq.(11)

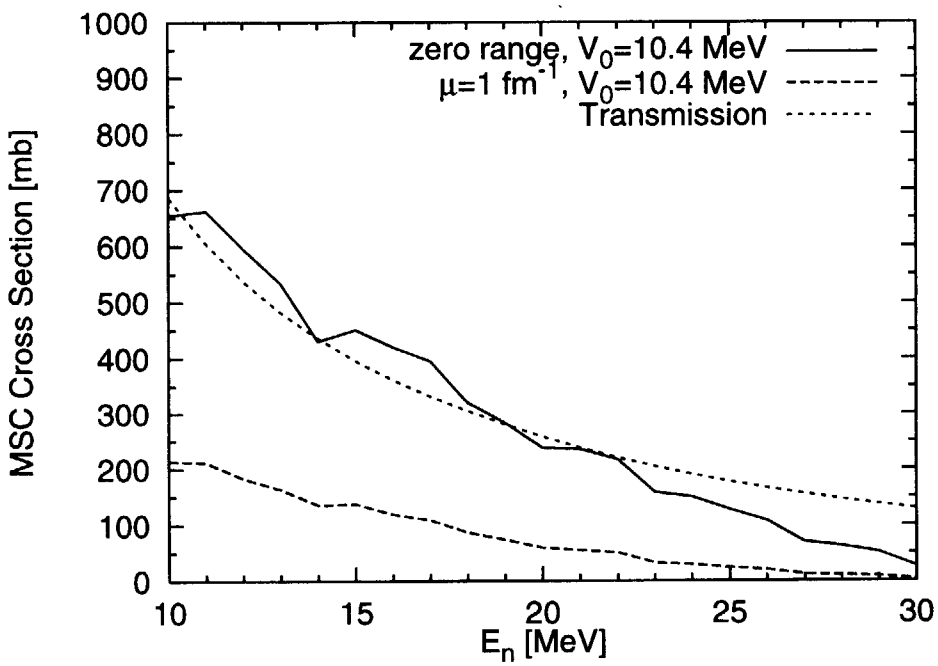

Fig.4: Comparison of the total MSC cross sections calculated from Eq.(9) and Eq.(11)

3.34

Measurement of Cross Sections Producing Short-lived Nuclei By 14 MeV Neutron -Cd,Sn,Te,Nd,Gd,Re-

H.Sakane, T.Iida*, A.Takahashi**, H.Yamamoto, K,Kawade

Department of Energy Engineering and Science, Nagoya University

* Department of Electronic, Information Systems and Energy Engineering, Osaka University

** Department of Nuclear Engineering, Osaka University

e-mail:h956316m@eds.ecip.nagoya-u.ac.jp

Nine neutron activation cross sections producing the nuclei with half-lives between 25sec and 22min were measured at energy range between 13.4 and 14.9 MeV by activation method. The (n,p) and (n,α) reaction cross sections were measured for the isotopes of ^{110}Cd, ^{112}Sn, ^{122}Te, ^{130}Te and ^{185}Re and those of ^{130}Te, ^{148}Nd and ^{158}Gd, respectively. The present results were compared with our systematics proposed on the basis of 58 cross section data of (n,p) and 33 data of (n,α) reaction. Good agreements have been seen between them.

1. Introduction

Neutron activation cross section data around 14 MeV are important from the view point of fusion reactor technology, especially for calculations on radiation damage, nuclear transmutations, induced activity and so on. However the cross sections for short-lived nuclei have not often been measured in reasonable accuracy, or there are no available data in some reactions because of difficulty in measuring short-lived activities. In the view point of gas production, we need to know the (n,p) and (n,α) reaction cross sections, although cross sections producing short-lived nuclei are not important for the problem induced activity. The nine (n,p) and (n,α) cross section data for short-lived nuclei were measured by using Intense D-T neutron source (OKTAVIAN) at Osaka University.

2. Experimental

Experiments were carried out at the Intense 14 MeV Neutron Source Facility (OKTAVIAN) at Osaka University. A pneumatic sample transport system was used for irradiation. The angles of the irradiation position to the d^+ beam were 0,50,75,105,125,

155 degree, which covered the neutron energies ranging from 14.9 to 13.4 MeV. The distance between the T-target and the irradiation position was 15 cm. When high flux was required, an additional tube was set at 1.5 cm in 0 degree. The induced activities were measured by 12% and 16% HPGe detectors. The neutron flux at the irradiation position was measured by substandard $^{27}Al(n,p)^{27}Mg(T_{1/2}=9.462$ min) reaction, whose cross sections were determined by referring the $^{27}Al(n,\alpha)24Na$ reaction (ENDF/B-VI). The samples were sandwiched between two aluminum foils of 10mm×10mm×0.2mm^t. The effective energy of incident neutron at the irradiation position was determined by the ratio of the $^{90}Zr(n,2n)^{89}Zr$ and $^{93}Nb(n,2n)^{92m}Nb$ cross sections (NB/Zr method [1]). Measured reactions and decay parameters are listed on Table 1. Corrections were made for time fluctuation of neutron flux, contribution of low energy neutron below 10 MeV, thickness of samples, self-absorption of the gamma ray and sum-peak effect of the gamma ray. The details of each correction are described elsewhere [2]. The total errors (δ_t) were described by combining the experimental errors (δ_e) and the errors of nuclear data (δ_r) in quadratic: $\delta_t^2=\delta_e^2+\delta_r^2$.

Table 1: Reactions and decay parameters [a)]

Reaction	$T_{1/2}$	Eγ(kev)	Iγ (%)	Q(MeV)
$^{110}Cd(n,p)^{110g}Ag$	24.6(2)s	657.5	4.5(2)	-2.02
$^{112}Sn(n,p)^{112m}In$	20.9(2)m	156.56	13.2(3)	-0.03
$^{112}Sn(n,p)^{112g}In$	14.4(2)m	617.1	4.6(6)	0.12
$^{122}Te(n,p)^{122m}Sb$	4.21(2)m	61.5	53.65(609)	-1.36
$^{130}Te(n,p)^{130m}Sb$	6.3(2)m	839.6	100	-4.18
$^{130}Te(n,\alpha)^{127m}Sn$	4.13(3)m	491.3	90(9)	1.80
$^{148}Nd(n,\alpha)^{145}Ce$	2.98(15)m	724.33	59(7)	5.34
$^{158}Gd(n,\alpha)^{155}Sm$	22.1(4)m	104.3	74.6(4)	5.15
$^{185}Re(n,p)^{185m}W$	1.67(3)m	131.55	4.33(16)	0.33
$^{27}Al(n,a)^{24}Na$ [b)]	14.959h	1368.6	99.994(3)	-3.13
$^{27}Al(n,p)^{27}Mg$ [c)]	9.462m	843.8	72.0	-1.83

a) taken from ref. [3] [4]

b) Standard reaction(ENDF/B-VI) used in this work

c)Secondary standard reaction used for short-lived nuclei

3. Result and discussion

The cross sections for 7 reactions were obtained at six energy points between 13.4 and 14.9 MeV and the slopes around 14 MeV were obtained for the first time. Numerical data of the present cross sections are given in Table 2. The excitation functions $\sigma(E_n)$ calculated by the systematics (1)~(6)(Kasugai et al. [5] [6]), together with the σ_{14} (mb)

calculated by the systematics (1)~(6)(Kasugai et al. [5] [6]), together with the σ_{14} (mb) and relative slopes S (/MeV) at 14 MeV are plotted in Fig. 1.

$$\sigma(E_n) = a(En-14.0)+\sigma_{14}. \quad (1)$$

$$S = a/\sigma_{14} \quad (2)$$

For (n,p) reaction ($26 \leqq A \leqq 187$),

$$\sigma_{14} = 1830(N-Z+1)\exp(-50.7(N-Z+1)/A). \quad (3)$$

$$S = -0.271+0.811(N-Z)/A+14.57((N-Z)/A)^2+0.037\,E_{th} \quad (4)$$

For (n,α) reaction ($26 \leqq A \leqq 187$),

$$\sigma_{14} = 434.8\exp(-33.4(N-Z)/A). \quad (5)$$

$$S = -1.076+0.0788(E_{th}+V_\alpha) \quad (6)$$

where N, Z and A are neutron, proton and mass number of target nuclei. The E_{th} (MeV) and V_α (MeV) are threshold energy and Coulomb barrier, respectively. The σ_{14} and the relative slope S calculated by the systematics except for $^{112}Sn(n,p)^{112m}In$ are in good agreement with experimental values.

4. Conclusions

Nine neutron activation cross sections were obtained. The σ_{14} and the relative slope S of excitation functions calculated by our systematics agree well with present results except a case of $^{112}Sn(n,p)^{112m}In$. We concrete by our systematics well predicts the excitation functions around 14 MeV within ±30%. The studies of the systematics for (n,2n) and (n,np) reaction are now in progress.

References

[1] V.E.Lewis et al.:Nucl. Inst.Meth., 174, 141, (1980).

[2] K.Kawade et al.:JAERI-M 92-020 (1992).

[3] E.Browne et al.: "Table of Radioactive Isotope" John Wiley & Sons, New York (1986).

[4] R.B.Firestone et al.: "Table of isotopes 8th Edition" John Wiley & Sons, New York(1996).

[5] Y.Kasugai et al.: Ann. Nucl. Energy Vol. 23, 1429 (1996).

[6] Y.Kasugai et al.: to be published in.

Table 2 Activation cross sections of short-lived nuclei and comparison of systematics and experimental value

Reaction	Neutron Energy(MeV) 13.40	13.65	13.88	14.28	14.58	14.87	σ_{14} Cal/Exp*	Slope(S) Cal/Exp*
$^{110}Cd(n,p)^{110g}Cd$	9.4_{8}	9.6_{8}	9.9_{8}	10.4_{9}	11.4_{10}	11.7_{11}		0.88
$^{112}Sn(n,p)^{112m}In$	30.9_{29}	30.1_{30}	29.6_{28}	29.0_{28}	30.5_{33}	28.0_{28}		0.50
$^{112}Sn(n,p)^{112g}In$	42.5_{78}	41.0_{78}	41.2_{77}	42.0_{75}	42.3_{73}	39.7_{74}		1.08
$^{122}Te(n,p)^{122m}Sb$	1.25_{27}	1.27_{26}	1.32_{26}	1.50_{29}	1.55_{33}	1.84_{33}		0.81
$^{130}Te(n,p)^{130m}Sb$	0.31_{24}	0.28_{20}	0.35_{14}	0.47_{21}	0.52_{17}	0.54_{20}		1.28
$^{130}Te(n,\alpha)^{127m}Sn$	0.14_{10}	0.18_{12}	0.19_{13}	0.20_{12}	0.21_{7}	0.33_{10}		0.73
$^{148}Nd(n,\alpha)^{145}Ce$	0.82_{13}	0.88_{13}	0.90_{13}	1.01_{15}	1.03_{15}	1.12_{17}	0.83	1.00
$^{158}Gd(n,\alpha)^{155m}Sm$						0.89_{45}		
$^{185}Re(n,p)^{185m}W$	0.90_{38}					1.89_{74}		0.76

* Experimental value are calculated by the least squares method

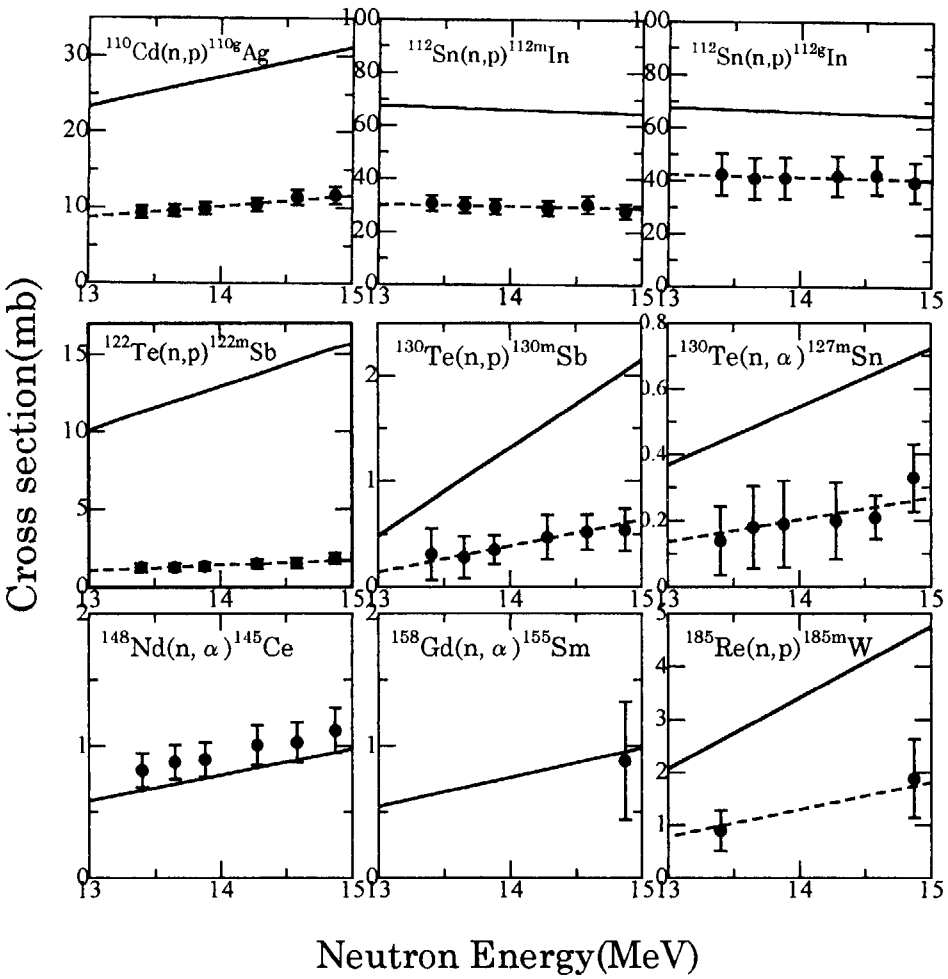

Fig.1 The experimental cross section data are compared with calculated values. The closed circles show the experimental cross sections, solid lines show the calculated ones and dotted lines show the calculated slopes.

3.35

Intercomparison of delayed neutron summation calculations among JEF2.2, ENDF/B-VI and JNDC-V2

M.Sagisaka, K.Oyamatsu*, Y.Kukita*
Department of Nuclear Engineering, Nagoya University
*Department of Energy Engineering and Science, Nagoya University
Furo-cho, Chikusa-ku, Nagoya, 464-01, Japan.
email : sagi@luna.nucl.nagoya-u.ac.jp

We perform intercomparison of delayed neutron activities calculated with JEF2.2, ENDF/B-VI and JNDC-V2 with a simple new method. Significant differences are found at $t < 20$ (s) for major fissioning systems. The differences are found to stem from fission yields or decay data of several nuclides. The list of these nuclides are also given for the future experimental determination of these nuclear data.

1. INTRODUCTION

The precise evaluation of delayed neutron properties is necessary for various reactor designs. We aim to improve delayed neutron summation calculations to have enough precision as has been achieved for decay heat summation calculations. At present, it is possible to calculate delayed neutron activities in the summation method for more than 50 fissioning systems. However, the accuracy of the delayed neutron calculations are inferior to that of integral measurements because the calculations essentially require fission yields and decay data of short-lived nuclides whose properties have not been measured so far. Recently, development of RI beam facilities enables us to measure the properties of these nuclides. Based on this observation, we need to identify key nuclides whose fission yields and decay data give rise to large uncertainties in the current delayed neutron calculations. In this paper, we attempt intercomparison of delayed neutron activities calculated with major nuclear data libraries, JEF2.2, ENDF/B-VI and JNDC-V2.

2. DELAYED NEUTRON SUMMATION CALCULATIONS

In the summation method, the number of a nuclide at a cooling time is calculated by simulating decay and build up of each nuclides. The number of ith nuclide $n_i(t)$ is obtained from coupled ordinary differential equations,

$$\frac{dn_i(t)}{dt} = -\lambda_i n_i(t) + \sum_j b_{j\to i}\lambda_j n_j(t) \tag{1}$$

with

$$n_i(0) = y_i\,. \tag{2}$$

Here λ_i and y_i are the decay constant and the independent fission yield of nuclide i, respectively. The symbol $b_{j\to i}$ represents the production rate of nuclide i from a decay of nuclide j. Then, the

delayed neutron activity from the ith nuclide is given by,

$$n_{di}(t) = P_{ni}\lambda_i n_i(t) \tag{3}$$

with P_{ni} being the delayed neutron emission probability.

3. NEW METHOD

We start with a vector of delayed neutron activities from individual nuclides;

$$\boldsymbol{n}_d(t) = \left(n_{d1}(t)\ ,\ n_{d2}(t)\ ,\ \cdots\ ,n_{dN}(t)\right). \tag{4}$$

We compare two vectors of the delayed neutron activities, $\boldsymbol{n}_d(t)$ and $\boldsymbol{n}'_d(t)$, which are calculated from different input nuclear libraries. First, we search for cooling times when the two vectors have marked differences. We use a quantity named 'overlap',

$$\mu(t) = \frac{\boldsymbol{n}_d(t)\cdot\boldsymbol{n}'_d(t)}{\left|\boldsymbol{n}_d(t)\right|\left|\boldsymbol{n}'_d(t)\right|} = \frac{\sum_{i=1}^{N} n_{di}(t)\cdot n'_{di}(t)}{\sqrt{\sum_{i=1}^{N}\left(n_{di}(t)\right)^2\sum_{i=1}^{N}\left(n'_{di}(t)\right)^2}}\ , \tag{5}$$

which is the directional cosine of the two vectors (see Fig. 1). The value of $1-\mu(t)$ gives a measure of the difference between the two vectors. Then, the sources of the difference can be identified using the following quantity

$$\varepsilon_i(t) = \frac{\frac{1}{2}\left(n_{di}(t) - n'_{di}(t)\right)^2}{\left|\boldsymbol{n}_d(t)\right|\left|\boldsymbol{n}'_d(t)\right|} = \frac{\frac{1}{2}\left(n_{di}(t) - n'_{di}(t)\right)^2}{\sqrt{\sum_{i=1}^{N}\left(n_{di}(t)\right)^2\sum_{i=1}^{N}\left(n'_{di}(t)\right)^2}}. \tag{6}$$

The value of $\varepsilon_i(t)$ represents the difference of the ith component between the two vectors. It is noted that

$$1-\mu(t) \approx \sum_{i=1}^{N}\varepsilon_i(t). \tag{7}$$

In this way, we can identify cooling times with distinct difference from the value of $1-\mu(t)$, and the sources of them from the $\varepsilon_i(t)$ values.

4. RESULTS

We make intercomparison of delayed neutron activities for ^{235}U(t), ^{235}U(f), ^{238}U(t), ^{239}Pu(t), ^{239}Pu(f). Figure 2 shows $1-\mu(t)$ for these fissioning systems after a fission burst. From this figure, we see that there are significant differences ($1-\mu(t) > 0.01$) at $t < 20$ (s) for all the fissioning systems. The value of $1-\mu(t)$ are large at short cooling times. This reflects large uncertainties in decay data and/or independent fission yields of short-lived nuclides. For example, $\boldsymbol{n}_d(t)$ for ^{235}U(t) calculated with ENDF/B-VI is remarkably different from the others due to too large

independent fission yield of ^{86}Ge in ENDF/B-VI as was reported by Miyazono et al[1].

It is interesting to see $1-\mu(t)$ in Fig. 3 and $n_d(t)$ in Fig. 4 for JEF2.2 and ENDF/B-VI. We can clearly see, from Fig. 3, significant differences in the two activity vectors between JEF2.2 and ENDF/B-VI at $t < 10$ (s) although the summed $n_d(t)$ values in Fig. 4 are in good agreement.

Table 1 lists nuclides (precursors) whose delayed neutron activities are significantly different ($\varepsilon_i(t)>0.01$) among the libraries. The nuclides listed in Table 1 cover more than 70 per cent of the $\sum \varepsilon_i(t)$ values at the two cooling times. We also list the yields or decay data of these nuclides, whose values are significantly different among the libraries. From this table, we see that the dependence on the input nuclear data library stems from only several yield and decay data values. Among them, as shown in Fig. 5, the discrepancy in the Pn values is remarkably large beyond the assigned uncertainty values in these libraries.

5. CONCLUSION

We make intercomparison of delayed neutron activity vectors calculated with JEF2.2, ENDF/B-VI and JNDC-V2. For major fissioning systems, the vectors are significantly different among the libraries at $t < 20$(s) even if the $n_d(t)$ values are in good agreement. These differences are large at short cooling times. This means that delayed neutron activities from individual precursors are different among the major libraries because fission yields and decays data of short-lived nuclides are not known well.

We also identify delayed neutron precursors, whose activities are significantly different among the libraries. The number of these precursors are limited. However, there are distinct differences in yields or decay data values of these nuclides. We note remarkable differences of the Pn values beyond the estimated uncertainty values in the libraries.

Our conclusion is summarized as follows;

(1) Delayed neutron activities from individual precursors are significantly different among the three major libraries at short cooling times, even if the aggregate activities are in good agreement.

(2) These differences stem from yields or decay data of several precursors.

(3) Values of Pn of several key precursors are remarkably different among the libraries beyond the estimated uncertainty values.

From this study, we expect that precise experimental determination of several key decay data will greatly improve the aggregate delayed neutron calculations at short cooling times. Together with results from uncertainty analyses using ENDF/B-VI[1], we are preparing the priority list for measurements.

REFERENCES

[1] T.Miyazono et al., JAERI-Conf 97-005 (1997)

[2] K.Oyamatsu et al., Proc. Nucl. Data for Sci. and Thechnol., Trieste, Italy 1997 to be published.

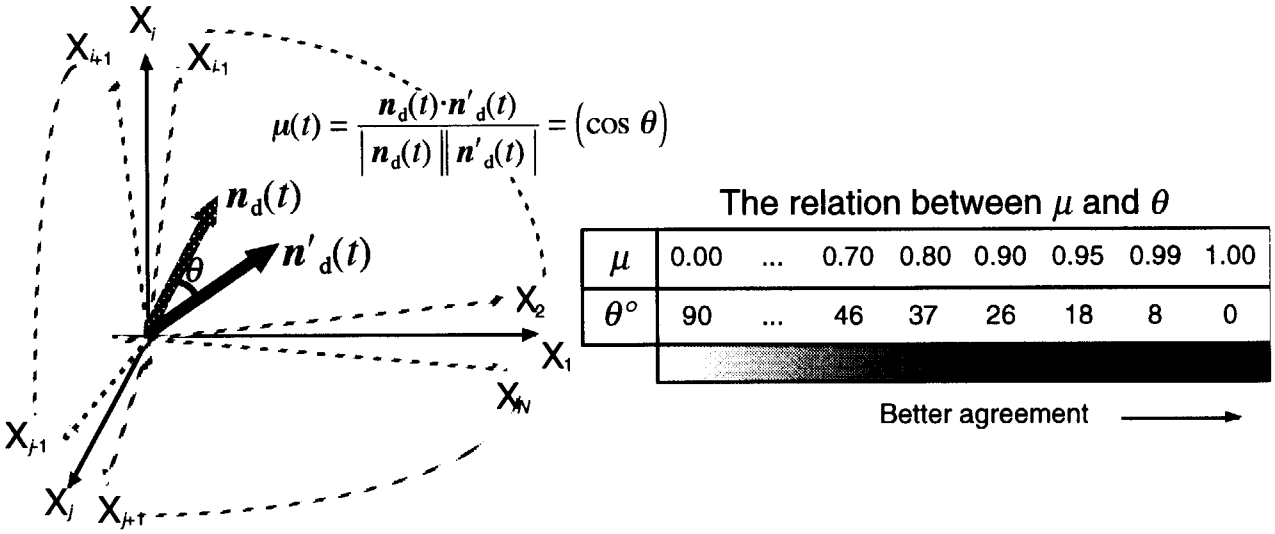

μ	0.00	...	0.70	0.80	0.90	0.95	0.99	1.00
$\theta°$	90	...	46	37	26	18	8	0

Fig. 1. Definition of 'overlap' μ.

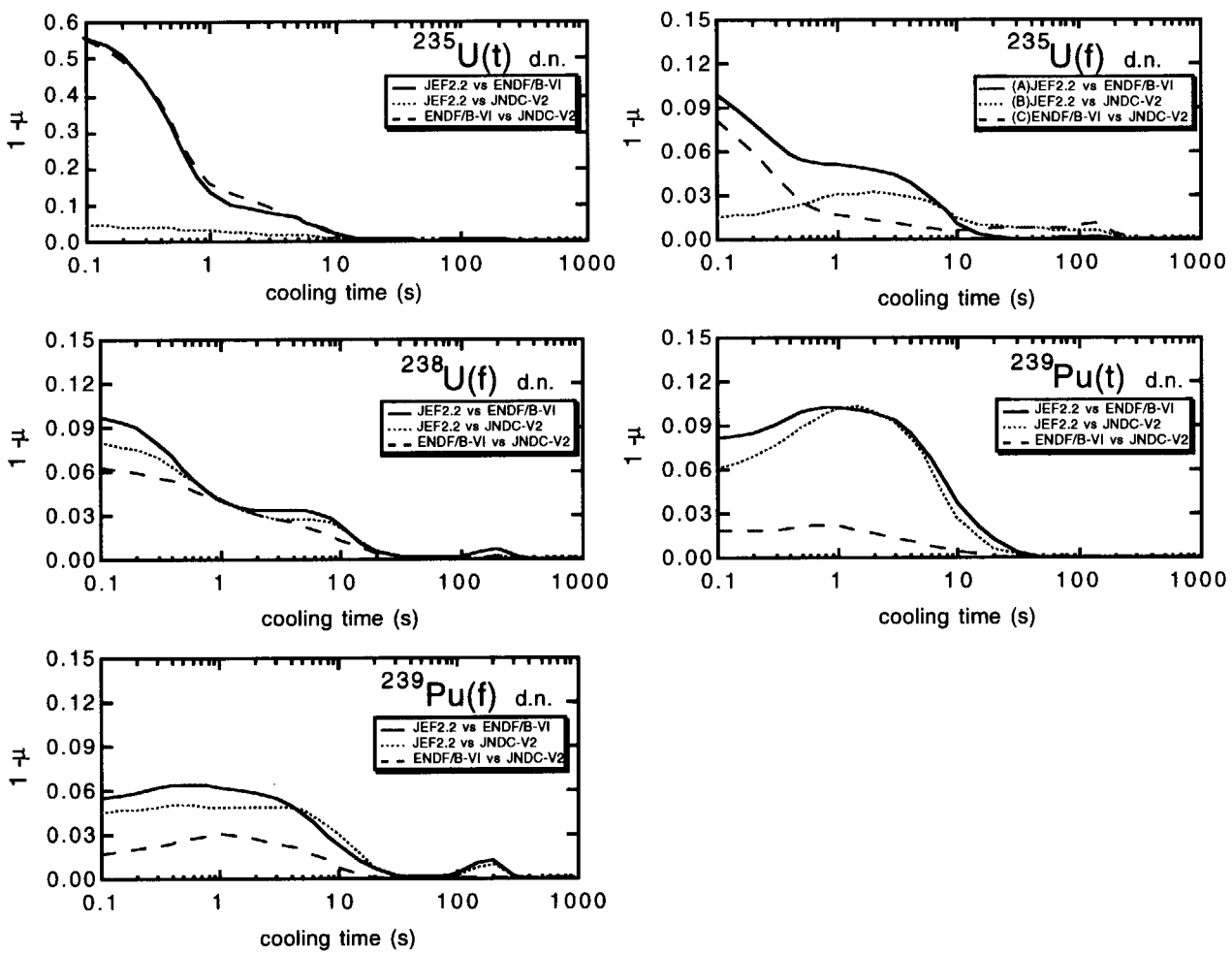

Fig. 2. Overlap between summation calculations with the three libraries for major fissioning systems.

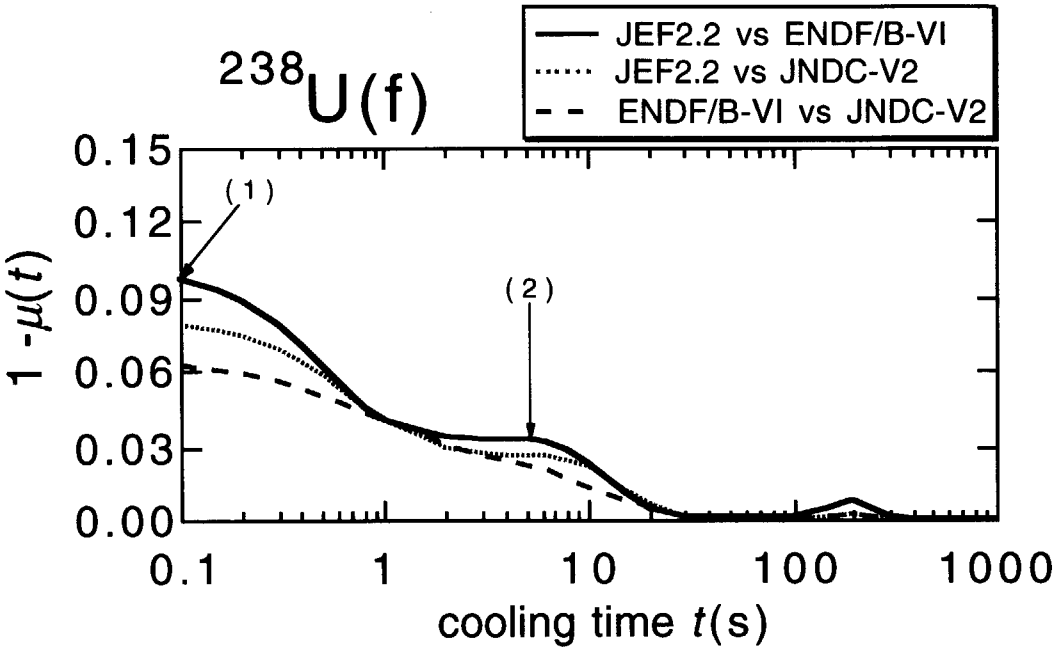

Fig. 3. Overlap of delayed neutron activities with three libraries for ^{238}U(f).

Table 1. Nuclides with large $\varepsilon_i(t)$ values for ^{238}U(f).

No.	t[s]	FP	ε_i(A)	ε_i(B)	ε_i(C)	main cause	JEF2.2	ENDF/B-	JNDC-V2
(1)	0.1	^{96}Rb	0.030	0.010	0.090	*number*	5.48e-3	8.31e-3	3.98e-3
		^{137}Sb	0.010	0.028	---------	P_n	0.996	0.200	0.200
						λ	1.925	1.451	0.571
		^{142}I	0.009	0.016	---------	P_n	0.545	0.160	0.130
						number	4.60e-4	2.96e-4	1.98e-4
		^{97}Rb	0.010	0.015	---------	*number*	1.34e-3	5.95e-4	5.67e-4
		^{141}I	---------	0.006	0.013	P_n	0.220	0.390	0.217
						number	3.16e-3	2.17e-3	1.53e-3
		^{145}Cs	0.004	0.010	---------	*number*	7.77e-3	4.95e-3	4.28e-3
(2)	5	^{85}As	0.010			*number*	5.49e-4	7.33e-4	5.56e-4
				---------	0.019	P_n	0.594	0.710	0.500
		^{90}Br	0.003	---------	0.011	*number*	1.62e-3	2.41e-3	1.52e-3
		^{139}I	0.005	0.009	---------	*number*	6.19e-3	4.32e-3	4.90e-3
		^{105}Nb	---------	0.009	---------	P_n	0.0001	0.022	0.045

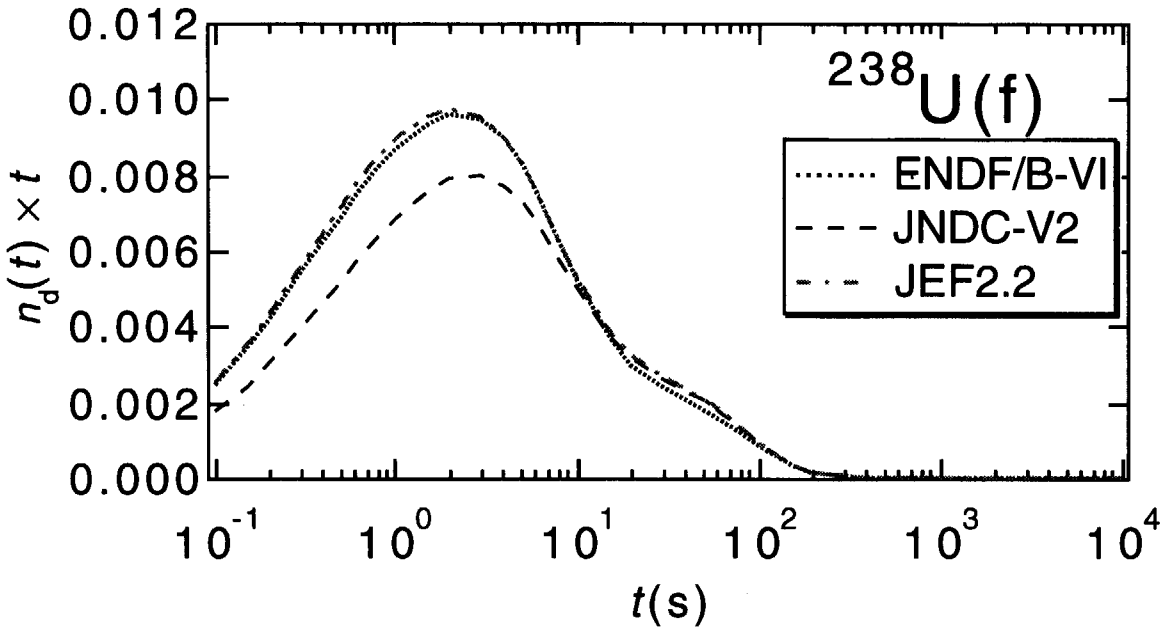

Fig. 4. Aggregate delayed neutron activities for ^{238}U(f).

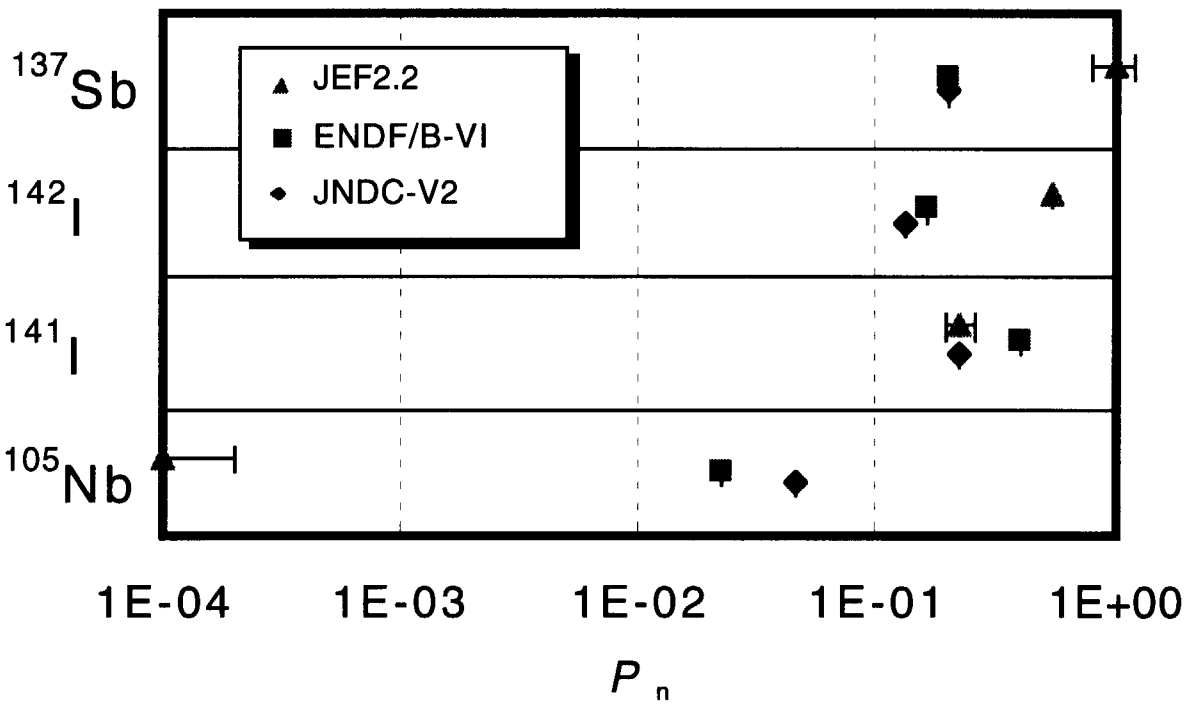

Fig. 5. Delayed neutron emission probabilities of ^{137}Sb, ^{142}I, ^{141}I and ^{105}Nb.

3.36

Easy-to-use Application Programs for Decay Heat and Delayed Neutron Calculations on Personal Computers

Kazuhiro Oyamatsu

Department of Energy Engineering and Science, Nagoya University
Furo-cho, Chikusa-ku, Nagoya, 464-01, Japan

Application programs for personal computers are developed to calculate the decay heat power and delayed neutron activity from fission products. The main programs can be used in any computers from personal computers to main frames because their sources are written in Fortran. These programs have user friendly interfaces to be used easily not only for research activities but also for educational purposes.

1. Introduction

Fission product properties are key nuclear data required at every stage in the nuclear fuel cycle. For our fission product studies based on the summation method, we have been developing application programs for personal computers to calculate the decay heat and delayed neutron activity, using fission yields and decay data in three major nuclear data libraries, JNDC nuclear data library of fission products version 2 (Japan), ENDF/B-VI (USA) and JEF2.2 (Europe).

At the same time, the fission product properties are also of interest for people who are not working in nuclear science, engineering or industry. Based on this recognition, we decide to make our programs open not only to researchers but also to general public, hoping that they will be useful especially for educational purposes. In this paper, we present a brief description of the family of our programs.

2. Features

Handy

The programs run on personal computers.

Easy-to-use

User friendly interface is provided although the interface is provided only for Macintosh (Apple Computer) at present.

Easy data transfer

The output files are text files. Therefore, the output data can be easily transferred to Excel (Microsoft Corporation), Transform (Fortner Research LLC) or any other application programs for detailed analyses.

Portable

The main programs are written in Fortran so that they can be easily run on other platforms.

3. Numerical method

Bateman equations are solved analytically. Therefore, the calculations with our programs are exact for a burst fission. However, no neutron capture process is taken into account at present. Consequently, the calculations for finite or infinite irradiations may not be very accurate probably at cooling times longer than 10^4 s.

4. Input nuclear data

Fission yields and decay data are required to calculate yields of individual nuclides at a cooling time after irradiation. As for the fission yields, our programs use only independent fission yields of fission product nuclides because the evaluation of cumulative fission yields requires branching ratios in decay chains, whose values are sometimes inconsistent between the fission yield file and decay data file even in a single nuclear data library. Actually, this is the case with ENDF/B-VI at present.

Our programs can perform fission product calculations with the above input data in JNDC nuclear data library version 2, ENDF/B-VI or JEF2.2. The fission yields and decay data can be taken from different libraries. For example, the calculations can be performed with fission yields in JNDC2 and decay data in ENDF/B-VI.

5. Program family

At present, four programs are available. Among them, three programs calculate the aggregate decay heat power and delayed neutron activity as functions of cooling time. They are decay97, decaysat97 and decayfinite97 for a fission burst, infinite irradiation and finite irradiation, respectively.

The definitions of the irradiation and cooling times are shown in Fig. 1. The fission rate is taken to be constant, $F(t)=1$ (fission/s), in the finite and infinite irradiation calculations. The infinite irradiation is defined as the limiting case of the finite irradiation with the irradiation time $T \rightarrow \infty$.

The other program, distel97, calculates yields of individual nuclides at a cooling time after a fission burst, as well as decay heat powers and delayed neutron activities from these nuclides. This program is useful to examine decay and buildup of each nuclide.

6. How to use the four programs

In this section, we describe the usage of our programs with their front-ends for Macintosh. These programs run under Japanese system (OS8). Consequently, some Japanese

words appear in dialog boxes or menu bars (Figs. 2, 5, 6, 7 and 10). However, these words are written in English under English systems.

6.1 decay97 and decaysat97

Step 0 : Prepare a cooling time file (Fig. 2).

Before you run decay97 or decaysat97, you have to prepare a text file that contains cooling times (one cooling time per line) with your favorite text editor. You can give any file name to the cooling time file.

Step 1 : Open a HyperCard stack, decay97 front-end (decaysat97 front-end) and a panel shown in Fig. 3 (Fig. 4) appears.

Step 2 : Choose a decay data file.

Push "Choose a decay data file" button, and a dialog box appears (Fig. 5). Choose a decay file from the following three files;

decaydatajndc2.dat (JNDC2), decaydatab6.dat (ENDF/B-VI), and decaydatajef22.dat (JEF2.2).

Step 3 : Choose a fission yield file.

Push "Choose a fission yield file" button, and a dialog box appears (Fig. 6). Choose a decay file from the following three folders; yieldsJNDC2 (JNDC2), yieldsB6 (ENDF/B-VI) and yieldsJEF2.2 (JEF2.2). A fission yield file contains independent fission yields of fission-product nuclides for a given fissioning system in a given library.

Step 4 : Choose a cooling time file.

Push "Choose a cooling time file" button, and choose the file that you created in Step 0.

Step 5 : Run decay97 or decaysat97.

Push "Run decay97" or "Run decaysat97" button and the main program starts to run.

Step 6 : You can open the output file, decayheat.dat from decay97 (or decaysat.dat from decaysat97), with a text editor. Figure 7 shows a sample of decayheat.dat. In the output file, the following values are listed at each cooling time t in s;

Pb : β decay heat power in MeV/s.

Pg : γ decay heat power in MeV/s.

Pa : α decay heat power in MeV/s.

d.n. act. : delayed neutron activity in 1/s.

6.2. decayfinite97

You need to specify an irradiation time in a dialog box (Step 2). Except for it, the usage is the same as those for decay97.

Step 0 : Prepare a cooling time file.

Step 1 : Open a HyperCard stack, decayfinite97 front-end (Fig. 8).
A panel similar to decay97 front-end appears. This panel has the same buttons as those in decay97 front-end, but there is an additional box for irradiation time.
Step 2 : Input an irradiation time in the dialog box.
Step 3 : Choose a decay data file.
Step 4 : Choose a fission yield file.
Step 5 : Choose a cooling time file.
Step 6 : Run decayfinite97. For the symbols in the output file, see Step 6 of decay97.

6.3 distel97

You don't have to create a cooling time file. Instead, you need to specify a cooling time in a panel (Step 2). Except for it, the usage is the same as the one for decay97.
Step 1 : Open a HyperCard Stack, distel97 front-end (Fig. 9).
A panel similar to decay97 front-end appears. This panel has the same buttons as those in decay97 front-end, but there is an additional box for cooling time.
Step 2 : Input a cooling time in the box.
Step 3 : Choose a decay data file.
Step 4 : Choose a fission yield file.
Step 5 : Run distel97. The output file (Fig. 10) contains the yield, β and γ decay heat powers together with the delayed neutron activity at the cooling time for each fission-product nuclide (isotope). The symbols in the output file are defined in the same way as those in Step 6 of decay97.

7. Remarks

The development of our programs is still in progress. Especially, the front-ends are provided only for Macintosh. However, the main programs are easily used on the other platforms, PC and Unix systems because they are written in Fortran.

The present programs will be available in the near future at our web page http://www9.nucl.nagoya-u.ac.jp/~oyak.

The programs described in this paper can be used and freely distributed unless any part of the programs or data is modified.

The present author keeps the copyright of the programs and front-ends described in this paper. However, the author is not responsible to any damages due to the use of these programs.

Lastly, we welcome any suggestions, and volunteers to work with us for the future development of the programs. We hope that our programs are useful for not only researchers and evaluators but also for anyone who is interested in the fate of fission product properties created in nuclear reactors.

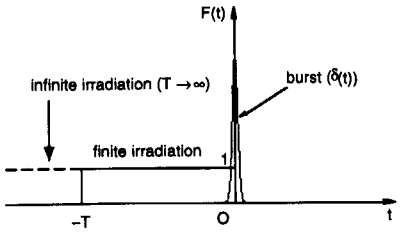

Fig. 1. Definitions of irradiation and cooling times. Infinite irradiation is defined as the limitting case of finite irradiation with T → ∞.

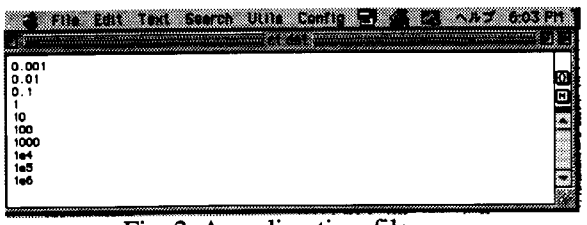

Fig. 2. A cooling time file.

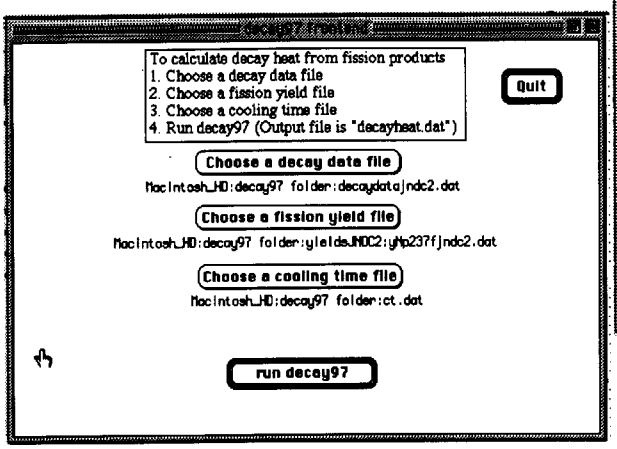

Fig. 3. The frontend of decay97 for a fission burst.

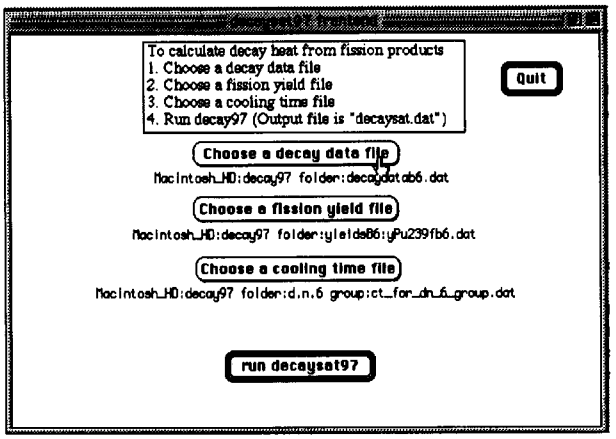

Fig. 4. The frontend of decaysat97 for infinite irradiation.

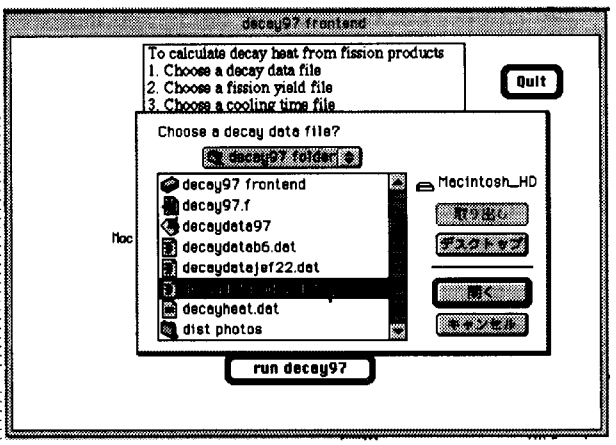

Fig. 5. Choose a decay data file.

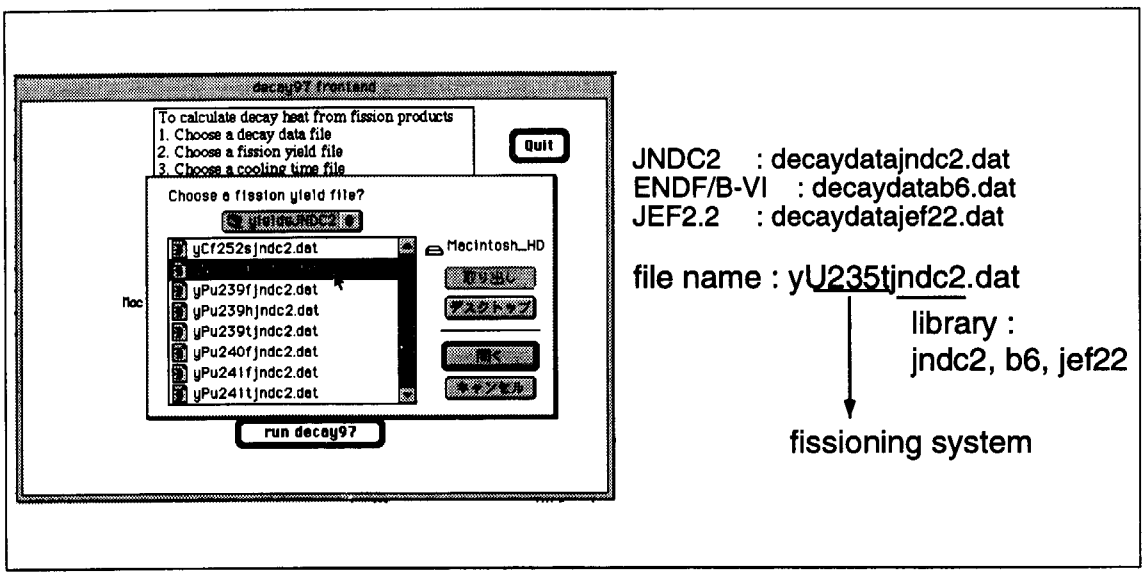

Fig. 6. Choose a fission yield file.

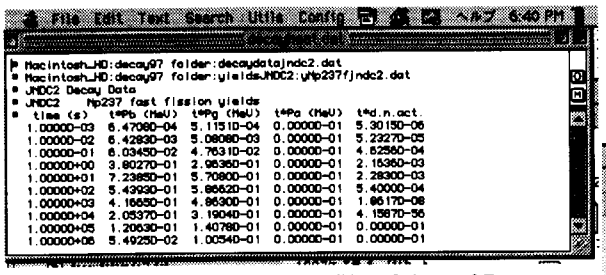

```
Macintosh_HD:decay97 folder:decaydatajndc2.dat
Macintosh_HD:decay97 folder:yieldsJNDC2:yNp237fjndc2.dat
JNDC2 Decay Data
JNDC2    Np237 fast fission yields
  time (s)   t*Pb (MeV)  t*Pg (MeV)  t*Pa (MeV)  t*d.n.act.
 1.00000-03  6.47080-04  5.11510-04  0.00000-01  5.30150-06
 1.00000-02  6.42830-03  5.08080-03  0.00000-01  5.23270-05
 1.00000-01  6.03450-02  4.76310-02  0.00000-01  4.82560-04
 1.00000+00  3.80270-01  2.96360-01  0.00000-01  2.16360-03
 1.00000+01  7.23850-01  5.70800-01  0.00000-01  2.28300-03
 1.00000+02  5.43930-01  5.85520-01  0.00000-01  5.40000-04
 1.00000+03  4.16650-01  4.86300-01  0.00000-01  1.86170-08
 1.00000+04  2.05370-01  3.19040-01  0.00000-01  4.15870-56
 1.00000+05  1.20630-01  1.40780-01  0.00000-01  0.00000-01
 1.00000+06  5.49250-02  1.00540-01  0.00000-01  0.00000-01
```

Fig. 7. The output file of decay97.

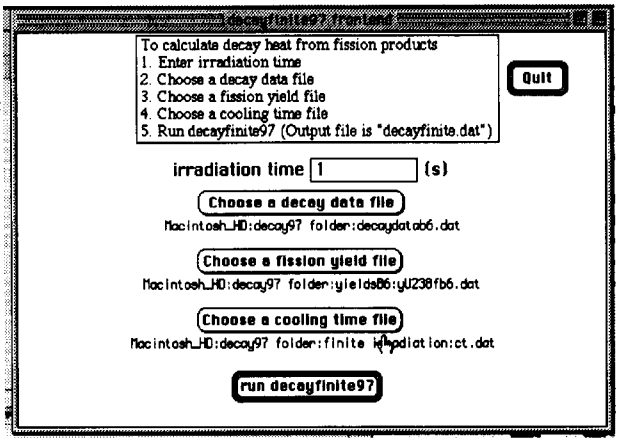

Fig. 8. The frontend of decayfinite97 for finite irradiation.

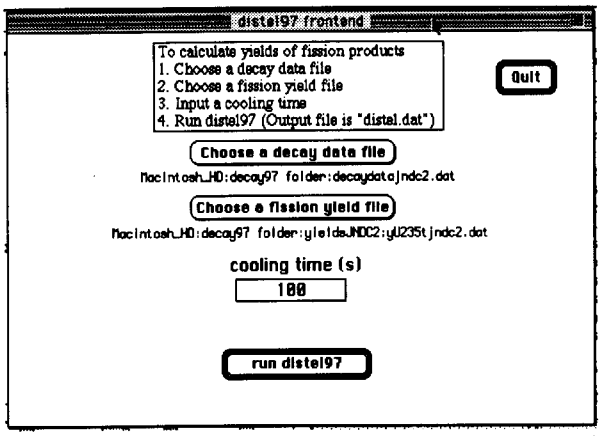

Fig. 9. The frontend of distel97 to calculate yields of fission-product nuclides, and their β, γ and delayed neutron activities after a fission burst.

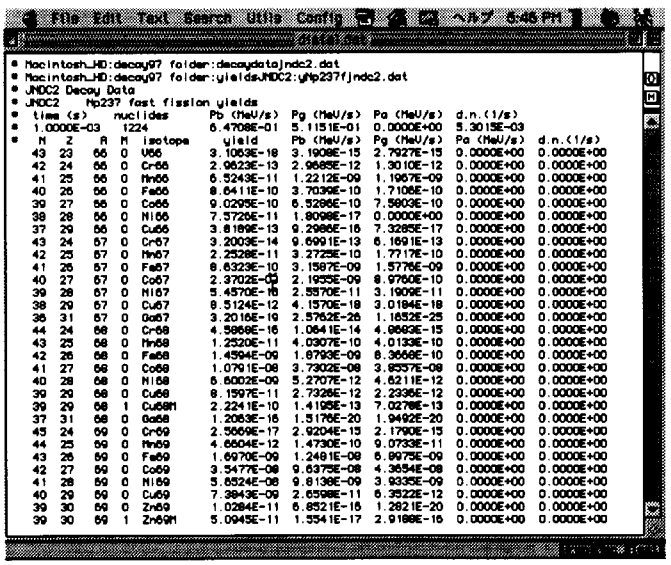

```
Macintosh_HD:decay97 folder:decaydatajndc2.dat
Macintosh_HD:decay97 folder:yieldsJNDC2:yNp237fjndc2.dat
JNDC2 Decay Data
JNDC2    Np237 fast fission yields
time (s)    nuclides      Pb (MeV/s)  Pg (MeV/s)  Pa (MeV/s)  d.n.(1/s)
1.0000E-03   1224         6.4708E-01  5.1151E-01  0.0000E+00  5.3015E-03
 N   Z   A  M  isotope      yield     Pb (MeV/s)  Pg (MeV/s)  Pa (MeV/s)  d.n.(1/s)
43  23  66  0  V66        3.1063E-18  3.1908E-15  2.7927E-15  0.0000E+00  0.0000E+00
42  24  66  0  Cr66       2.9623E-13  2.9685E-12  1.3010E-12  0.0000E+00  0.0000E+00
41  25  66  0  Mn66       6.5243E-11  1.2212E-09  1.1967E-09  0.0000E+00  0.0000E+00
40  26  66  0  Fe66       8.6411E-10  3.7036E-10  1.7108E-10  0.0000E+00  0.0000E+00
39  27  66  0  Co66       9.0295E-10  6.5286E-10  7.5903E-10  0.0000E+00  0.0000E+00
38  28  66  0  Ni66       7.5726E-11  1.8098E-17  0.0000E+00  0.0000E+00  0.0000E+00
37  29  66  0  Cu66       3.8169E-13  9.2986E-16  7.3285E-17  0.0000E+00  0.0000E+00
43  24  67  0  Cr67       3.2003E-14  9.6991E-13  6.1691E-13  0.0000E+00  0.0000E+00
42  25  67  0  Mn67       2.2528E-11  3.2725E-10  1.7717E-10  0.0000E+00  0.0000E+00
41  26  67  0  Fe67       8.6323E-10  3.1587E-09  1.5776E-09  0.0000E+00  0.0000E+00
40  27  67  0  Co67       2.3702E-09  2.1955E-09  8.9760E-10  0.0000E+00  0.0000E+00
39  28  67  0  Ni67       5.4570E-10  2.5570E-11  3.1909E-11  0.0000E+00  0.0000E+00
38  29  67  0  Cu67       8.5124E-12  4.1570E-18  3.0184E-18  0.0000E+00  0.0000E+00
36  31  67  0  Ga67       3.2016E-19  2.5762E-26  1.1652E-25  0.0000E+00  0.0000E+00
44  24  68  0  Cr68       4.5868E-16  1.0641E-14  4.8693E-15  0.0000E+00  0.0000E+00
43  25  68  0  Mn68       1.2520E-11  4.0307E-10  4.0133E-10  0.0000E+00  0.0000E+00
42  26  68  0  Fe68       1.4594E-09  1.6793E-09  8.3668E-10  0.0000E+00  0.0000E+00
41  27  68  0  Co68       1.0791E-08  3.7302E-08  3.8537E-08  0.0000E+00  0.0000E+00
40  28  68  0  Ni68       6.5002E-09  5.2707E-12  4.6211E-12  0.0000E+00  0.0000E+00
39  29  68  0  Cu68       8.1597E-11  2.7326E-12  2.2396E-12  0.0000E+00  0.0000E+00
39  29  68  1  Cu68M      2.2241E-10  1.4195E-13  7.0278E-13  0.0000E+00  0.0000E+00
37  31  68  0  Ga68       1.2063E-16  1.5176E-20  1.9492E-20  0.0000E+00  0.0000E+00
45  24  69  0  Cr69       2.5669E-17  2.9204E-15  2.1790E-15  0.0000E+00  0.0000E+00
44  25  69  0  Mn69       4.6604E-12  1.4730E-10  9.0733E-11  0.0000E+00  0.0000E+00
43  26  69  0  Fe69       1.6970E-09  1.2481E-08  6.9975E-09  0.0000E+00  0.0000E+00
42  27  69  0  Co69       3.5477E-08  9.6375E-08  4.3654E-08  0.0000E+00  0.0000E+00
41  28  69  0  Ni69       5.8524E-08  9.8138E-09  3.9335E-09  0.0000E+00  0.0000E+00
40  29  69  0  Cu69       7.3843E-09  2.6598E-11  6.3522E-12  0.0000E+00  0.0000E+00
39  30  69  0  Zn69       1.0284E-11  6.8521E-16  1.2821E-20  0.0000E+00  0.0000E+00
39  30  69  1  Zn69M      5.0945E-11  1.5541E-17  2.9188E-16  0.0000E+00  0.0000E+00
```

Fig. 10. The output file of distel97.

3.37

Consistency among Integral Measurements of Aggregate Decay Heat Power

H. Takeuchi, M. Sagisaka, K. Oyamatsu, Y. Kukita
Department of Energy Engineering and Science, Nagoya University

Persisting discrepancies between summation calculations and integral measurements force us to assume large uncertainties in the recommended decay heat power. In this paper, we develop a hybrid method to calculate the decay heat power of a fissioing system from those of different fissioning systems. Then, this method is applied to examine consistency among measured decay heat powers of ^{232}Th, ^{233}U, ^{235}U, ^{238}U and ^{239}Pu at YAYOI. The consistency among the measured values are found to be satisfied for the β component and fairly well for the γ component, except for cooling times longer than 4000 s.

1. Introduction

There are persisting discrepancies in the decay heat between summation calculations and integral measurements. However, there has been no way to judge which is more reliable. In this paper we develop a new method to examine consistency among the measured decay heat powers for different fissioning systems. With this method, we examine the measured decay heat powers at YAYOI[1-3] for ^{232}Th, ^{233}U, ^{235}U, ^{238}U and ^{239}Pu.

2. New method

The decay heat power is a linear function of independent fission yields. The yields for different fissioning systems are similar to each other. In the matrix representation of the summation method, we use a vector of independent fission yields, y. We can express the decay heat power, P, with y, as

$$P=\boldsymbol{E}\boldsymbol{\Lambda}_0\exp(\boldsymbol{\Lambda}t)y, \tag{1}$$

$$\exp(\Lambda t) = I + \Lambda t + \frac{1}{2!}(\Lambda t)^2 + \cdots, \quad (I: \text{ unit matrix}) \tag{2}$$

where $\boldsymbol{\Lambda}$ and $\boldsymbol{\Lambda}_0$ represent matrices with decay constant,

$$\Lambda=\begin{pmatrix} -\lambda_1 & b_{2\to1}\lambda_1 & \cdots & b_{N\to1}\lambda_1 \\ b_{1\to2}\lambda_2 & -\lambda_2 & \cdots & b_{N\to2}\lambda_2 \\ \vdots & \vdots & \ddots & \vdots \\ b_{1\to N}\lambda_N & b_{2\to N}\lambda_N & \cdots & -\lambda_N \end{pmatrix} \quad \text{and} \quad \Lambda_0=\begin{pmatrix} -\lambda_1 & 0 & \cdots & 0 \\ 0 & -\lambda_2 & \cdots & 0 \\ \vdots & \vdots & \ddots & \vdots \\ 0 & 0 & \cdots & -\lambda_N \end{pmatrix}, \tag{3}$$

respectively. In these matrices, λ_k and $b_{j\to k}$ are the decay constant of nuclide k, and the branching ratio from nuclide j to nuclide k, respectively. The vector $\boldsymbol{E}$ is the average decay energy vector,

$$\boldsymbol{E}=(E_1 \quad E_2 \quad \cdots \quad E_N). \tag{4}$$

In our new method, we start with writing y for a fissioning system as a linear combination of yield vectors of other N fissioning systems,

$$y=a_1y_1+a_2y_2+\cdots+a_Ny_N+y_R, \tag{5}$$

where y_R is the residual vector that can not be written with the N vectors. The values of the coefficients, a_i, are chosen to minimize $|y_R|$,

$$|y_R| = \min \quad \Leftrightarrow \quad \begin{cases} y \cdot y_1 = a_1 |y_1|^2 + a_2 y_2 \cdot y_1 + \cdots + a_N y_N \cdot y_1 \\ y \cdot y_2 = a_1 y_1 \cdot y_2 + a_2 |y_2|^2 + \cdots + a_N y_N \cdot y_2 \\ \vdots \\ y \cdot y_N = a_1 y_1 \cdot y_N + a_2 y_2 \cdot y_N + \cdots + a_N |y_N|^2 . \end{cases} \tag{6}$$

Then, the values of the coefficients, a_i, are obtained from

$$\begin{pmatrix} a_1 \\ a_2 \\ \vdots \\ a_N \end{pmatrix} = \begin{pmatrix} |y_1|^2 & y_2 \cdot y_1 & \cdots & y_N \cdot y_1 \\ y_1 \cdot y_2 & |y_2|^2 & \cdots & y_N \cdot y_2 \\ \vdots & \vdots & \ddots & \vdots \\ y_1 \cdot y_N & y_2 \cdot y_N & \cdots & |y_N|^2 \end{pmatrix}^{-1} \begin{pmatrix} y \cdot y_1 \\ y \cdot y_2 \\ \vdots \\ y \cdot y_N \end{pmatrix} \tag{7}$$

Furthermore, the above-mentioned linearity leads to a similar expression for the decay heat power, P, with the same coefficients, a_i,

$$P = a_1 P_1 + a_2 P_2 + \cdots + a_N P_N + P_R. \tag{8}$$

Here, P_i denotes the decay heat power of fissioning system i. The residual term P_R can be calculated in the summation method using the yield vector y_R. Note that P_R is expected to be small because $|y_R|$ is minimized. Equation (8) gives a relation among integral measurements of N+1 fissioning systems by putting the measured values into P_i.

We summarize, in Table 1, the nuclear properties required in the new method, summation calculation and integral measurement. Summation calculations fully require decay data. The new method partly requires them, because the decay data are required only when we calculate the residual term P_R.

3. Results

We examine the measured decay heat for Th232, U233, U235, U238 and Pu239 at YAYOI reactor. From Eq. (8), the following five consistency equations should be satisfied among the five measured decay heat values for the β and γ component separately.

$$P(\text{Th232}) = a_1 P(\text{U233}) + a_2 P(\text{U235}) + a_3 P(\text{U238}) + a_4 P(\text{Pu239}) + P_R(\text{Th232}), \tag{9}$$

$$P(\text{U233}) = b_1 P(\text{Th233}) + b_2 P(\text{U235}) + b_3 P(\text{U238}) + b_4 P(\text{Pu239}) + P_R(\text{U233}), \tag{10}$$

$$P(\text{U235}) = c_1 P(\text{Th233}) + c_2 P(\text{U233}) + c_3 P(\text{U238}) + c_4 P(\text{Pu239}) + P_R(\text{U235}), \tag{11}$$

$$P(\text{U238}) = d_1 P(\text{Th233}) + d_2 P(\text{U233}) + d_3 P(\text{U235}) + d_4 P(\text{Pu239}) + P_R(\text{U238}), \tag{12}$$

$$P(\text{Pu239}) = e_1 P(\text{Th233}) + e_2 P(\text{U233}) + e_3 P(\text{U235}) + e_4 P(\text{U238}) + P_R(\text{Pu239}). \tag{13}$$

The fission yields and decay data in ENDF/B-VI are used to calculate the coefficients a_1-a_N, y_R and P_R. Initially, we calculate the values of the coefficients a_i, b_i, c_i, d_i and e_i from Eq. (7). As shown in Table 2, the coefficient values are not necessarily positive. Except for Eq. (11), we have negative terms in Eq. (9), (10), (11) and (12). We see from Table 2 that the cancellation due to the negative terms are relatively large in these four equations. Then, the residual yield vector y_R are calculated from the following equations;

$$y_R(\text{Th232}) = y(\text{Th232}) - \{a_1 y(\text{U233}) + a_2 y(\text{U235}) + a_3 y(\text{U238}) + a_4 y(\text{Pu239})\} \tag{14}$$

$$y_R(\text{U233}) = y(\text{U233}) - \{b_1 y(\text{Th233}) + b_2 y(\text{U235}) + b_3 y(\text{U238}) + b_4 y(\text{Pu239})\} \tag{15}$$

$$y_R(\text{U235}) = y(\text{U235}) - \{c_1 y(\text{Th233}) + c_2 y(\text{U233}) + c_3 y(\text{U238}) + c_4 y(\text{Pu239})\} \tag{16}$$

$$y_R(\text{U238}) = y(\text{U238}) - \{d_1 y(\text{Th233}) + d_2 y(\text{U233}) + d_3 y(\text{U235}) + d_4 y(\text{Pu239})\} \tag{17}$$

$$y_R(\text{Pu239}) = y(\text{Pu239}) - \{e_1 y(\text{Th233}) + e_2 y(\text{U233}) + e_3 y(\text{U235}) + e_4 y(\text{U238})\} \tag{18}$$

In Table 3, we list values of $|y_R|/|y|$ together with important nuclei which gives dominant contributions to $|y_R|$. We see that $|y_R|/|y|$ is relatively large for the lightest and heaviest fissile, ^{232}Th and ^{239}Pu, as well as the heaviest even-A fissile ^{238}U.

Now, we examine whether Eqs. (9)-(13) are satisfied among the measured decay heat powers at YAYOI. The results are shown in Figs. 1-5. They show that the consistency equations are satisfied for the β component and reasonably well for the γ component, except for cooling times longer than 4000 s. Even at t < 4000 s, the equations sometimes break down slightly beyond the experimental uncertainties. However, the violation is not so large to reject the consistency. Actually, such small deviations may stem from P_R because P_R/P amounts to 7-18 % (Tables 4-8). Therefore, the YAYOI values for the five systems are good for the β decay heat and reasonable for the γ decay heat at t < 4000 s, but may not be so at longer cooling times.

To examine the residual term P_R, we list, in Tables 4-8, values of P_R/P and nuclides each of which gives more than 20% of P_R. The P_R/P values are much smaller than the $|y_R|/|y|$. It is noted that no nuclides in Tables 3 are listed in Tables 4-8. This implies that the decay heat calculations are not very sensitive to the independent fission yields because most of the short-lived nuclides have already decayed at the cooling times 10-10^4 s. Furthermore, it should also noted that nuclides in Table 3 and Tables 4-8 often belong to different decay chains. This suggests the importance of the decay data (branching ratios, decay constants and decay energies) in the decay heat calculations.

In the present method, the decay heat power, except for P_R, is calculated with decay data which is implicitly contained in the measured decay heat. Therefore the above smallness of the P_R/P values supports the effectiveness of the method for the decay heat calculations.

4. Conclusion

We propose a hybrid method to calculate the decay heat making full use of measured decay heat powers for different fissioning systems. The method is found to work well for the decay heat calculation although 10-20 % of the decay heat power should rely on the summation calculations.

The method is used to examine the consistency among the measured decay heat powers at YAYOI for the fast neutron fissions of Th232, U233, U235, U238 and Pu239. The results are as follows;

1. Consistent for the β decay heat at t<4000 s,
2. Reasonably consistent for the γ decay heat at t<4000 s.
3. Not consistent for either β or γ decay heat at t>4000 s.

Now, we are going to apply this method to find out good decay heat powers from available results of measurements using the consistency analyses as in the present paper. Then, with the good measured decay heat powers for several fissioning systems, we plan to evaluate decay heat powers for fissioning systems for which no measurements have not been performed so far.

References

[1] M. Akiyama, et al.: J. Atom. Enter. Soc. of Japan, 24, 709(1982)
[2] M. Akiyama, et al.: J. Atom. Enter. Soc. of Japan, 24, 803(1982)
[3] M. Akiyama, Proc. Int. Conf. on Nucl. Data for Sci. and Tech., Antwerp, 1982, p.273.

Table 1. Nuclear properties required for decay heat evaluation.
(●:required, △:partly required, ×:not required)

Nuclear properties	Summation method	New method	Integral measurement
Independent fission yields	●	●	×
Decay constants	●	△	×
Branching ratios	●	△	×
Average decay energies	●	△	×

Table 2. Values of coefficients a_i, b_i, c_i, d_i and e_i.

Coefficients	1	2	3	4
a_i	0.42	0.36	0.79	-0.71
b_i	0.15	0.82	-0.54	0.45
c_i	0.08	0.51	0.39	0.15
d_i	0.36	-0.67	0.78	0.38
e_i	-0.31	0.53	0.29	0.36

Table 3. Values of $|y_R|/|y|$ and important nuclides. The listed nuclides covers 50 % of $|y_R|$.

Fissioning system	$|y_R|/|y|$	Important nuclides
Th232	53.9 %	^{137}Cs, ^{86}Se, ^{87}Se, ^{102}Zr
U233	34.9 %	^{93}Sr, ^{100}Zr, ^{92}Sr
U235	27.5 %	^{133}Te, ^{134}Te, ^{100}Zr, ^{132}Te, ^{96}Sr
U238	40.9 %	^{103}Zr, ^{102}Zr, ^{100}Y, ^{135}Te, ^{136}Te
Pu239	40.9 %	^{104}Mo, ^{103}Mo

Table 4. Values of P_R/P and nuclides each of which gives more than 20% of P_R for Th232.

t (s)	β decay heat		γ decay heat	
	P_R/P(Th232)	Nuclide*	P_R/P(Th232)	Nuclide*
450	11.6 %	^{137}Xe, ^{90}Rb, ^{89}Kr, ^{102}Tc	9.3 %	^{90}Rb, ^{89}Kr, ^{89}Rb, ^{101}Mo
900	9.9 %	^{102}Tc, ^{139}Cs, ^{89}Rb, ^{137}Xe, ^{84}Br	7.4 %	^{89}Rb, ^{101}Mo, ^{84}Br, ^{102}Tc
1600	12.6 %	^{84}Br, ^{102}Tc, ^{89}Rb	8.9 %	^{89}Rb, ^{84}Br, ^{101}Mo, ^{102}Tc
2000	14.0 %	^{84}Br, ^{89}Kr	9.9 %	^{89}Rb, ^{84}Br, ^{101}Mo

Table 5. Values of P_R/P and nuclides each of which gives more than 20% of P_R for U233.

t (s)	β decay heat		γ decay heat	
	P_R/P(U233)	Nuclide	P_R/P(U233)	Nuclide
450	11.5 %	^{137}Xe	14.2 %	-
900	10.7 %	^{94}Y	13.3 %	^{89}Rb
1600	10.4 %	^{94}Y	12.9 %	^{89}Rb
2000	11.0 %	^{94}Y	13.1 %	^{89}Rb

Table 6. Values of P_R/P and nuclides each of which gives more than 20% of P_R for U235.

t (s)	β decay heat		γ decay heat	
	P_R/P(U235)	Nuclide	P_R/P(U235)	Nuclide
450	-11.3 %	-	-10.0 %	-
900	-10.6 %	-	-10.5 %	^{104}Tc
1600	-10.5 %	-	-11.0 %	^{104}Tc
2000	-10.6 %	-	-10.9 %	^{104}Tc

Table 7. Values of P_R/P and nuclides each of which gives more than 20% of P_R for U238.

t (s)	β decay heat		γ decay heat	
	P_R/P(U238)	Nuclide	P_R/P(U238)	Nuclide
450	17.1 %	^{137}Xe	17.7 %	-
900	16.3 %	-	17.7 %	-
1600	14.8 %	-	17.1 %	-
2000	13.7 %	-	16.9 %	-

Table 8. Values of P_R/P and nuclides each of which gives more than 20% of P_R for Pu239

t (s)	β decay heat		γ decay heat	
	P_R/P(Pu239)	Nuclide	P_R/P(Pu239)	Nuclide
450	11.6 %	^{105}Tc, ^{104}Tc, ^{107}Ru	9.3 %	^{104}Tc, ^{93}Sr, ^{105}Tc, ^{108}Rh ···
900	9.9 %	^{105}Tc, ^{104}Tc	7.4 %	^{104}Tc, ^{89}Rb, ^{93}Sr ^{105}Tc
1600	12.6 %	^{104}Tc	8.9 %	^{104}Tc, ^{89}Rb
2000	14.0 %	^{104}Tc	9.9 %	^{104}Tc, ^{89}Rb

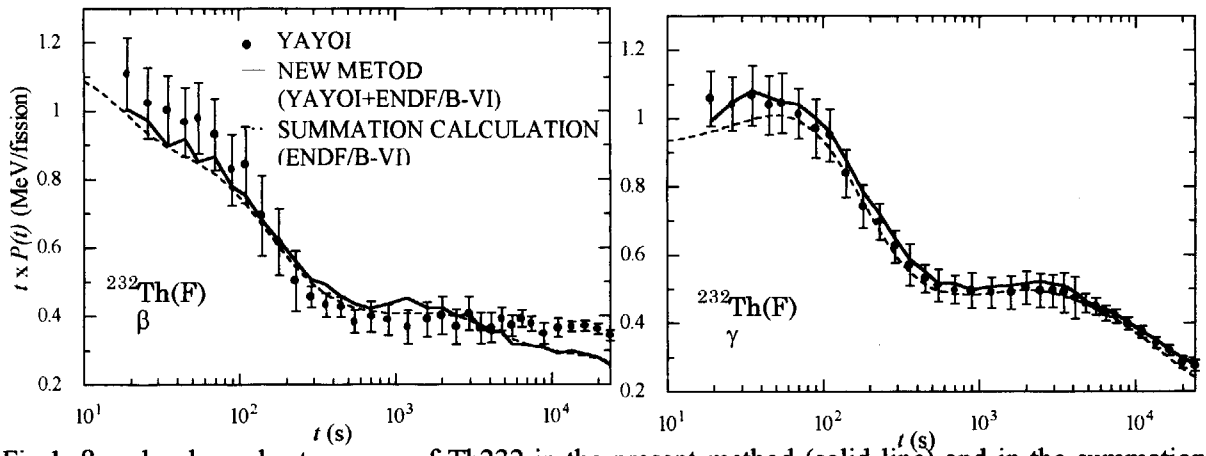

Fig.1. β and γ decay heat powers of Th232 in the present method (solid line) and in the summation method (dashed lines). Also shown are values obtained in the YAYOI experiment.

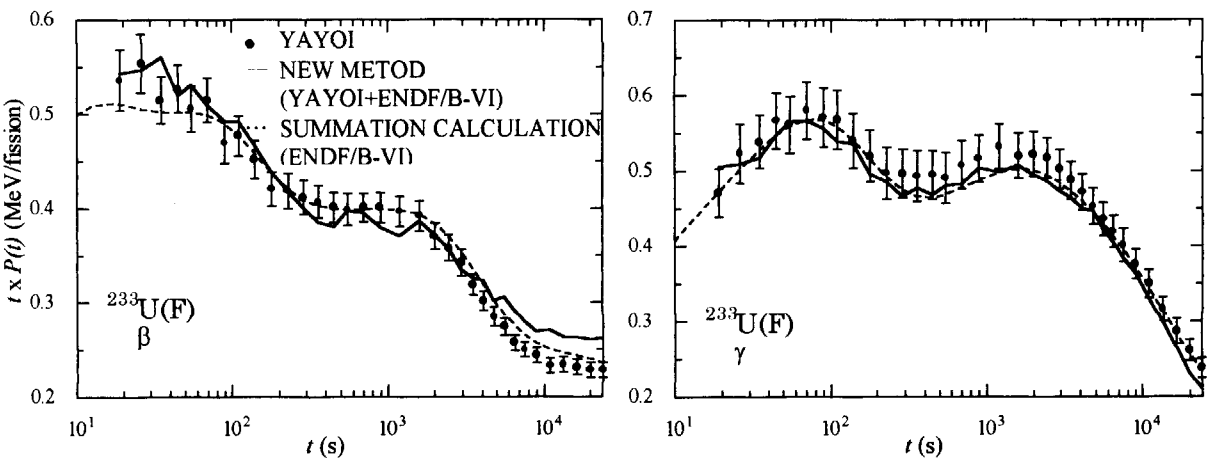

Fig.2. β and γ decay heat powers of U233 in the present method (solid line) and in the summation method (dashed lines). Also shown are values obtained in the YAYOI experiment.

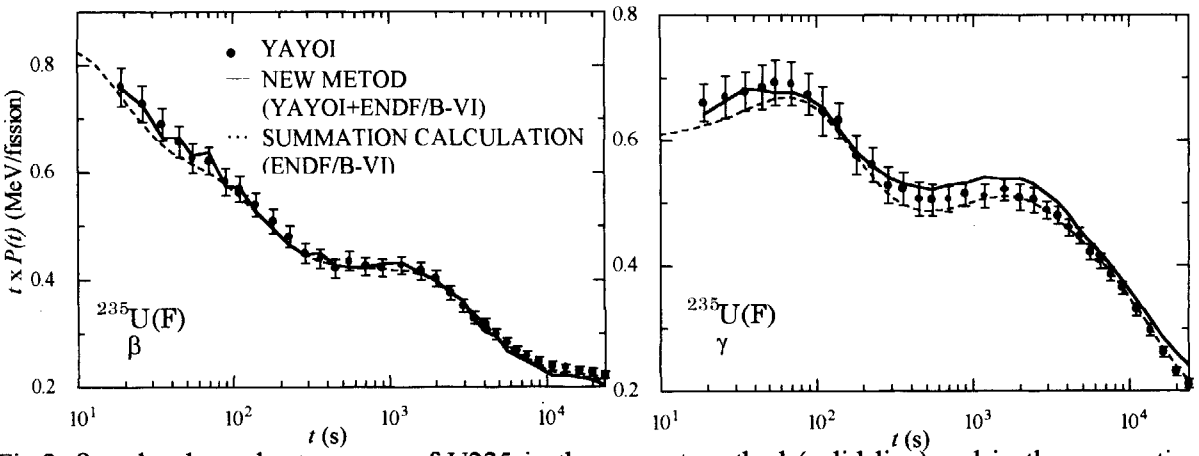

Fig.3. β and γ decay heat powers of U235 in the present method (solid line) and in the summation method (dashed lines). Also shown are values obtained in the YAYOI experiment.

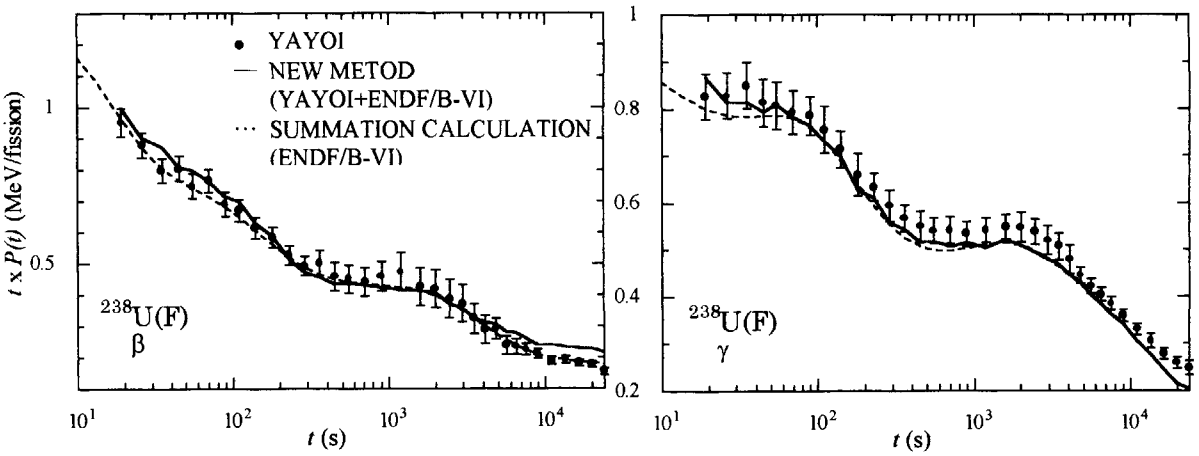

Fig.4. β and γ decay heat powers of U238 in the present method (solid line) and in the summation method (dashed lines). Also shown are values obtained in the YAYOI experiment.

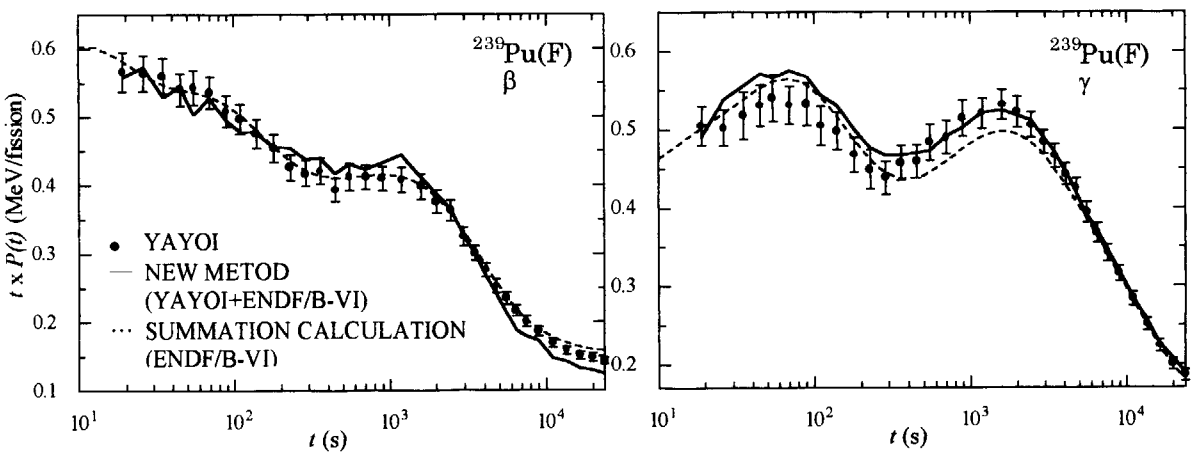

Fig.5. β and γ decay heat powers of Pu239 in the present method (solid line) and in the summation method (dashed lines). Also shown are values obtained in the YAYOI experiment.

(SND-97)

3.38 Quantum Recurrence and Integer Ratios in Neutron Resonances

Makio OHKUBO †
1663-39, Senba-cyo, Mito-shi, Ibaraki-ken, 310 Japan

Abstract
Quantum recurrence of the compound nucleus in neutron resonance reactions are described for normal modes which are excited on the compound nucleus simultaneously. In the structure of the recurrence time, integer relations among dominant level spacings are derived. The "base modes" are assumed as stable combinations of the normal modes, preferably excited in many nuclei.

1. Introduction

On the physical nature of the compound nucleus formed by neutron resonances, the statistical theories prevail. Most of the observed data of the nearest neighbor level spacings agree to the Wigner distribution, the long range correlations to the $\Delta 3$ statistics, and the strengths to the Porter-Thomas distributions. These distributions are predicted from the Random matrix theories(GOE), which are based on the complexity of the compound nucleus. Therefore the neutron resonances are believed to be a typical quantum chaos.[1,2].

However, non-statistical natures in observed neutron resonances are long reported. One of them is frequent appearance of dominant level spacings among resonance levels, which can be observed by Dij (spacings between arbitrary two levels) distributions or by Fourier analysis [3,4,5,6,7,8,9].

In these analyses[7,8,9], a strange fact was reported that the same dominant spacings or that with simple integer ratios are widely observed in different nuclei. For example, typical dominant spacings described are; 4.4eV for Hf-177, 5.5eV for Sb-123, 14.6eV for U-238, 17.6eV for Er-168, 142eV in As-75, 570eV in mix of Th-232,U-238, and Pu-240,242, so on. There are integer ratios among them; 5.5(Sb-123)/4.4(Hf-177) = 5/4, 14.6(U-238)/17.6(Er-168)=5/6, 14.6(U-238)/4.4 (Hf-177)=10/3, 142(As-75)/570(Th-232,U-238,Pu-240,Pu-242 mix)=1/4, etc. These integer ratios will never stems from the chaotic nature of the compound nuclei upon which statistical theories(GOE) are found. These integer ratios imply that the neutron resonances must be a rather simple regular systems, of which regularity may be a facet of quantum physics at highly excited states.

In this article, we describe the quantum recurrence of the compound nucleus by Feynman path integral for the normal modes which are excited simultaneously. A possible reason of the integer ratios in dominant spacings are considered based on the structures of the recurrence time. The "base modes" are assumed as stable combinations of normal modes, preferably excited in many

nuclei.

2. Decomposition into Normal Modes and Quantum Recurrence

The compound nuclear states excited by neutron resonances are time periodic functions. We assume that the excitation can be approximately decomposed into several integrable normal modes, which are possible to be excited simultaneously, such as many modes of collective vibrations and rotations, and many type of single particle excitations around the core, as shown schematically in Fig.1. These time dependent motions induce neutron density oscillations on the compound nuclear surface, of which frequencies are synchronized with these motions of the normal modes. At resonances, recurrence frequency(or its beat) of the compound nucleus resonates with the de Broglie wave frequency of the incident neutron. Recurrence of these normal modes in semi-classical model are described in [10], which we call I below.

In the following, quantum recurrence of M-normal modes is considered, where the details of these normal modes except frequencies are not important here. Because of independence of the normal mode, time development of the compound nucleus is the product of these modes, which can be described by the Feynman path integral.[11]

For the excitation of the compound nucleus, oscillation amplitude of each normal mode is assumed to be small, and the potential energies are proportional to the square of the displacement from the equilibrium position. The Lagrangean for the total system is described as

$$L = \sum (\dot{Q}_j^2 - \omega_j^2 Q_j^2) = \sum L_j , \qquad \text{.....} \qquad (2.1)$$

where Q_j ,$\dot{Q}_j$ are displacement from the equilibrium and its time derivative for j-th normal mode, respectively, ω_j is corresponding oscillating frequency, and L_j. is Lagrngean for j-th normal mode. Action integral S is

$$S = \int L\,dt = \sum \int L_j\,dt = \sum S_j . \qquad \text{.....} \qquad (22)$$

For the compound nuclear system, the wave function and the propagator are the products of each normal mode, as

$$\phi(x,t) = \prod \phi_j(x,t), \qquad \text{.....} \qquad (2.3)$$

$$K(t,t_0) = \prod K_j(t, t_0). \qquad \text{.....} \qquad (2.4)$$

The time development of the wave function $\phi_j(x)$ from t= t_0 to t=t can be described by a propagator $K_j(t, t_0)$ as,

$$\phi_j(x,t) = \int K_j(t, t_0)\ \phi_j(x, t_0)\,dx. \qquad \text{.....} \qquad (2.5)$$

$K_j(t, t_0)$ is written by a Feynman path integral, as

$$K_j(t, t_0) = \int D_j.\ \exp((i/\hbar)\, S_j) \qquad \text{.....} \qquad (2.6)$$

$$= F_j(t)\ \exp((i/\hbar) S_j), \qquad \text{.....} \qquad (2.7)$$

where the exponential term is path integral along the classical trajectory, and

$F_j(t)=\int D_j$ is path integral on all the available paths deviated from the classical trajectory. For each normal mode, the Lagrangean and its action integral S_j oscillates. S_j is written for $x_1 = x_2$, and $T=t_2-t_1$, as,

$$S_j = (m\,\omega_j/2\sin\omega_j T)\,2(x_1^2)[\cos\omega_j T - 1], \quad \text{..... (2.8)}$$

and $F_j(t)$ is written as,

$$F_j(t) = (m\,\omega_j/ih\sin\omega_j T)^{1/2}. \quad \text{..... (2.9)}$$

Though S_j and $F_j(t)$ diverge at $T = 2n\,\pi/\omega_j$ (n : integer), $K_j(t)$ and $\phi_j(x,t)$ are periodic function of time with a period $\tau_j = 2\,\pi/\omega_j$,as

$$K_j(t) = K_j(t + n\,\tau_j), \quad \text{(n : integer) ..... (2.10)}$$

$$\phi_j(x, t) = \phi_j(x, t + n\,\tau_j). \quad \text{(n : integer) ..... (2.11)}$$

As to recurrence of the total system, we can define the total recurrence time τ, which is essentially equal to the least common period of τ_j (j=1,2,...M), after which K(t) and $\phi(x, t)$ recurs to the initial value, as,

$$K(t) = K(t + \tau), \quad \text{..... (2.12)}$$

$$\phi(x, t) = \phi(x, t + \tau). \quad \text{..... (2.13)}$$

Determination of the total recurrence time τ is discussed in the following .

3. Recurrence Time for Multiple Oscillators

The concept of the recurrence for a independent multiple oscillator system can be seen in Fig.2 of I, as a toy model of rotating disks. The average recurrence frequency($=1/\tau$) was already derived in Eq.(3.5) of I, as a function of number of oscillators M, angular frequency ω_j, and the tolerable phase error d_j . The validity of Eq.(3.5) in I was confirmed by a computer simulation of the recurrence of multiple oscillators, of which frequencies are randomly sampled. For the quantum system, the tolerable phase error is $\triangle\theta=1$ rad., which is the uncertainty relation itself, as

$$\triangle E\triangle t \sim \hbar\triangle\omega\triangle t \sim \hbar\triangle\theta \sim \hbar, \quad \text{..... (3.1)}$$

where $\triangle E$ is uncertainty in energy, $\triangle t$ that in time, $\triangle\omega$ that in frequency, and $\triangle\theta$ that in phase angle.

Therefore the average recurrence frequency is derived in Eq.(3.8) in I, as,

$$1/\tau = f(M) = (\omega_1 + \omega_2 + .. \omega_M)/(2\,\pi)^M. \quad (s^{-1}). \text{..... (3.2)}$$

Eq.(3.2) is rewritten by total excitation energy E_x of the compound nucleus as,

$$1/\tau = f(M) = (E_x/h)/(2\,\pi)^{M-1}. \quad (s^{-1}) \quad \text{..... (3.3)}$$

Average recurrence time τ increases exponentially with M as,

$$\tau = (h/E_x)\exp(\beta M), \quad \text{..... (3.4)}$$

where $\beta = \ln(2\,\pi) \sim 1.84$.

On the other hand, for a quantum system having level spacing D, the recurrence time is formally given by,

$$1/\tau \sim D/h. \quad (s^{-1}) \quad \text{..... (3.5)}$$

By equating $1/\tau$ in Eq.(3.3),(3.5), a simple relation is derived as,

$$E_x/D = (2\,\pi)^{M-1}, \quad \text{..... (3.6)}$$

$$\text{or} \quad M = 1 + \ln(E_x/D)/\ln(2\,\pi). \quad \text{..... (3.7)}$$

In Eq.(3.7), M the number of normal modes excited simultaneously is expressed only by E_x/D, where h is dropped out naturally. From the experimental data of

D and E_x, M versus mass number are shown in Fig.4 of I. M are found to be nearly equal to the number of excitons in the exciton model of the nuclei, and the ratios between them are nearly 1, as shown in Fig.5 of I. Average energy of a normal mode is $E_x/M \sim 1$ MeV.

4. Mode Combinations

For the increase of cooperated normal modes, the total recurrence time τ is elongated, with average elongation rate of 2π per addition of a normal mode, as in Eq.(3.4). The average total recurrence energy E_r is defined by Eq.(3.3) as

$$E_r = h/\tau(M) = E_x/(2\pi)^{M-1}. \qquad (4.1)$$

As the total recurrence time is the least common multiple period for each normal mode, therefore the elongation rates are integer, from 2,3,4,....., to about 15. As illustrated in Fig.2, these normal modes are shown as points, and resonances A and B are shown as circles in which several points are enclosed. If the resonance A and B have common point(s), the recurrence times τ_A, τ_B are integer multiples of recurrence time τ_C of the common point(s). That is,

$$\tau_A = \tau_C\, n_1 n_2 \ldots n_K, \qquad (4.2)$$

$$\tau_B = \tau_C\, n_1' n_2' \ldots n_K'. \qquad (4.3)$$

where $n_1, n_2, \ldots n_K, n_1', n_2' \ldots, n_K'$ are integers. Then the ratio τ_A/τ_B is an integer ratio as,

$$\tau_A/\tau_B = n_1 n_2 \ldots n_K / n_1' n_2' \ldots n_K'. \qquad (4.4)$$

If the overlapping of resonances A and B is appreciable, and if K=K'=1, the ratio τ_A/τ_B is a simple integer ratio j/k (j,k : integer< ~15).

5. Base Mode

As described in the introduction, it is suggested that the same modes might be excited in the compound nuclei of wide mass region. It is considered that there might be combinations of normal modes, called "base mode", which are preferably and frequently excited in certain energy regions. This is a similar concept to chemical bases OH^-, SO_4^{--}, NH_4^+, ...which simplify the understanding of chemical reactions. When the other modes are excited beside the base mode, total recurrence times are elongated to integral multiple of that of the base mode. Then there will be integer ratios among the recurrence times of these resonance family with the same base mode. This will be a reason of the multiple integer ratios among level spacings in certain neutron energy region. In Fig.3, combinations of normal modes with increasing M are illustrated including base modes as examples. Overtone and coupling of the normal modes are neglected here. For the dominant spacings of the four nuclides Sb-123, Er-168, Hf-177, and U-238, we can assume as a base mode of 88 eV. The base mode of 88eV itself is composed of the ~7 normal modes. Combinations of the modes are illustrated in Fig.4. The base modes have two concepts: independence and affinity of normal modes. The base modes will be profoundly related to the shell stabilization effects stated by Sukhoruchkin[12], where the rést mass of electron m_e= 511keV and its family multiplied by integer ratios play important roles in nuclear level dispositions and spacings. Further investigation is needed to clarify the base modes.

The present work is partially supported by the REIMEI Research Resource of JAERI.

[1] M.L.Mehta, Random Matrix and the Statistical Theory of Energy Levels (Academic, New York,1967)
[2] O.Bohigas and M.Giannoni, Chaotic Motion and Random Matrix Theory, Lecture Note of Physics Vol 209 (Springer Verlag,Baerlin,1984) pp 1-99.
[3] K.Ideno and M.Ohkubo: J.Phys.Soc.Jpn. 30,620(1971), K.Ideno: ibid. 37,581 (1974)
[4] S.I.Sukhoruchkin; Sov.J. Nucl. Phys. 10,285(1970); Proceedings of the International Conference on Statistical Properties of Nuclei (Plenum, New York,1972), p. 215
[5] C.Coceva, F.Corvi,P.Giacobbe,and M.Stefanon; Proceedings of the International Conference on Statistical Properties of Nuclei (Plenum, New York,1972), p.447
[6] F.N.Belyaev and S.P.Borovlev, Yad.Fiz.27,289(1978)
[7] G.Rohr; Low Energy Nuclear Dynamics, World Scientific, 1995, p 130
[8] K.Ideno; Int.Conf. Neutron in Research and Industry, Proc. SPIE 2867, G.Vourvopoulos ed. 1997 Washington, pp.398-403
[9] S.I.Sukhoruchkin; ISINN-3, Dubna 1995,
[10] M.Ohkubo: Phys.Rev.C 53, 1325(1966)
[11] R.P.Feynman and A.R.Hibbs: Quantum Mechanics and Path Integral, (McGrow-Hill, 1965)
[12] S.Sukhoruchkin: ISINN-4, p379, Dubna 1996. ; "Low Energy Nuclear Dynamics", Oganessian ed. ,World Scientific (1995),p647

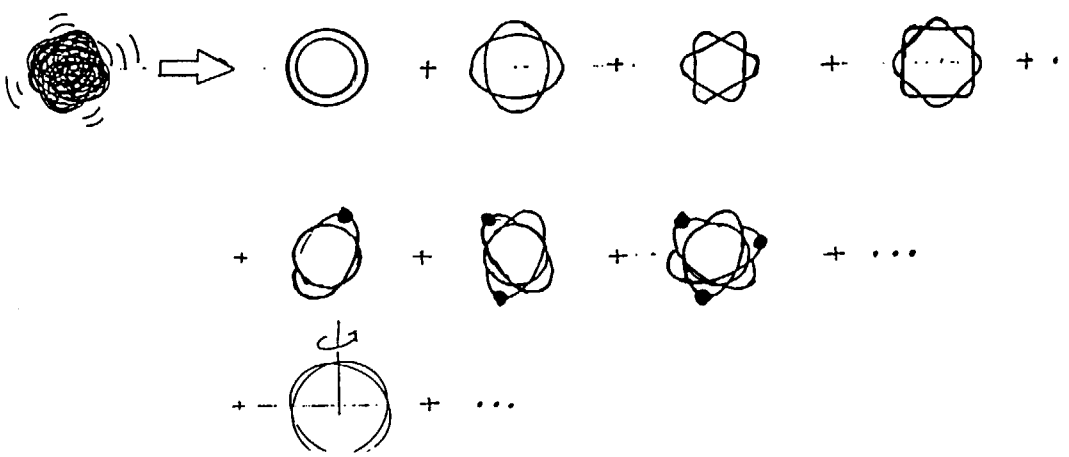

Fig.1 Decomposition into normal modes

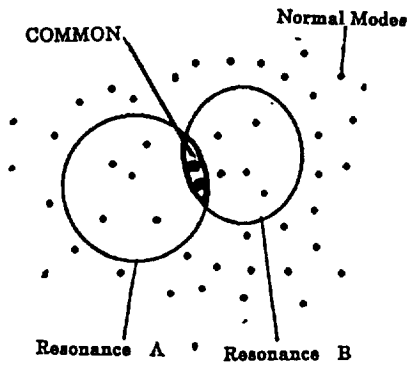

Fig.2 Resonances with common normal modes

number of coupled modes	average recurrence energy
1	8 MeV
2	1.27
3	200 keV
4	32
5	5
6	800 eV
7	130
8	20
9	3

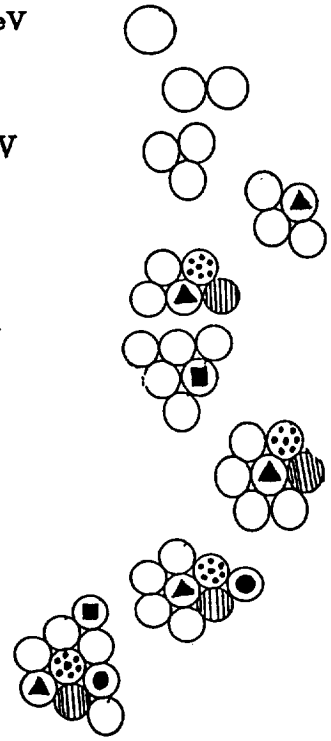

Fig.3 Mode coupling and slow-down of recurrence energy

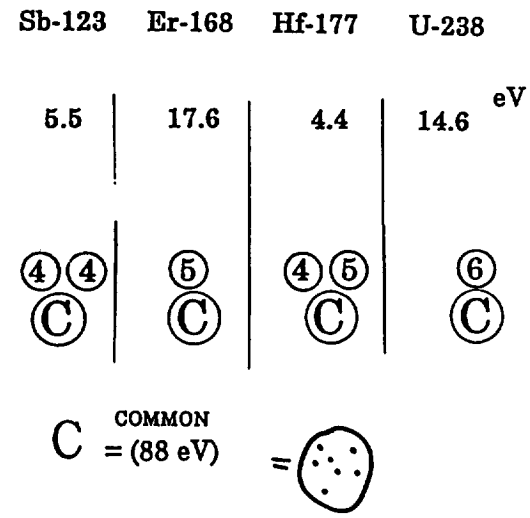

Fig.4 Sub-harmonic mode coupling

3.39 A Database for Transmutation of Nuclear Materials on Internet

Mitsutane FUJITA, Misako UTSUMI and Tetsuji NODA
National Research Institute for Metals
1-2-1, Sengen, Tsukuba, Ibaraki 305 Japan
fujita@tamamo.nrim.go.jp

A database system on Internet for nuclear material design and selection used in various reactors are developed in NRIM site of "Data-Free-Way". In order to retrieve and maintain the database, the user interface for the data retrieval was developed where special knowledge on handling of the database or the machine structure is not required for end-user. It is indicated that using the database, the possibility of nuclides and radioactivity in a material can be easily retrieved though the evaluation is qualitatively.

1. Introduction

In the data system for nuclear material design and selection used in various reactors, huge material databases and several kinds of tools for data analysis or simulation code of the phenomena under irradiation are required. Thus, a database on transmutation for nuclear materials had constructed on PC [1]. The database converted to a system used on Internet. As a database for nuclear material design and selection used in various reactors are developed in NRIM site of "Data-Free-Way"[2.3]. A database storing the data on nuclear reaction needs to calculate of the simulation. Using the database, we can retrieve the data of nuclear reaction for material design on the Internet and understand qualitatively the behavior of nuclear reaction such as the transmutation or decay. The database is required for the friend user-interface for the retrieval of necessary data. In the paper, features and functions of the developed system are described and especially, examples of the easy accessible search of nuclear reactions are introduced.

2. Outline of the database on transmutation for nuclear materials

2.1 Database system

In the database of transmutation for nuclear materials, the data of nuclear reaction for material design is stored and we can understand qualitatively the behavior of nuclear reaction such as the transmutation or decay. The database is managed by ORACLE where RDBMS (relational database management system) is supported on work station with unix OS.
As the RDBMS and WWW were connected, user are able to retrieve necessary data using Netscape or Explorer as a user-interface through the Internet.

Fig. 1 shows the home page in the WWW of NRIM site on "Data-Free-Way". Users are accessed the database by selecting the term of "transmutation of material" in the home page. Then. the opening screen of the database as shown Fig. 2 is appeared. Users are able to select various interface for retrieval and obtain the necessary data.

2.2 Data structure

The database consists of five main tables and three supplemental tables, as shown Fig. 3. Main tables are element, isotope, spontaneous decay, transmutation and cross section table. The element table has the data such as element name, atomic weight and etc. These data are input values obtained from ordinary periodic table. The data in the isotope table consist of the natural abundance ratio, half-life data, gamma-ray or beta-ray energy and maximum permissible concentration in air (MPC), which are taken from isotope table. The spontaneous decay table has the data of decay mode and branching ratio. The transmutation table has the data of

transmutation process, produced nuclide and etc.. The neutron cross-section table stores the data with 42-energy group covering from thermal neutron energy to 15MeV. Fig. 4 is shown a example of ^{180}W drown by the data in this table. It is defined that high neutron energy is more than 0.1MeV and low one is less than 0.1MeV.

The supplemental tables are three kinds of spontaneous decay, decay mode, gamma energy

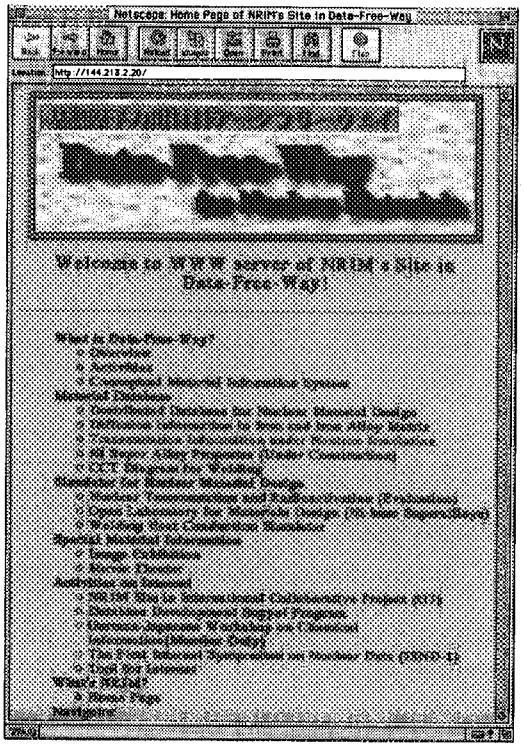

Fig. 1 WWW of NRIM's home page in "Data-Free-Way" system.

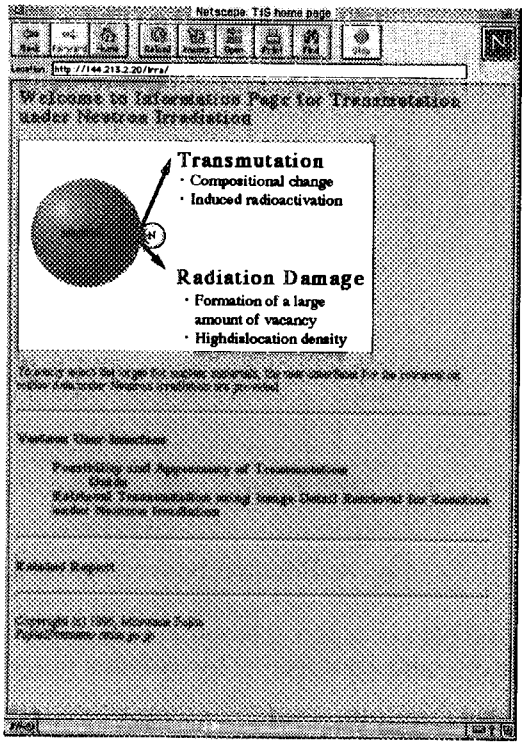

Fig. 2 Opening screen of the for transmutation under neutron irradiation.

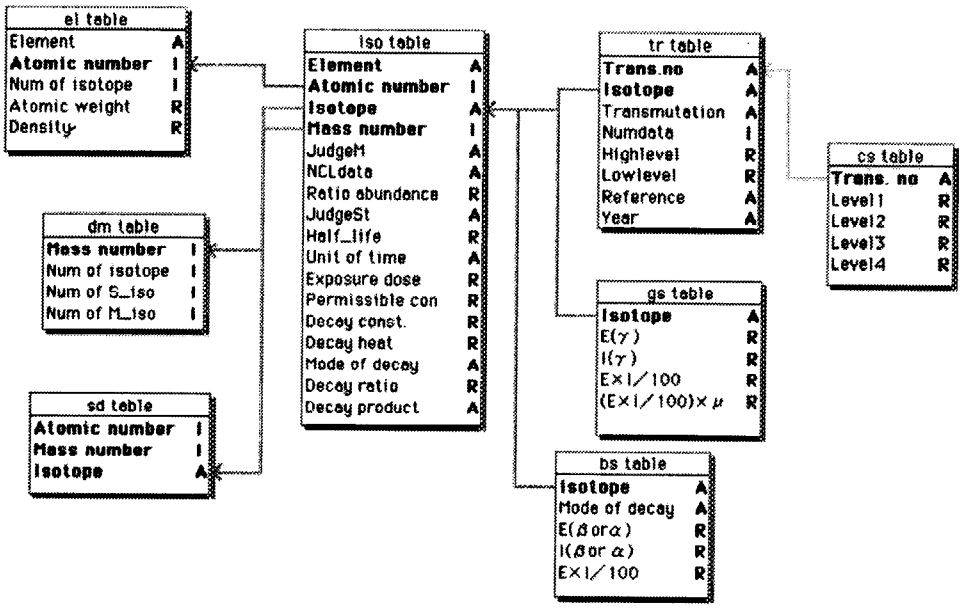

Fig. 3 The data structures of the database on transmutation for nuclear materials.

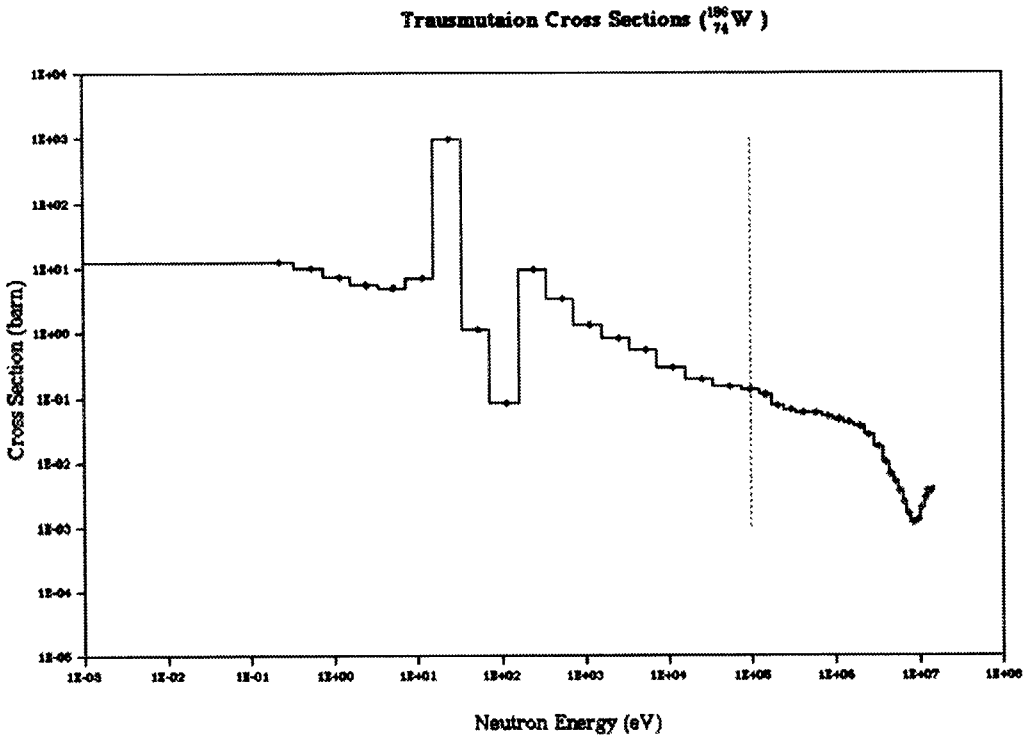

Fig. 4 Relation between cross section of nuclear reaction and neutron spectrum.

and beta or alpha. These tables play the roles due to aid the retrieval and the calculation of heat. Both tables are related by a certain unique key mutually.

2.3 Stored data

Various data, which are required for simulation on nuclear reaction, have been collected and stored in the database from reports as follows.

I. Nuclear data such as neutron cross-section are collected from JAERI's CRROSLIB, ENDF/B-6, JENDL-3 and FENDL 1.1. The number of element stored in the database is 54 at present, however, this will increase to be 89 in near future.

II. The data on element and isotope are collected from
   a. "Table of Radioactive Isotopes" E. Browne and R. B. Firestone, 1986, LBLU of C, John Wiley & Sons,
   b. "Chart of the Nuclides" compiled by Y. Yoshizaw and T. Horiguchi and M. Yamada, 1980, JNDC and NDC in JAERI.

In the near future, the system will be used through the Internet and the improvement will be being done to consider step reaction including many unstable nuclides.

3. Functions and user-interface

3.1 Functions

Fig. 2 shows opening main menu screen of the database. This database has four retrieval functions of nuclear reaction process, properties of radioactive isotope, spontaneous decay of each isotope and decay of produced nuclides after nuclear reaction. We can understand qualitatively the behavior of nuclear reaction such as the transmutation or decay.

3.2 User-interface for retrieval data

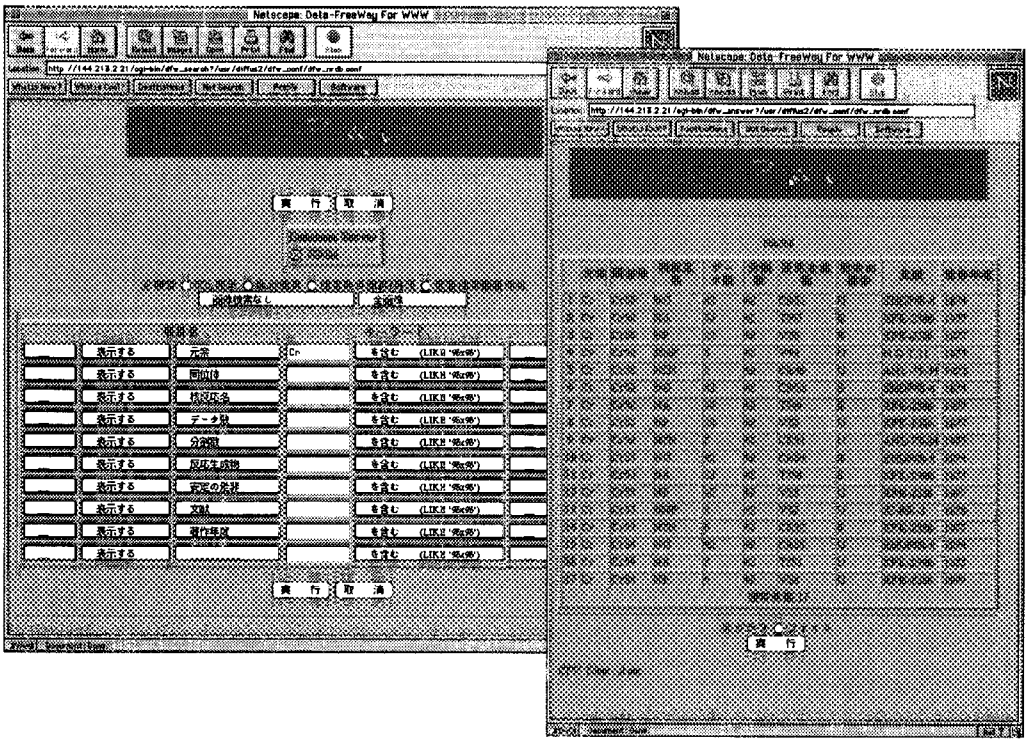

Fig. 5 Screen to retrieve data on nuclear transmutation and the results of Cr atomic element.

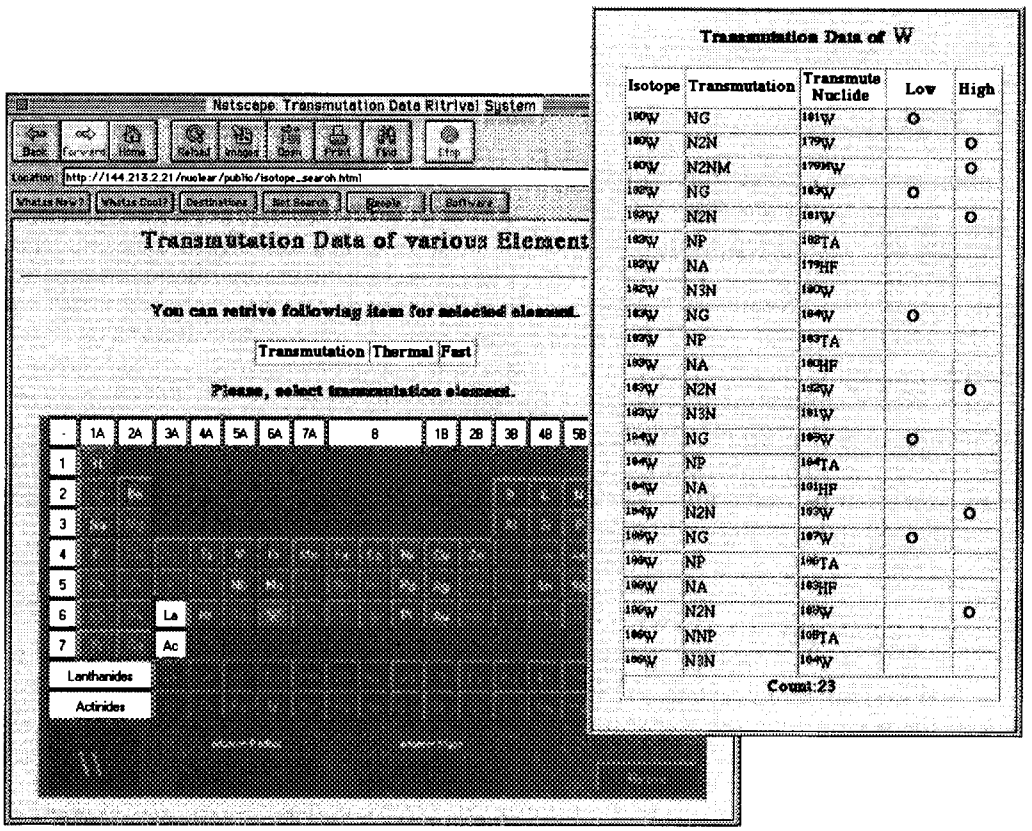

Fig. 6 Screen to retrieve data on nuclear transmutation using periodic table and the results of ^{186}W .

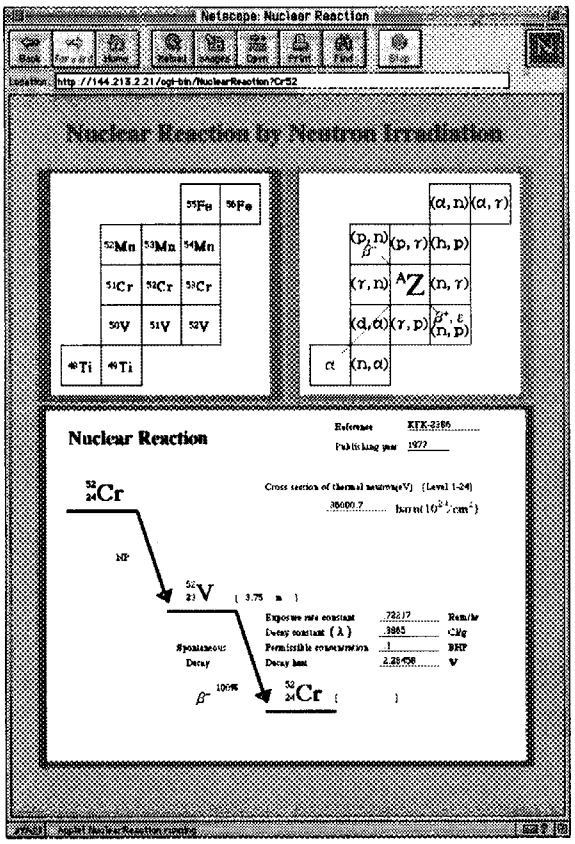

Fig. 7 Screen to retrieve data on nuclear transmutation and decay process and the results.

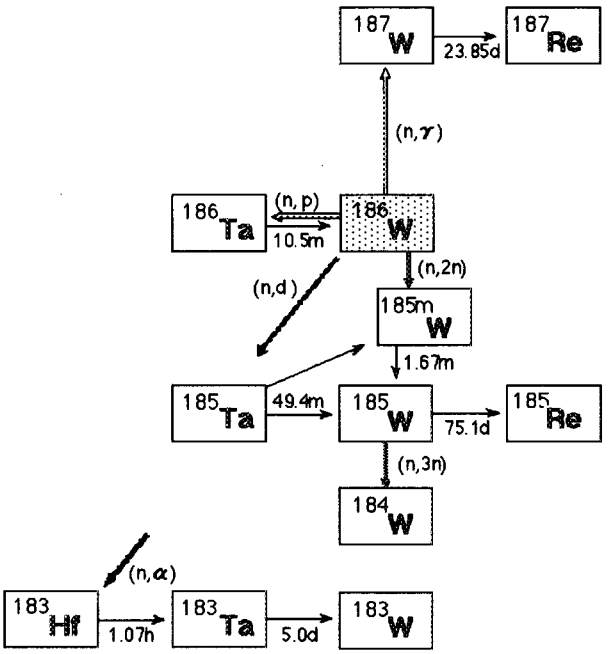

Fig. 8 Nuclear reaction for first step of ^{186}W.

After choosing one of four functions on opening screen, various screens corresponding to the function appear as shown Fig. 5,6,7. Fig 5 shows a screen to retrieve data related all item in main five tables. Retrieved results indicates nuclear reaction, transmuted nuclides and stability of the nuclide in stable isotope of Cr. Fig. 6 shows either the nuclide is easily formed by neutron energy in each nuclear transmutation of ^{180}W or not. Fig. 7 shows screen that by selecting the desired nuclear reaction in right folder, it is possible to know records on a given transmutation and spontaneous decay in the reaction process as shown ordinary in Fig. 8 in under folder. Fig. 8 shows nuclear reaction for first step of ^{186}W.

The user-interface (i.e. folder) of the database performs an important role either useful system or not. Using this user-interface, end-user can easily obtain the necessary information by the easy operation for retrieving, because a screen provided with pop-up and pull down menu, is employed to be mainly operated by micro-mouse in addition to keyboard.

4 Example of system operation

Type 316 stainless steel is used as the structural material of the fuel sub-assemblies in the sodium cooled fast breeder reactors. This steel is regarded as a candidate material for blanket structures of the fusion reactors. However it is required that materials should have a high resistance against swelling and low radioactivation under the high-energy neutron irradiation environment such as in fusion reactors. Ferritic 9Cr1WVTa steel is also being considered as an alternate candidate structural material to type 316 stainless steel [3]. An amount of He formation and radioactivity under neutron irradiation of both steels will be evaluated as an example of application of the present simulation system.

Using the nuclide database, the possibility of large amount of He formation and radioactivity

Table 1 Results of retrieval for long half-life on the products of nuclear reaction of the first

step caused by neutron irradiation to both type 316 stainless and ferritic steel.

(a) type 316 stainless steel (Fe,Cr,Ni,Mo,Ti,Cu,C,Mn,Si,S,P,O,N,B)

Isotope	Transmutation	Transmuted Nuclide	Half-life	Unit	Decay heat	Fast	Thermal
B10	NP	Be10	2.0000e+6	y	1.8500e-1		
C13	NG	C14	5.7300e+3	y	5.2300e-1		
C13	NA	Be10	2.0000e+6	y	1.8500e-1	○	
N14	NP	C14	5.7300e+3	y	5.2300e-1		○
O17	NA	C14	5.7300e+3	y	5.2300e-1		
Fe54	NG	Fe55	2.7000e+0	y			○
Fe54	NNP	Mn52	4.0000e+6	y			
Fe56	N2N	Fe55	2.7000e+0	y			
Ni58	NG	Ni59	7.5000e+4	y	3.5400e-1		○
Ni58	NA	Fe55	2.7000e+0	y			
Ni60	NP	Co60	5.2690e+0	y	2.6200e+0		
Ni60	N2N	Ni59	7.5000e+4	y	3.5400e-1		
Ni61	NNP	Co60	5.2690e+0	y	2.6200e+0		
Ni62	NG	Ni63	1.0000e+2	y	2.2000e-1		○
Ni64	N2N	Ni63	1.0000e+2	y	2.2000e-1	○	
Cu63	NA	Co60	5.2690e+0	y	2.6200e+0		
Cu63	NP	Ni63	1.0000e+2	y	2.2000e-1		
Mo92	NG	Mo93	3.5000e+3	y			
Mo92	NP	Nb92	3.0000e+7	y	1.5000e+0		
Mo92	NNP	Nb91	6.8000e+2	y			
Mo94	NP	Nb94	2.0000e+4	y	1.7400e+0		
Mo94	N2N	Mo93	3.5000e+3	y		○	
Mo95	NNP	Nb94	2.0000e+4	y	1.7400e+0		
Mo96	NA	Zr93	2.0000e+6	y	2.5000e-1		

(b) ferritic 9Cr-1WVTa steel (Fe,Cr,W,V,Ta,C,Mn,Si,S,P,O,N,B)

Isotope	Transmutation	Transmuted Nuclide	Half-life	Unit	Decay heat	Fast	Thermal
B10	NNP	Be9					
B10	NP	Be10	2.0000e+6	y	1.8500e-1		
B11	NP	Be11	1.3800e+1	s	4.7400e+0		
V51	NP	Ti51	5.7600e+0	m	1.6300e+0		
Cr50	NP	V50				○	
Cr50	NNP	V49	3.3000e+2	d			
Cr52	NP	V52	3.7500e+0	m	2.2000e+0	◇	
Cr53	NP	V53	1.6100e+0	m	1.8300e+0		
Cr53	NNP	V52	3.7500e+0	m	2.2000e+0		
Cr54	NP	V54	4.9800e+1	s	3.4100e+0		
Fe54	NP	Mn54	3.1221e+2	d	8.3500e-1	○	
Fe54	NNP	Mn53	4.0000e+6	y			
Fe56	NP	Mn56	2.5790e+0	h	2.2700e+0		
Fe56	NNP	Mn55					
Fe57	NP	Mn57	1.6100e+0	m	9.4400e-1		
Fe57	NNP	Mn56	2.5790e+0	h	2.2700e+0		
Fe58	NP	Mn58	6.5300e+1	s	3.2400e+0		
Ta181	NP	Hf181	4.2400e+1	d	6.6500e-1		
W182	NP	Ta182	1.1500e+2	d	1.2000e+0		
W183	NP	Ta183	5.1000e+0	d	4.1900e-1		
W184	NP	Ta184	8.7000e+0	h	1.8600e+0		
W186	NP	Ta186	1.0500e+1	m	1.7300e+0		
W186	NNP	Ta185	4.9000e+1	m	6.2600e-1		

in the candidate materials can be easily evaluated qualitatively. The possibility of He formation is known by retrieving cross section size of (n, alpha;) reaction on compositional atoms of materials. The radioactivity is known by retrieving half-life of transmuted products of compositional atoms of material. Table 1 shows transmuted products with half-life of more than one year in type 316 and ferritic steel. These result suggest that type 316 stainless steel has more radioactive nuclides and is radioactivated more easily than ferritic 9Cr-1WVTa steel under neutron irradiation. It is found that this system will be frequently used by nuclear material scientists as a material information tool, if this system is jointed to networking system such as "Data-Free-Way"[2]~[3].

5. Summary

1) A database on transmutation for nuclear materials with user friendly interface was constructed in WWW server on the Internet. (http://inaba.nrim.go.jp//Irra/)
2) The database consists of mainly four tables stored the information of atomic element , isotope, transmutation and cross section for 42 neutron energy group.
3) The compositional change and radioactivity in materials can be easily evaluated qualitatively.
4) The radioactivity is known by retrieving half-life of transmuted products of compositional atoms of material. Transmuted products with half-life of longer than one year in type 316 and ferritic steel. These result suggest that type 316 stainless steel has more radioactive nuclides and radioactivated more easily than ferritic 9Cr-1WVTa steel for reduced activationunder neutron irradiation .

References

[1] Fujita M., M. Utsumi, T. Noda; JAERI-Conf 97-004 p.208
[2] Nakajima H., Yokoyama N., Ueno F., Kano S., Fujita M., Kurihara Y. and Iwata S., J. Nucl. Mater. vol.212-215 (1994) p.1171-1714.
[3] Ueno F., Kano S., Iwata S.,Fujita M., Kurihara Y., Nakajima H., Yokoyama N. and Iwata S., J. Nucl. Sci. Technol, vol.31 (1994) p.1314-1334.

3.40 Systematics of nuclear mass and level density formulas

H.Nakamura
Nuclear Engineering Division, Fuji Electric Co., Ltd
1-1 Tanabe-Shinden, Kawasaki 210, Japan

The phenomenological models of the nuclear mass and level density are close related to each other, the nuclear ground and excited state properties are described by using the parameter systematics on the mass and level density formulas. The main aim of this work is to provide in an analytical framework the improved energy dependent shell, pairing and deformation corrections generalized to the collective enhancement factors, which offer a systematic prescription over a great number of nuclear reaction cross sections. The new formulas are shown to be in close agreement with not only the empirical nuclear mass data but the measured slow neutron resonance spacings, and experimental systematics observed in the excitation energy dependent properties.

I. INTRODUCTION

In recent years the most statistical theory calculations of nuclear reactions have been carried out still by using the semiempirical level density formula proposed by Gilbert and Cameron [1] in 1965 , which is based essentially on the Fermi-gas (FG) model and seems to be enough to predict the level densities at the narrow range of excitations. However, it has been in fact well established [2] that the extrapolation of this formula to a wide range of excitation energies is subject to large errors, and that washing out of shell effects should be considered. The main aim of the present work is to find a new set of parameter systematics for both the mass formula and the level density formula on the basis of the new single-particle state density model, which leads consistently to the nuclear ground and excitation properties. In this model, an analytical expression similar to the previous KRK model [3] is adopted for the single-particle states, but introducing the shell-pairing correlation terms in a new way [4]. This report presents a brief review on the recent developments of the systematics of parameters for the ground state (mass formula) and for the excited state (level density formula), and the predictions of the current model are compared with those of FG and KRK models by using the neutron resonance spacings, and the empirical evaporation process data.

II. FORMULA OF NUCLEAR LEVEL DENSITY

In the framework of the statistical model [1] the nuclear level density is described by means of the grand partition function. For realistic analyses the distribution function $g(\varepsilon)$ for the single-particle state density is written in terms of the harmonic oscillator model, considering only fundamental harmonics for the main-shell with the sub-shell associated to the pairing interaction [4] :

$$g(\varepsilon) = \sum_{X} g_{0X}[1 + f_X \cos \omega_S(\varepsilon - \varepsilon_X)] \cdot [1 - \cos \omega_P(\varepsilon - \lambda)], \tag{1}$$

where g_{0X} is the single-particle state density, f_X the amplitude of main-shell, ω_S the harmonic oscillator frequency related to the main-shell spacing $\hbar\omega_{sh}$, $\omega_S = 2\pi/\hbar\omega_{sh}$, ω_P the frequency related to the sub-shell spacing, ε_X the main-shell position, λ the Fermi level, and the subscript x stands for proton or neutron shell. By using the single-particle state density of Eq.(1), the excitation-energy dependences of both the shell and pairing effects can be considered. The foregoing descriptions for the nuclear statistical properties are only for intrinsic excitation levels of nuclei. On the other hand, the importance of considering the collective contributions on the level density have been pointed out [5] and the following nuclear level density formulas are used :

$$\rho_{sph}(U,J) = \rho_0(U,J)K_{vib}(U), \qquad \rho_{def}(U,J) = \rho_0(U,J)K_{rot}(U)\cdot K_{vib}(U) \tag{2}$$

where ρ_{sph} and ρ_{def} are the level densities for the spherical and for the deformed nucleus respectively, and $\rho_0(U,J)$ is that of the intrinsic excitation levels. The factors K_{rot} and K_{vib} in the definition (3) are the rotational and vibrational enhancement factors [6, 7], and each factor is written as respectively

$$K_{vib}(U) = \exp(0.0555A^{2/3}\, t^{4/3}), \qquad K_{rot}(U) = I_{\perp}\, t, \tag{3}$$

The spin cut-off factor σ^2, which appears in the levell density $\rho_0(U,J)$, is replaced by the effective spin cut-off factor σ^2_{eff} for deformed nuclei :

$$= I_{\perp}^{2/3} I_{\parallel}^{1/3}\, t, \qquad I_{\parallel} = I_r(1-\frac{2\delta}{3}), \qquad I_{\perp} = I_r(1+\frac{\delta}{3}), \tag{4}$$

where $I_{\parallel}$ and I are the parallel and perpendicular moments of inertia, and the value of the classical eccentricity parameters δ for the quadrupole deformation is considered at the next section.

III. SYSTEMATICS OF GROUND AND EXCITED STATE PARAMETERS

In this section the nuclear ground state correction energies E_S and E_P are combined with the shell and pairing correction terms of the nuclear mass formula. For the ground state energies we can use the typical mass formula by Myers and Swiatecki [8] based on the generally accepted definition of liquid drop model. The basic assumption made for the empirical mass $M(Z,N,\theta)$ is the independence of the corrections due to proton from those due to neutrons :

$$M(Z,N,\theta) - M_0 = S_Z + S_N, \tag{5}$$

where M_0 is the mass of an undistorted liquid drop, θ the deformation magnitude, S_Z and S_N are the empirical average shell correction energies including the pairing and deformation energies, and its values are obtained by means of the iteration procedure by using those of Myers and Swiatecki formula as the first guess. The systematics for the shell and pairing corrections E_{SX} and E_{PX} are obtained by fitting the empirical average shell correction S_X to the empirical mass data of 1988 compilation [9]. On the other hand, for deformed nuclei the deformation energy E_D is written from Myers and Swiatecki formula :

$$E_D = -M_1\theta^2 + E_S\{1-\exp(-\theta^2)\}, \tag{6}$$

where M_1 is a coefficient specifying the stiffness of the liquid drop against small spheroidal distortions, then, the value of deformation magnitude θ^2 is obtained for $E_D > 0$. The relations between the traditional quadrupole deformation parameters δ, β and ε are given as [5]

$$\delta \approx 0.945\,\beta\{1-\frac{4}{3}\pi^2(\frac{a}{r_0})^2 A^{-2/3}\}+0.34\,\beta^2, \qquad \beta^2 = \frac{4\pi}{5}\varepsilon^2, \tag{7}$$

then, the value of δ, Eq.(4), can be determined from the relations $\varepsilon^2 = \theta^2\varepsilon_0^2$ and Eq.(7).

The final theoretical error σ_{th}-value, which is a measure of overall quality for fitting acculacies of the mass formula [10] are easily obtained within a few iterations. For total 1655 nuclei (A=28~265), those error are σ_{th} = 1.280 MeV for Myers and Swiatecki formula, = 0.563 MeV for the current one. The improvement in fitting accuracy of the current mass formula is due mainly to the polynomial fitting

approach to express the shell and pairing corrections.

Free parameters to be fixed for the excited states are α, ω_0 in Eq.(8) :

$$a_0 = \alpha A, \qquad \omega_S = \omega_0 A^{1/3}, \tag{8}$$

where a_0 is the asymptotic level density parameter and the values of α and ω_0 are the mass independent constants. In the present work the neutron resonance spasings for the wide mass range (A=40--253) including deformed nuclei listed in Ref.11 (Table 1) are used. The results of the first simple analysis by using the current level density (LD) model are shown in FIG.1. A measure of the quality associated with the systematics is taken from the linear least-squares fits

$$\chi^2 = \Sigma(a_{0i} - \alpha \cdot A_i)^2 \tag{9}$$

and the values of parameters α and ω_0 are determined by minimizing the quantity χ^2. Another quantity of systematics is the root mean squares (rms) deviation of α by using weights based on error of observed spacings data. Values of α, ω_0 and χ^2 are shown on FIG.1, where the collective enhancement factors are not applied. FIG.1 shows that the rather good systematics of Eq.(8) seems to be obtained over the wide mass range including deformed nuclei without the collective enhancement factors. As shown in FIG.2, however, another systematics is deduced, where the collective enhancement factors, $K_{vib}(U)$ and $K_{rot}(U)$ in Eq.(3), are taken into account. The final systematics FIG.2 is the linear relation $a_0 = \alpha A$ obtained by using the same spacings data as for FIG.1, with the exception of three different mass ranges for spherical or deformed nuclei, where values of the deformation parameter δ are determined based on Eqs.(6) and (7). We can compare in more details the foregoing systematics with another kind of experimental data also listed in Ref.11 (Table 2). Those level density are connected with the total state density defined by

$$\rho_t(U) = \sum_J \rho(U,J) \approx \frac{\omega(U)}{\sqrt{2\pi}\sigma} \tag{10}$$

Typical results are selected and shown in FIG.3 for the comparison with experimental data of ^{41}Ca, ^{55}Mn, ^{56}Fe and ^{60}Ni , and in FIG.4 for ^{209}Po and ^{230}Th. Values of α and ω_0 are determined from the following procedures : 1) For FG model the values of α are determined by normalyzing to the experimental value at the arbitrary excitation energy points shown in figures, 2) All α and ω_0 values for KRK model are taken from a systematics same as FIG.1, 3) For cases of the current model the values are taken from FIG.2. The results of analyses with three diferent LD models are shown in FIG.3 and 4. FIG.3 shows that the predictions of the present model describe the experiments at lower and higher energy parts better than those of two models of FG and KRK. With the exception of FG model any normalization to the experimental point is not applied for both models. FIG.4 is for the cases of heavy nuclei, spherical ^{209}Po and deformed ^{230}Th. In ^{230}Th it is clear that the collective rotational enhancement factor gives a weaker energy dependence and descrives the experiment much better than no enhancement factor cases.

V. CONCLUSIONS

A semiempirical nuclear mass and level density formulas with its new parameter systematics are presented. The main advantage of the present models is no use of separate tables of the shell, pairing and deformation correction energies in the statistical theory analysis for a large number of reactions. The s-wave neutron resonance spacings for the mass range A = 40~253 including deformed nuclei were used to obtain the systematics of the simple linear relations with respect to the excited states. parameters. The

result of analyses shows that the foregoing systematics of the current model is consistent with the experimental energy dependences of the level density, and that the predictions of the present formulas will be superior to those of the previous models.

References ;
[1] A.Gilbert. and A.W.G.Cameron, Can.J.Phys.43,1446 (1965).
[2] H.Vonach ,*et al.*, Phys.Rev.C 38,2541(1988).
[3] S.K.Kataria., V.S.Ramamurthy and S.S.Kapoor, Phys.Rev.C18,549(1978).
[4] H.Nakamura, IAEA Reports, INDC(JPN)-173/U (1994), INDC(JPN)-175/U (1996).
[5] .A.Bohr and B.Mottelson, Nuclear structure, vol. II (Benjamin,New York,1975)
[6] S.Bjornholm, A.Bohr and B.Mottelson, Proc.Conf.on Physics and Chemistry of Fission,Vol.1, p.367, (IAEA,Vienna,1974).
[7] A.V.Ignatyuk, K.K.Istekov and G.N.Smirenkin, Sov.J.Nucl.Phys.29, 450(1979).
[8] W.D.Myers and W.J.Swiatecki, Nucl.Phys.81,1(1966), and Ark.Fys.36,343(1967).
[9] A.H.Wapstra, G. Audi and R Hoekstra., At.Data and Nucl.DataTables,39,281(1988).
[10] P. Moller and J.R.Nix, ibid.,39,213(1988).
[11] A.S.Iljinov, *et al.*, Nucl.Phys. 543,517(1992).

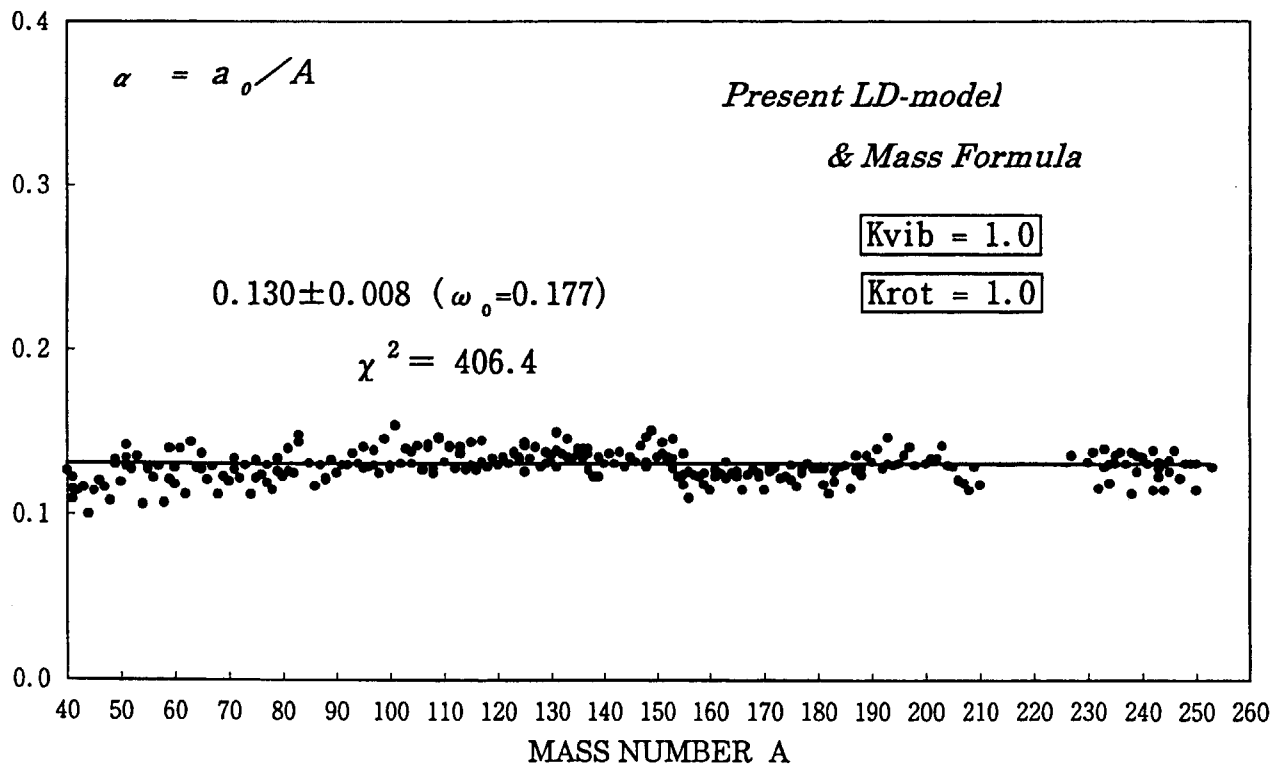

FIG.1 Systematics of the asymptotic level density parameter extracted using the s-wave neutron resonanse spacings. The collective enhancement factors are not applied for all cases.

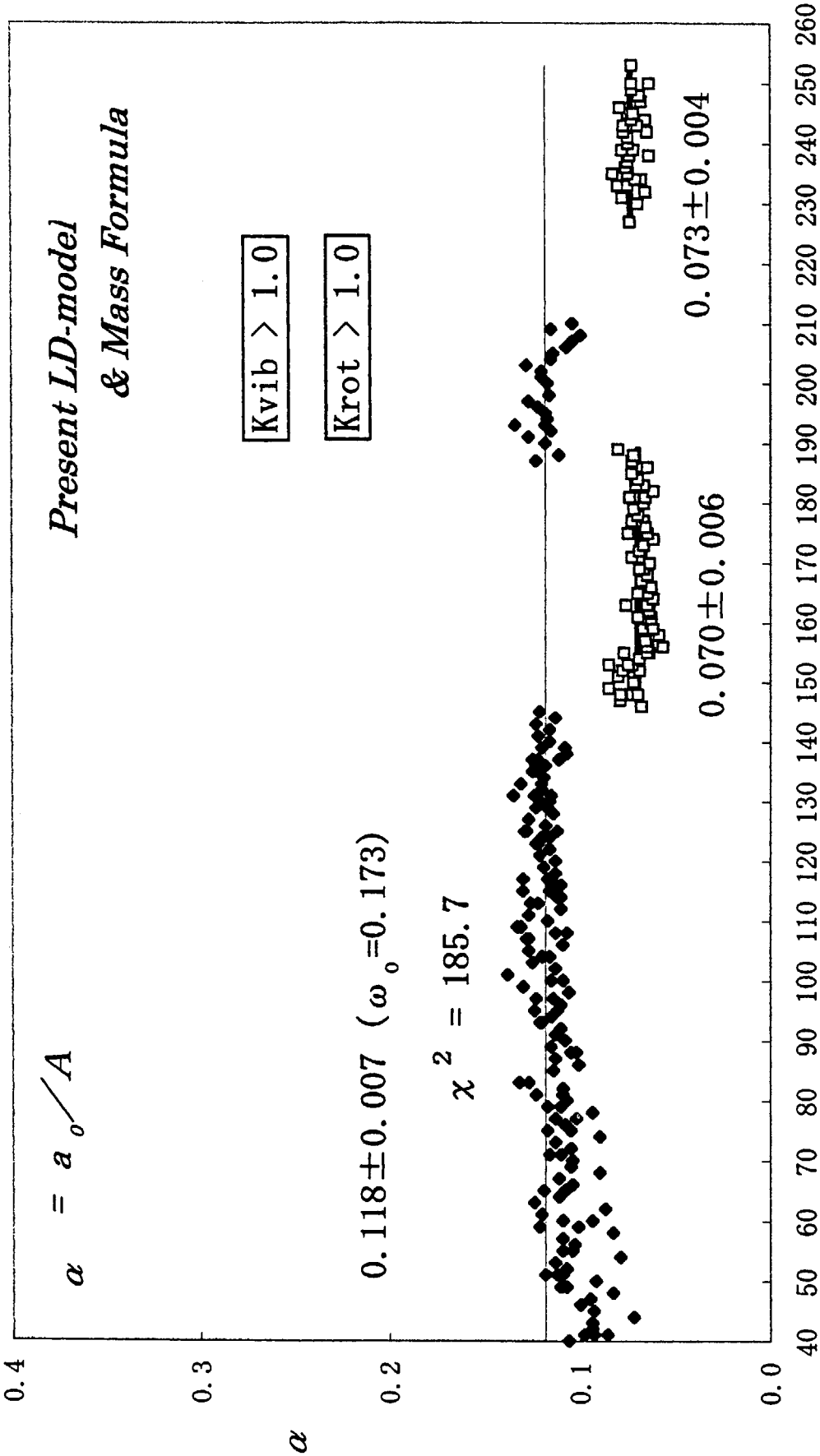

FIG.2 Same as FIG.1, but taking into account collective enhancement factors (Kvib and Krot). This systematics is applied only for the present level density model.

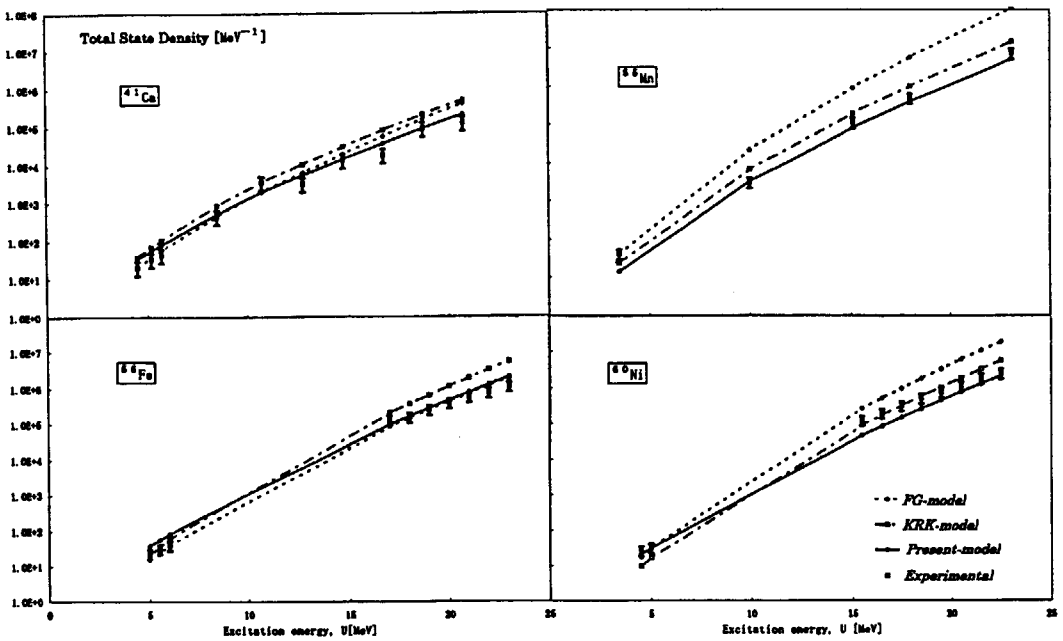

FIG.3 Energy dependence of the total state density for nucleides ^{41}Ca, ^{55}Mn, ^{56}Fe, ^{60}Ni. Resuls of three different models (FG, KRK and current LD) are shown with experimetal points.

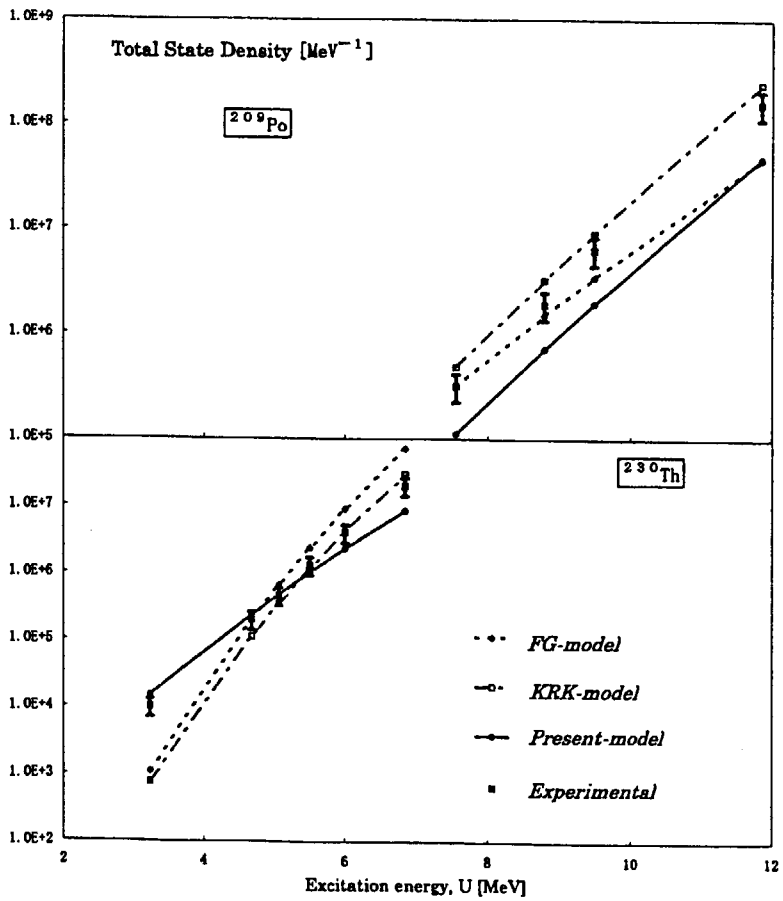

FIG.4 Same as FIG.3 for ^{209}Po and ^{230}Th.

Appendix: Participants List

Akino, F.	JAERI
Ando, Y.	Toshiba Co.
Andoh, M.	JAERI
Aoki, T.	Fuji Electric Co., Ltd.
Aoyama, T.	PNC
Aruga, T.	JAERI
Asano, Y.	JAERI
Baba, M.	Tohoku Univ.
Fujita, M.	NRIM
Fukahori, T.	JAERI
Fukasaku, Y.	NESI
Fuketa, T.	IES
Funabiki, J.	MRI
Goto, M.	JAERI
Hanaki, H.	Hitachi Ltd.
Harada, M.	Kyushu Univ.
Harima, Y.	CRC
Hasegawa, A.	JAERI
Hatsukawa, Y.	JAERI
Hayashi, K.	HEC
Hiramoto, J.	KCC
Hirasawa, Y.	Tohoku Univ.
Hori, J.	Tokyo Inst. of Tech.
Horiguchi, T.	Hiroshima Univ.
Ibaraki, M.	JAERI
Ichihara, C.	Kyoto Univ.
Iga, K.	Kyushu Univ.
Igarasi, S.	
Igashira, M.	Tokyo Inst. of Tech.
Iimura, H.	JAERI
Ikeda, Y.	JAERI
Ishikawa, M.	PNC
Itagaki, Y.	PNC
Ito, C.	PNC
Iwamoto, O.	JAERI
Iwashita, M.	IHI
Kai, T.	Kyoto Univ.
Kaise, Y.	ARTECH
Katakura, J.	JAERI
Katoh, T.	Gifu College of Medical Tech.
Kawade, K.	Nagoya Univ.
Kawai, M.	KEK
Kawano, T.	Kyushu Univ.
Kikuchi, T.	JAERI
Kim, Guinyun	POSTEC
Kitao, K.	DEI
Kitazawa, H.	Tokyo Inst. of Tech.
Kitsuki, H.	Kyushu Univ.
Kobayashi, H.	Rikkyo Univ.
Kobayashi, K.	JAERI
Kobayashi, K.	Hitachi Ltd.
Ko-Ko-Oo	Osaka Univ.
Konno, C.	JAERI

Kosako, K.	SAEI
Kurosawa, N.	V.I.C.
Lee, Young-Ouk	KAERI
Liem Peng Hong	BATAN
Maekawa, A.	Hitachi Ltd.
Maekawa, H.	JAERI
Makiguchi, H.	JNF
Maruyama, H.	Hitachi Ltd.
Matoba, M.	Kyushu Univ.
Matsufuji, N.	NIRS
Matsumoto, H.	MHI
Matsunobu, H.	DEI
Mio, K.	IHI
Miura, T.	Tohoku Univ.
Mizumoto, M.	JAERI
Momota, T.	
Murasaki, J.	JAERI
Murata, I.	Osaka Univ.
Murata, T.	AITEL
Nagao, T.	JAERI
Nagao, Y.	JAERI
Nagaya, Y.	JAERI
Naito, Y.	NAIS
Nakagawa, M.	JAERI
Nakajima, K.	JAERI
Nakajima, Y.	RIST
Nakamura, H.	Fuji Electric Co., Ltd.
Nakamura, S.	PNC
Nakano, D.	Osaka Univ.
Nakano, Y.	JAERI
Nakashima, H.	JAERI
Narita, T.	JAERI
Nauchi, Y.	Tohoku Univ.
Nishio, K.	Kyoto Univ.
Noda, T.	NRIM
Nomura, Y.	JAERI
Ohkawachi, Y.	PNC
Ohkubo, M.	
Ohsawa, T.	Kinki Univ.
Ohta, H.	CRIEPI
Oigawa, H.	JAERI
Okajima, S.	JAERI
Okochi, H.	JGC
Okuno, H.	JAERI
Oyama, Y.	JAERI
Oyamatsu, K.	Nagoya Univ.
Ozaki, S.	Kyushu Univ.
Raman, S.	ORNL
Sagisaka, M.	Nagoya Univ.
Saito, K.	Tohoku Univ.
Saitou, M.	HEC
Saji, E.	TSI
Sakamoto, Y.	JAERI

Sakane, H.	Nagoya Univ.
Sanami, T.	Tohoku Univ.
Sasa, T.	JAERI
Sasahara, A.	CRIEPI
Sasaki, K.	PNC
Shibata, K.	JAERI
Shibata, K.	Hitachi Ltd.
Shibata, T.	KEK
Shigetome, Y.	PNC
Shigyo, N.	Kyushu Univ.
Shikazono, N.	RIST
Shimada, S.	JAERI
Shindo, R.	JAERI
Shinohara, N.	JAERI
Sugai, H.	JAERI
Sugi, T.	ITIRO
Sugimoto, M.	JAERI
Sugino, K.	PNC
Sukegawa, T.	JAERI
Sun Weili	Kyushu Univ.
Sun-Tae Hwang	KAIST
Suyama, K.	JAERI
Suzuki, S.	PNC
Suzuki, T.	JAERI
Tahara, Y.	MHI
Takada, H.	JAERI
Takamatsu, M.	PNC
Takao, Y.	Kyushu Univ.
Takeda, T.	Osaka Univ.
Takeuchi, H.	Nagoya Univ.
Teshigawara, M.	JAERI
Than Win	Tohoku Univ.
Tsujimoto, K.	JAERI
Tsukiyama, T.	HEC
Utsumi, M.	NRIM
Uwamino, Y.	RIKEN
Watanabe, T.	KHI
Watanabe. K.	JAERI
Yamaguchi, M.	HEC
Yamamoto, A.	Kyoto Univ.
Yamamoto, T.	JAERI
Yamanaka, A.	Hitachi Ltd.
Yamane, T.	JAERI
Yamano, N.	SAEI
Yamaoka, M.	Toshiba Co.
Yokoyama, K.	PNC
Yoshida, H.	Kyushu Univ.
Yoshida, T.	Musashi Inst. of Tech.
Yoshizawa, Y.	College of Industrial Tech.
Zukeran, A.	Hitachi Ltd.

国際単位系（SI）と換算表

表1　SI基本単位および補助単位

量	名称	記号
長さ	メートル	m
質量	キログラム	kg
時間	秒	s
電流	アンペア	A
熱力学温度	ケルビン	K
物質量	モル	mol
光度	カンデラ	cd
平面角	ラジアン	rad
立体角	ステラジアン	sr

表2　SIと併用される単位

名称	記号
分，時，日	min，h，d
度，分，秒	°，′，″
リットル	l，L
トン	t
電子ボルト	eV
原子質量単位	u

1 eV=1.60218×10^{-19}J

1 u=1.66054×10^{-27}kg

表5　SI接頭語

倍数	接頭語	記号
10^{18}	エクサ	E
10^{15}	ペタ	P
10^{12}	テラ	T
10^{9}	ギガ	G
10^{6}	メガ	M
10^{3}	キロ	k
10^{2}	ヘクト	h
10^{1}	デカ	da
10^{-1}	デシ	d
10^{-2}	センチ	c
10^{-3}	ミリ	m
10^{-6}	マイクロ	μ
10^{-9}	ナノ	n
10^{-12}	ピコ	p
10^{-15}	フェムト	f
10^{-18}	アト	a

表3　固有の名称をもつSI組立単位

量	名称	記号	他のSI単位による表現
周波数	ヘルツ	Hz	s^{-1}
力	ニュートン	N	$m\cdot kg/s^2$
圧力，応力	パスカル	Pa	N/m^2
エネルギー,仕事,熱量	ジュール	J	N·m
工率，放射束	ワット	W	J/s
電気量，電荷	クーロン	C	A·s
電位，電圧，起電力	ボルト	V	W/A
静電容量	ファラド	F	C/V
電気抵抗	オーム	Ω	V/A
コンダクタンス	ジーメンス	S	A/V
磁束	ウェーバ	Wb	V·s
磁束密度	テスラ	T	Wb/m^2
インダクタンス	ヘンリー	H	Wb/A
セルシウス温度	セルシウス度	℃	
光束	ルーメン	lm	cd·sr
照度	ルクス	lx	lm/m^2
放射能	ベクレル	Bq	s^{-1}
吸収線量	グレイ	Gy	J/kg
線量等量	シーベルト	Sv	J/kg

表4　SIと共に暫定的に維持される単位

名称	記号
オングストローム	Å
バーン	b
バール	bar
ガル	Gal
キュリー	Ci
レントゲン	R
ラド	rad
レム	rem

1 Å=0.1nm=10^{-10}m

1 b=100fm^2=10^{-28}m^2

1 bar=0.1MPa=10^5Pa

1 Gal=1cm/s^2=10^{-2}m/s^2

1 Ci=3.7×10^{10}Bq

1 R=2.58×10^{-4}C/kg

1 rad=1cGy=10^{-2}Gy

1 rem=1cSv=10^{-2}Sv

（注）

1．表1－5は「国際単位系」第5版，国際度量衡局1985年刊行による。ただし，1 eVおよび1 uの値はCODATAの1986年推奨値によった。

2．表4には海里，ノット，アール，ヘクタールも含まれているが日常の単位なのでここでは省略した。

3．barは，JISでは流体の圧力を表わす場合に限り表2のカテゴリーに分類されている。

4．EC閣僚理事会指令ではbar，barnおよび「血圧の単位」mmHgを表2のカテゴリーに入れている。

換　算　表

力	N(=10^5dyn)	kgf	lbf
	1	0.101972	0.224809
	9.80665	1	2.20462
	4.44822	0.453592	1

粘　度　1 Pa·s(N·s/m^2)=10 P(ポアズ)(g/(cm·s))

動粘度　1m^2/s=10^4St(ストークス)(cm^2/s)

圧力	MPa(=10bar)	kgf/cm^2	atm	mmHg(Torr)	lbf/in^2(psi)
	1	10.1972	9.86923	7.50062×10^3	145.038
	0.0980665	1	0.967841	735.559	14.2233
	0.101325	1.03323	1	760	14.6959
	1.33322×10^{-4}	1.35951×10^{-3}	1.31579×10^{-3}	1	1.93368×10^{-2}
	6.89476×10^{-3}	7.03070×10^{-2}	6.80460×10^{-2}	51.7149	1

エネルギー・仕事・熱量	J(=10^7 erg)	kgf·m	kW·h	cal(計量法)	Btu	ft·lbf	eV
	1	0.101972	2.77778×10^{-7}	0.238889	9.47813×10^{-4}	0.737562	6.24150×10^{18}
	9.80665	1	2.72407×10^{-6}	2.34270	9.29487×10^{-3}	7.23301	6.12082×10^{19}
	3.6×10^6	3.67098×10^5	1	8.59999×10^5	3412.13	2.65522×10^6	2.24694×10^{25}
	4.18605	0.426858	1.16279×10^{-6}	1	3.96759×10^{-3}	3.08747	2.61272×10^{19}
	1055.06	107.586	2.93072×10^{-4}	252.042	1	778.172	6.58515×10^{21}
	1.35582	0.138255	3.76616×10^{-7}	0.323890	1.28506×10^{-3}	1	8.46233×10^{18}
	1.60218×10^{-19}	1.63377×10^{-20}	4.45050×10^{-26}	3.82743×10^{-20}	1.51857×10^{-22}	1.18171×10^{-19}	1

1 cal= 4.18605J（計量法）

= 4.184J（熱化学）

= 4.1855J（15℃）

= 4.1868J（国際蒸気表）

仕事率　1 PS(仏馬力)

= 75 kgf·m/s

= 735.499W

放射能	Bq	Ci
	1	2.70270×10^{-11}
	3.7×10^{10}	1

吸収線量	Gy	rad
	1	100
	0.01	1

照射線量	C/kg	R
	1	3876
	2.58×10^{-4}	1

線量当量	Sv	rem
	1	100
	0.01	1

（86年12月26日現在）